

JOURNAL OF THE MYANMAR ACADEMY OF ARTS AND SCIENCE



Physics and Computer Studies

Vol. XIX, No.2, January, 2023

Myanmar Academy of Arts and Science

Journal of the Myanmar Academy of Arts and Science

Vol. XIX, No.2

Contents

Section (i), Physics

Sr. No.	Title	Page
1	Thet Ni Moe , Innovative Design of Electronic Ballot for General Election	1
2	Khin San Yee , Graphical Teaching Aid for Astable and Monostable Circuits Utilizing Arduino Mega	9
3	Wint Shwe War Hlaing , Esp8266 Asynchronous Web Server Based Real Time Temperature Monitoring by Contactless IR Thermometer for Social Distancing	19
4	Nwe Wai , Effect of Complexing Agent (Na_2EDTA) on the Deposition of Copper Tin Sulphide Thin Films	29
5	Nay Min Aung , Code Tracking for GPS Signal Processing	37
6	Pwint Yi Thein , Study on Effect of Isovalent Barium Ions Substitution on Structural Features, Ferroelectric Properties and Bandgaps of Lead Titanate Time-Table	45
7	Cho Cho Khin , Effect of Sintering Temperature on Structural and Mechanical Properties of Beta-Tricalcium Phosphate	57
8	Ni Lar , Structure Characterization of Titanium Dioxide Films on Silicon Substrate	67
9	Su Su Tha , Influence of Copper Substitution on Electrical Properties of Mg-Cu-Zn Ferrite	75
10	Hnin Yu Khaing , Optical and Antibacterial Properties of Colloidal Gold Nanoparticles	83
11	Mono Zaw , Effects of Annealing Temperature on Optical and Electrochemical Properties of Spray-Pyrolysed WO_3 Films	87
12	Kyaw Kyaw , Synthesis and Optical Properties of Titanium Dioxide Nanoparticles Using Sol-Gel Method	93
13	Nu Nu Swe , Controlling the Appliances and Monitoring Data from Local Web Server Using ESP32 and HTML	101
14	Mi Yin Sa Nine , Prototype Hardware Design and Software Development of Password Coded ESP32 Web Server Based Home Appliances Controlling System Accessible from Anywhere Using Ngrok Software	113
15	Zin Min Myat , Microwave-Assisted Green Synthesis and Characterization of Titanium Oxide Nanoparticles Using <i>Centella asiatica</i> (L.) Leaf Extract and their Antimicrobial Activity	125
16	Zayar Pyae Phyoe Aung , Design and Assembling of Simple Homemade Electrospinning Device for Nanofibers Production	133
17	Hnin Aye Khine , Gmail Notification with Photograph from Motion Activated Camera Using ESP32_Cam and Microwave Motion Sensor for Security Purpose	139
18	Aung Zaw Myint , Design and Construction of Frequency, Inductance Logical Condition, Circuit Continuity and Current Data Acquisition System	151

<u>Sr. No.</u>	<u>Title</u>	<u>Page</u>
19	Zin Mar Aung , Preparation and Characterization of Kaolinite Clay for Production of Natural Pozzolan	161
20	Zin Min Tun , Physicochemical Characteristics of Activated Carbon from Rice Husk Biochar	169
21	Kyaw Thu , Temperature and Shading Dependence of the Potential Induced Degradation Effect of Solar Panel	177
22	Aye Aye Myint , Trace Elements Analysis of Sediment in Dohtawady River from Mandalay Region	185
23	Saine Lai Wai , Investigation of Radionuclide Concentration in Soil Samples Collected from Minhla Coal Mine Region	195
24	Win Mar , Investigation on Shielding Properties of Some Composite Materials by Using NaI(TL) Detector	203
25	Chan Myae Aung , Observation of a Single-Strangeness Hypernucleus Event in Kek-Ps E 373 Experiment	213
26	Nyi Nyi Soe , Calculation of the Ranges and Position Angles of Single- Λ Hypernucleus Event in Nuclear Emulsion	223
27	Htaik Nandar Kyaw , Formation of $^{15}_{\Lambda}N$ Hypernucleus in J-Parc E07 Experiment	231
28	Khaing Pwint Wai , Investigation of Triaxiality in Medium-mass Germanium Isotopes	241
29	Aye Aye Maw , Measurements of Iodine Contents in Seaweed (Kalamoat Seigh) (<i>Catenella SP</i>) from Various Places in Mon State	249
30	Ei Ei San , Investigation of the Radon Gas Concentration inside Heinda Tin Mine in Dawei Township, Tanintharyi Division, Myanmar	259
31	Khin Than Tint , Estimation of Binding Energy of Xi-Minus Hyperon in a Nucleus from Single- Λ Hypernucleus Event	265
32	Hein Nay Zar Wann , Measurement of Radon Concentration in Soil Gas Using RAD7 from Byut Myaung and Kalain Gold Mines at Bago Region	275
33	Shwe Sin Oo , Relativistic and Non-Relativistic Momentum Space Wavefunctions for Charmonium and Bottomonium States	285
34	Thei` Theint Theint Aung , Numerical Simulations of Binary Neutron Star Mergers	291
35	Khin Sandar Khaing , Assessment of Solar Energy Potential for Two Selected Areas in Yangon Region	299

Journal of the Myanmar Academy of Arts and Science

Vol. XIX, No.2

Contents

Section (ii), Computer Studies

Sr. No.	Title	Page
1	Chaw Su Lwin , *Firebase as a Backend Service in Mobile and Web Application Development	309
2	Kyaw Thiha , Effective Student Collaborative System Based on Clustering Analysis	319
3	Tin Nilar Win , Knowledge-Based Recommendation System for Travel Destination	329

INNOVATIVE DESIGN OF ELECTRONIC BALLOT FOR GENERAL ELECTION

Thet Ni Moe¹, Khin San Yee², Aye Aye Myint³

Abstract

An innovative design of electronic voting system is introduced. It is intended to use in coming general election 2020 in Myanmar. The voting system consists of an Arduino Mega 2560 development board, a 3.5 inch TFT (Thin Film Transistor) color graphic liquid crystal display with micro SD card module, a non-contact distance sensor module, voting input switches, control input switches for polling officers, reset input switch, display LED indicators and two 3.7V rechargeable li-ion batteries. The system is capable of detecting and counting the incoming voter and votes. The voting was restricted exactly only one vote for each voter. The list of candidate and operating information are display on the LCD. The voting results are stored in a micro SD card. The circuit design helps the electoral process more efficient and speed up the processing of results and voting easier.

Keywords: Arduino MEGA, 3.5 inch TFT LCD, Micro SD Card, Printed Circuit Board (PCB)

Introduction

An election is a formal group decision-making process by which a population chooses an individual to hold public office. Elections have been the usual mechanism by which modern representative democracy has operated since the 17th century. The vote is a formal indication of a choice between two or more candidates or courses of action, expressed typically through a ballot or a show of hands. The ballot is a system of voting secretly and in writing on a particular issue. The voting can be used to choose someone or something. People choose the leader or ruler by voting.

In some cases, vote decisions are made for projects that will develop the country or destroy the natural resources. In practice, a secret ballot is used to prevent voters from being intimidated or threatened and protect their privacy.

Now, Myanmar is one of the democracy countries and general elections are made on every five years. There are many difficulties, large budget costing, and upcoming arguments on every general election. Therefore, an innovative design of electronic ballot was designed and presented to use in coming general election 2020. The system design is large and complex, but it is reliable and easy to use for both voters and polling officers.

The system design consists of an Arduino Mega 2560 development board, a large TFT color LCD display with micro SD card module, a non-contact distance ranging sensor module (HCSR04), a piezo buzzer, a few input switches, two LEDs, and two 3.7V li-ion batteries. The system is constructed on a specially designed printed circuit board. The Arduino Mega is loaded with a program code to operate the circuit.

The system design will automatically detect the presence of voter. If there is a voter in front of the sensor, the red LED illuminates and LCD describes the presence of voter and counts the number of voter in the system memory. At the moment, the voter can search the candidate and vote using input switches given for voter. The voting can be made only one time for each visitor by created program code. After voting was successful for the voter, he or she has to leave from the sensor area within a few seconds. If the voter is not leaving within the predefined period, an alarm

¹ Dr, Associate Professor, Department of Physics, Kyaukse University

² Dr, Associate Professor, Department of Physics, Kyaukse University

³ Dr, Associate Professor, Department of Physics, Kyaukse University

will continuously generate from the buzzer. When the voter leaves the area, the alarm will stop and the green LED illuminated, illustrating it is ready for next voter. The counted votes are stored in a micro SD card for voting officers. Moreover, the system provided to view or delete the result on the system LCD by using some input switches. Basic structure of the system design is illustrated with a block diagram in Figure 1.

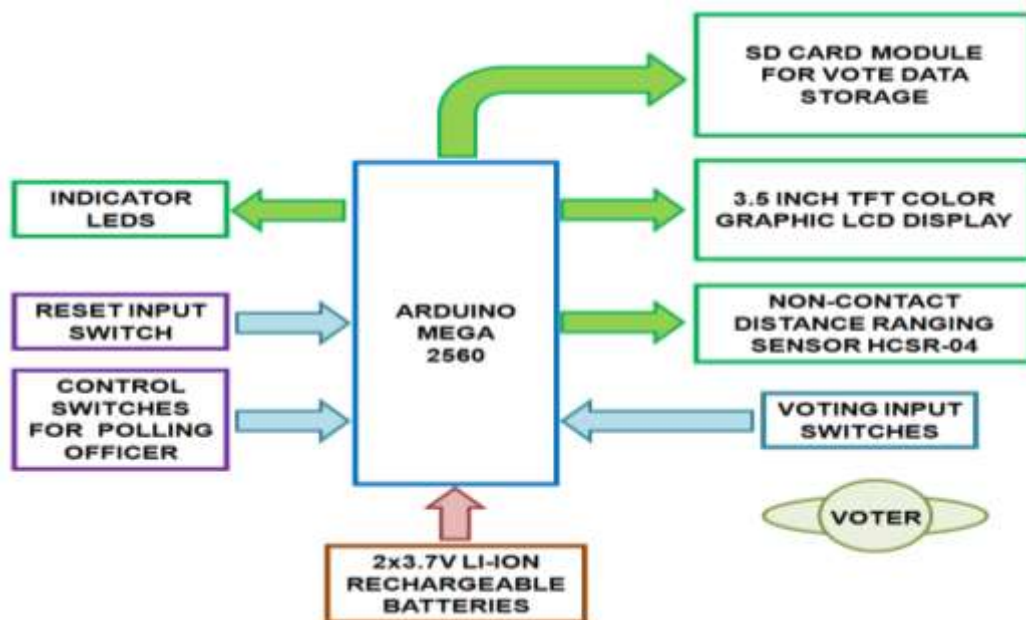


Figure 1 Block diagram of electronic ballot for General Election

Construction of the Circuit

The circuit construction was made on the fabricated printed circuit board. The use of fabricated printed circuit board in construction saves short circuits and loose contacts on the circuit board. Moreover, it is simple and easy to build the circuit. Some of the collected components are illustrated with a photo in Figure 2.

The fabricated PCB board has no outline drawing on the components side of the circuit board. Therefore, it is important to insert the components with the correct orientation and correct position on the board. But on the circuit PCB, wire connections are made very well and no jumpers are necessary on the components side. The resistors and other components were inserted and soldered in the following arrangement;

- Resistors
- Male terminal pins for Arduino Mega
- Button switches
- Female terminals for graphic LCD
- LEDs
- Piezo Buzzer
- Ultrasonic ranging module



Figure 2 Components of electronic ballot for general election

The soldering side and components side photos of connecting resistors and male terminal pins are illustrated in Figure 3a and 3b. There are only two resistors and they are 560Ω for two LEDs. The male terminal pins are used to connect with Arduino Mega development board.

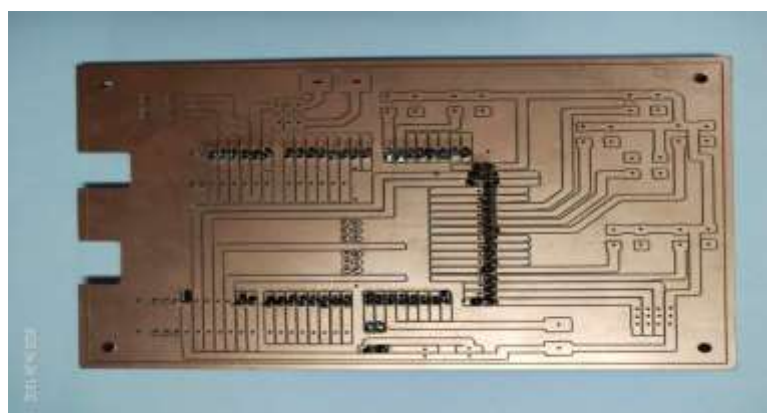


Figure 3a Soldering side of the resistors and male terminal pins

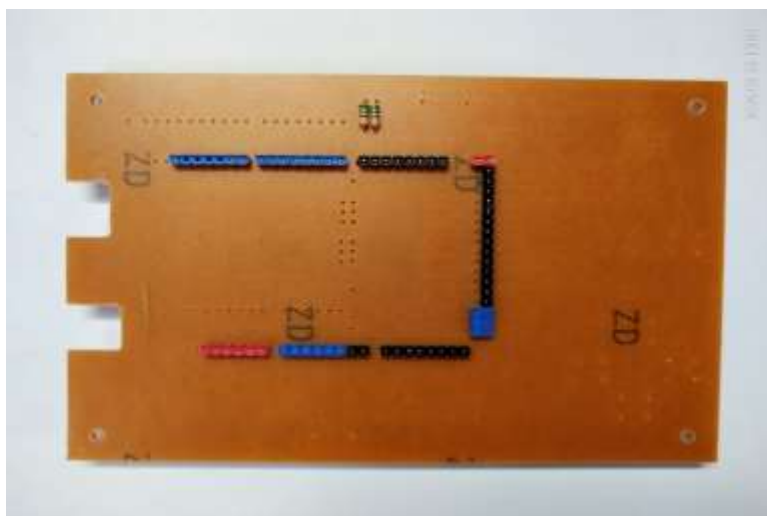


Figure 3b Components side of the resistors, and male terminal pins

Then nine input switches, female terminal pins for LCD, LEDs, piezo buzzer, and female pins for ultrasonic sensor module are inserted and soldered as shown in Figure 4a and 4b. Finally, the Arduino Mega, sensor module (HCSR04) and 3.5 inch TFT LCD are inserted on the circuit terminals as shown in Figure 5.

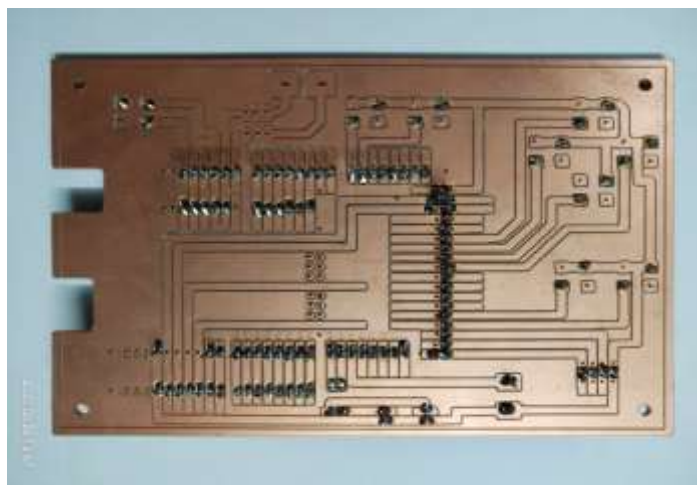


Figure 4a Soldering side of the constructed circuit board

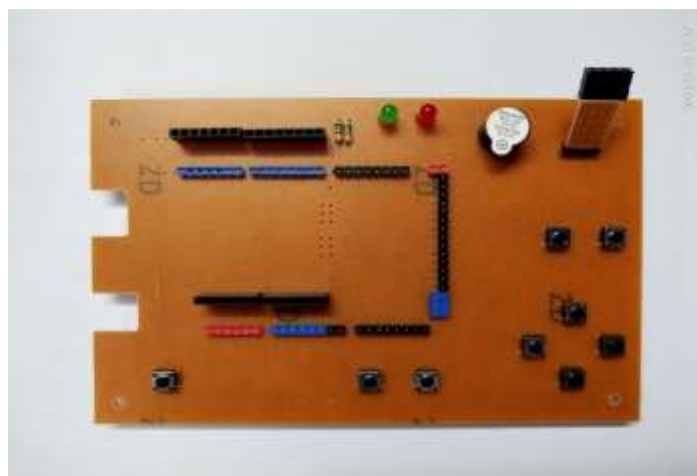


Figure 4b Components side of the constructed circuit board



Figure 5 Installation of circuit board with Arduino Mega, LCD and HCSR 04

Program Explanation

There are 517 program lines in the program. The program coding is written by using Arduino IDE software. The programming language is simplified C programming language. Flowchart diagram is very helpful in developing a program code. It is shown in Figure 6. An illustration of flowchart is used to briefly describe the flow of program. They are Adafruit_GFX, Adafruit TFTLCD, SPI, SD, WWPROM, and MCUFRIEND_kbv libraries. Then the defining the 16 bit color code with suitable color names for various colors. The void setup () routine starts from line 70 and end in line 110. In this routine, EEPROM memories are assigned with suitable names, setup I/O pin directions, initialize the LCD and SD card modules. Then the display illuminates the title and default background for the system.

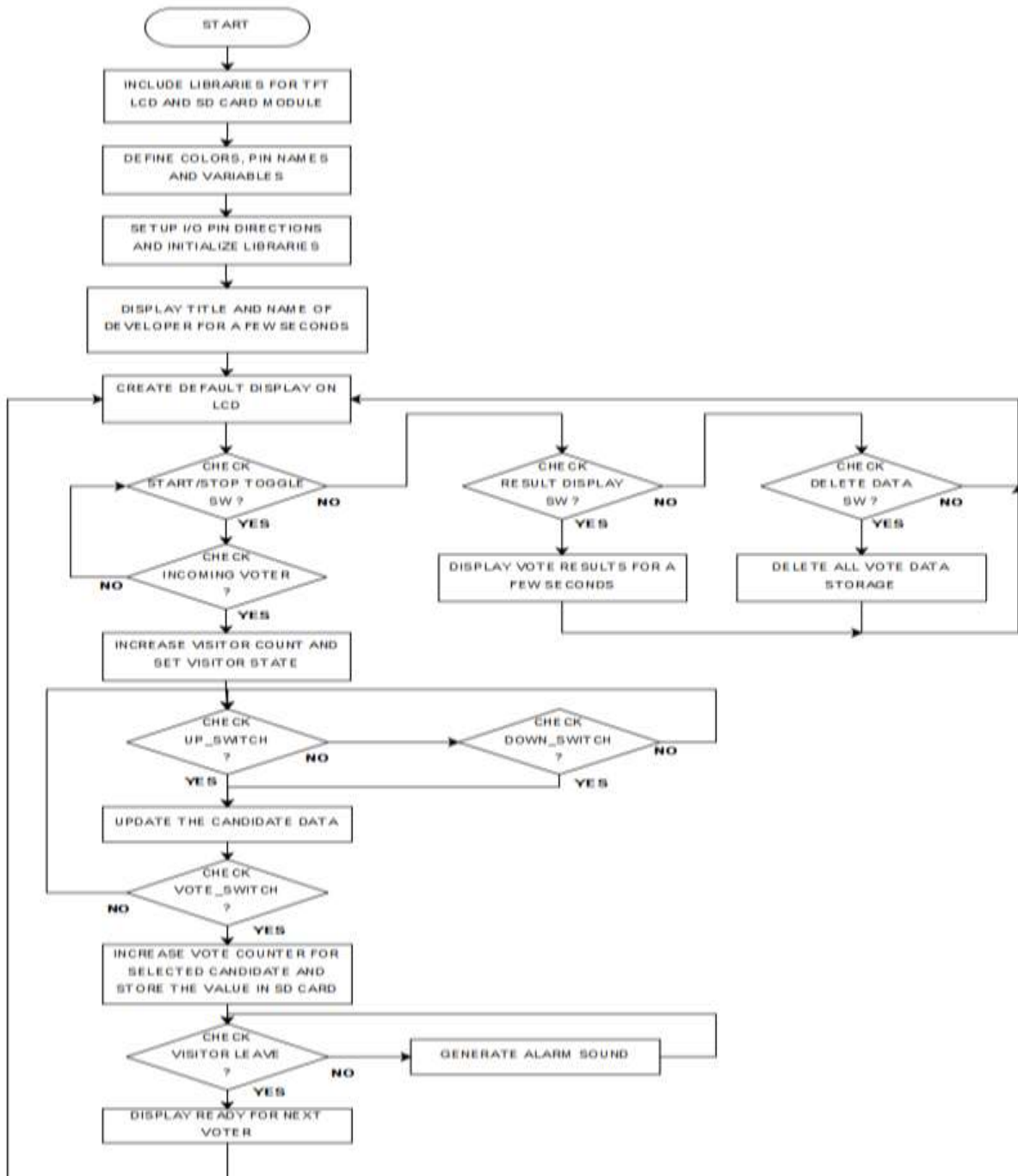


Figure 6 Flowchart diagram of the program

Circuit Operation

The whole circuit operation is user friendly, reliable and easy to use. The system can be power by three different methods, connecting with a USB cable to B type connector on Arduino Mega or using a 9V dc adaptor connect to the dc terminal socket on the Arduino Board or using batteries connected on the Vin pin terminals on power terminal of Arduino Mega. In this experimental and development, it is illustrated by connecting with USB (A-B) cable with a PC. But in the earlier schematic, it will be using two rechargeable li-ion batteries.

The parts and functions of components are illustrated with labels as shown in the Figure 7. The Arduino Mega is connected under the shield circuit board. It is the controller of every component on the circuit board. The board consists of 256K byte of program memory, 8K byte of RAM memory and a total of 70 I/O pins. Moreover, the board provided two on board voltage regulators 5V and 3.3V for other components on the circuit design. But the board itself cannot operate the system. Therefore, a program code was created and uploaded into the memory of microcontroller by using Arduino IDE software. The program coding was the most difficult part in this research and development of electronic ballot circuit.

As soon as the power supply is connected, the display initiated title of the project and name of developer for a few seconds. Each screen displays are illustrated in Figure 8. In this screen the background color is red and a title was created with white fonts for Candidate data. The voting area is labeled on a white square box. In this developing, a light green rectangular box is created under the vote area box to view the currently counted votes. But it is only for program developing.

Then a white horizontal stripe is in the 2/3 of the screen. It is used to display the operating information. Under the white stripe, the red background is again created for system information. There are two yellow colored boxes for visitor sensor and visitor counter. On initial background, it is assumed to be no visitor and the display area describes “No Visitor” on the area. But at the same area, a green LED sign is indicated on the LCD for detection of no visitor. On the area of visitor counter, there is no count on the display. On the lower right corner of the LCD, the system status is indicated for initial system status. It is OFF in the light green area. On the circuit there are a total of nine switches. They are divided for voter input switches and ballot officer switches. The voter input switches are up, down and enter switches. The ballot officer switches are start/stop, result and delete switches. Then the program checks the non-contact sensor module for incoming voter or visitor. If there is no visitor in front of the sensor, the Green LED is illuminated on both LCD and on the circuit board.

In this screen the candidate data started for the first candidate by display no of candidate, name and his or her party. On the white stripe, a string was illuminated “Vote for your candidate!”. On the visitor sensor area, the label changes to “Detect” and the Red LED illuminated on the LCD. Then the voter can press ENTER switch only one time for the selected candidate. When the voting is completed, a tick mark appeared on the vote area and vote counter was display under the vote area as shown in Figure 9.

On the white stripe, the label changes to “YOUR VOTE IS SUCCESSFUL”. Then the sensor check for the visitor to leave the area. If the voter is not leaving within 3000 ms, an alarm sound will be generated. If the voter is leaving before 3000 ms, the alarm will not sound and it will be ready for next voter.

After voting's are completed for every voter in the township, the polling officer can press the start/stop switch to stop the voting system. Then the storage results for each candidate can be read by pressing the RESULT switch. The result display photo of the system is shown in Figure 10 and 11.

The storage data on the SD card can be used as evidence of vote results for election.

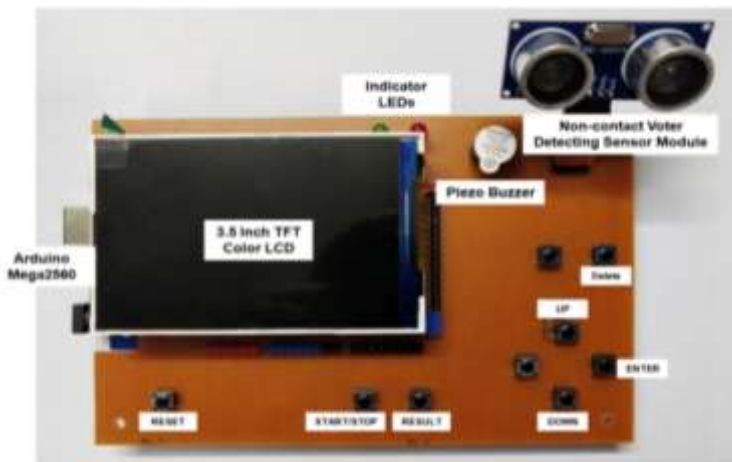


Figure 7 Name and function of components on the circuit board



Figure 8 The name of circuit developer illuminated on the LCD



Figure 9 The LCD display after voting successful



Figure 10 The LCD display for voting results



Figure 11 The photo of deleting voting results

Conclusion

The design of electronic ballot is not a new idea, but it is innovated to be secure and reliable. The system is very perfect to use in general election. It is restricted and limited only one vote for each voter. Moreover, the system stores the vote count permanently in a micro SD card for evidence of voting results. Although there are only five candidates in the prototype design, the number of candidates can be increased from the program code. The system provided information of each candidate and an audible alarm if the visitor is not leaving from the voting cell or voting area after a successful vote. The whole system can be operated with two rechargeable li-ion batteries. And the stored vote counts will not disappear while the battery is changing. The system will be a great help in general election forwarding the route to democracy in Myanmar.

Acknowledgement

I would like to express my special thanks to Dr Aung Khin Myint, Rector, Kyaukse University to allow to present this research. My sincere thanks are due to Dr Cherry Than, Professor and Head, Department of Physics, Kyaukse University for her kind encouragements throughout the research.

References

- Arduino homepage on Arduino Uno [online].
Available: <http://arduino.cc/en/Main/arduinoBoardUno> “Atmega328 datasheet”, [online].
- Brian Evans, (2011). Beginning Arduino Programming: Springer Science + Business Media, LLC., 233 Spring Street, 6th floor, New York.
- Marston R.M., 1996 “Modern CMOS Circuit Manual” (London: B H Newnes)
- Michael McRoberts., (2013). Beginning Arduino: Springer Science + Business Media, LLC., 233 Spring Street, 6th floor, New York, NY 10013.

GRAPHICAL TEACHING AID FOR ASTABLE AND MONOSTABLE CIRCUITS UTILIZING ARDUINO MEGA

Khin San Yee¹, Thet Ni Moe², Aye Aye Myint³

Abstract

An electronic device is created and constructed. It is intended to become a kind of teaching aid for electronic lecturers and students. The circuit was designed to help calculating various outputs of the 555 timer ICs in Astable mode and Monostable mode. Calculations can be easily made for frequency, period, duty cycle, and delay time outputs. Moreover, schematic displays and input values of the components can be display with graphical colorful images. The circuit design consists of Arduino Mega development board, a few input switches, a 3.5in TFT color LCD display, a piezo buzzer, and two 3.7V li-ion batteries. The whole circuit is operated by a program code created by using Arduino IDE software. The complete circuit was constructed on a specially created printed circuit board.

Keywords: Arduino MEGA, LCD, Buzzer, 2 x 3.7V Li-ion Batteries

Introduction

Education plays an important role in both development of our country and living standard. Ministry of education is making researches to develop the quality of education in Myanmar, such as adding the new courses and subjects, removing the unreasonable lessons. While preparing the courses, it is important to consider the application of various teaching aids. Teaching aids are objects (such as a book, picture, or map) or devices (such as a projector, DVD or computer), 3D models, or instruments used by a teacher to enhance understanding a lesson in a classroom or in a practical room. Therefore, research on development of teaching aids becomes important in modern education.

Therefore, a kind of teaching aid is designed for electronic students. It is intended to help in learning 555 timer IC in electronic lab or studying electronic circuits. The circuit is designed to be visually illustrate the schematic and components. Moreover, calculation can be made by using input data for various output results within a few seconds. The circuit design utilized a microcontroller development board (Arduino Mega), a 3.5 inch tft LCD display, a piezo buzzer, a few input switches and two li-ion batteries. The processing of input data and calculations were made with a program code. It is the most difficult part in the design. The program coding was created with Arduino IDE software. The basic structure of the circuit design is illustrated with a block diagram in Figure 1.

¹ Dr, Associate Professor, Department of Physics, Kyaukse University

² Dr, Associate Professor, Department of Physics, Kyaukse University

³ Dr, Associate Professor, Department of Physics, Kyaukse University

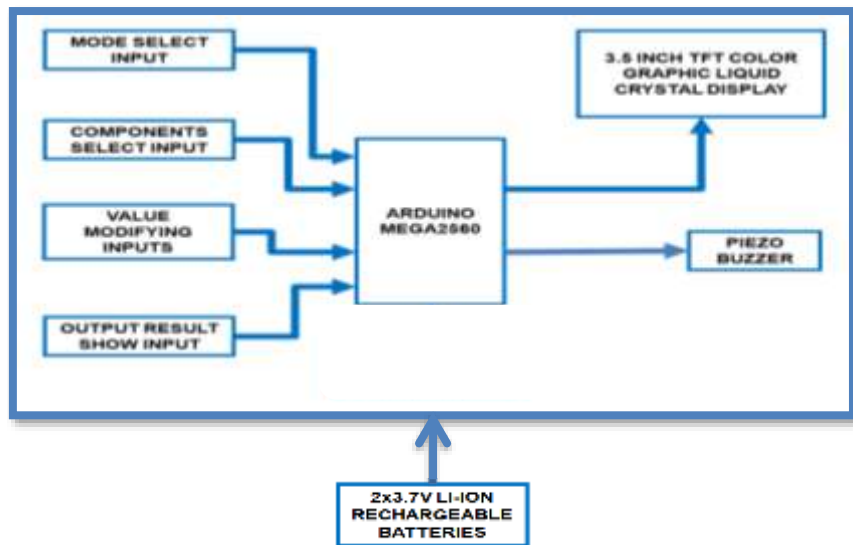


Figure1 Block diagram of astable and monostable training aid system

Arduino Mega2560 Module

The Arduino Mega2560 board is a microcontroller board included in the ATmega2560 microprocessor. It has 54 digital input/output pins, 14 pins of these 54 pins are used in PWM output. 16 analog pins and 4 UARTs pins to hardware serial ports are also included. The crystal oscillator in the Arduino Mega is 16MHz and includes everything to support a microcontroller, such as a USB connection, reset button, ICSP header, and a power jack. The Arduino Mega2560 board is shown in Figure 2.

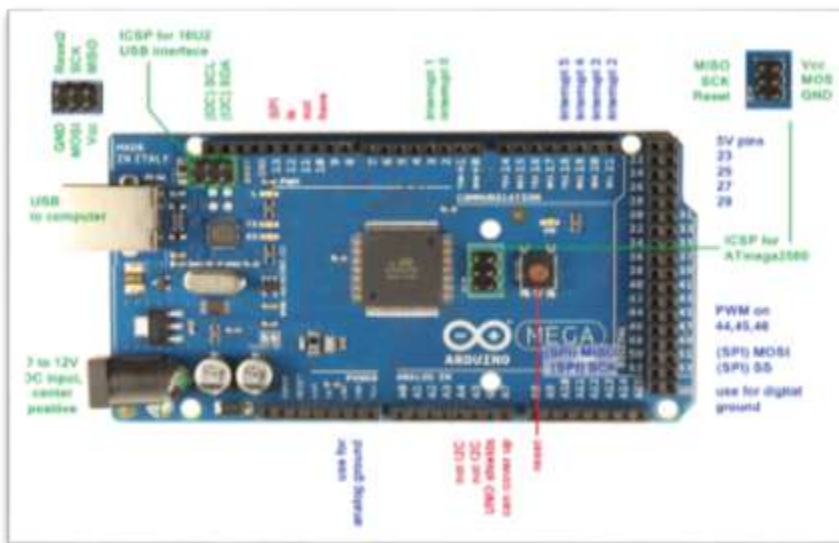


Figure 2 The Arduino Mega2560 Board

3.5 Inch TFT LCD Module

The 3.5 inch TFT LCD module is available in 320x480 resolutions and 65K color display. It uses 8-bit line parallel port communication, and the driver IC is ILI9486. The module includes an LCD display, 5V to 3.3V level conversion circuit, which can be directly, plugged into the Arduino Uno and Mega2560 development boards.

Moreover, the board consists of built in SD card expansion function. Front view photo of 3.5 inch TFT LCD Shield and pin out diagram of 3.5 inch TFT LCD shield as shown in Figure 3 and 4. The module can be directly inserted into the Arduino Mega2560, without adding manual jumpers or wires as shown in Figure 5.



Figure 3 Front view photo of 3.5 inch TFT LCD Shield

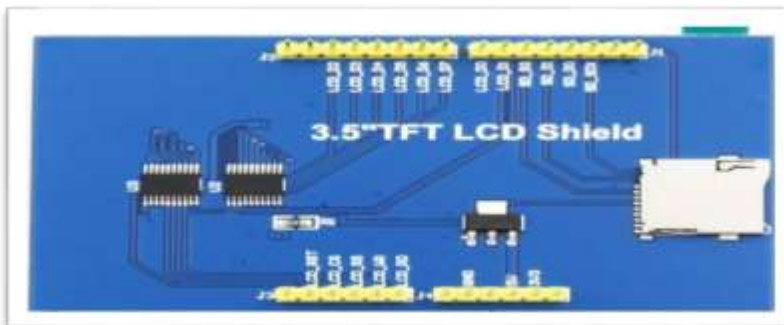


Figure 4 Pin out diagram of 3.5 inch TFT LCD Shield



Figure 5 The LCD is connected with Arduino Mega2560 board

Circuit explanation

The schematic of Astable and Monostable Teaching Aid circuit is shown in Figure 6. In the schematic there are some electronic components and modules. They are Arduino Mega2560, a 3.5inch TFT Color LCD display module, a few input switches, a piezo buzzer, and two 3.7V rechargeable li-ion batteries. The microcontroller development board Arduino Mega is the heart of the circuit in this design. The board was chosen for consisting a large amount of program memory and plenty of I/O pins.

Moreover, the board was combined together with programmer and regulated power supplies. But the controller board itself cannot operate the circuit of Astable and Monostable Teaching Aid. The LCD-RD pin is connected with A0, the LCD-RW pin is connected with A1, the

LCD-RS is connected with A2, the LCD-CS is connected with A3 and finally the LCD-RST pin is connected with connected with A4 as shown in Figure 7. A piezo buzzer is used in the circuit.

The positive side of the piezo buzzer is connected with the digital input pin 18 of the microcontroller and negative side of the buzzer is connected with the ground line as shown in the schematic. The last part in the circuit is power supply. The input of arduino mega can be range from 7 to 12V dc. Therefore, a pair of 3.7V rechargeable li-ion batteries is used in the circuit. But there is a power on/off switch between the battery and VIN of the Arduino Mega. There are 5V and 3.3V regulator outputs on the Arduino Mega and they can be used to power the other components on the circuit.

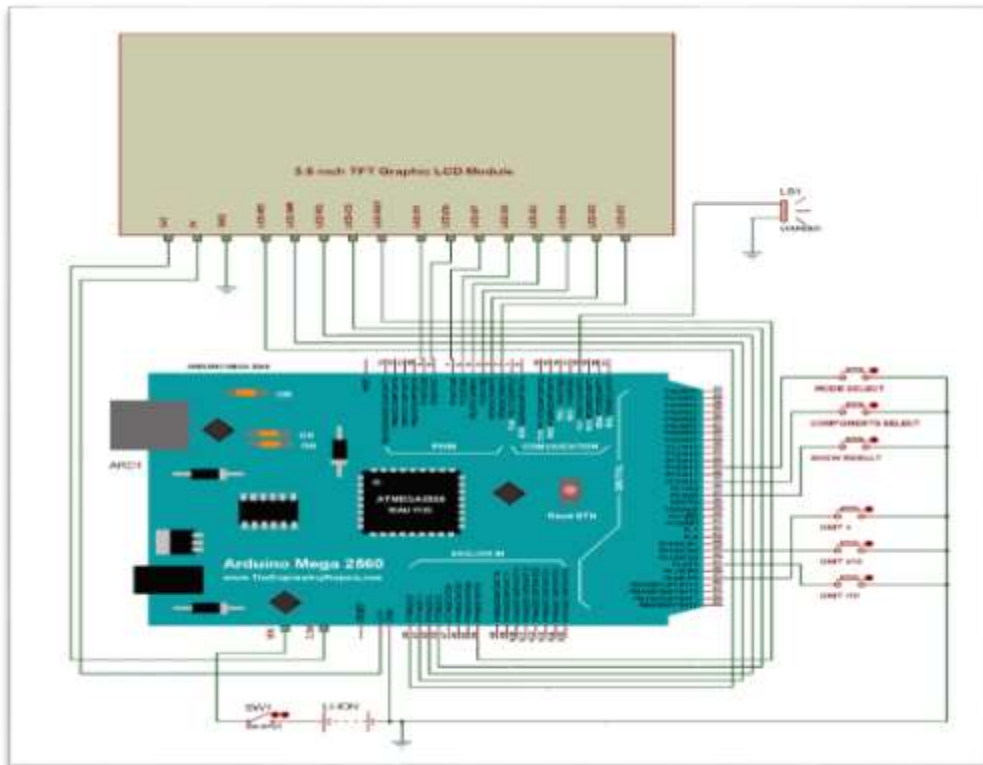


Figure 6 Schematic diagram of teaching aid for astable and monostable circuit

Program Explanation

A flowchart diagram is created to help during program development and to explain. It is shown in Figure 7. The flowchart is started by adding library files for 3.5 inch TFT LCD displays. Then the names of color are defined with 16 bit numerical values. At the same time pin naming, defining variables and sw input state variables are made for the program. Then the Input/ Output pin settings are made and libraries are initializing in the void setup routine.

Moreover, some default settings are made in this routine. The title of the circuit is display with large white color fonts on dark blue screen in the same routine. Then the program looping started by checking the ASTABLE or MONOSTABLE mode select input switch. Then the program checks for press of show results input switch. If the switch is not press, the program will loop back to modify the input values. If the show result switch is pressed, the calculations will be made for the periods, frequency and duty cycle values and display on the LCD for five seconds. After five seconds, the values are hidden again and only the component values are display on the LCD.

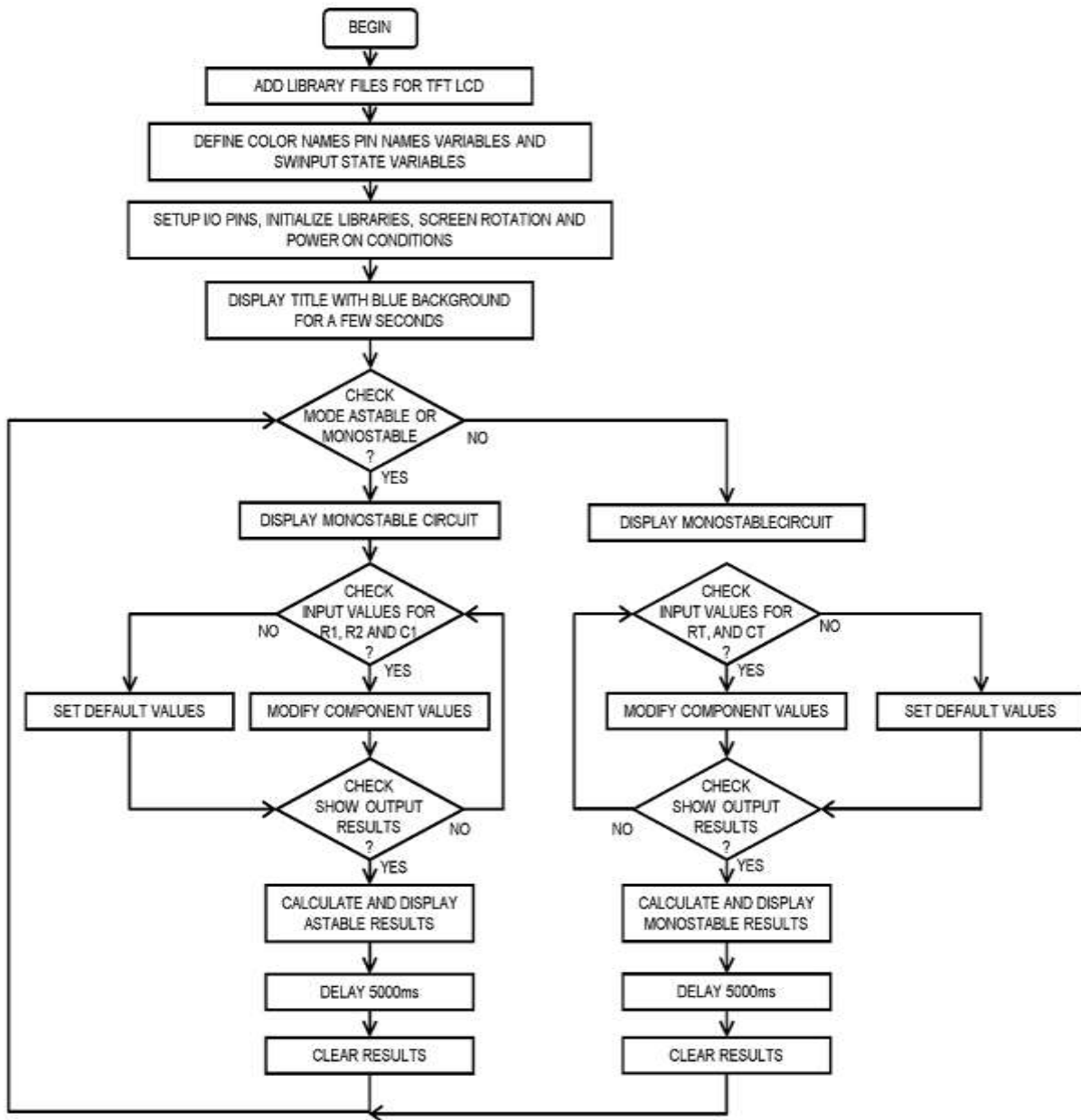


Figure 7 Flowchart diagram of the program

Circuit Operation

The operation of circuit is design to be user friendly. But there will be difficulties in changing required values for resistors and capacitors. The whole circuit operation can be modify and operate by editing the program code which is created with Arduino IDE software. The size of compiled program code is larger than 32K byte, therefore, Arduino Mega is chosen instead of Arduino Uno. The compiled size of program code is 35.6K bytes and RAM memory usage is 920 bytes.

When the power supply is connected or USB connection is made with the Arduino Mega board. The program code uploaded in the microcontroller starts executing the program. In the very first state of programming, title displays are created on the LCD display for a few seconds. The title display consists of two pages. The font size is 3 and the colors of characters are white, but the

background is blue color. The teaching aid for astable and monostable circuit is shown in Figure 8. The result of title display is illustrated with Figure 9 and 10.

Then the astable circuit diagram and monostable circuit diagram and created for the program and tested. In this case, the default selection of circuit is astable circuit. But the circuit selection can be change to monostable circuit by pressing mode select input switch. Pressing the mode select input switch will toggle the two circuit. The selection of each circuit photos are illustrated in Figure 11 ,12 13 ,14,15 and 16.



Figure 8 The teaching aid for astable and monostable circuit

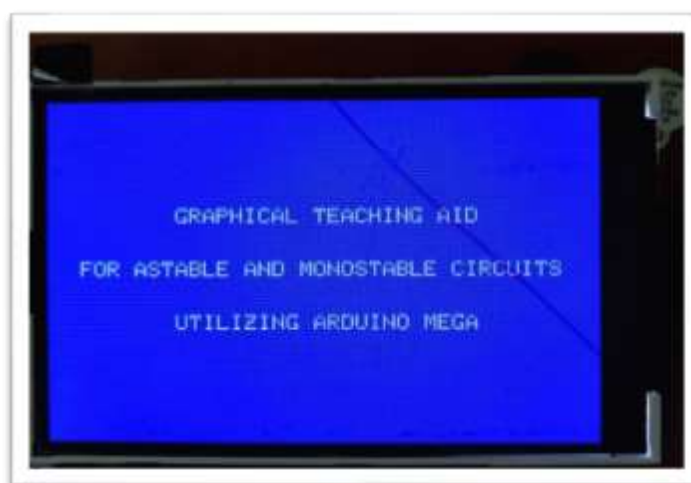


Figure 9 The graphic LCD display illuminating the first page of title

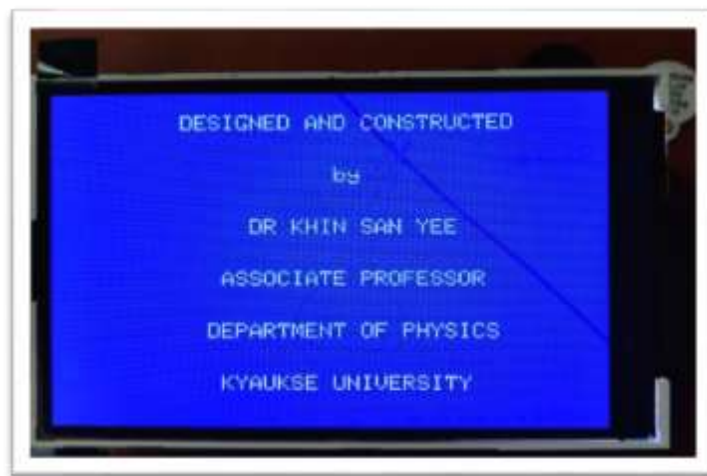


Figure 10 The graphic LCD display illuminating the second page of title

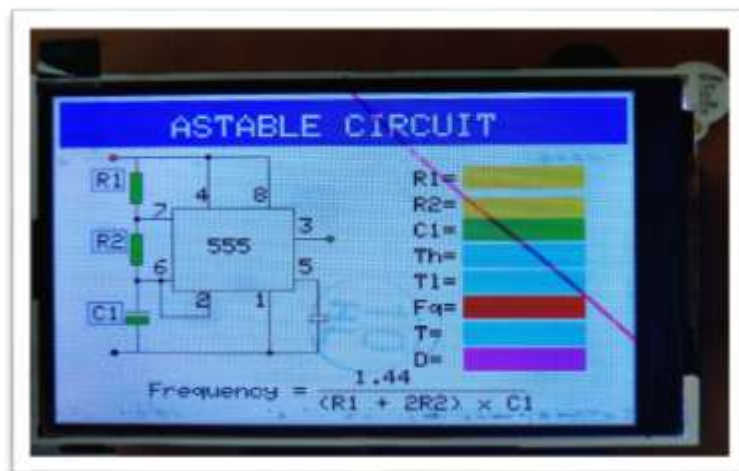


Figure 11 The operating mode selected for astable circuit

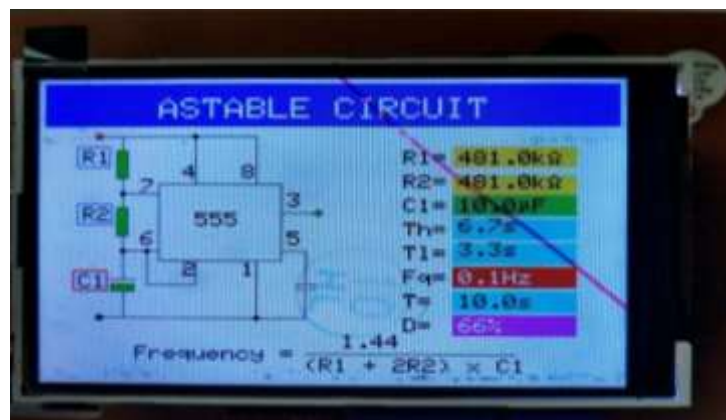


Figure 12 The calculated results for astable circuit

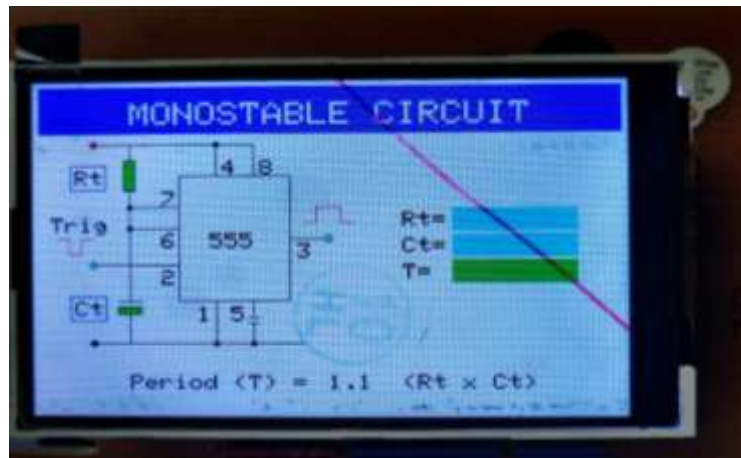


Figure 13 The operating mode selected for monostable circuit

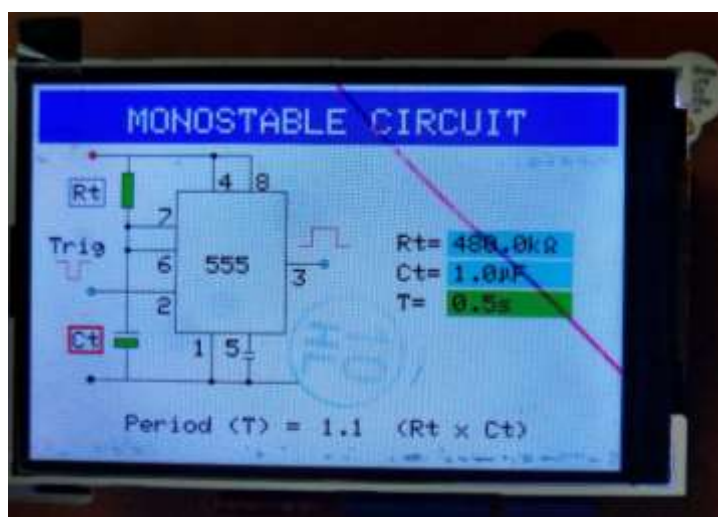


Figure 14 The calculated results for monostable circuit

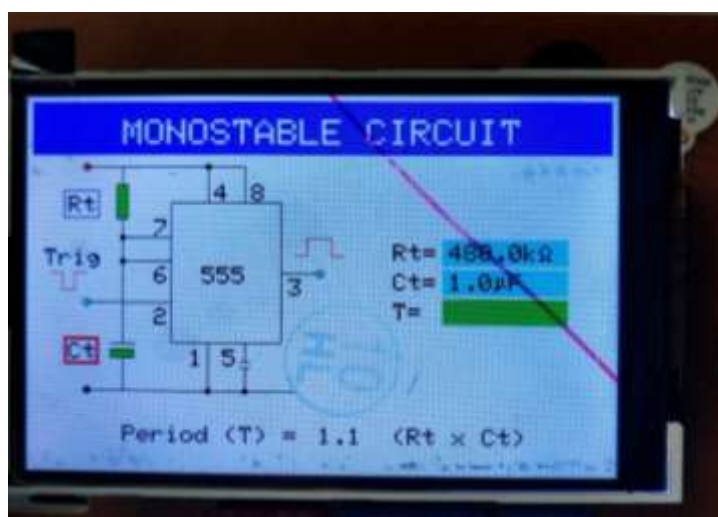


Figure 15 The Ct component was selected for monostable circuit

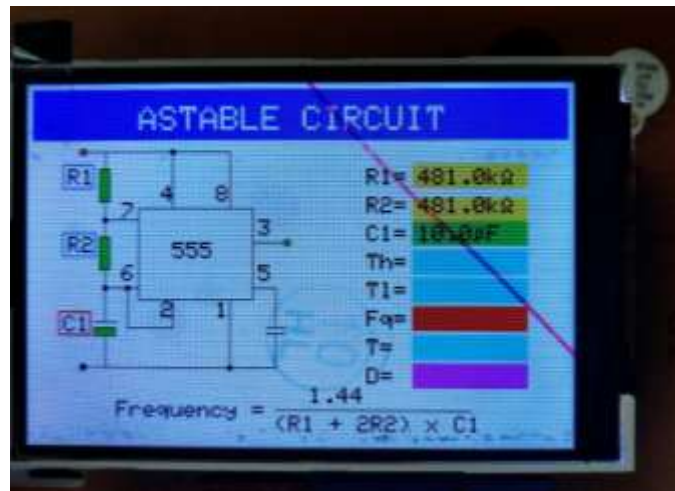


Figure 16 The C1 component was selected for astable circuit

Conclusion

The graphical teaching aid for astable and monostable circuit is tested and the output results are illustrated with photos. Practicing and understanding to the operation of the circuit will be very helpful to the users. In electronic practical, the experiments of astable circuit wiring and construction on project board output results can be easily tested with the help of constructed training aid circuit. The manual calculation for the output values of resistors and capacitors in various parameters in astable and monostable circuit confuse with the multiplier and divider units.

The application of the training aid will calculate correct value outputs for each circuit within a second by just pressing show result switch. For the further development in the training aid, the explanation of each pins and operations can be added in the design. The extra switches are used to upgrade or modify the circuit operations. More and more teaching aid or training aid are required to research and develop to upgrade the quality of education.

Acknowledgement

Firstly, I most respectfully express the gratitude to Dr Aung Khin Myint, Rector of Kyaukse University, for his permission to conduct this research paper. Secondly, I also thank to Dr Su Su Win, Pro-rector of Kyaukse University, for her kind permission to carry out this paper. I am indebted to Professor Dr Cherry Than, Professor & Head, Department of Physics, Kyaukse University, for her kind permission to undertake this paper.

References

- Brian Evans, Beginning Arduino Programming, (New York: 2011)
- Marston R.M, Modern CMOS Circuit Manual (London: 1996)
- Michael McRoberts, Beginning Arduino (New York: 2013)
- Nick Dossis, Everyday Practical Electronics (London: 2002)

ESP8266 ASYNCHRONOUS WEB SERVER BASED REAL TIME TEMPERATURE MONITORING BY CONTACTLESS IR THERMOMETER FOR SOCIAL DISTANCING

Wint Shwe War Hlaing*

Abstract

The commercial hand-held contactless thermometers are used to measure the body temperature to detect the virus-infected persons within a distance of about 3 feet. It is not a sufficient distance for virus protection without personal protective equipment (PPE) suit. The web server based on the contactless infra-red (IR) thermometer can measure the body temperature and display it on the PC monitor or mobile phone at the distance of 150 feet indoor and 300 feet outdoor from the sensor module. Since ESP8266 MCU is the Wi-Fi chip with microcontroller capability, it is suitable to use in the hardware interfacing and software development of a web server based contactless IR thermometer. Web server-client communication takes place by using the Hypertext Transfer Protocol (HTTP). Web server home page is created by using Hypertext Markup Language (HTML) and Cascading Style Sheet (CSS). Since asynchronous Javascript and XML (AJAX) are used in a web server system, the real time-temperature readings are automatically updated without the requirement to refresh the web server home page.

Keywords: ESP 8266 MCU, contactless, web server, HTTP, HTML, CSS, AJAX.

Introduction

Physician, nurse, and medical aid monitor the body temperature with a hand-held contactless IR thermometer to detect the virus-infected person within 3 feet distance without PPE suit. If the distance is too close, the virus can infect another. To avoid virus infection, the contactless IR thermometer is upgraded by using a web server. The contactless IR temperature sensor, microcontroller, WiFi module are mainly required. MLX90614 is used as a contactless IR temperature sensor. The Microcontroller is functioned as the data processing and these processed data are transmitted to a web server via WiFi. Since ESP8266 NODE MCU is, generally, the combination of microcontroller and WiFi module, it is used to implement the contactless IR thermometer system.

ESP8266 can be used as the control device that can connect to the WiFi network using HTTP and creates a web server with HTML and CSS. When the connected device accesses under the same web server, ESP 8266 reads the temperature from the MLX90614 sensor and sends it to the web browser of which device works under the same WiFi. Data is displayed once on the monitor of a PC or Android phone only if a web server is refreshed. In practice, its delay time is considered to measure the body temperature of many people. It can be solved by using the asynchronous Javascript and Xml (AJAX) that call the function repeatedly.

Experimental Procedure

Hardware, Software Equipments

The main components are ESP8266 NODE MCU and the contactless IR temperature sensor MLX 90614. ESP 8266 board, ESP8266 library and MLX 90614 library are required to be included in Arduino IDE. Web server home page is created by using HTML and CSS. Server to client or client to server is communicated on the HTTP platform.

* Dr, Lecturer, Department of Physics, University of Yangon

ESP 8266 NODE MCU

ESP8266NODE MCU is the microcontroller with integrated WiFi. NODE MCU is the combination of node and MCU (microcontroller unit). It composes of ESP-12E module containing ESP8266 chip 32-bit reduced instruction set controller (RISC) processor which supports real-time operating system (RTOS) and operates with adjustable frequency 80Hz to 160Hz. For program and data storage, 128KB RAM and 4MB flash memory have already added inboard. These memories are enough to make up the webpage, AJAX data which have large strings. Since ESP8266 is attached to WiFi, it can connect to WiFi network or can interact with the internet. Moreover, it can set up its own network as a server. CP 2102 USB- to-UART controller chip which included in ESP8266 board converts USB signal to serial data for communication with the computer [Abhijit Mukherjee, 2020].

There are 17 general purpose input-output (GPIO) pins in ESP8266 NODE MCU as shown in Figure 1. These pins are assigned to some peripheral capabilities including an analog-to-digital converter (ADC), universal synchronous receiver and transmitter (UART), pulse width modulation (PWM), serial peripheral interface (SPI), inter-integrated circuit (I2C), and inter-integrated sound(I2S). These pins are multiplexing features, that is; a single GPIO pin can multiplex as PWM / SPI / I2C [Vowstar, 2020].

Contactless IR Temperature sensor MLX 90614

MLX 90614 is an infrared sensor which is used to measure the temperature without contact. It consists of an infrared-sensitive thermopile detector MLX 81101 and the signal conditioning MLX 90302. An optical filter that cuts off the visible and near-infrared radiation is attached to the module to protect sunlight and ambient diffuse light. The high accuracy and high resolution of that thermometer are obtained due to the consisting of low noise amplifier, high-resolution 17-bit ADC, and the digital signal processing system of MLX90302 in MLX 90614 module.

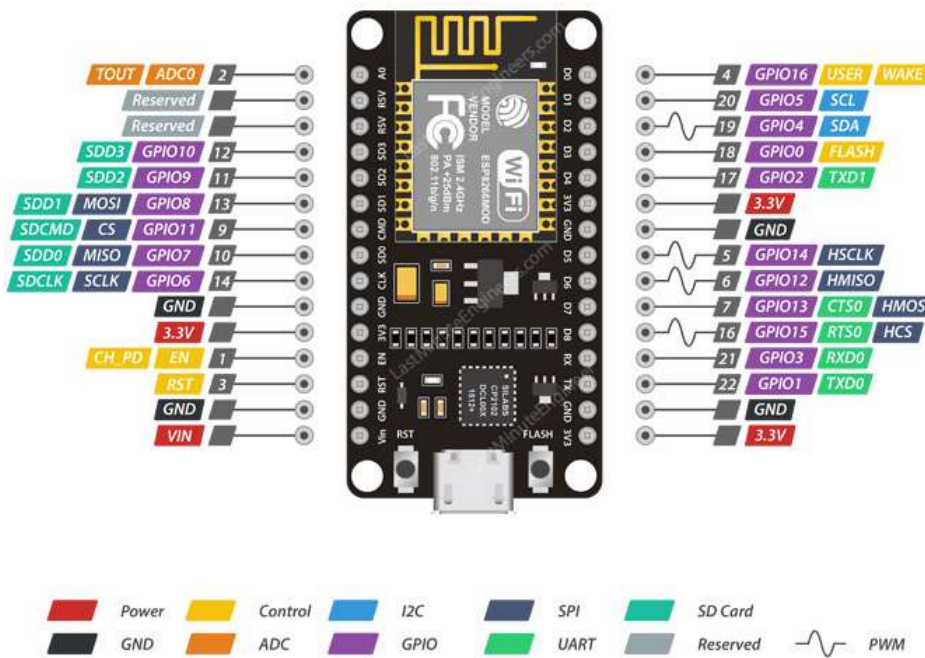


Figure 1 Pin assignment of ESP8266 NODE MCU

According to Stefan-Boltzmann law, the thermal (IR) energy emitted from any object that isn't below absolute zero (0K) is directly proportional to the fourth power of its absolute temperature. The infrared thermopile inside the MLX90614 detects how much IR energy is being emitted by materials in its field of view (FOV), it produces an electrical signal proportional to that. The MLX90614 produces both object temperature and ambient temperature. The object temperature is the non-contact measurement from the sensor, while the ambient temperature measures the temperature on the cover of the sensor. The object temperature measurements can vary from -70 to 382.2 °C (-94 to 719.96 °F), while the ambient temperature reading varies from -40 to 125 °C. The resolution of both the ambient temperature and object temperatures is ± 0.5 °C.

The MLX90614 (as shown in Figure 2) used in this research is rated for a 3V operating voltage with a single infrared sensor and an internal filter. This sensor has both digital pulse width modulation (PWM) and System Management Bus (SMBus) output. SMBus is a 2 wires interface based on the I2C principle. SMBus can be regarded as an I2C connection. A default I2C address of 0x5A is in MLX90614. By reconfiguring the address of an MLX90614, the multiple devices (up to 127) can be added to the same bus to get a larger temperature map [Melexis, 2020].



Figure 2 MLX 90614 IR sensor

Web Server and Client

Web server is one that stores, processes, and transfers the web pages to the client which is the web browser on a smartphone, tablet, and personal computer (PC). The request and response between the web server and client takes place using a hypertext transfer protocol (HTTP) capability. A client initiates to request the server for a web page using HTTP. The server also responds with the content of that web page or error if it cannot be able to process. Web server home pages are mostly made of HTML documents.

ESP8266 NODE MCU can connect to the WiFi network and act as a web server. Moreover, it can set up its own network to connect other devices. It can operate in three different modes: station (STA) mode, soft access point (AP) mode, and both at the same time. In this research, the system is implemented in the station (STA) mode.

System Operation

ESP8266 NODE MCU detects the digital signal from the MLX 90614 sensor and processes to convert the temperature. And then, it acts as web server in station mode. ESP8266 gets the internet protocol (IP) from the wireless router or WiFi hot spot and delivers the web pages to the devices that are requested under the same WiFi network. The operation of a web server based temperature monitoring system is categorized into two sections; hardware interface and software development.

Hardware Interface

Since the MLX 90614 IR sensor is inter-integrated circuit (I2C), it composes only two serial communication pins of serial clock (SCL) and serial data (SDA). From the data sheet of ESP8266 GPIO 5(D1) and GPIO 4 (D2) are SCL and SDA of ESP8266 respectively. So, SCL pin and SDA pin of MLX 90614 is connected to D1 and D2 of ESP8266, respectively as shown in Figure 3. The block diagram of the working principle of a web server based temperature monitoring system is shown in Figure 4.

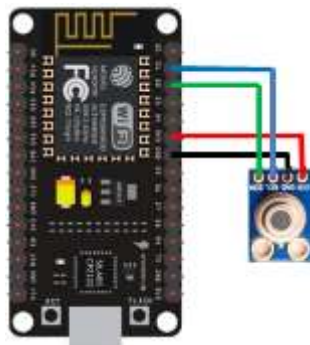


Figure 3 Circuit connection of ESP8266 and MLX90614 sensor

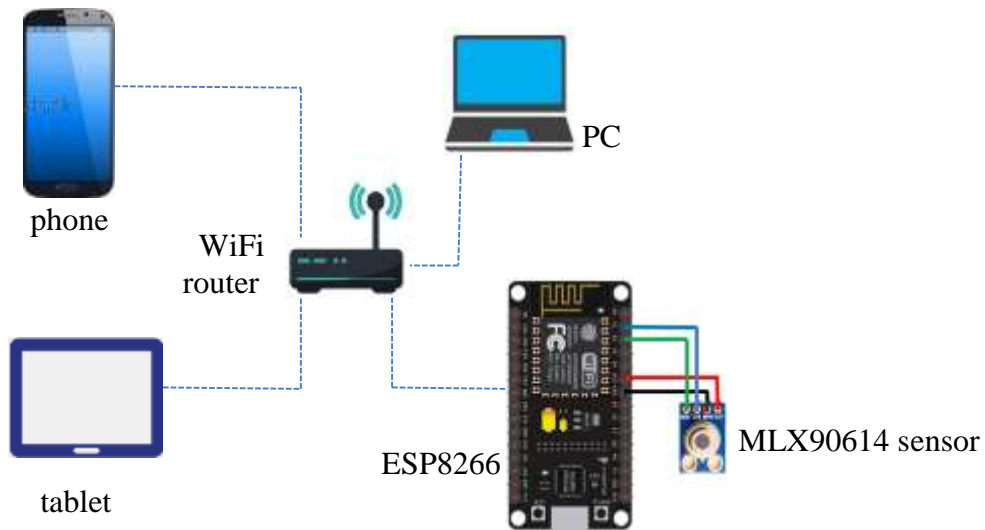


Figure 4 Block diagram of web server based communication

Software Development

ESP8266 is compatible with Arduino IDE. ESP8266 board and library are not included in the default Arduino IDE so that they are required to install in Arduino IDE. http://arduino.esp8266.com/stable/package_esp8266com_index.json is pasted into the “Additional Board Manager URLs” Field of preference in the IDE window as shown in Figure 5. After the URL path is defined, ESP8266 board can be installed using the board manager, as in Figure 6 [Santos R, 2020].

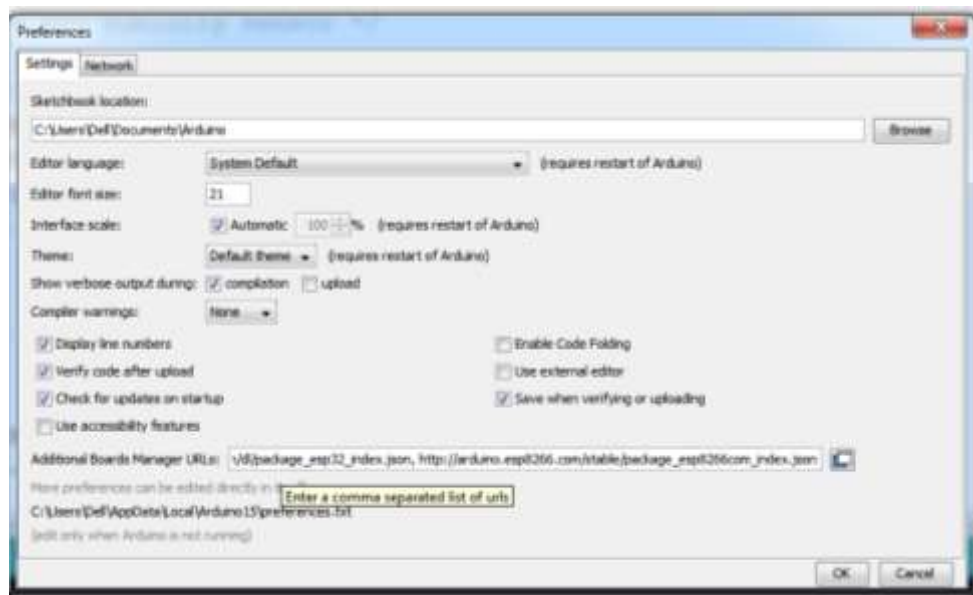


Figure 5 Including ESP8266 board

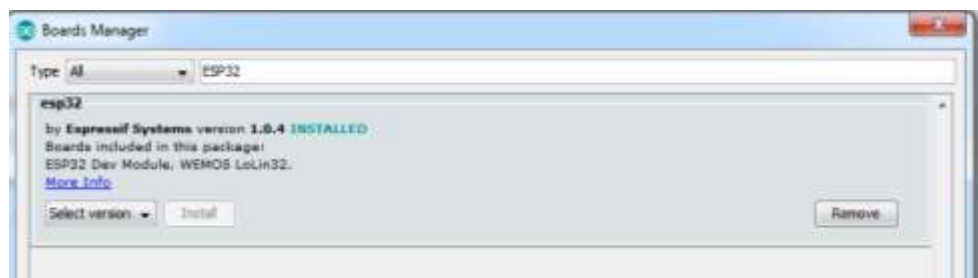


Figure 6 Installing ESP8266 library

As ESP8266NODE MCU is configured as station (STA) mode, it will communicate the local WiFi network. It needs to define the network credentials of service set identifier (SSID) and password.

```
const char* ssid    = "xxxxxxxxxxxxxx";
const char* password = "xxxxxxxxxxxx";
WiFiServer server(80);
```

Web server is at Port 80 which has assigned to use internet communication with HTTP. While ESP8266 is connecting the network, connectivity status is examined with Wifi.status() function. If it is connected, the IP address is obtained by using Wifi.localIP() function. When the server receives a request on the root path, it will trigger the function. When the ESP8266 web server receives a request from the client, Send.HTML() function generates the web page. Server.send() function takes temperature data as the parameters of HTML content. CSS is used to design the web page style such as font family, display, margin, and text alignment. The icon used to display temperature reading is a scalable vector graphics (SVG) defined in <svg> tag.

The temperature is displayed once when the webserver is refreshed. The asynchronous Javascript and Xml (AJAX) is used to automatically upload temperature. Java script setInterval()

function is used to call the function repeatedly. AJAX script process to 1) request data from the server, 2) receive data from the server and 3) send data to the server.

Results and Discussions

Cerebration

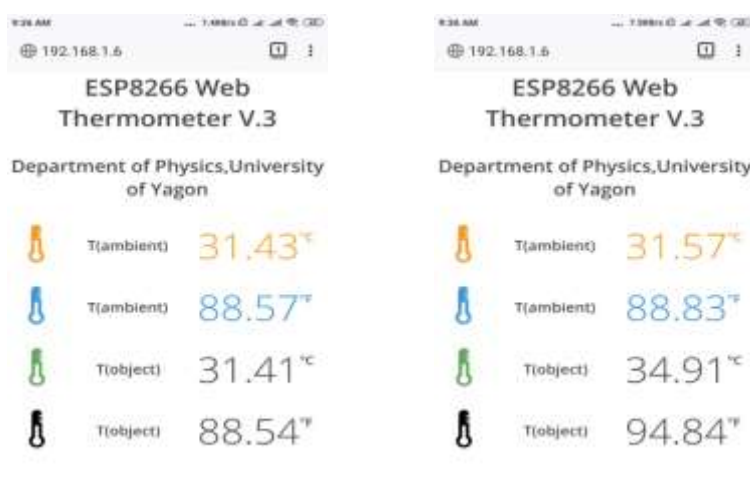
Web server-based contactless IR thermometer is designed and constructed by using ESP8266 and MLX 90614 temperature sensor as shown in Figure 7. While the program is uploading to ESP8266, it connected to the local WiFi network. If it is connected to a WiFi network, an IP address can be obtained on the serial monitor by pressing the RST (reset) button fixed on the ESP8266 board. An IP address is found that <http://192.168.1.6> as shown in Figure 8. If this IP address is inserted in the web browser of PC, tablet, or phone, the data can be visualized on the PC monitor, smartphone, and serial monitor as illustrated in Figure 9 to Figure 10, respectively. One set of data consists of ambient temperature and object temperature in degree Fahrenheit ($^{\circ}\text{F}$) and in degree Celsius ($^{\circ}\text{C}$) each.



Figure 7 Contactless thermometer

```
COM20
09:32:49.238 -> ..
09:32:50.238 -> WiFi connected..!
09:32:50.238 -> Got IP: 192.168.1.6
09:32:50.238 -> HTTP server started
09:32:54.119 -> ;l d□□| □$□| □ d□ c<
09:32:54.279 -> Ahkee
09:32:55.359 -> ....
09:33:00.120 -> WiFi connected..! ↓
09:33:00.120 -> Got IP: 192.168.1.6
09:33:00.120 -> HTTP server started
```

Figure 8 Obtaining IP address

**Figure 9** Temperatures on PC monitor**Figure 10** Temperatures on smartphone**Figure 11** Temperature on serial monitor

Discussions

Without AJAX script, the set of temperature can be monitored on the PC or phone only if the webserver is refreshed. Due to the manual refresh, it takes a delay time so that it is not convenient to measure the body temperature of many people. The program including AJAX script is uploaded and the temperature reading is automatically uploaded without a manual refresh of the webserver. It is obviously seen that there are three sets of temperature readings within one second, as shown in Figure 11.

If ESP8266 creates an own WiFi network as a soft access point (AP), the maximum number of clients that can be connected to AP is limited to five. In this research, the webserver in station (STA) mode is communicated to more than five numbers of clients such as PSs, phones, and tablets.

The set of temperature monitor on both laptop and phone at the same time is illustrated in Figure 12. It is seen that the decimal values of temperature are a little different because the clock speed in the performance of devices such as PC, phone had different.

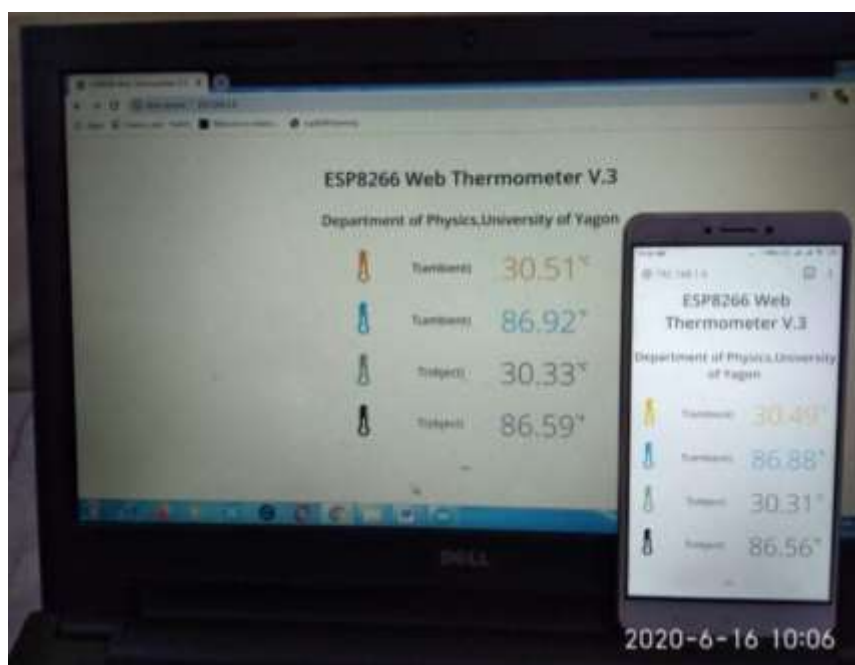


Figure 12 Temperature reading on both devices at the same time

Conclusion

Social distancing is one of the recommended preventive measures in the virus pandemic. When the body temperature is monitored by using a hand-held IR thermometer, the distance between two persons is a close distance about 3 feet. This distance is not safe for medical aid without PPE suit. This web server based contactless IR thermometer can measure the body temperature at the distance of 150 feet indoor and 300 feet outdoor. The temperature can be monitored on PC, tablet, and phone which is in the safe zone by connecting the webserver via WiFi hot spot or WiFi router. The cost of a set of web server IR thermometer plus internet charges is approximately equivalent to the cost of a PPE suit. Although it uses the electronic components and network, it is a user-easy device. The output temperature resolution is 0.14°C within the object temperature range -20°C to 120°C . As temperature uploading is reliably fast, it is useful to monitor the body temperature of many people safely and precisely.

Acknowledgements

I would like to express my profound thanks to Professor Dr Khin Khin Win, Head of Department of Physics, University of Yangon, for her advice, kind permission, and encouragement through the research period.

I sincerely thank all of Professors from the Department of Physics, University of Yangon for their kind encouragement to carry out this research.

I deeply grateful to Professor Dr Ohn Than (Retired), Head of Department of Physics, Kyaukse University who supports with the continuous guideline about the hardware and software of ESP8266 and web server.

References

- Abhijit Mukherjee, (2020) *ESP8266-based Contactless Thermometer*. Shanghai, China
- Melexis, (2020) *MLX90614 Non-Contact Infrared Thermometer*. Rare components, India.
- Santos Rui, (2020) *ESP8266 Web Server with Arduino IDE*. Random Nerd Tutorial Lab. No Starch Press, America.
- Santos Rui, (2020) *ESP 32 troubleshooting guide*. Random Nerd Tutorials Lab. No Starch Press, America.
- Santos Rui, Santos Sara. (2019) *Home Automation Using ESP8266*. No Starch Press, America.
- Vowstar, (2020) *NodeMUC*. GitHub, Inc., China.

EFFECT OF COMPLEXING AGENT (Na₂EDTA) ON THE DEPOSITION OF COPPER TIN SULPHIDE THIN FILMS

Nwe Wai¹, Kyay Mon Htwe², Than Zaw Oo³

Abstract

Copper tin Sulphide (CTS) thin films were prepared by chemically bath deposited in aqueous solutions containing sources of copper, tin and sulphur. The effect of different molar concentration of complexing agent on the growth of thin films was reported. The structure, optical and surface topography characteristics of thin films of copper tin sulphide grown on glass substrates were investigated by X-ray diffraction, UV-Vis spectrophotometry and atomic force microscopy techniques. The X-ray diffraction showed that the most prominent peak at $2\theta = 50.60^\circ$ which belong to (223) plane of Cu₄SnS₄. The atomic force microscopy indicated that the film deposited at the concentration of 0.1 M complexing agent exhibited narrow optical band-gap which is the requisite for light absorber layer in solar cell application. The band gap energy was found to be 1.5 eV with direct transition.

Keywords –copper tin sulphide, complexing agent, chemical bath deposition

Introduction

Solar cell energy applications took a great importance in the last few decades. This is because of the energy crisis and population caused by the traditional energy sources lie fossil fuels. So it's important to develop low cost light absorber materials for thin film solar cell energy applications. Recently, relatively high efficient materials were discovered and investigated for example copper indium gallium diselenide (CIGS) and CdTe. Such materials have the problems of being expensive and lower availability, especially indium tellurium and gallium. Also the toxicity of elements lie cadmium makes these materials lower applicable.

Copper containing chalcogenides, especially compounds of group I-IV-VI have been reported to have wide applications in photovoltaic devices, light emitting diodes, nonlinear optical materials. Copper and tin could form several ternary sulphides[1]. Wu et al. reported five stable phases of ternary copper tin sulphides in the Cu–Sn–S system in the temperature range of 400–650°C: Cu₄SnS₄, Cu₂SnS₃, Cu₂Sn₃S₇, Cu₅Sn₂S₇, and Cu₁₀Sn₂S₁₃. Phase relations in a 500°C isothermal section show the first three of these phases lying on the Cu₂S-SnS₂ line. A monoclinic cell with $a = 12.68 \text{ \AA}$, $b = 7.351 \text{ \AA}$, $c = 12.76 \text{ \AA}$, and $\beta = 109.60^\circ$ for Cu₂Sn₃S₇ and an orthorhombic (OR) cell with $a = 13.5 \text{ \AA}$, $b = 7.66 \text{ \AA}$, and $c = 6.395 \text{ \AA}$ for Cu₄SnS₄ are the crystal structures reported[2]. The compound Cu₂SnS₃ is reported as dimorphic or polymorphic with a phase transition occurring at 780 °C. The high temperature form of this material is isomorphic with cubic ZnS (sphalerite), and the low temperature phase could be tetragonal, monoclinic, or triclinic.²⁻⁴ The unit cell of triclinic Cu₂SnS₃ is reported to be identical to that of the mineral mohite (triclinic),² with $a = 6.64 \text{ \AA}$, $b = 11.51 \text{ \AA}$, $c = 19.93 \text{ \AA}$, $\alpha = 90^\circ$, $\beta = 109.75^\circ$, and $\gamma = 90^\circ$. On the basis of ellipsometric studies, Fiechter *et al.* reported for the material a fundamental band gap of 0.93 eV and a high absorption coefficient of 105 cm⁻¹ in the visible region.

In this work, Cu₄SnS₄ thin films were prepare by chemical bath deposition method using Na₂EDTA as a complexing agent. The effect of Na₂EDTA on the properties of thin films was studied. X-ray diffraction was used to study the structural properties of films. Meanwhile, the morphological and optical properties of CTS films were investigated by using atomic force microscope and UV –Vis spectrometer, respectively.

¹ Lecturer, Department of Physics, University of Magway.

² Lecturer, Department of Physics, University of Magway.

³ Professor, Department of Physics, Yangon University

Experimental Details

The *CTS* thin films were prepared by the chemical bath deposition (CBD) method on the glass substrates. All the chemicals used for the deposition were prepared in distilled water. The *CTS* thin films were prepared from an acid bath using copper sulphate ($\text{CuSO}_4 \cdot 5\text{H}_2\text{O}$), tin chloride ($\text{SnCl}_2 \cdot 2\text{H}_2\text{O}$) and sodium thiosulphate ($\text{Na}_2\text{S}_2\text{O}_3 \cdot 5\text{H}_2\text{O}$) acted as a source of copper, tin and sulphide ion, respectively. The disodium ethylenediaminetetraacetic acid (Na_2EDTA) was used as a complexing agent during deposition process. It is used to chelate with Cu^{2+} and Sn^{2+} to obtain Cu-EDTA and Sn-EDTA complex solution which can improve the lifetime of the deposition bath as well as the adhesion of deposited films on the glass substrate. In order to investigate the effect of complexing agent, we prepare precursor solution with complexing agent by varying molar concentration (0.05M - 0.15M) and without complexing agent.

The glass substrates were thoroughly cleaned before dipping into the reaction bath. To do this, the substrates were degreased by washing with detergent solution. Thereafter they were degreased with ultrasonic cleaner using distilled water, acetone and isopropyl alcohol (IPA) for each 15 minutes. The degreased, cleaned surface has the advantage of providing nucleation centre for the growth of the films, hence, yielding highly adhesive and uniformly deposited films.

In the preparation of reference solution, 0.05 M SnCl_2 and 0.05 M CuSO_4 were added in 100 ml beaker. Then this solution was stirred about 10 minutes and 0.05M $\text{Na}_2\text{S}_2\text{O}_3$ solution was then added into a beaker slowly under stirred condition. The resultant solution was stirred for 20 min. The pH values of the chemical bath were adjusted to pH 1.5 by adding hydrochloric acid.

For deposition of *CTS* films on the glass substrate, they were immersed vertically into acid bath. The deposition process was carried out for 2 hours at 50 °C. After deposition the glass substrates with *CTS* films were washed by distilled water to remove the contamination in the surface. The flow chart for growth process of *CTS* thin films is shown in Figure 1.

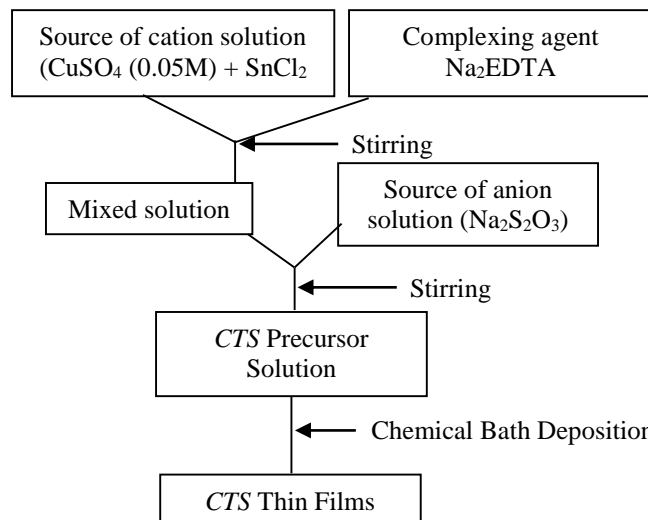


Figure 1 The flow chart for growth process of *CTS* thin films

Results and Discussion

In this section, the effect of complexing agent Na₂EDTA concentration on the optical and surface topography of *CTS* films were discussed.

Figure 2 shows the XRD patterns of *CTS* thin films chemically deposited with different molar concentrations of complexing agent (0.05 - 0.15M). The *CTS* thin films were found to be polycrystalline in nature. All the samples show four diffraction peaks at 26.69°, 30.80°, 47.22°, and 50.60° which are indexed to the (311), (112), (620), and (223) reflections of orthorhombic Cu₄SnS₄ structure. The intensity of observed major diffraction peaks increased with increasing molar concentration of complexing agent indicating the better crystallinity of *CTS* films with EDTA. The observed *d*-spacing values were compared with standard *d*-spacing values and are in good agreement with standard *d*-spacing values.

The peak positions (2θ) of the (311), (112), (620) and (223) reflections were used to calculate the lattice parameters using the following Equation

$$d = \frac{1}{[\left(\frac{h^2}{a^2} + \frac{k^2}{b^2} + \frac{l^2}{c^2}\right)]^{1/2}}$$

where, *d* is the interplanar spacing that is determined from Bragg's Law ($2d \sin\theta = \lambda$, λ is the wavelength of X-ray and θ is the Bragg's angle). The lattice parameter values for the dominant orthorhombic structure are $a = 13.6840$ Å, $b = 7.5001$ Å, $c = 6.4647$ Å for *CTS* (Non EDTA), $a = 13.6025$ Å, $b = 7.6484$ Å, $c = 6.4411$ Å for *CTS* (0.05M EDTA), $a = 13.6329$ Å, $b = 7.7164$ Å, $c = 6.4291$ Å for *CTS* (0.1M EDTA), and $a = 13.6440$ Å, $b = 7.7422$ Å, $c = 6.3244$ Å for *CTS* (0.15M EDTA). It is found that the lattice constants of *CTS* structure are not significantly altered upon introducing EDTA.

A peak of *CTS* corresponding to the plane (223) was selected to determine the crystallite size of *CTS* thin film using Scherer's equation:

$$t = \frac{0.9\lambda}{\beta \cos\theta}$$

where, *t* is the crystallite size, λ is the X-ray wavelength, β is the Full-width half-maximum (FWHM) of the peak and θ is the Bragg's angle. The crystallite size of *CTS* thin film is estimated to be 109 nm, 102 nm, 73 nm, and 82 nm for *CTS* thin film without EDTA, with 0.05 M, 0.10 M and 0.15 M EDTA respectively.

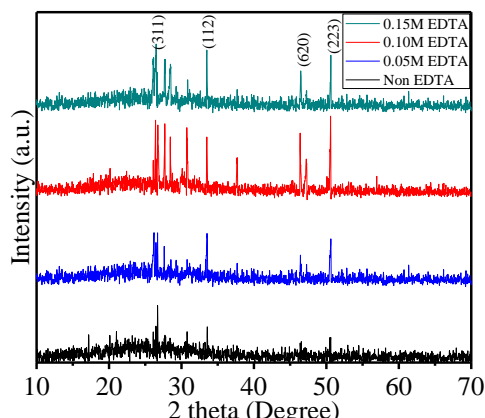


Figure 2 XRD diffraction patterns of *CTS* thin films with different molar concentration of complexing agent

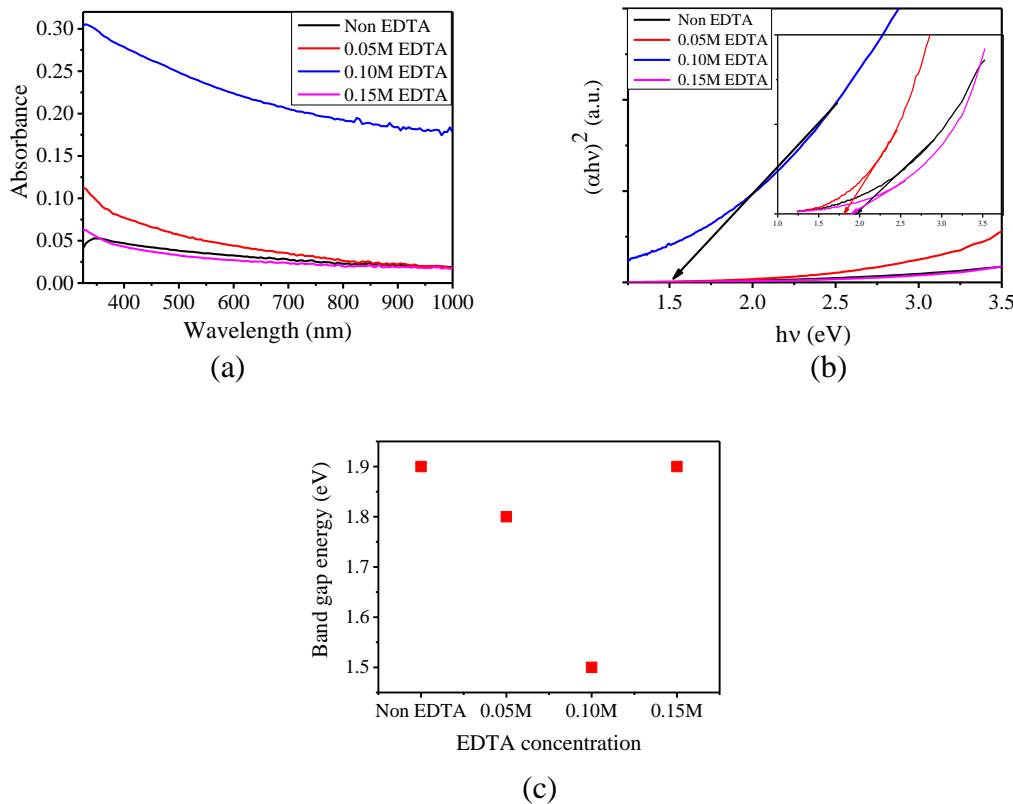


Figure 2 (a) Absorption spectra, (b) Plot of $(\alpha h v)^2$ Vs. $h v$ for *CTS* films with varying Na₂EDTA concentrations and (c) plot of E_g Vs EDTA concentration

The optical properties of *CTS* films deposited in the solution with different Na₂EDTA concentrations were observed by using UV-vis Spectrophotometry. Figure 3 (a) shows the absorption spectra of *CTS* films with varying Na₂EDTA concentration. As seen in Figure 3, the absorption of *CTS* film with 0.1M Na₂EDTA is higher than those without Na₂EDTA and with 0.05 M Na₂EDTA. This higher absorption indicates the formation of more Cu₄SnS₄ with better adhesion to the substrate under this condition. Upon further increasing EDTA concentration to 0.15 M, the absorption of *CTS* films decreased again which is probably due to the fact that complexing reaction would complete at EDTA concentration of 0.10 M and exceeding concentration of complexing agent (0.15M) hindered the deposition of *CTS* films.

Band-gap energy is a key criterion to determine if the material of interest can be used as light absorber material in solar cells. The optical band-gap energies of *CTS* films were calculated on the basis of the optical absorption spectra using Equation (3).

$$\alpha = \frac{A(hv - E_g)^n}{hv} \quad (3)$$

where, α is absorption coefficient, $h\nu$ is the incident photon energy, A is the proportionality constant, E_g is the band-gap energy and n is either 2 for indirect band gap semiconductor or 1/2 for direct band-gap semiconductor. Since *CTS* is a direct band-gap semiconductor, the optical band-gap of *CTS* was attained by plotting $(\alpha h v)^2$ versus incident photon energy ($h\nu$). Figure 3 (b) shows the plot of $(\alpha h v)^2$ vs. $h\nu$ for the *CTS* films with different Na₂EDTA concentrations where the optical band gap was deduced from the extrapolation of the linear part of the plot. The obtained band gap energies are plotted against the EDTA concentration and the plot is shown in Figure 3 (c). It is observed that the band-gap energy of *CTS* film (Non EDTA) is about 1.9 eV. The band gap energy of the *CTS* films decreased to 1.8 eV at 0.05M and 0.15 M EDTA concentration. The

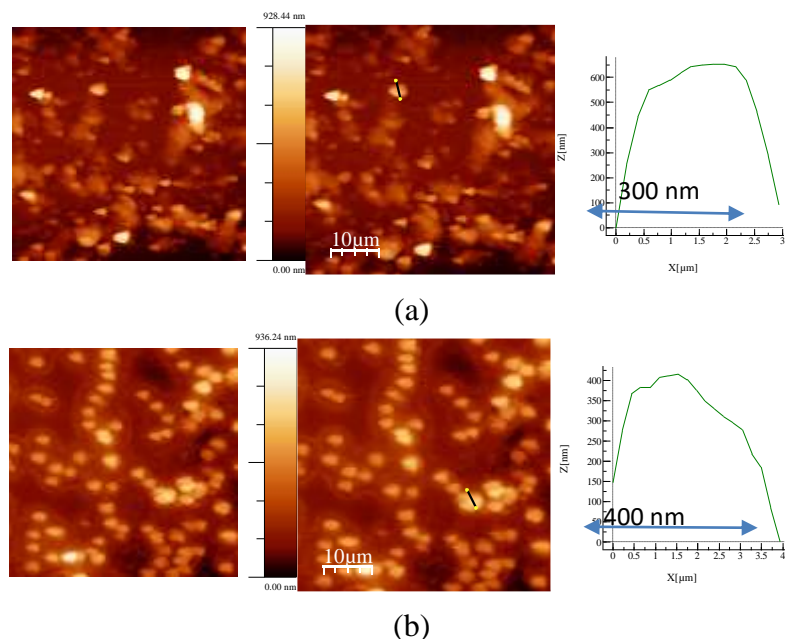
lowest band gap energy of 1.5 eV was realized for EDTA concentration of 0.1 M. The direct band gap energy of 1.5 eV is good enough for light harvesting in solar cell.

The atomic force microscopy measurements were performed to study the differences in the surface topography for the samples deposited under different concentrations of Na₂EDTA. Figure 4 shows three dimensional AFM images for an area of 50μm x 50μm of CTS films. The morphological features are readily recognized by visual inspection of Figure 4. Comparing the AFM images, it is clearly seen that the surface of the film deposited at 0.10M Na₂EDTA was found to cover the surface of the substrate completely (Figure 4 (c)).

A detail analysis on size and shape of the grains seen on the surface of the films were performed by generating the line profiles shown on the right side of the AFM images. From the line profiles, the average grain size is 300 nm, 400 nm, 800 nm and 300 nm for CTS film with Non EDTA, 0.05M EDTA, 0.10M EDTA and 0.15M EDTA respectively. There are several big grains in the film obtained by 0.10M EDTA solution, which is due to the agglomeration of the smaller crystallites. However, the images show the film is more uniform and compacter than that prepared in the other concentrations of Na₂EDTA. The thin film obtained with Non EDTA and 0.05M EDTA are very thin, not compact and incomplete coverage over the substrate surface (Figure 4 (a) and (b)).

The thickness of the films was studied using AFM images. At the right side of the images, an intensity strip is shown, which indicates the depth and height along the z-axis. The thickness of the film was increased from 930 nm to 2200 nm as the concentration of Na₂EDTA increased from 0.05M to 0.1M. However, the thickness was reduced (595 nm) as the concentration of EDTA was further increased to 0.15M. It is probably due to the complexing reaction was complete with high concentration (0.1M) of complexing agent. Therefore, hinders the deposition of the films. The thicknesses of the films were listed in Table 1.

The roughness parameter is the most used parameter for observation of changes in surface topography. The surface roughnesses of the films were obtained using the analysis software (WSxM 5.0). The roughness values are calculated over the surface area of 50μm x50μm of CTS films and listed in Table 1. It is noted that the RMS (root mean square) roughness increase with increasing the concentration of the solution up to 0.10M EDTA. This may be due to the larger grain size of films. But the molar concentration (0.15M EDTA), the RMS (root mean square) roughness decrease again which is due to the thickness of the film was reduced.



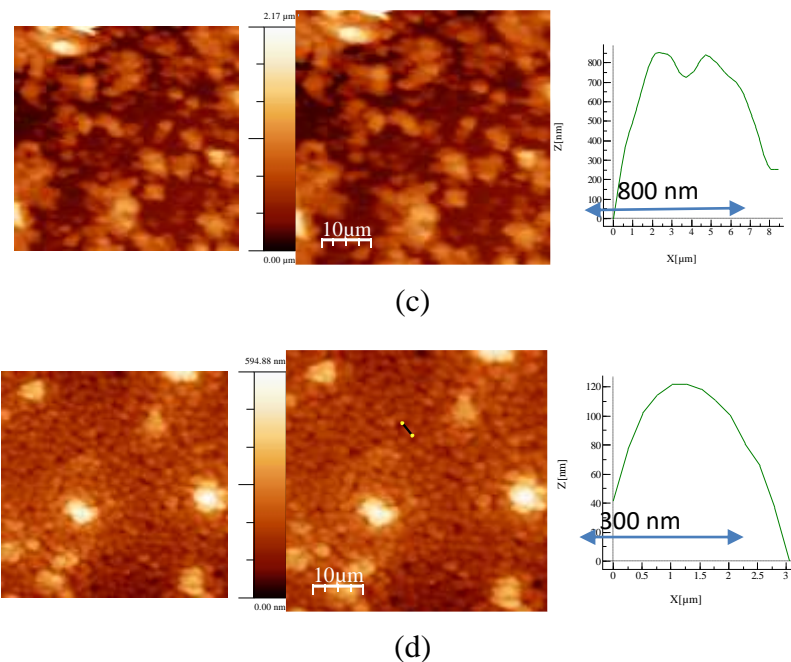


Figure 4 Atomic force microscopy images of *CTS* thin films chemically deposited in the solution of different concentration of (a) Non EDTA (b) 0.05M EDTA (c) 0.10M EDTA (d) 0.15M EDTA. The line profiles correspond to the markings in the AFM images.

Table 1 The film thickness and RMS (root mean square) roughness for *CTS* films

EDTA concentration	Film thickness (nm)	RMS roughness (nm)
Non	~930	103.29
0.05M	~935	108.40
0.10M	~2200	254.10
0.15M	~595	59.39

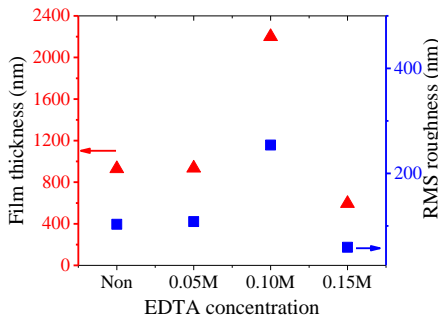


Figure 5 Plot of film thickness and RMS surface roughness of *CTS* films against EDTA concentration

Summary and Conclusion

Copper tin sulphide (*CTS*) films were deposited on glass substrates using chemical bath deposition method. The effect of complexing agent (Na_2EDTA) concentration on the structural, optical properties and surface topography were investigated. The XRD showed that *CTS* films exhibit orthorhombic structure with preferential orientation along the (223) plane. The *CTS* films deposited with 0.1M Na_2EDTA concentration have narrow optical band-gap which is the requisite for light absorber layer in solar cell application. The band gap was found to be 1.5 with direct transition.

Acknowledgements

First of all, I would like to thank Dr Khin Maung Oo, Rector, University of Magway, and Dr Than Than Oo, Pro-rector, University of Magway for their kind permission to carry out this work. Also, I am thankful to Professor, Dr Sandar Maung, Professor, Head of Department of Physics, University of Magway, for her encouragement for my research. Finally, I am deeply grateful to Dr Than Zaw Oo, Professor, Department of Physics, Yangon University, for his excellent advice and continuous guidance throughout this research work.

References

- A. Kassim *et al.*, J. Chem. Chem. Eng., **29** (1) (2010) 97.
- A. Kassim *et al.*, Bull. Chem. Soc. Ethiop., **24** (2) (2010) 259.
- A. Kassim *et al.*, Mater. Sci.(Medziagotyra), **14** (2008) 101.
- C. Gautier *et al.*, Thin Solid Films, **315**(1998) 118.
- M. Atif *et al.*, Appl. Surf. Sci., **253** (2006) 1198.
- M. Ristov *et al.*, Sol. Energ. Mater. Sol. Cells, **69**(2001) 17.
- N. Kamoun *et al.*, Thin Solid Films **515** (2007) 5952.
- S. Seghaier *et al.*, Mater. Chem. Phys., **97**(2006) 71.
- W. Li *et al.*, J. Solid State Electrochem., **10** (2006) 48.
- Z. Zainal *et al.*, Mater. Sci. Eng., **107** (2004) 181.

CODE TRACKING FOR GPS SIGNAL PROCESSING

Nay Min Aung¹

Abstract

This paper presents the code tracking method for software defined GPS receiver. A number of methods have been developed to enhance the robustness of Global Positioning System (GPS) receivers when there are a limited number of visible satellites. In this work, code tracking method is developed to improve the accuracy of positions of GPS receiver. The GPS signal consists of the navigation data, the carrier and code sequences for each of the satellite. The signal of each satellite is demodulated using Delay Lock Loop (DLL) for code tracking. The code tracking output errors feedback to Numerically Control Oscillator (NCO) frequency for exact signal lock between GPS signal and NCO signal. In position calculation, each channel of code is controlled by individual loop filter. The code tracking method for software defined GPS receiver is implemented by using MATLAB.

Keywords: *GPS software receiver, code tracking method, Delay Lock Loop, MATLAB, Numerically Control Oscillator*

Introduction

Satellite based navigation systems provide real time position, velocity and timing information of receiver. The most commonly used navigation system in today's world is Global Positioning System (GPS). The GPS system is a code division multiple access (CDMA) digital communication link. CDMA is a spread spectrum multiple access technique. Each satellite's signal consists of a sinusoidal carrier, a digital navigation message, and a unique wide bandwidth pseudo random noise (PRN) sequence. The navigation data from the satellites comprises of the orbital information of the satellite and precise timings.

Theoretical Background

2.1 Coarse Acquisition (C/A) Code Sequence

Each satellite has two unique codes spreading sequences. The first one is the coarse acquisition code (C/A), and the other one is the encrypted precision code (P(Y)). The C/A codes have a very wide bandwidth and are used to spread the spectrum of the data message over a wider bandwidth. The C/A codes are transmitted at a chipping rate of 1.023 Mbps. The code phase is the point in the current data block where the C/A code begins. If a data block of 1 ms is examined, the data include an entire C/A code and one beginning of a C/A code.

2.2 Coarse Acquisition (C/A) Code Tracking

To obtain a perfectly aligned replica of the code, code tracking loop is implemented. The goal of the code tracking loop is to keep track of the code phase of a specific code in the signal. The code tracking loop in the GPS receiver is a delay lock loop (DLL) called an early-late tracking loop. DLL block diagram with six correlators is shown in Figure (2). After multiplying the incoming signal with a perfectly aligned local replica of the carrier wave, the signal is multiplied with three code replicas, namely early, prompt and late, with a spacing of $\frac{1}{2}$ chips. After the second multiplication, the three outputs are integrated and dumped. The output of these integrations is numerical value indicating how much the specific code replica correlates with the incoming signal. A perfectly tuned code loop with highest correlation at prompt output is shown in figure (1). The

¹ Lecturer, Department of Physics, Monywa University

prompt replica of the code has a phase shift obtained from the acquisition. The early and late have additional shift of $-1/2$ and $+1/2$ chip from the prompt.

The common DLL discriminators are:

Coherent: $I_E - I_L$: Requires a good tracking loop for optimal functionality.

Noncoherent:

$(I_E^2 + Q_E^2) - (I_L^2 + Q_L^2)$: Early minus Late power, response is nearly the same as the coherent discriminator.

$\frac{(I_E^2 + Q_E^2) - (I_L^2 + Q_L^2)}{(I_E^2 + Q_E^2) + (I_L^2 + Q_L^2)}$: Normalized Early minus Late power, helps keep track in noisy signals when the chip error is larger than $1/2$ chips.

$I_P(I_E - I_L) + Q_P(Q_E - Q_L)$: Dot product, it is the only DLL discriminator that uses all six correlators.

The implemented tracking loop discriminator is the Normalized Early Minus Late power discriminator. This discriminator is described as

$$D = \frac{(I_E^2 + Q_E^2) - (I_L^2 + Q_L^2)}{(I_E^2 + Q_E^2) + (I_L^2 + Q_L^2)}$$

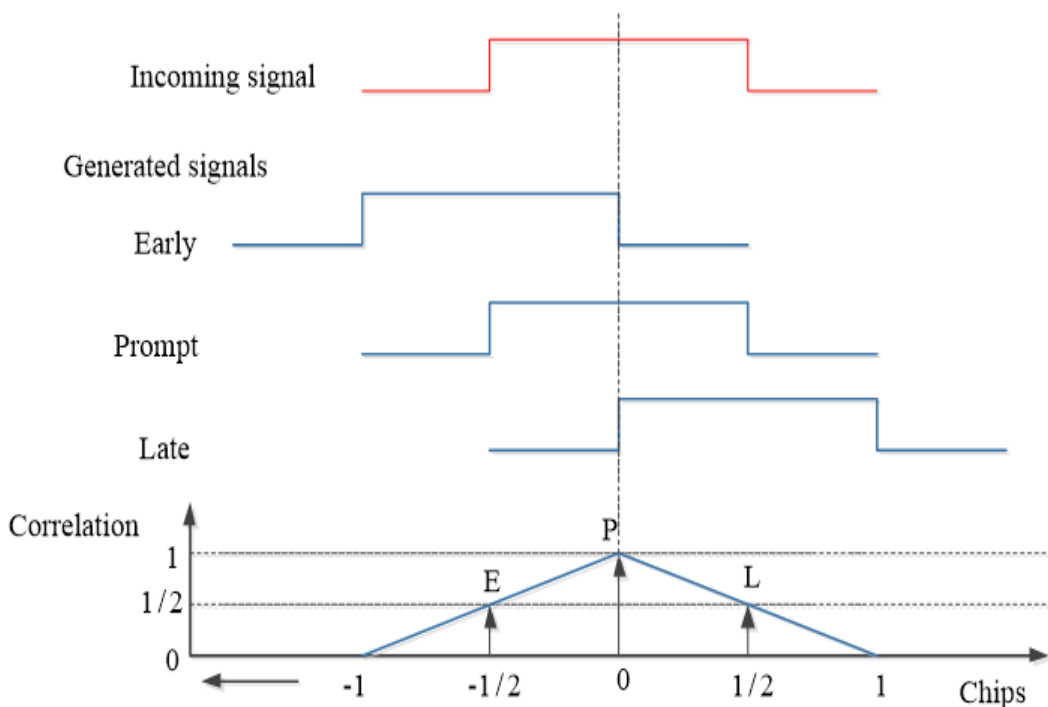


Figure 1 A perfectly tuned code loop with highest correlation at prompt output

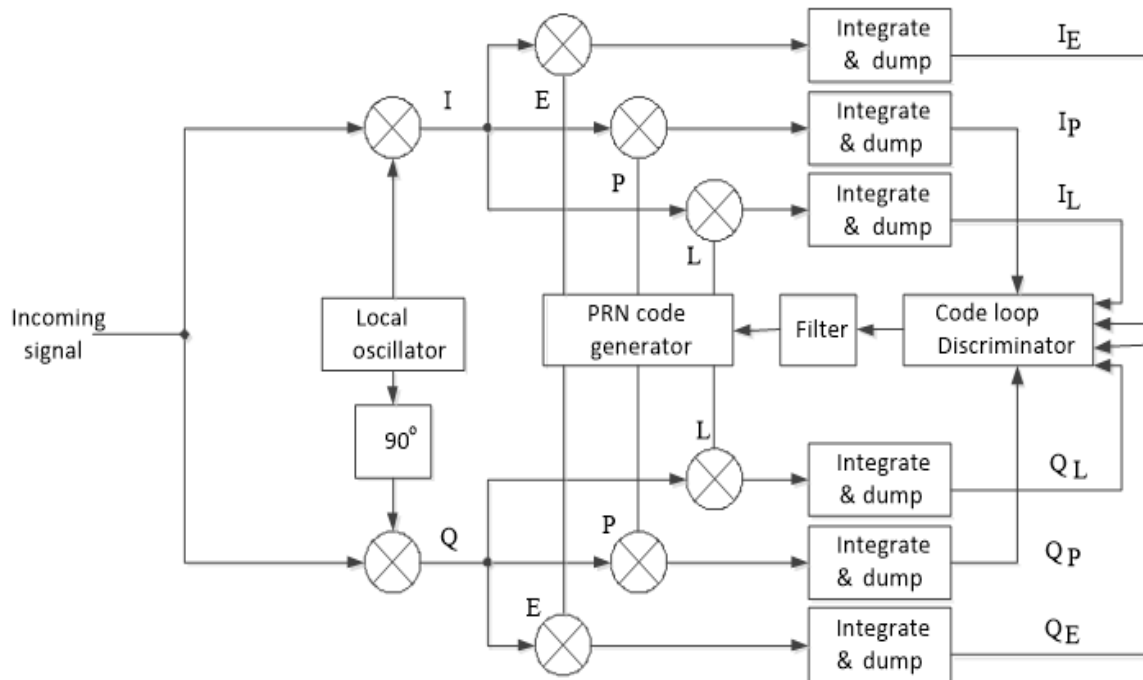


Figure 2 Delay Lock Loop (DLL) block diagram with six correlators

Experiment

3.1 Experiment apparatus

In this experiment, the GPS signal is captured by SiGe SE4110L front-end receiver and the sampling parameters are

- frequency of the received signal is about 1575.42 MHz
- intermediate frequency (IF) 1.364MHz and
- sampling frequency is 5.456MHz.

3.2 Received satellites positions skyplot

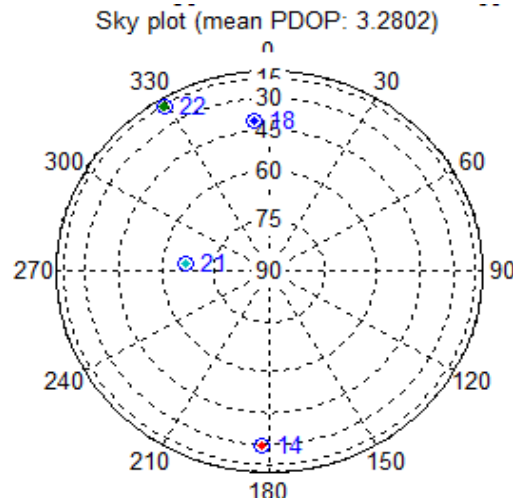


Figure 3 Mean position dilution of precision

The position dilution of precision plot shows satellites coverage on the receiver position with respective latitude and longitude coordinates. In Figure-3, the four satellites are scattered with the different elevation angles.

Result and Discussions

The I-prompt and Q-prompt arms of GPS signals are compared for each satellite (PRN) that all the power is in the in-phase of signal. Each of the scatter points has the phase angle from the discriminator output on the discrete time scatter plot. From discrimination data, the satellite number (PRNs) 14 and 18 have weak signal as shown in figures 4(a), (b) and figures 5(a), (b). The discrete time scatter points are scattered and continuous in both sides of Q prompt and I prompt for weak signal.

The satellite number (PRNs) 21 and 22 have strong signal as shown in figures 6(a), (b) and figures 7(a), (b). For the strength signal the power has in the I-prompt arm and Q-prompt arm has near zero in correlation. The discrete time scatter points are collected and separated in both sides of Q prompt and I prompt for strong signal. From the discrimination data of GPS signal, the satellite PRNs 21 and 22 have strong signals than PRNs 14 and 18.

The scattered positions variation from mean position is shown in figure (8). This discrimination data depends on the position of GPS receiver and the strong signal provide the exact position of the GPS receiver.

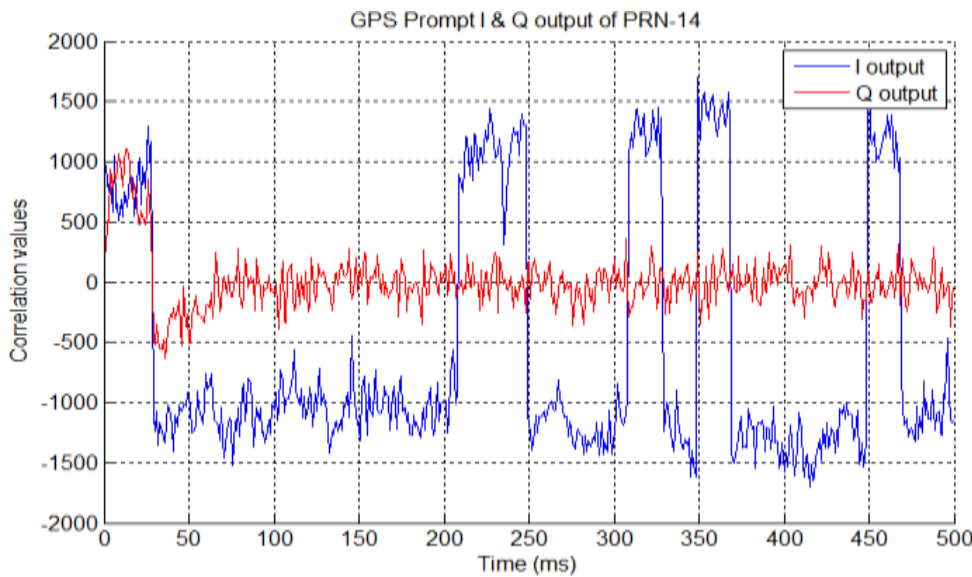


Figure 4(a) Output of prompt arms for C/A code-14

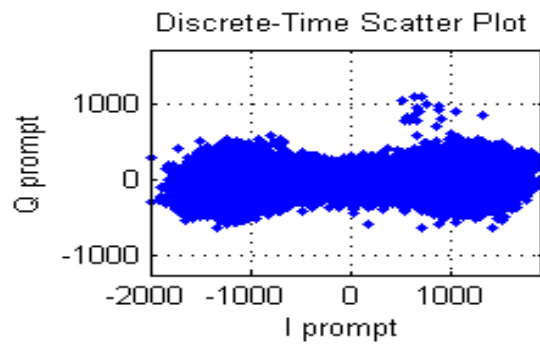


Figure 4 (b) Discrete time scatter plot for PRN -14

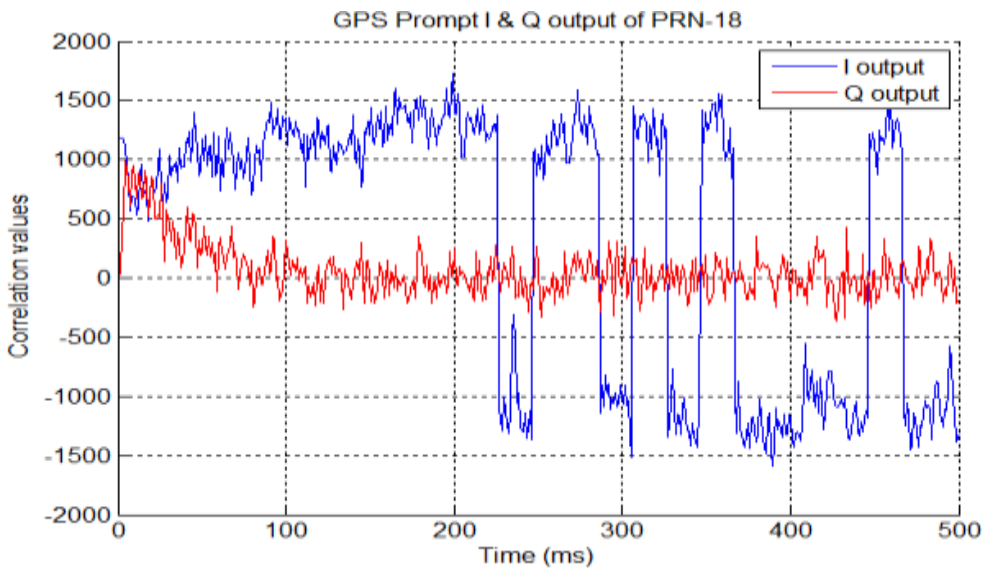


Figure 5 (a) Output of prompt arms for C/A code-18

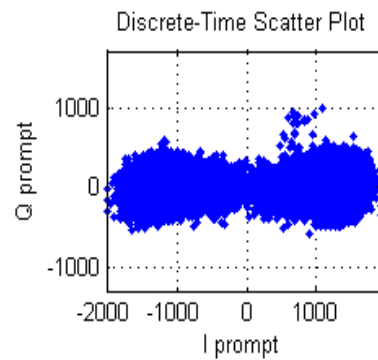


Figure 5 (b) Discrete time scatter plot for PRN -18

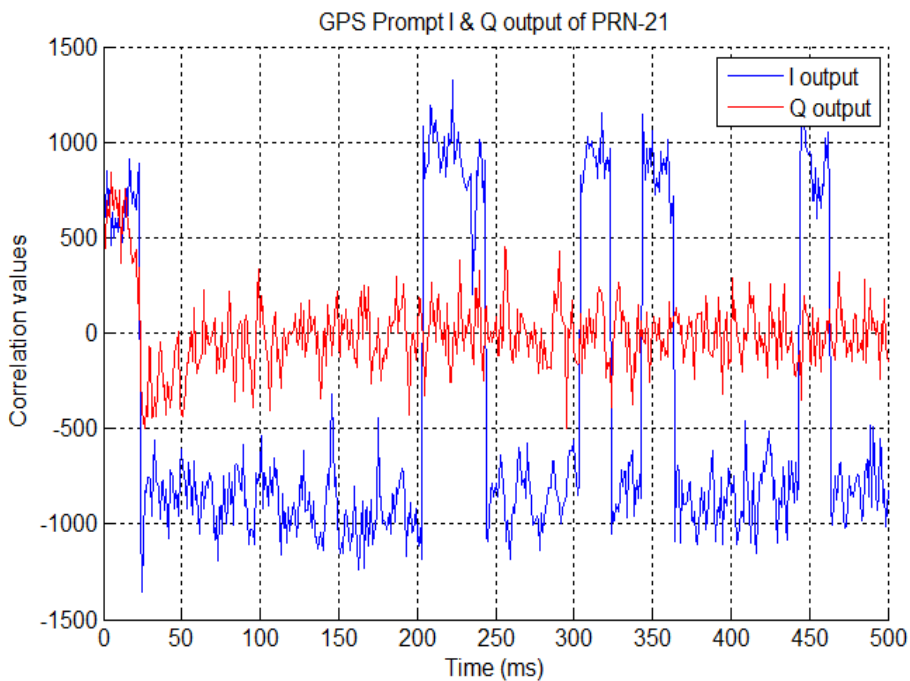


Figure 6 (a) Output of prompt arms for C/A code-21

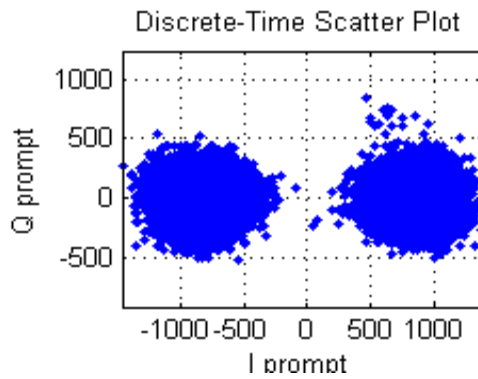


Figure 6 (b) Discrete time scatter plot for PRN -21

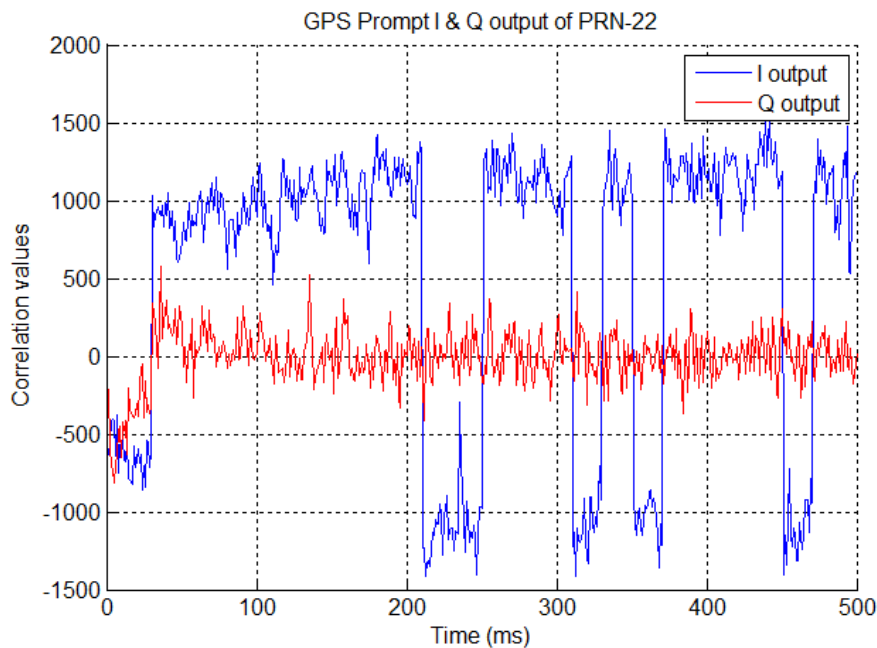


Figure 7 (a) Output of prompt arms for C/A code-22

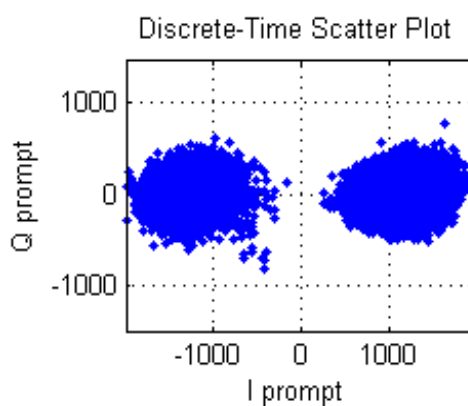


Figure 7 (b) Discrete time scatter plot for PRN -22

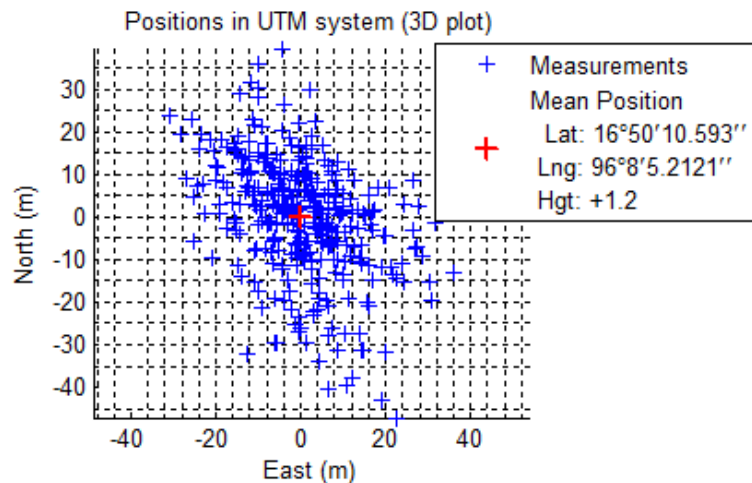


Figure 8 The scattered positions variation from mean position

The measurement points show the track of positions of the GPS receiver with latitude and longitude coordinates. The mean measurement position shows the positions of the GPS receiver with latitude, longitude and altitude coordinates.

Conclusion

The code tracking loop is based on delay lock loop filter design which relates between the GPS receiver navigation solutions and the code phase and carrier frequency of the received signal. The code tracking algorithm has been developed in MATLAB-based software for GPS satellite data demodulation. The GPS signals are down-convert to baseband signal and discriminated for error values. Then the errors are filtered and given the command NCO to add the generated frequency. Minimum four satellites are required for receiver position calculation and the code tracking are important for exact receiver position. The results demonstrate that if there are four or fewer satellites available, the proposed code tracking loop can maintain tracking on a satellite signal and generate reasonable navigation solutions.

Acknowledgements

The author is very grateful to Professor Dr Ye Chan within the Department of Physics, Universities' Research Centre, University of Yangon, for his valuable guidance throughout this work.

References

- E. D. Kaplan and C. Hegarty, “Understanding GPS: Principles and Applications”, 2nd Ed, Artech House Inc, 2006.
- K. Borre, D. Akos, N. Bertelsen, P. Rinder, and S. H. Jensen, “A Software-Defined GPS and Galileo Receiver: A Single-Frequency Approach”. Springer, New York, 2007.
- Z. Zhu, G. Tang, Z. Cheng and K. Huangfu, “GPS Signal Tracking Algorithm Based-on Vector Delay Locked Loop”. Progress in Natural Science, 2009.

STUDY ON EFFECT OF ISOVALENT BARIUM IONS SUBSTITUTION ON STRUCTURAL FEATURES, FERROELECTRIC PROPERTIES AND BANDGAPS OF LEAD TITANATE

Pwint Yi Thein^{1,*}, Lai Lai Khine², Ye Myint Win³, Amy Than⁴,
Mar Mar Myint¹ and Yin Yin Swe¹

Abstract

Isovalent Ba ions substituted lead titanate is studied by means of its structural features, ferroelectric properties and bandgaps. Analar grade PbO, TiO₂ and BaCO₃ are chosen and used as starting materials. Three starting materials are weighted and mixed by the stoichiometric composition: Pb_(1-x)Ba_(x)TiO₃, where x = 0, 1 mol%, 2 mol%, 3 mol%, 4 mol% and 5 mol% respectively. The mixture powders are grinded by using agate mortar for each 5 hrs. Then, the mixture powders are conventionally sintered at 700°C for each 5 hrs. After first sintering process, the mixture powders are grinded again by using ball milling for each 5 hrs. Finally, the mixture powders are sintered at 700°C for each 5 hrs. X – rays diffraction technique is used to examine the phase formation and structural features of PbTiO₃:Ba specimens. From the XRD studies, lattice constants, lattice distortion, unit cell volume, crystallite size and lattice micro strain are estimated. Ferroelectric properties of PbTiO₃:Ba specimens are characterized by using Sawyer – Tower circuit. Spontaneous polarization, remanent polarization and coercive field of PbTiO₃:Ba specimens are evaluated. Optical bandgaps of PbTiO₃:Ba specimens are studied by using UV – Vis spectrophotometer. From the absorption spectra, bandgaps are calculated. XRD results indicates that, there are no significant change of tetragonal perovskite type PbTiO₃ structure after Ba substitution. A little changes of structural features are observed and it is due to appearance of micro strain and defects, dislocations and vacancies in host PbTiO₃ structure during the doping mechanism. Ferroelectric properties, such as spontaneous polarization, remanent polarization and coercive field slightly increase as additional Ba content increases, due to second- order hybridizations, caused by isovalent Ba ions in PbTiO₃ lattice. Optical bandgap of PbTiO₃ is enhanced when additional Ba content is raised. It is expected that, there are a quantum confinement effect in PT: Ba specimens.

Keywords: PbTiO₃, additional Ba content, structural features, ferroelectric properties, bandgap

Introduction

Intensive research has been focused on ferroelectric materials in the last decade with particular emphasis on new processing and characterization techniques. Materials with perovskite - type crystalline structure are developed for their potential applications in the field of electronic, microelectronic and optoelectronic devices. In particular, the PbTiO₃ material has piezoelectric and ferroelectric properties at room temperature with bandgap of 3.4 eV in the tetragonal symmetry, special group P4mm and lattice parameters a = b = 3.904 Å and c = 4.152 Å [Zelezly V. et al., 2016].

In the cubic symmetry, PbTiO₃ materials has spacial group Pm3m with lattice parameter a = 3.865 Å and bandgap is around 3.6 eV. PbTiO₃ has received special attention due to it's applications, such as pyroelectric infrared detectors, piezoelectric sensors, optical switches, DRAM and NVRAM devices. There is a tetragonal to cubic phase transition at ~ 490 °C in PbTiO₃, which changes the piezoelectric and ferroelectric properties. Pure PbTiO₃ has large tetragonal

¹ Department of Physics, Nationalities Youth Resource Development Degree College, (Yangon), Myanmar.

² Department of Physics, University of Dagon, Myanmar.

³ Department of Physics, Defence Services Academy, Pyin Oo Lwin, Myanmar.

⁴ Department of Physics, University of Yangon, Myanmar.

* - Corresponding author, Susan74june@gmail.com.

distortion at room temperature, approximately 1.064, which introduces a stress upon the cooling through the phase transition [Zelezly V. 2016; Moudavi S. J. and Pourhabib -Yekta A. 2011].

For the electronic, microelectronic and optoelectronic applications, the properties of PbTiO₃ based materials can be enhanced by substitutions of the alkali, rare - earth, and transition metals/materials in the perovskite type PbTiO₃ based materials. At present, much attention has been paid to the lead based perovskite - type compounds and their solid solutions, due to a variety of physical properties and a wide range of industrial applications. Depending on the ionic/covalent radii and charge, ordering of cations may occur which gives rise to different structural and physical properties. Considerable amount of works has been carried out on A site, B site and A/B site in ABO₃ - type PbTiO₃ with different substituents. However, an annealing process is often accompanied by undesired secondary phases, such as substituent oxides. In the recent years, the substitutions of suitable ions either A, B and A/B site in the perovskite lattice has governed much attention [Scott J. F. 2008].

Among the suitable substituents, Ba ions are widely used to examine the structural, optical, magnetic, ferroelectric and piezoelectric properties of PbTiO₃ [Zhen X. et al.,2012; Ponte F. M. 2016]. In this research work, Ba substituted PbTiO₃ specimens are studied by means of its structural features, ferroelectric properties and optical bandgaps.

Experimental Procedure

Additional Ba substituted PbTiO₃ specimens are prepared by using conventional solid state sintering. Analar grade PbO, TiO₂ and BaO are used as starting materials. Three starting materials are weighted and mixed by the stoichiometric composition: Pb_(1-x) Ba_(x) TiO₃, where x = 0, 1 mol%, 2 mol%, 3 mol%, 4 mol% and 5 mol% respectively. The mixture powders are grinded by agate mortar for each 5 hrs. After that, the mixture powders are conventionally sintered at 700°C for each 5 hrs. After first sintering, the mixture powders are grinded again by using ball - milling process for each 5 hrs. Then, the mixture powders are conventionally sintered again, for each 5 hrs. X - rays diffraction technique is used to determine the phase formation and structural features of the PbTiO₃: Ba specimens by means of Rigaku Multiflux with Cu k_α monochromatic radiation ($\lambda = 1.542 \text{ \AA}$). PbTiO₃: Ba specimens are scanned from 2Θ ($\Theta = \text{Bragg's angle}$) in the range from 10° to 70° with a scanned speed of 0.01°/sec. Applied voltage and current of the Rigaku Multiflux are set to be 50 kV and 50 mA.

X - rays spectra are recorded at room temperature. From the x-rays spectra, lattice constants, lattice distortion, unit cell volume, crystallite size and lattice micro strain are estimated. Furthermore, effects of additional Ba substitution on lattice constants, lattice distortion and unit cell volume are studied.

PbTiO₃: Ba specimens are uniaxially pressed with 19.5 tons press into circular shape disc with 20 mm in diameter and 3.5 mm in thickness. Silver pastes are coated onto both surface of the specimens with the area of (7.06 mm²). Sawyer - Tower circuit is used to characterized the ferroelectricity of PbTiO₃: Ba specimens. Thermal hysteresis loops were recorded on oscilloscope (Gwinsteck, GDS -1152 A-U, 50 MHz). Applied voltage and frequency will set to 10Vpp and 10 kHz. Ferroelectric properties, such as spontaneous polarization, remanent polarization and coercive field of the PbTiO₃:Ba specimens are evaluated.

Optical bandgaps of the PbTiO₃: Ba specimens are determined by using UV - Vis spectrophotometer (UV 1800 Shimadsu) in the wavelength from 190 nm to 700 nm with 1.0 nm resolution and wavelength accuracy is $\pm 0.01 \text{ nm}$. UV 1800 consists of deuterium: tungsten halogen lamp source and attached with UV Probe. The optical bandgap measurement involves the excitation of electrons from valence band to conduction band using photons of selected frequency.

The process does not change the number of carriers involved and total numbers of carriers presented in the PbTiO₃: Ba specimens remain the same. From the absorption spectra, optical bandgaps of PbTiO₃: Ba specimens are studied.

Results and Discussion

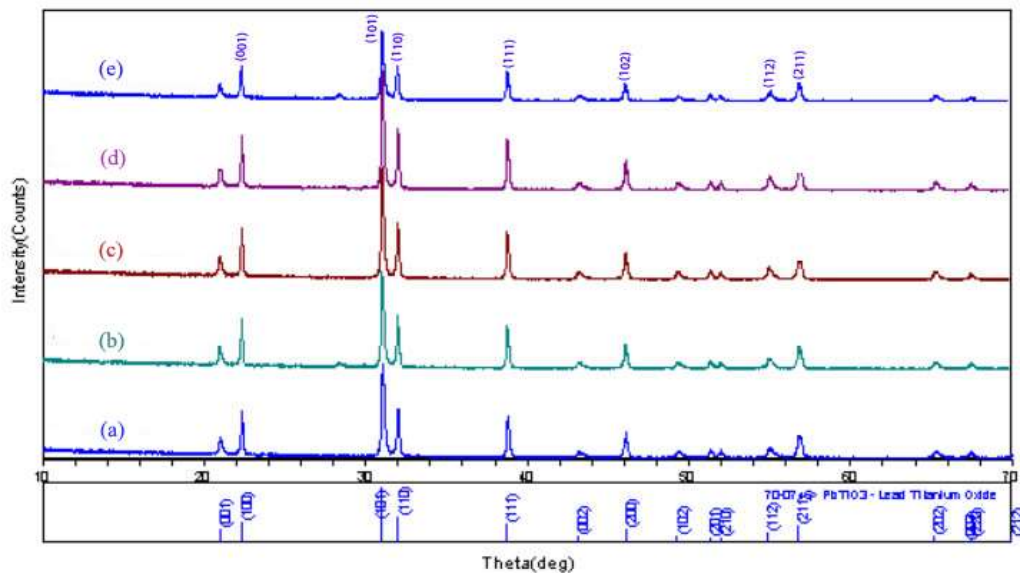


Figure 1 XRD spectra of (a)PbTiO₃ : Ba (1 mol %)specimens (b)PbTiO₃:Ba (2mol %) specimens (c)PbTiO₃ : Ba (3mol %) specimens (d)PbTiO₃:Ba (4mol %) specimens and (e)PbTiO₃:Ba (5mol %) specimens

X - diffraction spectra of PbTiO₃: Ba specimens are shown in figure (1). Peak search algorithm, known as Jade software is used to identify the unknown peaks in this research work. Only diffraction peaks from polycrystalline, tetragonal, perovskite - type PbTiO₃ structure with reference (70 - 0746 > JCPDS file) are observed. In addition, (101) peak is the most intense peak, known as Bragg peak and a little shift of (101) peak position (2Θ value) is obtained in all spectra. These results can be interpreted as additional Ba substituents are diluted into host PbTiO₃ structure. Furthermore, sharp diffraction peaks are found in all spectra. It is due to higher degree of crystallinity of PbTiO₃: Ba specimens. From the x-rays spectra, lattice constants of the PbTiO₃: Ba specimens are examined by using the equation (1):

$$\frac{1}{d^2} = \frac{h^2+k^2}{a^2} + \frac{l^2}{c^2} \quad (1)$$

Where, d = interplanar spacing

h, k, l = miller indices

a, c = lattice parameters

Interplanar spacing ‘d’ values from (110) and (101) planes are substituted in equation (1) and, lattice parameters ‘a’ and ‘c’ are estimated.

Unit cell volumes of PbTiO₃: Ba specimens are estimated by using the equation (2):

$$\text{Unit cell volume} = a \times a \times c \quad (2)$$

Lattice constants, lattice distortion and unit cell volume of PbTiO₃: Ba specimens are listed in table (1).

Table 1 List of lattice constants, lattice distortion and unit cell volume of PbTiO₃:Ba specimens.

Ba Content (%)	Lattice parameter "a (Å)"	Lattice parameter "c (Å)"	Lattice distortion	Cell Volume (x 10 ⁻³⁰ m ³)
1	3.897	4.134	1.0608	62.792
2	3.899	4.131	1.0595	62.815
3	3.902	4.129	1.0582	62.859
4	3.905	4.126	1.0566	62.906
5	3.908	4.124	1.0553	62.971

Crystallite size and lattice micro strain of the PbTiO₃:Ba specimens are investigated by using the Debye - Scherrer equations (3) and (4) :

$$D = \frac{0.9\lambda}{\beta \cos\theta} \quad (3)$$

$$\varepsilon = \frac{\beta}{4\tan\theta} \quad (4)$$

In this equation, β is full width at half of the most intense peak maximum (FWHM) and λ is the wavelength of the using X-ray and Θ is the peak position, is known as Bragg's angle.

Crystallite size and lattice micro strain of PbTiO₃: Ba specimens are listed in table (2).

Table 2 List of crystallite size and lattice micro strain of PbTiO₃: Ba specimens.

Ba Content (%)	Crystallize size (nm)	Micro strain (x 10 ⁻³)	FWHM of (101) plane (Rad) (x10 ⁻³)
1	29.52	4.073	4.887
2	29.34	4.098	4.917
3	29.08	4.134	4.961
4	28.87	4.164	4.997
5	28.64	4.198	5.037

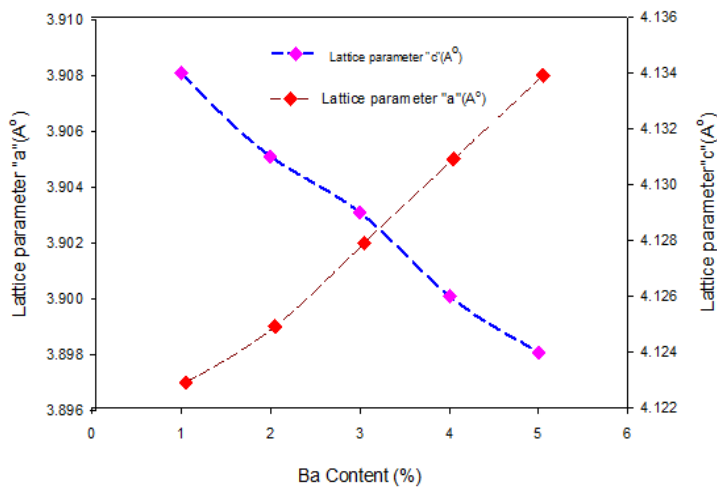


Figure 2 Variation of additional Ba content with lattice constants of sPbTiO₃:Ba specimens.

Figure (2) shows the variation of additional Ba content with lattice constants of PbTiO₃:Ba specimens. It is obvious that, lattice constant " a " increases with increasing additional Ba content, on the other hand, lattice constant " c " decreases.

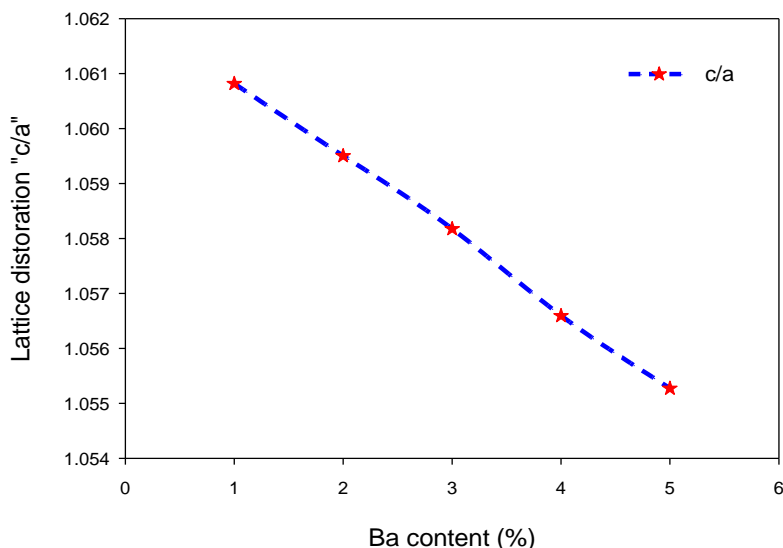


Figure 3 Influence of additional Ba content on the lattice distortion (c/a) of PbTiO₃: Ba specimens.

Figure (3) depicts the influence of additional Ba content on the lattice distortion (c/a) of PbTiO₃: Ba specimens. It is studied that; lattice distortion is lowered when the additional Ba content is raised.

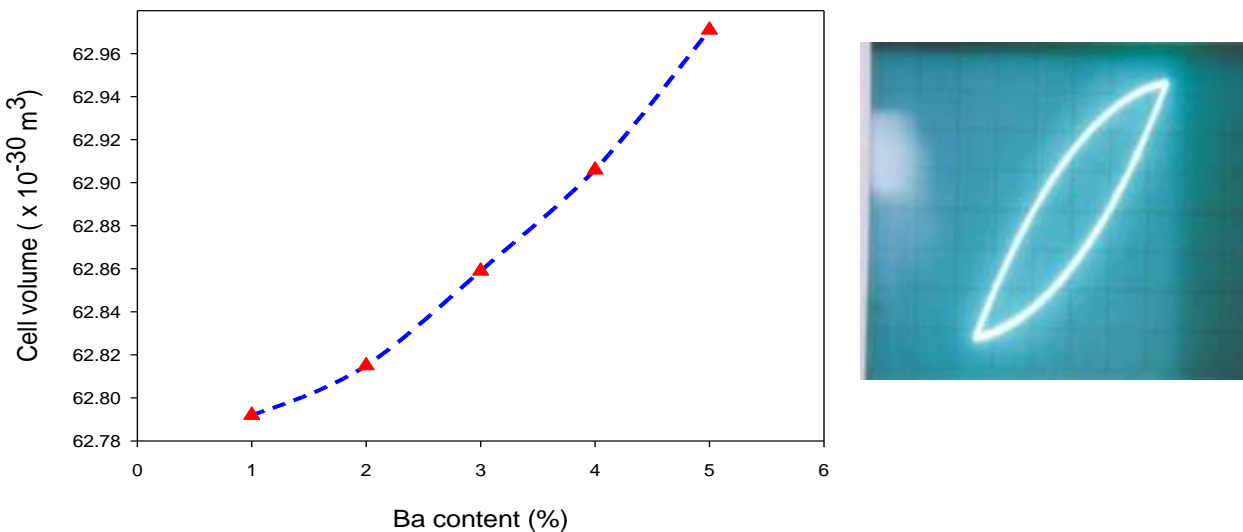


Figure 4 Effect of additional Ba content on unit cell volume of PbTiO_3 : Ba specimens.

Figure (4) illustrates the effect of additional Ba content on unit cell volume of PbTiO_3 :Ba specimens. It is found that, unit cell volume slightly increases as additional Ba content increases.

During the doping process, there are appearance of lattice micro strain, defects, dislocations and vacancies in host PbTiO_3 specimens. Consequently, variations of additional Ba content with structural features are observed.

Ferroelectricity of PT: Ba specimens is examined by using Sawyer - Tower circuit, as depicted in figure (5).

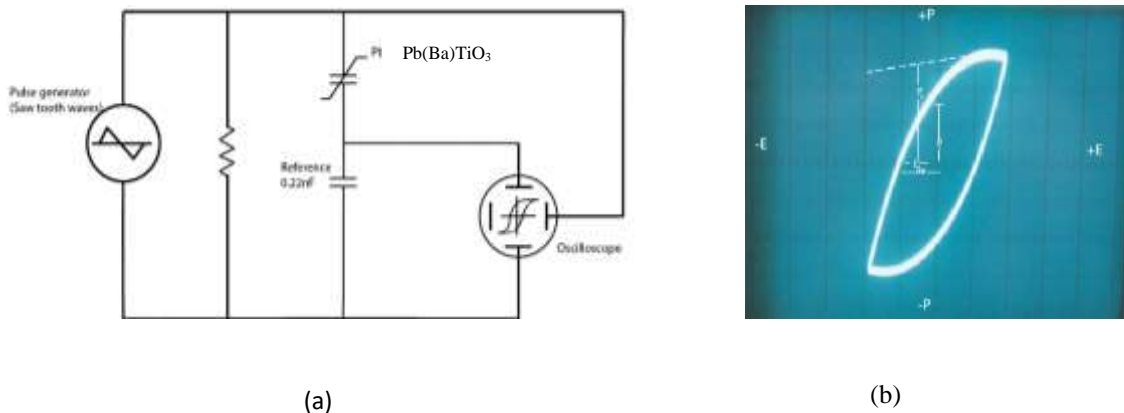
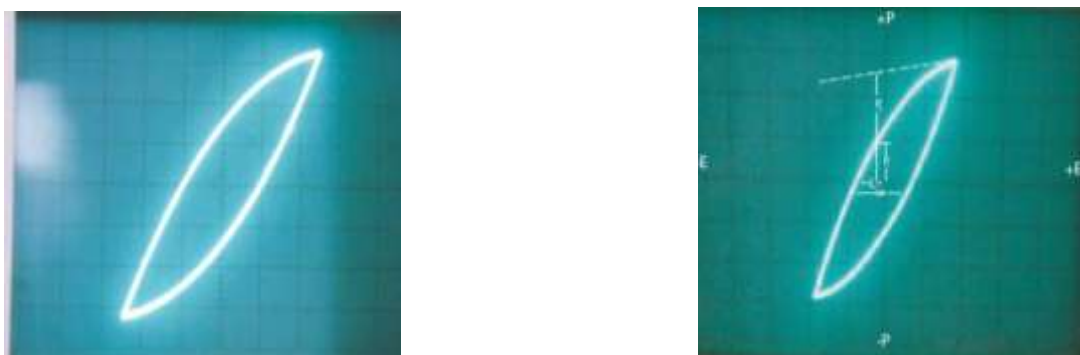


Figure 5 (a) Sawyer - Tower circuit , and (b) estimation of P_r , P_s , and E_c .



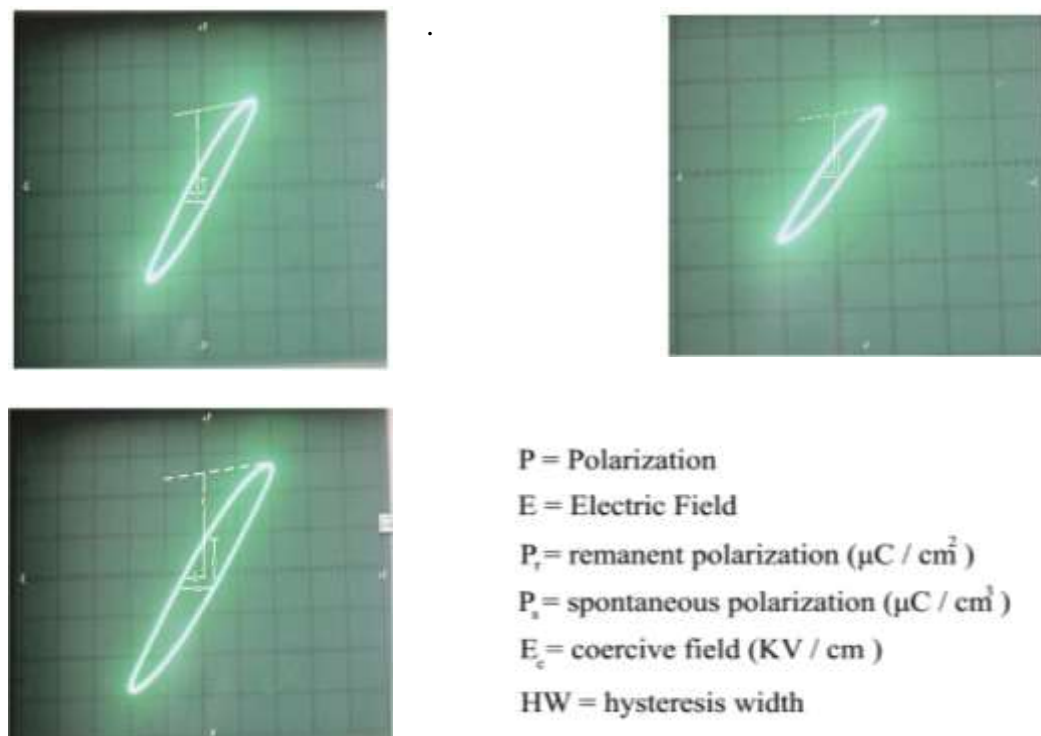


Figure 6 Ferroelectric hysteresis loops of Ba modified PbTiO_3 structures of (a) $\text{PbTiO}_3 : \text{Ba}$ (1 mol %) specimens (b) $\text{PbTiO}_3 : \text{Ba}$ (2 mol %) specimens (c) $\text{PbTiO}_3 : \text{Ba}$ (3 mol %) specimens (d) $\text{PbTiO}_3 : \text{Ba}$ (4 mol %) specimens and (e) $\text{PbTiO}_3 : \text{Ba}$ (5 mol %) specimens

According to first principle calculations on ferroelectric perovskite, hybridization between the electronic states of A or B ions and oxygen atom is essential for ferroelectricity. In addition, polarization in lead titanate arises from the distortion caused by $6s^2$ lone pairs of Pb combined with the displacement of empty Jahn Teller (J T) Ti d^6 ions [Turik A. V. and Khasabov A. G. 2000]. Situation, remanent, and coercivity are observed in all thermal hysteresis loops, as displayed in figure (6). Ferroelectric parameters, such spontaneous polarization, remanent polarization and coercive field are estimated and listed in table (3).

Table 3 List of ferroelectric parameters of $\text{PbTiO}_3 : \text{Ba}$ specimens.

Ba Content (%)	Spontaneous polarization $P_s(\mu\text{C}\cdot\text{cm}^{-2})$	Remanent polarization $P_r(\mu\text{C}\cdot\text{cm}^{-2})$	Coercive field $E_c (\text{kV cm}^{-1})$
1	11.4	2.4	3.6
2	11.6	2.6	3.9
3	11.9	2.8	4.1
4	12.2	3.1	4.3
5	12.6	3.4	4.6

It is studied that, ferroelectric parameters are enhanced when additional Ba content is raised. It may be due to, second - order hybridizations between Ti - O and Pb (Ba) - O, lead to enhance the ferroelectricity in $\text{PbTiO}_3 : \text{Ba}$ specimens.

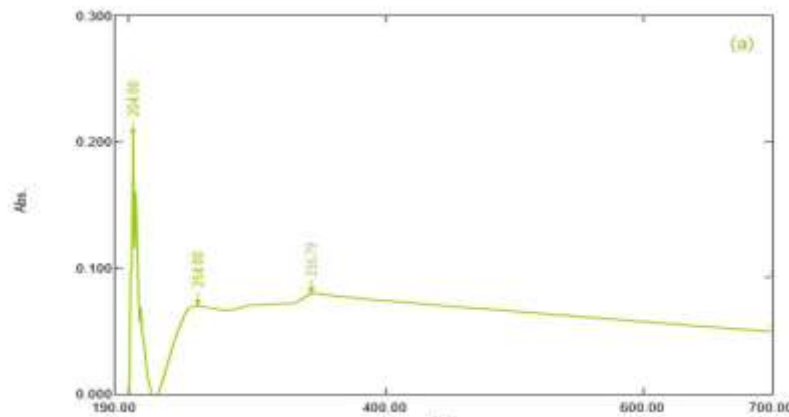


Figure 7 (a) UV-Vis absorption spectrum of PbTiO₃:Ba (1 mol %) specimens

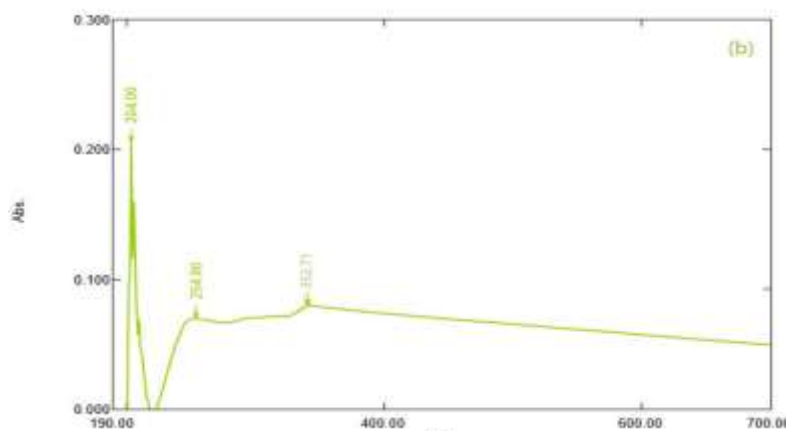


Figure 7 (b) UV-Vis absorption spectrum of PbTiO₃:Ba (2 mol %) specimens

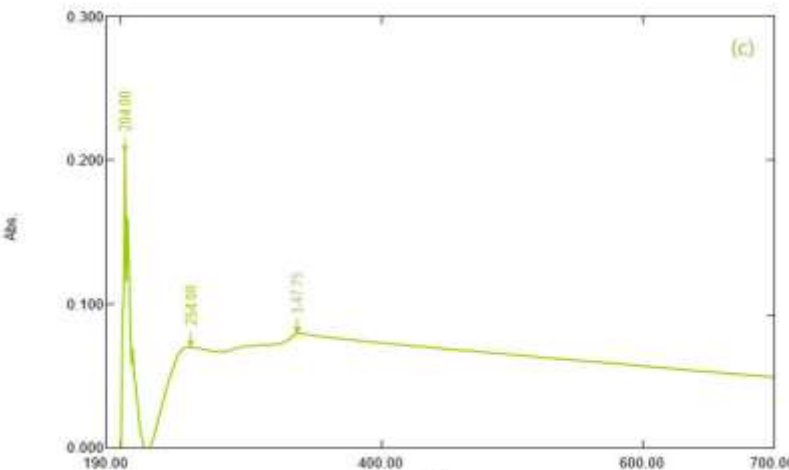


Figure 7 (c) UV-Vis absorption spectrum of PbTiO₃:Ba (3 mol %) specimens.

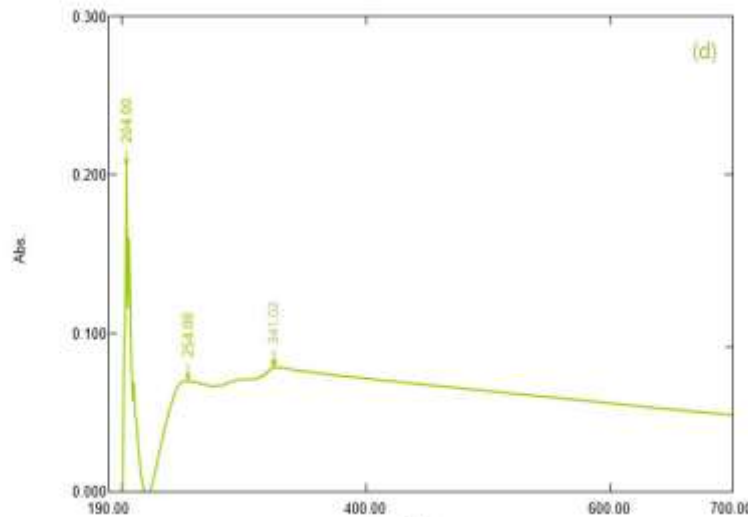


Figure 7 (d) UV-Vis absorption spectrum of $\text{PbTiO}_3:\text{Ba}$ (4 mol %) specimens.

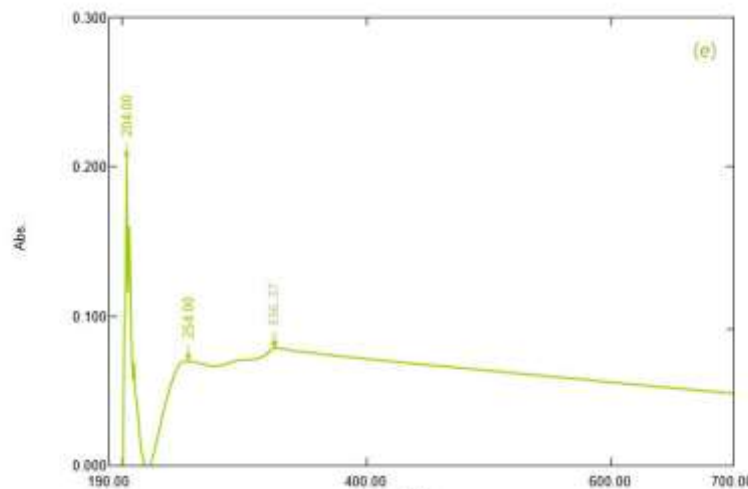


Figure 7 (e) UV-Vis absorption spectrum of $\text{PbTiO}_3:\text{Ba}$ (5 mol %) specimens.

Figure (7) shows the optical absorption spectra of $\text{PbTiO}_3:\text{Ba}$ specimens. It is obvious that absorbance increases with increasing additional Ba content. Optical bandgap is the exciton energy which determine the onset of vertical inter band transition. An exciton is a bound state of an electron and hole which are held together by electrostatic Coulomb force. An exciton forms when a photon is absorbed by a semiconductor ($\text{PbTiO}_3:\text{Ba}$), so optical bandgap is threshold for photons to be absorbed. From the optical absorption spectra, bandgap is estimated by using the following equation (5):

$$E_c = \frac{hc}{\lambda} \quad (5)$$

Where, h = Planck's constant,

c = speed of light and

λ = wavelength in nm, which is the absorption edge value from the spectra.

Optical bandgaps of $\text{PbTiO}_3:\text{Ba}$ specimens are listed in table (4).

Table 4 List of optical bandgaps of PbTiO₃: Ba specimens.

Ba Content (%)	Edge value from absorption spectrum (nm)	Optical bandgap (eV)
1	356.79	3.46
2	352.71	3.50
3	347.75	3.55
4	341.02	3.62
5	336.37	3.67

It is studied that, optical bandgap increases as additional Ba content increases in PbTiO₃ specimens. It is expected that, there are quantum confinement effect in PbTiO₃: Ba specimens. The quantum confinement is observed when the particle size (in nano scale) decreases in confining dimension makes the discrete energy level and ultimately bandgap energy also increases. It is also believed that, the conduction band is dominated by Ti⁴⁺ cations, the valence band is mainly by oxygen anions.

Conclusion

Additional Ba substituted PbTiO₃ specimens are studied by means of its structural features, ferroelectric behavior and optical bandgaps. Structural features of PbTiO₃:Ba specimens are examined by using x - rays diffraction technique. XRD results indicate that, there are no considerable change of tetragonal, perovskite - type PbTiO₃ structure after Ba substitutions. A little change of structural features is observed and it is due to appearance of lattice micro strains, defects, dislocations and vacancies in host PbTiO₃ structure during the doping process. Ferroelectricity of PbTiO₃:Ba specimens is investigated by using Sawyer - Tower circuit. Ferroelectric parameters are enhanced when the additional Ba substitution is raised in PbTiO₃ specimens. It is possibly due to second - order hybridizations between Ti - O and Pb (Ba) - O are responsible for the enhancement of ferroelectric parameters in PbTiO₃: Ba specimens. Optical bandgaps of PbTiO₃:Ba specimens are studied by using UV - Vis spectrophotometer. Optical bandgap increases as additional Ba content increases in PbTiO₃ specimens. It is expected that, there are quantum confinement effects in PbTiO₃:Ba specimens. PbTiO₃ : Ba specimens are potential candidate for dynamic random access memory (DRAM) and non-volatile random access memory (NVRAM) devices.

Acknowledgement

The authors would like to thank the Universities ' Research Center (U R C, University of Yangon for XRD investigations and AMTT Co.Ltd. for UV - Vis spectrophotometer examination

References

- Moudai S. J. and Pourhabib - Yekta A. (2011); " A First Principle Calculation of the Structural and Optical Properties of PbTiO₃ in Paraelectric Phase ", Chinese Journal of Physics, vol 50 (4), pp 628 - 637.
- Ponte F. M. et al., (2016); "Structural, Optical and Piezoelectric Properties of (Pb,Ba)(Ti,Fe)O₃ Perovskite: A Macroscopic and Nanoscale Properties Approach ", Journal of Materials Chemistry, vol 4, pp 9331 - 9342.
- Scott J. F. (2008); " Ferroelectrics Go Banana ", Journal of Physics Condensed Matter, vol 20, 021001.
- Turik A. V. and Khasabov A. G. (2000); " Origin of Ferroelectricity in PbTiO₃ " Ferroelectrics, vol 237 (1), pp 64 - 71.
- Zelezly V. et al., (2016); " The Variation of PbTiO₃ Bandgap at Ferroelectric Phase Transition ", Journal of Physics Condensed Matter, vol 28, 025501.
- Zhen X. et al., (2012); " Doping and Phase Transformation of Single Crystal Pure Perovskite PbTiO₃ Fibers with TiO₆ Edge Shared Octahedra ", Crystal Engineering Communication, vol 14, pp 4520 - 4524.

EFFECT OF SINTERING TEMPERATURE ON STRUCTURAL AND MECHANICAL PROPERTIES OF BETA-TRICALCIUM PHOSPHATE

Cho Cho Khin¹, Nay Win Tun², Aye Aye Thant³, and Khin Khin Win⁴

Abstract

β -tricalcium phosphate powders were synthesized by the wet chemical precipitation method starting from calcium nitrate tetrahydrate, $\text{Ca}(\text{NO}_3)_2 \cdot 4\text{H}_2\text{O}$, and diammonium hydrogen phosphate, $(\text{NH}_4)_2\text{HPO}_4$. The pH of the mixed solution was controlled at pH-10 by adding sodium hydroxide solution. The β -TCP pellets were sintered at 800°C, 900°C, 1000°C, and 1100°C for 6 h each. The structural and mechanical properties of β -TCP pellets were characterized by using XRD, SEM, Hardness tester, and Archimedes' method respectively. The dense microstructure without pores could be obtained at the sintering temperature of 1100°C. The hardness and compressive strength increased with increasing temperature. The maximum compressive strength of β -TCP pellets was obtained at 1100°C. The behavior of bioceramic was investigated such that porosity decreased when the bulk density and temperature increased accordingly. In this research, the sintering temperature at 1100°C provided maximum density and hardness which may be applied as a bone replacement.

Keywords: β -tricalcium phosphate, XRD, SEM, hardness, relative density, porosity

Introduction

Calcium phosphate ceramics are widely used as synthetic bone substitutes. Among the calcium phosphate ceramics, beta-tricalcium phosphate bioceramics are widely used for hard tissue regeneration due to their excellent biocompatibility and their close similarity to biological apatite present in human bones. β -TCP is known to be highly resorbable *in vivo* with new bone ingrowths replacing the implanted β -TCP [Yong-Seok, J., et al., 2018]. In the physiological environment, they can gradually degrade, absorb, and promote bone growth. Ultimately, they are capable of replacing the damaged bone with new tissue [Behzad, M., et al., 2012]. It has good biodegradability and a higher dissolution rate in the body's environment after implantation, which is absorbed and replaced by new bone. In the present research, the wet chemical precipitation method was carried out to prepare β -TCP and the effect of sintering temperature on structural and mechanical properties of β -TCP pellets were investigated.

Materials and Method

Experimental Procedure

β -TCP powders were synthesized by the wet chemical precipitation method starting from calcium nitrate tetrahydrate with diammonium hydrogen phosphate. The Ca:P molar ratio of β -TCP is 1.5. Keeping that ratio constant, the amounts of required raw materials were calculated. Calcium nitrate tetrahydrate and diammonium hydrogen phosphate solutions were prepared by dissolving the crystals in distilled water and stirred at room temperature. The prepared solution of $(\text{NH}_4)_2\text{HPO}_4$ was added slowly drop-wise into the $\text{Ca}(\text{NO}_3)_2 \cdot 4\text{H}_2\text{O}$ solution. The pH of the mixed solution was controlled at a pH value of 10 by adding sodium hydroxide solution. The obtained white suspension was stirred for 12 h. The synthesized precipitate was washed with distilled water as well as ethanol. After filtration, the filter cake dried at 80°C for 24 h. The dried powders were calcined at 700°C for 2 h. The synthesized β -TCP powders were pressed into pellets by the

¹ Lecturer, Department of Physics, Mawlamyine University

² Dr, Assistant Lecturer, Department of Physics, Dagon University

³ Dr, Professor, Department of Physics, University of Yangon

⁴ Dr, Professor and Head of Department, Department of Physics, University of Yangon

hydraulic press. The pellets were sintered at 800°C, 900°C, 1000°C, and 1100°C for 6 h each. The phase formations of these samples were characterized by using X-ray Diffraction analysis. The morphological features of β -TCP pellets were studied by a scanning electron microscope. The values of hardness were measured by using the hardness tester (EH-01). The compressive strengths were calculated from the hardness data. The bulk density and porosity were measured by using Archimedes' method. Figure 1 shows the flowchart of the sample preparation processes of β -TCP sample for pH-10.

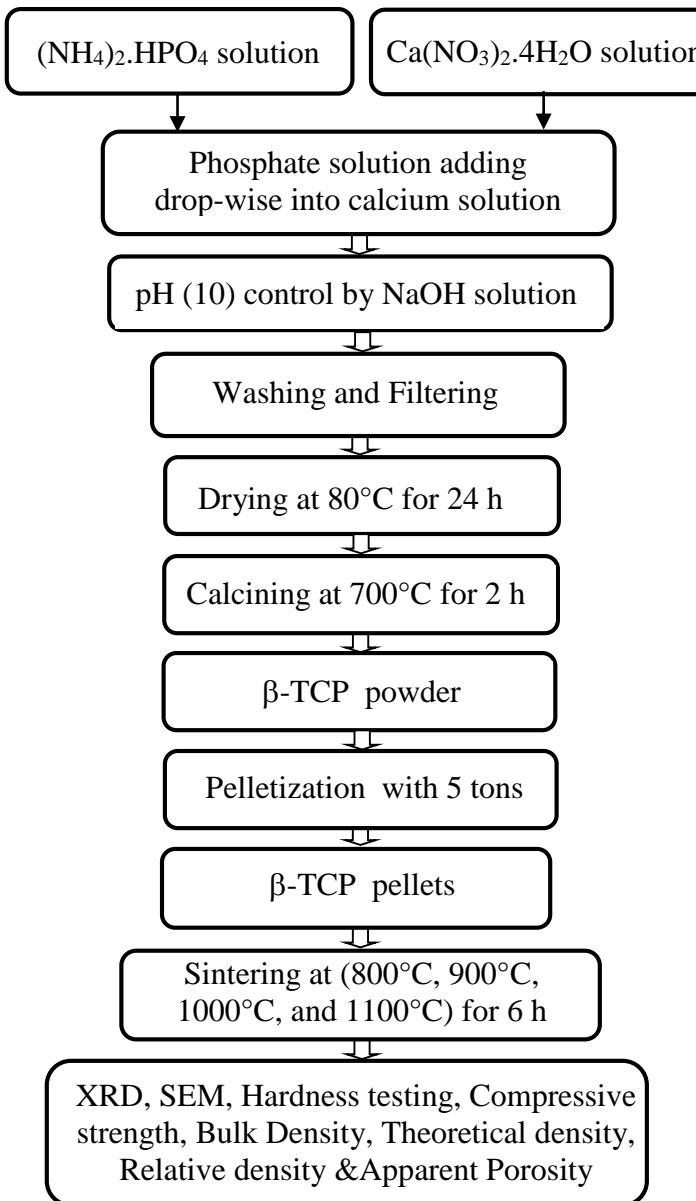


Figure 1 Flowchart of sample preparation processes of β -TCP sample for pH-10

Results and Discussion

Phase Formation by XRD Analysis

X-ray Diffraction (XRD) analysis was carried out to study the phase formations of β -TCP pellets. The XRD spectra of β -TCP pellets at 800°C, 900°C, 1000°C, and 1100°C for pH-10 is shown in Figure 2.

All peaks were well matched with the standard profile of whitlockite $\text{Ca}_3(\text{PO}_4)_2$. The XRD spectra exhibit that the phase in each sintered pellet is the rhombohedral structure of β -TCP. Thus, the β -TCP pellet was indicated the pure phase. The peaks were sharper as the sintering temperature was increased. The results show that the sintered pellets contain only a single phase β -TCP structure.

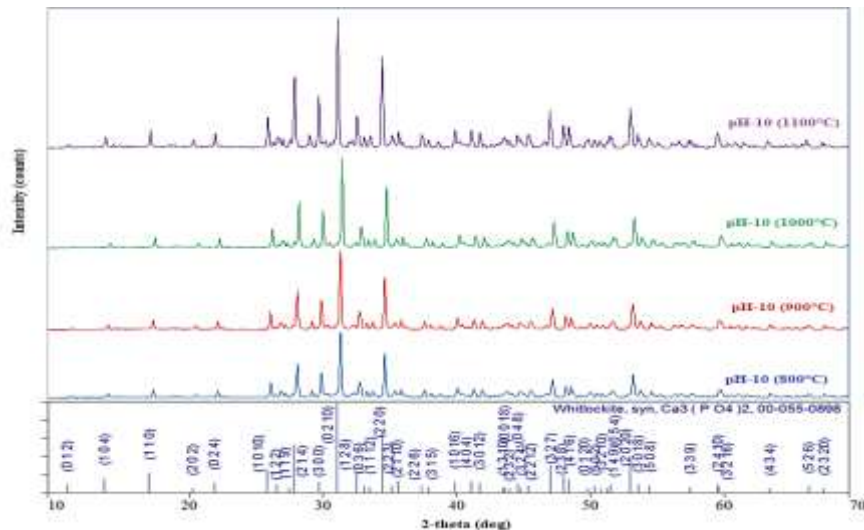


Figure 2 XRD spectra of β -TCP pellets sintered at 800°C, 900°C, 1000°C, and 1100°C for pH-10

Determination of Lattice Parameters, Crystallite Size, and Theoretical density

The lattice parameters ‘a’ and ‘c’ were calculated by using the ‘d’ value of the intense peak. The crystallite sizes were calculated by Debye Scherrer equation using FWHM and Bragg angle obtained from the XRD data. The values of crystallite size and lattice parameters of sintered pellets at 800°C, 900°C, 1000°C, 1100°C for 6 h are summarized in Table 1. It was investigated that the lattice parameters of the pellets well agree with the typical values for β -TCP structure as discussed in other research of β -TCP [Yashima, M., et al., 2003]. It was found that the crystallite size is in the nano-range and increased with increasing temperatures in Figure 3.

According to the XRD data, the unit cell volume in the β -TCP pellets was calculated and then the theoretical densities of the β -TCP pellets were calculated. The results were represented in Table 1. It was found that the theoretical densities of the β -TCP pellets lie in the range of 3.02 g cm^{-3} - 3.07 g cm^{-3} . However, the literature value of the theoretical density for β -TCP pellet is 3.07 g cm^{-3} . Thus, the obtained theoretical density of pure β -TCP pellet is in agreement with the literature value.

Table 1 The value of crystallite size, lattice parameter and theoretical density of β -TCP pellets for pH-10

Sintered Temperature (°C)	Crystallite Size D (nm)	Lattice Parameter ‘a’ (Å)	Lattice Parameter ‘c’ (Å)	Theoretical density (g cm^{-3})
800	58.15	10.44	37.38	3.07
900	62.52	10.46	37.44	3.05
1000	69.21	10.48	37.60	3.02
1100	71.83	10.44	37.40	3.06

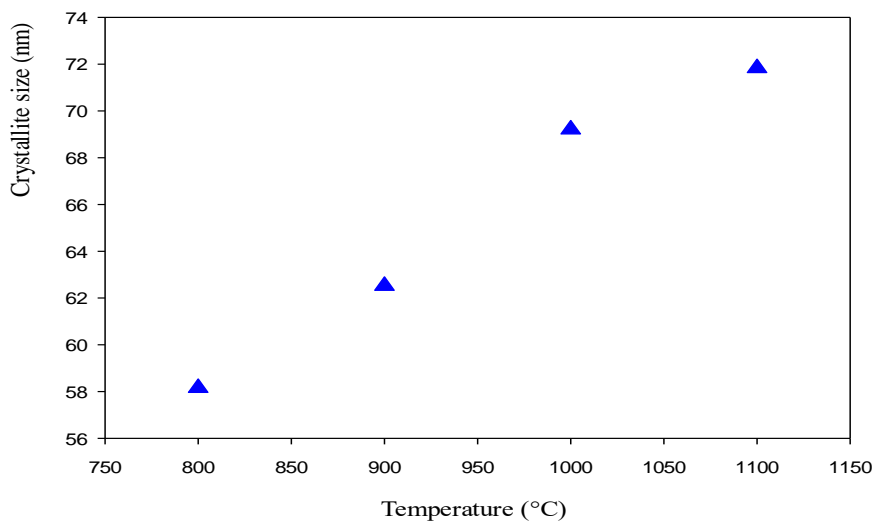


Figure 3 The crystallite size of β -TCP pellets at different sintering temperature for pH-10

Morphological Feature by SEM Analysis

The surface morphology features of β -TCP pellets were studied by a scanning electron microscope. SEM micrographs of β -TCP pellets obtained by sintering at 800°C, 900°C, 1000°C, and 1100°C for 6 h are shown in Figure 4 to Figure 7 respectively. The sintering temperature at 800°C in Figure 4 shows the particles in the sample were irregular in shape and highly agglomerated microstructure. The sintering temperature at 900°C in Figure 5 shows the highly reactive irregular particles in the sample were joined by neck growth and a continuous pore channel was formed. The fracture surface of the sample sintered at 1000°C in Figure 6, the grain boundaries and isolated pores were visible. Sintering temperature at 1100°C in Figure 7, the surface of the sample was highly dense and larger grain size with no pores. From the SEM micrographs of pellets that were sintered at different temperatures, it is noted that the grain size is increased with increasing temperatures as shown in Table 2. Therefore, it can be said that the pores become smaller with the increase in sintering temperature, and finally the dense microstructure without pores could be obtained at the sintering temperature of 1100°C.

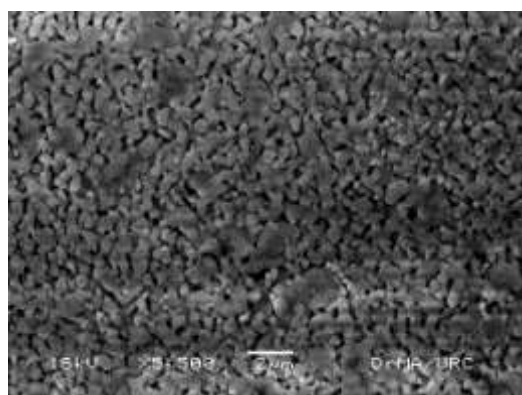


Figure 4 SEM micrograph of β -TCP pellet at 800°C for pH-10

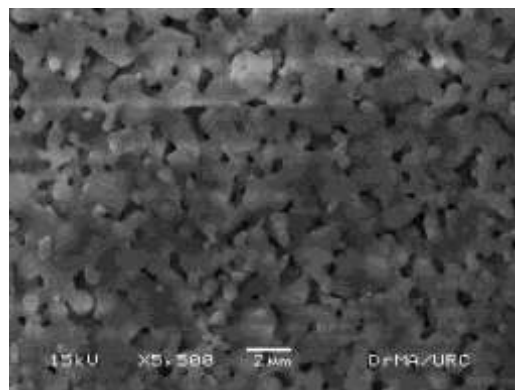


Figure 5 SEM micrograph of β -TCP pellet at 900°C for pH-10

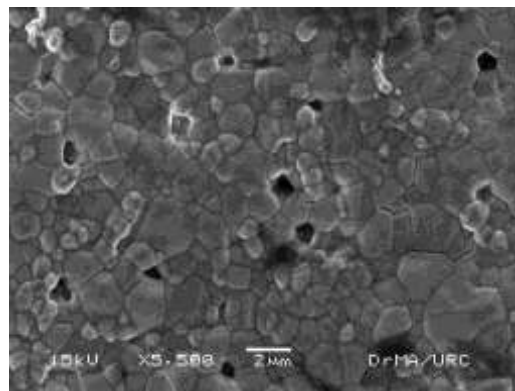


Figure 6 SEM micrograph of β -TCP pellet at 1000°C for pH-10

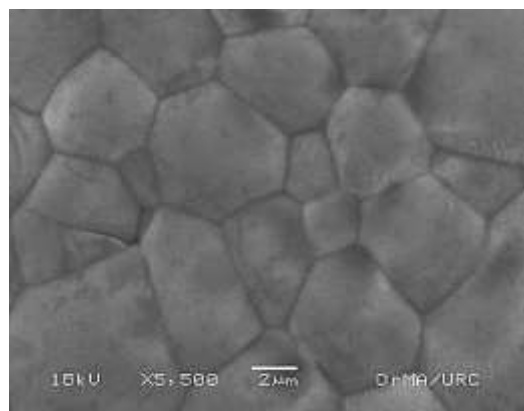


Figure 7 SEM micrograph of β -TCP pellet at 1100°C for pH-10

Table 2 The average value of grain size of β -TCP pellets at different sintering temperatures for pH-10

Sintered Temperature (°C)	Grain size (μm)
800	0.82
900	1.01
1000	1.06
1100	4.38

Study on Mechanical Properties of Sintered β -TCP Pellets

In this study, the thickness and diameter of the β -TCP pellets for pH-10 were measured by using a digital caliper. And then the values of the hardness of the β -TCP pellets were measured by using the hardness tester (EH-01). The compressive strengths of the β -TCP pellets were calculated by using the Hertz equation. The effect of sintering temperature on the hardness and compressive strength of β -TCP were investigated and the data are summarized in Table 3. The variation of hardness and compressive strength of β -TCP pellets with different temperatures are shown in Figure 8 and Figure 9 respectively. It was found that the hardness increases with increasing sintering temperature. The maximum hardness is found to be 484.8 N at 1100°C. The compressive strength of the sample which is determined from the hardness value shows the same trend as the hardness accordingly. The maximum compressive strength was found to be 10.29 MPa at 1100°C. It can be said that the hardness and compressive strength of β -TCP is increased with increasing sintering temperature.

Table 3 The values of hardness and compressive strength of β -TCP pellets for pH-10

Sintered Temperature (°C)	Hardness P (N)	Compressive Strength σ_{comp} (MPa)
800	139.8	2.86
900	172.3	3.56
1000	263.3	5.52
1100	484.8	10.29

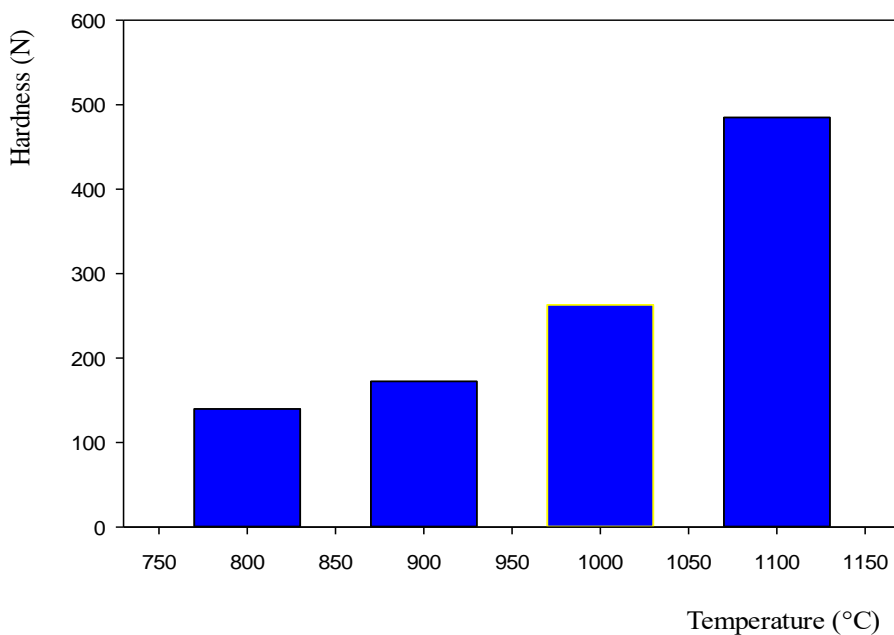


Figure 8 The variation of hardness value of β -TCP pellets at different sintering temperature for pH-10

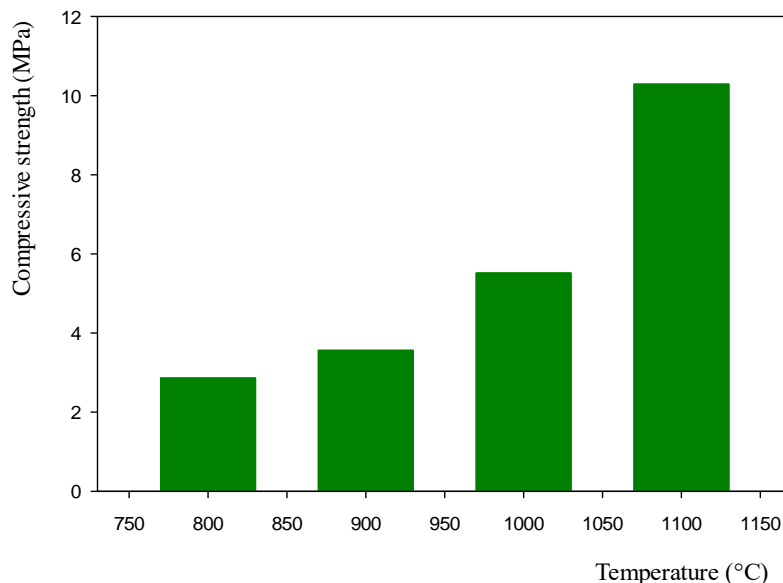


Figure 9 The variation of compressive strength of β -TCP pellets at different sintering temperature for pH-10

Estimation of Bulk Density, Relative Density, and Apparent Porosity of β -TCP Pellets

The bulk density and apparent porosity of the β -TCP pellets sintered at different temperatures for pH-10 were measured based on the Archimedes' method. The measured bulk density and apparent porosity of β -TCP pellets were represented in Table 4. The bulk density increases with increasing temperature and the porosity decrease with increasing temperature accordingly. It was found that the sample β -TCP at 1100°C exhibits the largest bulk density with the smallest porosity in Figure 10.

Figure 11 shows the relative densities of the β -TCP pellets sintered at different sintering temperatures for pH-10. It was found that relative density is increased with increasing sintering temperature. The relative density of β -TCP pellets increased up to 93.81% at 1100 °C. It can be said that the β -TCP pellet sintered at 1100°C was composed of a highly compact structure.

Table 4 The values of bulk density, relative density, and apparent porosity of β -TCP pellets for pH-10

Sintered Temperature (°C)	Bulk density (g cm^{-3})	Relative density (%)	Apparent Porosity (%)
800	2.65	86.32	26.47
900	2.71	88.27	23.53
1000	2.76	89.90	18.18
1100	2.88	93.81	9.37

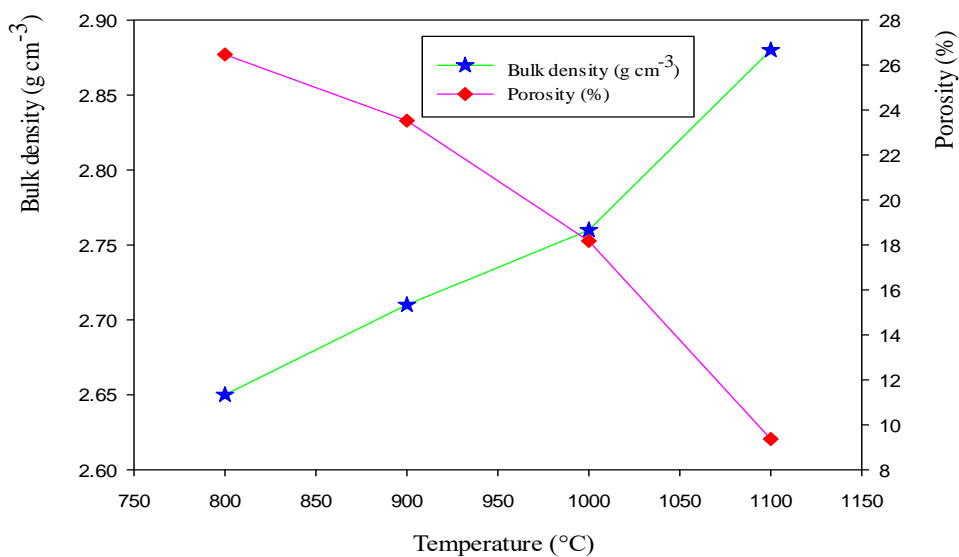


Figure 10 Comparison between bulk density and porosity of β -TCP pellets at different sintering temperature for pH-10

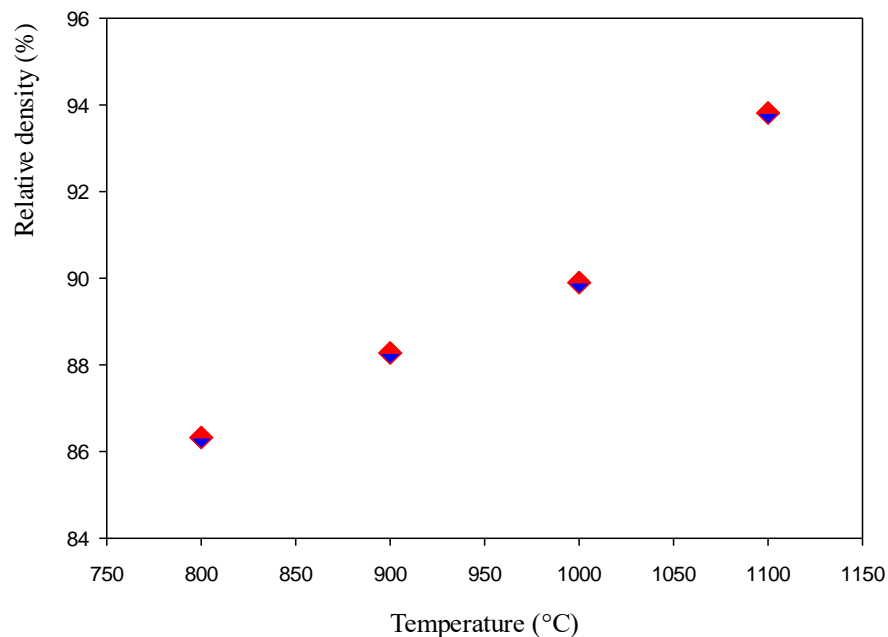


Figure 11 The relative density of β -TCP pellets at different sintering temperature for pH-10

Conclusion

β -TCP pellets were synthesized by the wet chemical precipitation method. The XRD analysis has revealed that the phase precipitated out in the samples is the rhombohedral structure of β -TCP. The lattice parameters and theoretical density of β -TCP pellets well agree with the typical values for β -TCP structure. Moreover, the crystallite size of β -TCP is obtained in nano-range and found to be increased with increasing temperatures. The XRD results proved that the single phase β -TCP was successfully obtained at different sintering temperatures with increased crystallite size. After sintering at different temperatures, the average grain size has increased with

increasing temperature. This increase in grain size with the temperature well agrees with the increase in crystallite size. This finding pointed out that the synthesis route is consistent with different sintering temperatures. The hardness and compressive strength of β -TCP pellets are found to increase with increasing sintering temperature. The hardness and compressive strength of β -TCP exhibit a larger value at 1100°C. The bulk density and relative density increase with increasing temperature and the porosity decreases with increasing temperature accordingly. It was found that the sintered β -TCP sample at 1100°C possesses the lowest porosity as it exhibits the largest compressive strength and bulk density with no pores in SEM analysis. The results showed that an increase in sintering temperature decreased the porosity and increased the mechanical properties of β -TCP. The results proved that the sintering temperature at 1100°C showed the most optimum properties of hardness, relative density, and microstructural features. Based on the results obtained, it is concluded that the sintering temperature could effect on structural and mechanical properties of beta-tricalcium phosphate.

Acknowledgements

The authors are grateful to the Department of Physics and Universities' Research Centre, University of Yangon, for the supports with research facilities and also. The authors are also grateful to the colleagues from the Department of Physics, Mawlamyine University for their encouragement to this work.

References

- Asmaam, M. et al., (2018) "Effect of physical and chemical parameters on the β -Tricalcium phosphate synthesized by the wet chemical method" Mediterranean Journal of Chemistry, 7(3), 234-242.
- Bahman, M., et al., (2011), "Synthesis of nano-sized β -tricalcium phosphate via wet precipitation", Processing and Application of ceramics, vol.4, pp. 193-198.
- Bahzd, M., et al., (2012), "Sintering effects on the hardness of β -TCP", Journal of Ceramic Processing Research, Vol. 13, No.4, pp. 486-490.
- Behzad, M., et al., (2014), "Densification and mechanical behavior of β -tricalcium phosphate bioceramics", International Letters of Chemistry, Physics and Astronomy, vol. 36, pp. 37-49.
- Chuthathip, M., et al, (2014), "Effect of Sintering Temperatures on the Microstructure and Properties of β -TCP" Australian Journal of Basic and Applied Sciences, 8(5) Special 2014, pp. 492-497.
- Nahar, U. K., et al., (2017) "Characterization of Beta-Tricalcium Phosphate (β - TCP) Produced at Different Process Conditions", J Bioengineer & Biomedical.
- Pham, T. K., (2007), "Synthesis of β -TCP powder via Wet precipitation and Hydrothermal methods", University Sains Malaysia.
- Tarek, A. E., et al., (2007), "Preparation and characterization of calcium phosphate ceramics containing some rare earth oxides for using as biomaterials", Mansoura University, Physics Department.
- Xing, Z., (2007), "Preparation and Characterization of Calcium Phosphate Ceramics and Composites as Bone Substitutes", University of California, San Diego.
- Yashima, M., et al., (2003), "Crystal structure analysis of β -TCP $\text{Ca}_3(\text{PO}_4)_2$, by neutron powder diffraction", Journal of Solid State Chemistry, Vol. 175, pp. 272-277.

STRUCTURE CHARACTERIZATION OF TITANIUM DIOXIDE FILMS ON SILICON SUBSTRATE

Ni Lar¹, Min Maung Maung², and Khin New Oo³

Abstract

Transparent semiconducting thin films of titanium dioxide (TiO_2) were deposited on silicon substrate by the spray method. The microstructure of the TiO_2 films were characterized by X-ray diffraction (XRD), Fourier Transform Infrared Spectroscopy (FTIR) and Raman Spectroscopy. The XRD analysis revealed that the films were polycrystalline with an anatase crystal structure and a preferred grain orientation in the (101) direction. Strong LO-phonon Raman spectra modes especially B_{1g} (393.29 cm^{-1}) and E_g (634.84 cm^{-1}) in Raman spectra and the absorption peak at 739 cm^{-1} in absorbance spectra by FTIR also indicated the existence of anatase phase TiO_2 in these films.

Keywords: TiO_2 thin films, silicon substrate, XRD, FTIR, Raman, spray pyrolysis.

Introduction

The development of new materials, blends, composites and advanced materials is a necessity for modification of mechanical, electrical, optical and thermal properties of thin films to fulfill the demand for improved materials in industries. The studies of semi-conducting thin film are being pursued with increasing interest on the account of their proven and potential applications in many semiconductor devices. Titanium dioxide (TiO_2) is a widely recognized candidate for photovoltaic (PV) applications because of its photoactive and electrical properties. It is a large band gap (3–3.2 eV) semiconductor with remarkable electrical and optical properties such as high refractive index, good transmission in the VIS and NIR regions, and high dielectric constant. TiO_2/Si structures constitute a primary component in the fabrication of photovoltaic and optoelectronic devices and recent research has paid special attention to the search for novel appropriate techniques to enhance their efficiency. Titanium dioxide thin film has been one of the most extremely studied oxides because of its role in various applications namely photo-induced water splitting, dye synthesized solar cells, environmental purifications gas sensors display devices, batteries etc. The present research work, on the spray-pyrolysis processing, structure, optical and electrical properties of TiO_2 thin films as a function of deposition and annealing temperatures was discussed. The energy band gap of TiO_2 thin film was evaluated with the aid of UV spectrophotometer.

Materials and Method

Preparation of Silicon Substrate

The substrates used in the study were antimony doped n-type silicon with the resistivity value $1\text{--}10 \Omega\text{-cm}$. The dimension of silicon substrates was $1 \times 1\text{cm}^2$. Firstly, the substrate is cleaned with HF: DI (1:5) for 10 minutes to remove native oxide and immerse in acetone for 10 minutes. Then, the substrate is immersed in methyl alcohol for 10 minutes to remove the impurities. After that, it is rinsed into deionized water (DI water) for a few minutes and then dried at room temperature.

¹ Lecturer, Department of Physics, Mawlamyine University.

² Dr, Professor, Department of Physics, University of Yangon.

³ Lecturer, Department of Physics, Mawlamyine University.

Deposition of TiO₂/SiO₂/Si Film

TiO₂ solution was deposited on n-type silicon substrates by spray pyrolysis process. The prepared nanosized TiO₂ powder was put into 250 ml beaker. The methoxy-ethanol and the deionized water were mixed at the ratio of 2:1. The mixed solution and the TiO₂ powder 10 g were stirred with the magnetic stirrer about 10 minutes. The homogeneous solution was poured into container of spray gun. The substrate temperature was set up at different temperature 100°C, 200°C, 300°C, 400°C and 500°C respectively. The spray gun was sprayed to the silicon substrates by pulsed spray solution feed. After depositing, they were slowly dried at room temperature. Schematic diagram of TiO₂ powder deposition is shown in Figure 1.

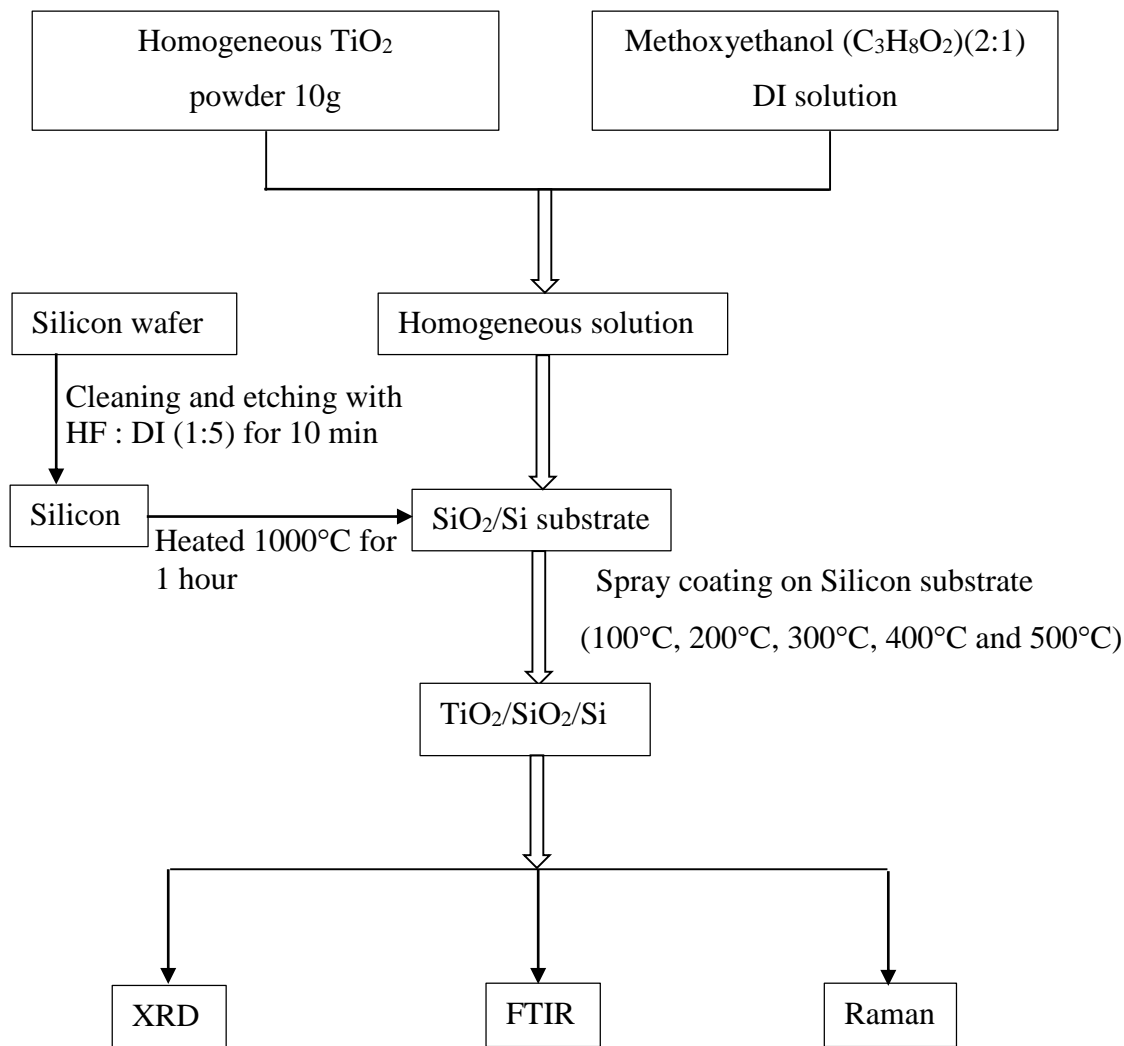


Figure1 Flow chart of the deposition of TiO₂/SiO₂/Si film

Results and Discussion

Structural Properties of TiO₂ Thin Films

The crystallographic structure of the films was studied by X-ray diffraction (XRD), using X-ray diffractometer with (Cu K α = 1.5406 Å) radiation, for 2 θ values in the range of 10 – 70°. The crystalline sharp peaks in the diffraction pattern were identified by using the International Centre for Diffraction Data (ICDD). The crystallite size was calculated by using Scherer's equation;

$D = (k\lambda)/(\beta \cos\theta)$ where, β is the peak width measured at half intensity (radian), λ is the wavelength measured in Å, k is the particle shape factor or Scherer constant ($k= 0.9$) and D is the crystallite size of the crystallites (Å).

The XRD spectra for TiO_2 thin films on Si substrates at 100°C, 200°C, 300°C, 400°C and 500°C were depicted in Figure 2. The crystallite sizes estimated by using Scherer's equation were found to be $\text{TiO}_2/\text{SiO}_2/\text{Si}$ films are shown in Table 1. XRD diffraction peaks belonging to (101), (103), (004), (112), (200), (105), (211), (213), (204), and (116) were observed in all these films which are well matched with the powder diffraction data of 21-1272>Anatase, syn- TiO_2 . Figure 2 shows the crystallite size of the films as a function of annealing temperatures. Importantly a preface orientation is seen along the (101) and (200) planes in all the annealed films. This shows that annealing of these samples at these temperatures have induced in some constructive features. Table 1 shows all the samples have Anatase phase was obtained. It was found that the crystallite size decreases with increasing process temperature. The c/a ratio of analyzed samples was obtained around 2.45 and it was agreed with the standard value of Anatase TiO_2 structure.

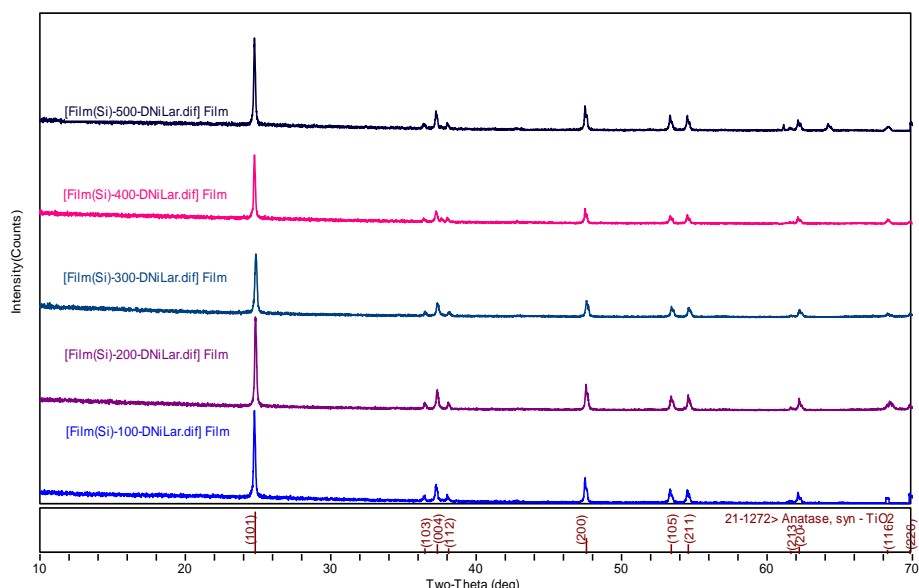


Figure 2 X-ray diffraction pattern of $\text{TiO}_2/\text{SiO}_2/\text{Si}$ film at 100 °C

Table 1 Structural properties of $\text{TiO}_2/\text{SiO}_2/\text{Si}$ films

Temperature (°C)	Phase name	Crystallite Size (nm)	c/a ratio
100	Anatase	43.71	2.44
200	Anatase	43.3	2.45
300	Anatase	43.24	2.46
400	Anatase	42.28	2.45
500	Anatase	34.42	2.44

FTIR analysis of TiO₂ thin film on silicon substrate

The FTIR pattern of TiO₂ synthesized by spray method with methoxy-ethanol in range of 500-3200 cm⁻¹ was shown in figure 3. The bond structure of Ti-O and Ti-O-Ti was observed in the range of 700 to 1000 cm⁻¹. The band in the wave number range of 1000 to 1200 cm⁻¹ corresponds to the formation of Si-O-Si, Si-C and Si-O-C bonds. The peak at 1430 cm⁻¹, 1720 cm⁻¹ and 2360 cm⁻¹ arises due to C = C, C = O and O = C = O bonds. All these bands with corresponding wave number were summarized in table 2. The peak at 739 cm⁻¹ is attributed to the formation of amorphous form of TiO₂. The broader peak at 1110 cm⁻¹ corresponds to the formation of SiO₂ which indicates that the oxidation of substrate had also happened. Some carbonaceous contamination had also appeared at 1430 cm⁻¹ and 1720 cm⁻¹. This carbon contamination had appeared due to already present carbon in the silicon wafers during the manufacturing process. Small peak at 2360 was attributed to CO₂ which arises due to the cavity formed between the sample surface and IR source as contamination during analysis. The similar kind of FTIR spectra was observed by increasing process temperature. There was an increase in the intensity of Si – O – Si bond which indicated the increase of oxidation of Si substrate.

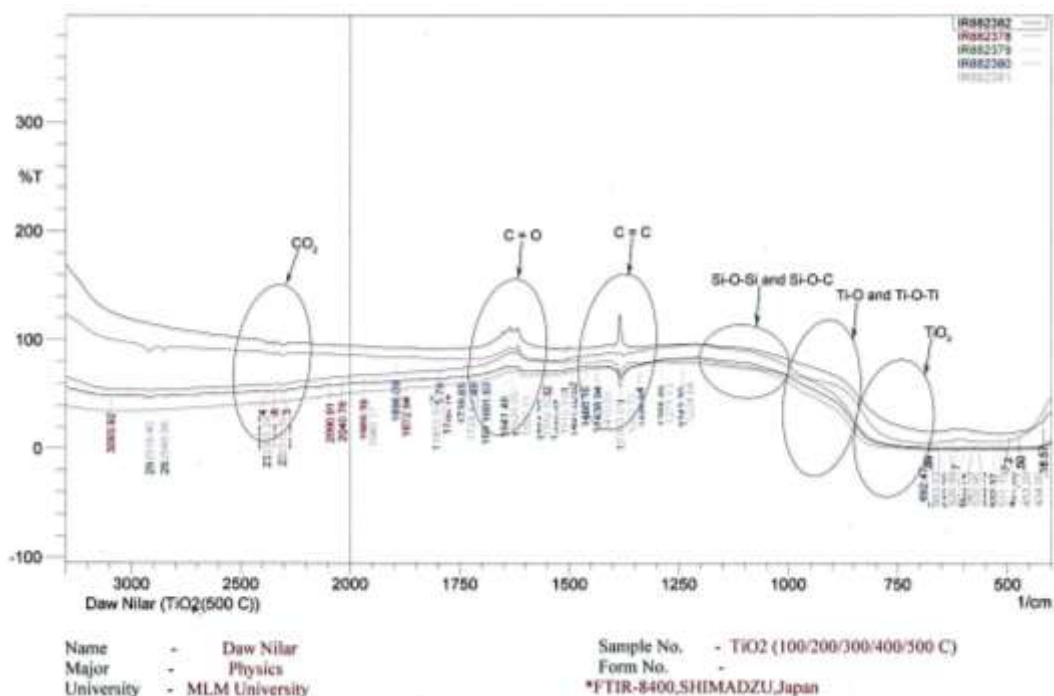


Figure 3 FTIR spectra of TiO₂ film

Table 2 FTIR frequencies and band assignment for the TiO₂ thin films deposited on Si wafer for spray method

Wavenumber (cm ⁻¹)	Band Assignment
700-1000	Ti - O, Ti - O - Ti
739	TiO ₂
1000-1200	Si – O – Si, Si – O - C
1430	C = C
1720	C = O
2360	CO ₂

Raman Scattering Analysis

The structure of TiO₂ thin films was also investigated by Raman spectroscopy. The Raman spectrum of TiO₂ nanoparticles has been extensively studied due to the unusual broadening and shifts of the Raman lines with decreasing particle size and because the intense E_g line appears as the most sensitive line to reveal size effects. The Raman peaks of TiO₂ film were assigned as E_g, E_g, B_{1g}, A_{1g} + B_{1g} and E_g modes of anatase phase. The Raman spectra having six Raman active modes, A_{1g} + 2 B_{1g} + 3 E_g of anatase. The Raman active spectra of the TiO₂ film were shown in figure 4. Five distinct peaks were being observed having bands centered at 139.47 cm⁻¹ (E_g), 198 cm⁻¹ (E_g), 393.29 cm⁻¹ (B_{1g}), 511.4 cm⁻¹ (A_{1g} + B_{1g}), and 634.84 cm⁻¹ (E_g). All the Raman bands characteristic to the anatase phase of TiO₂ could be recorded. The appearance of an intense peak at 139.47 cm⁻¹ mode meant that there was a certain degree of long-range order possessed by the TiO₂ nanocrystals.

It was the strongest peak and it was attributed to arise from the external vibration of the anatase structure. This peak was also broadened which was attributed to either phonon confinement effect or the surface pressure that was present in materials having sizes of nanometer scale. The intense low frequency band at 139.47 cm⁻¹ was observed due to O–Ti–O bending vibrations and was assigned as characteristic feature of the anatase phase. The weak vibrational mode at 790 cm⁻¹ was due to the bending vibration of Si–O–Si groups belonging to the substrate.

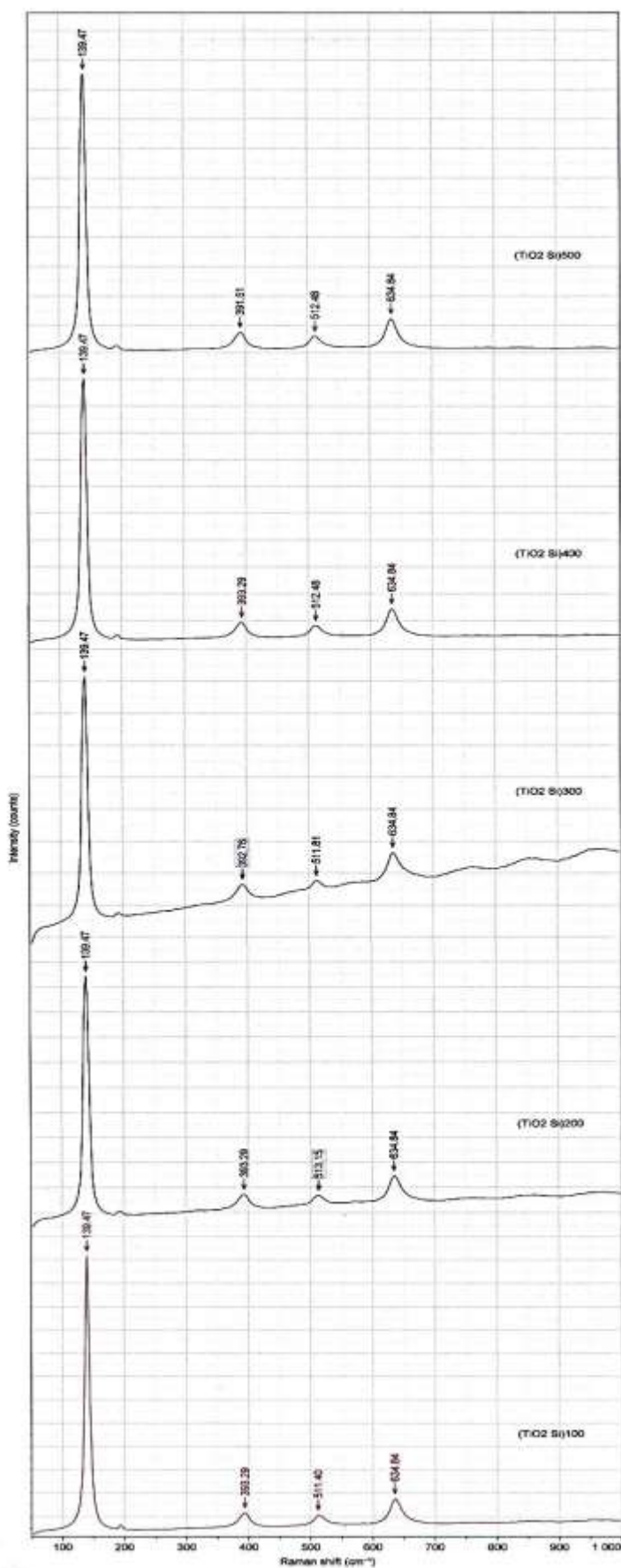


Figure 4 The Raman active spectra of the TiO_2 film

Conclusion

TiO₂ compact layer was successfully deposited onto silicon substrate using spray pyrolysis techniques. X-ray Diffraction studies revealed that TiO₂ compact layer had tetragonal crystalline structure with cell parameters $a = 3.86818\text{\AA}$ and $c = 9.47376\text{\AA}$, the c/a ratio was obtained around 2.45. Raman spectroscopy showed that TiO₂ compact layer had an intense peak at 139.47 cm⁻¹ mode. The absorption peak at 739 cm⁻¹ in absorbance spectra by FTIR also indicated the existence of anatase phase TiO₂ in these films. FTIR and Raman spectroscopy indicate that TiO₂ crystallizes in anatase structure from temperature at 100 to 500°C.

Acknowledgements

The authors are grateful to the Department of Physics and Universities' Research Centre, University of Yangon, for the supports with research facilities and also. The authors are also grateful to the colleagues from the Department of Physics, Mawlamyine University for their encouragement to this work.

References

- Chen, X. & Mao, S.S. (2007). "Titanium dioxide Nanomaterials: Synthesis, properties, modifications and applications" Chem. Rev.; 107: 2891.
- Cromer, D.T. & Herrington, K. (1955). "The structures of anatase and rutile". J. Am. Chem. Soc, 77: 4708.
- Mo, S., & Ching, W. (1995). "Electronic and optical properties of three phases of titanium dioxide: Rutile, anatase and brookite" Phys. Rev B, 51: 13023.
- Setiawati, E. & Kawano, K. (2008). "Stabilization of anatase phase in the rare earth; Eu and Sm ion doped nanoparticle TiO₂" J. Alloys Compd.; 451 (1-2): 293- 296.
- Simons, P Y. & Dachille, F. (1967). "The structure of TiO₂II, a high- pressure phase of TiO₂" Acta Cryst, 23: 334.
- Thamaphat, K., Limsuwan, P. & Ngotawornchai, B. (2008). "Phase Characterization of TiO₂ Powder by XRD and TEM". J. (Nat. Sci.); 42: 357-361.
- Wu, F., Li, X., Wang, Z., Guo, H., Wu, L., Xiong, X. & Wang, X. (2011). "A novel method to synthesize anatase TiO₂ nanowires as an anode material for lithium-ion batteries" J. Alloys Compd., 509 (8): 3711- 3715.

INFLUENCE OF COPPER SUBSTITUTION ON ELECTRICAL PROPERTIES OF Mg-Cu-Zn FERRITE

Su Su Tha¹, Hsan Htoo²

Abstract

Magnesium copper zinc ferrites with the general formula $Mg_{0.5}Cu_xZn_{0.5-x}Fe_2O_4$ ($x=0, 0.1, 0.2, 0.3, 0.4, 0.5$) were prepared by mixing stoichiometric proportions of magnesium, copper, zinc and ferrite nitrates with calculated amount of citric acid. Before mixing, four raw samples were checked by XRD to confirm these samples are pure or not. Four raw samples, magnesium nitrates: copper nitrate: zinc nitrates: ferric nitrates ($Mg(NO_3)_2 \cdot 6H_2O$, $Cu(NO_3)_2 \cdot 6H_2O$, $Zn(NO_3)_2 \cdot 6H_2O$, $Fe(NO_3)_3 \cdot 9H_2O$) were mixed with citric acid ($C_6H_8O_7$) in different ratios in the beaker and stirring at $70^\circ C$ until to get viscous gel. And then the samples were calcined at $800^\circ C$ for 2 hr. The structural analysis, crystallize size and surface morphology investigation of as prepared samples were studied by Powder X-ray Diffractometer (XRD) and Scanning Electron Microscopy (SEM) techniques. The temperature dependent resistivity of Mg-Cu-Zn ferrites were analysis in various concentration of copper.

Keywords: XRD, SEM and Resistivity

Introduction

With the rapid development of mobile communication and information technology, small, inexpensive, high performance electronic devices are in high demand. Recently, we have witnessed the rapid development of surface mounting devices (SMD) using multilayer chip inductors (MLCI), which utilize alternating coats of ferrite and electrical paste, followed by co-firing. High temperature co-firing (normally higher than $1000^\circ C$) causes a decrease in inductance due to the interfacial reaction (via diffusion) between ferrite and silver, usually use as electrode material. This interfacial reaction can be suppressed by co-firing at a temperature lower than the melting point of Ag (approximately $960^\circ C$). Therefore, low temperature sintering is of great importance to suppress the interfacial diffusion. Whereas, Mg-Cu-Zn ferrites are more suitable to overcome these problems. The citrate precursor method is a promising technique for the synthesis of certain technical ceramics. Since all the reactants are solutions, they can be uniformly mixed on an atomic or molecular level, and the amount of the reactants can be accurately controlled. This wet chemical method has unique advantages over conventional sintering processes in terms of obtaining nanoparticles that can be densified easily at lower temperature. The aim of this work is to present a novel and economical method of preparation of Mg-Cu-Zn ferrite by the citrate precursor method in order to achieve sintering at lower temperatures.

The spinel ferrite (MFe_2O_4 , M = a divalent cation) belongs to an important class of magnetic materials, because of their remarkable magnetic properties particularly in radio frequency region, physical flexibility high electrical resistivity, mechanical hardness and chemical stability. For its excellent properties, more attention was paid to Mg-Cu-Zn ferrite, which is mainly applied in electrical devices and in catalysis.

Materials and Methods

Experimental Procedure

The samples of $MgCuZnFe_2O_4$ mixed ferrite were prepared by mixing magnesium nitrate, zinc nitrate, copper nitrate and ferric nitrates with calculated amount of citric acid. Four raw

¹ PhD Candidate, Lecturer, Department of Physics, Mawlamyine University.

² Dr., Associate Professor, Department of Physics, Kalay University.

samples were checked by XRD to confirm these samples are pure or not. The different ratios of the six mixtures were starting at 70°C to get viscous gel. And then the samples were pre sintering at 70 °C until to get dry powder. Then the powder samples were sintering at 800 °C for 2 hours. During heating the crucible, the crystal water was gradually vaporized. When a crucible temperature was reached to the critical temperature, large amounts of foams produced with appearance of spark at one corner which spread through the mass in the container. Flow diagram of the sample preparation procedure of magnesium copper zinc ferrite is given in Figure 1.

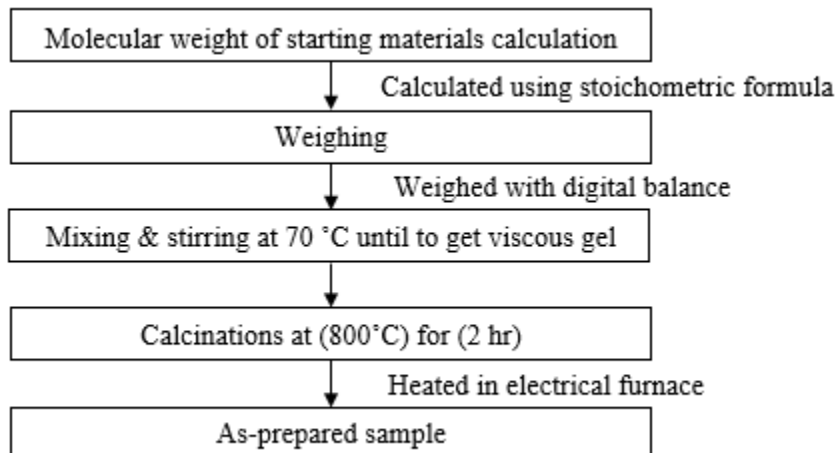


Figure 1 Flow diagram of the sample preparation procedure of magnesium copper zinc ferrite

Results and Discussion

X Ray Diffraction Measurement

X-ray diffraction is the most widely used and least ambiguous method for the precise determination of the positions of atoms in molecules and solids. In X-ray diffraction (XRD) measurement, a beam of X-ray directed on a crystalline material may experience diffraction (constructive interference) as a result of its interaction with a series of atomic plane according to Bragg's law. Since interplanar spacing is a function of the miller indices, lattice gathering much useful information relating the crystal structure. The value of interplanar spacing, d_{hkl} is function of miller indices (h, k and l) as well as the lattice parameter. The lattice parameters of the unit cell of the cubic represent:

$$\frac{1}{d^2} = \left[\frac{h^2 + k^2 + l^2}{a^2} \right]$$

where d = interplanar spacing

a = lattice parameter

(h k l) = Miller indices

The crystallite size can be measured as following Debye-Scherrer formula.

$$D = \frac{k \lambda}{B \cos \theta}$$

Where, D = Crystallite size (\AA)

λ = The wavelength of X-ray use (1.5405 \AA)

B = Full Width Half Maximum of dominant peak (radians)

θ = Angle of diffraction (radians)

k = scherrer constant

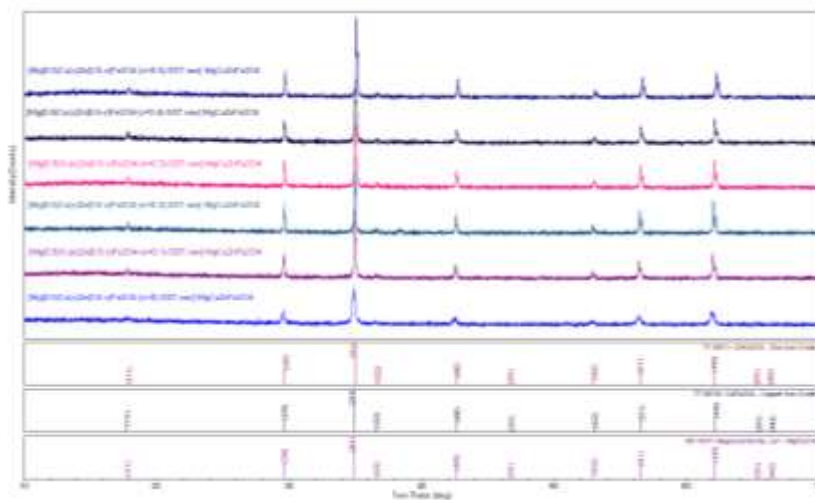


Figure 2 Peak comparisons of XRD patterns for $\text{Mg}_{(0.5)}\text{Cu}_{(x)}\text{Zn}_{(0.5-x)}\text{Fe}_2\text{O}_4$ samples

Table 1 Comparisons of lattice parameters and crystallite sizes for $\text{Mg}_{(0.5)}\text{Cu}_{(x)}\text{Zn}_{(0.5-x)}\text{Fe}_2\text{O}_4$ sample

x	Lattice (a) (\AA)	Crystallize Size (nm)
0.00	8.5489	20.73
0.10	8.6126	47.19
0.20	8.5334	44.68
0.30	8.5632	44.61
0.40	8.5483	29.63
0.50	8.5192	37.26

Surface Morphology Investigation using SEM

Scanning electron microscopy (SEM) as shown in the following figure is a widely spread technique, used in materials and biological sciences as well as in industry. Modern scanning electron microscopies combine high spatial resolution imaging and analysis capabilities with easy to handle hardware and user-friendly computer-based interface. The scanning electron microscope (SEM) is a type of electron microscope that creates various images by focusing a high energy beam of electrons onto the surface of a sample and detecting signals from the interaction of the incident electrons with the sample's surface. The type of signals gathered in a SEM varies and can include secondary electrons, characteristic X-rays, and back scattered electrons. The focused electron beam is scanned across the sample surface, generating different signals. The richness in signal opens up the possibility to investigate a wide range of materials properties. The two most commonly used signals for imaging in the SEM are secondary electrons and back scattered electrons.

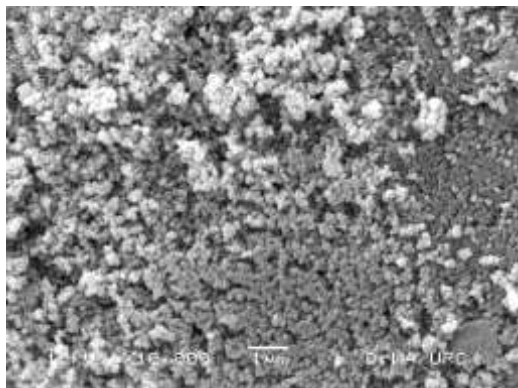


Figure 3 SEM image of $Mg_{(0.5)}Zn_{(0.5)}Fe_2O_4$ (800°) sample

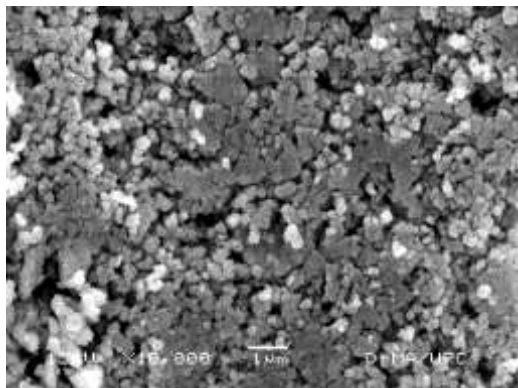


Figure 4 SEM image of $Mg_{(0.5)}Cu_{(0.1)}Zn_{(0.4)}Fe_2O_4$ (800°C) sample

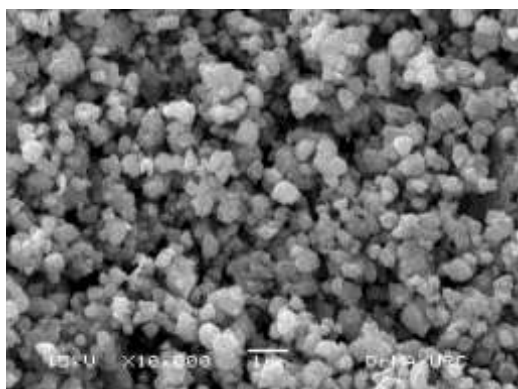


Figure 5 SEM image of $Mg_{(0.5)}Cu_{(0.2)}Zn_{(0.3)}Fe_2O_4$ (800°C) sample

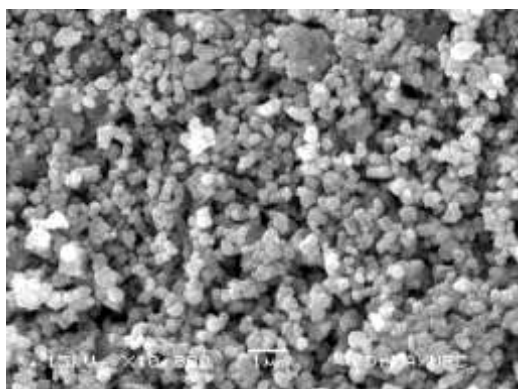


Figure 6 SEM image of $g_{(0.5)}Cu_{(0.3)}Zn_{(0.2)}Fe_2O_4$ (800°C) sample

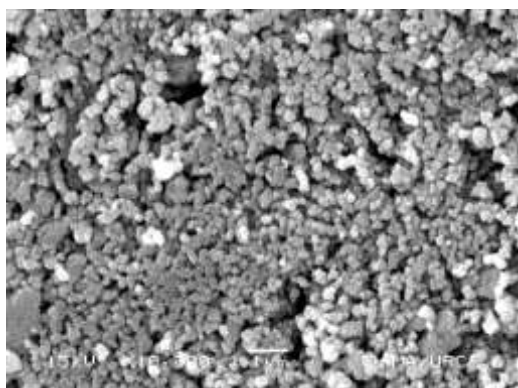


Figure 7 SEM image of $Mg_{(0.5)}Cu_{(0.4)}Zn_{(0.1)}Fe_2O_4$ (800°C) sample

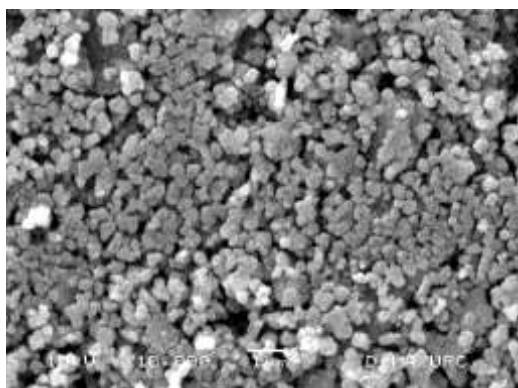


Figure 8 SEM image of $Mg_{(0.5)}Cu_{(0.5)}Fe_2O_4$ (800°C) sample

Table 2 Comparisons of grain size for $Mg_{(0.5)}Cu_{(x)}Zn_{(0.5-x)}Fe_2O_4$ sample

x	Grain size (μm)
0.0	0.186
0.1	0.199
0.2	0.205
0.3	0.209
0.4	0.232
0.5	0.269

The microstructure and morphology have an important role in determining the magnetic and electric transport properties and those were examined by a high resolution scanning electron microscope. These studied for the materials are essential in order to understand the relationship between their processing parameters as well as the behavior when used in practical applications. The morphology of the as prepared sample was achieved by using SEM technique. SEM images with same magnification for the $Mg_{(0.5)}Cu_{(x)}Zn_{(0.5-x)}Fe_2O_4$ samples are given in Figure 3 to 8. These images display formation of spongy and homogeneous material. Average grain size was determined using Image J software. The surface morphology of the $Mg_{(0.5)}Cu_{(x)}Zn_{(0.5-x)}Fe_2O_4$ (calcined at 800°C)sample as seen from the SEM photographs consists of grain size varying from (0.186) to (0.269) μm and it was generally uniform in grain size. There can be concluded that the grain size increases with increasing the molar ratio of Cu substitution.

Temperature Dependent Electrical Resistivity

The measurements on electrical resistivity were performed on the final sintered pellets. An Aplab LCR meter (MT-4080D) assisted by a temperature controller was used to observe the temperature dependent resistivity. In the first step, the dimension of the sample of the sample was measured by using slide caliper. Then, the sample was sandwiched between two copper plates that serve as two electrodes. To ensure better electrical contact, silver paste was evenly applied on both surfaces of the sample.

The sample was placed in a sample holder that was immersed in a heating chamber surrounded by asbestos. Each copper plate was brought into contact with copper rod from the chamber. Thermal conducting mica shield was used between the sample and the chamber to have a good thermal conductivity and to protect from electrical conduction. The resistances were measured over a temperature range from 300K to 700K at interval of 20K by using Aplab LCR meter. The J-type thermocouple was inserted near the sample to record its temperature. Temperature of the specimen was kept constant by a controller. Figure illustrates sample holder for resistivity measurement. The resistivity of each sample was calculated by using the following relation:

$$\rho = \frac{RA}{l}$$

Where l is the thickness of the sample in cm, A is the area of the electrode in contact with sample (πr^2) in cm^2 and R is the resistance in Ω . The relationship between resistivity and temperature can be expressed as:

$$\rho = \rho_0 \exp(E_a / k_b T)$$

Where, ρ_0 is the resistivity extrapolated to T , E_a is the activation energy, k_B is the Boltzmann constant and T is the absolute temperature. This equation can be converted in the form of linear equation. From the plot of $\log(\rho)$ versus temperature ($1000/T$), the activation energy is calculated. The electrical resistivity is found that the resistivity of all the samples decrease with increase in temperature, and then the resistivity becomes stable above temperature 400K. Kumar et al, studied electrical properties of a series of copper substituted Mg-Zn ferrites with the compositional formula $Mg_{(0.5)}Cu_{(x)}Zn_{(0.5-x)}Fe_2O_4$. Experimental results that they satisfied, showed that DC electrical resistivity decreases with increase of temperature ensuring the semiconducting nature of the ferrites “Kumar et al., 2014”. The decrease in resistivity with temperature may be attributed to the increase in drift mobility of the charge carriers.

Figure 9 shows the variation of the electrical resistivity of Cu concentration of $Mg_{(0.5)}Cu_{(x)}Zn_{(0.5-x)}Fe_2O_4$. It has been observed that room temperature resistivity values of bulk

samples are seen to vary between 1.0×10^7 ohm-cm to 8.7×10^7 ohm-cm. The resistivity values of $\text{Mg}_{(0.5)}\text{Cu}_{(x)}\text{Zn}_{(0.5-x)}\text{Fe}_2\text{O}_4$ increases with increase in concentration of copper $x=0.1$ to $x=0.3$. The resistivity values of copper substituted $\text{Mg}_{(0.5)}\text{Cu}_{(x)}\text{Zn}_{(0.5-x)}\text{Fe}_2\text{O}_4$ decrease with increase in concentration of copper $x=0.3$ to $x=0.5$. The resistivity values of $\text{Mg}_{(0.5)}\text{Cu}_{(x)}\text{Zn}_{(0.5-x)}\text{Fe}_2\text{O}_4$ decreases as increase in the temperature range between 300K to 400K and then the resistivity will becomes stable above temperature 400K in Figure 9(a) to (e).

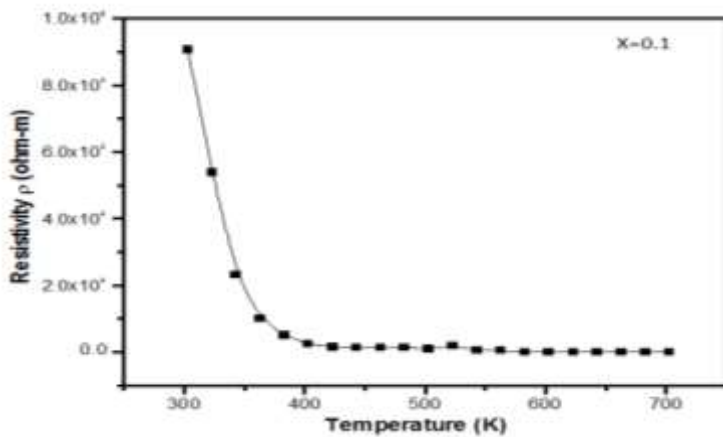


Figure 9 (a) Temperature dependent resistivity curves for $\text{Mg}_{(0.5)}\text{Cu}_{(x)}\text{Zn}_{(0.5-x)}\text{Fe}_2\text{O}_4$ with Cu content ($x=0.1$)

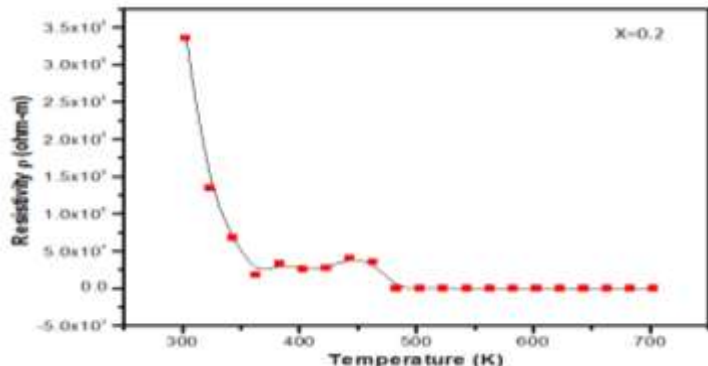


Figure 9 (b) Temperature dependent resistivity curves for $\text{Mg}_{(0.5)}\text{Cu}_{(x)}\text{Zn}_{(0.5-x)}\text{Fe}_2\text{O}_4$ with Cu content ($x=0.2$)

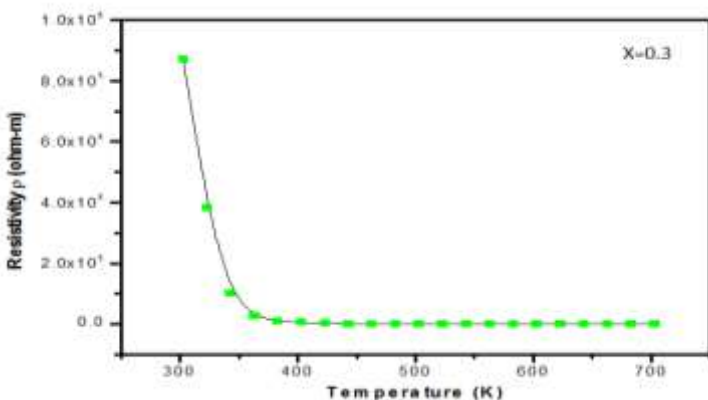


Figure 9 (c) Temperature dependent resistivity curves for $\text{Mg}_{(0.5)}\text{Cu}_{(x)}\text{Zn}_{(0.5-x)}\text{Fe}_2\text{O}_4$ with Cu content ($x=0.3$)

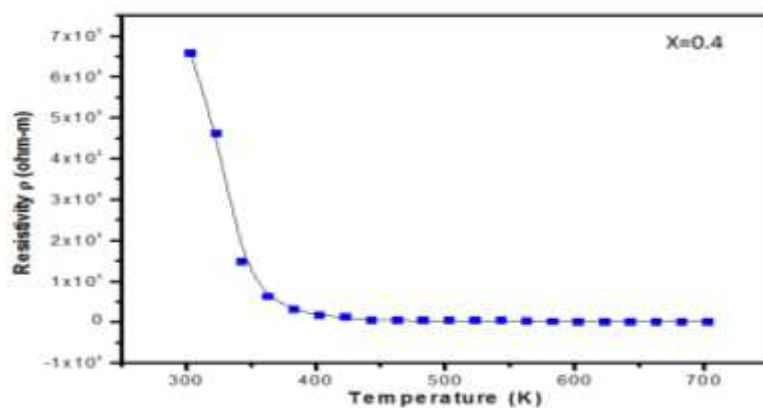


Figure 9 (d) Temperature dependent resistivity curves for $Mg_{(0.5)}Cu_{(x)}Zn_{(0.5-x)}Fe_2O_4$ with Cu content ($x=0.4$)

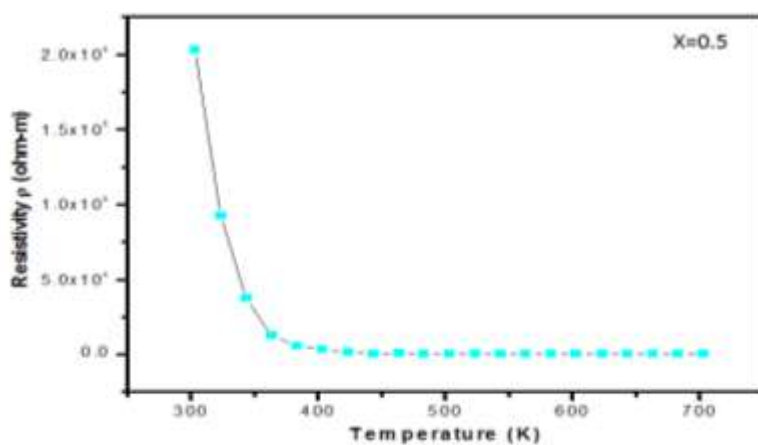


Figure 9 (e) Temperature dependent resistivity curves for $Mg_{(0.5)}Cu_{(x)}Zn_{(0.5-x)}Fe_2O_4$ with Cu content ($x=0.5$)

Table 3 The variation of resistivity with different Cu concentration at 373K

Cu Concentration	R (Ω)	Resistivity (Ωm)
0.1	1151383.04	282592.00
0.2	6562009.80	1610560.00
0.3	19073807.13	4681418.00
0.4	7862017.54	1929630.00
0.5	2298976.93	564254.00

Conclusion

Magnesium copper zinc ferrites $Mg_{(0.5)}Cu_{(x)}Zn_{(0.5-x)}Fe_2O_4$ has been determined in various ratios as ($x=0.0, 0.1, 0.2, 0.3, 0.4, 0.5$). The preparation method for the investigated system is sol gel method. According the XRD results, the crystallize sizes of ferrite samples were calculated to be 20.73, 47.19, 44.68, 44.61, 29.63 and 37.26 nm at the various ratios of ($x=0.0, 0.1, 0.2, 0.3, 0.4, 0.5$) respectively. And lattice parameters are nearly the same as 8.6 Å. It was clear that the crystallize size of ferrite sample with mixed ratio of ($x=0.0$) (or) $Mg_{(0.5)}Zn_{(0.5)}Fe_2O_4$ was smallest crystallite size about 20.73nm among all samples. But the crystallize size of ferrite sample with mixed ratio of ($x=0.4$) (or) $Mg_{(0.5)}Cu_{(0.4)}Zn_{(0.1)}Fe_2O_4$ was smallest crystallize size about 29.63 nm

among four mixed samples. X-ray diffraction analysis clearly revealed that all the ferrites have the structure cubic spinel. According of SEM results, grain size of as prepared samples are varying from (0.186) to (0.269) μm and it was generally uniform in grain size. It can be concluded that the grain size increases with increasing the molar ratio of Cu substitution.

The resistivity values of $\text{Mg}_{(0.5)}\text{Cu}_{(x)}\text{Zn}_{(0.5-x)}\text{Fe}_2\text{O}_4$ decreases as increase in the temperature range between 300K to 400K and then the resistivity will be stable above 400K as shown in figures.

Acknowledgements

The authors are grateful to the Department of Physics and Universities' Research Centre, University of Yangon, for the supports with research facilities and also. The authors are also grateful to the colleagues from the Department of Physics, Mawlamyine University for their encouragement to this work.

References

- Bondyopadhyay, A. K. (2010). "Nano Materials" (New Delhi: New Age)
- Kittle, C, (2005). "Introduction to Solid State Physics", (New York: Wiley)
- Nakamura, T. (2017). "Journal of Magnetism and Magnetic Material". Mater. 168, 285-291.
- Pillai S. O. (2006). "Solid State Physics" (New Delhi: New Age)
- Qi, X., Zhou, J., Yue, Z., Gui, Z., Li, L. (2002). "Journal of Magnetism and Magnetic Material". Mater. 251, 316-322.
- Zhang, H., Li, L., Wu, P., Zhou, J., Ma, Z. & Gui, Z. (2000). "Journal of Magnetism and Magnetic Materials". Mat. Res. Bull. 352, 207-2215.
- Zhang, H., Ma, Z., Zhou, J., Yue, Z., Li, L. & Gui, Z. (2000). "Journal of Magnetism and Magnetic Materials". Mater. 213, 304-308.

OPTICAL AND ANTIBACTERIAL PROPERTIES OF COLLOIDAL GOLD NANOPARTICLES

Hnin Yu Khaing¹, Kyaw Kyaw², Than Than Win³, Yin Maung Maung⁴

Abstract

Colloidal gold nanoparticles in spherical shape had been synthesized from chloroauric acid (HAuCl_4) by one of the solution method such as chemical reduction method. The colloidal gold nanoparticles were characterized with scanning electron microscopy (SEM) for morphological properties, X-ray diffraction method (XRD) for structural analysis and UV-VIS absorption spectroscopy for optical properties. It was found that the concentration of the precursors solution affected the size of the nanoparticles. In this nanoparticles fabrication method, the size of nanoparticles could be controlled by varying amount of sodium citrate. The antibacterial properties of gold nanoparticles had been studied.

Keywords: Colloidal, HAuCl_4 , SEM, XRD, Antibacterial properties

Introduction

Chemistry of gold colloids began from the 19th century, when Michael Faraday performed his well known experiments for gold colloids generation. His experiments yield deep red gold solution by reduction of tetrachloroaurate with the help of white phosphorus [Schmid G, Corain B.]. At the start of the 20th century, Wilhelm Ostwald pointed out that in the nm range, the properties of metal particles were mainly defined by surface atoms and he reasoned that these nanoparticles, called colloids, should show novel properties with respect to bulk particles. The trimness of gold to the nanometer range has dramatic consequences for its physical and chemical properties [Khan I, Saeed K.]. These consequences are also well-founded for other metals however, Gold is an outstanding example.

Gold nanoparticles are very attractive because of their size and shape dependent properties [Eustis S]. For example, gold nanoparticles have a characteristic red color, but anisotropic gold nanorods dramatically changed in color. The color changing properties is due to the collective oscillation of the electrons in the conduction band, known as the surface plasmon oscillation [Liz Marzan L]. The oscillation frequency of gold is usually in the visible region and so it has the strong surface plasmon resonance absorption in visible region. Gold nanoparticles can generate and enhance electromagnetic fields that affect its environment. It can be used in many applications such as solar cell, photocatalysis and biomedicine. Gold nanoparticles have been prepared using various methods such as chemical reduction method, photochemical using UV irradiation method, sonochemical method, sonoelectrochemical, etc. In this research work gold nanoparticles were synthesized as size and shape controlled synthesis with the help of chemical reduction method. Structural, morphology and absorption spectra of the gold nanoparticles were analyzed.

Experimental Procedure

Gold foil (99.99%, ~250mg), hydrochloric acid, nitric and trisodium citrate dihydrate ($\text{Na}_3\text{C}_6\text{H}_5\text{O}_7 \cdot 2\text{H}_2\text{O}$) were used as starting materials for gold nanoparticles synthesis. Deionized water was used as the reaction solvent. 15 ml of Hydrochloric acid and 1 ml of nitric acid were mixed and stirred at 400 rpm for 15 min in a beaker. 250 mg of gold foil was placed in the acids

¹ Lecturer, Department of Physics, Yenangyaung Degree College

² Lecturer, Department of Physics, University of Mandalay

³ Professor (Head), Department of Physics, Pin Lone University

⁴ Professor, Department of Physics, University of Yangon

solution and stirred under fume hood at 50 °C until all of the gold dissolved. The resulting solution of tetrachloroauric acid could be used without further treatment for nanoparticle synthesis. 7 ml of aqueous tetrachloroauric acid was diluted with deionized water to make 1.00 mM solution in a chemically cleaned glass beaker. The obtained diluted solution was vigorously stirred at 70 °C. While stirring vigorously, as prepared various amount of tri-sodium citrate solution were quickly added to the each tetrachloroauric acid solutions. The color of solution changed within several minutes from orange to dark brown and then to red or purple color depending on the size of the nanoparticles. The obtain colloidal solution were filtered and washed with deionized water and centrifuged at 3500 RPM for 15 min and the liquid was decanted and fresh DI water was added to disperse the sediment. This step was repeated until the decanting liquid had a pH ≈ 5. The obtained nanoparticles were annealed at 100 °C for 30 min. The structural and morphological properties of the obtained nanoparticles were characterized with XRD and SEM. Surface Plasmon resonance (SPR) absorption properties were analyzed with UV-Vis spectroscopy.

Results and Discussion

XRD analysis

X-ray diffraction (XRD) was conducted on RIGAKU multiflex X-ray diffractometer in 10°-70° 2θ range. Fig. 1. showed the XRD profiles of gold nanopartilces synthesized form 2 ml, 2.5 ml, 3 ml, 3.5 ml and 4 ml, respectively. It could be seen from the profile that all the diffraction peaks corresponding to the diffraction planes (111), (200), and (220) were indexed to the gold metal with face centered cubic structure. Lattice constants obtained from XRD patterns were observed to be $a = 4.078 \text{ \AA}$ in good agreement with the standard diffraction pattern of cubic gold metal (JCPDF 04-0784).

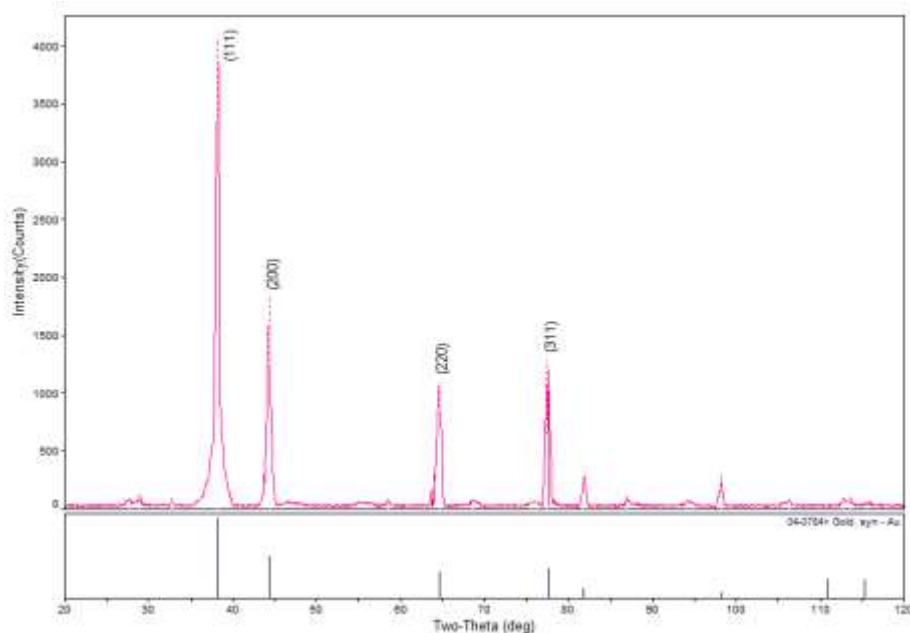


Figure 1 XRD profile of obtained gold nanoparticles.

SEM analysis

SEM microscopy was conducted to investigate the surface morphological properties of the obtained gold nanoparticles. The SEM micrograph of obtained nanoparticles was shown in Fig. 2. The SEM micrograph indicates that the shape and morphology of gold nanoparticles changed with increasing tri-sodium citrate amount. These images revealed that the individual particles were

composed by the agglomeration of particles of various shapes. This indicates that amount of tri-sodium citrate solution influences strongly on morphology of gold nanoparticles.

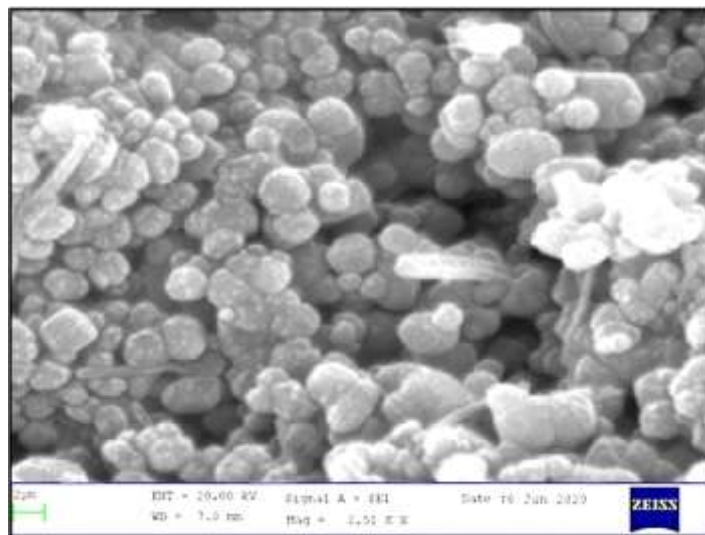


Figure 2 The SEM micrograph of obtained gold nanoparticles.

UV-Vis Analysis

Surface plasmon absorption spectra of gold nanoparticles prepared with different amounts of trisodium citrate solution were shown in Fig 3. It could be seen from the figure, the maximum absorption peaks were shifted to the shorter wavelength (from 539.9 to 521.1 nm) and the full width at half maximum (FWHM) of the spectrum is decreased with increasing amount of trisodium citrate from 2 ml to 4 ml. Therefore, the amount of citrate solution determines the size of the nanoparticles. As amount of trisodium citrate solution increased, the SPR bands increasingly broaden and a red shift occurred. In the case of gold nanoparticles, a red shift of plasmon resonances was caused by the increasing size of the nanoparticles, for example, from 520 nm for a ~30 nm particles to 540 nm for a ~50 nm particles. The UV-Vis results were also confirmed by the SEM observation

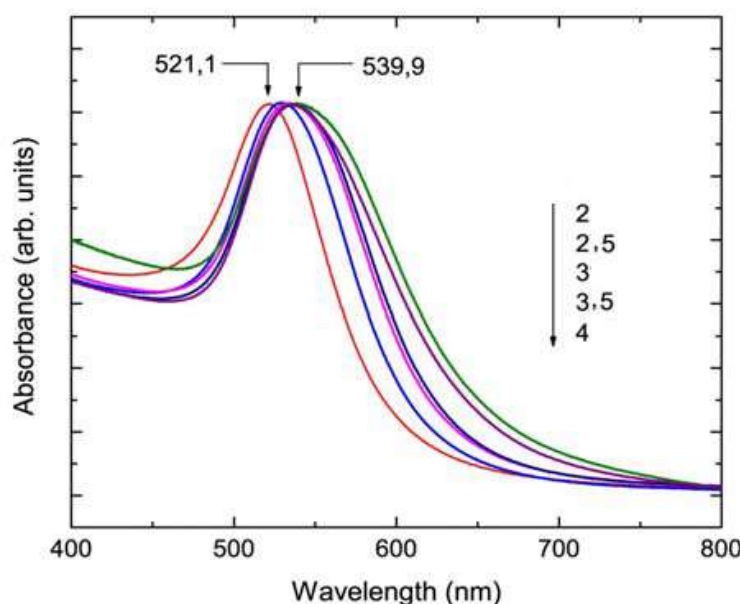


Figure 3 Surface plasmon absorption spectra of gold nanoparticles.

Conclusion

The colloidal gold nanoparticles had been prepared by chemical reduction method. In this present work reported a significant advance in terms of the realization of a simple chemical method, which could synthesize the size-controlled gold nanoparticles rapidly under ambient conditions. From XRD data it was confirmed that all the samples were good crystalline in nature with face center cubic structure. Synthesized gold nanoparticles were considered to have a wide range of applications in nanotechnology, catalyst, pharmaceutical, and energy industries.

Acknowledgments

I would like to thank Professor Dr Soe Myint, Head of Department of Physics, Yenangyaung Degree College, for his kind permission to carry out this work.

References

- Eustis S and El-Sayed M A (2006) Journal of Chemical Society Review vol. 35 pp. 209.
- Kaushik Mallick, Wang Z L and Tarasankar P. (2001) Journal of Photochemistry and Photobiology A: Chemistry vol. 140 pp.75.
- Kenji O, Yoshiteru M, Yamamoto T A, Yasuaki M and Yoshiro Na (2007) Journal of Materials Letters vol. 61 pp.3429.
- Kimling J, Maier M, Okenve B, Kotaidis V, Ballot H, Plech A. (2006) “Turkevich method for gold nanoparticle synthesis revisited” The Journal of Physical Chemistry B vol.110(No.32): pp. 157.
- Liz-Marzan L M (2004) Journal of Materials today vol. 7 pp.26.
- Polte J, Ahner TT, Delissen F, Sokolov S, Emmerling F, Thünemann AF, Krahnert R. (2010) “Mechanism of gold nanoparticle formation in the classical citrate synthesis method derived from coupled in situ XANES and SAXS evaluation”, Journal of the American Chemical Society. Vol.132(No.4) pp.1296-301.
- Rayavarapu R G, Petersen W, Ungureanu C, Post J N, van Leeuwen T G and Manohar S (2007) International Journal of Biomedical Imaging Article ID 29817.
- Sau T K, Anjali P, Jana N R, Wang Z L and Tarasankar P (2011) Journal of Nanoparticle Research vol. 3 pp.257.
- Shang Y, Min C, Hu J, Wang T, Liu H, Hu Y. (2013) “Synthesis of gold nanoparticles by reduction of HAuCl₄ under UV irradiation” Journal of Solid State Sciences. Vol. 15: pp17-23.

EFFECTS OF ANNEALING TEMPERATURE ON OPTICAL AND ELECTROCHEMICAL PROPERTIES OF SPRAY-PYROLYSED WO_3 FILMS

Mono Zaw¹, Aung Chan Thar², Nyein Wint Lwin³ and Than Zaw Oo⁴

Abstract

Tungsten trioxide (WO_3) thin films were coated onto fluorine tin oxide (FTO) coated glass substrates by spray pyrolysis technique and annealing at different temperatures (300°C, 400°C and 500°C). The presented work studied the effect of annealing temperature on the surface morphology, optical and electrochemical properties of WO_3 films by using scanning electron microscopy (SEM), atomic force microscopy (AFM), UV-vis spectroscopy and cyclic voltammetry (CV). Optical study showed that the decreased optical transmission and band gap was observed in WO_3 film at higher annealing temperature (400°C and 500°C). The electrochemical study revealed that anodic peak current density was higher in WO_3 film annealed at 400°C in KI electrolytic solution. Upon modulating the annealing temperature, change in optical and electrochemical properties of WO_3 films was correlated to surface morphology change in WO_3 films.

Keywords: Optical properties, Tungsten trioxide film, Annealing temperature, Electrochromism

Introduction

Electrochromic (EC) materials and devices are reversible change in color, or optical density, with a change in voltage or electric potential [Ruyu H.Y. *et al.*, J. Materials Science, **39** (2004) 4377].

The important feature of electrochromic glass is the ability to response toward the apply voltage in shortest time and endurance to maintain in color shape after apply voltage. A lot of attention has been devoted in the latter application due to the potential for significant energy saving by reducing cooling and heating loads and a better management of the natural light [Rajeshwar A.W. *et al.*, J. Electroanalytical Chemistry, **612** (2008) 112]. The application of the electrochromic smart glass include anti-glare automobile rearview mirrors, sun-roofs, electronic shutters, hydrogen sensors, displays and energy efficient “smart” windows [Gillaspie D.T. *et al.*, J. Materials Chemistry, **20** (2010) 9585]. They can be built in a form of electrochromic device with one or two electrochemically active coatings that change color during an oxidation-reduction process.

Electrochromic (EC) devices can be made from organic and inorganic materials. The advantage of inorganic materials based electrochromic device is that they are much more stable in sunlight and have longer lifetime. Transition metal oxides (inorganic materials) such as tungsten trioxide (WO_3), nickel oxide (NiO), molybdenum trioxide (MoO_3) and iridium trioxide (IrO_3) have been widely used in electrochromic materials. The electrochromic (EC) materials change their optical properties when charge insertion or extraction and this may cause the material change its color. Materials that change color upon charge insertion are called cathodic while materials that change color upon charge extraction are called anodic. Oxides of Tungsten (W), Titanium (Ti) and Molybdenum (Mo) exhibit cathodic electrochromism and oxides of Vanadium (V), Nickel (Ni) and Iridium (Ir) exhibit anodic electrochromism. [Niklasson G.A. *et al.*, J. Materials Chemistry, **17** (2007) 127]

¹ Assistant Lecturer, Department of Physics, University of Mandalay, Mandalay, Myanmar

² Dr, Lecturer, Department of Physics, Mohiny Degree Collage, Kachin, Myanmar

³ Dr, Professor, Department of Physics, University of Mandalay, Mandalay, Myanmar

⁴ Dr, Professor, Universities’ Research Centre, University of Yangon, Yangon, Myanmar

Tungsten trioxide (WO_3) is the most studied among the electrochromic materials and exhibits an n-type semiconducting behavior with a band gap energy of 2.5-3.3 eV [Jayachandran M. *et al.*, Transactions of the SAEST. **40** (2005) 42]. There are various choices for preparing WO_3 films with the development of thin film technology. These include sputtering, chemical vapor deposition, spray pyrolysis, evaporation, sol-gel and laser ablation deposition. Among these, spray pyrolysis method is the most cost-effective for producing large-area films, and enables a better control over the film growth and hence more homogenous and more transparent films are yielded [Daniel M.F. *et al.*, J. Solid State Chemistry, **67** (1987) 235.]

Materials and Methods

Tungsten trioxide (WO_3) powder (0.05 M) was dissolved in 50 ml of ammonia at 80°C under continuous stirring for 30 min to form tungsten trioxide (WO_3) precursor solution. The obtained WO_3 solution was diluted with 10 ml of deionized water and then cooled down to room temperature and filtered. After that, the final WO_3 solution was sprayed on the FTO substrate (substrate temperature is 300°C) by using spray pyrolysis method to obtain WO_3 films. The resulting WO_3 films with the WO_3 concentration of 0.05 M were annealed at different temperatures (300°C, 400°C and 500°C) for 1 hour.

The surface feature of WO_3 films was measured by scanning electron microscopy (SEM) and atomic force microscopy (Nanosurf Naio AFM). The optical properties of WO_3 films were performed using UV-vis spectrophotometry (Genesys 10S). The electrochemical properties of WO_3 films were characterized by cyclic voltammetry (CV) (Electrochemical Workstation-CorrTest CS350).

Results and Discussion

3.1 Surface morphology of WO_3 Films

The surface morphology of WO_3 films was examined by Scanning Electron Microscopy (SEM) and Atomic Force Microscopy (AFM). Figure 3.1 (a-c) shows the SEM micrograph of WO_3 films for different annealing temperatures in two dimensional view. From the SEM micrograph, the surface feature of WO_3 films annealed at 300°C reveals the cracking surface. This cracking is formed so many gap on the WO_3 films. The surface morphology of WO_3 films for 400°C and 500°C are relatively the same with a rough surface and uniformly covered. In addition, the solvent evaporation can cause defects in the surface, such as pores, cracks etc. Moreover, the surface morphology of WO_3 films was shown with three dimensional view by AFM technique. Figure 3.2 (a-c) shows the AFM micrograph of WO_3 films for different annealing temperatures. Like the case of SEM results, the surface morphology of WO_3 thin films annealed at 400°C shows better surface conformation rather than that of other WO_3 samples. It may provide the better performance of electrochromic device.

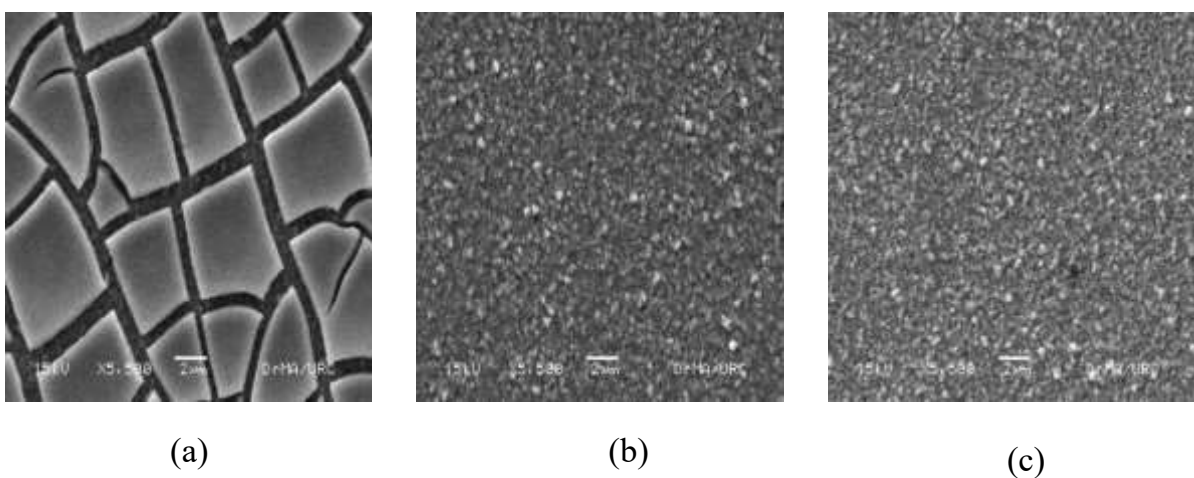


Figure 3.1 SEM micrograph of WO_3 films with different annealing temperatures (a) 300°C, (b) 400°C and (c) 500°C

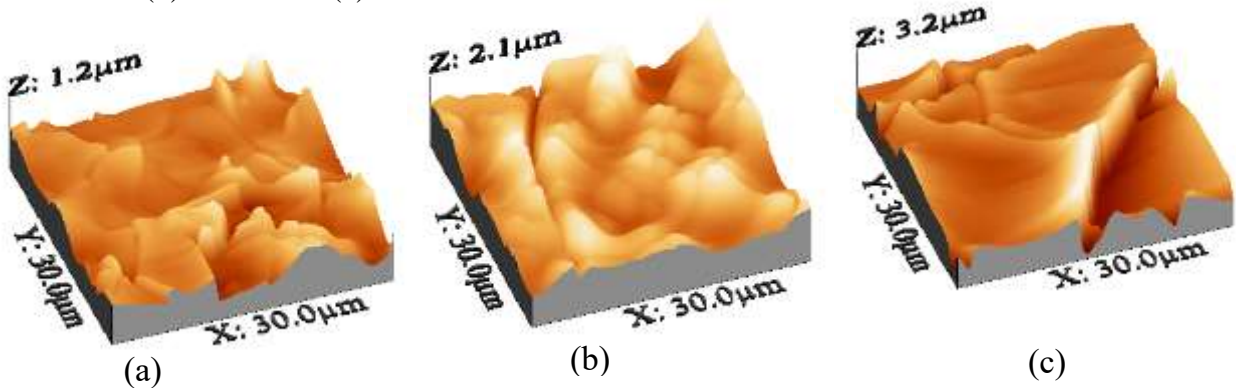


Figure 3.2 AFM micrograph of WO_3 films with different annealing temperatures (a) 300°C, (b) 400°C and (c) 500°C

3.2 Optical Transmission and Band Gap Energy of WO_3 Films

The optical properties of WO_3 films were investigated varying with annealing temperatures. The optical transmission spectra of WO_3 films were measured by UV-vis spectrophotometry. The optical transmission spectra of WO_3 films with different annealing temperatures are depicted in Figure 3.3 (a). From this figure, the values of the optical transmission in the visible region are listed in Table 3.1. The highest optical transmission of WO_3 films is observed at 300°C. It may be due to the surface defects (larger number of holes and cracking) of WO_3 films. The optical transmission of WO_3 films for 400°C and 500°C are almost overlap in the visible region. Upon increasing annealing temperatures, the optical transmission of WO_3 films decreased. It is due to the fully coverage of the sample and better surface formation of WO_3 films. The optical transmission of WO_3 films decreased upon increasing annealing temperatures which is ascribed to the surface conformity of WO_3 films at higher annealing temperatures.

The optical band gap energy of WO_3 films was determined from Tauc's plot equation, $(\alpha h\nu)^n = A(h\nu - E_g)$, where α is absorption coefficient, $h\nu$ is incident light energy, and E_g is the band gap of the material. The exponent ' n ' examine the transition type of the material. The value of n is 1/2 for indirect transition and is 2 for direct transition. The value of the optical band gap of WO_3 films was obtained by extrapolating the linear portion of the curve to photon energy axis. Figure 3.3 (b) shows the plot of the $(\alpha h\nu)^{1/2}$ versus $h\nu$ graph. The values of the band gap energy of

WO_3 films are listed in Table 3.1 for all annealing temperatures. The optical band gap energy values of WO_3 films decreased upon increasing annealing temperatures.

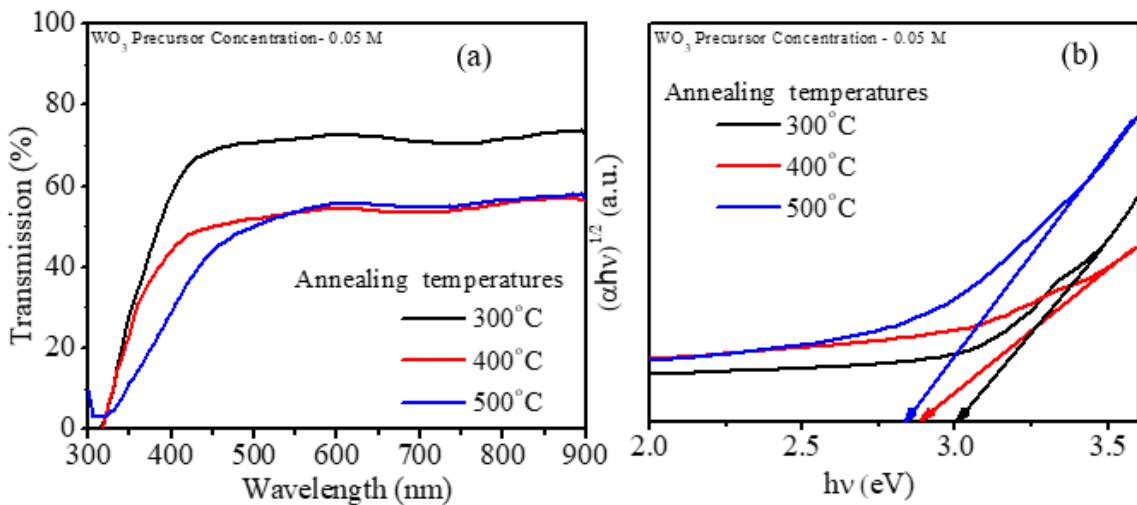


Figure 3.3 (a) Optical transmission spectra and (b) Plot of $(\alpha h\nu)^{1/2}$ versus $h\nu$ of WO_3 films with different annealing temperatures

Table 3.1 The value of optical transmission and band gap energy of WO_3 films with different annealing temperatures

Annealing Temperatures	Transmission (%)	Band gap energy (E_g) (eV)
300°C	75	3.0
400°C	50	2.9
500°C	55	2.7

3.3 Electrochemical Properties of WO_3 Films

Effect of annealing temperatures on electrochemical properties of WO_3 films were explored by cyclic voltammetry (CV). CV measurement is important for determining the performance of electrochromic device. Figure 3.4 (a-c) shows the CV graph of WO_3 films for all annealing temperatures with different scan rate in potassium iodide (KI) electrolytic solution. The cyclic voltammograms of WO_3 films were recorded in the potential range from -0.4 V to $+0.2$ V for each scan rate. The values of the anodic peak current density of WO_3 films for different annealing temperatures are obtained from the CV graph. As can be seen in the CV graph, the highest anodic peak current density of WO_3 films was observed at the annealing temperature 400°C for each scan rate. It is agreed with the earlier speculation of AFM results. The better surface homogeneity of WO_3 films annealed at 400°C gives the highest anodic peak current density for each scan rate. The values of the anodic peak current density of WO_3 films with different annealing temperatures are listed in Table 3.2. As can be seen in Figure 3.5, the highest anodic peak current density of WO_3 films was observed at the annealing temperature 400°C for different scan rates.

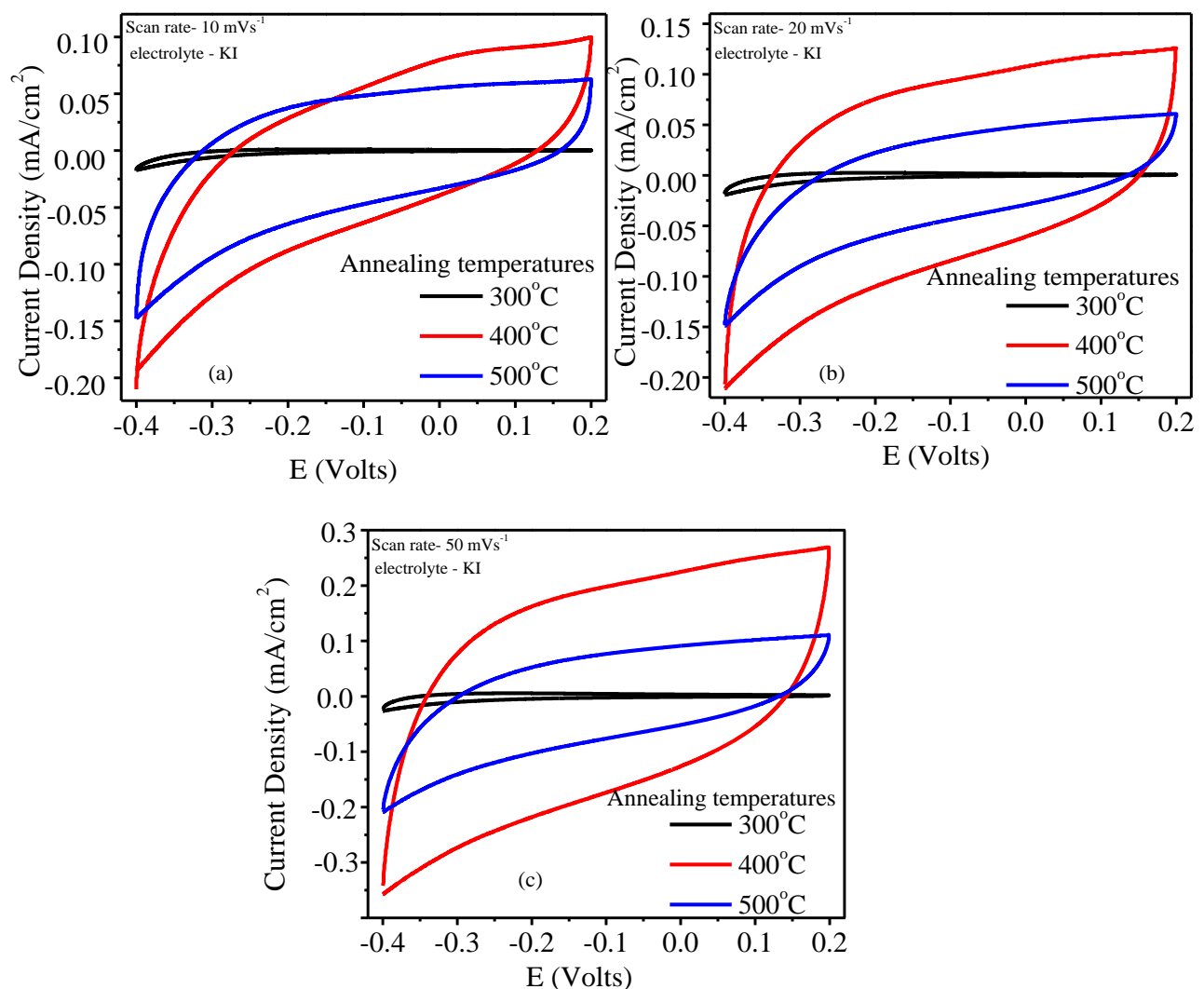


Figure 3.4 (a–c) Cyclic voltammogram of WO_3 films annealed at different temperatures (300°C , 400°C and 500°C) in KI electrolytic solution

Table 3.2 The values of anodic peak current densities of WO_3 films with different annealing temperatures in KI electrolytic solution

Scan Rate (mV/s)	Annealing Temperature	Anodic Peak Current Density (mA/cm^2)
10	300°C	0.01
	400°C	0.09
	500°C	0.05
20	300°C	0.01
	400°C	0.12
	500°C	0.06
50	300°C	0.01
	400°C	0.24
	500°C	0.09

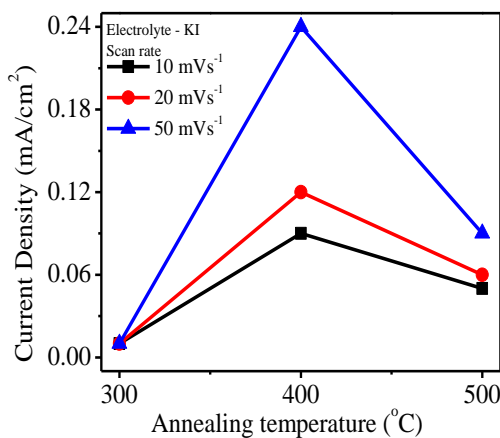


Figure 3.5 Plot of current density (mA/cm^2) Vs annealing temperature ($^\circ\text{C}$) of WO_3 films for all scan rates in KI electrolytic solution

Summary and Conclusion

Tungsten trioxide (WO_3) thin films were prepared from WO_3 aqueous solution by sol-gel method. The resulting WO_3 solution was transferred onto the substrate by spray pyrolysis method. The obtained WO_3 thin films were characterized by scanning electron microscopy (SEM), atomic force microscopy (AFM), UV-vis spectrophotometry and cyclic voltammetry (CV) by varying the annealing temperatures. The optical transmission and band gap energy of WO_3 films decreased upon increasing annealing temperatures. The electrochemical behavior of WO_3 films varying with annealing temperatures are tested by cyclic voltammetry (CV). The highest anodic peak current density of WO_3 films was observed at the annealing temperature 400°C for each scan rate in KI electrolytic solution. It may be due to the complete coverage of WO_3 thin films altered by annealing and it has sufficient colored species.

Acknowledgement

The authors special thanks to ISP (International Science Program), Sweden, for their support in measurement of cyclic voltammetry (Electrochemical Workstation- CorrTest CS350) and also grateful thank to all the Materials Science Laboratory members (University of Mandalay) for their helpful discussion.

References

- Daniel M.F. *et al.*, J. Solid State Chemistry, **67** (1987) 235.
- Gilliaspie D.T. *et al.*, J. Materials Chemistry, **20** (2010) 9585
- Jayachandran M. *et al.*, Transactions of the SAEST. **40** (2005) 42.
- Niklasson G.A. *et al.*, J. Materials Chemistry, **17** (2007) 127.
- Ruyu H.Y. *et al.*, J. Materials Science, **39** (2004) 4377.
- Rajeshwar A.W. *et al.*, J. Electroanalytical Chemistry, **612** (2008) 112.

SYNTHESIS AND OPTICAL PROPERTIES OF TITANIUM DIOXIDE NANOPARTICLES USING SOL-GEL METHOD

Kyaw Kyaw¹, Hnin Yu Khaing², Than Than Win³, Yin Maung Maung⁴

Abstract

The main objective of this research work was to synthesize and to characterize titanium dioxide (TiO_2) nanoparticles using sol – gel method with different weight ratio of NaOH. The optical properties and band gap energies of obtained nanoparticles were investigated with UV-Vis spectroscopy. The crystal structural and morphological properties of fabricated TiO_2 nanoparticles were characterized with XRD and SEM techniques. From the results of investigating methods, it was revealed that the fabricated particles were good agreement with standard physical properties of TiO_2 nanoparticles and they could be used in Solar cells, waste water treatment and industrial applications.

Keywords: TiO_2 , NPs, NaOH, SEM, XRD, UV-Vis

Introduction

Nowadays nanoparticles are the most widely used in the worldwide. They are like cornerstones of nanotechnology, nanoscale science and the interdisciplinary field of various science area. Nanotechnology is the studying of extremely small structures reducing bulk state materials as a result of size in nanoscale. These nanoparticles are very attractive because of its properties that is very different from bulk material. Nanoparticles have between the range size of 1 nm to 100 nm [Djouadi D., Aksas A.]. Titanium dioxide nanoparticles have one of great attractive significant interesting materials for scientists and physicists due to their properties. Titanium dioxide (TiO_2) is n - type semiconductor and it has wide energy band gap ($> 3eV$). TiO_2 exists in three different crystalline phases: anatase (tetragonal), rutile (tetragonal), and brookite (orthorhombic). Both anatase and rutile have tetragonal crystal structure but belong to different phase. As a bulk material rutile is the stable phase, however solution phase preparation methods for TiO_2 generation favors the anatase structure. The c/a ratio of tetragonal anatase phase has greater than one and rutile phase has less than one [Galioglu S]. TiO_2 nanoparticles were synthesized by various methods. These are hydrothermal method, sol-gel method, chemical method and so on. From these methods, sol-gel method is one of the most promising methods due to low cost, low temperature and ease fabrication than the other method. In this research, TiO_2 nanoparticles were prepared by sol – gel method and they were deposited onto glass substrates using spin coating method. The structural, morphological and optical properties of fabricated particles and thin films were investigated.

Experimental Procedure

In this research, $TiCl_3$ is used as precursor for synthesis of nanoparticles. According to the stoichiometric balance reaction equations were;



3.5ml of $TiCl_3$ was mixed again with 5 ml of hydrochloric acid and they were stirring at 300 rpm under aluminum fume hood for 30 min. After stirring, 0.1g, 0.3 g and 0.5 g amount of

¹ Lecturer, Department of Physics, University of Mandalay

² Lecturer, Department of Physics, Yenangyaung Degree College

³ Professor (Head), Department of Physics, Pin Lone University

⁴ Professor, Department of Physics, University of Yangon

sodium hydroxide were mixed into the solution. The exothermic reactions were observed and it released heat energy. And then the mixed solutions were continuously stirring at constant speed for 1 h to obtained homogenous solutions. In order to remove the produced impurities of reaction, the obtained solutions were annealed at 300°C for 1 h in the atmospheric pressure. After heating process was done the white color amorphous TiO₂ were obtained. The obtaining amorphous white TiO₂ were washed 3 times to removed sodium chloride ions by filtration process with de-ionized water. And then they were centrifuged to separate the dregs at speed 1500 rpm for 10 min. Subsequently white TiO₂ were annealed at 300°C to remove the absorbed water for 2 h. Finally, pure white TiO₂ nanoparticles were obtained. The obtained TiO₂ powders were mixed in 2.5 ml of ethanol and 2.5ml of acetone using magnetic stirrer for 5 min. The 200 µl of TiO₂ colloidal solution was deposited on the glass substrates using spin coating process at 2000 rpm for 20 s. The obtained TiO₂ coated glasses, were annealed on the hot plate at 150°C and 30 min. the obtained TiO₂ thin films were characterized by UV-Visible spectroscopy to determine its optical properties. The other properties such as structural and morphological properties were also investigated.

Results and Discussion

XRD analysis

In this XRD analysis, the diffraction angle 2θ was started from 10° to 70°. The XRD profiles of the TiO₂ nanoparticles were shown in Fig 1 (a, b, c and d) respectively. From these figures, all of the diffraction peaks showed anatase phase of TiO₂ tetragonal structure, which were good agreement with the standard library of Join Committee for Powder Diffraction Studies (JCPDS). The crystallite sizes were calculated using Debye-Scherrer's formula the average crystallite size of anatase TiO₂ synthesis nanoparticles was found in the range of 16nm to 35nm.

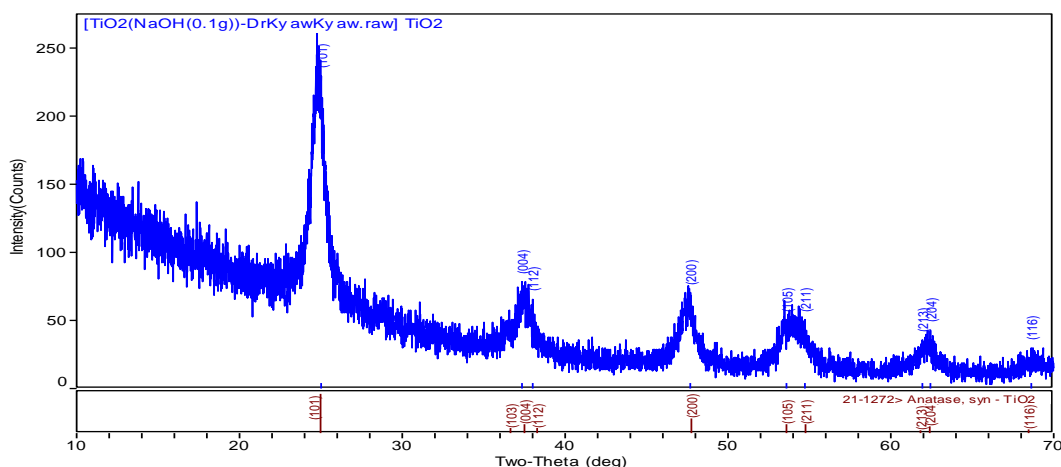


Figure 1 (a) XRD profiles of TiO₂ nanoparticles from NaOH(0.1g).

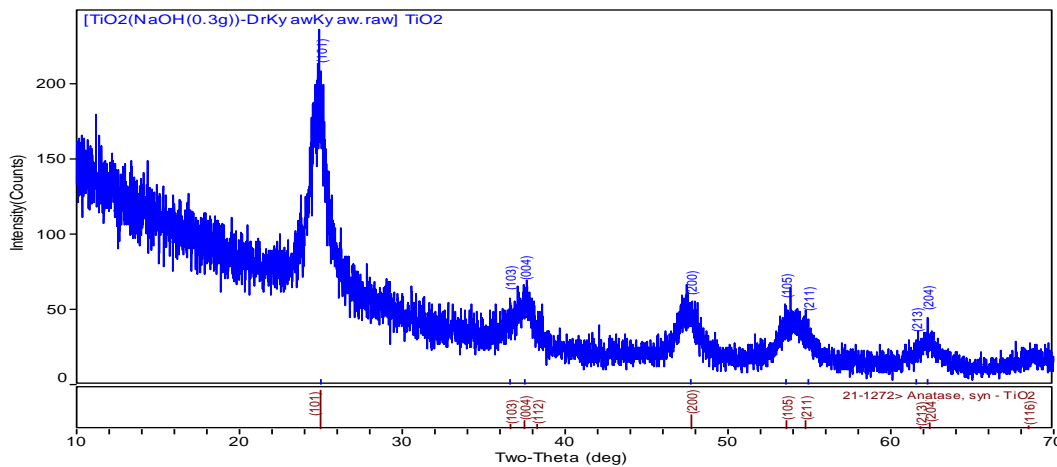


Figure 1 (b) XRD profiles of TiO_2 nanoparticles from $\text{NaOH}(0.3\text{g})$.

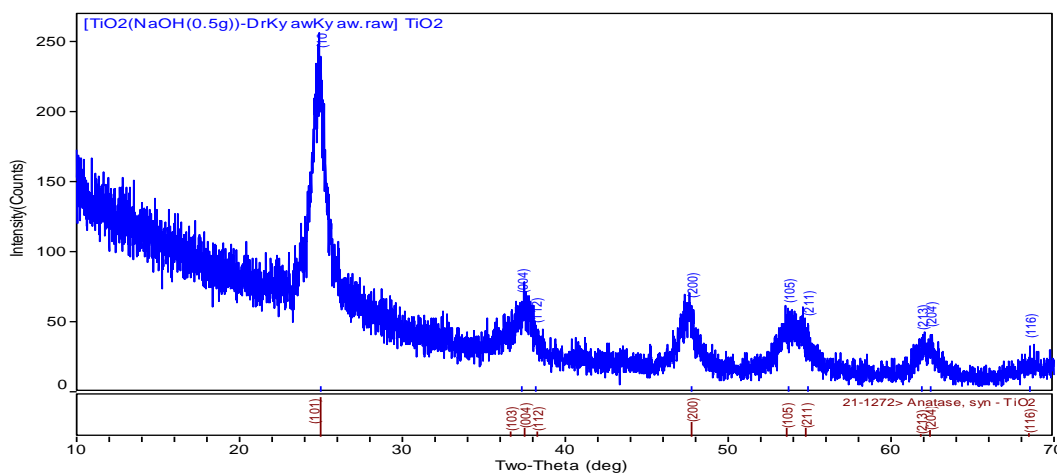


Figure 1 (c) XRD profiles of TiO_2 nanoparticles from $\text{NaOH}(0.5\text{g})$.

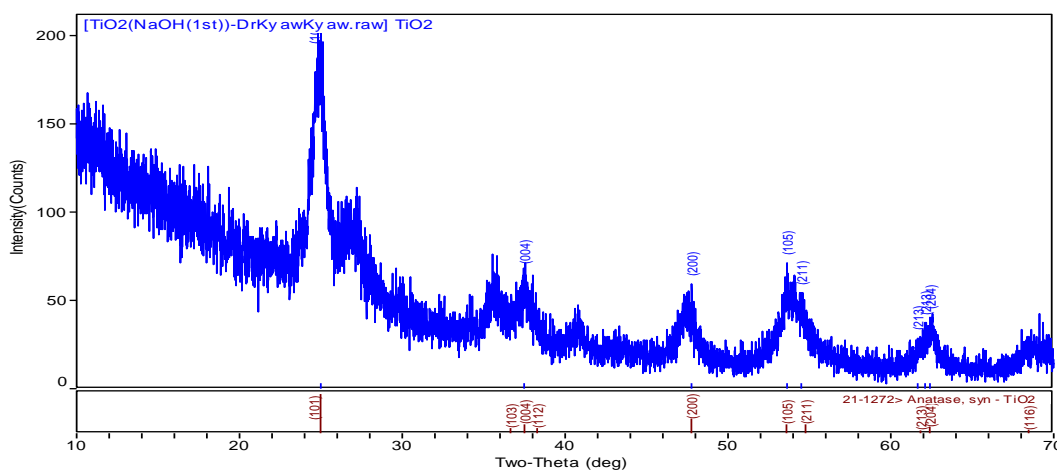


Figure 1 (d) XRD profiles of TiO_2 nanoparticles from $\text{NaOH}(0.5\text{g})$ with deionized water.

SEM analysis

The Fig 2(a, b, c and d) showed the SEM images of the TiO₂ nanoparticles prepared by sol-gel method with different amount of NaOH. In the Fig 2(a) the nanoparticles were formed in irregularly shape, overlapped and extremely agglomerated. Fig 2(b) illustrated the SEM result of TiO₂ nanoparticles synthesized with 0.3 g of NaOH. It was observed that the particles became tiny size and spherical shape. It can be observed from the Fig 2(c), some grains were agglomerated in some regions and some grains were separated by pores. Moreover, they were formed in spherical shape and overlapped in some regions. In Fig 2(d), the particles were formed spherical shapes and they had uniform nanoparticles sizes.

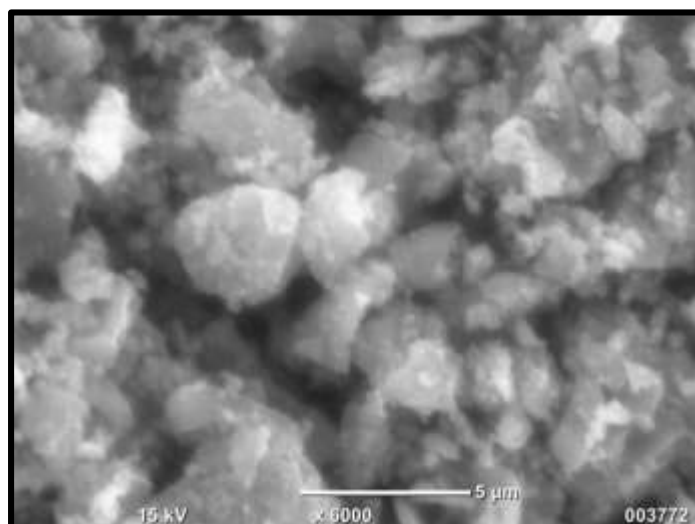


Figure 2 (a) The SEM micrographs of TiO₂ nanoparticles with NaOH (0.1 g).

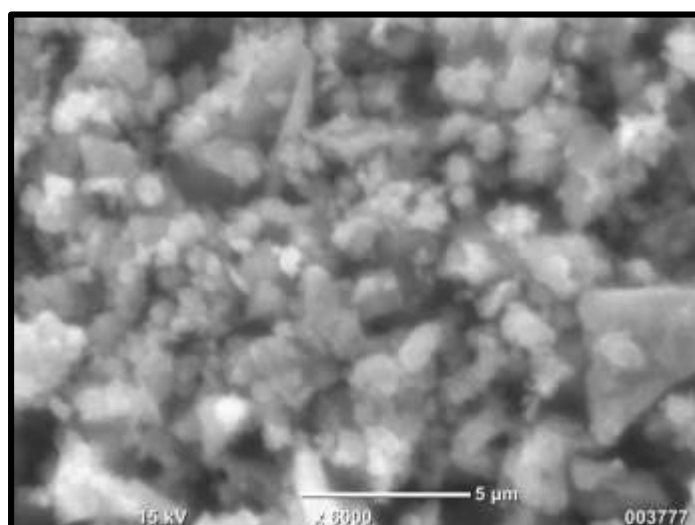


Figure 2 (b) The SEM micrographs of TiO₂ nanoparticles with NaOH (0.3 g).

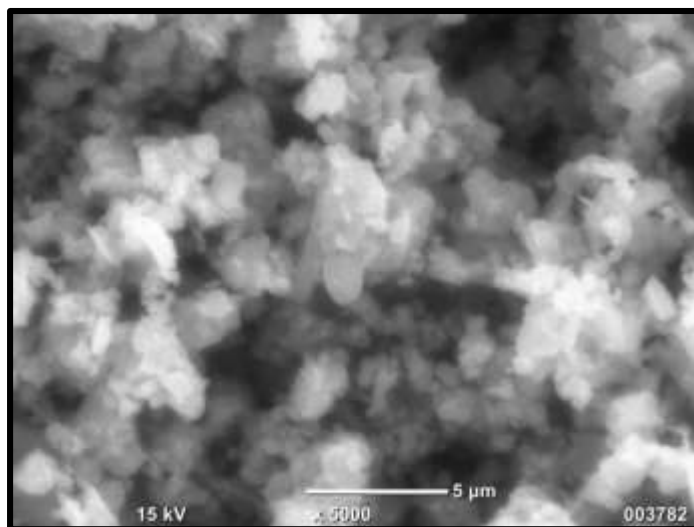


Figure 2 (c) The SEM micrographs of TiO₂ nanoparticles with NaOH (0.5 g).

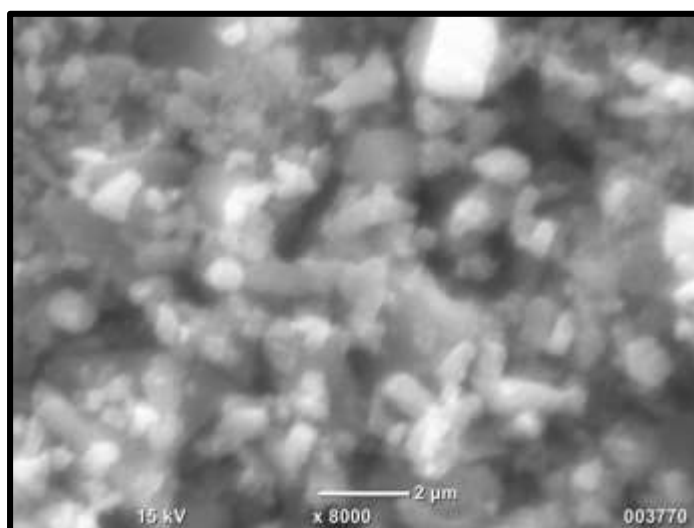


Figure 2 (d) The SEM micrographs of TiO₂ nanoparticles with NaOH (0.5 g) and deionized water.

Energy Band Gap From UV-Vis Analysis

Tauc's relation was used to calculate band gap energies. A plot of variation of $(\alpha h\nu)^2$ versus $h\nu$ were shown in Fig 3 (a, b, c and d). The band gap energies were evaluated using extrapolation of the linear part of the curve. The obtained band gap energies of TiO₂ nanoparticles were listed in Table 1.

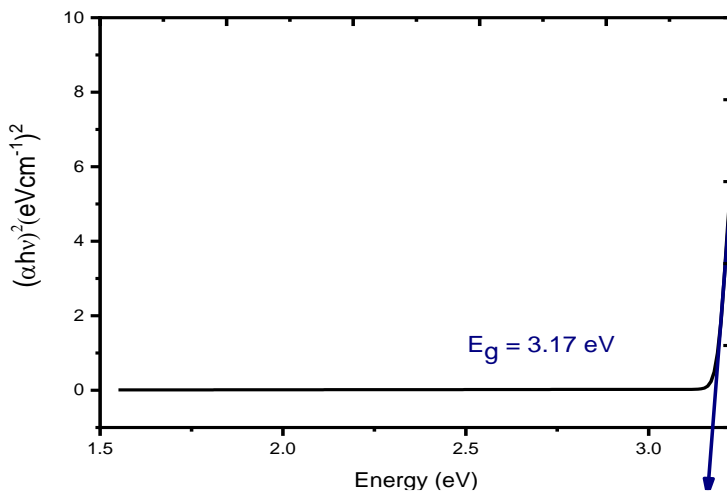


Figure 3 (a) The plot of extrapolation for TiO_2 nanoparticles from NaOH (0.1 g).

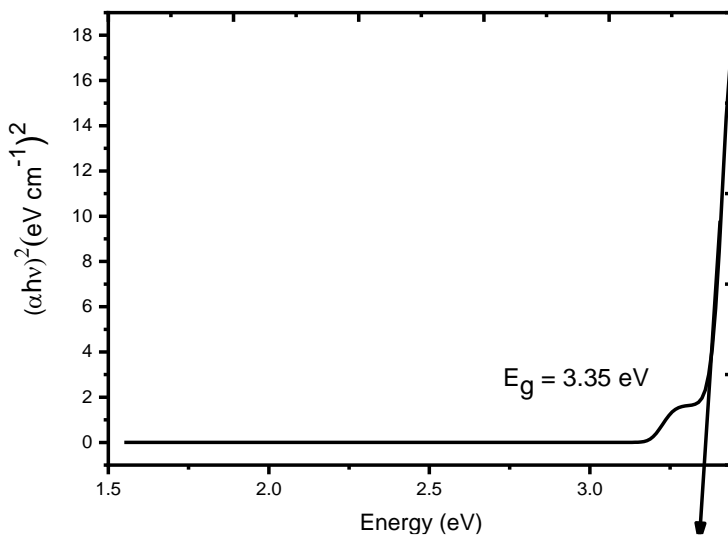


Figure 3 (b) The plot of extrapolation for TiO_2 nanoparticles from NaOH (0.3 g).

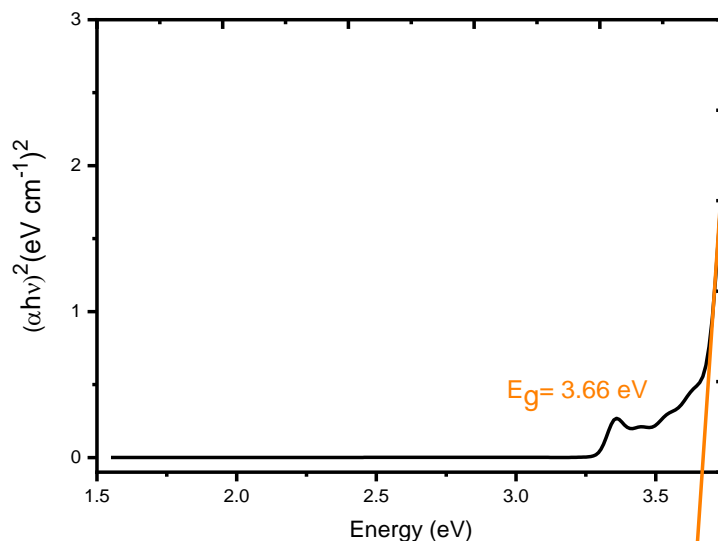


Figure 3 (c) The plot of extrapolation for TiO_2 nanoparticles from NaOH (0.5 g).

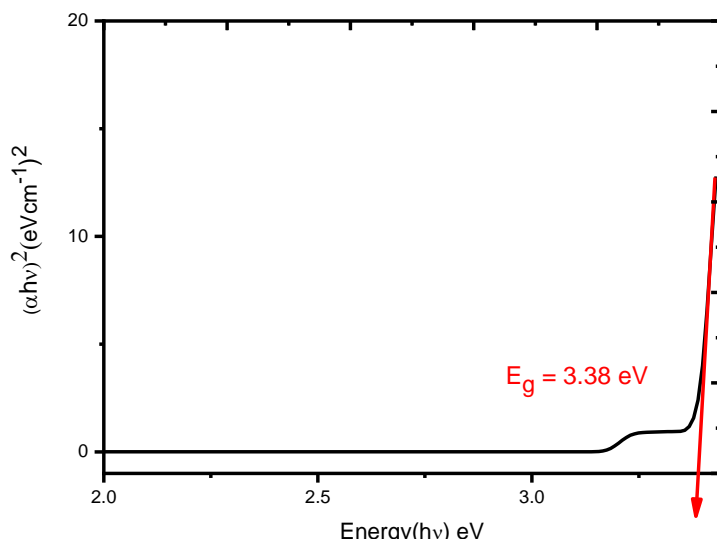


Figure 3 (d) The plot of extrapolation for TiO_2 nanoparticles from NaOH (0.5 g) with deionized water.

Table 1 The band gap energies of TiO_2 nanoparticles.

No	NaOH (g)	Band gap energy (eV)
1	0.1	3.17
2	0.3	3.35
3	0.5	3.66
4	0.5 with H_2O	3.38

Conclusion

Titanium dioxide (TiO_2) nanoparticles using sol – gel method with different mass ratio of NaOH from 0.1 g to 0.5 g were successfully synthesized. UV-Vis analysis showed that the maximum absorption peaks for TiO_2 nanoparticles were found between 300 nm and 400 nm. The band gap energies of nanoparticles were varied from 3.17 eV to 3.66 eV due to the effect of NaOH content increase. The crystal structural and morphological properties of fabricated TiO_2 nanoparticles were characterized with XRD and SEM techniques. From XRD analysis, it was observed that the fabricated TiO_2 nanoparticles had polycrystalline nature and it's crystal structure were tetragonal with anatase phase. The grain formation was obviously formed in SEM micrographs. Some grains were agglomerated in some region and some were separated by pores. It could also be noted that one grain composed of approximately 20 crystallites. From this study it was concluded that the obtained TiO_2 nanoparticles were quite suitable to be used in photovoltaic applications such as solar cells.

Acknowledgments

This research work was totally implemented at materials research lab, Department of Physics, University of Mandalay.

References

- Djouadi D., Aksas A. and Chelouche A. (2011) Journal of Physical Sciences vol. 10 pp.76.
- Galioglu S. (2014) Journal of Microporous and Mesoporous materials. Vol.196 pp.136.
- Han Y., Kim H. S. (2012), Journal of Nanomaterials. Vol.1 pp.2.
- Hwang I. S., Choi. J. K., Kim S. J., Dong K. Y., Kwon J. H., Ju B. K., (2009) Journal of Sensor & Actuator B - Chem vol.142 pp.105.
- Junbo W., Minge Y., Yingmin L. C., Licheng, (2015), Journal of Non-Cryst Solids, 351 pp.228-232.
- Kusumawardani C., and Indriana K. (2010), Journal of Science. Vol. 1 pp 1.

CONTROLLING THE APPLIANCES AND MONITORING DATA FROM LOCAL WEB SERVER USING ESP32 AND HTML

Nu Nu Swe¹, Mi Yin Sa Nine², Hnin Aye Khine³, Ohnmar Soe⁴

Abstract

Physical data can be sending (writing) to or receiving (reading) from the web server using ESP32 which is a device of combination of microcontroller and Wi-Fi, generally. Physical data such as temperature, humidity and voltage are detected (read condition) from the DHT11 sensor and potentiometer by using microcontroller and these are monitored on web page. And then, the home appliance can be controlled by the touching or clicking the word or symbol on the web page on laptop or smart phone as writing action. In this research, a LED is controlled instead of the home appliance and the potentiometer is used behalf of voltage source to be measured. ESP32 is compatible to Arduino IDE but ESP32 board is not included in Arduino IDE as default. The board is installed in the IDE. Coding composes of data writing to / reading from web, connecting to web server and web page management. Web page is created by using hypertext markup language (HTML).

Keywords: ESP 32, Wi-Fi, Read/write, client, web server, HTML.

Introduction

The data can be writing to or read on the web server with the help of ESP32. Arduino IDE can be compatible to ESP32. There are no ESP boards in the default Arduino IDE. The ESP boards are needed to include in Arduino IDE. The physical data (such as voltage, temperature, humidity) are detected from the potentiometer and DHT 11 and then data are visualized on the web page using the local Wi-Fi router or Wi-Fi hot spot of phone. By the writing section, the electrical appliance can be controlled from the web page on the specified webserver. Programmer code is written by Arduino language and HTML.

Materials Required

In this research, ESP32 is used as the main processing unit and DHT11, potentiometer and electrical appliance (such as LED) are used to implement the data reading /writing action.

Web Server

A web server processes incoming network requests over Hypertext Transfer Protocol (HTTP) and several other related protocols. The primary function of a web server is to store, process and deliver web pages to clients. The communication between client and server takes place using the Hypertext Transfer Protocol (HTTP). Web servers can frequently be found embedded in printers, routers and webcams which are serving only a local area network (LAN). The web server may then be used as a part of a system for monitoring or administering the device. This usually means that additional software not to be installed on the client computer since only a web browser which is included the most required operating system.

¹ Dr, Associate Professor, Department of Physics, Yangon University of Education

² Dr, Lecturer, Department of Physics, Myeik University

³ Dr, Lecturer, Department of Physics, Yangon University of Education

⁴ Dr, Lecturer, Department of Physics, Yangon University of Education

ESP32

ESP32 development board is equipped with ESP-WROOM-32 module which contains dual-core 32-bit microprocessor attached with Wi-Fi and dual mode Bluetooth. Moreover, consists of two CPU cores which can be controlled individually. It operates at 80 MHz to 240MHz adjustable clock speed and performs 600 Dhystone million instructions per second (DMIPS).

ESP32, is the various memory types which are 448KB for ROM, 520KB of SRAM and 4MB of flash memory. In sleep mode condition, 8KB memory can be used for real time controller fast/slow SRAM. These memories are sufficient to run with the string that make web pages, JSON/XML data is utilized in Internet of Things(IoT)devices. ESP32 integrates Wi-Fi transceiver, classic Bluetooth and Bluetooth low energy (BLE) so that it can connect to Wi-Fi network and interact with internet. ESP32 can set up its own network which can directly be connected by other devices.

ESP32 possesses the multiplexed general-purpose input output (GPIO)pins which are shown in Table 1.

Table 1 Peripheral Input /Output of ESP32

No	Pin Name	Function
1.	Touch pad	Capacitance touch sensing
2.	ADC	(Analog-to-converter) channels of 12- bit SAR-ADC. The ADC range can be varied 0-1V,0-1.4V,0-2V and 0-4V.
3.	DAC	(Digital-to-analog converter) channels of 8-bit
4.	I2C	(inter-integrated circuit) uses to interface the sensors
5.	UART	(Universal asynchronous receiver/transmitter). One is used to load serially.
6.	CAN2.0	Controller area network
7.	SPI	(Serial peripheral interface) use to interface the sensors.
8.	I2S	(inter-integrated sound) use to interface sound
9.	RMII	(Reduced media-independent interface)
10.	PWM	(Pulse width modulation) pins for controlling device

ESP32 is highly integrated with built-in antenna switches, RF, power amplifier, low-noise receive amplifier, filters, and power management modules. The internal block diagram is shown in Figure1.

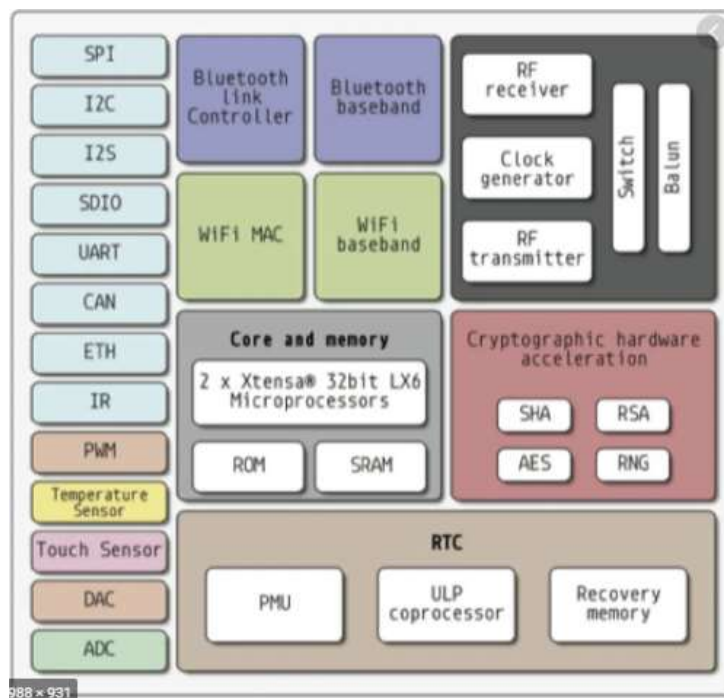


Figure 1 Function Block Diagram of ESP32

DHT 11

The DHT11 is a digital temperature and humidity sensor as shown in Figure 2. It is composed of a capacitive humidity sensor and a thermistor to measure the surrounding air, and a digital signal is produced on the data pin. Table 1 shows the pin description of DHT11. Single-bus data format is used for communication and synchronization between MCU and DHT11 sensor. It is about 4ms for one communication process. The data consists of decimal and integral parts. A complete data transmission is 40bit, and the sensor sends higher data bit first. Data format is the sum of 8bit integral RH data, 8bit decimal RH data, 8bit integral T data, 8bit decimal T data and 8bit check sum. If the data transmitted correctly, the check-sum should be the last 8bit of "8bit integral RH data + 8bit decimal RH data + 8bit integral T data + 8bit decimal T data". Data transmission is expressed in Figure 3.

Table 2 Pin Description of DHT 11

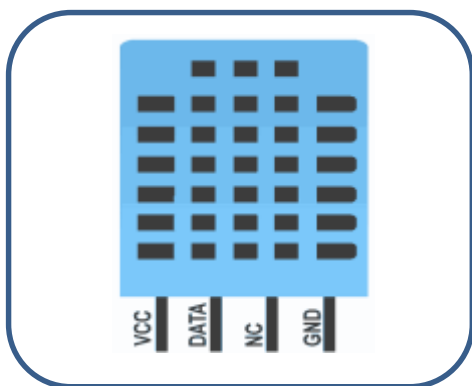


Figure 2 The Photo of DHT 11

Pin No	Pin Name	Pin Description
1	VCC	Power supply 3.3 to 5.5 Volt DC
2	DATA	Digital output pin
3	NC	Not in use
4	GND	Ground

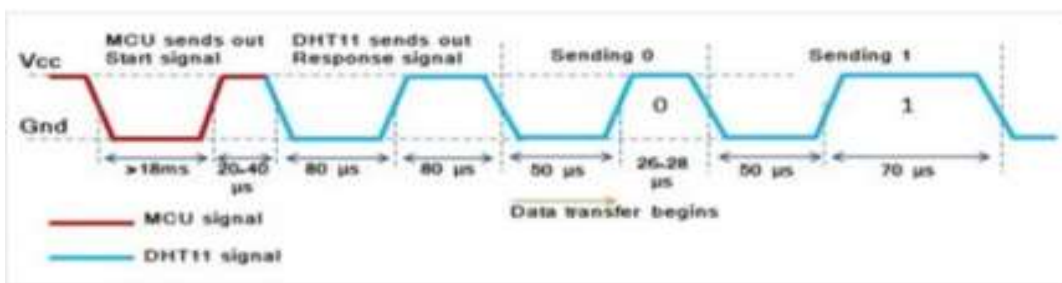


Figure 3 Data Transmission

Operation

In this research, the temperature and humidity are detected from DHT11 sensor and the voltage is detected from potentiometer by ESP32. The data are transferred to the webserver via Wi-Fi which is associated with ESP32. The web page style can be designed in option. There are two main sections hardware preparation and software preparation for implementation of data monitoring on web server.

Hardware Preparation

There is more GPIOs in ESP32 which is more functionalities compared to the ESP8266. For the ESP32, one can decide which pins are UART, I2C, or SPI – it is needed to set that on the code. This is possible due to the ESP32 chip's multiplexing feature that allows to assign multiple functions to the same pin. If the pins are not set them on the code, the pins will be used as default as shown in Figure 2. DHT 11 is a sensor which produces the digital output. The data pin of DHT 11 is connected to GPIO 23 pin of ESP32, the wiper pin of potentiometer is connected to GPIO 34 pin to read the value of voltage. The LED is wired to GPIO 2 pin to be controlled by clicking or touching the switch or symbol on web page. The schematic circuit diagram is shown in Figure 4. The Figure 5 shows the block diagram of the working principle of data monitoring on web server via Wi-Fi.

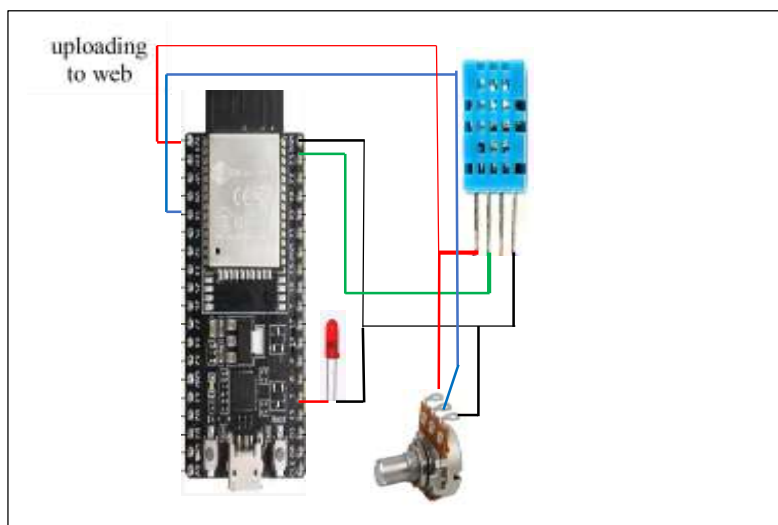


Figure 4 Schematic Circuit Connection

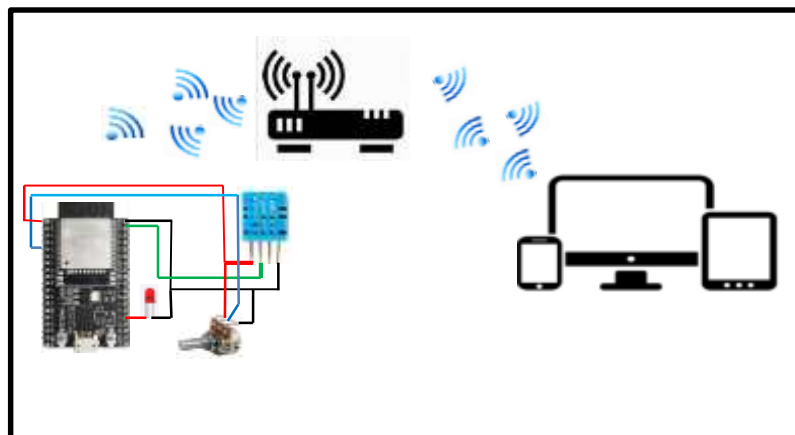


Figure 5 Block Diagram of Data Read/ Write

Software Preparation

First of all, ESP32 library and ESP32 board must be added in Arduino IDE by the following procedures.

- 1) In Arduino IDE, go to File> Preferences.
- 2) Https://dl.espressif.com/dl/package_esp32_index.json enter into the “Additional Board Manager URLs” field as shown in the figure 6. Then, Click the “OK” Button.
- 3) Open the board manager: tool>board>board manger and install ESP32 as in Figure 7.



Figure 6 Including ESP32



Figure 7 Installing ESP32

Software coding composes of four sections; 1) accessing web server, 2) data reading, 3) appliance controlling(writing) and 4) web page preparation.

DHT11 library is used to detect the temperature and humidity from sensor.

```
#include "DHT.h"
#define DHTPIN 23
#define DHTTYPE DHT11
```

Temperature and humidity data are obtained by using the following commands.

```
DHT dht(DHTPIN, DHTTYPE);
dht.readTemperature( )
dht.readHumidity( )
```

To get the value of analog voltage

```
#define ANALOG_PIN_0 34
int analog_value = 0;
float volt=0;
analog_value =0;
analogRead(ANALOG_PIN_0);
volt= analog_value*5/4096;
```

To connect Wi-Fi set point, the following instructions are used;

```
#include <Wi-Fi.h>
const char* ssid    = "xxxxxxxxxxxx";
const char* password = "xxxxxxxxxxxx";
Wi-FiServer server (80);
```

To connect Web server and find out the IP address,

```
Wi-Fi.begin(ssid, password);
while (Wi-Fi.status() != WL_CONNECTED)
{
delay (500);
Serial.print(".");
}
Serial.println("");
Serial.println("Wi-Fi connected.");
Serial.println("IP address: ");
Serial.println(Wi-Fi.localIP());
server.begin();
}
```

Sending data to web server and web page style preparation are as follows;

```

client.println("<!DOCTYPE html><html>");
client.println("<head><meta name=\"viewport\" content=\"width=device-width, initial-
scale=1\">");
client.println("<link rel=\"icon\" href=\"data:,>");
client.println("</style></head><body><h1>ESP32 WEb Server data sending and
receiving</h1>");
client.println("<h2>Dr Nu Nu Swe, Associate Professor, YUOE.</h2>");
client.print("Current Temperature is: ");
client.print(localTemp);
client.print(" oC<br>");
client.print("Current Humidity is : ");
client.print(localHum);
client.print(" %<br>");
client.print("<br>");
client.print("Voltage measured: ");
client.print(volt);
client.print("V");
client.print("<br>");
client.print("<br>");
```

Receiving data to control the appliance (LED) is as;

```

client.print("Click <a href=\"/H\">ON</a> to turn the LED on.<br>");
client.print("Click <a href=\"/L\">OFF</a> to turn the LED off.<br>");
```

Results

After the completion of circuit connection, the program is uploaded as following procedures;

- 1) **Tools > Board** and select **ESP32 Dev Module** in Figure 8.
- 2) **Tools > Port** and select the COM port which ESP32 to be connected. Click the upload button.
- 3) Press the ESP32 on board BOOT button after seeing “connecting” dots on debugging window in Figure 9.

After uploading. Then, serial monitor is opened and press RST button to obtain IP address as shown in Figure 10.

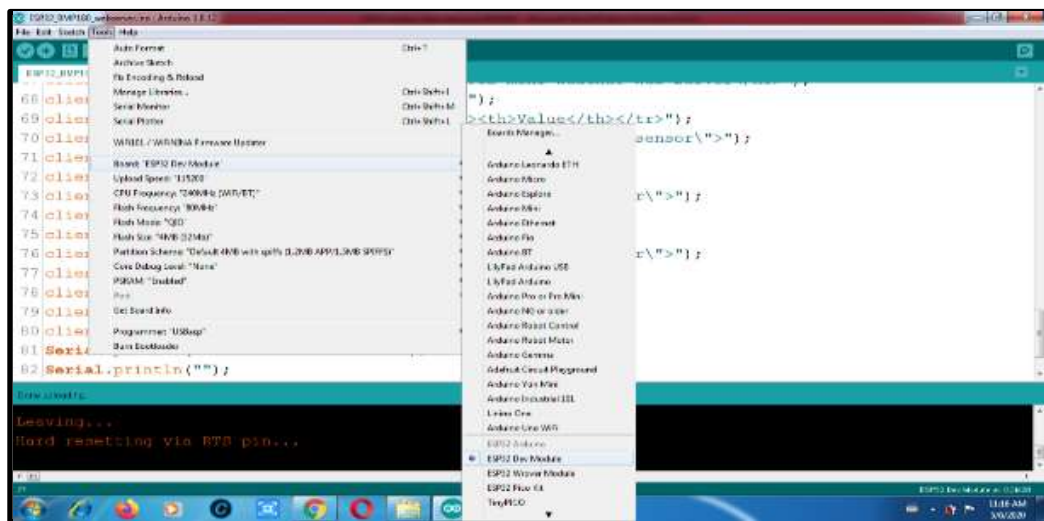


Figure 8 Selection Board

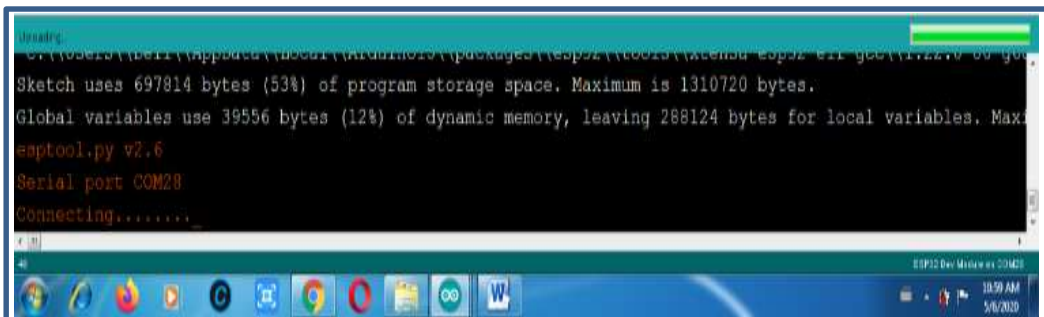


Figure 9 Press BOOT Button After seeing “Connection”

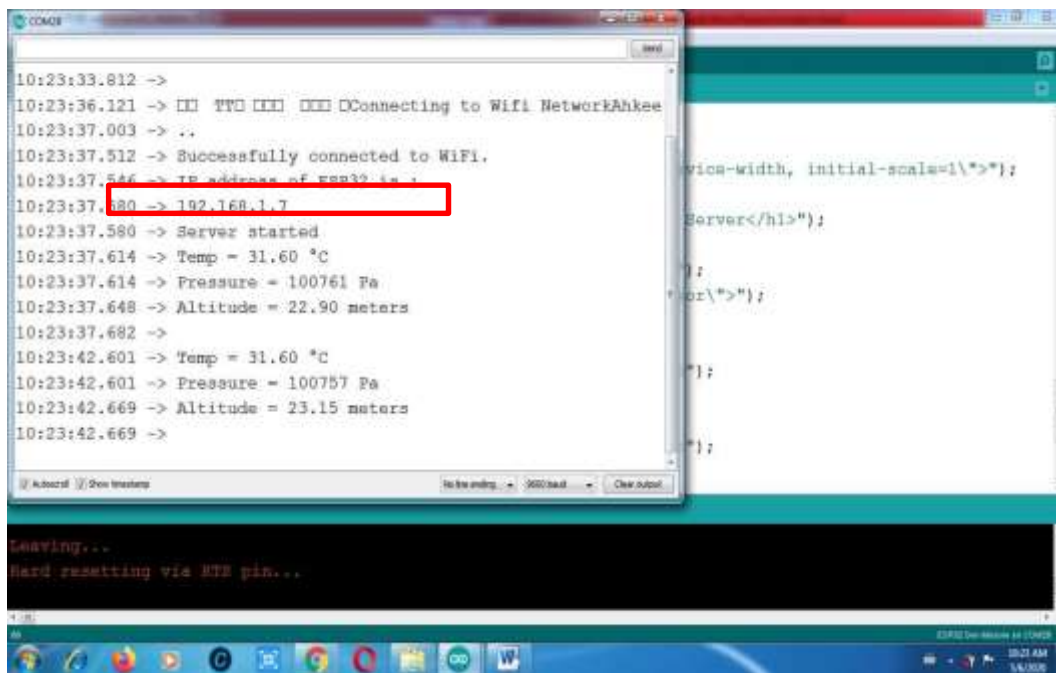


Figure 10 Pressing RST Button to get IP Address

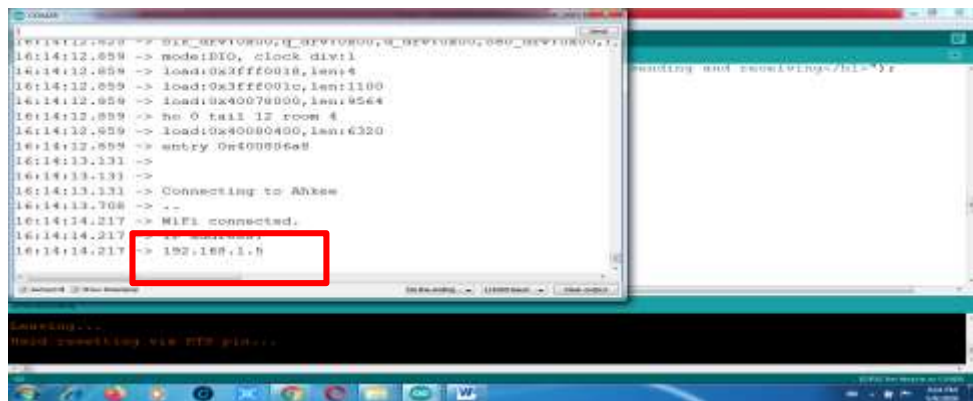


Figure 11 Obtaining IP Address

One can access web server on the specific local network. By typing the IP address of <http://192.168.1.7> on a browser, the data can be visualized on the PC as well as on Serial monitor as illustrated in Figure 12 and 13. The data can be also visualized on the web page on the smart phone as shown in Figure 14.

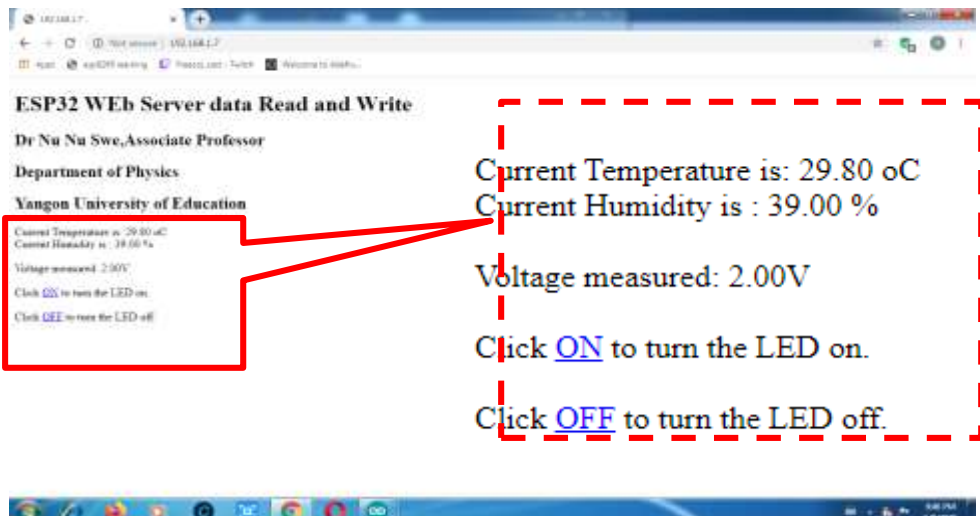


Figure 12 Monitoring data and controlling LED from PC.

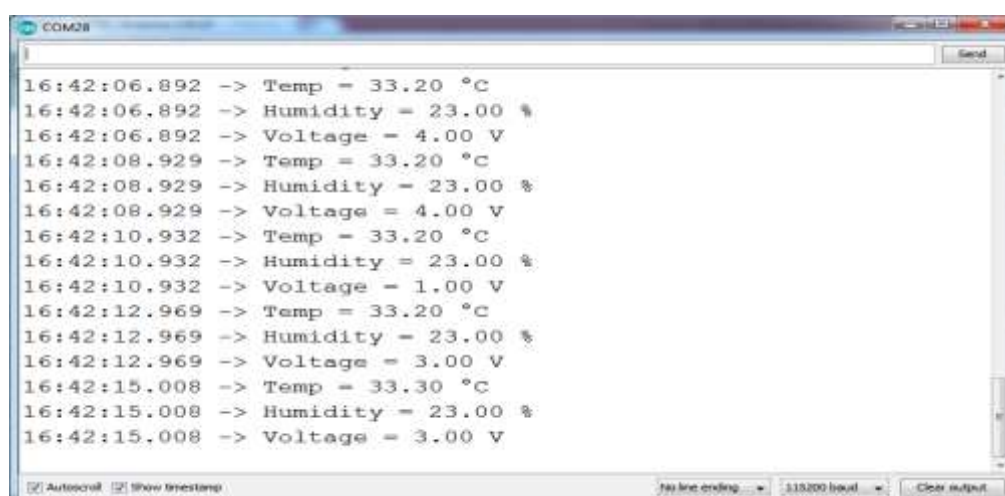


Figure 13 Data on Serial Monitor

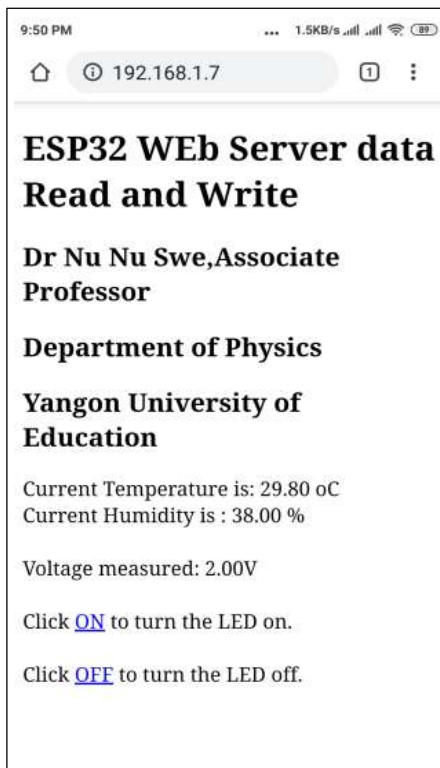


Figure 14 Monitoring Data at <http://192.168.1.7>,and controlling LED from Phone

Discussion

There are a few problems when the new code (sketch) is uploaded to ESP32. The first problem is “COM port is not available”. It might be seen when the USB driver is missing or USB cable without data wires. If USB driver is missing CP2102 driver is installed. The another problem is “Failed to connect to ESP32: Timed out Connecting” It will occur when ESP32 is failing to connect with IDE, it means that ESP32 is not in flashing/uploading mode. It can be corrected as the hold-down the “**BOOT**” button in your ESP32 board while the uploading the code. After seeing the “**Connecting....**” message in Arduino IDE, the finger should release from the “**BOOT**” button.

Conclusion

The local Wi-Fi router or phone Wi-Fi or fiber network are used as internet service provider (ISP). IP address of the website which is specified in this research is 192.168.1.7. It can be used in the local area network (LAN). If the public domain is available, the data on web page can be visualized from any other place with internet access. This system can be used to send secure message. This system can be used as home appliances monitoring and controlling system using the smoke sensor, flame sensor, gas sensor and current sensors. But it can be used in the Wi-Fi coverage area about thirty meters of radius. If the system can be monitoring sensor and controlling appliances at anywhere, it will integrate the software such as “ngrok”, IoT cloud server and hardware such as GSM module.

Acknowledgements

I would like to thank Pro-rectors, Yangon University of Education, Dr Pyone Pyone Aung and Dr Kay Thwe Hlaing for their kind permission to take part in this research work.

I also thankful to Professor Dr Khin Swe Oo, Head of Department of Physics, Yangon University of Education, for giving advice and encouragement through the research period.

I deeply grateful to Professor Dr Ohn Than (Retired), Head of Department of Physics, Kyaukse University who supports the continuous guideline about the Arduino hardware and software.

Also, Thankful all my colleagues for their participation in this research work.

Finally, I pay my thank and respect to my parents.

References

- https://en.wikipedia.org/wiki/Web_server
- <https://en.wikipedia.org/wiki/ESP32>
- https://www.waveshare.com/wiki/DHT11_Temperature-Humidity_Sensor
- https://www.mouser.com/datasheet/2/891/esp-wroom-32_datasheet_en-1223836.pdf
- Rui Santos, "Learn ESP32 withArduino IDE" Random Nerd Tutorial Lab,2020
- Purdun J, "Beginning C for Arduino" Apress, NY, 2012
- Rui Santos,"ESP 32 troubleshooting guide" Random Nerd Tutorial Lab,2020

PROTOTYPE HARDWARE DESIGN AND SOFTWARE DEVELOPMENT OF PASSWORD CODED ESP32 WEB SERVER BASED HOME APPLIANCES CONTROLLING SYSTEM ACCESSIBLE FROM ANYWHERE USING NGROK SOFTWARE

Mi Yin Sa Nine¹, Nu Nu Swe², Ohnmar Soe³, Hnin Aye khine⁴

Abstract

Web server based appliances controlling system is mostly built up by using any microcontroller and Wi-Fi or Bluetooth module. The system can control appliances in the coverage range of Wi-Fi or Bluetooth, not from anywhere. To solve this, the controlling system which is accessible from anywhere with internet access is built up by using ESP32 and ngrok software. ESP 32 is connected to the local network and IP address is obtained. This IP is inserted to the terminal window of ngrok software and a uniform resources locator (URL) is obtained. For security purposes, the password coded program is developed by using “base64encode” software. Using this URL and password, the home appliances are monitored and controlled from anywhere with internet access in the world. The web server home page is created with HTML (hypertext markup language) and CSS (cascading style sheets) to control the devices as well as to express the current status of home appliances. The communication between a web server and clients takes place via Hypertext Transfer Protocol (HTTP). This system is useful to monitor the status of home appliances and to control the switch “on” and “off” of the devices from anywhere with internet access.

Keywords: ESP 32 web server, HTTP, HTML.CSS, ngrok, Base64encode

Introduction

Internet of things (IoT) based Home automation system is mostly implemented by using microcontrollers that are communicating the cloud server such as “thingspeak”, “firebase”, “blynk”, “azure”, “adafruit io” etc via the internet. Phone screen pages are created by the MIT inventor 2 app or Blynk app separately. In this research, the home automation system is developed by using ESP32 as hardware and HTML, CSS, ngrok and base64encode as software. ESP 32 is a system on chip (soc) with integrated Wi-Fi and dual-mode Bluetooth and it is compatible with Arduino IDE. One of the features of ESP32 is that it can connect to a Wi-Fi network or it can set up a web server itself. ESP32 is used as a web server to communicate between servers and clients. The web server homepage is created by HTML tags and CSS functions to express the current status of appliances and to control the devices. The web server such as ESP32 is communicated to a local existing network via the Wi-Fi hotspot of a phone while the Android phone, laptop, or tablets are communicated to the same router with Wi-Fi or Ethernet cable. So, all are on the same local area network. That means that the home appliances controlling system only works in the Wi-Fi network coverage area. This problem is solved by using “ngrok “software.

Web server based electric appliances can be controlled and monitored the latest state of devices from anywhere. Moreover, the web page is protected by the password by using Base64encode software.

¹ Dr, Lecturer, Department of Physics, Myeik University

² Dr, Associate Professor, Department of Physics, Yangon University of Education

³ Dr, Lecturer, Department of Physics, Yangon University of Education

⁴ Dr, Lecturer, Department of Physics, Yangon University of Education

Materials and Methods

The main components are ESP32 and 4-channel relay. ESP 32 board and ESP32 library are required to be included in Arduino IDE. Ngrok server software is used to control electric devices from anywhere. The web server home page is protected by using Base64encode. The web server home page is created by using HTML and CSS. Communication between Server and client takes place on the HTTP platform.

ESP 32

ESP32 development board equips Tensilica Xtensa dual-core 32 bit LX6 microprocessor. This processor operates at **80 to 240 MHz** adjustable clock frequency and performs at up to **600 DMIPS** (Dhrystone Million Instructions Per Second). ESP32 integrates Wi-Fi transceiver and dual-mode Bluetooth capabilities. It can not only connect to a Wi-Fi network and interact with the internet but also it can set up an own network. It composes 448KB of ROM, 520 KB of SRAM, and 4MB of flash memory which is sufficient to implement web pages, JSON / XML (, JavaScript Objects notation /Extensible Markup Language) data, and everything used in IoT devices.

ESP32 has many multiplexed I/O pins. They are; 1) fifteen ADC channels, 2) two UART interface, 3) twenty-five PWM outputs, 4) two DAC channels, 5) three SPI interface, 6) one I2C interface, 7) one I2S interface, 8) nine touchpads. These pins are multiplexing features, that is; a single GPIO pin can multiplex as PWM / SPI / I2C. There are two built-in sensors- Hall effect sensor and temperature sensor. The pin assignment and block diagram of ESP32 is as shown in figure 1 and figure 2, respectively.

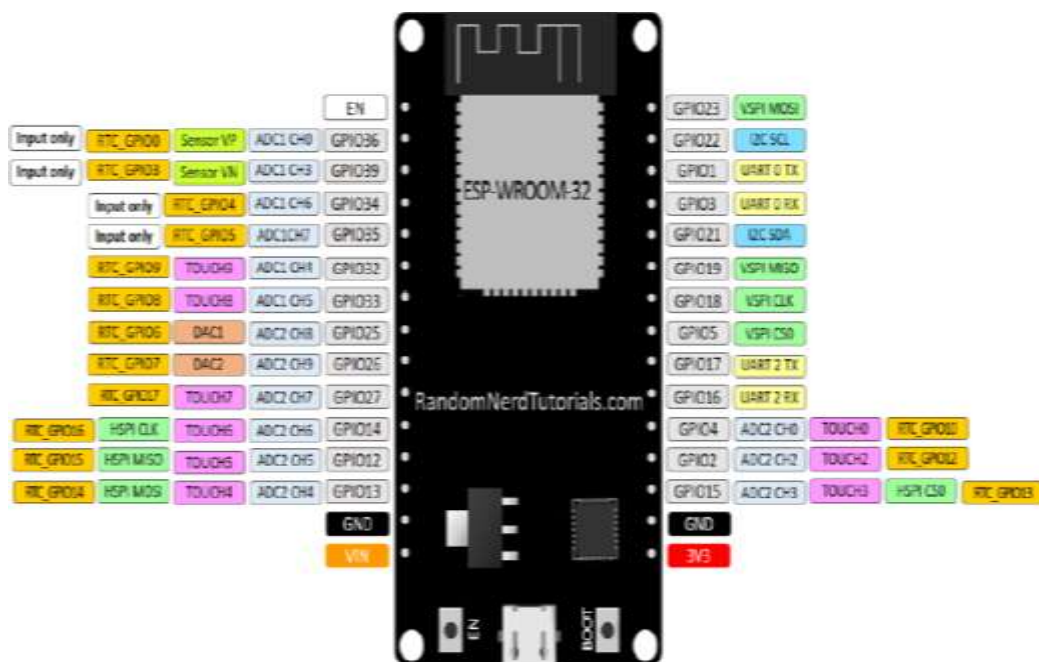


Figure 1 Pin assignment of ESP32

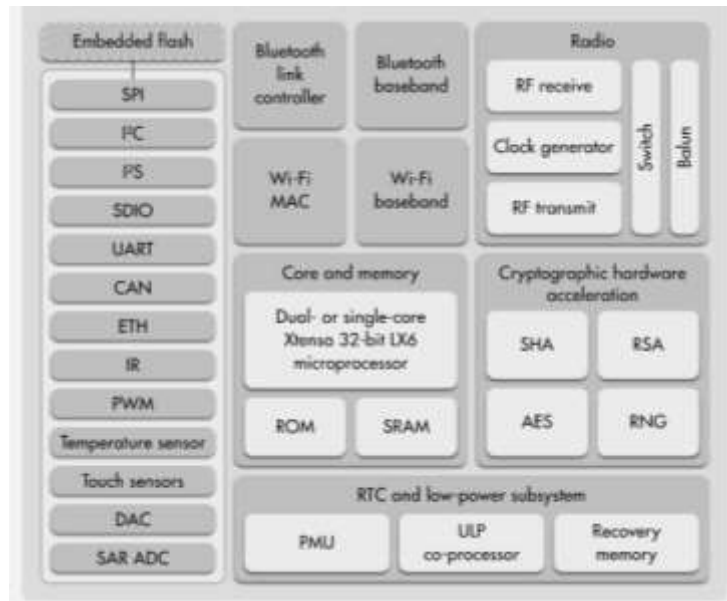


Figure 2 Block diagram of ESP32

Channel Relay

In this research, the relay is used instead of the various appliances to be controlled. The 4-channel relay can be used to control the large voltage and the large current load such as electric motor, stove, air-conditioner, lamp, and ac load. It can be controlled directly by the microcontroller. 5V 4-channel relay interface board needs a 15-20mA driver current in each channel. The 4-channel relay (as shown in figure 3) can operate under AC250V 10A or DC30V 10A. There are four LEDs to indicate the status of the output of the relay. The optocoupler is attached to the relay and it is optically isolated from high voltage for electrical safety purposes.



Figure 3 4-channel relay

HTML and CSS

Hypertext markup language (HTML) is a computer language which is making up of a set of instructions and data, for creating a web page. A web page is a document which can be viewed in a web browser. Web page composes of writing, picture, links, sound and video. HTML describes these kinds of content so that the web browser can express them correctly. Cascading style sheets (CSS) are a way to change the appearance of HTML. It is used to style HTML elements. Web server home pages are mostly created by HTML documents CSS.

Web Server and Client

A Web server is a computer that stores, processes, and transfers the web pages which contains HTML documents, CSS style sheets, images and JavaScript files to the clients. The request and response (communication) between the web server and the client takes place using hypertext transfer protocol (HTTP) capability. A client initiates to request the server for a web page using HTTP. The server also responses with the content of that web page or error if it cannot be able to process.

ESP32 can connect to the Wi-Fi network and it can operate in three different modes: station (STA) mode, soft access point (AP) mode, and both at the same time. In this research, the system is implemented in the station (STA) mode.

Ngrok software

To control the system from anywhere with internet access, the system will be run with “ngrok” server software in this research. Ngrok is just a messenger to the server. Ngrok is a cross-platform application that enables developers to expose a local development server to the internet with minimal effort. No public IP or domain name on the local network is needed.

System Operation

ESP32 acts as a web server in station mode. ESP32 gets the internet protocol (IP) address from the wireless router or Wi-Fi hot spot and delivers the web pages to the devices that are requested from anywhere with a Wi-Fi network. The operation of a web server based electrical appliances controlling system is in two sections; hardware interface and software development.

Hardware Interface

The 4- channel relay instead of air-conditioner, electric motor, stove and bedroom lighting operates in the system, GPIO 33, GPIO 25, GPIO 26 and GPIO 27 of ESP32 are connected to the IN1, IN2, IN3 and IN4 of 4- channel relay, respectively, as shown in figure 4. The block diagram of the working principle of the web server based home appliance controlling system is shown in figure 5.

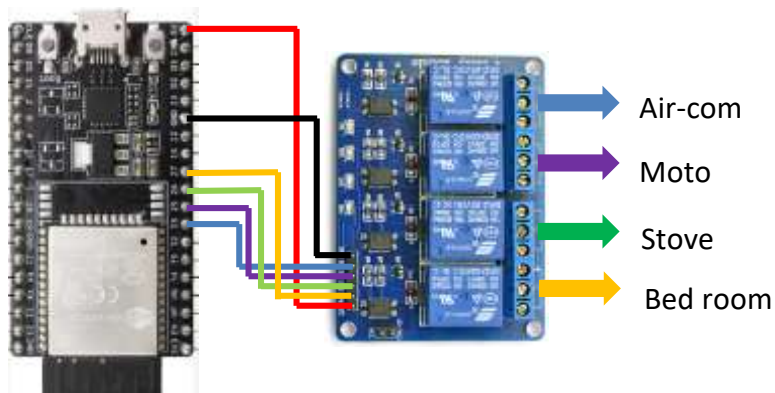


Figure 4 Circuit connection of ESP32 and 4-channel relay

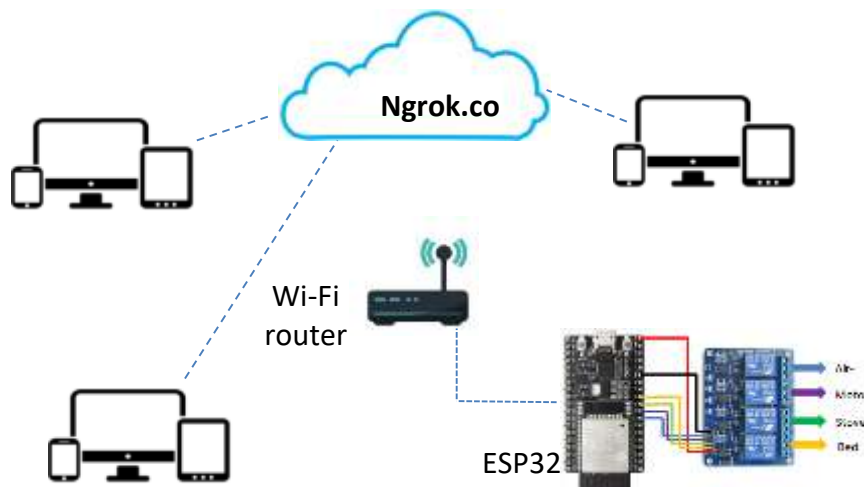


Figure 5 Block diagram of web server based communication

Software Development

ESP32 can run with Arduino IDE. But, the ESP32 board and library are not included in Arduino IDE so that they are needed to install in Arduino IDE. The URL of http://dl.espressif.com/dl/package_esp32_index.json is pasted into the “Additional Board Manager URLs” Field of preference in the IDE window as shown in figure 6. After URL path is defined, ESP32 board can be installed using the board manager, as in figure 7.



Figure 6 Including ESP32 board

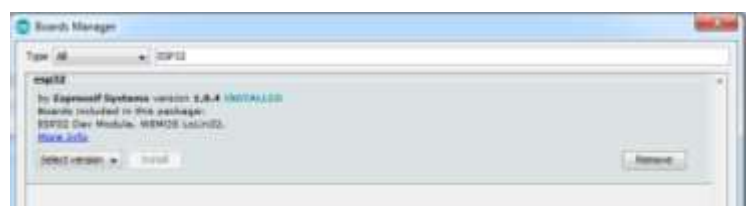


Figure 7 Installing ESP32 library

After the program has uploaded, ESP32 will communicate the local Wi-Fi network. It needs to define the network credentials of service set identifier (SSID) and password as;

```

const char* ssid    = "xxxxxxxxxxxxxx";
const char* password = "xxxxxxxxxxxx";
Wi-FiServer server(8888);

```

The web server is at Port 8888 which has assigned to use internet communication with HTTP. While ESP32 is connecting the network, connectivity status is examined with Wi-Fi.status() function. If it is connected, the IP address is obtained by using Wi-Fi.localIP() function. While the program is uploading, the BOOT push button is pressed. If the connecting dots are seen, the BOOT button is released. After uploading is finished, the serial monitor is open and the IP address is obtained by pressing the reset button as shown in figure 8.

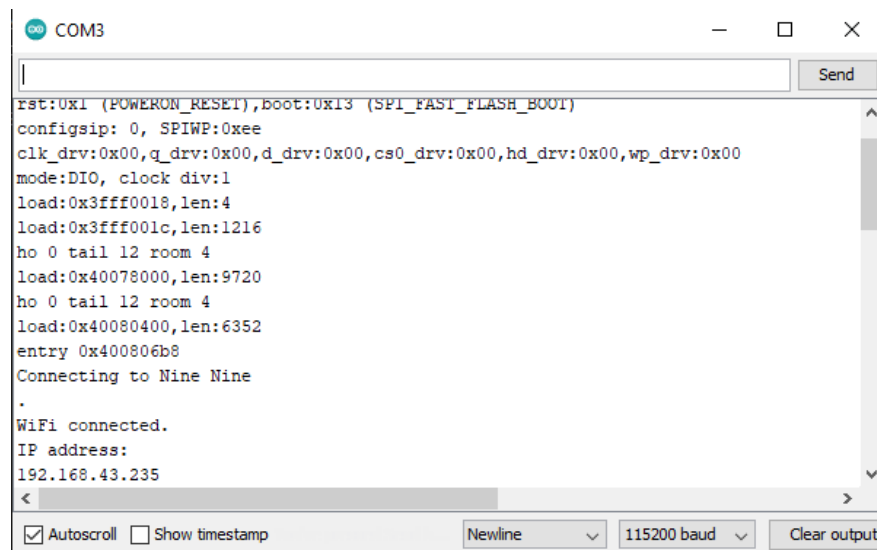


Figure 8 Obtaining IP address on serial monitor

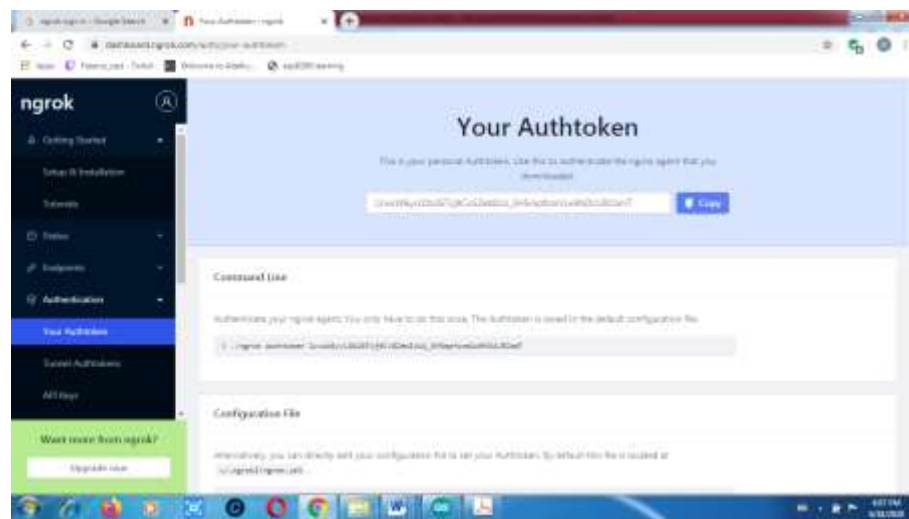
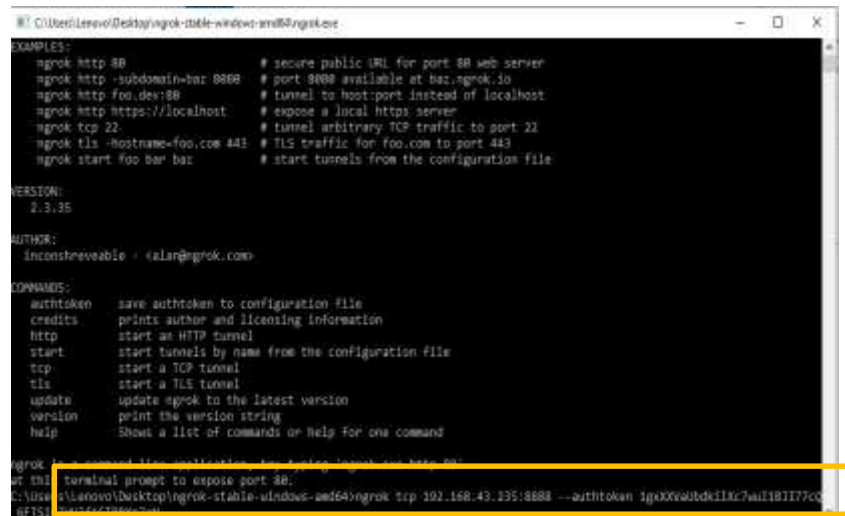


Figure 9 Getting tunnel authtoken from ngrok window



```
ngrok http 8888 --auth token
ngrok http -subdomain=bar 8888 # port 8888 available at bar.ngrok.io
ngrok http foo.dev:8888 # tunnel to host:port instead of localhost
ngrok http https://localhost # expose a local https server
ngrok tcp 22 # tunnel arbitrary TCP traffic to port 22
ngrok tls -hostname=foo.com 443 # TLS traffic for foo.com to port 443
ngrok start #go bar bar # start tunnels from the configuration file

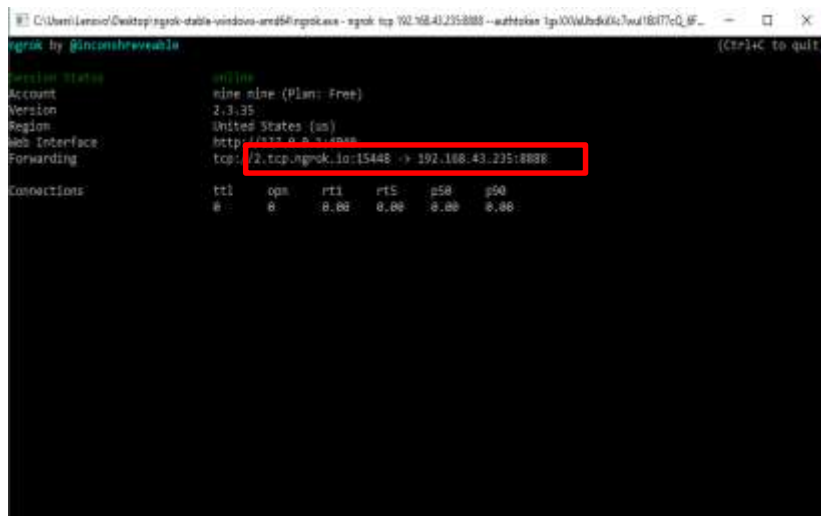
VERSION: 2.3.35

AUTHOR: unconsreveable <elar@ngrok.com>

COMMANDS:
auth token      save auth token to configuration file
credits         prints author and licensing information
http           start an HTTP tunnel
start          start tunnels by name from the configuration file
tcp            start a TCP tunnel
tls             start a TLS tunnel
update         update ngrok to the latest version
version        print the version string
help           Show a list of commands or help for one command

ngrok [options] [tunnels] [configuration]
at this terminal prompt to expose port 8888
C:\Users\elar\Downloads\ngrok-stable-windows-amd64>ngrok tcp 8888 --auth token 1gxXxwldkllc7u1B1T77cc
GETS1
```

Figure 10 Inserting the Ip address



```
ngrok by @unconsreveable
Version Status: 2021/09/09 00:00:00
Account: mine mine (Plan: Free)
Version: 2.3.35
Region: United States (us)
Web Interface: http://127.0.0.1:4040
Forwarding: tcp://2.tcp.ngrok.io:15448 → 192.168.43.225:8888

Connections: ttl opm rti rtS p50 p90
0 : 0 0.00 0.00 0.00 0.00 0.00
```

Figure 11 Obtaining URL from ngrok

Ngrok software is downloaded. The account is created and the “tunnel authtoken” is noted as shown in figure 9. Ngrok.exe file (in figure 10) is open and ESP IP address is filled up in the terminal window like the following format;

ngrok tcp ESP_IP_address:8888 --auth token tunnel_authtoken .

By pressing “enter”, the URL is expressed in the terminal window as illustrated in figure 11. When the URL <http://2.tcp.ngrok.io.15448> is pasted in a browser, the password security box has appeared as shown in figure 12. If the correct user name (SSID) and password is filled up, the webserver home page is ready to monitor and control the appliances as shown in figure 13. The web server which is accessible from anywhere in the world is ready to serve the appliances controlling.

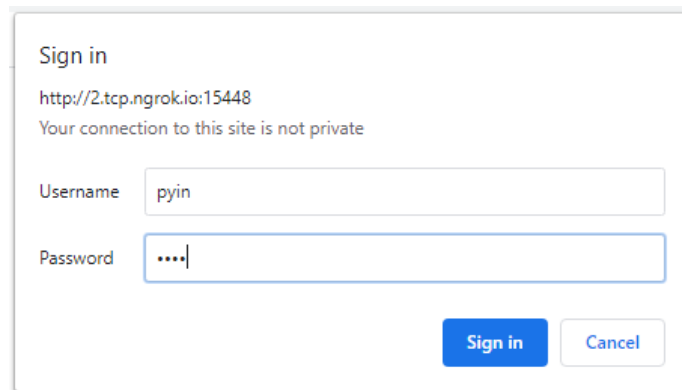


Figure 12 Password protecting the server

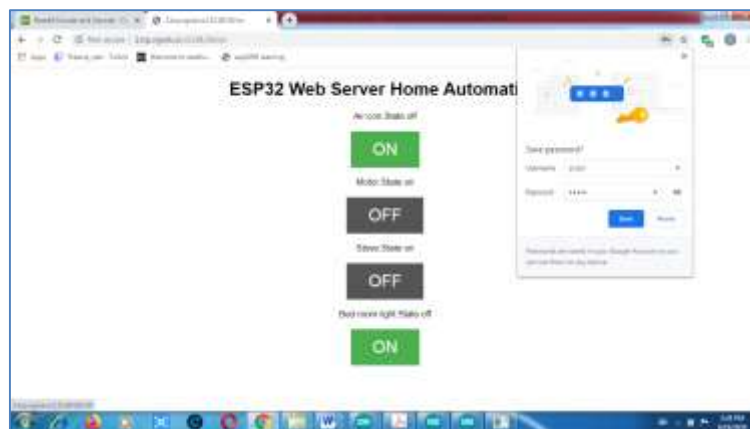


Figure 13 Web server being ready to monitor and control appliances

Results and Discussions

Results

The prototype design of home electrical appliances controlling system is implemented by using a 4-channel relay instead of home appliances such as air-conditioner, motor, stove, and lighting. The prototype system and the web server based operation are illustrated in figure 14. In this figure, the states of air-conditioner, motor, stove and lighting are in “off” condition and buttons are ready to be “on” condition. All LEDs are in “off” condition. That means all home appliances switch- off. The home appliances are controlled by the web page on PC as shown in figure15. In figure 15. (b), the air-conditioner is in “on” condition so that the button is ready to be switched off. The remaining appliances are in “off” condition and three LEDs are off. These buttons are ready to be switched on. In figure 15. (e). All home appliances are in “on” condition. All LEDs are switched on while all buttons are ready to be switched off. The home appliances controlling by the web page on a smart phone is illustrated in figure 16. The operation manner by phone is the same as that by PC.

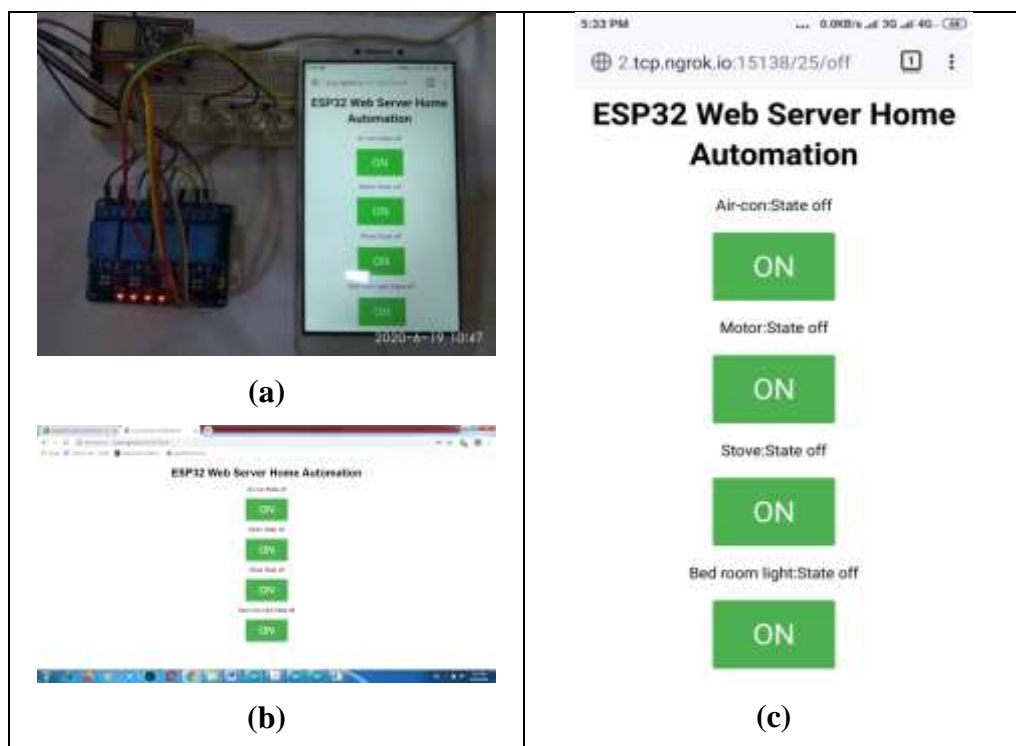


Figure 14 Circuit connection and webpages on PC and phone

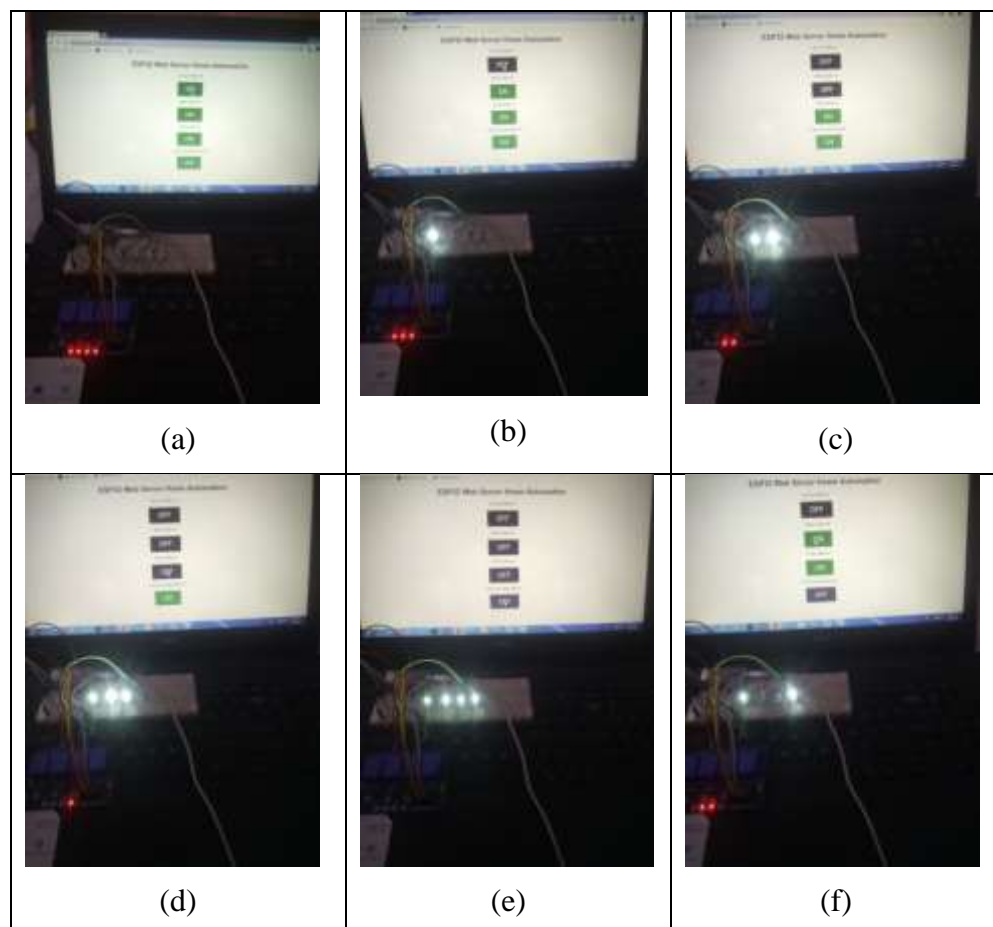


Figure 15 Appliances controlling by web page on PC

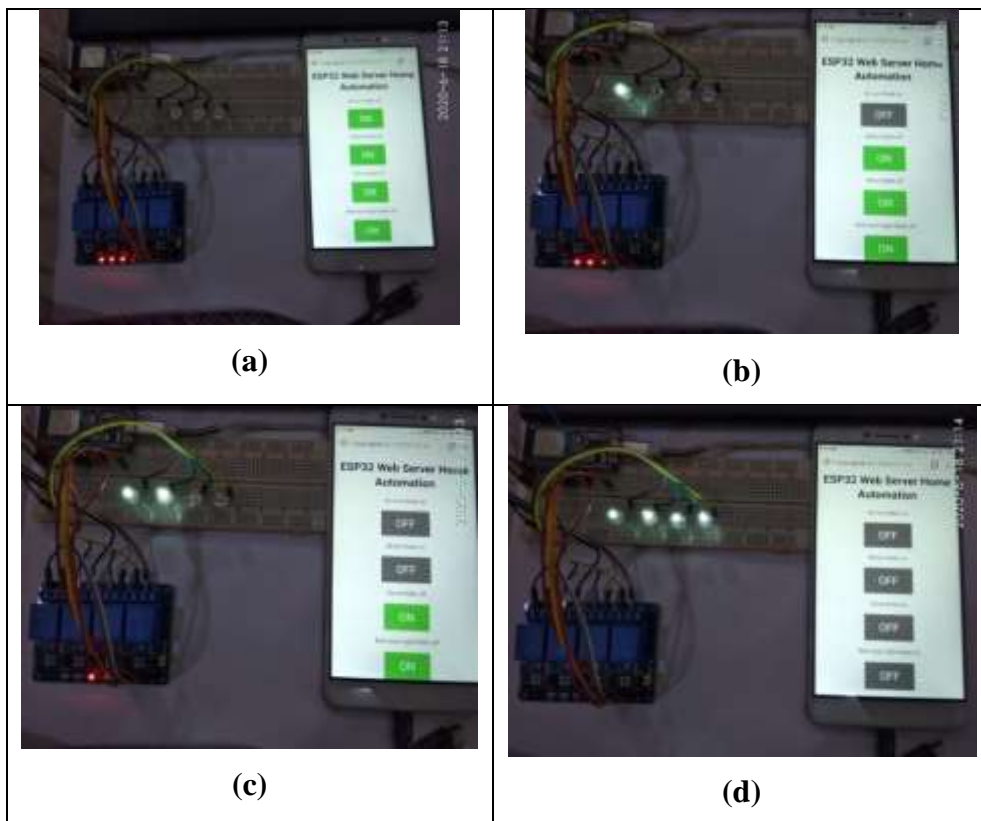


Figure 16 Appliances controlling by web page on phone

Discussions

The typical web server based electrical appliances can control the devices in the Wi-Fi coverage area, not anywhere. The system which is included with ngrok software can control the appliances anywhere with internet access. But, on the free plan, its URLs are randomly generated. One of the disadvantages is ngrok software running always-on PC to control the appliances from anywhere with internet access. When the PC is restarted, the auth token of ngrok is changed. The program is installed again with different auth token. The same URL every time can be used if the ngrok is upgraded to a paid plan.

This research demonstrates the prototype's 'hardware design by using a 4-channel relay instead of four home appliances. ESP32 consists of thirty-two general-purpose input-output (GPIO) pins. Among them, twenty-eight pins can be used as output pins so that twenty-eight home appliances can be controlled by an ESP32. The heavy-duty appliances can be controlled through the high power switching devices instead of a relay.

A password protected program is developed in this system; no one can control the appliances for the destructed purpose.

Conclusion

The webserver based appliances controlling system can monitor the electrical fixtures such as air-conditioner, motor, stove, and lighting whether they are “on” or “off”. And then, they are controlled by using a laptop, tablet, or phone from anywhere with a network. One can check the state of electrical device whether “on” or “off”. It can save the electrical cost and it can protect the electrical faults. One can start the air-conditioner or preheat the rice cooker or light on the rooms before you get home from work.

As the future work, the gas sensor, the heat sensor, the light sensor and the motion sensor are attached to this system, and the home automation system can be designed and constructed.

Acknowledgements

I would like to Dr. Ni Ni Oo, Rector, Myeik University and Dr. Win Win Than, Pro-rector, Myeik University for her kind permission to carry out this work.

I would like to express my deepest gratitude to Professor Dr. Khin Myo Ma Ma Saw, Head of Department of Physics, Myeik University for her encouragement and inspiring suggestions.

I deeply grateful to Professor Dr. Ohn Than (Retired), Head of Department of Physics, Kyaukse University who supports the continuous guideline about the hardware and software of ESp32 and web server.

Also, Thankful all my colleagues for their participation in this research work.

Finally, I pay my thank and respect to my parents.

References

- <https://electropeak.com/learn/create-a-web-server-w-esp32/>
- <https://lastminuteengineers.com/esp32-arduino-ide-tutorial/>
- <https://simple.wikipedia.org/wiki/HTML>
- https://simple.wikipedia.org/wiki/Cascading_Style_Sheets
- http://wiki.sunfounder.cc/index.php?title=4_Channel_5V_Relay_Module
- <https://www.pubnub.com/learn/glossary/what-is-ngrok/QQ>
- Rui Santos, “ESP8266 Web Server with Arduino IDE” Random Nerd Tutorial Lab,2020
- Rui Santos, “ESP 32 troubleshooting guide” Random Nerd Tutorial Lab,2020

MICROWAVE-ASSISTED GREEN SYNTHESIS AND CHARACTERIZATION OF TITANIUM OXIDE NANOPARTICLES USING *CENTELLA ASIATICA* (L.) LEAF EXTRACT AND THEIR ANTIMICROBIAL ACTIVITY

Zin Min Myat¹, Zin Min Tun², Toe Toe Wai³, Shwe Sin Aung⁴, Yin Maung Maung⁵

Abstract

Green synthesis of titanium oxide (TiO_2) nanoparticles was successfully developed by using *Centella asiatica* leaf extract. Metal oxide nanoparticles have a high specific surface area and a high fraction of surface atoms. Titanium oxide nanoparticles have unique properties as a consequence of this size, distribution and morphology and are a very important component in the rapidly developing fields of nanotechnology. In this research, titanium oxide nanoparticles with leaf extract percent were characterized by instrumental analysis such as X-ray Diffraction (XRD), Scanning Electron Microscopy (SEM), Fourier Transform Infrared Spectroscopy (FTIR) and UV-Vis Spectroscopy. Generated titanium oxide nanoparticles were investigated different degree of antimicrobial activity against micro-organisms and it was observed that the zone of inhibition whose diameters were estimated. This research can provide useful and comprehensive results because of their main physicochemical properties and some of their medical applications.

Keywords: *Centella asiatica* leaf extract, XRD, SEM, FTIR, UV-Vis and Antimicrobial activity

Introduction

Nanoparticles are the important role in nanotechnology that are being explored due to the diversity of potential applications in biomedical, optical, photocatalytic, sensing and electronic devices [G. Nabi et al 2018]. The metal oxide nanoparticles have received considerable attention on medical line due to their antibacterial properties, resistance against microbes, drug delivery, antibiotics and immune chromatography, tissue / tumour image, anticancer activities and identification of pathogens in clinical specimens. TiO_2 is the most promising material in the group of the metal oxides [Abou-Helal,M.O et al 2002]. In n - type semiconductor, titanium dioxide is a most important semiconductor due to its light absorption, surface adsorption and charge transport properties. TiO_2 has three crystal structures namely anatase, rutile, and brookite. In three phases, the anatase phase has got applications in photo-voltaic cells [Fujima and Donald 2000], photo catalysts and more applications for its antimicrobial properties. Metal oxide nanoparticles Nanoparticles can be made of Titanium oxide (TiO_2) by co-precipitation method [Castaneda L et al 2002]. In order to obtain these particles, titanium oxide (TiO_2) paricles is required and proposed mainly from the titanium tetra chloride, hydrochloric acid and ammonia used as the starting materials [Dahir, T.A.AL., (May 2013)]. Titanium oxide nanoparticles prepared by various methods like sol-gel method, chemical deposition method, solid state reaction method, hydrothermal method co-precipitation method and so on [Monoharan,C & Sridhar, R, (September, 2012)]. Among these, co-precipitation method is considered to be one of the best techniques and potentially advantageous in comparison to other method to produce pure phase formation of compound, low temperature preparation, highly purity and yield nanoparticles. Thin film of Titanium dioxide (TiO_2) has generated a lot of interest because of its attractive properties such as wide band gap, high refractive index, high dielectric constant, absence of nontoxicity and also it is

¹ Lecturer, Department of Physics, University of Yangon

² Lecturer, Department of Physics, Pathein University

³ Lecturer, Department of Physics, University of Yangon

⁴ Lecturer, Department of Physics, East Yangon University

⁵ Professor, Department of Physics, University of Yangon

considerable interest for both scientific and technical applications [Revathi, B. P. Perumal & Nachammai.J., (September 2018)].

Materials and Methods

Experimental Preparation of TiO₂ Nanoparticles

Materials

For the preparation of experimental details, all the chemicals (Titanium chloride (TiCl₄) and reagents used for the preparation of TiO₂ Nanoparticles were purchased from Academy chemical store in the downtown of Yangon. This chemical was analytically pure and directly used as received without further purification.

The materials used for the synthesis of centella asiatica leaves extract were collected from market.

Methods

The synthesis method consisted of two steps (1) the preparation of the centella asiatica leaf extract and (2) the synthesis of the TiO₂ nanoparticles.

Preparation of Centella asiatica Leaf Extract

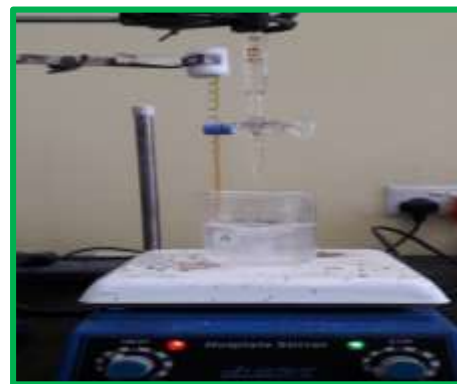
Fresh leaves of Centella asiatica were collected from the market. The leaves were cleaned thoroughly with tap water and distilled water. After cleaning the leaves, take 50 g of the leaves were crushed and grinded in mortal and pestle by adding deionized water dropwise. The paste is then mixed with 200 ml of distilled water and kept over the hot plate and boiled for 2 h at 80 °C. Then, it is set to get cool down and the extract solution was filtered by filter paper until no debris is present. The filtrate was stored for the synthesis of TiO₂ nanoparticles.

Synthesis of Titanium Oxide Nanoparticles with Centella asiatica Leaf Extact

Once the aqueous Centella asiatica leaf extract is obtained, to synthesis the TiO₂ nanoparticles, 1 g of titanium chloride (TiCl₄) was dissolved in 100 ml of distilled water. Distilled water was used as solvent. Different amount of leaves extract solution (30 ml and 60 ml) was added drop wise under constant stirring up to achieve the pH levels. Firstly, these solutions were subjected to stirring with magnetic stirrer for 4 h continuously. During this process, the whitish colour of the mixed solution changed into yellow with the addition of the leaf extract solution. After stirring process, TiO₂ nanoparticles were formed. The mixture solution was centrifuged and washed three times with deionised water to remove the by-product. The nanoparticles were left for drying at 100 °C for overnight and annealed at 500 °C for 1 h. Figure 1(a-d) showed the photos of experimental procedure of green synthesis of titanium oxide nanoparticles.

Characterization Techniques

The green synthesized silver nanoparticles will be characterized by XRD, SEM, FTIR and UV-vis spectroscopy for structural, morphological, chemical and optical properties. The antimicrobial activity will be studied with these titanium oxide nanoparticles using Centella asiatica leaf extract

**Figure 1(a)** Plant extracted solution**Figure 1(b)** Titanium oxide solution**Figure 1(c)** Heating Process**Figure 1(d)** TiO₂ Nanoparticles

Results and Discussions

XRD Analysis of Titanium Oxide (TiO₂) Nanoparticles

The titanium oxide nanoparticles by green synthesis were obtained and XRD technique was used to examine towards studying phase analysis, particle structure, and crystallographic investigation and lattice parameters. The phase analysis of powder was determined by using an X-ray Diffractometer (Rigaku RINT 2000). The XRD profiles of TiO₂ particles of different extract solution (30 ml and 60 ml) at 500 °C, thus obtained and shown in figure 2 (a & b). There were extra peaks on pattern of all particles because the results clearly proved the influence of the concentration of extract solution on the product composition and agreed with the typical TiO₂ pattern of anatase nano particles structure. All peaks were found to be well matched with the diffracted of standard. The intensity of (101) reflection was much stronger than that of remaining TiO₂ peaks. The XRD measurement showed that all peaks of TiO₂ were consisted with that TiO₂ standard (JCPDS) file having a tetragonal structure. The broad peaks in XRD patterns indicate fine crystallite size of the TiO₂ particles. The average crystallite size of TiO₂ particles were in the range of 42.39 nm. The crystallite size was calculated from the XRD peak broadening of peaks using Scherrer's formula. By analyzing XRD measurement, all the peak heights and peak positions were in good agreement with library file of XRD machine.

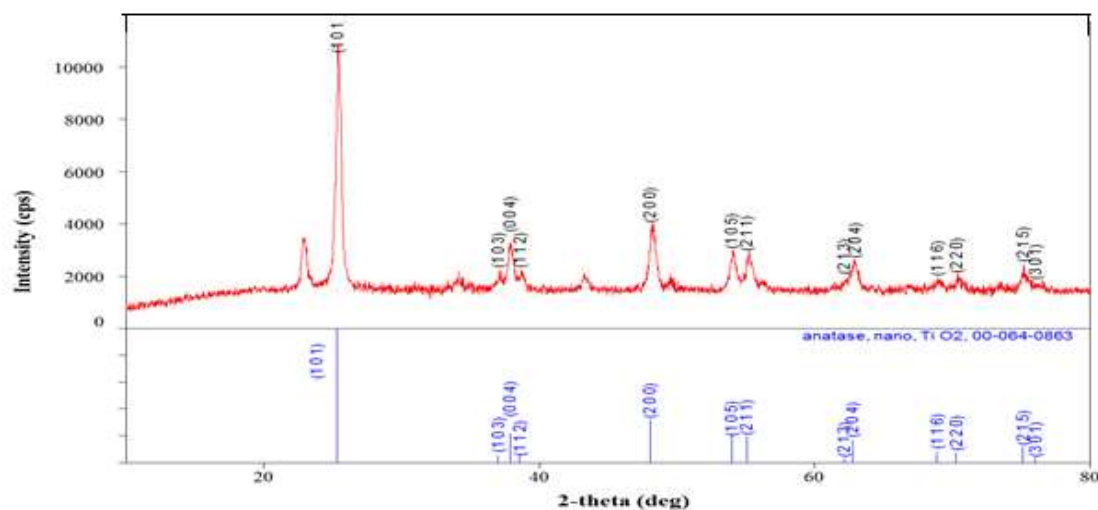


Figure 2 (a) XRD pattern of TiO₂ nanoparticles (30 ml of extract solution) at 500 °C

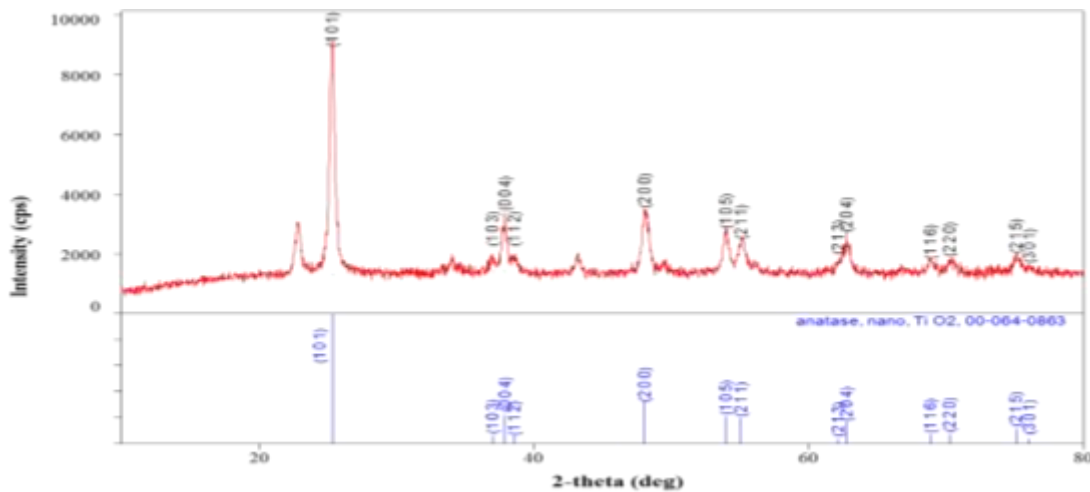


Figure 2 (b) XRD pattern of TiO₂ nanoparticles (60 ml of extract solution) at 500 °C

SEM Analysis of Titanium Oxide (TiO₂) Nanoparticles

The microstructural properties of TiO₂ nanoparticles by green synthesis were observed by using Scanning Electron Microscopy (SEM). Materials evolutions were obtained grain size, surface roughness and pore distribution. Figure 3 (a-b) showed the SEM photographs of TiO₂ crystalline powder with different extract solution at process temperature 500 °C. As detail analysis of SEM micrograph, it looked crack-free and little dense. Porosity and grain growth pattern were significantly observed on SEM images. These images were smooth and seemed to be front-oriented and the grain distribution was uniform but some of grain sizes were slightly larger. According to SEM results, these TiO₂ nanoparticles were composed of regular and sphere grains and TiO₂ nanoparticles were reported to be an average grain size of 35.53 nm for 30 ml of extract solution and 30.33 nm for 60 ml of extract solution with spherical shape by SEM images at process temperature 500 °C. These figures indicated that most of the grain size was regular structure and a few number of large grain size were found. It looks fairly dense and rough. These consisted of well-defined grain but marked difference. This fact indicated that structural properties were influenced by different extract concentration. From the images, it was clearly found that the little

amount of pores and grain growth were examined and the orientation of grain was towards left for all images. TiO_2 nanoparticles were reported to be an average grain size of 35.53 nm for 30 ml of extract solution and 30.33 nm for 60 ml of extract solution with spherical shape by SEM images. In these results, the average grain size of the TiO_2 nanoparticles were depended varying different extract solution of *Centella asiatica* Leaf.

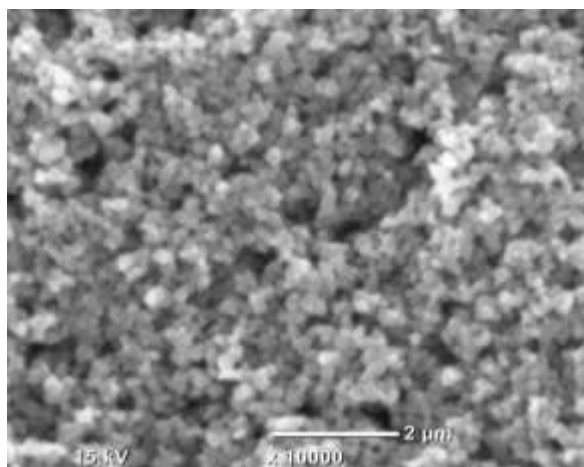


Figure 3 (a) SEM image of TiO_2 nanoparticles (30 ml of extract solution) at 500 °C

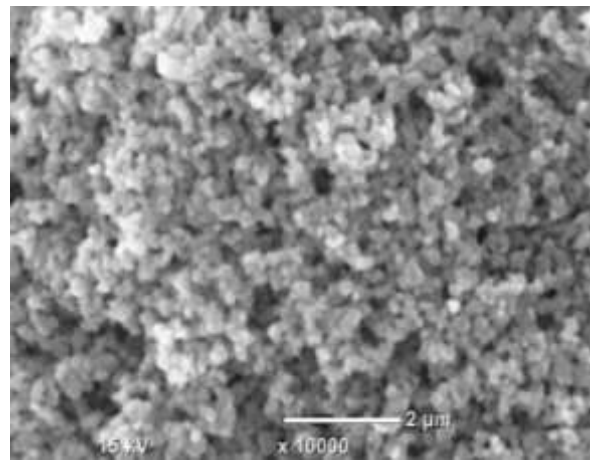


Figure 3 (b) SEM image of TiO_2 nanoparticles (60 ml of extract solution) at 500 °C

UV-Vis Analysis of Titanium Oxide Nanoparticles

The absorbance spectrum of titanium oxide TiO_2 nanopowders were measured by using UV-Vis Spectrometer. The optical absorption spectra for a range of samples of titanium oxide (TiO_2) nanoparticles (TiO_2) with different *Centella asiatica* leaf extract concentration was obtained in UV/ VIS/ NIR region (up to 1100 nm) using a SHIMADZU U-1800 UV/ VIS Double Beam Spectrophotometer. The wavelength range of spectrum lied between 190 nm and 400 nm. As the different leaf extracts were added to aqueous mixture solution, the colour of the solution changed from the whitish colour of the mixed solution changed into yellow and finally to colloidal pale yellow indicating titanium oxide nanoparticles (TiO_2) formation. The colour change is due to the Surface Plasmon Resonance phenomenon. From different literatures, it was found that the titanium oxide nanoparticles show SPR peak at around (370 nm – 431 nm). In this result, the dominant sharp band of titanium oxide nanoparticles (TiO_2) was observed around 385 nm in case of 30 ml extract solution whereas the band for 60 ml extract solution was found around 435 nm. The $(\alpha h\nu)^2$ and $h\nu$ characteristic curve of TiO_2 nanoparticles for 30 ml of extract solution and 60 ml of extract solution) at 500 °C were shown in figure 4 (a & b). On the characteristic curve, the extrapolating the straight line onto horizontal axis ($(\alpha h\nu)^2 = 0$), give the value of energy band gap and the obtained nanoparticles had a direct band gap 3.808 eV with 30 ml of extract solution and 3.295 eV with 60 ml of extract solution for the absorbance spectra. According these result, the intensity of absorption peak increases with increasing more extract solution. It was observed that the titanium oxide nanoparticles were dispersed in the aqueous solution with no evidence for aggregation in UV- Vis absorption spectrum.

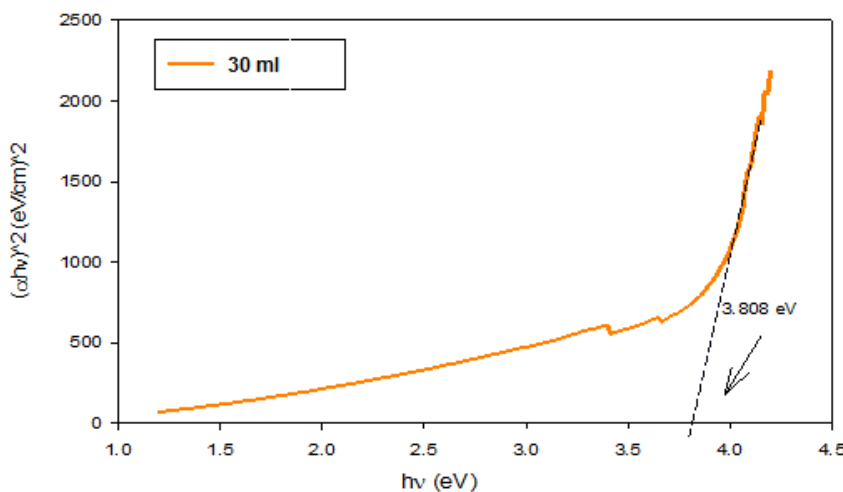


Figure 4 (a) Energy band gap calculation of TiO_2 Nanoparticles (30 ml extract solution)

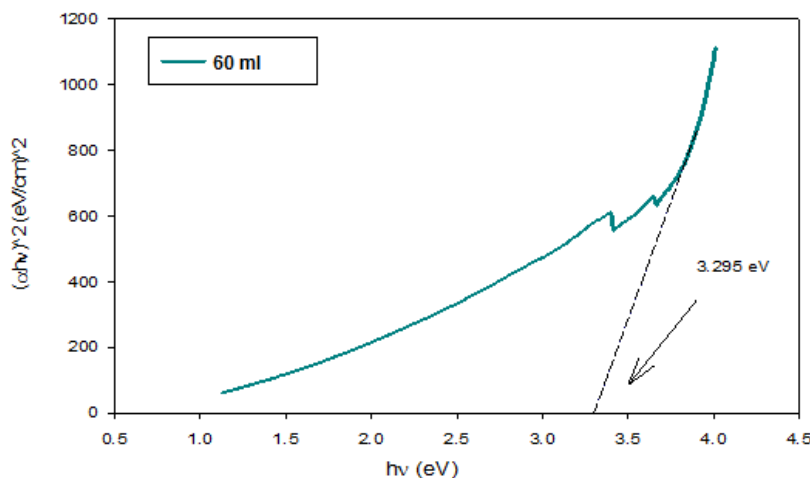


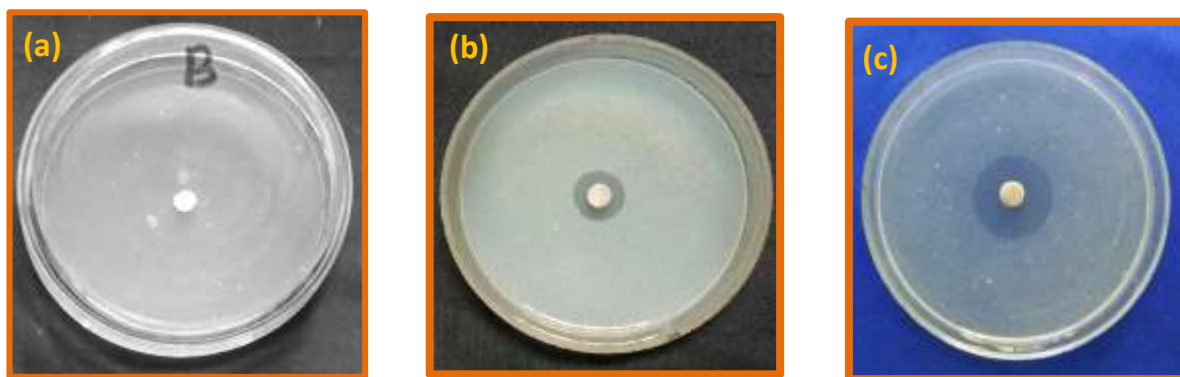
Figure 4 (b) Energy band gap calculation of TiO_2 Nanoparticles (60 ml extract solution)

Antimicrobial Activity of Titanium Oxide by paper disc diffusion assay

Isolated bacterial strains grown on nutrient agar were inoculated into 50 ml conical flasks containing 10 ml of sterile growth medium. Then, they were incubated at 30 °C for 72 hours on a reciprocal shaker at 200 rpm. In this research, test organisms were *Aspergillus flavous*, *Bacillus subtilis*, *Candida albicans*, *Escherichia coli*, *Pseudomonas flurorescens*, *Klebsiella pneumonia*. 0.3 ml of test organisms was added to assay medium, then poured into plates. After solidification, paper discs impregnated with broth samples were applied on the test plates and these plates were incubated for 24-36 hours at 30 °C. After for 24-36 hours, clear zones (inhibitory zones) surrounding the test discs indicate the presence of bioactive compounds which inhibit the growth of test organisms. The diameters of inhibition zones that appeared were shown in Table 1 and figure 5 (a-c) According to experimental result, the inhibition zone of 60 ml extract solution was showed more against on microorganism than 30 ml of extract solution.

Table 1 Inhibitory zone of titanium oxide nanoparticles with different extract solution

No	Test organisms	Inhibition zones (mm)		Diseases
		30 ml of extract solution	60 ml extract solution	
1	<i>Aspergillus flavous</i>	9	10	Bronchitis
2	<i>Bacillus subtilis</i>	16	30	Pathogenic group
3	<i>Candida albicans</i>	12	18	Skin infection
4	<i>Escherichia coli</i>	12	20	Cholera, diarrhea and vomiting
5	<i>Pseudomonas fluorescens</i>	8	8	Bacteria for leaf blight
6	<i>Klebsiella pneumonia</i>	14	28	Infections in the urinary tract, liver abscess

**Figure 5(a)** Control media without bacteria, **(b)** Zone of inhibition on *Bacillus subtilis* (30 ml extract solution) and **(c)** Zone of inhibition on *Bacillus subtilis* (60 ml extract solution)

Conclusion

In conclusion, the green synthesis of titanium oxide (TiO_2) nanoparticles has been demonstrated by the *Centella asiatica* leaf extract. Titanium oxide nanoparticles (TiO_2) have been appropriately characterized using XRD, SEM, and UV-Vis spectroscopy analysis. According to XRD analysis, all the peak heights and peak positions of different leave extract solution were in good agreement with library file of XRD machine. XRD analysis showed that nanoparticles were crystallized in the tetragonal structure and their average crystallite sizes were observed to be 42.39 nm for 30 ml of extract solution and 35.54 nm for 60 ml of extract solution. TiO_2 nanoparticles were reported to be an average grain size of 35.53 nm for 30 ml of extract solution and 30.33 nm for 60 ml of extract solution with spherical shape by SEM images. UV-Vis showed that the dominant sharp band of titanium oxide nanoparticles (TiO_2 NPs) was observed the intensity of absorption peak increases with increasing more extract solution. It was observed that the titanium oxide nanoparticles were dispersed in the aqueous solution with no evidence for aggregation in UV- Vis absorption spectrum. According to the antimicrobial experimental result, the inhibition zone of 60 ml extract solution was showed more against on microorganism than 30 ml of extract solution.

Acknowledgements

I would like to express my sincere thanks to Professor Dr Khin Khin Win, Head of the Department of Physics, University of Yangon for her kind encouragement and permission to perform this research work.

I would like to thank Professor Dr Aye Aye Thant, Professor Dr Yin Maung Maung, Professor Dr Than Zaw Oo, Department of Physics, University of Yangon, for their kind advice, encouragements and suggestions for this research.

References

- Abou-Helal,M.O & W.T.Seeber (2002), Preparation of TiO₂ thin films by spray pyrolysis to be used as photocatalyst, *Applied Surface Science* 195,53.
- Andoronic,L,Manolance,S & Duta,A.,(May 2007), *Journal of optoelectrics and advanced materials,"TiO₂ thin films prepared by spray pyrolysis deposition(SPD) and their photocatalytic activities"*,Vol.9,pp 1403-1406
- Castaneda,L., J.C.Alono,A. Ortiz, E & Andrade,J.M(2002)."*Spray pyrolysis deposition and characterization of titanium dioxide thin films*,*Material chemical physics*,Vol. 77,pp.938.
- Dhahir, T.A.AL., (May 2013), *Diyala Journal for Pure Science," Quantitative Phase Analysis for Titanium Dioxide from X- ray Powder Diffraction Data Using the Rietveld Method"*, Vol.9, Issue No.2, pp. 108.
- Gratzel,M & B.O Regan(1991), Low cost, high efficiency cell based on dye-sensitized colloidal TiO₂ films, *Nature* 353,pp737-740
- Monoharan,C & Sridhar,R,(September,2012) ,*International Journal of Recent Scientific Research , Physical Properties of Spray Pyrolysis TiO₂ Films*, Vol.3, Issue,9,pp.775-777.
- Masuda,Y., & Kato, K.,(February 2009), *Journal of the Ceramic Society of Japan, Synthesis and Phase Transformation of TiO₂ Nanocrystals in Aqueous Solutions , Vol.117,Issue No.3*,pp.373.
- Revathi,B.P.Perumal & Nachammai.J.,(September 2018),*Journal of Applied Science and Computations , Structural and Optocal Characterization of TiO₂ Thin Films Synthesized by Spray Pyrolysis Technique*,Vol.5,Issue 9, pp.124-129.

DESIGN AND ASSEMBLING OF SIMPLE HOMEMADE ELECTROSPINNING DEVICE FOR NANOFIBERS PRODUCTION

Zayar Pyae Phyo Aung¹, Su Su Lwin², Yin Maung Maung³, Than Than Win⁴

Abstract

A high technology is required in the production of nanofibers by electrospinning technique. This paper presents the work to implement design of the novel low-cost electrospinning system with inexpensive components. This home-made electrospinning device composed of three main components. They are Zero Voltage Switching (ZVS) flyback converter based home-made adjustable high-voltage power supply, stepper motor based homemade automatic injection pump and metallic collector plate. After a brief explanation to build the device using unexpensive components, the production zinc oxide (ZnO) nanofiber using low-cost homemade electrospinning device. The zinc oxide (ZnO) nanofibers were prepared from zinc acetate and poly vinyl alcohol (PVA). The fibers were deposited onto the aluminum substrate and calcined for 1 h at 600 °C. The properties of ZnO nanofibers were characterized by X-ray diffractometer (XRD) and field emission scanning electron microscope (FESEM).

Keywords: Nanofibers, electrospinning technique, Zero Voltage Switching (ZVS) driver and home-made automatic injection pump

Introduction

Electrospinning is a manner used for fabrication of nanofibers and based on the electrostatic phenomena used. The Basic components of electrospinning instruments are High voltage power supply, solution reservoir with frame and collector to collect nanofibers [Ayşe Gül Şener et al (2011)]. Electrospinning is a spinning technique using an electrostatic force approach to produce fibre from a polymer solution or fused [Dian Ahmad Hapidina (2017)]. The fibres produced from this method have a diameter range from nano to micrometers and a wider surface area than conventional spinning methods [Muhammad Miftahul Munir (2015)]. This method is in great demand because it can control production, fibre structure, porosity, orientation and dimensions of the fibre produced [Pravin Bhattacharai (2014)]. Zinc oxide (ZnO), an II-VI compound semiconductor, has a wide energy band gap of 3.37 eV, and large exciton binding energy of 60 MeV [Arini Nuran Binti Zulkifili (2015) & I. Jinchu (2015)]. It has a hexagonal wurtzite-type structure and is non-toxic and relatively cheap. ZnO in one-dimensional (1-D) nanostructures offer extra characteristics such as high aspect ratios, high electron mobility and possess both electrical and optical anisotropy. These unique multiple characteristics make ZnO suitable for various applications including solar cell, gas sensor and photodetector [Ngurah Ayu Ketut Umiati (2019)]. In this research work, the design of electrospinning device for production nanofiber material was carried out. The development of an electrospinning system is carried out using raw materials and components that are available from the local market. The material used for testing is zinc acetate with a mixture of polyvinyl alcohol (PVA). Characterization of the nanofiber structural and morphological were carried out using X-ray diffraction (XRD) and field emission scanning electron microscopy (FESEM).

¹ Demonstrator, Department of Physics, Myeik University, Myanmar.

² Demonstrator, Department of Physics, Myeik University, Myanmar.

³ Professor, Department of Physics, University of Yangon, Myanmar.

⁴ Professor, Department of Physics, Panglong University, Myanmar.

Experimental Procedure

Design of home-made electrospinning device

This home-made electrospinning device composed of three main modules. They are zero voltage switching (ZVS) flyback converter based home-made adjustable high-voltage power supply, stepper motor based homemade automatic injection pump and metallic collector plate.

ZVS flyback converter based home-made adjustable high-voltage power supply

The power supply was composed of four main parts. They are timer switch for automatic on/off system, 0-24 V AC to DC power supply, ZVS flyback converter and flyback transformer. The connecting diagram and the photo of automatic on/off variable high voltage power supply was shown in figure 1 (a) and 1 (b). So, the on/off time of this power supply can be programmable by the user easily. The input voltage is 12-36V and will give high voltage of direct current (DC). The differences between the input and output voltage is about 1000 V. When the input voltage applies 12 V, the output voltage can reach 50-100 W. If 24 V input applies the output voltage can reach more than 200 W.



Figure 1 (a) The connecting diagram of automatic on/off variable HV power supply

12 kV- 24.5 kV home-made high voltage power supply

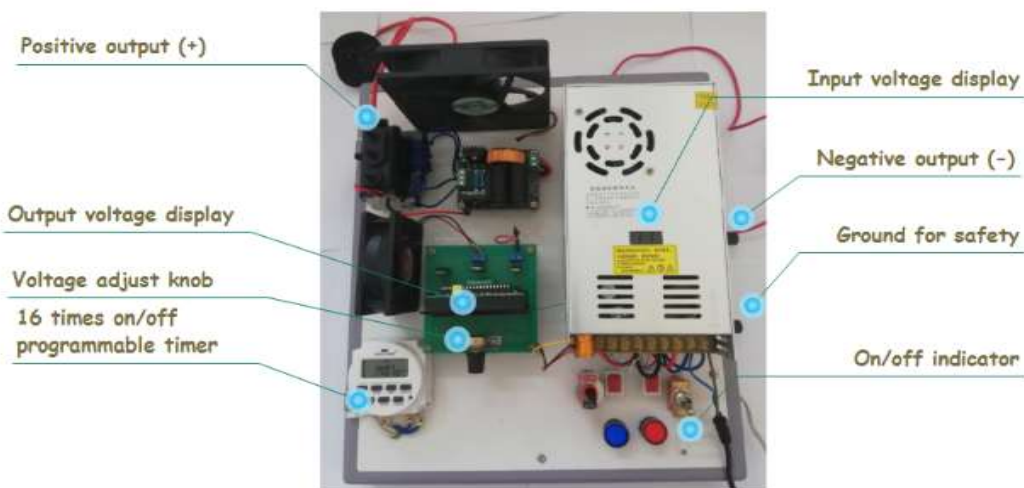


Figure 1 (b) The photo of automatic on/off variable HV power supply.

Homemade automatic injection pump

A small infusion pump used to gradually push small amounts of fluid from the syringe. Syringe pump flow rates can be adjusted by suing stepper controller. The standard volume syringe is 10 mL with an installed capacity of 1 syringe. In this syringe pump, Neam 17 stepper motor of restoration angle 180 degree was driven by Tb6560 stepper motor driver. The speed was control by stepper motor speed controller. The block diagram and the figure of injection pump was shown in figure 2.

Homemade Automatic Injection Pump

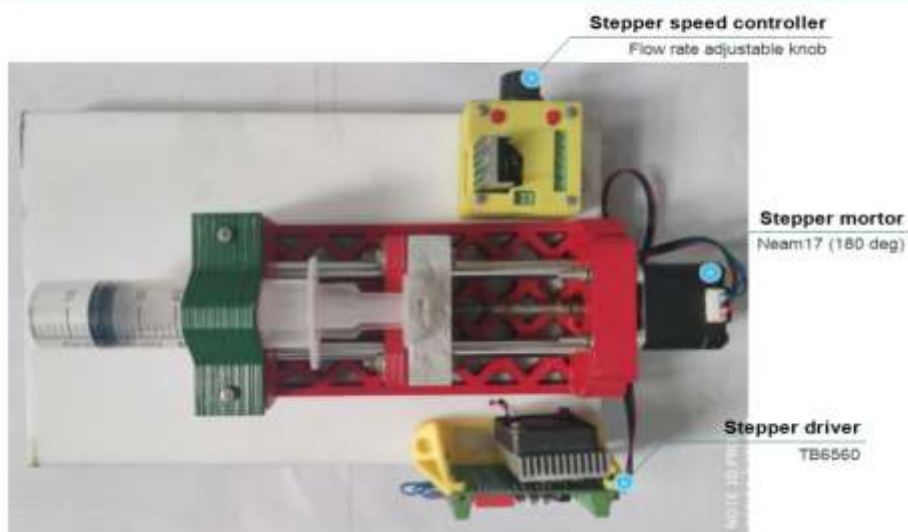


Figure 2 The homemade automatic injection pump

Preparation of ZnO nanofibers

10% poly vinyl alcohol PVA solution was prepared with distilled water by conventional method. Firstly, poly vinyl alcohol PVA, 10g was dissolved in distilled water, 100ml for 3days at 60°C. And then, 5 g of zinc acetate was dissolved in 10ml of distilled water for 1h at 60°C. Finally, PVA solution 40ml was mixed zinc acetate solution for 3h at 60°C. The PVA/zinc acetate solution

was filled into the 10 ml syringe. The block diagram for sample preparation was shown in figure 4. The tip of the emitter (needle) was connected to the positive terminal of high voltage power supply and the collector (aluminum foil) was connected with the ground. The collector (aluminum foil) was placed 7 cm below the emitter (tip of needle) to collect the nanofibers at a voltage of 24 kV and the running time was 15 min. The as-spun nanofibers were calcined at 600 °C for 1 h. The resulting fibers were analyzed by XRD and FESEM.

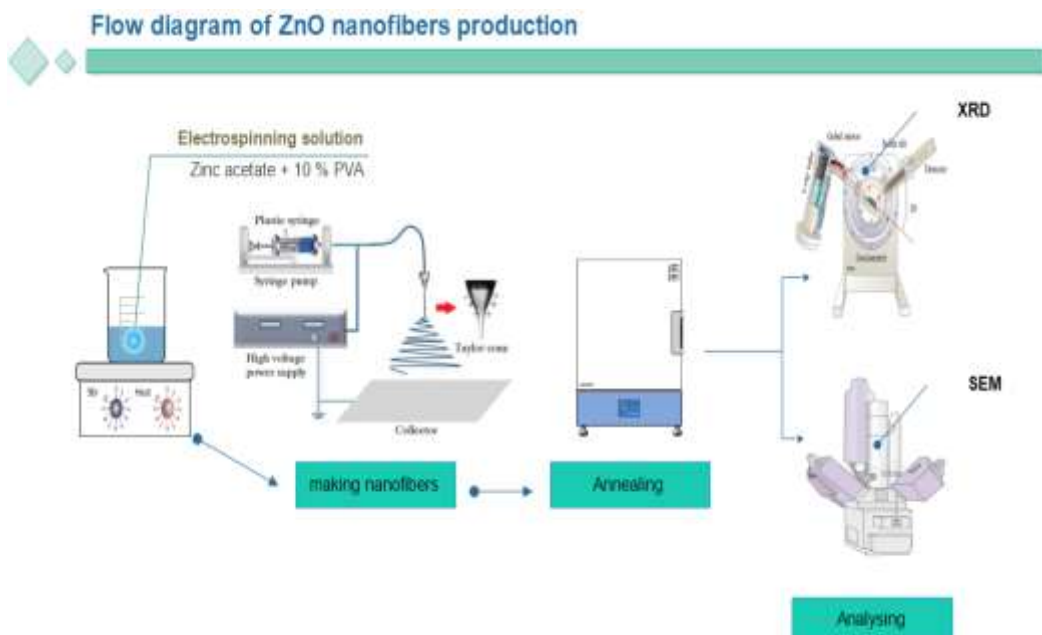


Figure 3 The flow diagram for the production of ZnO nanofibers production

Results and Discussion

High Voltage Power Supply (HVPS) Performance Test

The output voltage of HVPS was measured by Fluke 80k-40 and Fluke 179 multimeter. According to the measurement result the output voltage is about 1000 times larger than the input voltage. It was found that the single flyback can generate HV output voltage up to 34 kV but should not applied more than 24 kV. According to the stability test, there is no significant output voltage change within 3 h. The input voltage versus output voltage and the stability test result graph were shown in figure 4 (a) and 4 (b).

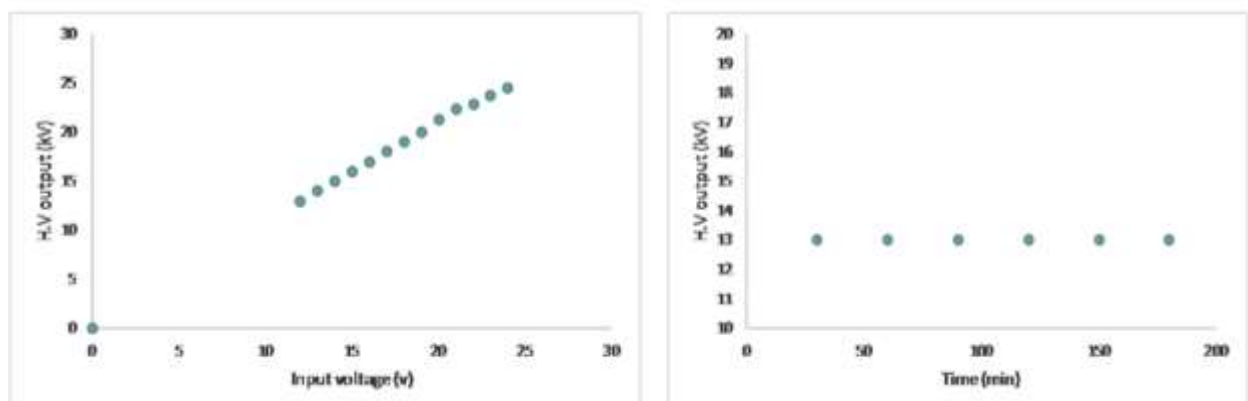


Figure 4 (a) The relationship between input and output voltage; (b) the output voltage stability test

XRD and FESEM analysis of ZnO nanofibers

The ZnO powder was determined by using X-ray Diffractometer (Rigaku RINT 2000). XRD was performed using monochromatic CuK α radiation ($\lambda=1.54056\text{ \AA}$) operated at 40kV (tube voltage) and 40mA (tube current). Sample was scanned from 10° to 70° in diffraction angle 2 θ with a step-size of 0.02°. The X-ray diffractograms of pure ZnO is shown in figure 5. The ZnO X-ray patterns present the higher crystallinity degree of investigated materials. The crystallite size (D) was calculated based upon on the all diffraction peak's (main peak's) broadening in the XRD pattern using the Debye Scherrer formula. The crystallite size is 42.69 nm. The FESEM images of ZnO nanofibers for different scale bar are shown in figure 6 (a) and 6 (b). It was observed that the high area density and there is no uniform distribution of diameter for all samples. The diameters of fibers change in between 46-106 nm. It was also found that some defects such as droplets, splitting and branched fibers. It could be due to the less flight time. Therefore, the fiber uniformity was significantly affected by the flow rate.

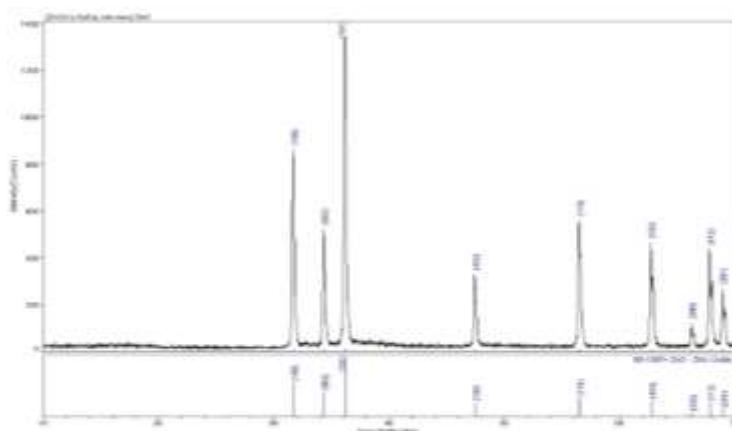


Figure 5 The XRD pattern of ZnO oxide

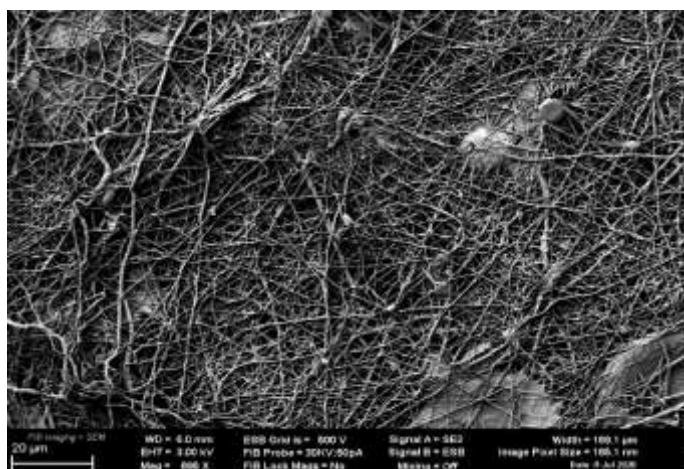


Figure 6 (a) FESEM image of ZnO nanofibers (20 μm)

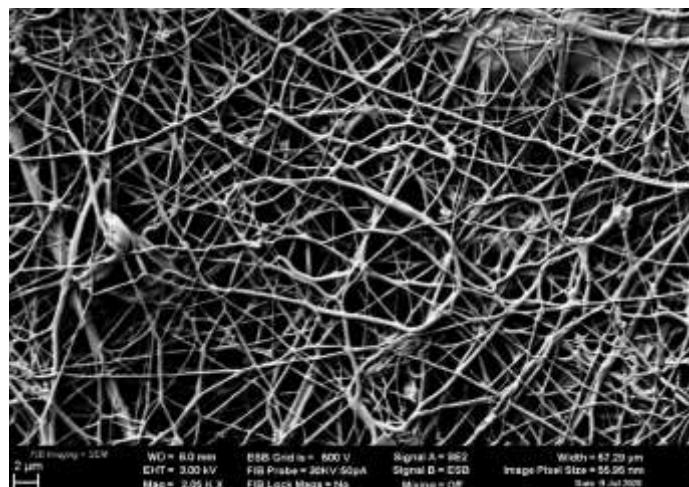


Figure 6 (a) FESEM image of ZnO nanofibers (2 μ m)

Conclusion

The electrospinning system has been implemented with an electrical power supply to generate a constant dc high voltage dc, an adjustable syringe pump, and flat collector. The single Mazzilli converter could generate HV up to 24 kV and the performance test showed that the converter has good stability over time. Electrospinning tests have been successfully carried out. According to the XRD analysis the resulting ZnO nanofibers was indicated the good crystalline nature. The average crystallite size of 42.69 nm was calculated by XRD profiles. Observation using FESEM shows that the fibre produced by electrospinning device in this work was in a nanometer scale.

Acknowledgements

I would like to express my gratitude to everyone who supported me throughout this research work.

References

- Ayşe Gül Şener, Ali Saffet Altay and Filiz Altay (2011) “Effect of Voltage on Morphology of Electrospun Nanofibers”, ELECO; I-324-I328.
- Arini Nuran Binti Zulkifili, Terauchi Kento, Matsutake Daiki, and Akira Fujiki (2015) “The Basic Research on the Dye-Sensitized Solar Cells (DSSC)”, Journal of Clean Energy Technologies, Vol. 3, No. 5, 382-387.
- Dian Ahmad Hapidina, Ismail Saleha, Muhammad Miftahul Munira, Khairurrijal (2017) “Design and Development of a Series-Configuration Mazzilli Zero Voltage Switching Flyback Converter as a High-Voltage Power Supply for Needleless Electrospinning” Engineering Physics International Conference, EPIC 2016, 509 – 515.
- I. Jinchu, C.O Sreekala, U.S. Sajeev3, K. Achuthan, K.S. Sreelatha (2015), “Photoanode Engineering Using TiO₂ Nanofibers for Enhancing the Photovoltaic Parameters of Natural Dye Sensitised Solar Cells”, Journal of nano and electronic physics, Vol. 7 No 4, 04002(4pp).
- Muhammad Miftahul Munir, Dian Ahmad Hapidin, and Khairurrijal (2015), “Designing of a High Voltage Power Supply for Electrospinning Apparatus Using a High Voltage Flyback Transformer (HVFBT)” Applied Mechanics and Materials Vol 771 (2015) pp 145-148.
- Ngurah Ayu Ketut Umiati, V.G.S. Kadarisman, Agus Subagio Kunto Wandono (2019) “A Simple Homemade Electrospinning for Nanoscale Fibres Production” E3S Web of Conferences 125.
- Pravin Bhattacharai, Keshar Bdr. Thapa, Rajesh Bdr. Basnet and Saurav Sharma (2014), “Electrospinning: How to Produce Nanofibers Using Most Inexpensive Technique? An Insight into the Real Challenges of Electrospinning Such Nanofibers and Its Application Areas” IJBAR (2014) 05 (09).

GMAIL NOTIFICATION WITH PHOTOGRAPH FROM MOTION ACTIVATED CAMERA USING ESP32_CAM AND MICROWAVE MOTION SENSOR FOR SECURITY PURPOSE

Hnin Aye Khine¹, Ohnmar Soe², Nu Nu Swe³, Mi Yin Sa Nine⁴

Abstract

Microwave motion sensor HW MS03 utilizes the Doppler shift phenomenon due to the relative motion. The sensor detects the slight movement and it triggers the microprocessor to operate the various functions. In this research, microwave motion sensor detects the motion of object and then it sends the digital signal to the microprocessor. The capturing the photograph and the Gmail with photograph sending to the specified address are implemented by microprocessor. ESP32_CAM is the microcontroller which is attached with OV2640 camera module, Wi-Fi and dual mode Bluetooth. It is reliably suitable to detect the trigger signal from microwave motion sensor, to capture the photograph and to connect the internet via Wi-Fi for sending the email. By using deep sleep mode which is one of the special features of ESP32_CAM, the energy consumption is reduced. After implementation of all functions, the processors and digital peripherals connection are in sleep mode until the next motion signal is detected. This system can be used in security monitoring, intelligent home appliances control system due to low energy consumption, cost effective system and reliable operation.

Keywords: ESP32_CAM, microwave motion sensor, deep sleep mode, Gmail

Introduction

The motion detector is a device which can detect the movement in the certain region in front of or around the detector. It is used to detect the motion of human beings or the objects for both safety and security purposes. When the sensor senses the movement, the signal is sent to control system. Some security system with motion sensor can be programmed to record the events via camera or send the alert via Gmail. In this research, microwave motion sensor HW MS03 is functioned as motion detector. As it uses Doppler Effect, it can detect the human beings as well as the objects. The main function of this research is the sending Gmail with photograph when the movement is detected. ESP32_CAM is a reasonable device to implement these functions because it has microprocessors, OV 2640 camera, Wi-Fi and dual mode Bluetooth. Camera can capture the image, Gmail can be sent via Wi-Fi and these functions can be processed by processors which are already attached to ESP32-CAM. ESP32-CAM is the module which composes ESP32-S attached with OV2640 camera. Deep sleep is one of the features of ESP32 which is used for power saving purpose. Initially, ESP32-CAM is already in deep sleep mode. When microwave motion sensor detects the movement of any body, it wakes up ESP32-CAM, starts to capture image and sends it via Gmail to the specified Gmail address. After all functions are completed, it goes back to sleep until next movement is detected. The block diagram of motion activated camera is shown in figure 1.

¹ Dr, Lecturer, Department of Physics, Yangon University of Education

². Dr, Lecturer, Department of Physics, Yangon University of Education

³. Dr, Associate Professor, Department of Physics, Yangon University of Education

⁴. Dr, Lecturer, Department of Physics, Myeik University

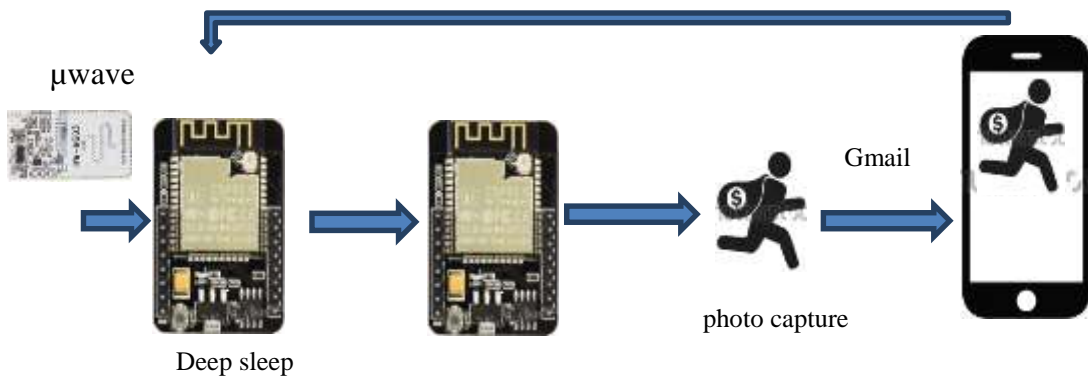


Figure 1 Block diagram of motion activated camera

Material and Method

The motion activated security camera is designed and constructed by using ESP32_CAM and microwave motion sensor HW MS03 module. FTDI adapter is used to upload the code. As the deep sleep mode is used, the system is slept all time after the capturing photograph and sending alert Gmail with photograph via Wi-Fi.

Microwave Motion Sensor HW MS03 Module

Microwave motion sensor HW MS03 is used the Doppler Effect which is the change in frequency of a wave due to the relative motion between source and observer. It can sense the movement of the living things or non-living things. It detects the movement of the objects without interference from temperature, humidity, airflow, dust, noise, light and dark and anti-jamming. The microwave motion detector module has wide coverage and no blind spots.

Microwave motion sensor emits continuously the microwave which is electromagnetic radiation whose frequency ranges from 0.3GHz to 300GHz. The sensor transmits the microwave into the surrounding and it detects any movement by analyzing the microwave frequency after reflection from object. Microwave motion sensor HW MS03 is illustrated in figure 2.



Figure 2 Microwave sensor HW MS03

ESP32_CAM

The ESP32-CAM is a rich-featured microcontroller that has an integrated Wi-Fi, dual mode Bluetooth, 2MP OV2640 video camera and micro SD card slot. It is ready for IoT (Internet of Things) devices which require a camera with advanced functions like video streaming and image recognition. The software distributed by Espressif includes a sketch that allows building a web-based camera with a sophisticated control panel. The ESP32-CAM module is made up of ESP32-S but it has fewer I/O pins than ESP32-S module because some of the GPIO pins are used internally for the camera and the micro SD card port. ESP32-CAM module has no USB port. The future technology devices international (FTDI) adapter is used to program. The photo of ESP32_CAM is shown in figure 3.



Figure 3 The photo of ESP32_CAM

The camera has 2 Megapixel sensor, the resolutions of camera are UXGA (320X240), SXGA (1280X1204), XGA (1024X768), SVGA (800X600), VGA (640X480) and CIF (400X296) and the image transferred rate is 15 to 60 fps (frame per second). Table1 shows the specifications of ESP32_CAM and the pin assignment of ESP32_CAM is illustrated in figure 4.

Table 1 Specifications of ESP32_CAM

Wifi	802.11b/g/n/e/i
Bluetooth	4.2 with BLE
Support interface	UART,SPI,I2C,PWM
Support SD card	Maximum 4G
Clock speed	Up to 160Mz
Computing power	Up to 600DMIPS
RAM	SRAM-520KB, PSRAM-4MB
IO port	9
Serial port rate	Default 115200bps
Image output format	Jpeg(only OV2640), bmp , grayscale
Power consumption	Deep sleep: 6mA ,5V Light sleep: up to 6.7mA ,5V

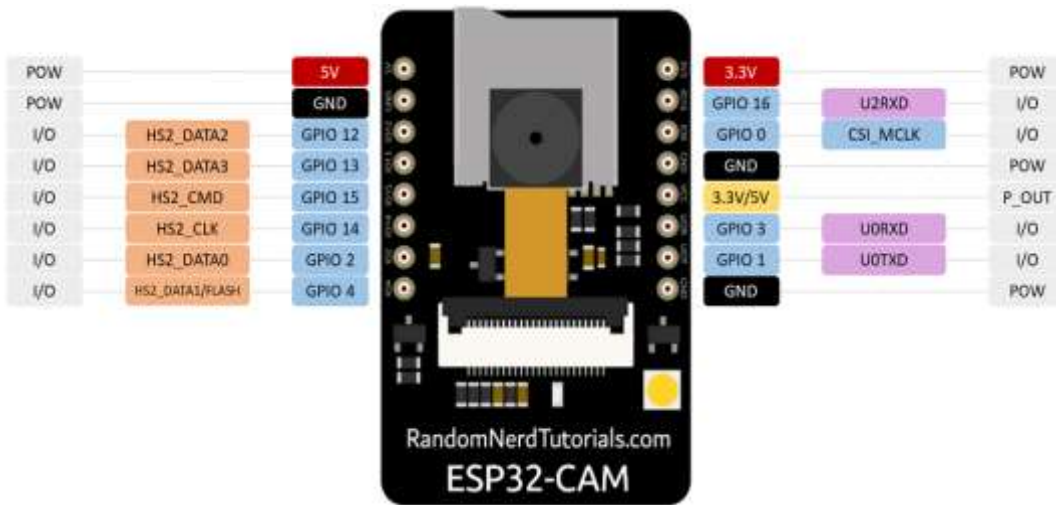


Figure 4 Pin assignment of ESP32_CAM

FTDI 232 Adapter

ESP32-CAM AI-Thinker has no USB connector, so FTDI is used for uploading the code to the board through the U0R and U0T pins (serial pins). The pin assignment of FTDI 232 is shown in figure 5.

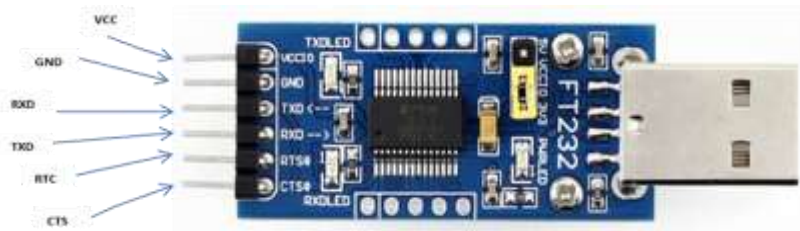


Figure 5 Pin assignment of FTDI 232

Hardware and Software Preparation

In motion activated camera system, ESP32_CAM and microwave motion sensor are used as main components. Arduino IDE is one of the languages which is compatible with ESP32_CAM but it is not included the default Arduino IDE. If ESP32 series device is used with Arduino IDE, the board manager is needed to add ESP32 board. This will be completed by inserting http://dl.espressif.com/dl/package_esp32_index.json link to Arduino IDE preferences “additional board manager URLs”. ESP32-CAM mail client library is also needed to install in the library manager. Before uploading the code, check the port and select the board “AI thinker ESP32_CAM” in tools menu.

Hardware Design

The code is uploaded to ESP32_CAM by using FTDI adaptor as shown in figure 6. In flashing mode, GPIO0 is grounded and Tx, Rx pins of FTDI are connected to U0R, U0T of ESP32_CAM respectively. The output pin of microwave motion sensor is connected to the GPIO13 pin of ESP32-CAM to send the signal. After uploading the code, GPIO0 is disconnected

from ground to operate the system as shown in figure 7. The system starts to operate by pressing the reset button.

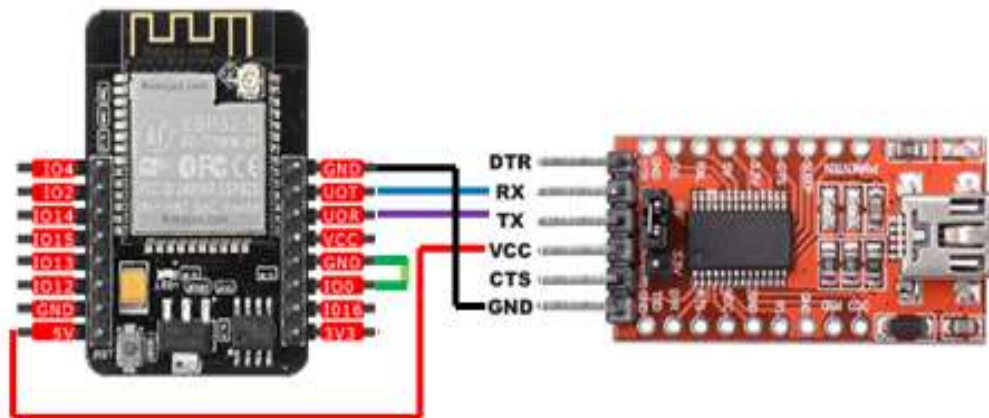


Figure 6 ESP32_CAM in flashing mode

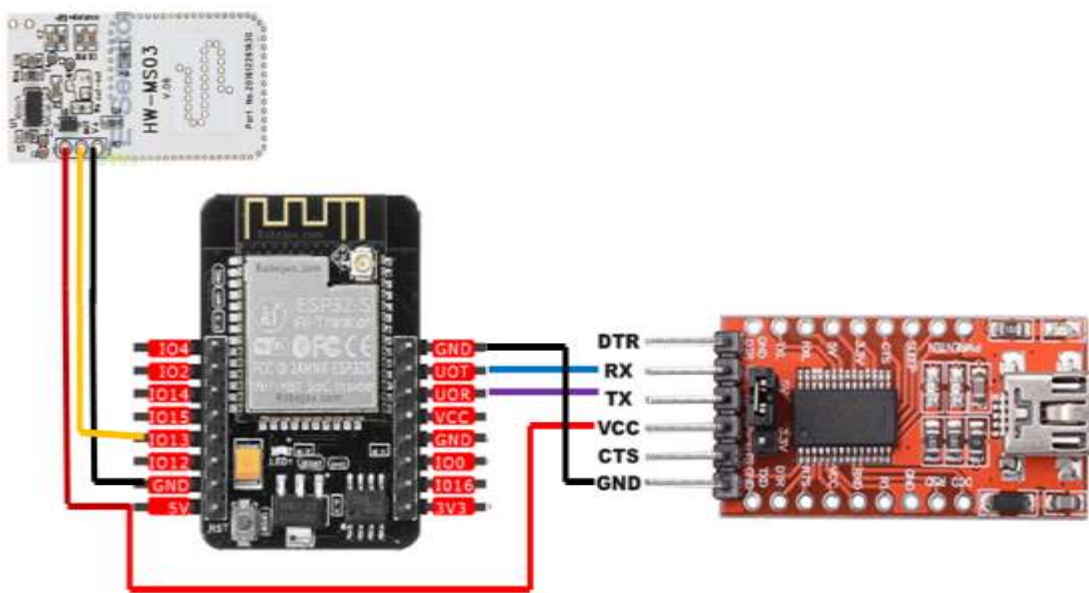


Figure 7 Circuit diagram of camera trap

The working principle of motion activated camera is as follows:

- ESP32_CAM being in deep sleep mode
- Microwave motion sensor triggers the ESP32_CAM to wake-up
- Take a photograph and save it temporarily on SPIFFS
- Connecting to Gmail address
- Sending the Gmail notification with photo captured
- ESP32 return to sleep again

The flow chart of work function of motion activated camera is shown in figure 8.

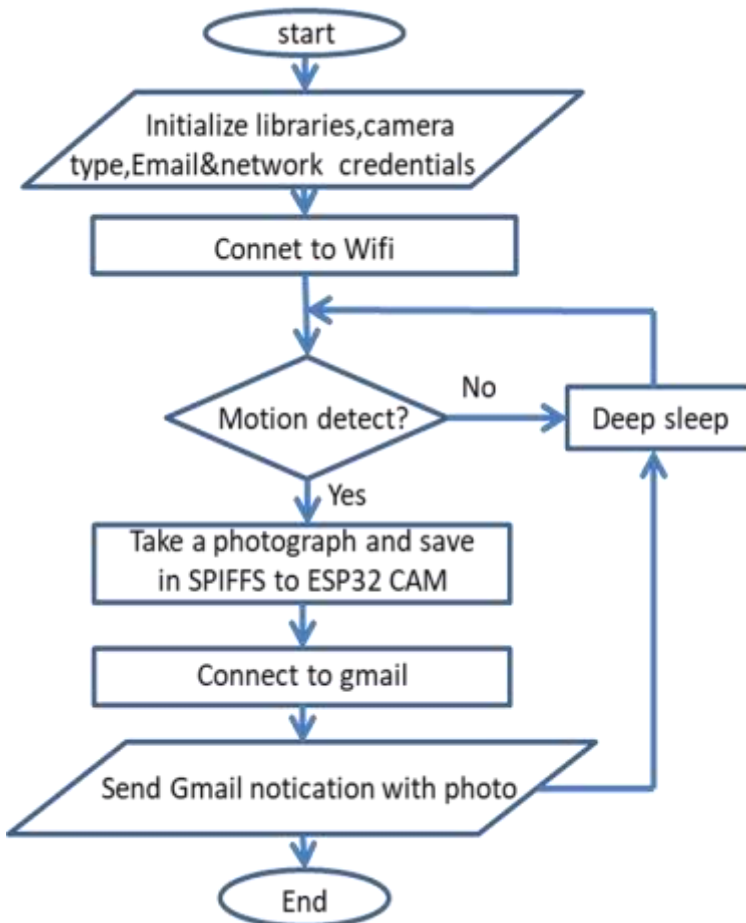


Figure 8 The flow chart of Work function of motion activated camera

Software Development

ESP32-CAM is in deep sleep mode. It will be wake up by the external wake up source. The microwave motion sensor HW MS03 is used as external wake up source. When it detects the movement, it sends the HIGH signal. All GPIO pins cannot be used as the wake up source. Only RTC GPIO pins can be used as the wake up sources. In this research, RTC GPIO13 is connected to the output pin of microwave motion sensor which is functioned as wake up source.

When the external trigger applied to ESP32-CAM, it takes a photograph and saves it temporarily on serial peripheral interface flash file system (SPIFFS) which is a light-weight file system for microcontrollers with an SPI flash chip. And then, it sends Gmail alert with photo captured. Finally, it is in deep sleep again until next trigger comes in. The deep sleep mode is an important function in software development to reduce the power consumption.

ESP32_CAM is capable of light sleep mode and deep sleep mode for power saving. In this research, deep sleep mode is used. In deep sleep mode, CPUs, RAM and all digital peripherals are powered off. RTC controller, RTC peripherals and RTC memories are still powered on. [4] The function “*esp_sleep_enable_ext0_wakeup (GPIO_NUM, status)*” is used to enable the device wakeup.

```

esp_sleep_enable_ext0_wakeup (GPIO_13 ,1)
esp_deep_sleep_start ();
  
```

fesp_sleep_enable_ext0_wakeup (GPIO_13, 1) means that the device will wake up when the trigger signal is high. To take the photograph, the following instruction is used. This creates the frame buffer that contains the photos.

```
Camera_fb_t* fb = esp_camera_fb_get();
```

As soon as photo has captured, temporarily save photo in SPIFFS and then sending notification to specified Gmail address. After that, the Wi-Fi is disconnected and the device is in deep sleep mode again.

```
WiFi.disconnect();
Delay(1000);
esp_deep_sleep_start();
```

Simple Mail Transfer Protocol (SMTP) server is an application. Its main purposes are sending, receiving and relaying the outgoing mails between sender and recipient. Anyone who has internet Gmail account can use SMTP. The emails are sent using the port 587 or 465.

```
#define smtpServerPort 465
```

Gmail account and password of sender and Gmail account of recipient are required for outgoing Gmail.

Results and Discussion

Results

Motion activated camera is implemented for photo capturing and sending Gmail alert with photos captured by using ESP32-CAM, microwave motion sensor and FTDI adapter as shown in figure 9. The code is uploaded to ESP32 CAM. If the movement of any object is detected, microwave motion sensor triggers ESP32_CAM to take the photo and sending the Gmail alert with photograph. The step by step working procedures from the motion activation to the successfully sending alert with photo via Gmail can be seen on serial monitor of arduino IDE as shown in figure 10. When ESP32_CAM detects the motion of the object, it connects the Wi-Fi and initiates the SPIFFS. And then, it captures the photo and connects SMTP to send the Gmail. After checking the Gmail address, the notification with photo is sent. The Gmail alert on the PC is shown in figure 11. Gmail notifications with photos are arrived on phone as shown in figure12. Figure13 shows Gmail with photo arriving on phone. The Photo captured is illustrated in figure 14.

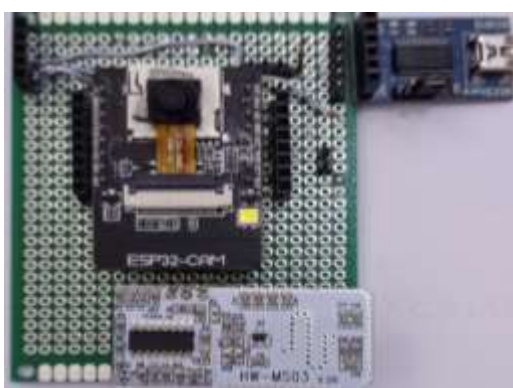
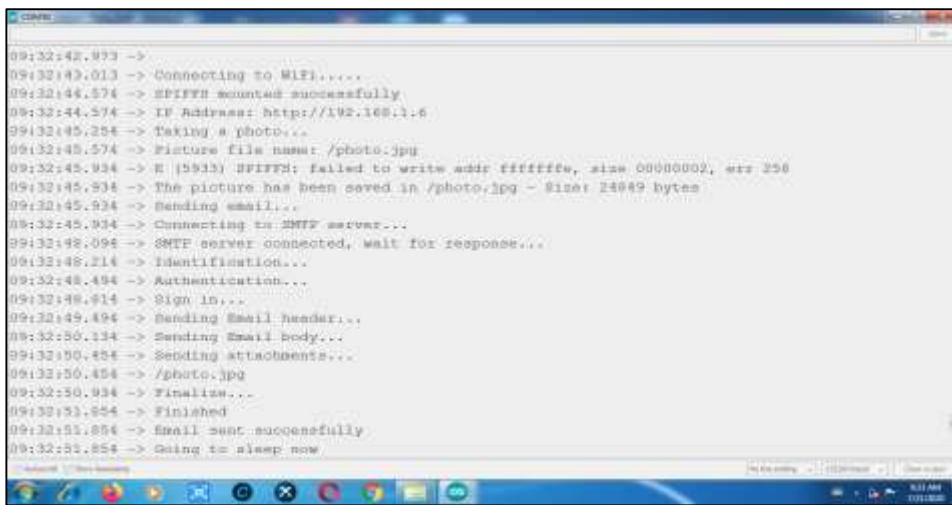


Figure 9 The photo of motion activated camera



```

09:32:42.873 -> Connecting to WiFi.....
09:32:43.013 -> Connecting to WiFi.....
09:32:44.574 -> SDFFF mounted successfully
09:32:44.574 -> IP Address: http://192.168.1.6
09:32:45.254 -> Taking a photo...
09:32:45.574 -> Picture file name: /photo.jpg
09:32:45.934 -> E (5913) SMTP: failed to write addr ffffff, size:00000002, err:256
09:32:45.934 -> The picture has been saved in /photo.jpg - Size: 24049 bytes
09:32:45.934 -> sending email...
09:32:45.934 -> Connecting to SMTP server...
09:32:45.934 -> SMTP server connected, wait for response...
09:32:45.934 -> Identification...
09:32:45.934 -> Authentication...
09:32:45.934 -> Sign in...
09:32:45.934 -> Sending Email header...
09:32:45.934 -> Sending Email body...
09:32:45.934 -> Sending attachments...
09:32:45.934 -> /photo.jpg
09:32:45.934 -> Finalize...
09:32:45.934 -> Finished
09:32:45.934 -> Email sent successfully
09:32:45.934 -> Going to sleep now

```

Figure 10 The working procedure of motion activated camera

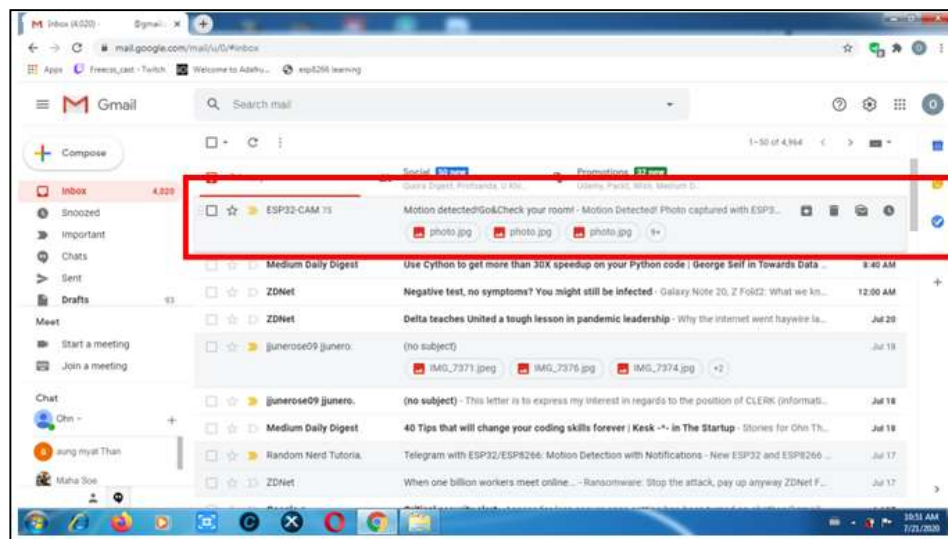


Figure 11 Gmail alert on PC

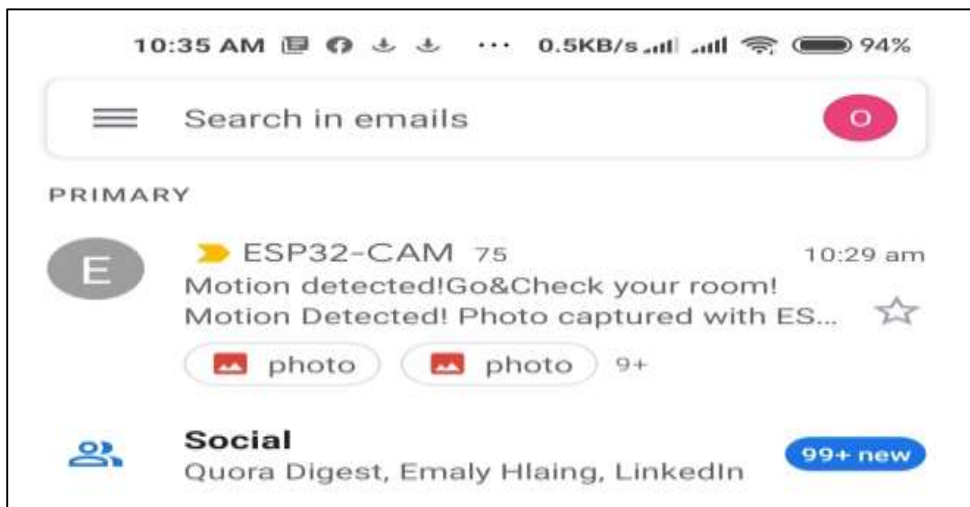


Figure 12 Gmail notification with photo arriving on phone

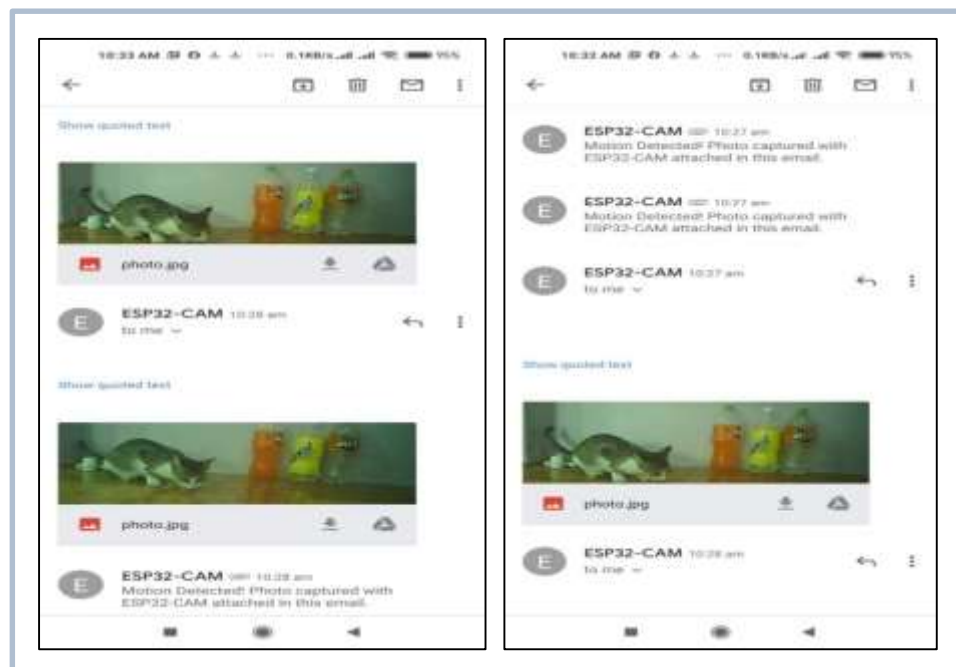


Figure 13 Gmail with photo arriving on phone



Figure 14 Photo captured by ESP32_CAM

Discussion

It takes time three seconds to capture the image from the motion activation to ESP32_CAM. The photos are saved in SPIFFS within one second. The time taken for sending Gmail takes six seconds. Total time elapsed from motion activation to sending Gmail is taken ten seconds. These procedures can be obviously seen in figure 10. Although the time seems to be short time, the fast moving objects cannot capture the proper sharp image. As the resolution of camera is 2 MP, the moderated quality photograph can be obtained. Less secure app access is allowed to send the new Gmail properly as shown in figure 15. Google will automatically turn off this setting if it is not being used.



Figure 15 Less secure app access allowing



Figure 16 Image distortion

Conclusion

Microwave motion sensor can make the false trigger due to the slight vibration such as curtain and itself movement. The microwave motion sensor detects the motion through wood and other building materials. The microwave can penetrate the many surfaces in the detecting area so that the microwave sensor can detect the motion where the detection is not required. The camera setting such as resolution, brightness, quality, contrast and exposure can be adjusted to get the sharp image in the detecting surrounding. For example, the value of quality can vary within 1 and 63. The value 1 is maximum quality and 63 is minimum quality. The camera with high resolution and maximum quality setting can capture the error image as shown in figure 16. GSM module does not use in this device. Instead of GSM module, simple mail transfer protocol (STMP) server is used. Although the cost for GSM module is reduced, the internet bill for sending mail will be accounted.

Acknowledgements

I would like to thank Pro-rectors, Yangon University of Education, Dr Pyone Pyone Aung and Dr Kay Thwe Hlaing for their kind permission to take part in this research work. I also thankful to Professor Dr Khin Swe Oo, Head of Department of Physics, Yangon University of Education, for giving advice and encouragement through the research period. I deeply grateful to Professor Dr Ohn Than, Head of Department of Physics, Kyaukse University, who supports the continuous guideline about the hardware and software for this research work. Finally, Thankful all my colleagues for their participation in this research work.

References

- [https://szhaiwang.en.made-in-china.com/product/cBIEGNzrEOhs/China-New-Model-Microwave-Radar Sensor-Module-for-Lighting-HW-MS03-.html/](https://szhaiwang.en.made-in-china.com/product/cBIEGNzrEOhs/China-New-Model-Microwave-Radar-Sensor-Module-for-Lighting-HW-MS03-.html/)
- <https://howtomechatronics.com/tutorials/arduino/how-pir-sensor-works-and-how-to-use-it-with-arduino/>
- <https://randomnerdtutorials.com/esp32-cam-pir-motion-detector-photo-capture/>
- https://docs.espressif.com/projects/esp-idf/en/latest/esp32/api-reference/system/sleep_modes.html
- <https://www.waveshare.com/ft232-usb-uart-board-type-a.htm>
- <https://randomnerdtutorials.com/esp32-cam-ai-thinker-pinout/>
- <https://www.ebay.com/itm/High-Performance-Motion-Sensor-Module-Radar-HW-MS03-2-4GHz-to-5-8GHz-Microwave-/193566412649/>
- Purdun J, “Beginning C for Arduino” Apress, NY, 2012
- RuiSantos ,“Learn ESP32 with Arduino IDE” Random Nerd Tutorial Lab,2020

DESIGN AND CONSTRUCTION OF FREQUENCY, INDUCTANCE LOGICAL CONDITION, CIRCUIT CONTINUITY AND CURRENT DATA ACQUISITION SYSTEM

Aung Zaw Myint¹, Win Kyaw², San Ngwe Oo³

Abstract

In the present work, data acquisition system is designed to measure frequency, inductance, current, digital logic condition and circuit continuity. The system is constructed using an Arduino mega 2560 development board, resistors, capacitors, comparator, and various sensors. The respective sensors sensed physical phenomenon and sent electrical signal to Arduino ATmega2560 microcontroller. The measuring results data are displayed on the LCD, stored in micro SD card and logged in excel sheet directly using the parallax data acquisition (PLX-DAQ) as the same time. The system is innovatively designed to measure five different types of physical quantities.

Keywords: Data acquisition, Arduino ATmega2560, sensors, micro SD card, parallax data acquisition (PLX-DAQ).

Introduction

A process of gathering and measuring electrical data information in a specific method is known as data acquisition. In the study of electronics, data acquisition system is essential to acquire the various parameters of electrical and physical properties to process a control system or to drive a prototype design [Simon, (2010)]. Data acquisition system is very important to develop analyses an electronic circuit, material science, thin film technology, developing solar cells and study of semiconductor researches. Data acquisition applications are usually controlled by software programs developed using various general-purpose programming languages such as Assembly, BASIC, C, C++, Fortran, Java, Lab VIEW, Pascal, etc. Data acquisition system is the process of sampling signals into digital numeric values to measure real world physical conditions. Data acquisition system convert analog waveforms into digital values for processing [Floyd, (2006)]. Data acquisition begins with the physical phenomenon using a sensor such as the temperature of a room, the intensity of a light source, or the force applied to an object [Karvinen, (2014)].

Materials and Method

Arduino Mega Microcontroller

An Arduino microcontroller is a microcontroller built onto a single printed circuit board. This board provides all of the circuitry necessary for a useful control task: microprocessor, I/O circuits, clock generator, RAM, stored program memory and any support ICs necessary. The microcontroller utilized in the circuit is chosen Arduino Mega 2560 has large numbers of digital and analog I/O pins, larger program memory in Arduino development boards, easy to upload the program code. This code can be created with higher level programming language. Arduino mega is the heart of the circuit in which a program code to operate the data acquisition system [John, (2013)]. The Arduino mega consists of 54 digital I/O pins and 16 analog input pins. The Arduino mega board is operated with 16MHz crystal oscillator. The component of Arduino mega microcontroller is shown in Figure 1.

¹ Dr, Lecturer, Department of Physics, Dagon University

² Dr, Professor, Department of Physics, Loikaw University

³ Dr, Associate Professor, Department of Physics, University of Computer Studies (Dawei)

Rotary Encoder Module

A rotary encoder-based menu is created to choose different measuring quantities by rotating the rotary encoder. Component of rotary encoder module is shown in Figure 2. A rotary encoder is a type of position sensor which is used for determining the angular position of a rotating shaft. It generates an electrical signal, either analog or digital, according to the rotational movement. Turning the rotor will change the menu and pressing the rotor will enter the selected menu and pressing again will return to start of the menu selection. Selections are made the menu in following order,

1. Logic Probe
2. Continuity Tester
3. Frequency Meter
4. Inductance Meter
5. Current Meter

Micro SD Card Module

In some data acquisition, micro-SD card is required to log the measuring results [Jack, (2015)]. Logging data to the micro SD card and exporting data to excel worksheet are at the time for measuring physical quantities. The terms SD card stands for “Secure Digital” Card, there are many types of SD cards. The SD cards can work in two operating modes, one is using the SD mode commands and the other is serial peripheral interface (SPI) mode. The SPI module consists of six pins and they are four SPI pins and two power pins. The component of micro SD card module is as shown in Figure 3. The data logging on SD memory card can be stored measuring data. While the data is logging on the micro SD card, the data can be exported to the excel worksheet by connecting the circuit using USB cable [Harold, (2011)]. The Parallax Data Acquisitions (PLX-DAQ) tool software is an add-in tool for Microsoft Excel.

LM311 Comparator IC

The LM311 device is single high-speed voltage comparator. This device is designed to operate from a wide range of power supply ± 15 V voltages for operational amplifiers and 5 V supplies for logic systems. The output levels are compatible with TTL circuits. The LM311 device is an 8-pin chip which has 2 power inputs which are VCC and VEE. The pin 7 is an open collector pin of the output transistor. All inputs and outputs can be isolated from system ground. The LM311 of output go high or low depending on the difference voltage between its two inputs (+, -). Component of LM311 comparator and pin out diagram are shown Figure 4.

Current Sensor Module

The current sensor module includes the famous ACS712 IC to measure current using the Hall Effect principle. This module can measure current AC or DC current up to 5 A. The device consists of a precise, low-offset, linear Hall circuit with a copper conduction path located near the surface of the die. Applied current flowing through this copper conduction path generates a magnetic field which the Hall IC converts into a proportional voltage. [Bhattacharya, (2015)]. The module is connected in series with the load and be extra cautious to avoid shorts. On the other side, it has three pins. The Vcc is connected to +5 V to power the module and the ground is connected to the ground. Then the analog voltage given out by the ACS712 module is read using any analog pin on the Microcontroller. Component of current sensor module and pin out diagram are shown in Figure 5.



Figure 1 The component of Arduino mega microcontroller



Figure 2 Component of rotary encoder module

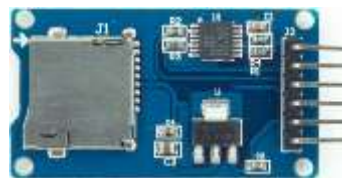


Figure 3 Component of micro SD card module

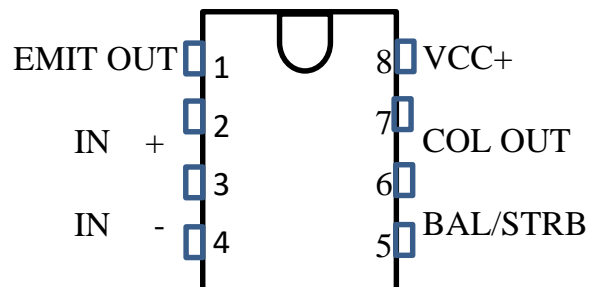


Figure 4 Component of LM311 comparator and pin out diagram



Figure 5 Component of current sensor module

Hardware Development and Operation

The main board consisted of Arduino Mega 2560 board, rotary encoder, alphanumeric liquid crystal display (LCD 20×4), a micro SD card module, comparator, current sensors and two lithium ion batteries. The block diagram of data acquisition system is shown in Figure 6. The flow chart of data acquisition system is shown in Figure 7. Data acquisition system is controlled by

software programs developed using Arduino C programming language. The Arduino IDE supports the languages C and C++ using special rules of code structuring. The Arduino IDE employed the program to convert executable code into a text file in hexadecimal encoding [Eide, (2008)].

The results of data acquisition system are illustrated with alphanumerical liquid crystal display LCD and sent to micro SD card. While the data is logging on the micro SD card, the data could be exported to the excel worksheet by connecting the circuit with computer using USB cable. PLX-DAQ is a simple add-on software to log Microsoft excel sheets for laboratory purpose. Parallax data acquisition tool (PLX-DAQ) software acquires up to 26 channels of data from any Parallax microcontrollers and drops the numbers into columns. PLX-DAQ provided easy spreadsheet analysis of data collected in the field that laboratory analysis of sensors and real-time equipment monitoring. Circuit diagram of data acquisition system is shown in Figure 8. The photograph of data acquisition system is shown in Figure 9.

For logic probe tester circuit, the Arduino mega board of an analog input pin A7 and a ground pin are applied. The logic conditions of a digital circuit board can be differentiated. Rotary encoder can be selected the condition of logic probe. Arduino microcontroller regarded input signal voltage level specifications as 0 to 0.8 V for logic LOW and 2 to 5 V as logic HIGH. The range can be converted by using 10 bits analog to digital conversion. The resolution is 4.88mV for each ten-bit digital values 1024. For 0.8 V, the digital value is 164($800 \text{ mV}/4.88 \text{ mV}$). The analog reading on analog input A7 pin between 0 and 164 can be concluded as logic LOW level. For 2 V, the digital value is 409($2000 \text{ mV}/4.88 \text{ mV}$). The analog reading on analog input A7 pin between 409 and 1023 can be concluded as logic HIGH level. But the voltage is detected between 0.8 to 2 V (the digital number between 164 and 409). The reading can be concluded neither logic LOW nor logic HIGH. In this condition, the logic probe will display FLOAT on the LCD display.

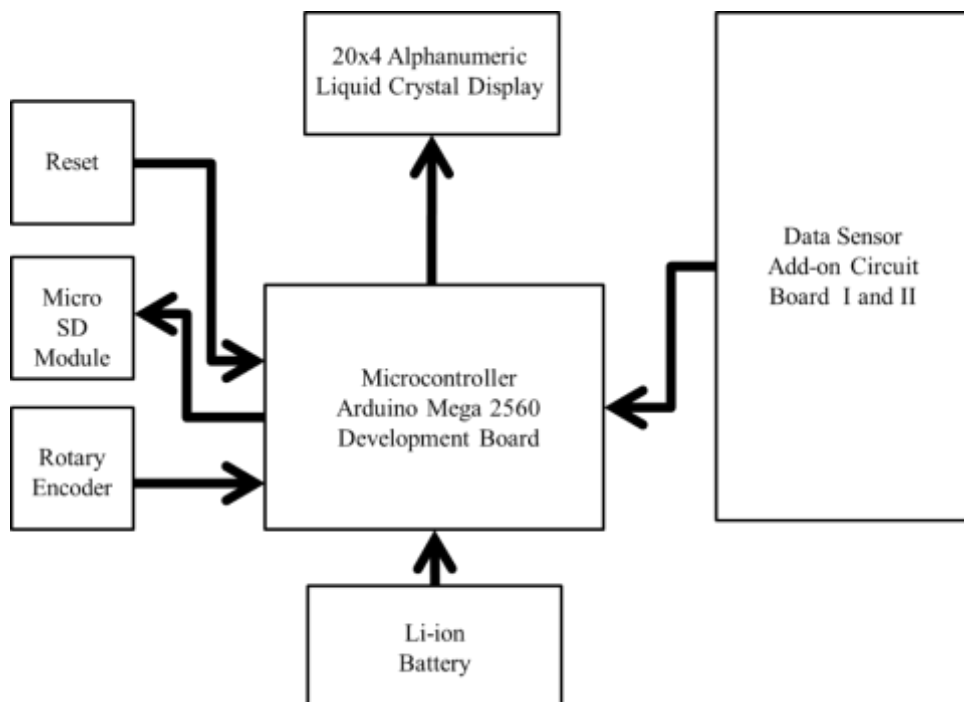


Figure 6 The block diagram of data acquisition system

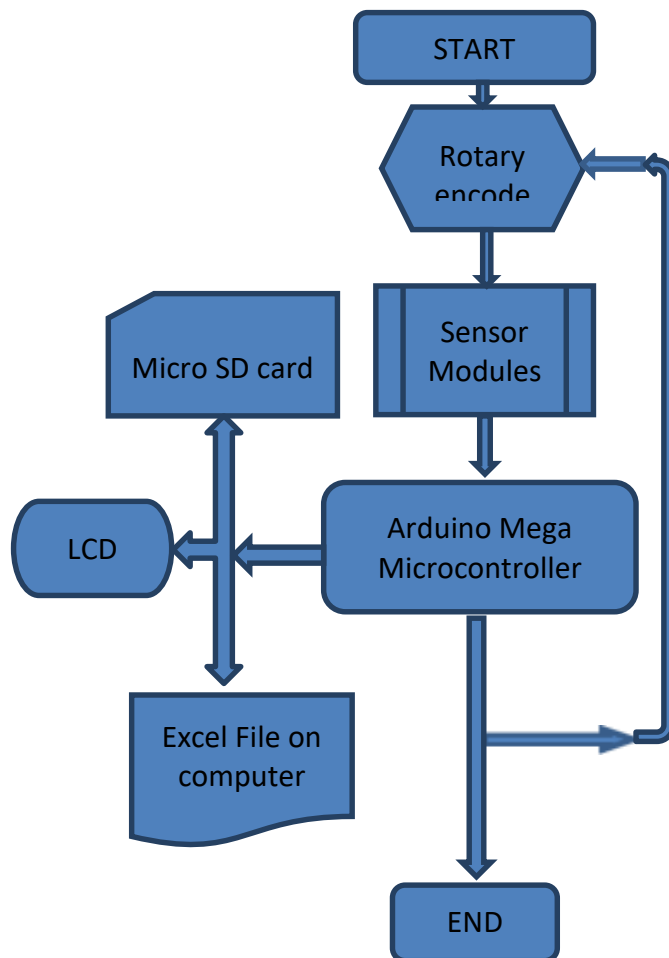


Figure 7 The flow chart of data acquisition system

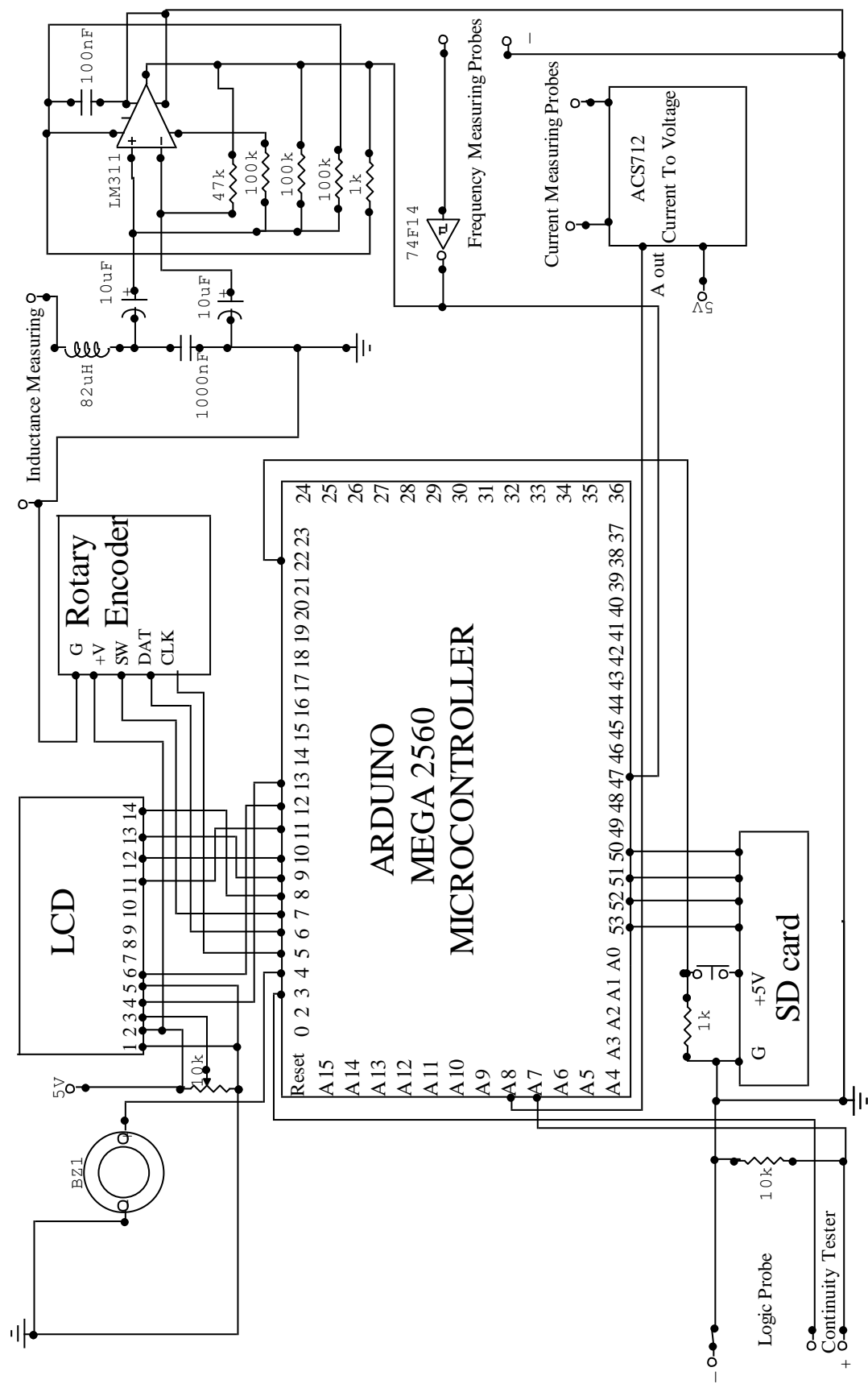


Figure 8 The schematic circuit diagram of data acquisition system

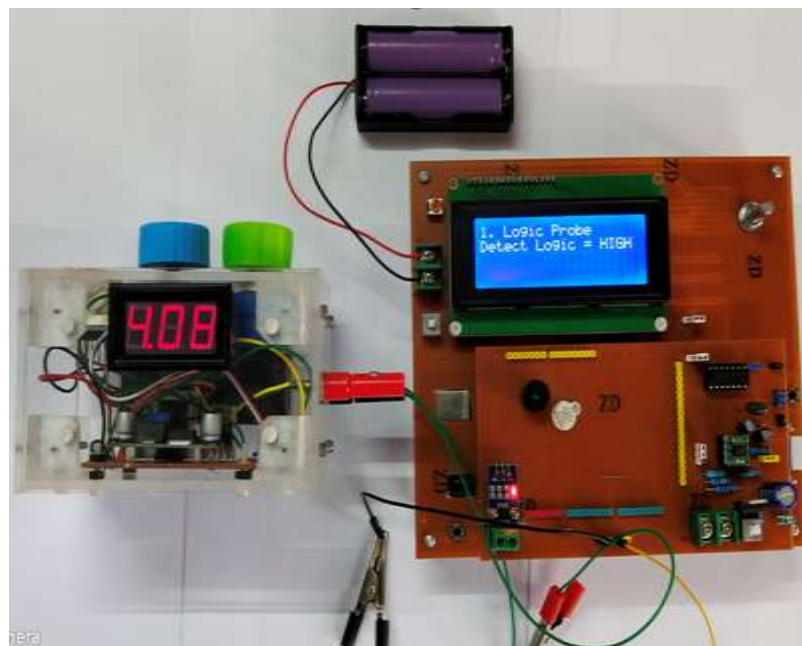


Figure 9 The photograph of data acquisition system

For continuity tester circuit, Arduino microcontroller of digital pin 3 and an analog pin A7 are applied. The continuity tester read the analog value under a specific condition. The buzzer is used to generate a sound under $50\ \Omega$ between two probes for continuity. The digital value is 1024 for 10-bit resolution. If the digital value is greater than 41(0.2 V), the buzzer would generate to continue. The connection between two points is successful. If the digital value is less than the 41, the connection of continuity testing is failed and buzzer would generate short tone.

The circuit is capable to measure both alternating current AC and direct current DC. The current sensor ACS712 is used to convert the current under measuring into relative voltage. The DC or AC current can be calculated from that voltage through the Arduino analog to digital converter. In this design, measurement of the current does not exceed 5Amp. The reading results are displayed on the LCD screen.

The frequency measuring circuit utilized an inverter IC 7414, two test probes and Arduino mega microcontroller of pin 47. The input frequency is feed to the input pin 47 through an inverter gate. The input pin 47 is available to read TTL logic level input. Pin 47 was specific for frequency counting library in programming. In this case, the counting begin is followed by a parameter called gate interval in milliseconds. The millisecond or micro second functions are limited to measure the periods of high frequencies. But Arduino programming in the frequency library file is capable of measuring high frequency values without error. Then the value of input frequency is counted and displayed on the LCD.

Measuring inductance values cannot be achieved only with microcontroller. Arduino mega microcontroller of pin 47 can be used to read the frequency value of inductor-capacitor (LC) circuit in frequency library for Arduino programming. Inductor-capacitor LC circuit is frequency resonator used as oscillator in series inductor and capacitor to oscillate. LC series circuit is one of the most important circuits used electrical and electronic circuits.

The LC meter is used a LM311 IC that functions as a frequency generator. The unknown inductance value can be obtained the relation of inductance and frequency $L = 1/(4\pi^2 C f^2)$. where L is the inductance in Henry (H), C was the oscillator capacitance in Farad (F) and f is the oscillation frequency in Hertz (Hz). Then an unknown inductance value is fed into the non-

inverting input pin of LM311 comparator. The output pin of LM311 comparator is fed into a specific input 47 pin of Arduino mega microcontroller.

Results and Discussion

The logic probe circuit can be differentiated three different logic levels for TTL input logic states. They are logic HIGH, FLOAT and logic LOW functions. The voltage between 0 to 0.8 V is logic LOW and 0.8 to 2 V is FLOAT. The voltage greater than 2 V and up to 5 V is logic HIGH. The continuity testing circuit is selected by using rotary encoder. If the two probes are disconnecting condition in testing circuit, LCD would display as “Fail” and the buzzer would generate a short beeping tone on every second. If the two probes are connecting condition in testing circuit, LCD will display as “Connected” and the buzzer would generate a continuous high frequency short beeping tone on every second.

The current sensor ACS712 is used as the current to voltage converter circuit. In this data collection, nichrome wire of load resistance that 7 ohms, 5 ohms, 2.7 ohms, 2.5 ohms and 2 ohms are tested with 3volts dc power supply. Comparison results of DAQ and digital multi-meter for measuring DC current using supply 3 V are shown in Table 1.

The pin 47 of Arduino mega microcontroller is connected with both inductance measuring circuit and frequency measuring circuit. In this measurement, an inverter gate (TTL7414) is added to achieve digital level on the frequency reading. Measuring Frequency is obtained from a portable digital signal generator. Other frequency data generated by an astable oscillator 555circuit is collected and compared with the portable digital oscilloscope. The data results are illustrated in Table 2. The most important part of inductance measuring circuit is the operational amplifier LM311N and LC circuit. The various inductors can be measured in this circuit. Comparison results of DAQ and color code values for measuring various inductors are illustrated in Table 3.

Table 1 Comparison results of DAQ and multi-meter for measuring current using supply 3V

No	Load Resistance(Ω)	Digital Multimeter current(A)	DAQ measuring current(A)	Deviation (A)
1	2	1.509	1.50	0.009
2	2.5	1.201	1.21	0.009
3	2.7	1.131	1.13	0.001
4	5	0.601	0.59	0.11
5	7	0.426	0.42	0.006

Table 2 Comparison results of DAQ and astable oscillator circuit for measuring frequency

No	Astable circuit (Hz)	DAQ measuring Frequency(Hz)	Deviation (Hz)
1	25.58	25.55	0.03
2	255.79	255.73	0.06
3	544.24	542.22	0.02
4	2.55E3	2.54E3	0.01
5	25.58E3	25.56E3	0.02

Table 3 Comparison results of DAQ and color code values for measuring various inductors

No	Marking color code (H)	Inductors values (μH)	DAQ measuring Inductance (μH)	Deviation (μH)
1	(Blue,gray,brown,gold)	$680 \pm 05\%$	675	05
2	$2\times$ (Blue,gray,brown,gold)	$1360 \pm 05\%$	1358	02
3	470 μH	$470 \pm 20\%$	471	01
4	820 H	$820 \pm 20\%$	818	02

Conclusion

The data acquisition system for five different quantities is successfully constructed. For measuring current system, large loading is required the current through. If the loads are very small, the reading cannot illustrate stable and correct reading. The reading is exactly for measuring the current between 400 mA and 5 A. In the frequency measurement, the range from 0.01 Hz to 100 GHz can be measured. Comparison results of DAQ and astable oscillator circuit for measuring frequency are shown in Table 2.

The inductance measuring system can measure larger than 10nH vales with acceptable results. But for the inductors in very small 0.01 nH range cannot be measure in stable. Comparison results of DAQ and color code values for measuring various inductors are shown in Table 3. The results are acceptable and most of data comparison approach to theoretical calculations. Finally, data acquisition is a process that begins with systematic data collection from various sources to achieve a beneficial decision.

Future Extension

In some of recent work, the innovative design of data acquisition system has been constructed for five different quantities to measure frequency, inductance, current, digital logic condition and circuit continuity. Especially for current measuring, ACS712 current sensor range from 400mA to 5A is used for large current. Current measuring for small amount of current range μA to nA will be designed and developed.

Acknowledgement

The authors would like to acknowledge Professor Dr Khin Khin Win, Head of Department of Physics, University of Yangon, for her valuable suggestion and comments for this work.

References

- Bhattacharya, S. K. (2015). Electrical measurement and control, kindle ed, INDIA VIKAS.
- Eide, A. R., Jenison, R. D., Northup, L. L. and Mickelson, S. (2008). Introduction to Engineering Problem Solving, 5th ed, New York: McGraw-Hill.
- Floyd, T. L (2006). Digital Fundamental, 9th ed, New Jersey: Prentice Hall.
- Harold, T. (2011). Practical Arduino Engineering, Paul Manning ed, (SBN-13: 978-1-4302-3886-7).
- Jack, J, Purdum. (2015). Beginning C for Arduino: learn C programming for the Arduino, 2nd ed, New York: (ISBN 9781484209400).
- John, B. (2013). Arduino Workshop, William Pollock (ISBN-13: 978-1-59327-448-1).
- Karvinen, T. and Karvinen, K. (2014). Getting Started with Sensors: Measure the World with Electronics, Arduino, and Raspberry Pi, Maker Media, Inc.
- Simon, M. (2010). 30 Arduino Projects for the Evil Genius, New York: McGraw Hill.

PREPARATION AND CHARACTERIZATION OF KAOLINITE CLAY FOR PRODUCTION OF NATURAL POZZOLAN

Zin Mar Aung¹, Mar Mar Swe²

Abstract

Kaolinite clay has been modified with thermal treatment for application as pozzolanic material in cement. The thermal analysis of kaolinite has been characterized by using Thermogravimetric/Differential Thermal Analysis (TG/DTA). In the result of TG-DTA, the endothermic peak (dehydroxylation temperature) has been observed at 542.95°C. Kaolinite clay has been heat-treated at three different temperatures; 600 °C, 700 °C, and 800 °C for two hours duration each. The phase analysis of kaolinite samples has been analysed by using X-ray Diffraction technique (XRD). The pozzolanic activity of metakaolinite samples has been revealed by strength activity index (SAI). Finally, the elemental content of the resultant metakaolinite sample has been analysed by Energy Dispersive X-ray Fluorescence (EDXRF). The XRD result has revealed that the original crystalline microstructure of kaolinite has transformed into an amorphous one after thermal treatment. According to EDXRF analysis, it has been found that kaolinite clay is suitable to be used as cement replacement. Based on the XRD and SAI test results obtained, it is revealed that metakaolinite produced from the treated temperature at 700 °C for 2 hours was adopted as pozzolanic material for natural pozzolan production.

Keywords: Kaolinite, Pozzolanic Material, TG/DTA, XRD, SAI, EDXRF.

Introduction

Ordinary Portland Cement (OPC) production releases massive CO₂ gases and generates SO₃ and NO_x gases, which caused the greenhouse effect and incurred serious environmental impacts. On the other hand, large amounts of energy and virgin materials were consumed in cement production. To reduce environmental damage and exploitation of natural resources, the cement industry is actively looking for solutions. Hence, several research activities are directed towards partial or full substitution of Portland cement with the pozzolanic binder in some applications.

In recent years, the use of calcined clays as a pozzolanic material for mortar and concrete has received considerable attention. One of such materials is metakaolinite (MK), which is obtained by thermal treatment of kaolinite clays in the range of 600-800 °C and mixed with lime or cement, MK acts as a highly reactive pozzolana. The production of calcined clay reduces the amount of energy used and CO₂ emissions because the activation temperatures of clay are lower than that of clinker and the decomposition of clays emits water vapor rather than CO₂.

Based on these backgrounds, an attempt has been made to utilize the kaolinite clay as construction materials to partially replace the use of cement in making concrete as pozzolanic material. Clay which is suitable to be used as a Pozzolanic material is very widespread and is readily available in almost all regions of the world. According to m geological surveys, kaolinite clay has been found in many areas of Myanmar. Kaolinite clay used in this study has been collected from Taungni Taung in Kyaukpadaung Township, Mandalay Division.

This research focuses on the effect of treated temperature of kaolinite on its microstructure, and the compressive strength of clay-based composite because the clay needs heat treatment before using as cement replacement material. Three tests were carried out to establish the pozzolanicity of kaolinite. The TG/DTA analysis highlights the temperature at which the MK formation phase occurred. This does not indicate the exact treated temperature at which the MK with the excellent pozzolans is produced. The first two tests (XRD and SAI) help to identify the exact treated

¹ PhD candidate, Lecturer, Department of Physics, University of Magway

² Dr, Lecturer, Department of Physics, University of Yangon

temperature. The third test is the chemical analysis of the MK. While the first two tests particularly seek to determine the exact treated temperature that produces highly reactive pozzolana, the third test was carried out on samples eventually prepared under these conditions. The results of SAI and chemical analysis tests are compared with the ASTM (American Society for Testing Material) standard for calcined natural pozzolan since this is an internationally accepted standard.

Materials and Methods

Sample preparation of metakaolinite fine powder

Kaolinite clay was collected from Taungni Taung in Kyaukpadaung Township, Mandalay Division. The raw kaolinite was dried under the sun and ground into a fine powder using pestle and mortar. The kaolinite powder was then sieved with a 200 mesh to obtain a fraction with a particle size of fewer than 74 μm . The kaolinite sample was analysed by Thermogravimetric Differential Thermal Analysis (TG/DTA) before thermal treatment.

The fine kaolinite powder was treated at different temperatures of 600 $^{\circ}\text{C}$, 700 $^{\circ}\text{C}$, and 800 $^{\circ}\text{C}$ for two hours each in a laboratory furnace. After treatment, metakaolinite obtained from treatment was allowed to cool down gradually in the furnace to the ambient temperature. Again the treated powder was ground and sieved with a 325 mesh to obtain a fraction with particle size of fewer than 45 μm . Finally, the obtained metakaolinite fine powder was characterized by X-ray Diffraction (XRD), and Energy Dispersive X-ray Fluorescence (EDXRF). Figure 1 shows the flow chart for the preparation of pozzolanic material.

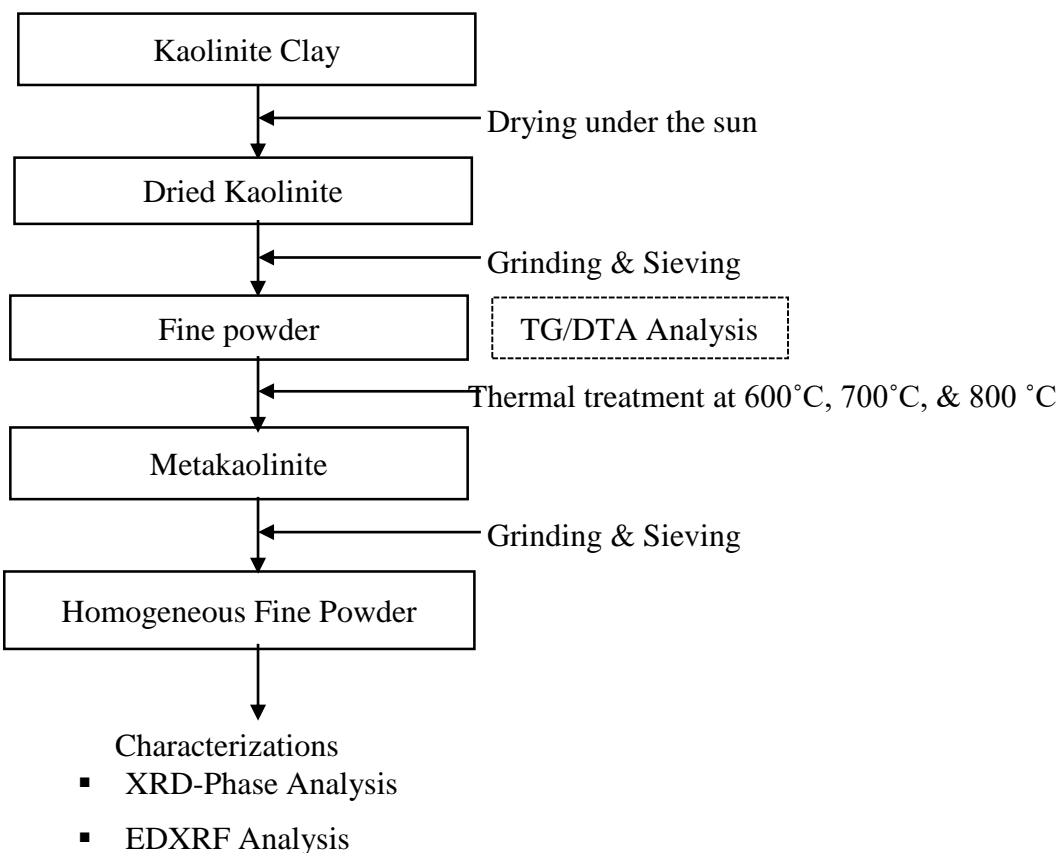


Figure 1 Flow chart for the preparation of pozzolanic material

Cement mortar processing for SAI test

The SAI values of metakaolinite samples with various treated temperatures (600, 700, and 800 °C) were also determined to support the result of XRD. Figure 2 shows the flow chart for the preparation of mortar cubes. The cement mortars were prepared in line with the requirements of ASTM C109/C109M-08. Table 1 shows the mixed proportions of various ingredients of the mortar specimen. The cement mortar cubes were prepared using a cement: sand ratio of 1:2.75 and a water: binder ratio of 0.48. These served as control cubes. Thereafter, metakaolinite obtained from each treated temperature was combined with cement at 20% cement replacement. This was used with sand in the same ratio to produce its respective mortar test cubes.

Mechanical mixing was used to combine all of the weighed ingredients. After mixing deionized water and cementitious material for 30 s, the sand was gradually added into the solution during the first 30 s of mixing. All of the materials were combined at high speed for the following 30 s, after which the mixer was turned off for 90 s: the material residues on the bowl walls were removed during the first 30 s, and then the mixture was allowed to stand. The mixer was restarted at high speed for an additional 60 s after the pause.

Then the cement mixture was gradually placed into the iron mold, which was made up of 50x50x50 mm cube specimens, at the end of the mixing period. The hand tamping method was used to finish the mortar consolidation in the mold. All of the cube compartments had a layer of mortar around 25 mm thick. In four rounds, the mortar in each cube compartment was tamped 32 times in roughly 10 s each round being at right angles to the other and consisting of eight contiguous strokes. The tamping pressure was exactly right to insure that the molds were evenly filled. After the first layer was tamped in all of the cube compartments, the remaining mortar was poured and tamped as specified for the first layer. After tamping, the mortar was brought to a flat surface and flushed with the top of the mold by sawing the straight edge of the trowel along the length of the mold.

The molds were then placed in a moist environment for 24 h. The specimens were then taken from the mold and cured for 28 days in saturated lime water. The cured specimens were then allowed to dry in the air for 12 h before being tested for their strengths. Finally, the compressive strength values of the mortar cubes were determined using the Compressive Testing Machine. The sides of the cubes were loaded uniformly with a compressive strength machine until fracture appeared. The maximum load in kN at which fracture occurred was recorded and used to calculate the compressive strength as

$$R_c = \frac{1000F_c}{A_r}$$

Where

R_c = compressive strength, MPa

F_c = maximum load at which fracture occurs, kN

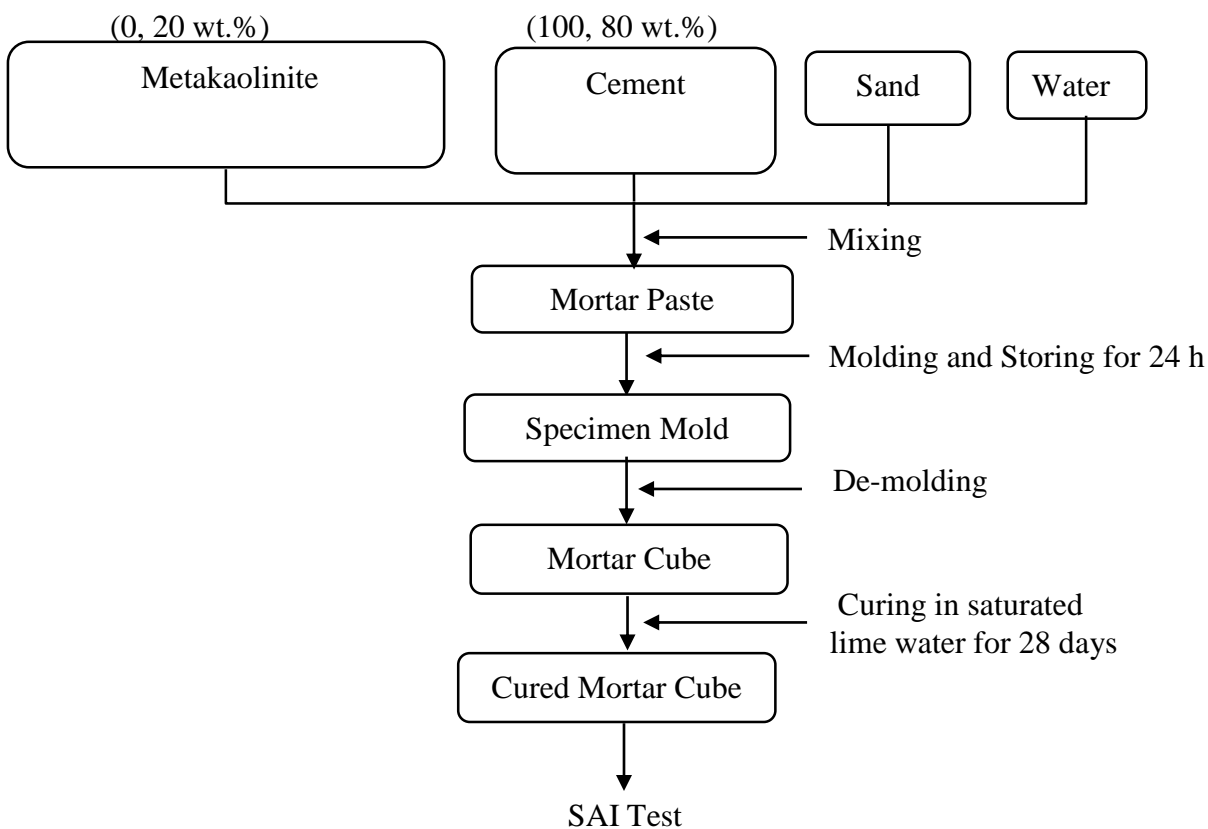
A_r = area of a face of the cube, mm²

For each crushing test, 2 cubes were used and the average was taken for the compressive strength.

The pozzolanic activity of the metakaolinite samples with various treated temperatures was revealed by strength activity index (SAI) test. The average strength for each temperature was compared with that for control to give the SAI. The metakaolinite sample with the highest SAI value is assessed as natural pozzolan with the highest pozzolanicity. This result should agree with the result of XRD. Besides, the SAI for each temperature should satisfy a minimum of 75% as required for natural pozzolans.

Table 1 Mixed proportions of various ingredients of the mortar specimen

No	Materials	For Compressive Strength test	Remarks
1	Specimen	50 mm Cube	Materials required for 6 specimens
2	Cementitious materials (Cement + Metakaolinite)	500 gm	
3	Sand	1375 gm	
4	Water	242 ml	

**Figure 2** Flow chart for the preparation of mortar cubes

Results and Discussion

TG-DTA Analysis

Thermal behavior of starting kaolinite clay was analysed using TG-DTA and shown in Figure 3. In the TGA curve, the material has a total mass loss of 13 % at 600 °C. The mass loss was 2.11 % in the temperature range 37. 45-480 °C, corresponded with the release of free or absorbed water from kaolinite surface. The second significant mass loss in the TGA curve was 10.86% in the temperature range 480-590°C which was associated with dehydroxylation of kaolinite and formation of disordered material metakaolinite. The observed endothermic peak with a maximum at 542.95 °C may be attributed to the dehydroxylation process.

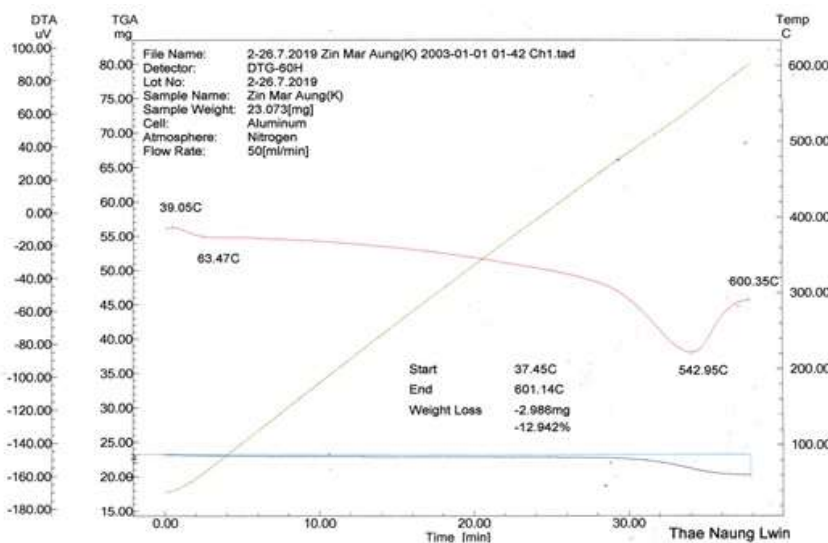


Figure 3 TG/DTA curve of Kaolinite

XRD Analysis

The XRD patterns of raw and treated samples with thermal treatment at 600 °C, 700 °C, and 800 °C are shown in Figure 4. It is seen that the mineral constituent of the starting clay is kaolinite. Based on XRD result obtained, it has been observed that the original crystalline microstructure of the kaolinite has transformed into an amorphous one after thermal treatment. Importantly, much broader diffused peaks with maximum intensity at $2\theta = 20.910$ are observed at treated temperature 700 °C. The amorphous structure is a characteristic of the excellent pozzolanic activity of pozzolan material. Therefore, the treated sample at 700 °C may have potential application for pozzolan production.

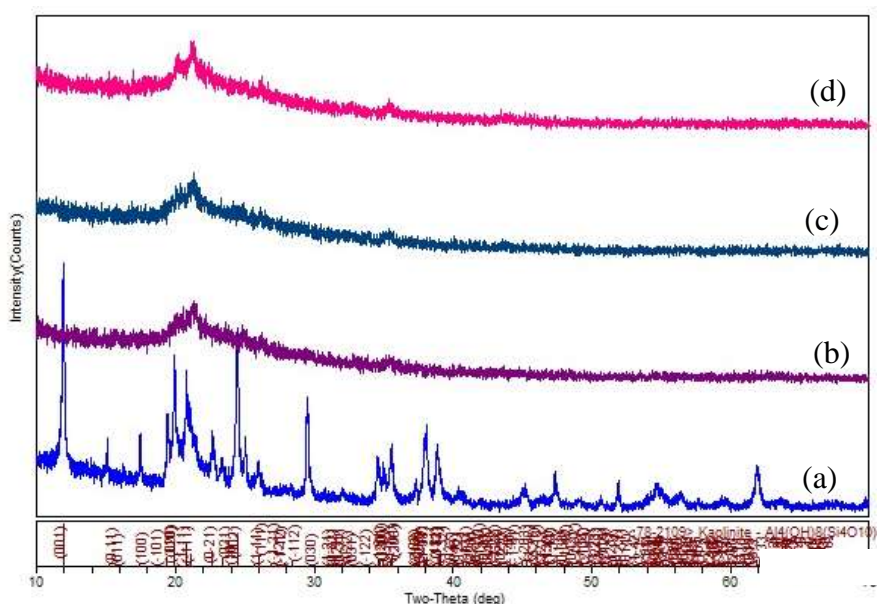


Figure 4 XRD of kaolinite samples: (a) raw kaolinite; (b) thermally treated at 600 °C; (c) thermally treated at 700 °C; (d) thermally treated at 800 °C

SAI Test

The SAI test was used to support the result of the XRD test. The strength index provides the pozzolanic activity of MK samples with various treated temperatures (600, 700, and 800 °C). The photograph of the Ministry of Construction's certificate was shown in Figure 5. Table 2 shows the compressive strength and strength activity index of specimens and the effect of treated temperature on the SAI of MK samples was also compared in Figure 6. According to the ASTM specification, the SAI for each temperature should satisfy a minimum of 75% as required for natural pozzolans. The results obtained show that all of the MK samples with various treated temperatures are assessed as pozzolans. The highest amount of SAI value was found in MK sample with the treated temperature at 700 °C. The results obtained from the SAI test are in good agreement with XRD results.

MINISTRY OF CONSTRUCTION DEPARTMENT OF HIGHWAYS MINI - LABORATORY MAGWAY REGION COMPRESSIVE STRENGTH TEST RESULTS												(1)
Register No	Date (Moulded)	Date (Tested)	Age	Weight (Kg)	Specimen Size			Load at Failure (KN)	Compressive Strength		Average Compressive Strength (Mpa)	Remark
					Length (mm)	Breadth (mm)	Height (mm)		(MPa)	(Psi)		
ပုဂ္ဂနယ်အတွက် ပစ္စည်းမှု လောင်းလာ ပစ္စည်းမှု ပုဂ္ဂနယ်												
1	10.3.2020	7.4.2020	28	0.29	50.556	50.560	51.230	126.76	49.59	7191	51.72	7498.82
2	10.3.2020	7.4.2020	28	0.30	51.496	50.963	51.563	141.30	53.84	7807		
3	10.3.2020	7.4.2020	28	0.28	51.090	50.730	50.810	129.54	49.98	7247	50.19	7276.96
4	10.3.2020	7.4.2020	28	0.28	50.890	50.230	51.790	128.81	50.39	7307		
5	10.3.2020	7.4.2020	28	0.28	50.910	50.590	50.276	149.10	57.89	8394		
6	10.3.2020	7.4.2020	28	0.28	51.410	50.630	50.467	159.72	61.36	8898	59.63	8645.87
7	10.3.2020	7.4.2020	28	0.28	51.060	50.890	50.256	127.38	49.02	7108	49.15	7126.61
8	10.3.2020	7.4.2020	28	0.28	51.493	50.280	50.576	127.58	49.28	7145		
Remark: Tested on received basis.												

Figure 5 The photograph of the Ministry of Construction's certificate

Table 2 Compressive strength and strength activity index of specimens

Sample Name	Compressive Strength (MPa)	SAI (%)
OPC	51.72	-
MK-600	50.19	97.04
MK-700	59.63	115.29
MK-800	49.15	95.03

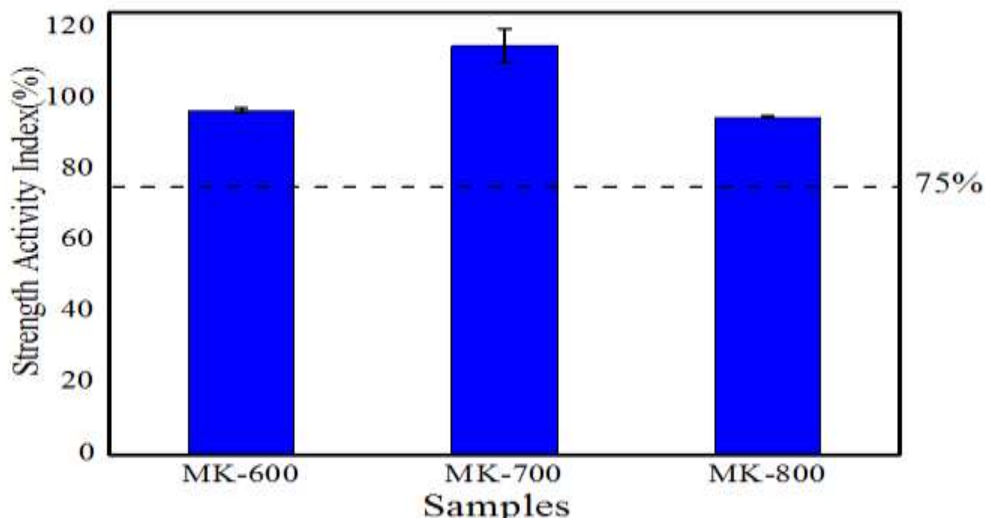


Figure 6 Effect of treated temperature on strength activity index of metakaolinite samples
(dotted line: reference for minimum requirement of natural pozzolans)

EDXRF Analysis

The chemical composition of MK at treated temperature 700 °C is shown in Table 3. The result was compared with the requirements for classifying a material as a pozzolan as established by ASTM. The result of the chemical analysis showed that the resultant MK sample passed the ASTM requirements with the constituents of SiO₂, Al₂O₃, and Fe₂O₃ totaling 98.581%. This is more than the required 70% minimum. Another condition was seen to be satisfied as well signifying the suitability of the heat-treated clay as a pozzolan. Therefore, the EDXRF analysis has confirmed that kaolinite from Taungni Taung, Kyaukpadaung Township is suitable to be used as pozzolanic material.

Table 3 The concentration of detectable oxides in metakaolinite sample

Oxides	Metakaolinite (%)	ASTM C618-05 requirement for pozzolans
SiO ₂	58.329	SiO ₂ +Al ₂ O ₃ +Fe ₂ O ₃ ≥70%
Al ₂ O ₃	40.048	
Fe ₂ O ₃	0.204	
SO ₃	0.762	4% max
CaO	0.106	
Others	0.549	

Conclusion

This study investigates the effect of treated temperature on kaolinite clay for natural pozzolan production. In the result of TG/DTA, the endothermic peak (dehydroxylation temperature) has been observed at 542.95 °C. Moreover, the XRD results clearly showed that the originally crystalline structure of kaolinite has transformed into an amorphous one after thermal treatment. Therefore, the heating time duration and treated temperature range play an important role in this study. EDXRF result has proved that metakaolinite is suitable for pozzolanic material due to its high content of silica and alumina. Based on the XRD and SAI test results obtained, it is concluded that metakaolinite produced from the treated temperature at 700 °C for two hours may have the potential to be applied as pozzolanic material for natural pozzolan production.

Acknowledgements

I would like to express appreciation to Dr Khin Maung Oo, Rector, University of Magway, for his kind permission and encouragements to carry out this work. I would like to express my profound thanks to Professor Dr Sandar Maung, Head of Department of Physics, University of Magway, for her kind permission and encouragements to carry out this work.

References

- Aliyu,U., Muhammad, B., and Nurabala, (2018), “Effect of Amorphous Silica Ash Used as a Partial Replacement for Cement on the Compressive and Flexural Strengths Cement Mortar.” Morozov, IOP Conf Series: Earth and Environmental Science 140, 012124.
- Gbenga,M.A., Olasunkanm ,A., and Adekitan, (2016), “Characterization of Ajedo Kaolinite clay for production of natural pozzolan.” World academy of science, engineering and technology, International journal of civil and environmental engineering, vol.10, No.9
- Ghassan,K.A., Mouin,A., and Panagiotis,G.A., (2013), “Natural Pozzolan as a Partial Substitute for Cement In Concrete.” The Open Construction and Building Technology, 7, 33-42
- Kaleeswari,G., Hanalakshmi,G., and Manikandan,N., March (2016), “Clay as a Partial Replacement of Cementitious Material in Cement.” International Journal of Advanced Research in Biology Engineering Science and Technology (IJARBEST) Vol.2, Issue3.
- Yang,H., and Jie, D., (2018), “Preliminary Investigation of Pozzolanic Properties of Calcined Waste Kaolin.” ISSN 1392-1320 Material Science Vol.24, No.2.

PYHSICOCHMICAL CHARACTERISTICS OF ACTIVATED CARBON FROM RICE HUSK BIOCHAR

Zin Min Tun¹, Zin Min Myat², Kyaw Zay Ya², Yin Maung Maung², Naw Htoo Lar Phaw¹

Abstract

Rice husk is an agricultural waste abundantly available in rice-producing countries. In this work, biochar is a solid material that is produced by heat decomposition of rice husk biomass by well-known pyrolysis method. Activated carbon was prepared by the conventional carbonization and KOH activation on a laboratory scale. The sample was calcined at 200 °C, 300 °C and 400 °C for 2 h to obtain biochar. The carbon structure of rice husk biochar activated carbon was examined by XRD. The chemical properties of the rice husk biochar activated carbon were confirmed by FTIR. The morphology of rice husk biochar activated carbon was determined by SEM. From FTIR analysis, three functional groups were found. According to SEM results, the average pore sizes of the samples were found to be about 6.15 µm at 200 °C, 5.80 µm at 300 °C and 4.13 µm at 400 °C respectively.

Keywords- Rice Husk biochar, Activated carbon, XRD, FTIR, SEM

Introduction

Biochar is charcoal used as a soil amendment for both carbon sequestration and soil health benefits. Biochar is a stable solid, rich in carbon, and can endure in soil for thousands of years [Lean, Geoffrey, 2011]. Biochar is produced by thermal decomposition of biomass under oxygen-limited condition (pyrolysis), and it has received attention in soil remediation and waste disposal in recent years. The characteristics of biochar are influenced mainly by the preparation temperature of biomass. Higher pyrolysis temperature often results in the increased surface area and carbonized fraction of biochar leading to high absorption capability for pollutants. Biochars derived from various source materials show different properties of surface area porosity and the amount of functional groups which are important concerning on the effect of biochar [Jingchun Tang , et al, 2013]. Biochar has been proved to be effective in improving soil properties and increasing crop biomass. It has also been suggested that it can even enhance crop resistance to disease. Biochar has recently been used to remediate soil with both heavy metal and organic pollutant [Jingchun Tang , et al, 2013, Luke Beesley, et al, 2011]. In addition to its potential for carbon sequestration and decrease greenhouse gas emission from agriculture, biochar is reported to have numerous benefits as a soil amendment, increased plant growth yield, improved water quality, reduced leaching of nutrients, reduced soil acidity, increased water retention and reduced irrigation and fertilizer requirements [Wen Wang, et al, 2013]. Bio-char is a stable solid, rich in carbon and can endure in soil for thousands of years. Biochar carbon species vary in complexity from graphite like carbon to high molecular weight aromatic rings, which are known to persist in soil for thousands to millions of years [Mohamad Azri Sukiran, et al, 2011].

Activated carbon, also called activated charcoal, is a form of carbon processed to have small, low-volume pores that increase the surface area [Bulletin of the American Physical Society, 2013] available for adsorption or chemical reactions [CPL Caron Link, 2008]. Activated is sometimes substituted with active. Due to its high degree of microporosity, one gram of activated carbon has a surface area in excess of 3,000 m² (32,000 sq ft) [Dillon, et al, 1989] as determined by gas adsorption [P. J. Paul.]. An activation level sufficient for useful application may be obtained

¹ Lecturer and Professor (Head), Department of Physics, Pathein University

² Lecturers and Professor, Department of Physics, University of Yangon

solely from high surface area. Further chemical treatment often enhances adsorption properties. Activated carbon is usually derived from charcoal and is sometimes used as biochar.

Materials and Method

The rice husks (RH) were cleaned with deionized water to remove the dust and impurities. These RHs were dried in sun for one day and then hand crushed to smaller pieces. Then, the smaller pieces of these RHs were dried at room temperature about one week. The weight of rice husks were measured with digital balance. And then, these raw RHs were carbonized in the muffle furnace at three different temperatures, which were 200 °C, 300 °C and 400 °C for 2 h respectively. After carbonization, these rice husk biochars were mixed with deionized water and KOH in a stainless steel beaker with weight ratio of KOH/RH biochar equal to 1:2. Water was evaporated at 120 °C for 6 h, and these dried mixtures were heated in the muffle furnace at 800 °C for 1 h. The products were cooled to room temperature and washed with HCl and deionized water until the pH of the washing solution reached 6-7. Finally, the activate carbon obtained from rice husk biochars. The carbon structure confirmation of rice husk activated carbon (RHAC) was confirmed by X-ray Diffractometry (XRD). The morphology and microporous structures of RHAC were determined by Scanning Electron Microscopy (SEM, JEOL 6000) and the chemical properties of biochars were examined by Fourier Transform Infrared Spectroscopy (FTIR, Thermo Scientific). The block diagram for experimental procedure of rice husk biochars was shown in Figure 1. Table 1 showed the weight loss and weight loss % of rice husk biochars.

Table 1 Weight loss and weight loss % of rice husk biochar

Temperature	W ₁	W ₂	Weight loss, W = W ₁ – W ₂	Weight loss %
200 °C	5.86 g	5.02 g	0.84 g	14.33 %
300 °C	5.89 g	3.36 g	2.53 g	42.95 %
400 °C	6.00 g	3.14 g	2.86 g	47.67 %

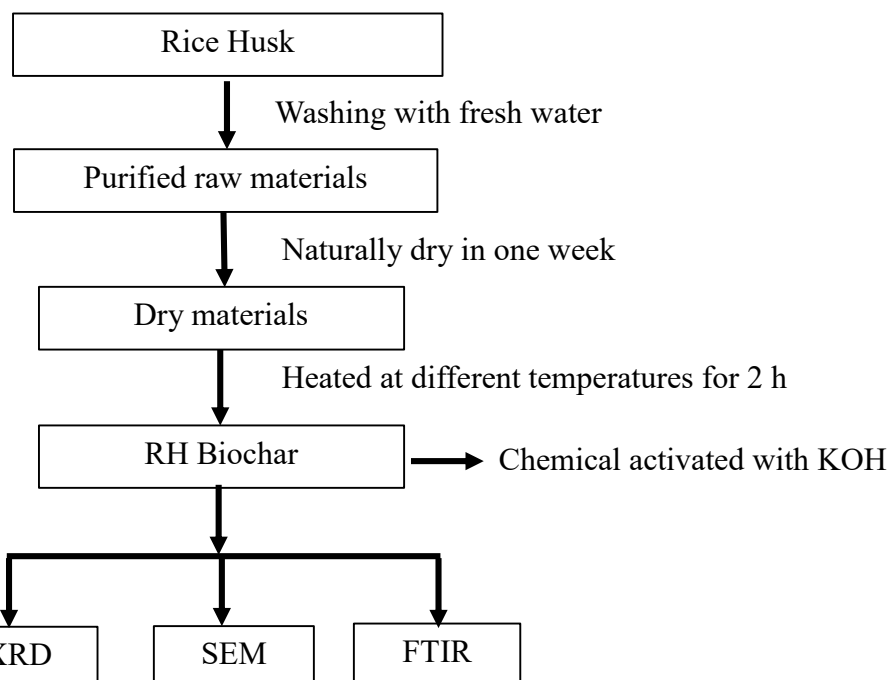


Figure 1 The block diagram for experimental procedure of coconut and peanut shell biochars

Results and Discussion

FTIR Analysis of Rice Husk Biochars

FTIR spectroscopy was applied to measure the chemical properties and absorption of energy from the range of 4000 cm^{-1} - 500 cm^{-1} by studied samples. Spectral registration was examined with use of solid-state samples which is made of a complex organic material. The FTIR analysis demonstrated the functional groups presented on rice husk biochar at different process temperatures. The functional groups of rice husk biochar have found to be O-H stretching vibration, C=O stretching vibration and C-O stretching vibration respectively. The spectrum of these samples showed some characteristic bands related to physical and chemical changes. As shown in Figure 2(a-c), the infrared spectra of these biochar types are comparable but there are some changes in the functional groups. The water O-H stretch can occur in the rice husk biochar for about 3324.85 cm^{-1} , 3240.00 cm^{-1} and 3236.43 cm^{-1} at three different temperatures. The absorption bands, between 3000 cm^{-1} - 3300 cm^{-1} indicated the presence of strong carboxylic acid O-H stretch. As observed peak of RH biochar, C=O stretching is associated with peak values 1599.15 cm^{-1} , 1601.15 cm^{-1} and 1637.85 cm^{-1} respectively. The presence of the band located at 1028.45 cm^{-1} - 1073.68 cm^{-1} showed the strong C-O stretching modes. According to FTIR analysis, all of the absorption bands are due to hydroxyl group in cellulose, carbonyl groups of acetyl ester in hemicellulose, and carbonyl aldehyde in lignin. Table 2 showed the FTIR analysis data of rice husk biochars at different temperatures.

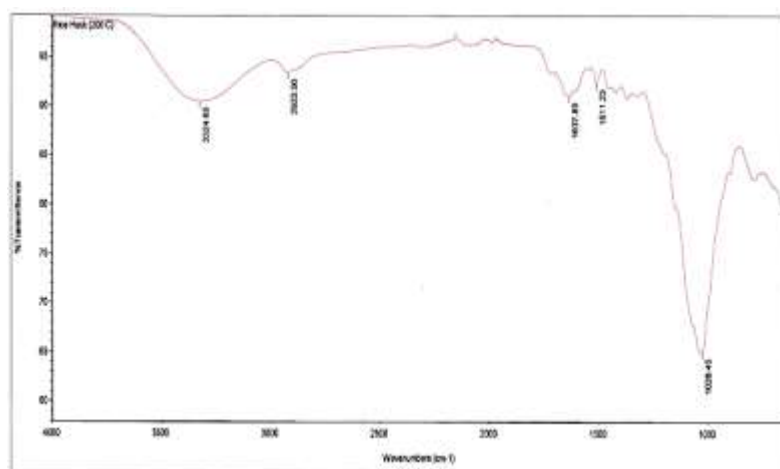


Figure 2(a) FTIR spectrum of rice husk biochar at $200\text{ }^{\circ}\text{C}$

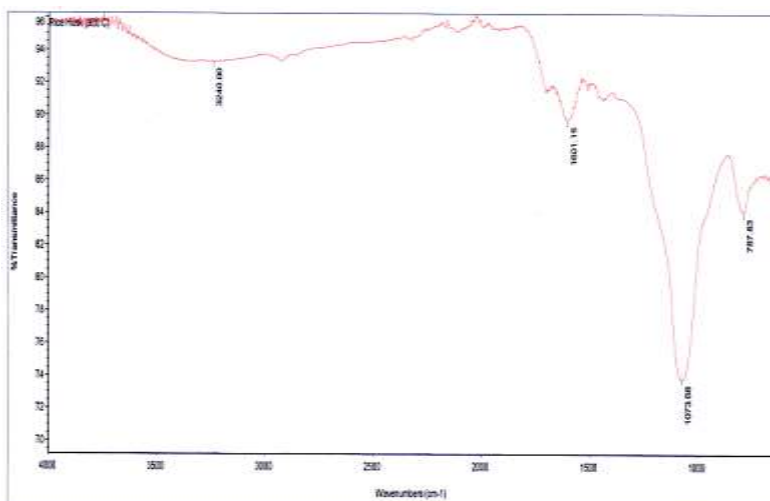


Figure 2(b) FTIR spectrum of rice husk biochar at $300\text{ }^{\circ}\text{C}$

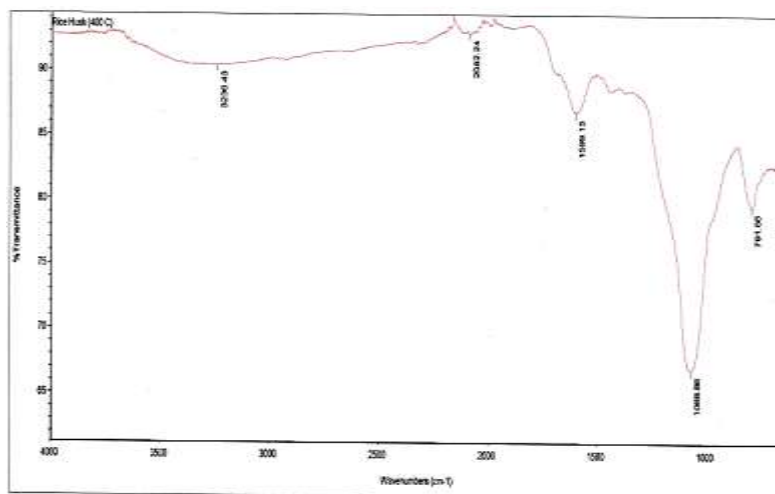


Figure 2 (c) FTIR spectrum of rice husk biochar at 400 °C

Table 2 FTIR analysis data of rice husk biochars at different temperature

Temperature (°C)	Wave numbers (cm ⁻¹)	Functional group
200	1637.85	C=O stretching
	2922.00	C-H stretching
	3324.85	O-H stretching
300	1073.66	C-O stretching
	1601.15	C-O stretching
	3240.00	O-H stretching
400	1599.15	C=O stretching
	2082.24	C-H stretching
	3236.43	O-H stretching

SEM Analysis of Rice Husk Biochars

SEM is one of the most versatile instruments available for the examination and analysis of the microstructure characteristics of a solid. The most important reason for using SEM is high resolution that can be obtained when bulk sample are examined. SEM micrographs for external morphology of rice husk biochar at temperatures 200 °C, 300 °C and 400 °C for 2 h were shown in Figure 3(a-c). According to Figure 3(a-c), the clear porous nature had observed the rice husk biochar at 200 °C, 300 °C and 400 °C. After increasing temperature, it was found that the rice husk biochar had more clearer porous nature and uniform with microporous structure. From SEM analysis as shown in Figure 3(a-c), it can be observed that the microstructure of rice husk biochar samples by varying the pore sizes with different temperatures. At 200 °C, the RH biochar had uniform porous nature and had large surface area. At 300 °C, the pores of biochar were non-uniform and not clear. At 400 °C, the pores were more uniformly microporous structure. For RH biochar, the average pore sizes of the samples were found to be about 6.15 µm at 200 °C, 5.80 µm at 300 °C and 4.13 µm at 400 °C respectively.

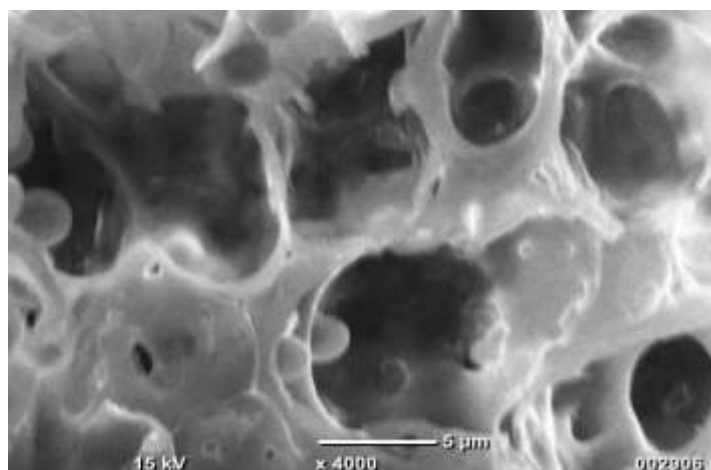


Figure 3(a): SEM micrograph of rice husk biochar at 200°C, (6.15 μm)

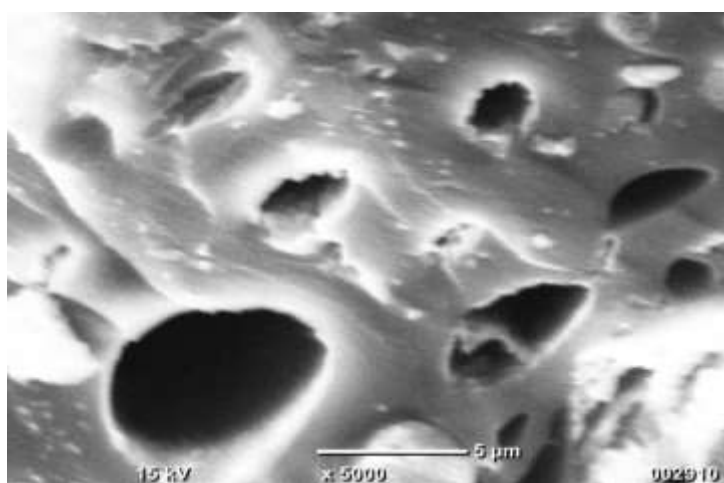


Figure 3(b): SEM micrograph of rice husk biochar at 300°C, (5.80 μm)

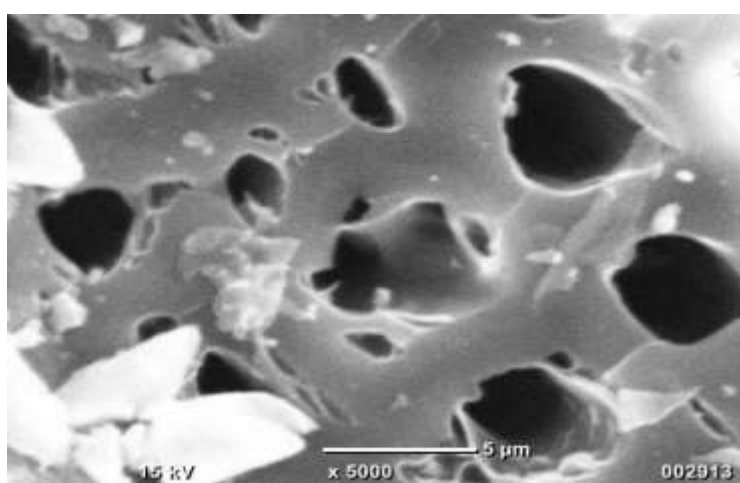


Figure 3 (c) SEM micrograph of rice husk biochar at 400°C, (4.13 μm)

X-ray diffraction analysis

X-ray diffraction is to determine the structure properties of rice husk biochar using monochromatic CuK α radiation ($\lambda = 1.54056 \text{ \AA}$) operated at 40 kV (tube voltage) and 40 mA (tube current). Analysis of rice husk biochar activated carbon at different temperature values (200 °C, 300 °C and 400 °C) for 2 h were shown in Figure 4(a-c).

From XRD results, these biochar exhibit the dominant diffraction peak located at around $2\theta = 20^\circ - 30^\circ$ that revealed the presence of amorphous structure which was disorderly stacked up by carbon rings. The XRD patterns of the rice husk biochar activated carbon showed the asymmetric (111) peak and (110) peaks maxima which were characteristic of graphite and carbon structures.

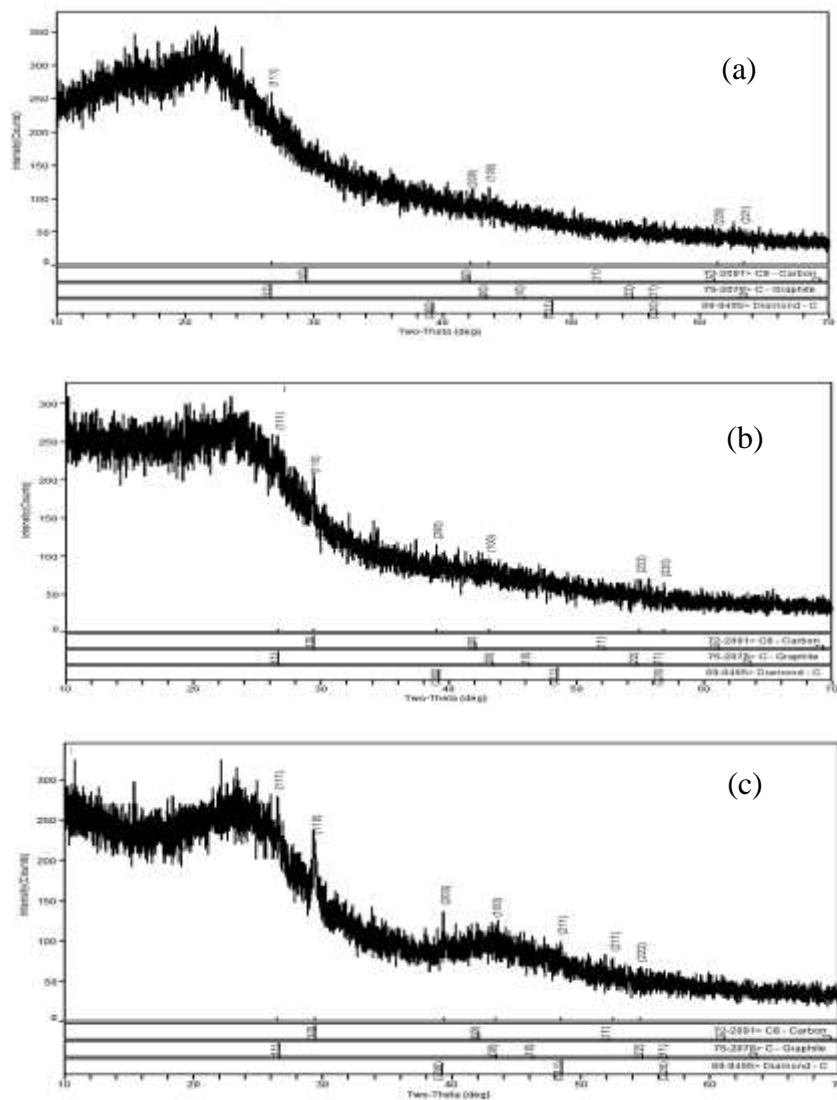


Figure 4(a-c) XRD patterns of Rice husk biochars activated carbon at different temperatures

Conclusions

In this research work, it was found that the weight loss % of RH biochar at different temperatures were 14.33%, 42.95% and 47.67% respectively. From the result, it can be observed that the weight and weight loss % of RH biochars were dependent on the calcinating temperature. The weight loss and weight loss % of RH biochars decreased with increasing calcinating temperatures.

For the results of FTIR analysis, all of the absorption bands are due to hydroxyl group in cellulose, carbonyl groups of acetyl ester in hemicellulose, and carbonyl aldehyde in lignin.

From SEM analysis, it can be observed that the porous structure of rice husk biochar samples by varying the pore sizes with different temperatures. For RH biochars, the average pore

sizes of the samples were found to be about 6.15 μm at 200 $^{\circ}\text{C}$, 5.80 μm at 300 $^{\circ}\text{C}$ and 4.13 μm at 400 $^{\circ}\text{C}$ respectively.

As the results of XRD analysis, there are several diffracted peaks were observed. They were not perfectly identified. It could be say that the RHAC samples were found to be amorphous structure with little crystalline. XRD patterns of RHAC were quite acceptable. Almost all the reflections were found to be consistent with carbon.

According to these analyzed results, rice husk was calicnated at 200 $^{\circ}\text{C}$, 300 $^{\circ}\text{C}$ and 400 $^{\circ}\text{C}$ to get the rice husk biochar, a pozzolanic material, which can be used in partial replacement of cement and soil amendment for agriculture. These rice husk activated carbon can also be used in removal of heavy metal from waste water solution for environment.

Acknowledgements

I would like to express my sincere gratitude to Professor Dr Naw Htoo Lar Phaw, Head of Department of Physics, Pathein University, for her kind permission.

I would also like to mention my gratitude to Professor Dr Yin Maung Maung, University of Yangon for his encouragement on this research.

I would like to thank all of my research colleagues for their advice and effort in this research.

References

- "Activated carbon monoliths for methane storage" (<http://meetings.aps.org/Meeting/MAR12/Session/W33.12>). Bulletin of the American Physical Society. 57 (1). 2012-03-01.
- "Adsorbed Methane Film Properties in Nanoporous Carbon Monoliths" (<http://meetings.aps.org/Meeting/MAR13/Event/186324>). Bulletin of the American Physical Society. 58 (1). 2013-03-20.
- Dillon, Edward C; Wilton, John H; Barlow, Jared C; Watson, William A (1989-05-01). "Large surface area activated charcoal and the inhibition of aspirin absorption". *Annals of Emergency Medicine*. 18 (5): 547–552.
- Jingchun Tang , Wenyng Zhu, Rai Kookana, Arata Katayama, "Characteristics of Biochar and Its Application in Remediation of Contaminated Soil", *J Biosci Bioeng*, Dec. 2013,116(6),653-9.
- Lean, Geoffrey, "Ancient skills' could reverse global warming", *The Independent*. October 2011.
- Luke Beesley, Eduardo Moreno-Jiménez et al, "A review of biochars' potential role in the remediation", *j.envpol*, 2011 Dec, 159(12), 3269-3282.
- Mohamad Azri Sukiran, Loh Soh Kheang, Nasrin Abu Bakar and Choo Yuen May, "Production and Characterization of Bio-Char from the Pyrolysis of Empty Fruit Bunches", *American Journal of Applied Sciences*, 8 (10): 984-988, 2011.
- P. J. Paul. "Value Added Products from Gasification–Activated Carbon", Bangalore: The Combustion, Gasification and Propulsion Laboratory (CGPL) at the Indian Institute of Science (IISc).
- "Properties of Activated Carbon", CPL Caron Link, accessed 2008-05-02".
- Wen Wang, Dominic C Moran, et al,"Economic Potential of Greenhouse Gas Mitigation Measures in Chinese Agriculture", *Report*, UK-China, Sustainable Agriculture Innovation Network-SAIN, July 2013.

TEMPERATURE AND SHADING DEPENDENCE OF THE POTENTIAL INDUCED DEGRADATION EFFECT OF SOLAR PANEL

Kyaw Thu¹, Yin Maung Maung², Than Than Win³

Abstract

This paper investigates on a simulation model for a PV panel to allow estimate the electrical behavior of the panel with respect changes on parameters of shade and temperature. The simulation model was implemented in Mat lab and accepted the I-V characteristic outputs as variable parameters the effects of shading and temperature of solar PV module. This model is quite and especially useful to analyze the performances of the PV modules under various operating conditions. It is simulating the parameters for the nonlinear I-V equations based on only the solar panel such as open circuit voltage, short circuit current, voltage and current at maximum power point at the standard test condition which are obtained from manufacturer's solar panel. The performance of PV panels is affected by the shading and temperature effect due to trees, passing of clouds, neighboring buildings. The aim of this research work is to use the change in electrical parameters with shading and temperature of PV solar cell and module. The simulation results show that the electrical parameter such as the open circuit voltage, short circuit, maximum power decreases as the shading and the ambient temperature increases.

Keywords: Photovoltaic Solar Module, Solar cells, Temperature, Shade, Simulation.

Introduction

Renewable energy resources are being developed important part of power generation in new centuries. In particular, solar photovoltaic PV is converted solar radiation directly to electricity; most solar power plants are being developed based on photovoltaic technology. For series-connected PV cells, although some the cells are being partially shaded, all the cells carry almost the same amount of current. While a small number of cells under shade produce less photocurrent, these cells are being also forced to carry the same current as the other fully illuminated cells. Moreover, in some cases it is difficult to avoid partial shading of solar panel due to the surrounding and environmental conditions, such as buildings, dust, bird droppings, and cloud cover throughout the day and in all seasons. It is made the study of partial shading of solar PV modules a main key issue. In recent years, the effects on partial shading on the solar PV array system performance have widely discussed [Ekpenyong, E.E, Idriss Hadj Mahammed, L. Fialho and A. Woyte]. The power reduced due to a shadowed panel has already been studied [Smita Ganesh Pachpande].

However, the power of PV modules is yielded a function of different weather conditions, including partial shaded conditions [Chia Seet Chin1] and configuration of PV array and partial shading [A. Woyte]. It is necessary to consider all these parameters to determine the performance of a PV system under the various conditions of shading. In this study, the main objective is to investigate the effects of partial shading and temperature caused by surrounding environmental conditions through the application of predefined configurations of the solar PV module system in series arrays cells. The study aims to find an equivalent electrical circuit model of the PV module when cells in the module are being connected in series in order to analyze the characteristics of the module under uniform operating conditions. All solar module parameters, including short-circuit current, open-circuit voltage, fill factor, efficiency and impact of series and parallel resistances are being changed due to changing the light intensity and temperature [Tuque and Heeds, 2003]. Therefore, it is necessary to study the effect of the light intensity and temperature on the output

¹ Lecturer, Department of Physics, Monywa University

² Dr, Professor, Department of Physics, University of Yangon

³ Dr, Professor, Department of Physics, Pinlon University

performance of the solar module. The electricity flows through an electrical circuit by changing the speed at which the electrons travel because of temperature effect. This is caused due to an increase in resistance of the circuit that results from an increase in temperature. In this work, the main point aims to investigate a detailed experimental of module PV parameters with light intensity and temperature are being studied.

Materials and Methods

Methods

In field testing, it is difficult to investigate the effects on partial shading and temperature because there are many time and weather conditions. Also, it is being challenged to uniformly measure the different level of intensity of shading and temperature under a number of different configurations of a shaded and temperature of PV module system. Alternatively, it is easily to carry out a simulation study with the help of a computer model. In this study, generalized MATLAB/Simulink models have developed and are capable of simulating any number of cells connected in series for any type of temperature and shading patterns.

Mathematical Modeling of a PV Cell and Module

A PV module consists of a number of solar cells, which convert light into electricity. The solar cell mainly depends on a diode, a photocurrent (I_{ph}), an internal resistor (R_s), and a shunt resistor (R_{sh}). Fig.1 shows a photovoltaic equivalent circuit of a single cell.

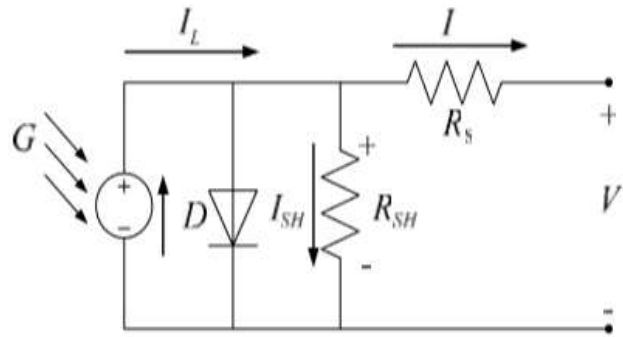


Figure1 Photovoltaic equivalent circuit of a solar cell

When a PV module collects irradiance energy from the sun by individual solar cells, it is charged with electric energy. The output of electric energy depends on intensity of irradiance (W/m^2), temperature (K), material, design of the PV module, and the photocurrent (I_{ph}) in series with the internal resistor (R_s) and parallel with a shunt resistor (R_{sh}). The basic equation of the current at the terminal of the solar cell and the maximum power output are formulated. The photovoltaic panel can be mathematically modelled as:

Basic mathematical equation of the output current (I) in Eq. (1)

$$I = I_{ph} - I_d \quad (1)$$

I_{ph} is the photocurrent, I_d is the diode current, which is related to the saturation current and is described by Eq. (2):

$$I_d = I_0 \left[\exp\left(\frac{V}{A.Ns.V_T.a}\right) - 1 \right] \quad (2)$$

where V is the voltage applied to the diode, then V_T can be expressed by the equation of $V_T = k \cdot \frac{T}{q}$. A is the diode ideality ranged between 1 and 2; N_s is the number of cells in a series for the output current; a is the diode emission coefficient. The photocurrent, I_{ph} , is generated from the incident solar irradiation and affected by the temperature (T). It can be expressed by Eq. (3):

$$I_{ph} = \frac{G}{G_{STC}} (I_{ph,STC} + K_I (T - T_{STC})) \quad (3)$$

Where $G_{STC} \left(\frac{W}{m^2} \right)$ is the irradiation at STC; $I_{ph,STC}$ is the current produced at STC; K_I is the temperature coefficient of the short-circuit current. The diode reverse leakage current, I_o , is influenced by the actual temperature and can be expressed in Eq. (4):

$$I_o = \frac{I_{SC,STC} + K_I (T - T_{STC})}{\exp(V_{OC,STC} + K_V K_I (T - T_{STC})) - 1} \quad (4)$$

where $I_{SC,STC}$ and $V_{OC,STC}$ are the short-circuit current and open-circuit voltage at STC; K_V is the temperature coefficient of the open-circuit voltage (V/Kelvin). In the PV module, the short-circuit current (I_{sc}) can be described when V_o across the PV module is equal to zero and I_{sc} , as expressed in Eq. (5):

$$I_{sc} = I_{PV} - I_d \left[\left(\exp \frac{I_{sc} R_s}{V_T \cdot a} \right) - 1 \right] - \frac{I_{sc} R_s}{R_{sh}} \quad (5)$$

Maximum power point of a PV module in Eq. (6):

$$I_{mp} = I_d \left[\exp \frac{V_{mp} + I_{mp} R_s}{V_T \cdot a} - 1 \right] - \frac{V_{mp} + I_{mp} R_s}{R_{sh}} \quad (6)$$

The maximum power, P_m , is calculated by $V_{mp} \times I_{mp}$ and described in Eq. (7):

$$P_m = V_{mp} \left[I_{PV} - I_d \left(\exp \frac{V_{mp} + I_{mp} R_s}{V_T \cdot a} - 1 \right) - \frac{V_{mp} + I_{mp} R_s}{R_{sh}} \right] \quad (7)$$

where shunt resistance of the PV module is expressed in Eq. (8):

$$R_{sh} = \frac{V_{mp} + I_{mp} R_s}{\left(V_{mp} I_{PV} + V_{mp} I - V_{mp} I \cdot \exp \left[\frac{q(V_{mp} + I_{mp} R_s)}{N_s K T_a} \right] - P_m \right)} \quad (8)$$

The I-V and P-V characteristics of the PV module operating at various temperatures and intensity of irradiance are determined.

Solar PV Cells and Module System

A solar PV panel module consists of a number of interconnected solar cells encapsulated into a stable module, and an array is constructed with a number of panels interconnected in series or parallel. A solar PV module system is comprised of the following components: (1) a number of solar cells, (2) a cells connected in series, and (3) a module system that includes a charge control system and a storage system based on a DC converter system for transmitting the electricity to a desired place, shown in Fig.2.

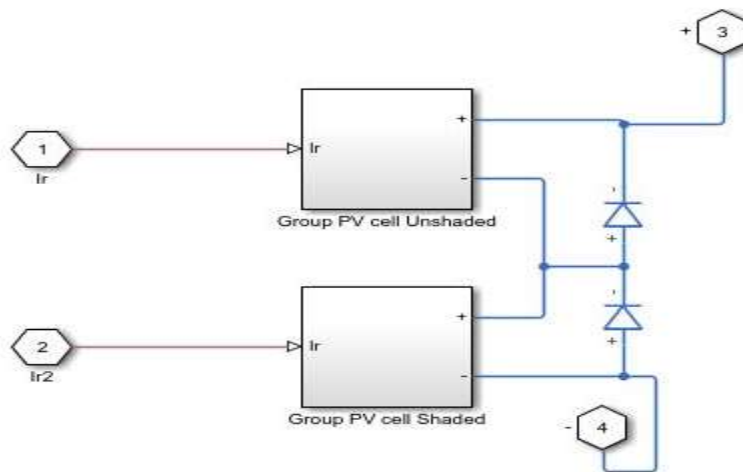


Figure 2 Solar PV Cells array configuration and system

Table 1 Typical electrical characteristics of 34 Watt PV panel

Parameter	Variable	Value
Maximum Power	P_m	34 W
Maximum Voltage	V_{mp}	5V
Maximum Current	I_{mp}	6.8A
Open Circuit Voltage	V_{oc}	6.3 V
Short Circuit Current	I_{sc}	7.3 A

A commercial PV module is interconnected in series, and this standard is used to investigate the effects on maximum power points reached while under partial shading conditions. A single PV module is constructed from 12 PV cells derived from a mono-crystalline material. Table 1 shows the electrical characteristics of 34 Watt module used in this research work under standard test conditions (STC), indicating that irradiance $G = 1000 \text{ W/m}^2$ with temperature (25°C to 37°C), and $\text{AM} = 1.5$ (Air Mass). These conditions define performance at incident sunlight of 1000 W/m^2 to 400 W/m^2 with decreasing 200 W/m^2 and temperature of 25°C . This research adopts the notions and characteristics of a simplified PV system that a single PV module 34 W is interconnected with PV cells. The Simulink models for the various configurations in series combination are shown below in Fig.3.

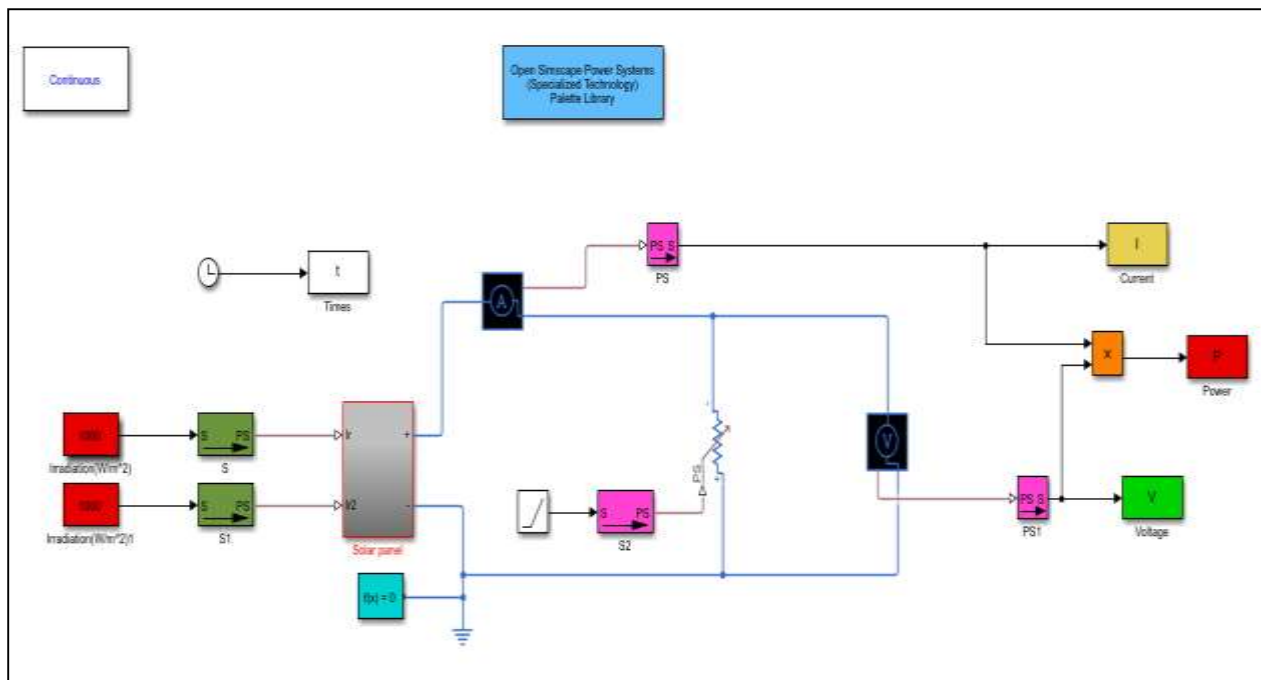


Figure 3 Simulink model with respect to PV module configuration

The module has been used for the panel configurations. For comparing the various configurations, several unique possible scenarios have been studied. I-V and P-V graphs for each of these possible scenarios have been simulated, and values of maximum power, voltage, and current obtained from the model has been simulated in this work. Table 1 Studies The series configurations of cells have been simulated. It is finding the parameters for the nonlinear I-V equations based on only the solar panel data such as open circuit voltage, short circuit current, voltage and current at maximum power point and temperature coefficient for voltage and current at the normal condition or the standard test condition which are obtained from manufacturer's solar panel.

Results

Simulation results show that when the panel temperature is 25 °C, short circuit current and maximum current of the panel increase as proportional to solar radiation level. On the other hand, there is a little increase in open-circuit voltage and maximum voltage of the panel. When the solar radiation level is increased from 200 W/m² to 1000 W/m², panel power increases. The solar radiation level is unchanged with 1000W/m² gradually increase from 25 °C to 37 °C panel temperature, but little decrease in open-circuit voltage and maximum voltage is observed. When the panel temperature under 25 °C and 37 °C are compared it is observed that as the panel temperature increases there is a little decrease in short circuit current and the maximum current values are nearly the same. On the contrary, open-circuit and maximum voltage values decrease in proportion to the increase in panel temperature. Therefore, panel power decreases.

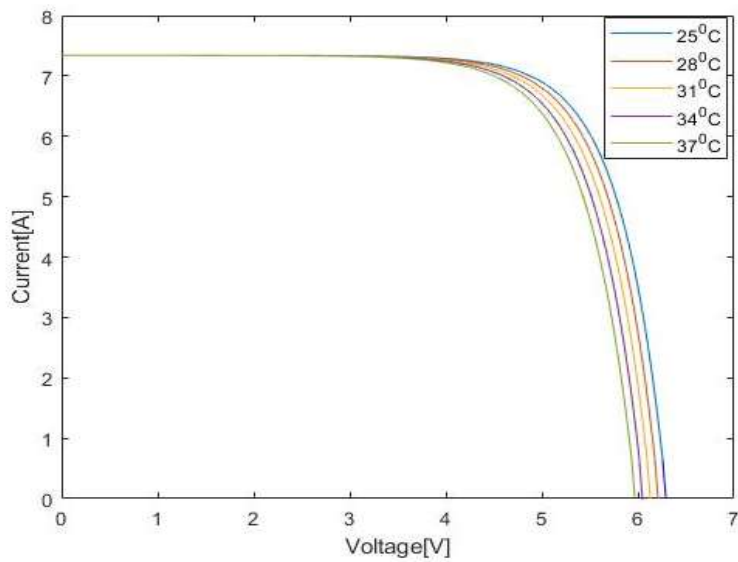


Figure 4 The I-V characteristics of PV panel at 25 °C to 37 °C temperatures

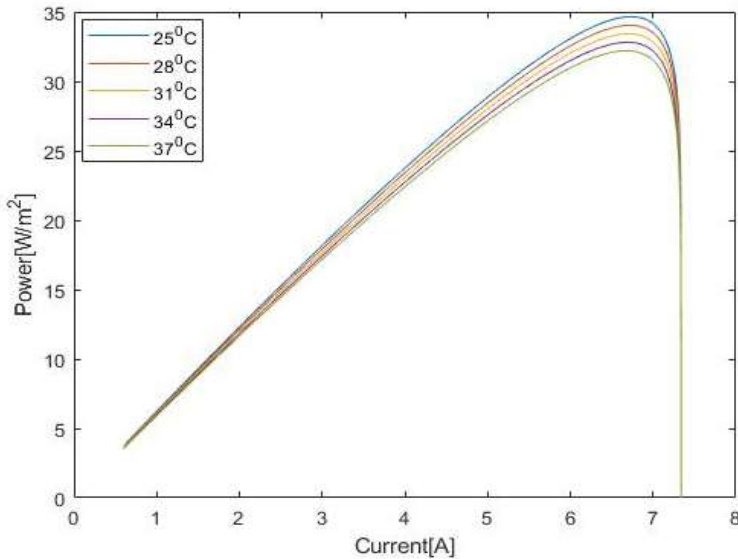


Figure 5 The P-I characteristics of PV panel at 25 °C to 37 °C temperatures

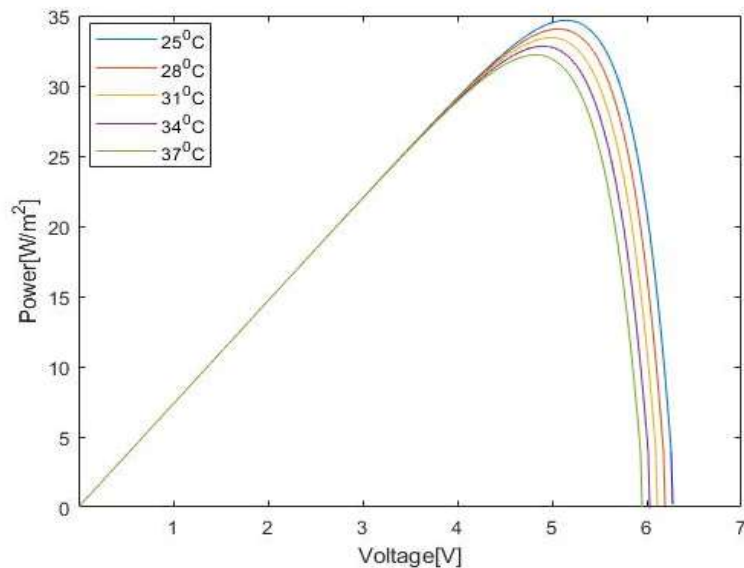


Figure 6 The P-V characteristics of PV panel at 25 °C to 37 °C temperatures

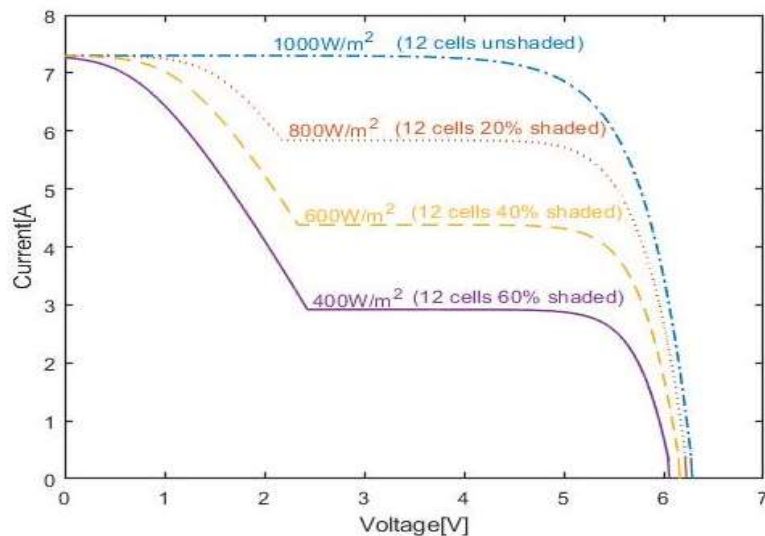


Figure 7 Simulated and the I-V curves without shading and simulated with shading.

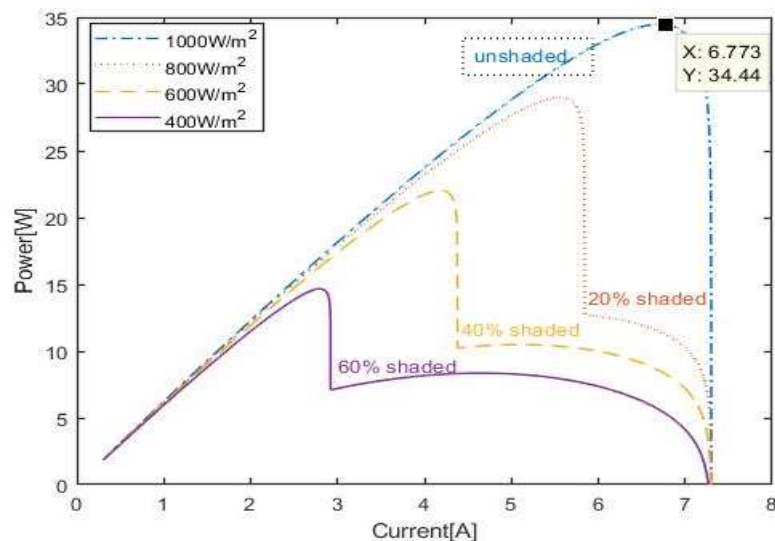


Figure 8 Simulated and P-I curves without shading and simulated with shading

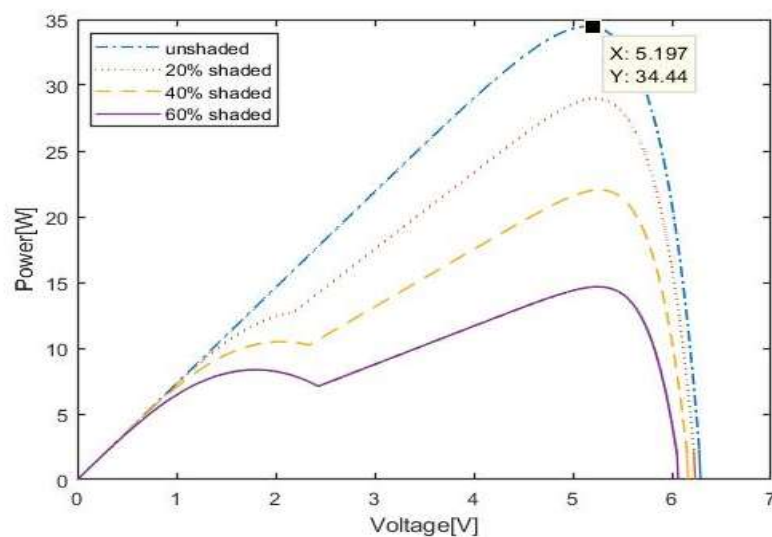


Figure 9 Simulated and P-V curves without shading and simulated with shading

The partial shading is given by the settings: $G = 1000 \text{ W/m}^2$ to $G=400 \text{ W/m}^2$ with decreasing 200 W/m^2 each. The I-V curves simulated and without shading and simulated with shading are respectively shown in Fig.7. When solar PV system is shaded partially, the power output decreases. The number of shaded modules increases, the number of peaks in power output more decreases. Position of maximum power point is independent with varying number of shaded cells. However, in case study of shading modules under varying solar irradiation, PV curve peaks are tended to be around 20 % ,40% and 60% of W/m^2 . A Matlab/Simulink model for the solar PV cells and modules is developed and presented in this research work. This model is based on the fundamental circuit equations of a solar PV module taking into the effects of physical and environmental parameters such as cell temperature, solar irradiation and shading condition. In addition, the proposed model is also used effectively to study the effect of shadow on operating characteristics of solar PV system. The higher percentage of shaded cells is the lower value of power output.

Conclusion

Analysis of various configurations with respect to environmental parameters has been investigated and more realistic models using MATLAB/Simulink have been developed. Solar cells are connected in a PV module with series were studied. The PV module electrical model is presented and demonstrated in Matlab for a typical 34W solar panel. Simulation results show that when the panel temperature is increased gradually 25°C to 37°C , open circuit voltage and maximum voltage of the panel decreases and also panel power decreases. Also, a Simulink model has been developed to simulate the behavior of PV modules with different configurations under variable shading conditions with temperature constant. In order to collect the maximum possible power output from partial shading caused by environmental conditions, it is recommended that the connection of a bypass diode in anti-parallel with a module or group of cells is required to avoid the stress on the shaded cells. This approach to PV module design would solve the problem of sensitivity of hot-spot as well as provide a higher power supply when compared to a solar PV module system without considering the configuration of bypass diode.

The results obtained from the Matlab model are quite credible and suitable for the manufacturer's solar panel kit. Model's aim is to achieve I-V characteristics similar to the data that presents the manufacturer's solar panel. An advantage of the presented simulation procedure is that the model developed here can be used for any cell and for any module by simply changing the specifications of the module used in the program.

Acknowledgement

The author would like to thank Professor Dr Shwe Sin Aung, Head of Department of physics, Monywa University for her kind permission to carry out this work. And then, I also would like to thank Professor Dr Yin Maung Maung, Department of physics, University of Yangon, Myanmar.

References

- A. Woyte, J. Nijs, and R. Belmans, (2003) "Partial shadowing of photovoltaic arrays with different system configurations: literature review and field test results," *Solar Energy*, vol. 74. Ekpenyong, E.E and Anyasi, F.I, (Nov.Dec. 2013), "Effect of Shading on Photovoltaic Cell," *IOSRJEEE*, Journal, Volume 8, Issue 2 PP 01-06.
- Chia Seet Chin1, (2011) "Maximum Power Point Tracking for PV Array under Partially Shaded Conditions", in Proceedings of the International Conference on Computational Intelligence.
- Idriss Hadj Mahammed and Amar Hadj Arab, (2017) "Outdoor study of Partial Shading effects on different PV modules Technologies," CPESE on Power and Energy Systems Engineering, International Conference, PP 81-85.
- L. Fialho and R. Melicio, (2013) "Effect of Shading on Series Solar Modules: Simulation and Experimental Results," in Proceedings of the International Conference, CETC, PP 295-302.
- Luque A. and Hegedus S. (2003), *Handbook of Photovoltaic Science and Engineering*, John Wiley and Sons Publication, NJ 07030, U.S.A.
- Smita Ganesh Pachpande, (May – June 2012) "Studying the effect of shading on Solar Panel using MATLAB", Volume 1, No.2.

TRACE ELEMENTS ANALYSIS OF SEDIMENT IN DOTHTAWADY RIVER FROM MANDALAY REGION

Aye Aye Myint¹, Thet Ni moe², Khin San Yi³, Sanda Tun⁴

Abstract

In this paper, Dohtawady River Sediments samples 1(RS-1), River Sediments sample 2(RS-2), River Sediments sample 3 (RS-3) and River Sediments sample 4 (RS-4) were collected from Mandalay region and analyzed to determine the elemental concentration by using Energy dispersive x-rays fluorescence (EDXRF) analysis. It was found that there are 14 element oxides such as Al_2O_3 , SiO_2 , Fe_2O_3 , SO_3 , K_2O , CaO , TiO_2 , Cr_2O_3 , MnO , Fe_2O_3 , CuO , ZnO , SrO , ZrO_2 in the three River Sediment samples, the value of pH and conductivity were also measured. These result values were compared and discussed.

Keywords: EDXRF (Energy Dispersive X-Ray Fluorescence), pH, conductivity

Introduction

Sediment is a naturally occurring material that is broken down by processes of weathering and erosion, and is subsequently transported by the action of wind, water, or ice, or by the force of gravity action on the particles. Sediments are most often transported by water (fluvial processes), but also wind (Aeolian processes) and glaciers. Beach sands and river channel deposits are examples of fluvial transport and deposition, though sediment also often settles out of slow-moving or standing water in lakes and oceans. Rivers draining densely populated and industrialized areas carry huge loads of heavy metals fixed to their suspended matter.

The behavior of these heavy metals in the transition from fresh water to sea water is not well understood. In the euphotic zone of the marine environment, the photosynthetic planktonic population comes into contact with some part of these solids, the composition of which again is not well yet worldwide basis. Eventually, these inorganic solids together with a proportion of the biomass settle out and are incorporated in to marine sediments. Investigations of sediments in estuaries and rivers have been stepped up in recent years in order to study mobilization and mixing effects and to trace down the extent and distribution of heavy metal contamination. Both with respect to environmental and geochemical problems, the suspended phase are a very important component of estuaries and oceans. Heavy metals, which are often concentrated in the particulate phase, belong doubtlessly to the most toxic pollutants in the environment.

Aquatic ecosystems are affected by several health stressors that significantly deplete biodiversity. In the future, the loss of biodiversity and its effects are predicted to be greater for aquatic ecosystems than for terrestrial ecosystems. Sediments form a natural buffer and filter system in the material cycles of water. Sediment in our rivers is an important habitat as well as a main nutrient source for aquatic organisms. Sediment strata serve as an important habitat for the benthic macro invertebrates whose metabolic activities contribute to aquatic productivity. Sediment is also the major site for organic matter decomposition which is largely carried out by bacteria. Important macro-nutrients are continuously being interchanged between sediments and overlying water. Furthermore, sediment has an impact on ecological quality, because of their quality, or their quality, or both. It is observed that continuous accumulation of pollutants due to biological and geochemical mechanisms, and cause toxic effect on sediment dwelling organisms

¹ Dr, Associate Professor, Department of Physics, Kyaukse University

² Dr, Associate Professor, Department of Physics, Kyaukse University

³ Dr, Associate Professor, Department of Physics, Kyaukse University

⁴ Dr, Associate Professor, Department of Physics, Kyaukse University

and fish, resulting in decrease survival, reduced growth, or impaired reproduction and lowered species diversity. Alkalinity may be caused by dissolved strong bases such as sodium hydroxide or potassium hydroxide (and other hydroxide containing compounds), and it may also be caused by dissolved carbonates, bicarbonates, borates and phosphates.

Materials and Method

Dohtawady River Sediment samples: River Sediment sample 1 (RS-1), River Sediment sample 2 (RS-2), River Sediment sample 3 (RS-3) and River Sediment sample 4 (RS-4) were collected from Mandalay region area. River Sediment sample 1 and sample 2 were collected from near the Shwesaryan pagoda, Pyin Oo Lwin Township in Mandalay region. River Sediment sample 3 and River Sediment sample 4 were collected from away from the Myitnge Bridge, Myit nge Township in Mandalay region.

River Sediment samples were collected in good quality glass container of (50) grams capacity without any air bubbles. The glass container were cleaned with nitric acid and dried. The glass container were tightly sealed after collection and labeled. Each River Sediment samples were prepared for energy dispersive X-rays fluorescence (EDXRF) analysis. The X-ray Fluorescence analysis system consist of Si (Li) detector with personal computer and X-rays analysis software and also used preamplifier and amplifier are used in experimental measurement. The value of pH and Conductivity were determined using pH meter and conductivity meter (Ecoscan Con 5) at Department of Chemistry, University of Mandalay.

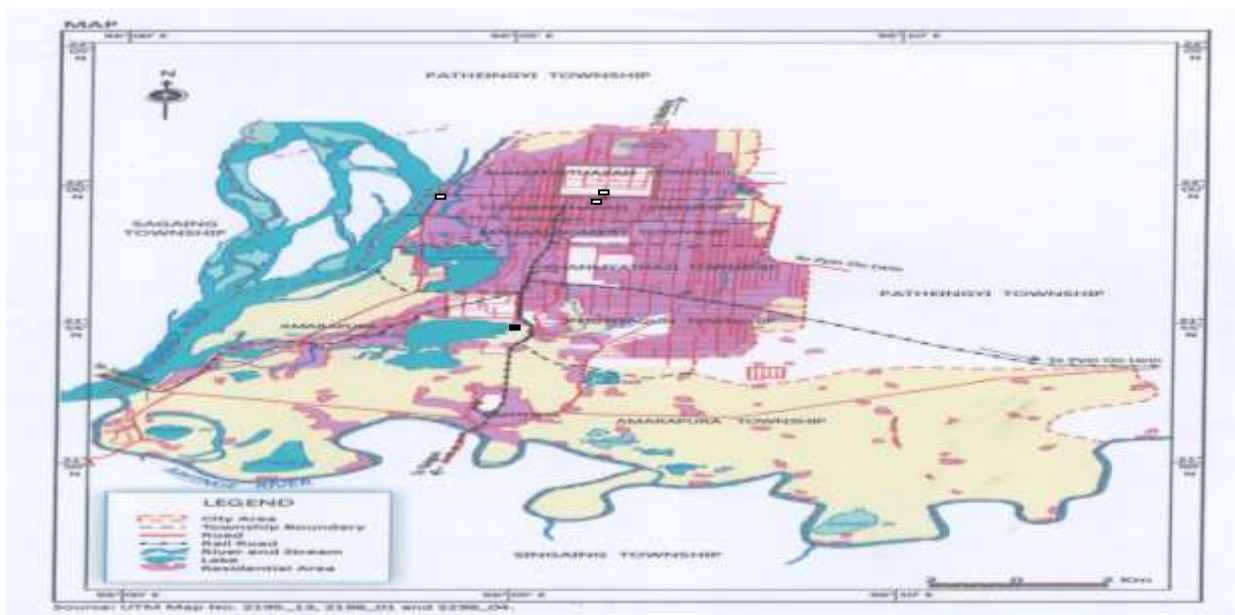


Figure 1 The collection sites Dohtawady River from Mandalay Environ



Figure 2 The photograph of sample collection

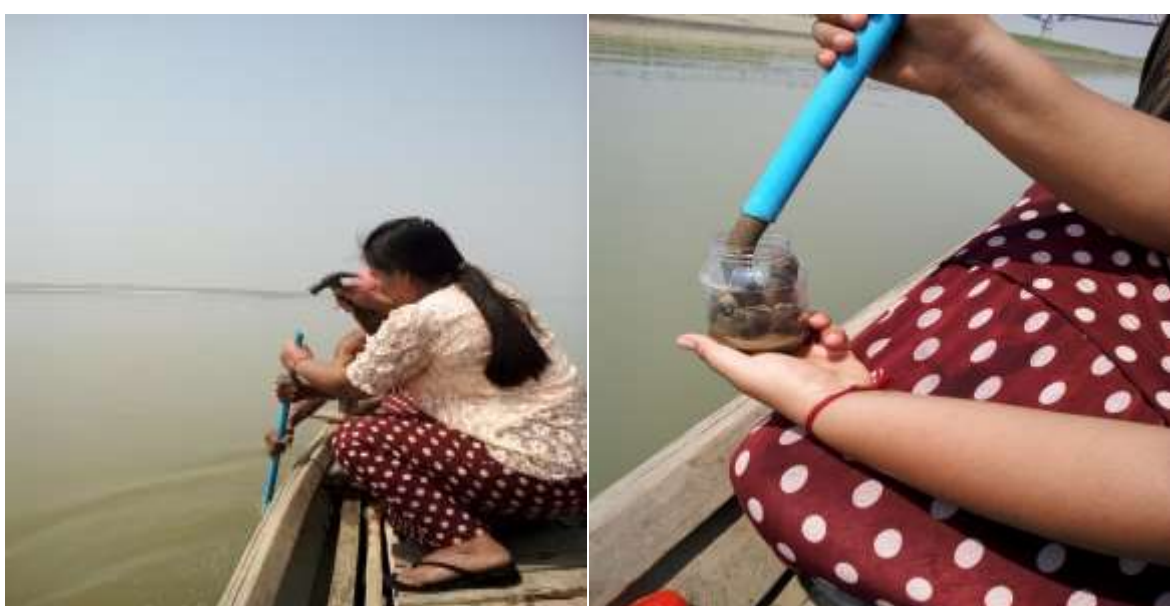


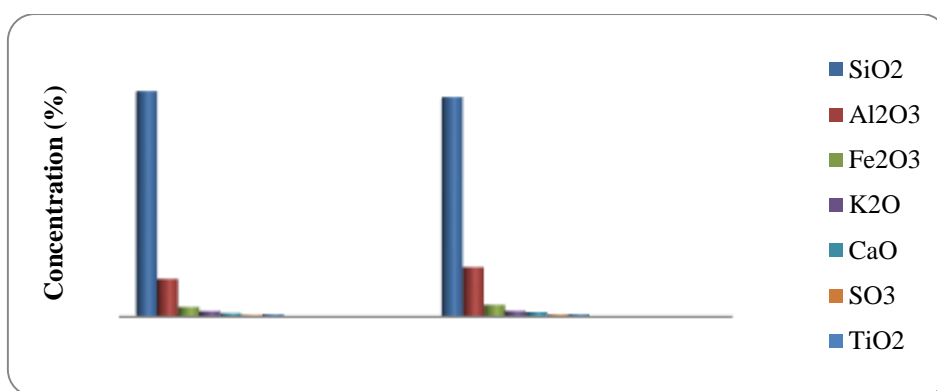
Figure 3 The photograph of sample collection

Experimental Results and Discussion

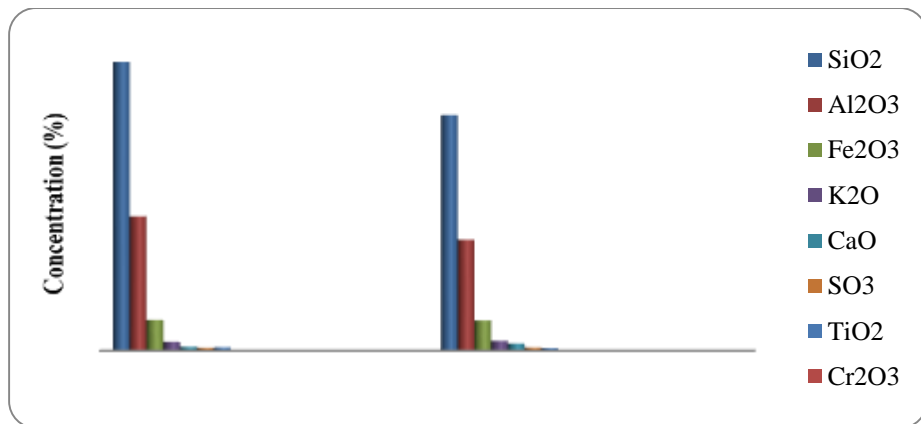
The concentrations of the elements of the Sediment samples were determined by EDXRF technique. The results were shown in following tables.

Table 1 The element oxides present in two kinds of samples (Pyin Oo Lwin)

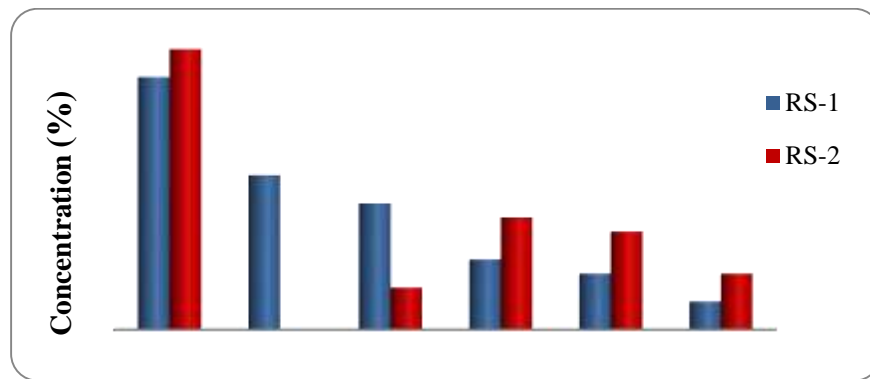
No	Elements Oxide	Concentration (%)	
		RS-1 (Sample 1)	RS-2 (Sample 2)
1	SiO ₂	71.998	70.124
2	Al ₂ O ₃	12.123	15.800
3	Fe ₂ O ₃	3.112	3.842
4	K ₂ O	1.749	1.823
5	CaO	1.118	1.504
6	SO ₃	0.545	0.719
7	TiO ₂	0.784	0.832
8	Cr ₂ O ₃	0.054	0.063
9	MnO	0.041	0.064
10	NiO	ND	0.028
11	SrO	0.019	0.027
12	CuO	0.019	0.009
13	ZnO	0.006	0.004

**Figure 4** Concentration of element oxides in samples (Pyin Oo Lwin)**Table 2** The element oxides present in two kinds of samples (Myitnge)

No	Element Oxide	Concentration (%)	
		RS-3 (Sample 3)	RS-4 (Sample 4)
1	SiO ₂	58.247	47.533
2	Al ₂ O ₃	27.11	22.38
3	Fe ₂ O ₃	6.198	6.125
4	K ₂ O	1.786	1.991
5	CaO	0.818	1.422
6	TiO ₂	0.703	0.567
7	SO ₃	0.592	0.651
8	MnO	0.190	0.136
9	Cr ₂ O ₃	0.059	0.047
10	NiO	0.039	ND
11	SrO	0.011	ND
12	CuO	0.005	0.002

**Figure 5** Concentration of element oxides in samples (Myint nge)**Table 3** Amount of trace element oxides in samples (Pyin Oo Lwin)

No	Elements Oxide	Concentration (%)	
		RS-1 (Sample 1)	RS-2 (Sample 2)
1	Cr ₂ O ₃	0.054	0.063
2	MnO	0.041	0.064
3	NiO	ND	0.028
4	SrO	0.019	0.027
5	CuO	0.019	0.009
6	ZnO	0.006	0.004

**Figure 6** Concentration of trace element oxides in samples (Pyin Oo Lwin)**Table 4** Amount of trace element oxides in samples (Myit nge)

No	Elements Oxide	Concentration (%)	
		RS-3(Sample 3)	RS-4(Sample 4)
1	Cr ₂ O ₃	0.059	0.047
2	MnO	0.190	0.135
3	NiO	0.039	ND
4	SrO	0.011	0.019
5	CuO	0.005	0.017

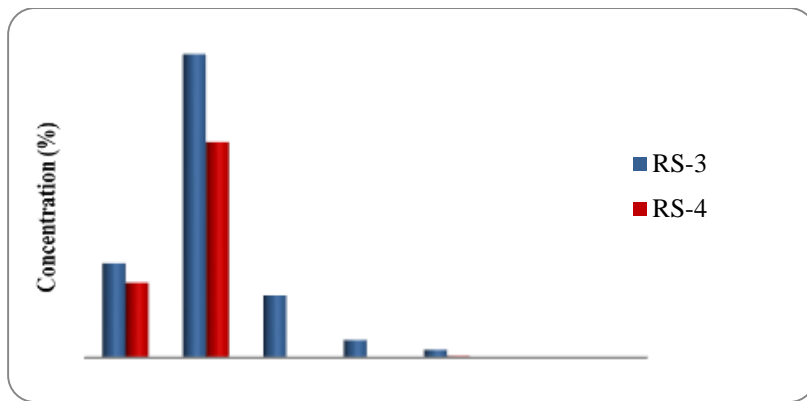


Figure 7 Concentration of trace element oxides in samples (Myint nge)

Table 5 Amount of trace toxic element oxides in samples (Pyin Oo Lwin)

No	Element Oxide	The amount determined (%) (RS-1)	The amount determined (%) (RS-2)
1	CuO	0.019	0.009
2	NiO	ND	0.028
3	ZnO	0.006	0.004

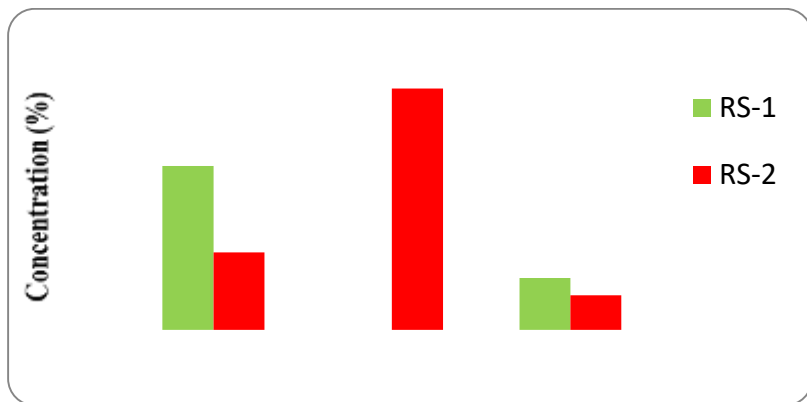
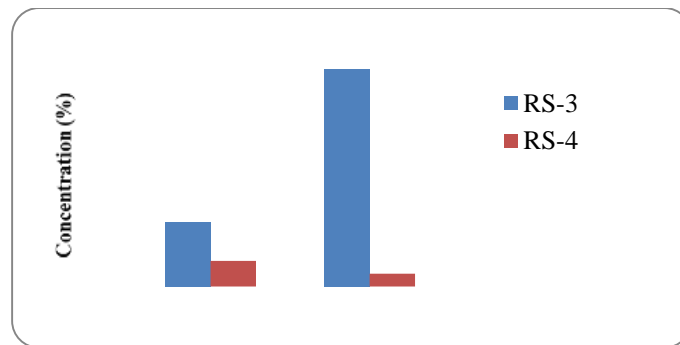


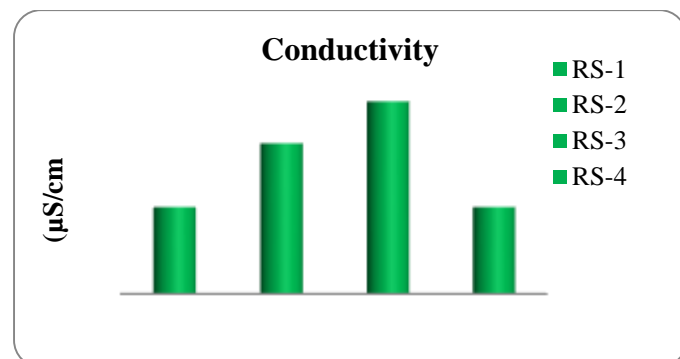
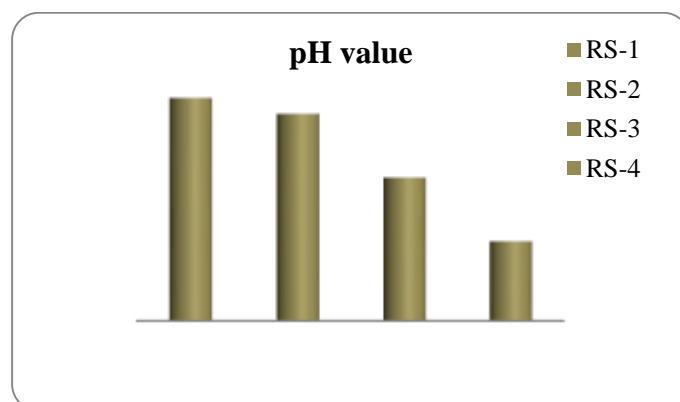
Figure 8 Concentration of toxic element oxides in samples (Pyin Oo Lwin)

Table 6 Amount of trace toxic element oxides in samples (Myit nge)

No	Element Oxide	The amount determined (%) (RS-3)	The amount determined (%) (RS-4)
1	CuO	0.005	0.002
2	NiO	0.039	ND

**Figure 9** Concentration of toxic element oxides in samples (Myint nge)**Table 7** The conductivity and pH values of four different samples

No	Samples code name	Conductivity ($\mu\text{S}/\text{cm}$)	pH value
1	RS-1	72.9	8.9
2	RS-2	78.7	8.8
3	RS-3	82.5	8.4
4	RS-4	72.9	8.0

**Figure 10** The Conductivity of different river sediment samples**Figure 11** The pH values of different river sediment samples

Dothatawady River Sediment samples: River Sediment sample 1 (RS-1), River Sediment sample 2 (RS-2), River Sediment sample 3 (RS-3) and River Sediment sample 4 (RS-4), were collected from Pyin Oo Lwin township and Myit nge township Mandalay region area.

The elements that contain in four kinds of samples of (Pyin Oo Lwin and Myit nge) were analyzed by using Energy Dispersive X-Ray Fluorescence (EDXRF) method. Most elements can exist as element oxides in sediment. Among the elements having atomic number 11 to 92, it was found that there are 13 element oxides such as Al_2O_3 , SiO_2 , SO_3 , K_2O , CaO , TiO_2 , Cr_2O_3 , MnO , Fe_2O_3 , NiO , CuO , ZnO , SrO , in the River Sediment sample 2 (RS-1). However, River Sediment sample 1 (RS-1) contains 12 element oxides that are found in RS-1. NiO is not found in RS-1. The element oxides present in the samples were described in Table (1) as the order of high to low concentration.

Twelve element oxides such as Al_2O_3 , SiO_2 , SO_3 , K_2O , CaO , TiO_2 , Cr_2O_3 , MnO , Fe_2O_3 , NiO , CuO , ZnO , SrO , are found in the River Sediment sample 3 (RS-3). However, River Sediment sample 3 (RS-3) contains 12 element oxides that are found in RS-3, NiO and SrO are not found in RS 4. The element oxides present in the samples were described in Table (2) as the order of high to low concentration.

Trace element oxides present in samples RS-1, RS-2 of Pyin Oo Lwin were also determined. It was found that Cr_2O_3 , SrO , CuO , MnO , NiO and ZnO were present in the samples and described in Table (3) and Figure (6).

Trace element oxides present in samples RS-3, RS-4 of Myit nge Cr_2O_3 , SrO , CuO , MnO and NiO were also determined and it was found that were present in the samples and described in Table (4) and Figure (7).

Some trace toxic element oxides present in samples RS-1, RS-2 of Pyin Oo Lwin were also determined and it was found that CuO , NiO and ZnO were present in the samples and described in Table (5) and Figure (8).

Some trace toxic element oxides present in samples RS-3 of Myit nge were also determined and it was found that CuO and NiO . River Sediment sample 4 (RS-4) contains only toxic element oxide of CuO , However NiO and ZnO are not found in RS 4, described in Table (6) and Figure (9).

The pH values of Dothatawady River Sediment samples are shown in Table (7). The pH values of River Sediment sample 1 (RS-1), River Sediment sample 2 (RS-2), River Sediment sample 3 (RS-3) and River Sediment sample 4 (RS-4) are found to be 8.9, 8.8, 8.4 and 8.0 respectively. RS-4 show the lowest value of pH (8.0). River Sediment sample 1 (RS-1) has the highest value of pH (8.9).

The Conductivity of Dothatawady River Sediment samples are presented in Table (7). Conductivity values range from 72.9-82.5 $\mu\text{S}/\text{cm}$. Dotetawady River Sediment sample 1 (RS-1) and (RS-4) have lowest conductivity value (72.9 $\mu\text{S}/\text{cm}$). The Dotetawady River Sediment sample 3(RS-3) has highest conductivity value (84.5 $\mu\text{S}/\text{cm}$).

Conclusion

In this paper, the quantitative data are measured by the EDX-7000 software, which is used in the calibration system with the internal standards. These data obtained in the samples were not considered on the organic compounds.

Four Dothatawady River Sediment samples (RS-1, RS-2, RS-3 and RS-4) were chosen for the study from Mandalay region area.

RS-2 sample contains thirteen element oxides such as Al_2O_3 , SiO_2 , SO_3 , K_2O , CaO , TiO_2 , Cr_2O_3 , MnO , Fe_2O_3 , NiO , CuO , ZnO , SrO . RS-1 sample contains twelve element oxides (except NiO). RS-3 sample contains twelve element oxides (except ZnO). RS-4 sample contains ten element oxides (except NiO , SrO and ZnO). The elements found in four Dohtawady River Sediment samples are very valuable macro and micro elements for plant growth.

One of the plants' nutrient, potassium (K) in four sediment samples are 1.749%, 1.823%, 1.786% and 1.991%. This means that the selected sediment samples can supply potassium nutrient to the plants. Among the four samples, RS-4 can support more potassium than that of others.

For agriculture, maximum permissible value of soil pH is 7.5-8.5. The pH values of four Dohtawady River Sediment samples are found to be 8.0-8.9.

For agriculture, the suitable conductivity is 100 $\mu\text{S}/\text{cm}$. Conductivity values of Dohtawady River Sediment samples are found to be 72.9-82.5 $\mu\text{S}/\text{cm}$. Therefore, conductivity values of four sediments samples fall in suitable conductivity value.

In Pyin Oo Lwin, for toxic elements, the amounts of copper and zinc of River Sediment sample RS-1 are higher than that of River Sediment sample RS-2. Then Nickel was detected River Sediment sample RS-2, but nickel toxic was not found in River Sediment sample RS-1.

In Myit Nge, for toxic elements, nickel and zinc does not found in River Sediment sample RS-4 but nickel toxic was detected in River Sediment sample RS-3. Copper contents of River Sediment sample RS-3 is higher than that of River Sediment sample RS-4. From the above data, Pyin Oo Lwin samples (RS-1, RS-2) contain more toxic elements than Myit nge samples (RS-3, RS-4).

From the point of view of elemental concentration, pH and conductivity, the four selected Dohtawady River Sediment samples are found to be used for the suitable to grow agriculture purpose.

Among these four Dohtawady River Sediment samples, the quality of Dohtawady River Sediments sample 4 (RS-4) is better than others.

Acknowledgements

I would like to express my special thanks to Dr Aung Khin Myint, Rector, Kyaukse University to allow to present this research. I would like to express my sincere thanks are due to Dr Cherry Than, Professor and Head, Department of Physics, Kyaukse University for her kind encouragements throughout the research.

References

- Agarwal, B. K., X-ray Spectroscopy: An Introduction (Heidelberg: Springer-Verlag, (1979).
- Biddle, M. B. *et al.*, Nuclear Instrument and Methods in Physics Research, B 251 (2012) 117.
- Campbell, I. *et al.*, The Use of EDXRF for Pharmaceutical Material Elemental Analysis, American Pharmaceutical review, (2012).
- M. Rozic and V. Orescanin, Nuclear Instrument and Methods in Physics Research, B 229 (2005).
- P Singh et al, X-Ray Physics, B 73 (2010).
- Shimadzu 2002 User Manual of Shimadzu EDX-700 X-ray Spectrometer Universities` Research Centre, Yangon University and Methods in Physics", *Research, B*, 251, pp 223.

INVESTIGATION OF RADIONUCLIDE CONCENTRATION IN SOIL SAMPLES COLLECTED FROM MINHLA COAL MINE REGION

Saine Lai Wai¹, Nay Win Oo²

Abstract

The aim of this research work is to investigate the radionuclides and calculate the activities of the collected samples from Kan Toke coal mine areas, Minhlha Township, Magway Region. The radionuclide concentrations in soil samples were examined by using NaI (Tl) gamma ray spectrometry. There are four soil samples. From the analysis of the obtained spectra, peaks of ^{212}Pb (77.11 keV), ^{212}Pb (238.63 keV), ^{228}Ac (338.32 keV), ^{208}Tl (583.19 keV), ^{208}Tl (860.56 keV), ^{214}Bi (1120.3 keV) and ^{40}K (1461 keV) were found. It is also found that the observed radionuclides except ^{40}K (1461 keV) are the decay products of ^{238}U and ^{232}Th natural radioactive series. The concentrations of these radionuclides were determined by Gamma Vision 32 software. The highest activity of ^{212}Pb (77.11 keV) was found in soil sample 1. The highest activity of ^{212}Pb (238.63 keV) was found in soil sample 3. The highest activity of ^{228}Ac (338.32 keV) was found in soil sample 3. The highest activity of ^{208}Tl (583.19 keV) was found in soil sample 3. The highest activity of ^{208}Tl (860.56 keV) was found in soil sample 1. The highest activity of ^{214}Bi (1120.3 keV) was found in soil sample 1. The highest activity of ^{40}K (1461 keV) was found in soil sample 4. The concentrations of radionuclides contained in Kan Toke coal mine areas are not very high compared with IAEA standard, the samples have very small amount of radionuclides.

Keywords: Soil Samples, NaI(Tl) Scintillation Detector, Activity, Radionuclides, Standard Gamma Sources.

Introduction

Soil

Soil is a material which nourishes and supports growing plants. (Includes rocks, water, snow, and even air – all of which are capable of supporting plant life). And soil is loose surface of the earth as distinguished from solid bedrock. Soil contains mixture of mineral matter, organic matter, water and air. (Example: Loam soil = 45% mineral matter, 5% organic matter, 20-30% water, and 20-30% air). This composition of loam soil is shown in Figure (1).

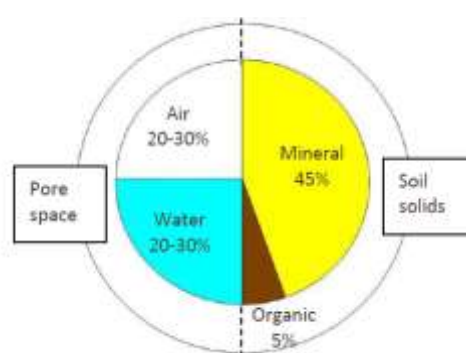


Figure 1 Composition of a loam surface soil when conditions are for plant growth

Soil is collection of natural bodies of the earth's surface, in places modified or even made by man or earthy materials, containing living matter and supporting or capable of supporting plants out-of-doors. Its upper limit is air or shallow water. Its lower limit is the lower limit of biologic

¹. Assistant Lecturer, Department of Physics, University of Magway

². Professor, Department of Physics, University of Mandalay

activity, which generally coincides with the common rooting depth of native perennial plants, the depth to which soil weathering has been effective, or both.

Soil is a collection of natural bodies occupying portions of the earth's surface that supports plants and that have properties due to the integrated effect of climate and living matter, acting upon parent material, as conditioned by relief, over periods of time.

Experimental Procedure

Sample Collection and Preparation

Four types of soil samples are collected from different places of Kan Toke coal mine area, Minhla Township, Magway Region. Soil sample 2 is about 200ft from soil sample 1, and soil sample 3 is also about 200ft from soil sample 2. Soil sample 4 is collected from the Gway Cho stream flowing across the coal mine areas. Soil samples were dried at shelter, avoiding the loss of any volatile radionuclide. The dried samples were pulverized and sieved to pass through a 1-2mm mesh. The meshed soil samples were transferred to plastic sample cup. The plastic sample cup used in this research was as shown in Figure (2). The detection system of the scintillation detector is shown in Figure (3).

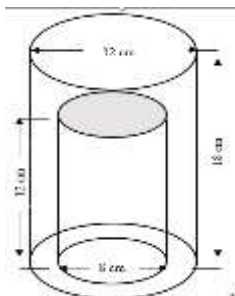


Figure 2 Plastic Sample Cup

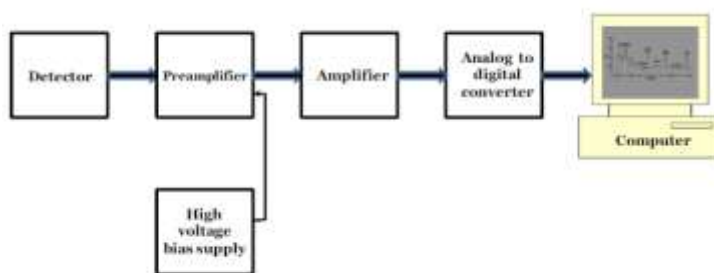


Figure 3 Experimental setup

Energy Resolution of the NaI(Tl) Detector

For a perfect detector, the photopeak is expected to be a delta function. Which is in contrast to the widened peaks in the measured energy spectrum, this widening contains contributions from a range of separate effects such as charge collection statistics, electronic noise, fluctuations in PMT gain, variations in the detector response over its active volume and drifts in parameters over the course of the measurement. The energy resolution is defined as the Full Width at Half Maximum (FWHM) in percentage.

$$R = \frac{\text{FWHM}}{H_0} \times 100\% \quad (1)$$

Where, FWHM is the full width at half maximum of the full-energy peak and H_0 is the mean pulse height corresponding to the same peak.

Experimental Set-Up

Gamma spectrometric analysis of the samples was performed with a computer based gamma spectrometry system for qualitative and quantitative determination of gamma emitting radionuclides. The system included Thallium doped, sodium iodide NaI(Tl) scintillation detector (Model 296) photomultiplier tube, high voltage power supply, preamplifier (Model 142 PC) fast spectroscopy amplifier (Model 671), a pulse stored multi-channel analyzer (MCA) together with Gamma Vision-32 software were installed in PC. The operation voltage for NaI(Tl) scintillation detector is 1000V. The whole system including detector and all other modules were from ORTEC.

The detector resolution was 8% at 662 keV energy of ^{137}Cs . The detectors were placed in low-background shields made of 7.5 cm thick old lead (Pb) rings, which were lined with cosmic rays, cadmium, other radiation in environment and copper to reduce the effect of X-rays.

Energy Calibration

The energy of radioactive elements in soil samples were unknown. The standard radioactive sources of known energies were used to calibrate the spectrometer. Four standard sources such as, 6 different energies including all ranges of energy low, medium and high, ^{241}Am (60 keV), ^{137}Cs (661.66 keV), ^{22}Na (511 keV and 1274.53 keV) and ^{60}Co (1173.24 keV and 1332 keV) were used for 600 seconds placing at 5 cm above the detector cap. The datas are as shown in Table (1) and the energy calibration curve is as shown in Figure (3). Establishing a direct relationship between photo peak energy and channel number could do the energy calibration process.

Table 1 The Standard Gamma Sources

Used in the Energy Calibration Data

Source	Energy (keV)	Channel
^{241}Am	60	91.1
^{137}Cs	661.66	621
^{22}Na	511	488.83
	1274.53	1168
^{60}Co	1173.24	1080
	1332	1218

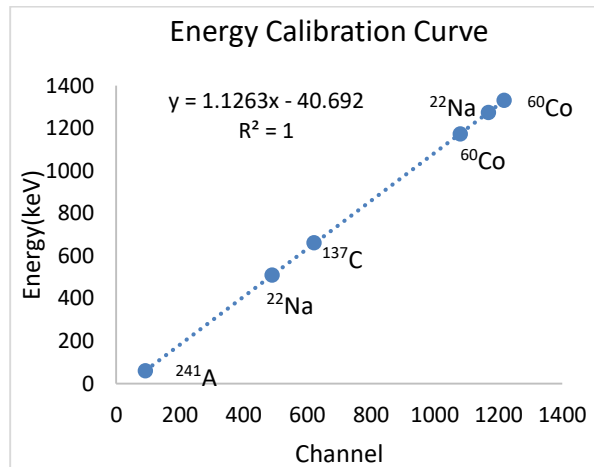


Figure 4 Energy Calibration Curve

Calculation of Activity

The activity of radionuclide present in the samples was calculated by following equation

$$A = \frac{N_A}{m \varepsilon P_\gamma T} \quad (2)$$

where, N_A = net count area for sample

m = mass of sample

P_γ = gamma ray intensity

T = counting time (in second)

ε = efficiency of the interest gamma energy

Experimental Procedure

In gamma ray spectroscopy system, sodium crystal mounted a photomultiplier tube, preamplifier, amplifier, a pulse store multi-channel analyzer (MCA), high-voltage power supply and data readout devices are included.

In this experiment, NaI (Tl) 3 inches x 3 inches scintillation detector is used to detect the gamma radiation after passing through the samples and then passed informations (electron pulses) are amplified by the preamplifier and the fast spectroscopy amplifier and collected by using MCA based on personal computer. The operating voltage used in scintillation detector is 1000V dc. First, the background was measured for three hours. This value is fixed for all measurements and measuring time is 10800 seconds in each sample. At the end of the counting period, the spectrum that was recorded may be displayed on the screen. The spectra stored in MCA were analyzed by the application of Gamma-Vision 32 software. Using the displayed information, unknown radioisotopes can be identified radionuclides with activity concentrations, a picture of the spectrum and then determination of the gross area and net area of full energy peak. The activities of different radionuclides can be calculated by using the equation (2).



Figure 5 Side view of the detection system



Figure 6 Diagram of the experimental arrangement of the detection system

Results and Discussion

The activity concentrations of radionuclides in soil samples were presented in Tables (2), (3), (4) and (5). The comparison of activity concentrations of radionuclides in soil samples were presented in Table (6). The activity concentrations of ^{212}Pb (77.11 keV) was found with values of 26.17 Bq/kg in sample 1, 20.7 Bq/kg in sample 2, 21.74 Bq/kg in sample 3 and 17.55 Bq/kg in soil sample 4. The highest activity of ^{212}Pb (77.11 keV) was found in soil sample 1. The activity concentrations of ^{212}Pb (238.63 keV) was found with values of 7.94 Bq/kg in sample 1, 9.34 Bq/kg in sample 2, 12.58 Bq/kg in sample 3 and 6.28 Bq/kg in soil sample 4. The highest activity of ^{212}Pb (238.63 keV) was found in soil sample 3. The activity concentrations of ^{228}Ac (338.32 keV) was found with values of 20.18 Bq/kg in sample 1, 27.31 Bq/kg in sample 2, 27.37 Bq/kg in sample 3 and 15.05 Bq/kg in soil sample 4. The highest activity of ^{228}Ac (338.32 keV) was found in soil sample 3. The activity concentrations of ^{208}Tl (583.19 keV) was found with values of 4.77 Bq/kg in sample 1, 5.29 Bq/kg in sample 2, 6.58 Bq/kg in sample 3 and 4.48 Bq/kg in soil sample 4. The highest activity of ^{208}Tl (583.19 keV) was found in soil sample 3. The activity concentrations of ^{208}Tl (860.56 keV) was found with values of 11.42 Bq/kg in sample 1 and 2.81 Bq/kg in sample 2. The highest activity of ^{208}Tl (860.56 keV) was found in soil sample 1. The activity concentrations of ^{214}Bi (1120.3 keV) was found with values of 10.13 Bq/kg in sample 1 and 0.03 Bq/kg in sample 2. The highest activity of ^{214}Bi (1120.3 keV) was found in soil sample 1. The activity concentrations of ^{40}K (1461 keV) was found with values of 203.63 Bq/kg in sample 1, 154.29 Bq/kg in sample 2, 163.34 Bq/kg in sample 3 and 304.06 Bq/kg in soil sample 4. The highest activity of ^{40}K (1461 keV) was found in soil sample 4. The background spectrum and soil sample spectrums were shown in Figure (6) to (10).

Table 2 Activity concentrations of radionuclides in soil sample 1

Sr.No	Radionuclide	Energy(keV)	Activity (Bq/kg)
1	^{212}Pb	77.11	26.17
2	^{212}Pb	238.63	7.94
3	^{228}Ac	338.32	20.18
4	^{208}Tl	583.19	4.77
5	^{208}Tl	860.56	11.42
6	^{214}Bi	1120.29	10.13
7	^{40}K	1461	203.63

Table 3 Activity concentrations of radionuclides in soil sample 2

Sr.No	Radionuclide	Energy(keV)	Activity (Bq/kg)
1	^{212}Pb	77.11	20.7
2	^{212}Pb	238.63	9.34
3	^{228}Ac	338.32	27.31
4	^{208}Tl	583.19	5.29
5	^{208}Tl	860.56	2.81
6	^{214}Bi	1120.29	0.03
7	^{40}K	1461	154.29

Table 4 Activity concentrations of radionuclides in soil sample 3

Sr.No	Radionuclide	Energy(keV)	Activity (Bq/kg)
1	^{212}Pb	77.11	21.74
2	^{212}Pb	238.63	12.58
3	^{228}Ac	338.32	27.37
4	^{208}Tl	583.19	6.58
5	^{40}K	1461	163.34

Table 5 Activity concentrations of radionuclides in soil sample 4

Sr.No	Radionuclide	Energy(keV)	Activity (Bq/kg)
1	^{212}Pb	77.11	17.55
2	^{212}Pb	238.63	6.28
3	^{228}Ac	338.32	15.05
4	^{208}Tl	583.19	4.48
5	^{40}K	1461	304.06

Table 6 Comparison of activity concentrations of radionuclides in soil samples

Sr.No	Radionuclide	Energy (keV)	Soil sample 1	Soil sample 2	Soil sample 3	Soil sample 4
1	^{212}Pb	77.11	26.17	20.7	21.74	17.55
2	^{212}Pb	238.63	7.94	9.34	12.58	6.28
3	^{228}Ac	338.32	20.18	27.31	27.37	15.05
4	^{208}Tl	583.19	4.77	5.29	6.58	4.48
5	^{208}Tl	860.56	11.42	2.81	ND	ND
6	^{214}Bi	1120.3	10.13	0.03	ND	ND
7	^{40}K	1461	203.63	154.29	163.34	304.06

Conclusion

In this research work, the soil samples from Kan Toke coal mine areas, Minhla Township, Magway Region were examined by using NaI (Tl) detector and analyzed by Gamma Vision 32 software. There are four soil samples. From the analysis of the obtained spectra, the radionuclides present in soil sample 1,2, 3 and 4 are [^{212}Pb (77.11 keV), ^{212}Pb (238.63 keV), ^{228}Ac (338.32 keV), ^{208}Tl (583.19 keV), ^{208}Tl (860.56 keV), ^{214}Bi (1120.3 keV) and ^{40}K (1461 keV)]. It is also found that the observed radionuclides except ^{40}K (1461 keV) are the decay products of ^{238}U and ^{232}Th natural radioactive series. The highest activity of ^{212}Pb (77.11 keV) was found in soil sample 1. The highest activity of ^{212}Pb (238.63 keV) was found in soil sample 3. The highest activity of ^{228}Ac (338.32 keV) was found in soil sample 3. The highest activity of ^{208}Tl (583.19 keV) was found in soil sample 3. The highest activity of ^{208}Tl (860.56 keV) was found in soil sample 1. The highest activity of ^{214}Bi (1120.3 keV) was found in soil sample 1. The highest activity of ^{40}K (1461 keV) was found in soil sample 4. The concentrations of radionuclides contained in Kan Toke coal mine areas are not very high compared with IAEA standard, the samples have very small amount of radionuclides.

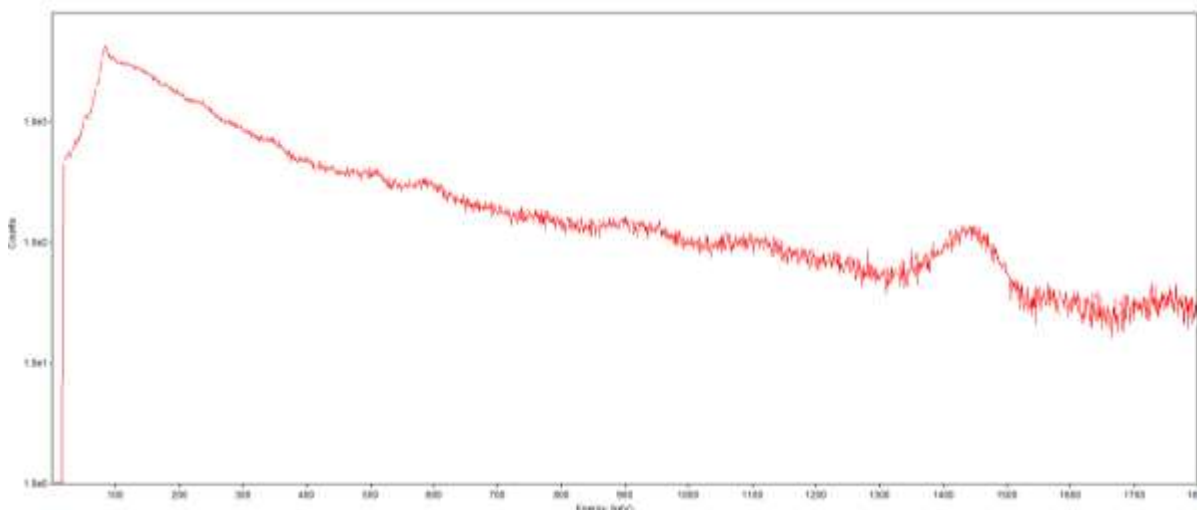


Figure 6 The energy spectrum of the background radiation

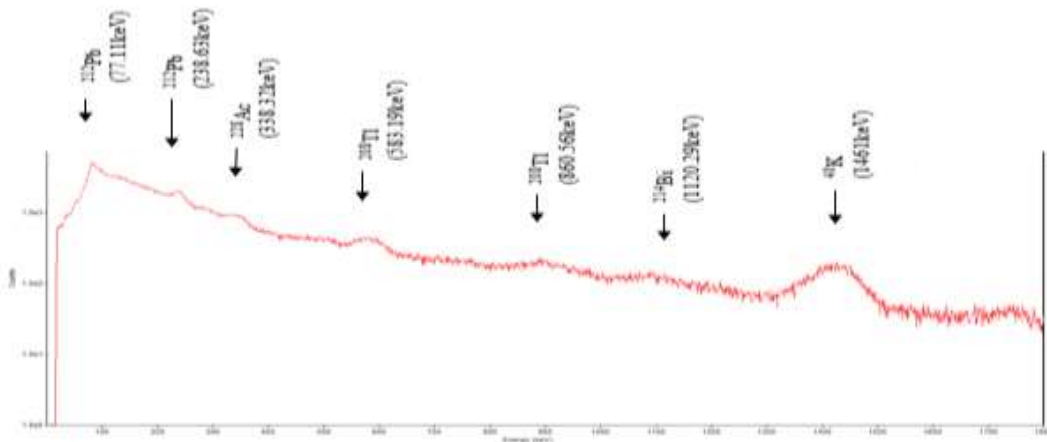


Figure 7 The energy spectrum of the soil sample 1

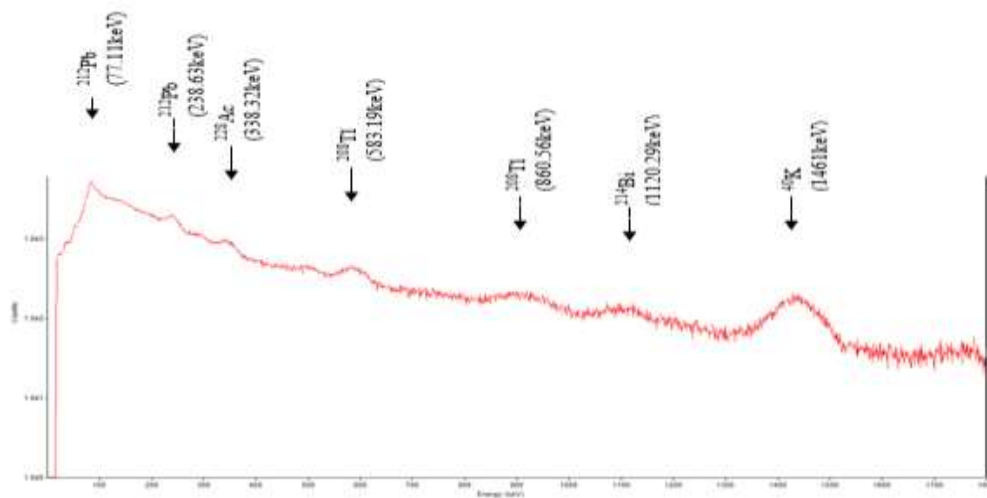


Figure 8 The energy spectrum of the soil sample 2

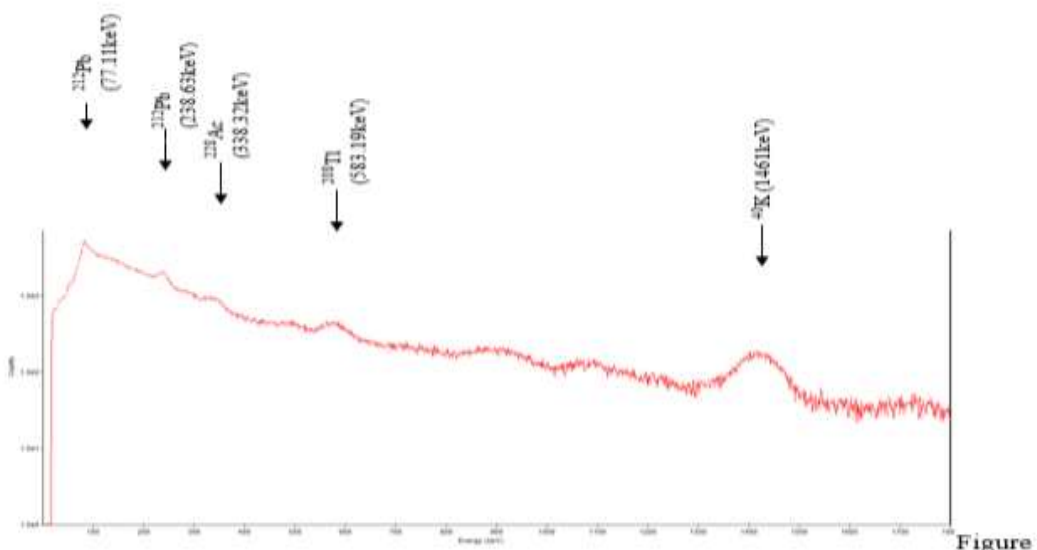


Figure 9 The energy spectrum of the soil sample 3

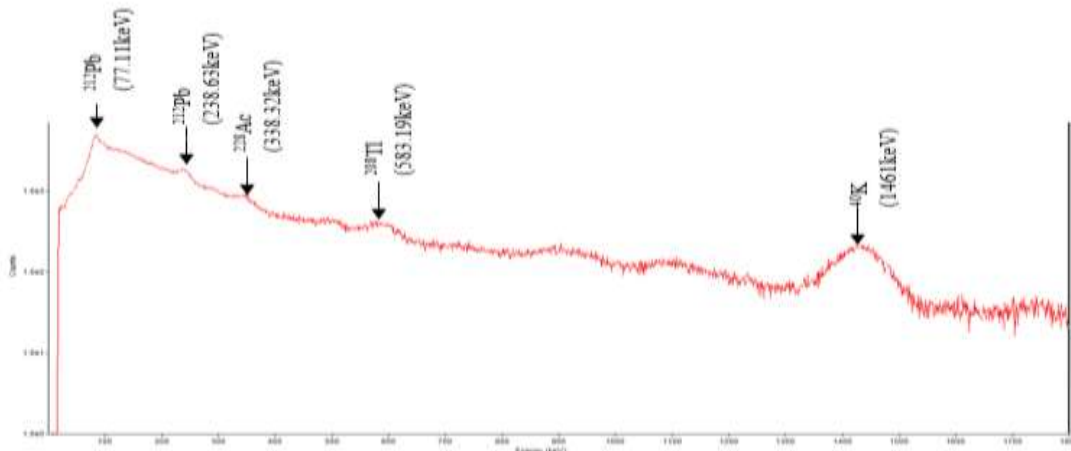


Figure 10 The energy spectrum of the soil sample 4

Acknowledgement

Author also thanks to Professor Dr Sandar Maung, Head of Department of Physics, University of Magway for her permission, and valuable discussion. Author gratefully acknowledges to Professor Dr Nay Win Oo, Department of Physics, University of Mandalay, for his patience, kindness, excellent advice and continuous guidance throughout this research work. Author deeply thanks to Dr Aye Aye Myint, Associate Professor, Department of Physics, Kyaukse University for her excellent advice, kindness and valuable discussion throughout this research.

References

- A.Faanu, (2011) “West African Journal of Applied Ecology”, Vol.19, pp 45
- G.Shanthi, at al, (2010) “ Radiation Production Dosimetry”, Vol.141, No.1, pp 91
- Hamamatsu, (2017) “Photomultiplier Tubes, Basics and Applications”, Fourth Edition, pp 159
- J.Fundam.Concepts, (2006) <https://extension.illinois.edu/soil/concepts/concepts>.
- S.Breur, (2013) “ The performance of NaI (Tl) scintillation detectors”.

INVESTIGATION ON SHIELDING PROPERTIES OF SOME COMPOSITE MATERIALS BY USING NAI(Tl) DETECTOR

Win Mar¹

Abstract

The high-density composite materials have similar behavior of heavy metals when increasing the proportion of material supported in composite material. In other word measure and determination for the amount of shielding required to provide personal protection on an environment with lowest costs and appropriate selecting materials to reduce radiation doses in industrial facilities and surrounding areas. In this research, the numerical buildup factor and the linear attenuation coefficient were accounted as a function for the concentration of cement in shields with 25%, 50% and 75% of iron powder. The shield thickness of shielding composite materials that supported by these concentrations of iron in cement powders in the range of (5-40) mm was done. From the results, it is found that the better attenuation coefficient become in its each composite sample, the more iron concentration increased in cement. In this research, it is cleared that the most iron concentration in cement is the best shielding ability.

Keywords: *attenuation coefficient, buildup factor, composite materials, personal protection, shielding materials.*

Introduction

Ionizing radiation is known to be harmful to human health and heredity. In the field of radiation protection, the shielding materials protected from gamma radiation, such as concrete, lead, requires large block and then high cost. Various materials which are used for shielding include aluminum, iron, cement and organic compounds. The shields could take different like blocks, plates, rods, pellets etc. which can act as fillers for ducts, trenches and penetrations. At the present time it is an important need to improve new shielding materials and also to develop properties of the conventional shielding materials. So, the composite material helps to solve the problem of shielding, these composite materials have properties of multiple commensurate with many industrial applications. Shielding pellets are useful in areas that are irregular in shapes or inaccessible to personnel.

Relation between Buildup Factor, Gamma Attenuation and Mean Free Path

The mean free path is the distance that a molecule travels between collisions. In particle physics the concept of the mean free path is not commonly used, being replaced by the similar concept of attenuation length. In particular, for high-energy photons, which mostly interact by electron-positron pair production, the radiation length is used much like the mean free path in radiography.

When a narrow parallel of photons passes through relatively thin shield as shown in Figure (1), the relative intensity of mono-energetic photons transmitted without interaction through a shield of thickness is:

$$\frac{I}{I_0} = e^{-\mu x} \quad (1)$$

Where I and I_0 are the shielded and initial beam intensities, respectively, μ is the linear attenuation coefficient (in cm^{-1}), and x is the shield thickness (in cm). Ideally, the beam should be well

¹ Associate Professor, Department of Physics, Meiktila University.

collimated, and the source should be as far away as possible from the detector. The absorber should be midway between the source and the detector, and it should be thin enough so that the likelihood of a second interaction between a photon already scattered by the absorber and the absorber is negligible. In addition, there should be no scattering material in the vicinity of the detector.

The linear attenuation coefficient can be considered as the fraction of photons that interact with the shielding medium per centimeter of shielding. It is also known as narrow beam conditions because the source and detector are assumed to be collimated and the measurement made at a short distance.

If the incident beam is broad as shown in Figure (2), then the measured intensity will be greater than that described by equation (1), because scattered photons will also be detected. Such conditions usually apply to the shields required for protection from gamma ray source. The increased transmission of photon intensity over the measured in good geometry can be taken into account.

$$\frac{I}{I_0} = B e^{-\mu x} \quad (2)$$

where B is the buildup factor for one energy at the shield thickness x.

This formula attempts to estimate the correct number of scattered photons that reach the detector (closest estimate) by using a correction factor to add in the Compton scatter and pair production photons that are ignored by the linear attenuation coefficient formula. Therefore, the value of B can be obtained by dividing equation (2) by equation (1).

The absorbance ratio (R_A) for radiation inside the material shield by the following form

$$R_A = e^{\mu x} \quad (3)$$

Where $R_A = \left(\frac{I_0}{I}\right)$

The above equation shows that the relationship absorbance ratio (R_A) to thickness of the material shield or absorbent is exponential, so this relationship can be converted to a linear relationship as in the following form:

$$\ln R_A = \mu x \quad (4)$$

The recent equation can be used to calculate the linear attenuation coefficient, which represents the slope of straight line of the relationship between (x) and ($\ln R_A$), i.e. μ =slope.

In addition to, we can be calculation standard of statistical deviation and fractional statistical deviation from follow:

$$S.D = B \left[\left(\frac{1}{I_g} \right) + \left(\frac{1}{I_{ob}} \right) \right]^{1/2} \quad (5)$$

$$F.S.D = \left[\left(\frac{1}{I_g} \right) + \left(\frac{1}{I_{ob}} \right) \right]^{1/2} \times 100\% \quad (6)$$

Where:

S.D = Standard of statistical deviation

F.S.D = Fractional statistical deviation

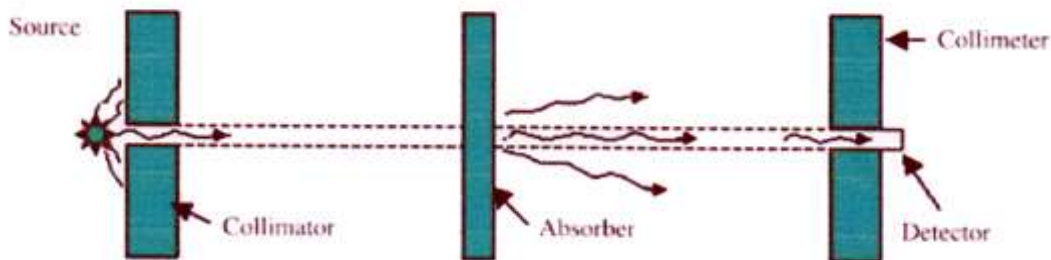


Figure 1 Measurement of the attenuation of gamma radiation under conditions of good (collimated) geometry.

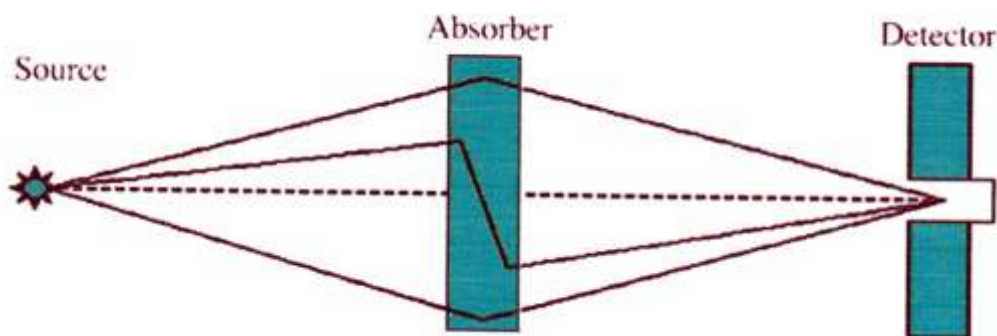


Figure 2 Gamma radiation attenuation under conditions of bad (broad beam) geometry showing the effect of photons scattered into the detector

Source for Gamma Rays

In the present work, gamma-ray source Cs-137 forms gamma disc shape from Nuclear Lab in University of Yangon is chosen. Cs-137 has one energy. It has an activity of $5 \mu\text{Ci}$, half-life is 30.17 years and energy of the source is 0.662 MeV.

Equipment

In the present work, the equipment used in gamma ray spectrometry were described as:

- (1) Thallium Activated Sodium Iodide detector (Model 802-5)
- (2) High Voltage Power Supply (Model 3002)
- (3) ST-360 Radiation Counter with Windows (Model ST- 360)

Sample Collection, Sample Preparation and Elemental Analysis

Iron powder was collected from Myanmar Supply Co., Ltd in Yangon Division. The brand of cement that used in this research was Double Rhinos cement.

Cement powder was poured into the mold and pressed with hydraulic press, weighting 5 tons into pellets. Each pellet has a thickness of 0.5 cm and 2.5 cm diameter. The above procedure was repeated for the mixture of iron (25-75%) in cement powder. These four types of sample preparation were performed at University Research Centre (URC) in University of Yangon.

The elemental analysis was done on cement powder and iron powder by using EDXRF method. The chemical compositions for iron powder and cement were shown in Table (1) and Table (2). The elemental analysis of these samples by EDXRF method was performed at Department of Chemistry in Monywa University.

Table 1 Chemical Composition for Iron

Mineral	Fe ₂ O ₃	CaO
Percent	99.872	0.128

Table 2 Chemical Composition for Cement

Mineral	CaO	SiO ₂	Fe ₂ O ₃	SO ₃	K ₂ O	TiO ₂	MnO	SrO	CuO	ZrO ₂	V ₂ O ₅	ZrO	NiO
Percent	78.277	12.188	5.133	2.758	1.183	0.313	0.076	0.067	0.024	0.018	0.018	0.014	0.002

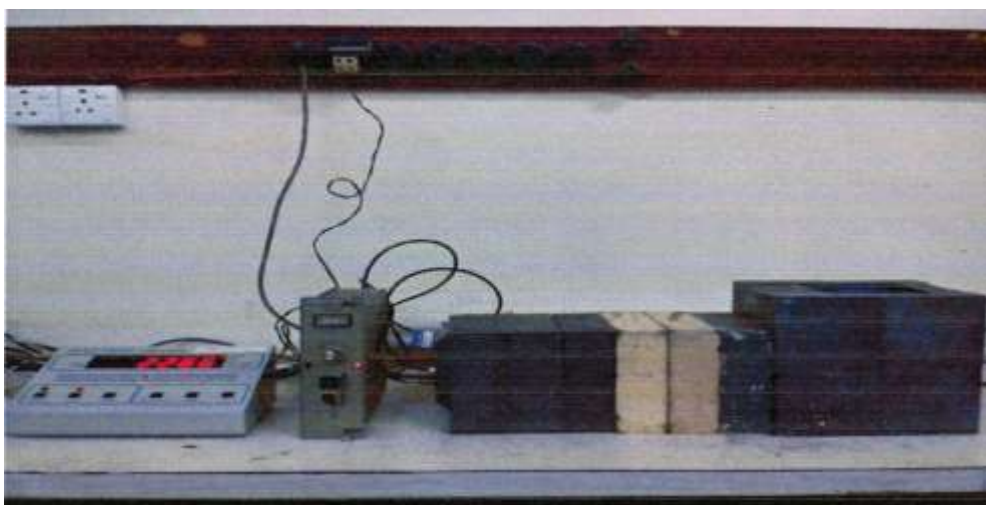


Figure 3 The operating system of NaI (Tl) detector and ST-360 radiation counter with high voltage power supply in the form of narrow beam (good geometry)

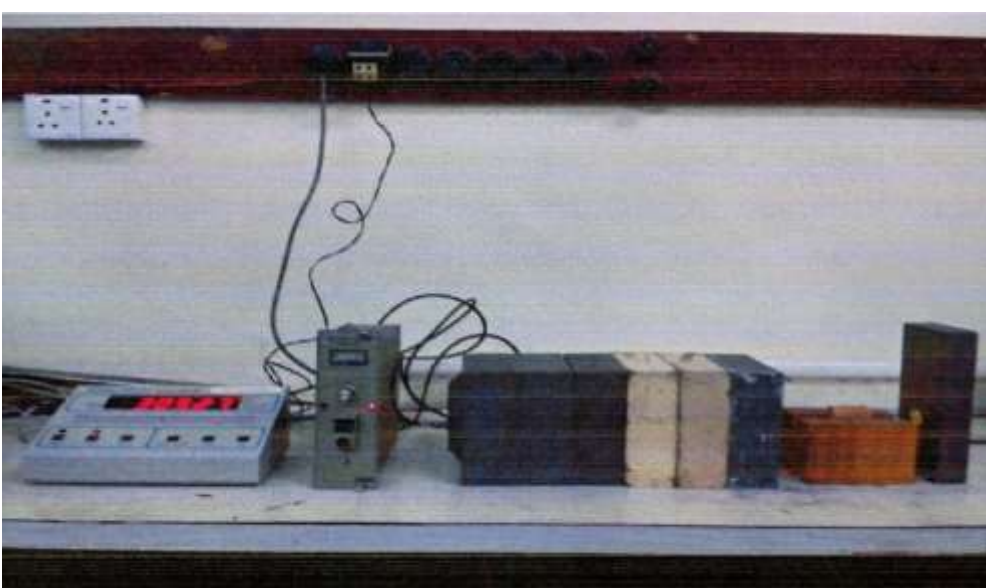


Figure 4 The operating system of NaI (Tl) detector and ST-360 radiation counter with high voltage power supply in the form of broad beam (bad geometry)

Experimental Setup and Procedure

The materials which used as absorbers are cement and composite slabs. These pellets of cement as composite materials were placed midway position between the source and detector. The detector was placed horizontally and the distance between the source and detector was 20cm. The Cs-137 source was fixed in the lead shield.

The sample was positioned on the wood stand for broad beam (bad geometry) as shown in Figure (4). The sample was positioned between two collimators beside source collimator and detector collimator for narrow beam (good geometry). Two lead blocks with 5mm diameter holes were used as collimators as shown in Figure (3).

The two collimators were aligned by passing through a steel rod. Then the alignment is checked by laser beam. The alignment shown the above Figure (3) was estimated to be accurate to within ± 0.5 mm.

First the gamma intensity I_{bad} (in the absence of the shield sample, without collimator) and I_{good} (in the absence of the shield sample, with collimator) were measured by the detector. Then, the sample position was placed at the centre of the source and detector for both bad (uncollimated) and good (collimated) geometry. The detector was located forward direction of the gamma beam. Measurements were made with different thickness for both bad (uncollimated) and good (collimated) geometry. Then, the sample was fixed 10cm from the detector and measured using above procedures were repeated, shown in Figures (3) and (4).

The transmitted gamma counts collections were done for 60s. Detector working voltage is 900 V (positive bias). For each thickness, the gamma intensity reaching the detector was measured and the results obtained were recorded.

Results

From the experiment, the intensity without absorber and with absorbers in broad beam and narrow beam geometry of different thickness for 25% concentration of iron powder in cement composite samples are recorded in Table (3). And then, the above procedure also done for 50% concentration of iron powder in cement composite samples, 75% concentration of iron powder in cement composite samples and 0% concentration of iron in cement samples, and are also recorded in Table (4), (5) and (6).

The buildup factor and the logarithm of the absorbance ratio ($\ln R_A$) for 25% concentration of iron in cement composite samples are calculated by using equation (1), (2) and (3). After that, the results are recorded in Table (3). The buildup factor and the logarithm of the absorbance ratio for 50% concentration of iron in cement composite samples, 75% concentration of iron in cement composite samples and 0% concentration of iron in cement samples are also calculated by using equation (1), (2) and (3) and also recorded in Table (4), (5) and (6).

It is found that, as the composite sample thickness increases the buildup factor will be increase accordingly with increasing the iron concentration in cement. Figure (5), (6), (7) and (8) show the logarithm of absorbance ratio versus the different thickness of 25% concentration of iron, 50% concentration of iron, 75% concentration of iron in cement composite samples and 0% concentration of iron in cement samples.

From the linear graph in each figure, the linear attenuation coefficients are obtained 0.15 cm^{-1} for 25% concentration of iron, 0.19 cm^{-1} for 50% concentration of iron, 0.24 cm^{-1} for 75% concentration of iron in cement composite samples and 0.11 cm^{-1} for 0% concentration of

iron in cement samples. The relation between linear attenuation coefficient (μ) and the different iron concentration in cement as shown in Figure (9).

It is cleared that, the highest concentration of iron in cement composite sample has the greatest attenuation coefficient for gamma ray while the lowest concentration of iron in cement sample having the smallest. From Table (1) and Table (2), iron powder consist mainly ironer and cement consist second more silica. The ionic silica bonds absorbed gamma ray energy more than other bonds.

Therefore, a composite sample of highest iron concentration would have highest attenuation coefficient, this implies a best absorber of gamma radiation in this research work. The determination of error associated with the measurement is a very important task. It is probably as important as the measurement. So, to reduce the error in the research work, the standard of statistical deviation (S.D) and fractional statistical deviation (F.S.D) for different thickness of each samples are calculated by using equation (5) and (6). The calculated values are recorded in Table (3), (4), (5) and (6).

Discussion

Gamma ray which is used widely in medical care, electricity generation and industry, it's the most penetrating of ionizing radiation that is known to be harmful to human health. Although, high density materials like lead are used to protect life from gamma hazardous radiation, it is toxic and heavy. Therefore, materials which are nontoxic and lighter shield should be used with personal. From the results, it is cleared that the minimum attenuation of gamma ray is with the cement sample which has 0% concentration of iron, while the attenuation amount of the composite sample is higher because it contains increasing concentration of iron. The composite sample which contains 50% concentration of iron powder increase more of gamma-ray attenuation where it was found by compared with other 25% concentration of iron powder in cement composite samples. Finally, a greater attenuation was noticed as the composite sample was loaded with 75% concentration in cement. From the research, it is found that the linear attenuation of the composites was found to increase with increased concentration content in the composite and the highest value was for most concentration of elemental in cement.

Table 3 Absorbance ratio (R_A), buildup factor (B), standard of statistical deviation (S.D) and fractional statistical deviation (F.S.D) values for 25% concentration of iron powder in cement

Sr. No.	Thickness of the shield (cm)	I _b	I _g	ln R _A	buildup factor (B)	S. D \pm	FSD %
1	0	65257	6441	0	1	0.0131	1.3061
2	0.5	46713	6050	0.0626	1.0121	0.0134	1.3439
3	1.0	43457	5700	0.1222	1.0136	0.0139	1.3812
4	1.5	40158	5400	0.1763	1.0198	0.0144	1.4160
5	2.0	37567	5050	0.2433	1.0245	0.0149	1.4606
6	2.5	34894	5000	0.2532	1.0280	0.0151	1.4674
7	3.0	33659	4500	0.3586	1.0319	0.0159	1.5413
8	3.5	31248	4250	0.4158	1.0386	0.0164	1.5831
9	4.0	30670	4000	0.4764	1.0415	0.0169	1.6289

Table 4 Absorbance ratio (R_A), buildup factor (B), standard of statistical deviation (S.D) and fractional statistical deviation (F.S.D) values for 50% concentration of iron powder in cement

Sr No.	thickness of the shield (cm)	I_b	I_g	$\ln R_A$	buildup factor (B)	S. D \pm	FSD %
1	0	65257	6441	0	1	0.0131	1.3061
2	0.5	46213	6000	0.0709	1.0219	0.0138	1.3490
3	1.0	42957	5650	0.1310	1.0286	0.0143	1.3868
4	1.5	39658	5240	0.2064	1.0314	0.0148	1.4358
5	2.0	37067	4950	0.2633	1.0349	0.0153	1.4743
6	2.5	34394	4650	0.3258	1.0391	0.0158	1.5178
7	3.0	33159	4300	0.4041	1.0419	0.0164	1.5744
8	3.5	30748	4050	0.4639	1.0461	0.0169	1.6194
9	4.0	30170	3800	0.5277	1.0498	0.0175	1.6688

Table 5 Absorbance ratio (R_A), buildup factor (B), standard of statistical deviation (S.D) and fractional statistical deviation (F.S.D) values for 75% concentration of iron powder in cement

Sr. No.	thickness of the shield (cm)	I_b	I_g	$\ln R_A$	buildup factor (B)	S. D \pm	FSD %
1	0	65257	6441	0	1	0.0131	1.3061
2	0.5	45713	5950	0.0793	1.0311	0.0139	1.3542
3	1.0	42457	5550	0.1489	1.0347	0.0145	1.3982
4	1.5	39158	5100	0.2334	1.0386	0.0151	1.4539
5	2.0	36567	4600	0.3366	1.0398	0.0159	1.5255
6	2.5	33894	4450	0.3698	1.0410	0.0161	1.5493
7	3.0	32659	4100	0.4517	1.0438	0.0168	1.6101
8	3.5	30248	2830	0.5198	1.0468	0.0174	16626
9	4.0	29670	3500	0.6099	1.0511	0.0182	1.7350

Table 6 Absorbance ratio (R_A), buildup factor (B), standard of statistical deviation (S.D) and fractional statistical deviation (F.S.D) values for 0% concentration of iron in cement samples

Sr. No.	thickness of the shield (cm)	I_b	I_g	$\ln R_A$	buildup factor (B)	S. D \pm	FSD %
1	0	65257	6441	0	1	0.0131	1.3061
2	0.5	47889	6020	0.0676	1.2078	0.0172	1.3469
3	1.0	44881	5600	0.1399	1.2191	0.0176	1.3925
4	1.5	42165	5200	0.2140	1.2293	0.0180	1.4409
5	2.0	39542	4850	0.2837	1.2371	0.0185	1.4883
6	2.5	36710	4550	0.3476	1.2454	0.0193	1.5333
7	3.0	34576	4250	0.4158	1.2558	0.0197	1.5831
8	3.5	32564	3950	0.4889	1.2631	0.0201	1.6386
9	4.0	30617	3650	0.5679	1.2661	0.0205	1.7009

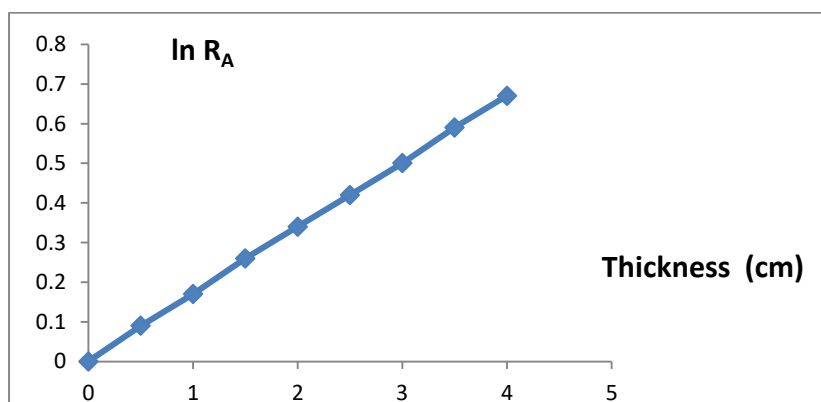


Figure 5 Logarithm of the absorbance ratio (intensity) versus different thickness of 25% concentration of iron in cement composite samples for good (collimated) geometry

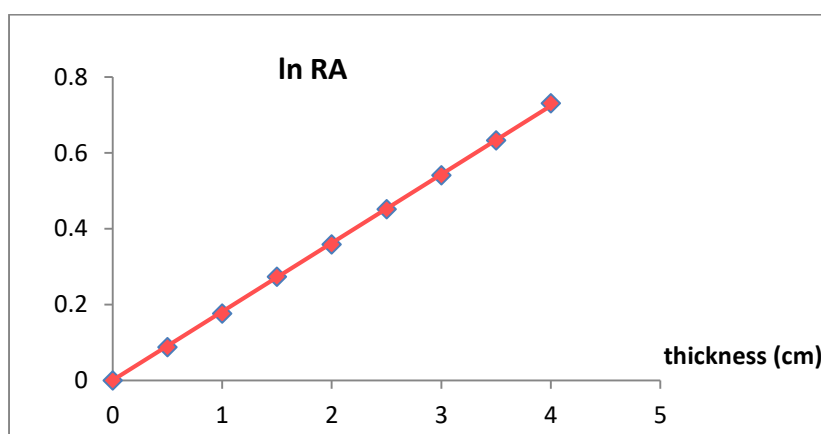


Figure 6 Logarithm of the absorbance ratio (intensity) versus different thickness of 50% concentration of iron in cement composite samples for good (collimated) geometry

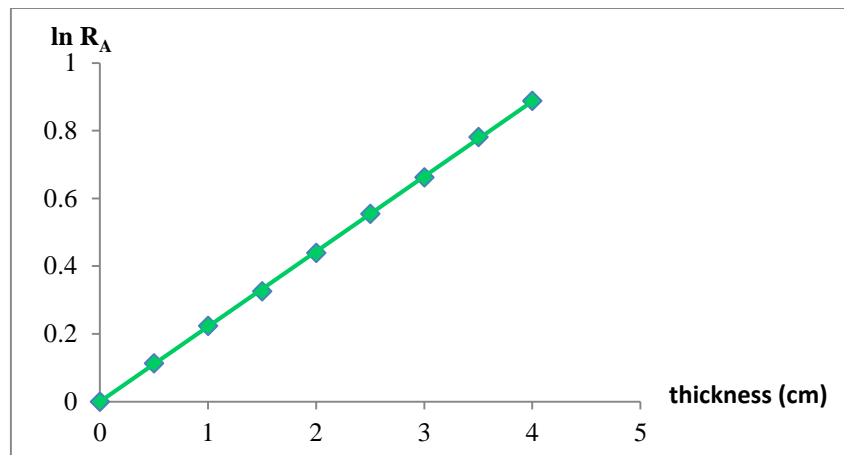


Figure 7 Logarithm of the absorbance ratio (intensity) versus different thickness of 75% concentration of iron in cement composite samples for good (collimated) geometry

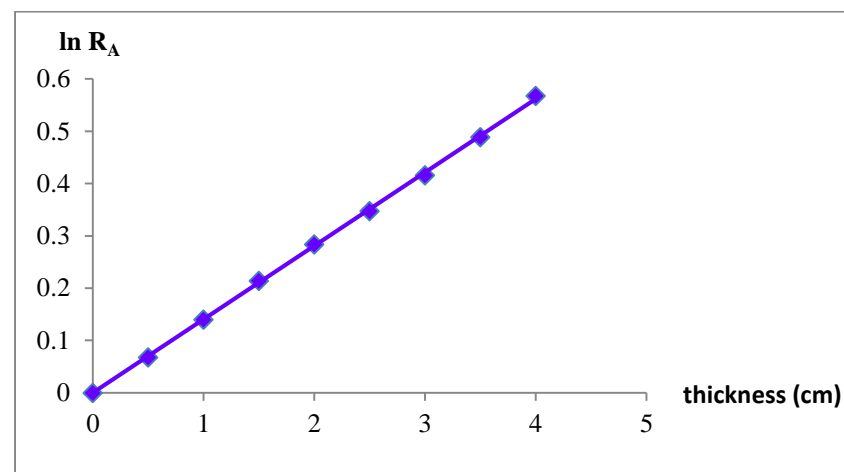


Figure 8 Logarithm of the absorbance ratio (intensity) versus different thickness of 0% concentration of iron in cement composite samples for good (collimated) geometry

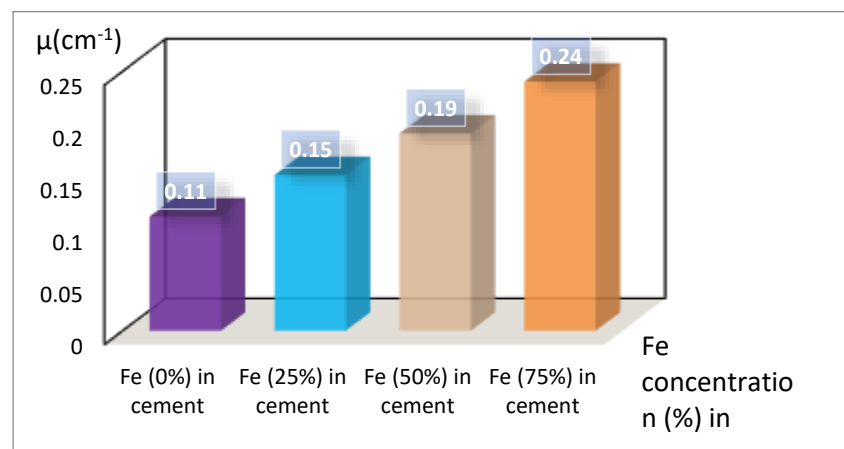


Figure 9 Relation between linear attenuation coefficient (μ) and iron powder concentration in cement

Conclusion

Materials which are environment friendly and nontoxic can be used with both personal and material lighter shield. So, composite material filled with elemental powder is now becoming more and more popular. The linear attenuation coefficient has been measured and calculated for composite samples for its use in radiation shielding, protection, and cancer treatment. The gamma rays photon beam (Cs-137 source) was used in the experimental work. It is found that the linear attenuation coefficient increases with increasing concentration of composite sample. So, composite material filled with highest concentration of iron elemental powder should be used as gamma shield.

Acknowledgement

The author would like to express my gratitude to Ministry of Education, the department of Higher education in Myanmar, University of Yangon, and Universities' Research Centre (URC) for all necessary facilities.

References

- Chilton AB, JK Shultz and RE Faw: Principles of Radiation Shielding, Prentice-Hall Inc N Jersey, 1984.
Cember H., (1990) Introduction to Health Physics. New York: Pergamon Press.
Knoll G. F, Radiation Detection and Measurement.3rd Edition. New York: John Wiley & Sons, 2000. P-48-55.
Turner J.E., (2007) "Atoms, Radiation and Radiation Protection", Wiley-VCH Verlag GmbH & Co.KGaA.

OBSERVATION OF A SINGLE-STRANGENESS HYPERNUCLEUS EVENT IN KEK-PS E 373 EXPERIMENT

Chan Myae Aung¹

Abstract

A single- Λ hypernucleus event is kinematically analyzed in this research paper. The analyzed event was observed in KEK-PS E373 experiment. In this research work, a single- Λ hypernucleus was produced by the direct process of hypernuclei studies. From the experimental studies, ranges of tracks #1, #2, #3, #4 and #5 are $40.10 \pm 0.30 \mu\text{m}$, $414.93 \pm 0.48 \mu\text{m}$, $9.11 \pm 0.03 \mu\text{m}$, $9.47 \pm 0.15 \mu\text{m}$ and $10800.90 \pm 0.00 \mu\text{m}$. By using these ranges, Q-value, total kinetic energy, reconstructed mass and mass difference are calculated. We checked conservation laws so that 167 decay modes are obtained. All negative Q-values are neglected as the first step of our analysis. Furthermore, comparison of Q-value and visible energy released are performed and then mass of single- Λ hypernucleus is calculated. Finally, we have obtained 13 decay modes. According to our calculated results, only two decay modes, ${}^6_{\Lambda}\text{Li} \rightarrow p + {}^4_2\text{He} + p + \pi^-$ and ${}^6_{\Lambda}\text{Li} \rightarrow p + p + {}^4_2\text{He} + \pi^-$ are possible with the same single-strangeness hypernucleus. Due to the percentage of mass difference, ${}^6_{\Lambda}\text{Li} \rightarrow p + p + {}^4_2\text{He} + \pi^-$ is more acceptable between the most possible two decay modes. Q-value and total kinetic energy or visible energy released of ${}^6_{\Lambda}\text{Li}$ are $35.27 \pm 0.00 \text{ MeV}$ and $35.25 \pm 0.06 \text{ MeV}$. The mass difference of the single- Λ hypernucleus is $0.019 \text{ MeV}/c^2$. According to our calculating results, a single- Λ hypernucleus was identified as a ${}^6_{\Lambda}\text{Li}$ hypernucleus.

Keywords: Single-strangeness, Single- Λ hypernucleus, nuclear emulsion, relativistic kinematics, range-energy relation

Introduction

Strangeness nuclear physics introduces “strangeness” quantum number into nuclear systems. In 1953, Gell-Mann, Nakano and Nishijima introduced a strangeness quantum number conserved under the strong interaction in order to explain the behaviour of the strange particles. Almost simultaneously the first strange hypernucleus event formed by a Λ hyperon bound to a nuclear fragment was observed by Danysz and Pniewski in nuclear emulsions exposed to cosmic rays.

Hyperons or strange particles are special class of baryons heavier than nucleons and consisting one or more strange quarks. A Λ hyperon consists of one up quark “u”, one down quark “d” and one strange quark “s”. So, the nuclear system which contains a Λ hyperon is called the single-strangeness hypernuclear system. Hyperons have the life time of the order of 10^{-10} s and they decay weakly while their formation time is in the order of 10^{-23} s which is typical for strong interaction. Their decay time is very much greater than that of their formation. Because of this strange property, the hyperons along with the K mesons are called strange particles. Being baryons, all hyperons are fermions. That is, they have half-integer spin and obey Fermi-Dirac statistics.

According to the recent data of Particle Data Group (PDG), the hyperons are classified into four main groups such as lambda (Λ), sigma (Σ), Xi (Ξ), omega (Ω). In the family of hyperons, Λ particle is the lightest particle, and it can stay in contact with nucleons inside nuclei and form hypernuclei. It carry zero charge and its mass is $1115.683 \pm 0.006 \text{ MeV}$. It can stay in contact with protons and neutrons because its mass is nearly equal to that of protons and neutrons. Hypernuclei are produced by two processes in nuclear emulsion. One is the direct production of Λ hyperon(s)

¹ Ph.D Candidate, Department of Physics, Defence Services Academy

and another process is the production of Λ hyperon via the Ξ^- atom. Λ hyperons are directly produced when K^- is bombarded the proton or Ξ^- atom. But, the production of Λ hyperon via the Ξ^- atom, when K^- is bombarded the proton of target nucleus, Ξ^- hyperon is emitted. Λ hyperon is produced from the decay of the emitted Ξ^- hyperon. In this research work, the analyzed single- Λ hypernucleus event was produced by the direct process called the direct production of Λ hyperons. The analyzed event was observed in KEK-PS E373 experiment.

Strangeness nuclear physics extends our knowledge on nuclear and hadron many-body system regarding hypernuclei, hyperon-nucleons systems and hyperon-hyperon systems. Hypernuclei studies are performed with the aim of investigating the hyperon-nucleon (Y-N) and hyperon-hyperon (Y-Y) interactions in theoretical approach. Otherwise, it is to understand the baron-baron (B-B) interactions in a uniform way. The nucleon-nucleon (N-N) interaction (nuclear force) is phenomenologically well known, but the physical understanding of the N-N interaction has not been achieved yet.

Baryon-baryon (B-B) interaction was expected to extend the nuclear force by adding the strangeness quantum number. For the experimental approach, nuclei with strangeness can be plotted in the three-dimensional nuclear chart. The knowledge of the (Y-N) and (Y-Y) interactions is essential to understand high-density nuclear matter in neutron stars where strangeness is expected to appear.

KEK-PS E373 Experiment

Experimental Procedure

The hybrid-emulsion experiment KEK-PS E373 was performed using a 1.66 GeV/c K^- beam at the K2 beam line of the proton synchrotron facility at KEK. In this experiment, (K^-, K^+) reactions were identified by a beam-line spectrometer for incoming K^- particles and a KURAMA spectrometer for outgoing K^+ . Ξ^- hyperons which were produced from the quasi-free p (K^-, K^+) Ξ^- reaction were detected by a scintillating microfiber bundle detector (SciFi-Bundle), and then entered a stack of emulsion plates. This experiment was designed to observe ten times more stopping Ξ^- hyperons in the emulsion than the previous experiment KEK-PS E176. To optimize the stopping rate in the emulsion, density of the target material should be high to decelerate the Ξ^- hyperons in the target and size of the target should be also optimized. An emulsion stack consisted of a thin emulsion plate located upstream followed by eleven thick emulsion plates. The thin plate had 70 μm thickness emulsion gel on both sides of a 200 μm thickness emulsion acrylic base film, and each thick plate had 500 μm thickness emulsion gel on both sides of a 500 μm thickness acrylic film. The schematic diagram of the experimental setup of KEK-PS E373 is shown in figure 2.

The positions and angles of the Ξ^- hyperons at the surface of the first emulsion thin plate were provided. The tracks of Ξ^- hyperons detected with the SciFi-Bundle detector which was sandwiched between the diamond target and the emulsion stack measured the position and angle of each Ξ^- hyperons were identified under a microscope, and then followed the tracks to their end points in the nuclear emulsion thin plate. The production of a double- Λ hypernucleus and its decay were searched for around the end points. Scintillating fiber (SciFi) detector, U-Block and D-block, were placed both upstream and downstream of the emulsion stack.

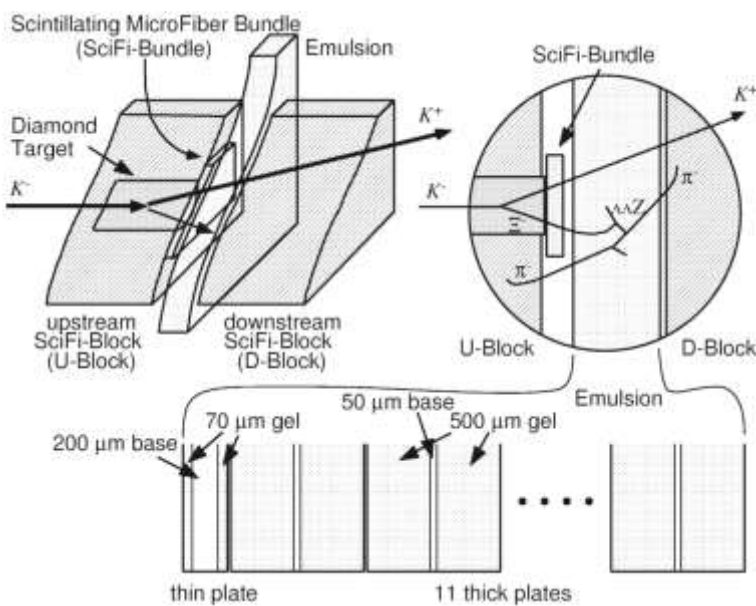


Figure 1 Schematic view of the experimental set-up of KEK-PS E373 experiment

Present Research of Single- Λ Hypernucleus Event

The analyzed event is detected in nuclear emulsion of KEE-PS E373 experiment. Nuclear emulsion is a three dimensional photographic plate and can be recorded as a photograph in which the tracks of charged particles are taken photographs. The analyzed event is identified as a single- Λ hypernucleus event which has a ${}^6_{\Lambda}\text{Li}$ hypernucleus and its decay species of protons, helium and pi-minus meson.

Aim

The analyzed event is performed with the aims of supporting for theoretical and experimental studies. Our analysis supports the nuclear forces (B-B interactions) for theoretical approach and extension of 3-D nuclear chart for experimental studies.

Overall Scanning Method

In the previous method, hybrid emulsion method, the number of double hypernuclei strongly depends on the detection efficiency of K^+ mesons by KURAMA spectrometer system. The overall scanning method is well known that the topology with three vertices is shown at the production and decay of double hypernuclei. The aim of intending to use the overall scanning method is to obtain ten times more double hypernuclei than that by hybrid emulsion method. Ξ^- hyperons are also produced via some other process such as $n(K^-, K^0)\Xi^-$, where K^0 mesons are not tagged by KURAMA spectrometer.

The overall scanning system was developed with fast image taking of the emulsion in the whole area and image processing to search for three vertices. In this system consists of an objective lens ($\times 50$) and a CCD camera (100Hz), where the image size is $120 \times 100 \mu\text{m}^2$. Four million images were taken in the emulsion of the KEK-PS E373 experiment, and then the events with at least one vertex were searched. When this system was developed, 1000 times faster scanning speed than that of the previous system was obtained. The α decay vertices of uranium and thorium series for calibration of the range-energy relation were detected by a new method, called overall scanning of the full emulsion volume. During test operations of this method, a twin single-hypernuclei event

was found among about 8 million pictures taken in a volume of 1.46 cm^3 emulsion exposed in the KEK-PS E373 experiment. By using this method, the KISO event was found in this experiment.

Event Description

The analyzed event is observed in KEK-PS E373 experiment. In the analyzed event, a Λ hyperon is produced by the direct process of beam interaction. A single- Λ hypernucleus (track #1) is produced at production point A and four charged particles (tracks #2, #3, #4 and #5) are emitted from the decay of single- Λ hypernucleus #1 at point B. This event has two vertex points; "A" which is the production vertex of track #1 and "B" which is the decay vertex of it. Therefore, the particle of track #1 can be identified as single- Λ hypernucleus. The photograph and schematic diagram are shown in figure 2.

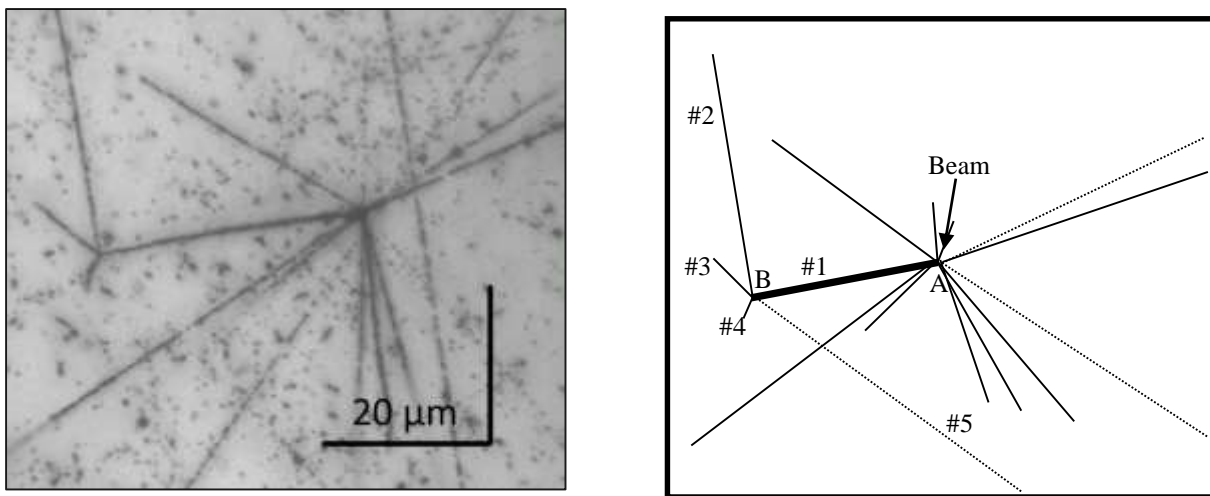


Figure 2 Photograph and Schematic diagram of analyzed single- Λ hypernucleus event

According to experimental results, ranges and position angles of single- Λ hypernucleus and its decay species are summarized in table 1.

Table 1 Ranges and position angles of tracks #1, #2, #3, #4 and #5

Track (#)	Range (μm)	θ (degree)	ϕ (degree)
#1	40.10 ± 0.30	52.69 ± 3.09	97.91 ± 2.61
#2	414.93 ± 0.48	111.28 ± 4.70	189.19 ± 5.12
#3	9.11 ± 0.03	76.71 ± 1.82	232.51 ± 4.30
#4	9.47 ± 0.15	321.25 ± 2.70	121.03 ± 4.31
#5	>10800.90	67.19 ± 4.71	43.29 ± 2.11

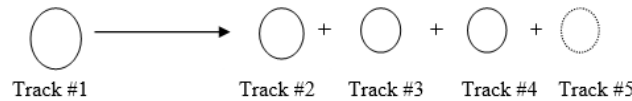
Choosing Possible Decay Modes

To choose the possible decay mode, we firstly checked the conservation laws which are charge, baryon number, lepton number and strangeness number. Moreover, mesonic or non-mesonic decay have to be considered. According to grain density and ionization measurements of experimental results, charged particle track #5 is a pi-minus meson. Therefore, non-mesonic decay was not considered at decay point B. According to visible structure and decay topology of the analyzed single- Λ hypernucleus event, a single- Λ hypernucleus (#1) decayed into only four charged particles (#2, #3, #4 and #5). After checking the conservation laws, 167 decay modes of all possible decay modes are obtained with pi-minus meson emission.

Track #1 → charged particles (#2, #3 and #4) + pi-minus meson (1)

Calculation of Q-value, Visible Energy and Kinetic Energy of Decay Pro of Single- Λ Hypernucleus

The Q-value of the reaction is defined as the difference between the sum of the masses of the initial and final states.



$$Q \text{ (MeV)} = [M(\text{track } \#1) - \{M(\text{track } \#2) + M(\text{track } \#3) + M(\text{track } \#4) + M(\text{track } \#5)\}]c^2 \quad (2)$$

At decay point B, Q-values of all possible decay modes are calculated. If Q-value is positive, the reaction is energetically possible. This reaction can be called exoergic reaction. If Q-value is negative, the reaction is not energetically possible. This reaction can be called endoergic reaction. First of particle identification steps, all negative Q-values are rejected from 167 decay modes. Only 12 decay modes of all possible decay modes are neglected because of negative Q-values. So, we have to consider only 155 decay modes which are positive Q-values to analyze our research work. In this research paper, visible energy released of 155 decay modes are calculated by using equation 3. The visible energy released is the sum of kinetic energies of emitted charged particles.

$$E_{\text{vis}} = KE(\text{track } \#2) + KE(\text{track } \#3) + KE(\text{track } \#4) + KE(\text{track } \#5) \quad (3)$$

Table 2 Kinetic energy of single- Λ hypernuclei and emitted charged particles

No	Decay Mode					KE of Charged Particles				
	Track #1	Track #2	Track #3	Track #4	Track #5	Track #1	Track #2	Track #3	Track #4	Track #5
1	${}^4_\Lambda\text{He}$	d	p	p	π^-	3.180	10.818	0.734	0.754	23.647
2	${}^4_\Lambda\text{He}$	p	d	p	π^-	3.180	8.173	0.883	0.754	23.647
3	${}^4_\Lambda\text{He}$	p	p	d	π^-	3.180	8.173	0.734	0.910	23.647
4	${}^6_\Lambda\text{Li}$	p	${}^4_2\text{He}$	p	π^-	3.553	8.173	2.613	0.754	23.647
5	${}^6_\Lambda\text{Li}$	p	p	${}^4_2\text{He}$	π^-	3.553	8.173	0.734	2.699	23.647
6	${}^7_\Lambda\text{Li}$	d	${}^4_2\text{He}$	p	π^-	3.696	10.818	2.613	0.754	23.647
7	${}^7_\Lambda\text{Li}$	d	p	${}^4_2\text{He}$	π^-	3.696	10.818	0.734	2.699	23.647
8	${}^7_\Lambda\text{Li}$	p	${}^4_2\text{He}$	d	π^-	3.696	8.173	2.613	0.910	23.647
9	${}^7_\Lambda\text{Li}$	p	d	${}^4_2\text{He}$	π^-	3.696	8.173	0.883	2.699	23.647
10	${}^8_\Lambda\text{Li}$	p	t	${}^4_2\text{He}$	π^-	3.818	8.173	0.959	2.699	23.647
11	${}^8_\Lambda\text{Li}$	p	${}^4_2\text{He}$	t	π^-	3.818	8.173	2.613	0.991	23.647
12	${}^8_\Lambda\text{Be}$	p	${}^3_2\text{He}$	${}^4_2\text{He}$	π^-	3.818	8.173	2.474	2.699	23.647
13	${}^8_\Lambda\text{Be}$	p	${}^4_2\text{He}$	${}^3_2\text{He}$	π^-	3.818	8.173	2.613	2.550	23.647

Kinetic energy of decay products of single- Λ hypernucleus is obtained by using range-energy software package. For example, Kinetic energies of charged particles are obtained by using the range-energy software package as presented in table 2.

Table 3 The Most Possible Mesonic decay modes with Q-value and E_{vis} comparison

No.	Decay mode	Q-value (MeV)	E _{vis} (MeV)
1	${}^4_{\Lambda}\text{He} \rightarrow d + p + p + \pi^-$	29.887±0.058	35.953±0.025
2	${}^4_{\Lambda}\text{He} \rightarrow p + d + p + \pi^-$	29.887±0.058	33.457±0.024
3	${}^4_{\Lambda}\text{He} \rightarrow p + p + d + \pi^-$	29.887±0.058	33.464±0.026
4	${}^6_{\Lambda}\text{Li} \rightarrow p + {}^4_2\text{He} + p + \pi^-$	35.272±0.000	35.187±0.030
5	${}^6_{\Lambda}\text{Li} \rightarrow p + p + {}^4_2\text{He} + \pi^-$	35.272±0.000	35.253±0.061
6	${}^7_{\Lambda}\text{Li} \rightarrow d + {}^4_2\text{He} + p + \pi^-$	30.272±0.058	37.832±0.033
7	${}^7_{\Lambda}\text{Li} \rightarrow d + p + {}^4_2\text{He} + \pi^-$	30.272±0.058	37.898±0.063
8	${}^7_{\Lambda}\text{Li} \rightarrow p + {}^4_2\text{He} + d + \pi^-$	30.272±0.058	35.343±0.034
9	${}^7_{\Lambda}\text{Li} \rightarrow p + d + {}^4_2\text{He} + \pi^-$	30.272±0.058	35.402±0.062
10	${}^8_{\Lambda}\text{Li} \rightarrow p + t + {}^4_2\text{He} + \pi^-$	28.514±0.058	35.478±0.062
11	${}^8_{\Lambda}\text{Li} \rightarrow p + {}^4_2\text{He} + t + \pi^-$	28.514±0.058	35.424±0.036
12	${}^8_{\Lambda}\text{Be} \rightarrow p + {}^3_2\text{He} + {}^4_2\text{He} + \pi^-$	29.365±0.071	36.993±0.067
13	${}^8_{\Lambda}\text{Be} \rightarrow p + {}^4_2\text{He} + {}^3_2\text{He} + \pi^-$	29.365±0.071	36.983±0.063

To choose the most probable decay modes, the visible energy released (E_{vis}) must be calculated. The total kinetic energy of emitted charged particles, E_{vis}, should be comparable with Q-value of the selected decay mode.

Mass of Single- Λ Hypernucleus

The reconstruction of the analyzed event was performed at point B by comparing the calculated masses and known masses of single- Λ hypernuclei for all possible decay modes.

Table 4 Calculated masses and known experimental masses of analyzed single- Λ hypernuclei

No.	Decay Mode	Known Experimental Mass (#1) (MeV)	Calculated Mass (#1) (MeV)
1	${}_{\Lambda}^4\text{He} \rightarrow d + p + p + \pi^-$	3921.642±0.058	3927.708±0.025
2	${}_{\Lambda}^4\text{He} \rightarrow p + d + p + \pi^-$	3921.642±0.058	3925.212±0.024
3	${}_{\Lambda}^4\text{He} \rightarrow p + p + d + \pi^-$	3921.642±0.058	3925.219±0.026
4	${}_{\Lambda}^6\text{Li} \rightarrow p + {}_{\Lambda}^4\text{He} + p + \pi^-$	5778.807 ± 0.000	5778.722 ± 0.030
5	${}_{\Lambda}^6\text{Li} \rightarrow p + p + {}_{\Lambda}^4\text{He} + \pi^-$	5778.807 ± 0.000	5778.788 ± 0.061
6	${}_{\Lambda}^7\text{Li} \rightarrow d + {}_{\Lambda}^4\text{He} + p + \pi^-$	6711.61±0.058	6718.715±0.033
7	${}_{\Lambda}^7\text{Li} \rightarrow d + p + {}_{\Lambda}^4\text{He} + \pi^-$	6711.61±0.058	6718.781±0.063
8	${}_{\Lambda}^7\text{Li} \rightarrow p + {}_{\Lambda}^4\text{He} + d + \pi^-$	6711.61±0.058	6716.226±0.034
9	${}_{\Lambda}^7\text{Li} \rightarrow p + d + {}_{\Lambda}^4\text{He} + \pi^-$	6711.61±0.058	6716.285±0.062
10	${}_{\Lambda}^8\text{Li} \rightarrow p + t + {}_{\Lambda}^4\text{He} + \pi^-$	7642.712±0.058	7649.676±0.062
11	${}_{\Lambda}^8\text{Li} \rightarrow p + {}_{\Lambda}^4\text{He} + t + \pi^-$	7642.712±0.058	7649.622±0.036
12	${}_{\Lambda}^8\text{Be} \rightarrow p + {}_{\Lambda}^3\text{He} + {}_{\Lambda}^4\text{He} + \pi^-$	7643.023±0.071	7650.651±0.067
13	${}_{\Lambda}^8\text{Be} \rightarrow p + {}_{\Lambda}^4\text{He} + {}_{\Lambda}^3\text{He} + \pi^-$	7643.023±0.071	7650.641±0.063

We assumed that a single- Λ hypernucleus (track #1) at rest decays into charged particles. The mass of a single- Λ hypernucleus was calculated from kinetic energy values of its decay products.

In our calculation, the masses of single- Λ hypernuclei are also calculated and compared with known experimental masses of these hypernuclei by using the following formula.

$$M(\#1) = M(\#2) + M(\#3) + M(\#4) + M(\#5) + KE(\#2) + KE(\#3) + KE(\#4) + KE(\#5) \quad (4)$$

Identification of Single- Λ Hypernucleus

The analyzed event has been identified as a single- Λ hypernucleus according to decay topology and its visible structure. Then, Q-values of all possible decay modes are calculated and negative Q-values are neglected. From all decay modes, only positive Q-values are considered to identify the most possible decay modes. To do this, the main performances of identification are to compare the Q-value and visible energy released and to evaluate calculated mass of a single- Λ hypernucleus and known experimental mass of the accepted event.

After completing our analysis, 13 decay modes are acceptable among the 155 decay modes. But, only two decay modes, ${}_{\Lambda}^6\text{Li} \rightarrow p + {}_{\Lambda}^4\text{He} + p + \pi^-$ and ${}_{\Lambda}^6\text{Li} \rightarrow p + p + {}_{\Lambda}^4\text{He} + \pi^-$, are the most acceptable decay modes. Therefore, the other 142 decay modes are not comparable not only with Q-values and visible energy released but also with calculated mass and known experimental mass. The results of accepted decay modes are summarized in table 4.

Results and Discussions

Detecting with overall scanning method, the analyzed event which was observed in KEK-PS E 373 experiment has been identified as a single- Λ hypernucleus event according to decay topology. In this research paper, kinematical analysis based on relativity theory is performed. In this analyzed event, the beam line with momentum of 1.67 GeV/c was accelerated and charged particles are produced at point A including a single-strangeness hypernucleus in nuclear emulsion. Our analysis is started at point B because the analysis on a hypernucleus can be performed only if physical properties of decay products of a hypernucleus are studied by using the relativistic kinematic.

At point B, the single- Λ hypernucleus of track #1 decays into four charged particles tracks #2, #3, #4 and #5. The charged particle track #1 is identified as pi-minus meson according to ionization measurement and grain density observation. So, only the mesonic decay is considered and the non-mesonic decay is neglected.

Moreover, Q-values and visible energy released are compared. The comparable values and positive Q-values are accepted. Performing the kinematical analysis, only two decay modes, ${}^6_{\Lambda}\text{Li} \rightarrow p + {}^4_2\text{He} + p + \pi^-$ and ${}^6_{\Lambda}\text{Li} \rightarrow p + p + {}^4_2\text{He} + \pi^-$, are possible with the highest possibility. Finally, the decay mode of ${}^6_{\Lambda}\text{Li} \rightarrow p + p + {}^4_2\text{He} + \pi^-$ is accepted as the mass difference value on which the ΔM (%) value is 0.000329 is the smallest among the most possible decay modes.

If all charged particles are emitted as decay products, the calculated masses of single- Λ hypernucleus should be equal to known mass. If neutral particles exist in decay products, the calculated masses of single- Λ hypernucleus should be less than known mass. In our results, the calculated masses of the accepted decay modes are nearly equal to known experimental mass because only charged particles are emitted.

According to those assumptions, it is found that the possible species of single- Λ hypernuclei is ${}^6_{\Lambda}\text{Li}$ and the charged particle decay products are possible to be protons, helium and pi-minus meson. The values of mass differences are shown in table 5 illustrating with percentages.

Table 5 Mass differences and percentages for each decay mode

No.	Decay Mode	ΔM (MeV)	ΔM (%)	Remark
1	${}^4_{\Lambda}He \rightarrow d + p + p + \pi^-$	-6.066	-0.15468	Rejected
2	${}^4_{\Lambda}He \rightarrow p + d + p + \pi^-$	-3.57	-0.09103	Rejected
3	${}^4_{\Lambda}He \rightarrow p + p + d + \pi^-$	-3.577	-0.09121	Rejected
4	${}^6_{\Lambda}Li \rightarrow p + {}^4_2He + p + \pi^-$	0.085	0.001471	Rejected
5	${}^6_{\Lambda}Li \rightarrow p + p + {}^4_2He + \pi^-$	0.019	0.000329	Acceptable
6	${}^7_{\Lambda}Li \rightarrow d + {}^4_2He + p + \pi^-$	-7.105	-0.10586	Rejected
7	${}^7_{\Lambda}Li \rightarrow d + p + {}^4_2He + \pi^-$	-7.171	-0.10684	Rejected
8	${}^7_{\Lambda}Li \rightarrow p + {}^4_2He + d + \pi^-$	-4.616	-0.06878	Rejected
9	${}^7_{\Lambda}Li \rightarrow p + d + {}^4_2He + \pi^-$	-4.675	-0.06966	Rejected
8	${}^7_{\Lambda}Li \rightarrow p + {}^4_2He + d + \pi^-$	-4.616	-0.06878	Rejected
9	${}^7_{\Lambda}Li \rightarrow p + d + {}^4_2He + \pi^-$	-4.675	-0.06966	Rejected
10	${}^8_{\Lambda}Li \rightarrow p + t + {}^4_2He + \pi^-$	-6.964	-0.09112	Rejected
11	${}^8_{\Lambda}Li \rightarrow p + {}^4_2He + t + \pi^-$	-6.91	-0.09041	Rejected
12	${}^8_{\Lambda}Be \rightarrow p + {}^3_2He + {}^4_2He + \pi^-$	-7.628	-0.0998	Rejected
13	${}^8_{\Lambda}Be \rightarrow p + {}^4_2He + {}^3_2He + \pi^-$	-7.618	-0.09967	Rejected

Conclusion

A single-strangeness hypernucleus observed in KEK-PS E373 experiment is kinematically analyzed in this research work. In this analyzed event a single- Λ hypernucleus decays into four charged particles including pi-minus meson. According to our calculated results, Q-value and total kinetic energy or visible energy released of ${}^6_{\Lambda}Li$ are 35.27 ± 0.00 MeV and 35.25 ± 0.06 MeV and its calculated mass and known experimental mass of ${}^6_{\Lambda}Li$ are 5778.788MeV and 5778.807 MeV while the mass difference percent is 0.000329. According to those results, it is found that the possible species of single- Λ hypernuclei is ${}^6_{\Lambda}Li$ and the charged particle decay products are possible to be protons, helium and pi-minus meson.

Acknowledgements

The author would like to thank Lieutenant Colonel Saw Myint Oo, Dean of Faculty of Physics, Defence Services Academy for his encouragement and permission to complete this work. The author also would like to Dr Htaik Nandar Kyaw who is the Lecturer from Physics Department of Defence Services Academy for her support to perform hypernuclear identification research works. Finally, the author sincerely thanks to all collaborators of KEK-PS E373 experiment for their discussions, supports and valuable advices to carry out hypernuclear research.

References

- Ahn J.K., *et al.*, (2013), Physical Review **C88** (014003).
- Danysz M., and Pniewski J., (1953), Philosophical Magazine **44**.
- Gal A., *et al.*, (2016) Strangeness in Nuclear Physics.
- Nakazawa K., (2010), Nuclear Physics **A835** (207-214).
- Nakazawa K., (2013), Few-Body System **54** (1279-1282).
- Takahashi H., (2003) “Study of Double-Hypernuclei with Hybrid-Emulsion Method” Ph.D Thesis, Kyoto University.
- Tamura H., (2008), Progress of Theoretical Physics, **Vol. 120**, No.5.
- Yoshida J., *et al.*, (2017) Nuclear Instruments and Methods in Physics Research **A847** (86-92).

CALCULATION OF THE RANGES AND POSITION ANGLES OF SINGLE- Λ HYPERNUCLEUS EVENT IN NUCLEAR EMULSION

Nyi Nyi Soe¹

Abstract

In this research work, the ranges and position angles of charged particle tracks which are emitted from a single- Λ hypernucleus event in KEK-PS E373 experiment. The positions (x, y, z) of a single- Λ hypernucleus event are measured in nuclear emulsion. In the analyzed event, the Ξ^- hyperon is stopped and decays into charged particles tracks #1 and #2 which has $4.27 \pm 0.001 \mu\text{m}$ range. The charged particle track #1 is a single- Λ hypernucleus according to its decay topology ($\#1 \rightarrow \#3 + \#4$). The ranges of charged particles tracks #1, #2, #3 and #4 are $24.7527 \pm 0.00047 \mu\text{m}$, $4.2698 \pm 0.000 \mu\text{m}$, $11.9915 \pm 0.00083 \mu\text{m}$, and $1486.8012 \pm 0.1358 \mu\text{m}$. The measurement of position angles (θ and ϕ) of charged particles is the main work for particles identification as well as that of ranges. The position angles of charged particles tracks #1, #2, #3 and #4 are $147.1130 \pm 0.4830^\circ$, $159.5224 \pm 0.2149^\circ$, $101.17061 \pm 0.3360^\circ$ and $73.1808 \pm 1.7845^\circ$ for the zenith angle (θ) and $2.4819 \pm 0.2775^\circ$, $-31.0295 \pm 0.4417^\circ$, $53.10747 \pm 0.6409^\circ$ and $57.1516 \pm 2.7838^\circ$ for the azimuthal angle (ϕ).

Keywords: Single- Λ hypernucleus, nuclear emulsion, range, position angles

Introduction

The hypernuclear physics has a great important in many branches of physics. Nuclei which consists of protons, neutrons and one or more hyperons are called hypernuclei. A hyperon is a strange hadron, larger mass than the nucleon and consisting one or more strange quarks (strangeness). Therefore, hyperons are also known as strange particle. Hyperons are made one or more strange (S) quark. Therefore, strange particle can enter deeply inside the core nucleus. There are four types of hyperons (strange particles); lambda (Λ), sigma (Σ), xi (Ξ), omega (Ω). Strange particles are produced by strong force and their life time have about 10^{-23} s . They decay by the weak force and decay relatively slow about 10^{-10} s . Among the family of hyperon, a Λ particle is lightest and it can stay in contact with nucleons inside the nucleus and form hypernuclei. As the internal structure, a single- Λ hypernucleus consists of protons, neutrons and one Λ hyperon. A single- Λ hypernucleus is generally described by a symbol ${}^A_\Lambda Z$ in which Z represents the element or charge of hypernucleus and A represents the total number of baryons in hypernucleus. For example, a single- Λ hypernucleus ${}^5_\Lambda \text{He}$ consists of 2 protons, 2 neutrons and one Λ hyperon as described in figure 1.

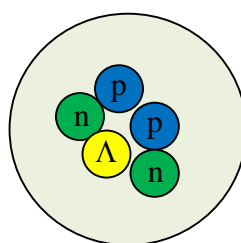


Figure1 Internal structure of ${}^5_\Lambda \text{He}$

Nuclear emulsion is one of the photographic films, which is used to detect three-dimensional tracks of charged particles. Hybrid emulsion experiments started in the 1950's. Firstly, nuclear emulsion was developed in cosmic-ray experiments with chamber and counters. For an emulsion plate, a transparent material is called base which is used to support against shrinkage and swelling

¹ Assistant Lecturer, Major, Department of Physics, Defence Services Academy

in its drying and developing process. The base is not sensitive to particles and that it is a dead space. Many different preprocessing of the base surface have been tried out for acrylic films and polystyrene films. Using those bases, two types of emulsion plates were developed. One is a plate called "thin plate" with 70 μm thick emulsion coated on both sides of the base, to be used for the tracking of Ξ^- particles predicted by a fiber-bundle tracker. Another type, the "thick plate", has a 500 μm thick emulsion coated on both sides of the thin base.

A hybrid-emulsion experiment, E176, was carried out at the KEK 12 GeV proton synchrotron to study the strangeness hypernucleus events in 1980s [1]. In this experiment 7 events of single- Λ hypernuclei were found among the 80 hyperon capture at rest in nuclear emulsion. Moreover, the experiment E373 was performed using a 1.66 GeV/c K^- beam at the K2 beam line of the proton synchrotron facility at KEK [2]. The purpose of this experiment is to get ten times higher statistics of Ξ^- hyperon and double strangeness nuclei than the previous experiment KEK-PS E176. After emulsion scanning, about 1000 Ξ^- stop events were observed in nuclear emulsion of KEK-PS E373 experiment [4]. Among them 46 events of single- Λ hypernucleus were detected. One of the 46 single- Λ hypernuclei is planned to analyzed and calculations of ranges and position angles using positions data are presented in this paper.

Calculation of Ranges and Position Angles of Single- Λ Hypernucleus Event

Event Description

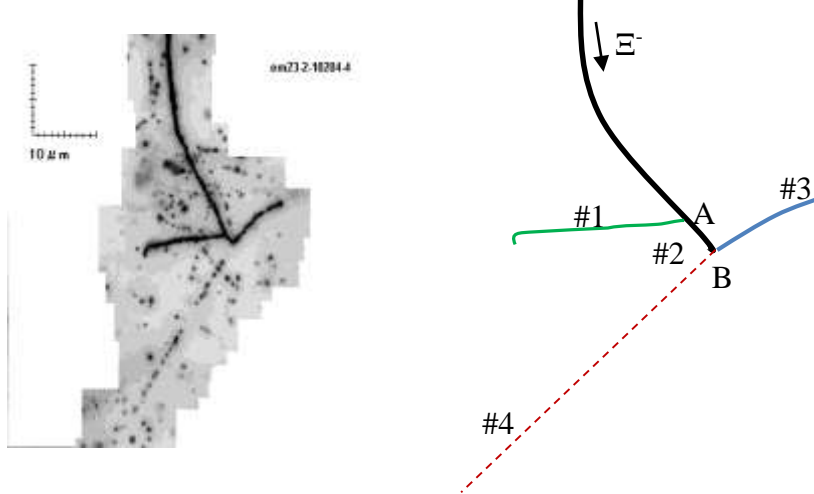


Figure 2 Photograph and schematic diagram of analyzed single- Λ hypernucleus event

The analyzed event is detected in module #023, plate #02 during the semiautomatic scanning of nuclear emulsion in KEK-PS E373 experiment. The event number is 10204-4. In the analyzed event, a Ξ^- hyperon is captured by the emulsion nucleus at point A, from which two charged particles track #1 and track #2 are emitted. The particle of track #2 decays into track #3 and track #4 at point B. So, point A is production point and point B is decay point of single- Λ hypernucleus track #2. The experimental data are provided by Professor Dr Nakazawa and KEK-PS E373 collaborators from Gifu University. Using these data, the ranges and position angles of the analyzed event are calculated. These experimental data for our analysis include in vital role. The range is defined as the distance travelled of a charged particle when passing through the nuclear emulsion before it decay. The photograph and schematic diagram of a single- Λ hypernucleus event are shown in figure 2.

Measurement of Positions (x, y, z) in Nuclear Emulsion and Calculation of Range

In the first step of the measurement, the points formed the tracks of charged particles are clicked. The points through the track travelled in nuclear emulsion are checked. If the points are along a straight line, we click these points between the starting and stopping points. If the points are not straight line, we click each point formed along the track travelled to obtain the accurate range. The range measurement of the charged particle tracks is as follows:

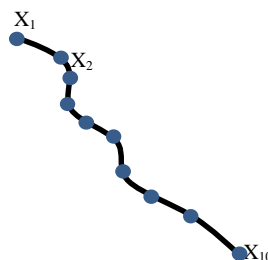


Figure 3 Measurement of a track from point to point

In nuclear emulsion, the tracks of charged particles are measured in three-dimension. The positions (x, y and z) of tracks #1, #2, #3 and #4 are measured in three times to obtain the accurate results.

$$\Delta x = x_2 - x_1, x_3 - x_2, x_4 - x_3, \dots \quad (1)$$

where, Δx refers to the range between each two click point and x_1, x_2, x_3 , and x_4 refer to the click points for first, second, third and fourth click points of our measurement in the x-direction. So, the measurement for "y" and z-direction are as in the x-direction. For the measurement, the positions (x, y, z) of charged particles tracks #1, #2, #3 and #4 are shown in table 1.

Table 1 Positions (x, y, z) of track #1, #2, #3 and #4

Track	x (mm)	y (mm)	z (mm)	Remark
#1	-104.06997	53.03572	-2.786	
	-104.06351	53.03600	-2.791	
	-104.05721	53.03807	-2.796	
#2	-104.06972	53.03572	-2.787	
	-104.07100	53.03649	-2.789	
#3	-104.07075	53.03649	-2.788	
	-104.07379	53.03244	-2.789	
#4	-104.07826	53.03115	-2.791	
	-104.07006	53.03594	-2.790	
	-104.02520	53.10542	-2.790	
	-103.98238	53.17091	-2.765	
	-103.92302	53.26002	-2.748	
	-103.86744	53.34064	-2.734	
	-103.82884	53.39874	-2.723	
	-103.78056	53.47005	-2.709	
	-103.72091	53.55768	-2.694	
	-103.69813	53.59066	-2.686	
	-103.77101	53.65645	-2.970	
	-103.74679	53.69172	-2.965	
	-103.72477	53.72648	-2.959	
	-103.68599	53.78332	-2.950	
	-103.6585	53.82436	-2.943	

The range of a charged particle is calculated by the formula,

$$R = \sqrt{\Delta x^2 + \Delta y^2 + (\Delta Z \cdot S)^2} \quad (2)$$

In the equation (2), “S” represents the shrinkage factor in the focusing direction of emulsion plate. The shrinkage factor “S” is defined as the ratio of the thickness of gel at exposure time and that at the measurement time. It is very important to measure the actual range of charged particles. In our analysis, the typical value of shrinkage factor is used. This typical value is 2.

In figure 2, a single- Λ hypernucleus track #2 decays into tracks #3 and #4. So, we calculate the range of track#1 as follows;

$$\Delta x_1=x_2-x_1=0.00646\text{mm}$$

$$\Delta y_1= y_2-y_1=0.00028\text{mm}$$

$$\Delta z_1=z_2-z_1=-0.005\text{mm}$$

So, $R_1= 0.0119084004$ mm using equation 2.

$$\Delta x_2=x_3-x_2=0.0063\text{ mm}$$

$$\Delta y_2= y_3-y_2=0.00207\text{mm}$$

$$\Delta z_2=z_3-z_2=-0.0055\text{ mm}$$

Therefore, $R_2=0.01284425553$ mm also using equation 2.

The total range of track #1 is as follows;

$$R_{\text{total}}= R_1+R_2= 0.02475265593\text{ mm which is the range of track } \#1 \text{ in nuclear emulsion.}$$

Track #1, #2 and #3 are stopped in plate 2 and track #4 is passed through plate 2 and stopped in plate 1. The ranges of tracks #2, #3 and #4 are calculated by using equation 2 as the same way in track #1 and the calculated results are presented in table 2.

Table 2 Calculated Results of Tracks #1, #2, #3 and #4 for each point

Track	$\Delta x(\text{mm})$	$\Delta y(\text{mm})$	$\Delta z(\text{mm})$	R (mm)	Total R (μm)
#1	0.00646	0.00028	-0.005	0.0119084	24.7527 ± 0.00047
	0.0063	0.00207	-0.0055	0.0128443	
#2	-0.00128	0.00077	-0.002	0.0042698	4.2698 ± 0.0001
#3	-0.00304	-0.00405	-0.0005	0.0051618	11.9915 ± 0.00083
	-0.00447	-0.00129	-0.0025	0.0068297	
#4	0.04486	0.06948	0.0125	0.0863996	1486.8012 ± 0.1358
	0.04282	0.06549	0.0125	0.0821431	
	0.05936	0.08911	0.0165	0.1120411	
	0.05558	0.08062	0.014	0.1018466	
	0.0386	0.0581	0.0115	0.0734477	
	0.04828	0.07131	0.0135	0.0902501	
	0.05965	0.08763	0.015	0.1101687	
	0.02278	0.03298	0.0085	0.0435386	
	-0.07288	0.06579	-0.2845	0.5774087	
	0.02422	0.03527	0.005	0.0439384	
	0.02202	0.03476	0.0065	0.0431524	
	0.03878	0.05684	0.009	0.0711244	
	0.02749	0.04104	0.007	0.0513418	

Calculation of Position Angles

The position angles of charged particles need to be measured because the main work of our analysis is to measure the ranges and position angle of analyzed event. We can decide what the particles are emitted from the analyzed event only when we know the position angles of charged particles which are observed in nuclear emulsion.

The angle θ is the zenith angle which is defined as the angle between the track of particles, ranges, and a vertical line, passing through the z-direction. The angle ϕ is the azimuthal angle which refers to the angle counterclockwise angle from the x-axis formed when the point is projected onto the xy-plane. The position angles (θ and ϕ) of charged particles tracks #1, #2, #3 and #4 are shown in figure 4.

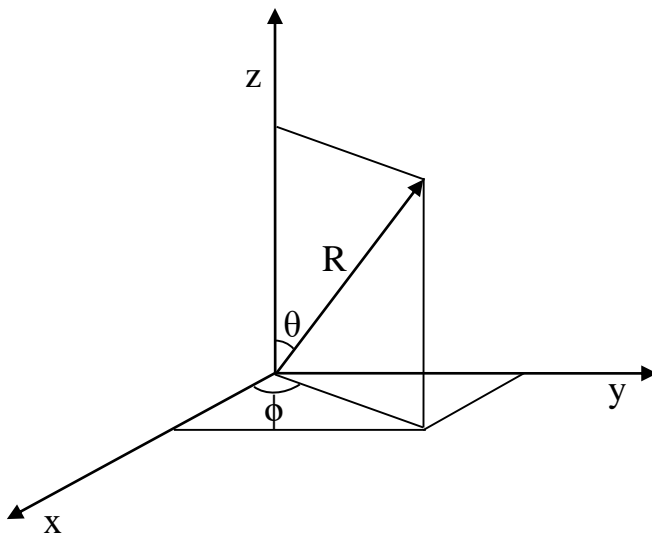


Figure 4. Schematic drawing for position angles θ and ϕ of the emitted tracks

To find the appropriate and accurate angles of charged particles #1, #2, #3 and #4, their ranges of which they are observed approximately about 10 μm are used. So, the angles of charged particles are also calculated by using the following formulae:

$$\theta = \cos^{-1} \left[\frac{\Delta z}{\sqrt{\Delta x^2 + \Delta y^2 + (\text{s.}\Delta z)^2}} \right] \quad (3)$$

$$\phi = \tan^{-1} \left[\frac{\Delta y}{\Delta x} \right] \quad (4)$$

The position angles of charged particles are summarized in table 3.

Table 3 Calculated Results of Angles θ and ϕ of #1, #2, #3 and #4

Track	θ (degree)	ϕ (degree)
#1	147.1130 ± 0.4830	2.4819 ± 0.2775
#2	159.5224 ± 0.2149	-31.0295 ± 0.4417
#3	101.17061 ± 0.3360	53.10747 ± 0.6409
#4	73.1808 ± 1.7845	57.1516 ± 2.7838

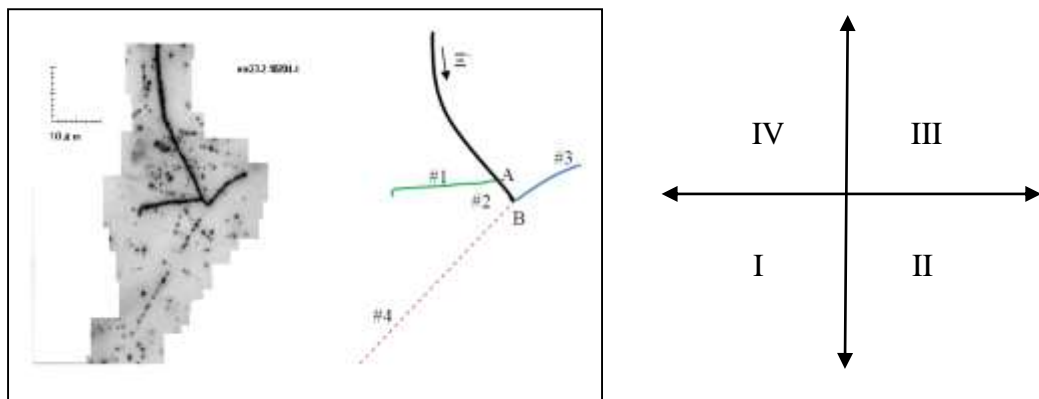


Figure 5 Photograph, schematic drawing and quadrant for position angle ϕ of the emitted tracks #1, #2, #3 and #4.

In figure 5, a photograph, schematic diagram and quadrant figure for position angle ϕ are presented. According to figure track #1 is located in quadrant IV ($270^\circ < \phi < 360^\circ$), track #2 is located in quadrant II ($90^\circ < \phi < 180^\circ$), track #3 is located in quadrant III ($180^\circ < \phi < 270^\circ$) and track #4 is located in quadrant I ($0^\circ < \phi < 90^\circ$). Due to their location the position angles are expressed in table 4.

Table 4 Calculated Results of Angles θ and ϕ of #1, #2, #3 and #4 due to their location

Track	θ (degree)	ϕ (degree)
#1	147.1130 ± 0.4830	357.5181 ± 0.2775
#2	159.5224 ± 0.2149	121.0295 ± 0.4417
#3	101.17061 ± 0.3360	216.8925 ± 0.6409
#4	73.1808 ± 1.7845	57.1516 ± 2.7838

Results and Discussions

We planned to identify a single- Λ hypernucleus event which was observed in nuclear emulsion of KEK-PS E373 experiment. In this paper, the ranges and position angles of emitted charged particle tracks from single- Λ hypernucleus are calculated using experimental data (positions x, y and z). According to present research, the following results are obtained.

Table 5 Calculated results of range and position angles of analyzed event

Track	R (μm)	θ (degree)	ϕ (degree)
#1	24.7527 ± 0.00047	147.1130 ± 0.4830	357.5181 ± 0.2775
#2	4.2698 ± 0.0001	159.5224 ± 0.2149	121.0295 ± 0.4417
#3	11.9915 ± 0.00083	101.17061 ± 0.3360	216.8925 ± 0.6409
#4	1486.8012 ± 0.1358	73.1808 ± 1.7845	57.1516 ± 2.7838

Conclusion

Our analysis of a single- Λ hypernucleus will provide to identify the hypernuclear species observed in nuclear emulsion. In hypernuclear physics, the understanding of nucleon-baryon interaction and baryon-baryon interaction is important. To do so, observations of more and more hypernuclei are needed and identification of observed event is important work. For hypernuclei identification work, kinematical analysis is usually used. Therefore, the measurement of range and position angles is very fundamental for hypernuclear research.

Acknowledgements

The author would like to thank Lieutenant Colonel Saw Myint Oo, Dean of Faculty of Physics, Defence Services Academy for his encouragement and permission to complete this work. The author also would like to express gratitude to Dr Htaik Nandar Kyaw who guides me to succeed on the hypernuclear research. Finally, the author would like to thank Professor Dr Kazuma Nakazawa who supports and gives me valuable advices to carry out hypernuclear research and all of the collaborators from KEK-PS E373 experiment.

References

- Danysz M., and Pniewski J, (1953) "Historical Development of Field of the Hypernuclei", Philosophical Magazine, Vol. 44, pp. 348.
- Danysz M., *et al.*, (1963) "The Identification of Hyperfragments", Nucl. Phys. Vol.49, pp.121-132.
- Rochester G. D., and Butler C. C., (1947) "Evidence for the Existence of New Unstable Elementary Particles", Nature, vol. 160, pp. 855.
- Tamura H., (2012) "Strangeness nuclear physics experiments at J-PARC", Prog. Theo. Expt, vol. 1, pp. 02B012.

FORMATION OF $^{15}_{\Lambda}$ N HYPERNUCLEUS IN J-PARC E07 EXPERIMENT

Htaik Nandar Kyaw¹, Hnin Yee Hlaing²

Abstract

In this research, a single- Λ hypernucleus which is detected in J-PARC E07 nuclear emulsion experiment is analyzed by relativistic kinematics. The ranges and position angles of charged particle tracks are measured in nuclear emulsion. Neutral particle emission in the decay products is checked by calculating the dot product of direction vector of hyperfragment and total momentum of decay products. The possible decay modes of single- Λ hypernucleus are considered and Q-values are calculated. Total energies of each decay product are obtained by range-energy relation and momentum conservation. The acceptable decay modes are chosen by comparing Q-values and total energy. Then, mass of possible hypernuclei is calculated by mass-energy relation. According to our analysis, a single- Λ hypernucleus is uniquely identified as $^{15}_{\Lambda}$ N which follows the $^{15}_{\Lambda}$ N \rightarrow $^{9}_{4}$ Be + $^{3}_{2}$ He + d + n decay mode with the mass 14141.58 ± 0.19 MeV/c² and binding energy 14.31 ± 0.19 MeV.

Keywords: Single- Λ hypernucleus, nuclear emulsion, relativistic kinematics, J-PARC

Introduction

Hypernuclei are bound systems of nucleons with one or more hyperons. Hyperons are unstable particles with a mean lifetime of the order of 10^{-10} s. In the family of hyperons, Λ is the lightest particle and it can stay in contact with nucleons inside nuclei and form hypernuclei. If a nucleus contains one Λ hyperon, it is said to be a single- Λ hypernucleus and a nucleus which made up of two Λ hyperons in addition to nucleons is called a double- Λ hypernucleus. Hyperons are free from Pauli's exclusion principle and they can travel deep inside of the nuclear medium until the core region of strange matter such as neutron stars that may exist in distant parts of the universe. The theoretical motivation of hypernuclear physics is to understand the baryon-baryon interaction in a unified way. Under the title of baryon-baryon interaction, nucleon-nucleon interaction can be studied by ordinary nuclei, hyperon-nucleon interaction can be studied by single- Λ hypernuclei and hyperon-hyperon interaction can also be studied by double- Λ hypernuclei. The experimental motivation of hypernuclear physics is to draw the three dimensional nuclear chart with number of protons, number of neutrons and strangeness. Therefore, more hypernuclei events are expected and hypernuclei searching experiments such as KEK-PS E176 and KEK-PS E373 are carried out at Japanese High Energy Accelerator Research Organization using p(K⁻,K⁺) Ξ^- reaction .

The J-PARC E07 experiment, which stands for Japan Accelerator Research Complex, is aimed to improve the roles of material science, life science, nuclear physics and particles physics, especially in astrophysics. The main purposes of this experiment are to detect about 10,000 Ξ^- stopped events by the hybrid emulsion method, automatic scanning method, combining the emulsion and counters and to identify clearly and accurately double hypernuclei. The J-PARC E07 experiment was performed at K 1.8 beam line in the J-PARC Hadron Experimental facility in 2016. This 1.8 GeV/c momentum was chosen to maximize the Ξ stopping yield in the emulsion. The emulsion scanning of the E07 experiment is ongoing now. At present, twice the statistics for Ξ^- stopping events than that of KEK-PS E373 experiment has been scanned. More than ten events

¹ Dr, Lecturer, Department of Physics, Defence Services Academy

² Assistant Lecturer, Captain, Department of Physics, Defence Services Academy

of double and twin- Λ hypernuclei have been observed up to the present. Further impressive events are expected to be observed in the next future.

In this research, a single- Λ hypernucleus event of J-PARC E07 experiment will be analyzed. The experimental data were supported by Professor Nakazawa who is the spokesperson of this experiment from Gifu University in Japan.

Analysis of Single- Λ Hypernucleus Event

Event Description

The analyzed single- Λ hypernucleus event is detected in module #75, plate #3 of J-PARC E07 experiment. The photograph and schematic diagram of analyzed event are presented in figure 1. In the analyzed event, a Ξ^- hyperon is captured by the emulsion nucleus at point A from which two charged particles tracks #1 and #2 are emitted. At point B, the particle of track #1 showed the topology of decayed into three charged particles track #3, track #4 and track #5. This event has two vertex points; one production vertex A and one decayed vertex B. Therefore, the particle of track #1 can be identified as single- Λ hypernucleus. The measured ranges and emitted angles are expressed in table 1.

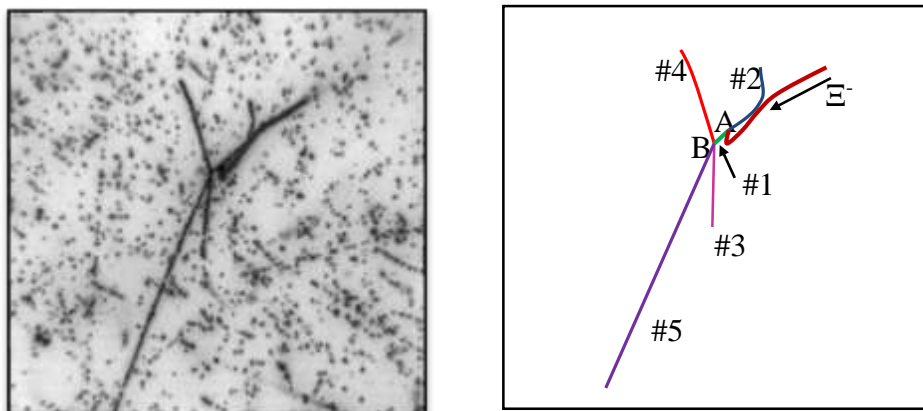


Figure 1 Photographs and schematic diagram of analyzed single- Λ hypernucleus in nuclear emulsion of J-PARC E07 experiment

Table 1 Measured ranges of hypernucleus track #1 and charged particle decay products

Vertex	Track	Range (μm)	θ (degree)	ϕ (degree)	Remark
A	#1	1.78 ± 0.00	87.09 ± 0.03	32.55 ± 0.31	Single- Λ hypernucleus
	#2	12.52 ± 0.00	94.59 ± 0.06	63.18 ± 0.24	
B	#3	13.65 ± 0.00	80.03 ± 0.09	85.91 ± 0.52	
	#4	14.67 ± 0.00	85.16 ± 0.04	69.76 ± 0.20	
	#5	101.11 ± 0.04	85.24 ± 0.07	64.45 ± 0.23	

Checking the Neutral Particles Emission at Point B

Present analysis is started from point B and possible decay modes have to choose at point B. At point B, track #1 single- Λ hypernucleus decays into charged particle tracks #3, #4 and #5. So, it is necessary to know neutral particle emission at point B and checked by calculating the dot product of direction vector of hyperfragment and total momentum of decay products such as

$$\cos\theta = \frac{\vec{V}_{HF} \cdot \vec{p}_{total}}{|\vec{V}_{HF}| \cdot |\vec{p}_{total}|} \quad (1)$$

where, \vec{V}_{HF} = the direction vector of hyperfragment

\vec{p}_{total} = the total momentum of the emitted tracks

If the angle θ becomes zero, there is no neutron emission. It means that the total momentum is zero and other neutral particles cannot be emitted at point B. If the angle θ has some value, the neutral particles will be emitted at point B. According to our calculation, the angle θ value is 39.56° and not equal to zero. So, we can consider that not only three charged particles tracks #3, #4 and #5 but also neutral particles can be emitted at the vertex point B and decay modes of single- Λ hypernucleus track #1 will be obtained.

Choosing the Possible Decay Modes at Point B

At point B, a single- Λ hypernucleus (track #1) is decayed into three charged particles and one or more neutral particles as follow.



Therefore, possible decay modes of single- Λ hypernucleus track #1 are chosen according to equation 2. Firstly, internal structures of possible single- Λ hypernuclei are considered. Track #1 decays into decay products of three charged particle tracks and neutral particles, the possible hypernucleus must be chosen ${}_{\Lambda}^{14}\text{C}$ to ${}_{\Lambda}^{15}\text{N}$.

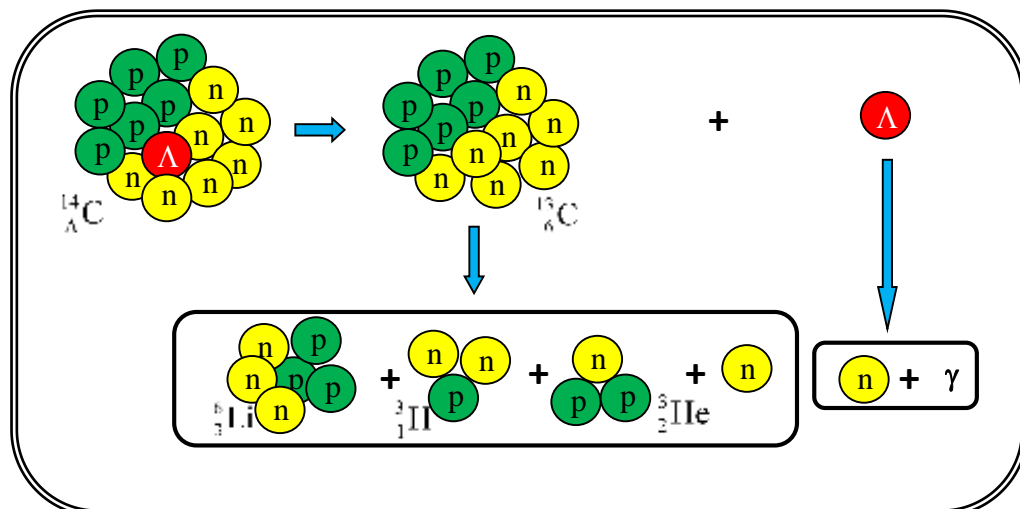


Figure 2 Decay of ${}_{\Lambda}^{14}\text{C}$ hypernucleus into three charged particles and two neutral particles

According to figure 2, a ${}_{\Lambda}^{14}\text{C}$ hypernucleus consists of 6 protons, 1 Λ hyperon and 7 neutrons (figure 2). It means that a Λ hyperon combines with a core nucleus ${}_{\Lambda}^{13}\text{C}$ to form a ${}_{\Lambda}^{14}\text{C}$ hypernucleus. In the analyzed event, a single- Λ hypernucleus has 3 charged particle decay products and it is assumed that a core nucleus decays into three charged particles Li^6 , H^3 and He^3 . Due to the dot product of hyperfragment direction vector and total momentum of decay products, neutral particle emission at point B is observed. Therefore, the possible decay mode becomes,



Similarly, all possible decay modes are chosen and 85 possible decay modes are obtained.

Calculation of Q-values and Total Energy at Point B

To check the possible decay modes that we have chosen in section 3.6.1 are energetically possible or not, the Q-values at point B are calculated. The Q-value is defined as the energy released or absorbed during the nuclear reaction. If the calculated Q-value is positive, it is defined as an exoergic reaction. If so reaction is energetically possible. If the calculated Q-value is negative, it is defined as an endoergic reaction. In this case, the reaction does not energetically possible and is not taken into the consideration for our analysis.

The Q-values of all possible decay modes are calculated by the formula,

$$Q = \sum M_{\text{initial state}} - \sum M_{\text{final state}} \quad (4)$$

$$Q(\text{MeV}) = [M({}^{14}_{\Lambda}Z)(\text{MeV}/c^2) - \{M(\#3) + M(\#4) + M(\#5) + M(n)\}(\text{MeV}/c^2)]c^2 \quad (5)$$

The lifetime of hypernuclei is very short ($\sim 10^{-10}$ s) and it decays itself without external effects in nuclear emulsion. So, an exoergic reaction is allowed in nuclear emulsion. Moreover, if Q-value is positive, the energy is released and this energy is shared by the decay products. Therefore, only exoergic reaction must be allowed for these decay modes. According to our calculation it is found that the calculated Q-values are all positive and all possible decay modes are taken into consideration to perform analysis.

The kinetic energies of charged particles which are called visible energy (E_{vis}) are obtained by range-energy relation calculation package by measuring its range. The kinetic energies of neutral particles (E_n) are calculated by momentum conservation. Total energy means that the sum of kinetic energies of charged particle decay products and that of neutral particles. If all charged particles are emitted Q-values should be equal to total kinetic energy. If neutral particles are contaminated in the decay products, Q-values should be less than total kinetic energy.

In the present analysis, a single- Λ hypernucleus decays into three charged particles and one or more neutral particles so that we should choose the possible decay modes which have smaller total energy than Q-values. In table 2, the comparisons of calculated Q-values and E_{total} for all possible decay modes are presented. Some decay modes have one neutron emission and some have two neutron emission. The decay modes which have more than two neutrons emission are rejected because of very small and negative Q-values.

Table 2 Comparison of Q-values and total energy for all possible decay modes at point B

No.	Possible Decay Modes	Q-value (MeV)	E_{total} (MeV)	Remark
1	${}^{14}_{\Lambda}C \rightarrow {}^6_3Li + {}^3_1H + {}^3_2He + 2n$	114.98 ± 0.33	$>60.31 \pm 0.01$	Acceptable
2	${}^{14}_{\Lambda}C \rightarrow {}^6_3Li + {}^3_2He + {}^3_1H + 2n$	114.98 ± 0.33	$>47.749 \pm 0.01$	Acceptable
3	${}^{14}_{\Lambda}C \rightarrow {}^3_1H + {}^6_3Li + {}^3_2He + 2n$	114.98 ± 0.33	$>62.14 \pm 0.01$	Acceptable
4	${}^{14}_{\Lambda}C \rightarrow {}^3_2He + {}^6_3Li + {}^3_1H + 2n$	114.98 ± 0.33	$>49.24 \pm 0.01$	Acceptable
5	${}^{14}_{\Lambda}C \rightarrow {}^3_1H + {}^3_2He + {}^6_3Li + 2n$	114.98 ± 0.33	$>117.28 \pm 0.01$	Rejected
6	${}^{14}_{\Lambda}C \rightarrow {}^3_2He + {}^3_1H + {}^6_3Li + 2n$	114.98 ± 0.33	$>116.94 \pm 0.01$	Rejected
7	${}^{14}_{\Lambda}C \rightarrow {}^6_3Li + {}^3_1H + {}^4_2He + n$	135.55 ± 0.33	119.54 ± 0.01	Acceptable

No.	Possible Decay Modes	Q-value (MeV)	E _{total} (MeV)	Remark
8	$^{14}_{\Lambda}C \rightarrow ^6_3Li + ^4_2He + ^3_1H + n$	135.55±0.33	85.065±0.01	Acceptable
9	$^{14}_{\Lambda}C \rightarrow ^3_1H + ^6_3Li + ^4_2He + n$	135.55±0.33	122.77±0.01	Acceptable
10	$^{14}_{\Lambda}C \rightarrow ^4_2He + ^6_3Li + ^3_1H + n$	135.55±0.33	87.38±0.01	Acceptable
11	$^{14}_{\Lambda}C \rightarrow ^3_1H + ^4_2He + ^6_3Li + n$	135.55±0.33	208.18±0.01	Rejected
12	$^{14}_{\Lambda}C \rightarrow ^4_2He + ^3_1H + ^6_3Li + n$	135.55±0.33	207.26±0.01	Rejected
13	$^{14}_{\Lambda}C \rightarrow ^6_3Li + ^2_1H + ^4_2He + 2n$	129.29±0.33	>69.62±0.01	Acceptable
14	$^{14}_{\Lambda}C \rightarrow ^6_3Li + ^4_2He + ^2_1H + 2n$	129.29±0.33	>46.22±0.01	Acceptable
15	$^{14}_{\Lambda}C \rightarrow ^2_1H + ^6_3Li + ^4_2He + 2n$	129.29±0.33	>71.55±0.01	Acceptable
16	$^{14}_{\Lambda}C \rightarrow ^4_2He + ^6_3Li + ^2_1H + 2n$	129.29±0.33	>47.53±0.01	Acceptable
17	$^{14}_{\Lambda}C \rightarrow ^2_1H + ^4_2He + ^6_3Li + 2n$	129.29±0.33	>118.94±0.01	Acceptable
18	$^{14}_{\Lambda}C \rightarrow ^4_2He + ^2_1H + ^6_3Li + 2n$	129.29±0.33	>118.32±0.01	Acceptable
19	$^{14}_{\Lambda}C \rightarrow ^7_3Li + ^3_1H + ^3_2He + n$	122.23±0.34	108.06±0.01	Acceptable
20	$^{14}_{\Lambda}C \rightarrow ^7_3Li + ^3_2He + ^3_1H + n$	122.23±0.33	87.96±0.01	Acceptable
21	$^{14}_{\Lambda}C \rightarrow ^3_1H + ^7_3Li + ^3_2He + n$	122.23±0.33	112.05±0.01	Acceptable
22	$^{14}_{\Lambda}C \rightarrow ^3_2He + ^7_3Li + ^3_1H + n$	122.23±0.33	91.42±0.01	Acceptable
23	$^{14}_{\Lambda}C \rightarrow ^3_1H + ^3_2He + ^7_3Li + n$	122.23±0.33	242.03±0.01	Rejected
24	$^{14}_{\Lambda}C \rightarrow ^3_2He + ^3_1H + ^7_3Li + n$	122.23±0.33	241.49±0.01	Rejected
25	$^{14}_{\Lambda}C \rightarrow ^7_3Li + ^2_1H + ^3_2He + 2n$	115.98±0.33	>63.29±0.01	Acceptable
26	$^{14}_{\Lambda}C \rightarrow ^7_3Li + ^3_2He + ^2_1H + 2n$	115.98±0.33	>47.64±0.01	Acceptable
27	$^{14}_{\Lambda}C \rightarrow ^2_1H + ^7_3Li + ^3_2He + 2n$	115.98±0.33	>65.58±0.03	Acceptable
28	$^{14}_{\Lambda}C \rightarrow ^3_2He + ^7_3Li + ^2_1H + 2n$	115.98±0.33	>49.56±0.01	Acceptable
29	$^{14}_{\Lambda}C \rightarrow ^2_1H + ^3_2He + ^7_3Li + 2n$	115.98±0.33	>136.50±0.03	Rejected
30	$^{14}_{\Lambda}C \rightarrow ^3_2He + ^2_1H + ^7_3Li + 2n$	115.98±0.33	>136.09±0.01	Rejected
31	$^{14}_{\Lambda}C \rightarrow ^7_3Li + ^2_1H + ^4_2He + n$	136.54±0.33	125.47±0.01	Acceptable
32	$^{14}_{\Lambda}C \rightarrow ^7_3Li + ^4_2He + ^2_1H + n$	136.54±0.33	85.40±0.02	Acceptable
33	$^{14}_{\Lambda}C \rightarrow ^2_1H + ^7_3Li + ^4_2He + n$	136.54±0.33	129.60±0.01	Acceptable
34	$^{14}_{\Lambda}C \rightarrow ^4_2He + ^7_3Li + ^2_1H + n$	136.54±0.33	88.48±0.02	Acceptable
35	$^{14}_{\Lambda}C \rightarrow ^2_1H + ^4_2He + ^7_3Li + n$	136.54±0.33	245.19±0.01	Rejected
36	$^{14}_{\Lambda}C \rightarrow ^4_2He + ^2_1H + ^7_3Li + n$	136.54±0.33	244.14±0.01	Rejected
37	$^{14}_{\Lambda}C \rightarrow ^7_3Li + ^1_1H + ^4_2He + 2n$	134.32±0.33	>72.62±0.01	Acceptable
38	$^{14}_{\Lambda}C \rightarrow ^7_3Li + ^4_2He + ^1_1H + 2n$	134.32±0.33	>46.35±0.01	Acceptable

No.	Possible Decay Modes	Q-value (MeV)	E _{total} (MeV)	Remark
39	$^{14}_{\Lambda}C \rightarrow ^1_1H + ^7_3Li + ^4_2He + 2n$	134.32±0.33	>74.98±0.01	Acceptable
40	$^{14}_{\Lambda}C \rightarrow ^4_2He + ^7_3Li + ^1_1H + 2n$	134.32±0.33	>48.04±0.01	Acceptable
41	$^{14}_{\Lambda}C \rightarrow ^1_1H + ^4_2He + ^7_3Li + 2n$	134.14±0.33	>138.15±0.01	Rejected
42	$^{14}_{\Lambda}C \rightarrow ^4_2He + ^1_1H + ^7_3Li + 2n$	134.14±0.33	>137.46±0.01	Rejected
43	$^{14}_{\Lambda}C \rightarrow ^7_3Li + ^1_1H + ^5_2He + n$	133.42±0.38	144.87±0.01	Rejected
44	$^{15}_{\Lambda}N \rightarrow ^9_4Be + ^2_1H + ^3_2He + n$	125.93±0.21	150.86±0.01	Rejected
45	$^{15}_{\Lambda}N \rightarrow ^9_4Be + ^3_2He + ^2_1H + n$	125.93±0.16	125.17±0.03	Acceptable
46	$^{15}_{\Lambda}N \rightarrow ^2_1H + ^9_4Be + ^3_2He + n$	125.93±0.16	158.96±0.01	Rejected
47	$^{15}_{\Lambda}N \rightarrow ^3_2He + ^9_4Be + ^2_1H + n$	125.93±0.16	132.60±0.03	Rejected
48	$^{15}_{\Lambda}N \rightarrow ^2_1H + ^3_2He + ^9_4Be + n$	125.93±0.16	448.23±0.02	Rejected
49	$^{15}_{\Lambda}N \rightarrow ^3_2He + ^2_1H + ^9_4Be + n$	125.93±0.16	447.56±0.02	Rejected
50	$^{15}_{\Lambda}N \rightarrow ^9_4Be + ^1_1H + ^3_2He + 2n$	123.70±0.16	>86.19±0.01	Acceptable
51	$^{15}_{\Lambda}N \rightarrow ^9_4Be + ^3_2He + ^1_1H + 2n$	123.70±0.16	>67.68±0.03	Acceptable
52	$^{15}_{\Lambda}N \rightarrow ^1_1H + ^9_4Be + ^3_2He + 2n$	123.70±0.16	>90.69±0.01	Acceptable
53	$^{15}_{\Lambda}N \rightarrow ^3_2He + ^9_4Be + ^1_1H + 2n$	123.70±0.16	>71.70±0.03	Acceptable
54	$^{15}_{\Lambda}N \rightarrow ^1_1H + ^3_2He + ^9_4Be + 2n$	123.70±0.16	>247.18±0.02	Rejected
55	$^{15}_{\Lambda}N \rightarrow ^3_2He + ^1_1H + ^9_4Be + 2n$	123.70±0.16	>246.70±0.02	Rejected
56	$^{15}_{\Lambda}N \rightarrow ^9_4Be + ^1_1H + ^4_2He + n$	144.27±0.16	168.58±0.01	Rejected
57	$^{15}_{\Lambda}N \rightarrow ^9_4Be + ^4_2He + ^1_1H + n$	144.27±0.16	123.37±0.03	Acceptable
58	$^{15}_{\Lambda}N \rightarrow ^1_1H + ^9_4Be + ^4_2He + n$	144.27±0.16	176.37±0.01	Rejected
59	$^{15}_{\Lambda}N \rightarrow ^4_2He + ^9_4Be + ^1_1H + n$	144.27±0.16	130.42±0.03	Acceptable
60	$^{15}_{\Lambda}N \rightarrow ^1_1H + ^4_2He + ^9_4Be + n$	144.27±0.16	451.46±0.02	Rejected
61	$^{15}_{\Lambda}N \rightarrow ^4_2He + ^1_1H + ^9_4Be + n$	144.27±0.16	450.29±0.02	Rejected
62	$^{15}_{\Lambda}N \rightarrow ^{10}_4Be + ^1_1H + ^3_2He + n$	130.51±0.16	160.13±0.01	Rejected
63	$^{15}_{\Lambda}N \rightarrow ^{10}_4Be + ^3_2He + ^1_1H + n$	130.51±0.16	129.53±0.03	Acceptable
64	$^{15}_{\Lambda}N \rightarrow ^1_1H + ^{10}_4Be + ^3_2He + n$	130.51±0.16	169.52±0.01	Rejected
65	$^{15}_{\Lambda}N \rightarrow ^3_2He + ^{10}_4Be + ^1_1H + n$	130.51±0.16	138.13±0.03	Rejected
66	$^{15}_{\Lambda}N \rightarrow ^1_1H + ^3_2He + ^{10}_4Be + n$	130.51±0.16	508.09±0.02	Rejected
67	$^{15}_{\Lambda}N \rightarrow ^3_2He + ^1_1H + ^{10}_4Be + n$	130.51±0.16	507.29±0.02	Rejected
68	$^{15}_{\Lambda}N \rightarrow ^{10}_5B + ^1_1H + ^3_1H + n$	131.04±0.16	165.18±0.01	Rejected
69	$^{15}_{\Lambda}N \rightarrow ^{10}_5B + ^3_1H + ^1_1H + n$	131.04±0.16	154.69±0.01	Rejected

No.	Possible Decay Modes	Q-value (MeV)	E _{total} (MeV)	Remark
70	$^{15}_{\Lambda}N \rightarrow {}^1_1H + {}^{10}_5B + {}^3_1H + n$	131.04±0.16	177.28±0.01	Rejected
71	$^{15}_{\Lambda}N \rightarrow {}^3_1H + {}^{10}_5B + {}^1_1H + n$	131.04±0.16	166.62±0.01	Rejected
72	$^{15}_{\Lambda}N \rightarrow {}^1_1H + {}^3_1H + {}^{10}_5B + n$	131.04±0.16	648.04±0.02	Rejected
73	$^{15}_{\Lambda}N \rightarrow {}^3_1H + {}^1_1H + {}^{10}_5B + n$	131.04±0.16	647.78±0.02	Rejected
74	$^{15}_{\Lambda}N \rightarrow {}^{10}_5B + {}^2_1H + {}^2_1H + n$	127.01±0.16	159.51±0.01	Rejected
75	$^{15}_{\Lambda}N \rightarrow {}^2_1H + {}^{10}_5B + {}^2_1H + n$	127.01±0.16	171.59±0.01	Rejected
76	$^{15}_{\Lambda}N \rightarrow {}^2_1H + {}^2_1H + {}^{10}_5B + n$	127.01±0.16	647.84±0.02	Rejected
77	$^{15}_{\Lambda}N \rightarrow {}^{11}_5B + {}^1_1H + {}^2_1H + n$	136.24±0.16	172.13±0.01	Rejected
78	$^{15}_{\Lambda}N \rightarrow {}^{11}_5B + {}^2_1H + {}^1_1H + n$	136.24±0.16	167.23±0.01	Rejected
79	$^{15}_{\Lambda}N \rightarrow {}^1_1H + {}^{11}_5B + {}^2_1H + n$	136.24±0.16	185.87±0.01	Rejected
80	$^{15}_{\Lambda}N \rightarrow {}^2_1H + {}^{11}_5B + {}^1_1H + n$	136.24±0.16	180.84±0.01	Rejected
81	$^{15}_{\Lambda}N \rightarrow {}^1_1H + {}^2_1H + {}^{11}_5B + n$	136.24±0.16	728.28±0.02	Rejected
82	$^{15}_{\Lambda}N \rightarrow {}^2_1H + {}^1_1H + {}^{11}_5B + n$	136.24±0.16	728.16±0.02	Rejected
83	$^{15}_{\Lambda}N \rightarrow {}^{11}_5B + {}^1_1H + {}^1_1H + 2n$	134.01±0.16	>91.57±0.01	Acceptable
84	$^{15}_{\Lambda}N \rightarrow {}^1_1H + {}^{11}_5B + {}^1_1H + 2n$	134.01±0.16	>99.12±0.01	Acceptable
85	$^{15}_{\Lambda}N \rightarrow {}^1_1H + {}^1_1H + {}^{11}_5B + 2n$	134.01±0.16	>394.51±0.02	Rejected

According to table 2, 45 possible decay modes are rejected because they have larger total energy than Q-values. In this case, we have found that 40 acceptable decay modes in which E_{total} are consistent with Q value within 3σ value. Therefore, 40 possible decay modes are acceptable and they are taken into considerations to calculate the possible mass and binding energy of single-Λ hypernucleus. In the next section, detailed calculation of possible mass and binding energy will be presented.

Calculation of the mass and binding energy of single-Λ hypernucleus (track #1)

The possible masses of single-Λ hypernucleus are calculated by extracting the kinetic energy of charged particle decay products at point B. At point B, a single-Λ hypernucleus decays into three charged particles and neutral particles. The possible masses of single-Λ hypernucleus can be calculated by using the formula,

$$M({}^A_{\Lambda}Z)c^2 = E_3 + E_4 + E_5 + E_n \quad (6)$$

where, M(^A_ΛZ) = mass of single-Λ hypernucleus

E₃ = the total energy of track #3 = KE₃ + M₃

E₄ = the total energy of track #4 = KE₄ + M₄

E₅ = the total energy of track #5 = KE₅ + M₅

E_n = the total energy of neutron = KE_n + M_n

The binding energy of a single-Λ hypernucleus is calculated by the formula

$$B_{\Lambda} = M(^{A-1}Z) + M_{\Lambda} - M(^{\Lambda}Z) \quad (7)$$

where, B_{Λ} = binding energy of a single- Λ hypernucleus

$M(^{A-1}Z)$ = mass of core nucleus

M_{Λ} = mass of Λ hyperon

$M(^{\Lambda}Z)$ = mass of a single- Λ hypernucleus

The total binding energy of any ordinary nucleus involves a vital role in nuclear stability. In hypernuclear physics, hypernuclear binding energies determine Y-N and Y-Y effective interaction strengths. The comparison of our calculated results of masses and binding energies of 40 acceptable single- Λ hypernuclei and previous experimental and theoretical values are expressed in table 3.

Table 3 Calculated mass and binding energy compare with known values

No.	Possible Decay Modes	Calculated Mass(MeV/c ²)	Known Mass(MeV/c)	Calculated BE(MeV)	Known BE(MeV)
1	$^{14}_{\Lambda}C \rightarrow ^6_3Li + ^3_1H + ^3_2He + 2n$	>13158.36±0.34	13213.03±0.33	<66.81±0.34	12.17 ±0.33
2	$^{14}_{\Lambda}C \rightarrow ^6_3Li + ^3_2He + ^3_1H + 2n$	>13145.80±0.34	13213.03±0.33	<79.37±0.34	12.17 ±0.33
3	$^{14}_{\Lambda}C \rightarrow ^3_1H + ^6_3Li + ^3_2He + 2n$	>13160.18±0.34	13213.03±0.33	<64.99±0.34	12.17 ±0.33
4	$^{14}_{\Lambda}C \rightarrow ^3_2He + ^6_3Li + ^3_1H + 2n$	>13147.29±0.34	13213.03±0.33	<77.88±0.34	12.17 ±0.33
5	$^{14}_{\Lambda}C \rightarrow ^6_3Li + ^3_1H + ^4_2He + n$	13197.02±0.34	13213.03±0.33	28.15±0.34	12.17 ±0.33
6	$^{14}_{\Lambda}C \rightarrow ^6_3Li + ^4_2He + ^3_1H + n$	13162.55±0.34	13213.03±0.33	62.62±0.34	12.17 ±0.33
7	$^{14}_{\Lambda}C \rightarrow ^3_1H + ^6_3Li + ^4_2He + n$	13200.25±0.34	13213.03±0.33	24.92±0.34	12.17 ±0.33
8	$^{14}_{\Lambda}C \rightarrow ^4_2He + ^6_3Li + ^3_1H + n$	13164.86±0.34	13213.03±0.33	60.31±0.34	12.17 ±0.33
9	$^{14}_{\Lambda}C \rightarrow ^6_3Li + ^2_1H + ^4_2He + 2n$	>13153.36±0.35	13213.03±0.33	<71.81±0.35	12.17 ±0.33
10	$^{14}_{\Lambda}C \rightarrow ^6_3Li + ^4_2He + ^2_1H + 2n$	>13129.96±0.34	13213.03±0.33	<95.21±0.34	12.17 ±0.33
11	$^{14}_{\Lambda}C \rightarrow ^2_1H + ^6_3Li + ^4_2He + 2n$	>13155.29±0.34	13213.03±0.33	<69.88±0.34	12.17 ±0.33
12	$^{14}_{\Lambda}C \rightarrow ^4_2He + ^6_3Li + ^2_1H + 2n$	>13131.27±0.34	13213.03±0.33	<93.90±0.34	12.17 ±0.33
13	$^{14}_{\Lambda}C \rightarrow ^2_1H + ^4_2He + ^6_3Li + 2n$	>13202.06±0.34	13213.03±0.33	<22.49±0.34	12.17 ±0.33
14	$^{14}_{\Lambda}C \rightarrow ^4_2He + ^2_1H + ^6_3Li + 2n$	>13202.06±0.34	13213.03±0.33	<23.11±0.34	12.17 ±0.33
15	$^{14}_{\Lambda}C \rightarrow ^7_3Li + ^3_1H + ^3_2He + n$	13198.86±0.34	13213.03±0.33	26.31±0.31	12.17 ±0.33
16	$^{14}_{\Lambda}C \rightarrow ^7_3Li + ^3_2He + ^3_1H + n$	13178.76±0.34	13213.03±0.33	46.41±0.34	12.17 ±0.33
17	$^{14}_{\Lambda}C \rightarrow ^3_1H + ^7_3Li + ^3_2He + n$	13202.85±0.34	13213.03±0.33	22.32±0.34	12.17 ±0.33
18	$^{14}_{\Lambda}C \rightarrow ^3_2He + ^7_3Li + ^3_1H + n$	13182.22±0.34	13213.03±0.33	42.95±0.34	12.17 ±0.33
19	$^{14}_{\Lambda}C \rightarrow ^7_3Li + ^2_1H + ^3_2He + 2n$	>13160.34±0.34	13213.03±0.33	<64.83±0.34	12.17 ±0.33
20	$^{14}_{\Lambda}C \rightarrow ^7_3Li + ^3_2He + ^2_1H + 2n$	>13144.69±0.36	13213.03±0.33	<80.48±0.36	12.17 ±0.33
21	$^{14}_{\Lambda}C \rightarrow ^2_1H + ^7_3Li + ^3_2He + 2n$	>13162.64±0.34	13213.03±0.33	<62.53±0.34	12.17 ±0.33

No.	Possible Decay Modes	Calculated Mass(MeV/c ²)	Known Mass(MeV/c)	Calculated BE(MeV)	Known BE(MeV)
22	$^{14}_{\Lambda}C \rightarrow ^3_2He + ^7_3Li + ^2_1H + 2n$	>13146.58±0.36	13213.03±0.33	<78.59±0.36	12.17 ±0.33
23	$^{14}_{\Lambda}C \rightarrow ^7_3Li + ^2_1H + ^4_2He + n$	13201.95±0.34	13213.03±0.33	23.22±0.34	12.17 ±0.33
24	$^{14}_{\Lambda}C \rightarrow ^7_3Li + ^4_2He + ^2_1H + n$	13161.89±0.36	13213.03±0.33	63.28±0.36	12.17 ±0.33
25	$^{14}_{\Lambda}C \rightarrow ^2_1H + ^7_3Li + ^4_2He + n$	13206.08±0.34	13213.03±0.33	19.09±0.34	12.17 ±0.33
26	$^{14}_{\Lambda}C \rightarrow ^4_2He + ^7_3Li + ^2_1H + n$	13164.97±0.36	13213.03±0.33	60.20±0.36	12.17 ±0.33
27	$^{14}_{\Lambda}C \rightarrow ^7_3Li + ^1_1H + ^4_2He + 2n$	>13151.33±0.34	13213.03±0.33	<73.84±0.34	12.17 ±0.33
28	$^{14}_{\Lambda}C \rightarrow ^7_3Li + ^4_2He + ^1_1H + 2n$	>13125.07±0.34	13213.03±0.33	<100.84±0.34	12.17 ±0.33
29	$^{14}_{\Lambda}C \rightarrow ^1_1H + ^7_3Li + ^4_2He + 2n$	>13153.70±0.34	13213.03±0.33	<71.47±0.34	12.17 ±0.33
30	$^{14}_{\Lambda}C \rightarrow ^4_2He + ^7_3Li + ^1_1H + 2n$	>13126.75±0.34	13213.03±0.33	<98.42±0.34	12.17 ±0.33
31	$^{15}_{\Lambda}N \rightarrow ^9_4Be + ^3_2He + ^2_1H + n$	14141.58±0.19	14142.34±0.16	14.31±0.19	13.59±0.15
32	$^{15}_{\Lambda}N \rightarrow ^9_4Be + ^1_1H + ^3_2He + 2n$	>14104.82±0.17	14142.34±0.16	<51.07±0.17	13.59±0.15
33	$^{15}_{\Lambda}N \rightarrow ^9_4Be + ^3_2He + ^1_1H + 2n$	>14086.32±0.19	14142.34±0.16	<69.57±0.17	13.59±0.15
34	$^{15}_{\Lambda}N \rightarrow ^1_1H + ^9_4Be + ^3_2He + 2n$	>14109.32±0.17	14142.34±0.16	<46.57±0.19	13.59±0.15
35	$^{15}_{\Lambda}N \rightarrow ^3_2He + ^9_4Be + ^1_1H + 2n$	>14090.34±0.19	14142.34±0.16	<65.55±0.19	13.59±0.15
36	$^{15}_{\Lambda}N \rightarrow ^9_4Be + ^4_2He + ^1_1H + n$	14121.44±0.19	14142.34±0.16	34.45±0.19	13.59±0.15
37	$^{15}_{\Lambda}N \rightarrow ^4_2He + ^9_4Be + ^1_1H + n$	14128.49±0.19	14142.34±0.16	27.40±0.19	13.59±0.15
38	$^{15}_{\Lambda}N \rightarrow ^{10}_4Be + ^3_2He + ^1_1H + n$	14181.35±0.17	14142.34±0.16	14.53±0.19	13.59±0.15
39	$^{15}_{\Lambda}N \rightarrow ^{11}_5B + ^1_1H + ^1_1H + 2n$	>14107.44±0.17	14142.34±0.16	<56.00±0.17	13.59±0.15
40	$^{15}_{\Lambda}N \rightarrow ^1_1H + ^{11}_5B + ^1_1H + 2n$	>14402.84±0.18	14142.34±0.16	<48.45±0.17	13.59±0.15

Results and Discussions

A single- Λ hypernucleus event of J-PARC E07 experiment is analyzed in the present paper. The experimental data are supported by Professor Nakazawa who is the Spokesperson of J-PARC E07 experiment. Analysis is started from decay point B of analyzed event. Neutral particle emission at point B is firstly checked by dot product of direction vector of hyperfragment and total momentum of decay products. It is found that the angle between direction vector and total momentum is not equal to zero and neutral particle emission at point B is observed. Therefore, 85 possible decay modes with neutral particle decay products of track #1 single- Λ hypernucleus are chosen. In order to check the possible decay modes are allowed or forbidden, Q-values at point B are calculated and it is found that all 85 decay modes are allowed in nuclear emulsion. Then, the total energies of decay products are calculated. Total energies mean that the sum of kinetic energies of charged particle and that of neutral particles decay products. The Q-values and total energies are compared in table 2. According to table 2, we have found that 40 acceptable decay modes in which E_{total} are consistent with Q value within 3σ value. Moreover, mass and binding energy of track #1 single- Λ hypernucleus for all possible decay modes are calculated by mass-energy relation

and hypernuclei binding energy formula. The results are summarized in table 3. According to table 2 and table 3, ${}_{\Lambda}^{15}\text{N} \rightarrow {}_4^9\text{Be} + {}_2^3\text{He} + {}_1^2\text{H} + \text{n}$ decay mode has comparable Q-value and E_{total} in which 125.93 ± 0.16 MeV Q-value and 125.17 ± 0.03 MeV E_{total} value. Moreover, it is observed that the calculated mass of single- Λ hypernucleus is 14141.58 ± 0.19 MeV/c². This value is consistent with the known experimental mass 14142.34 ± 0.16 MeV/c² of ${}_{\Lambda}^{15}\text{N}$ hypernucleus. Furthermore, the calculated binding energy for ${}_{\Lambda}^{15}\text{N}$ hypernucleus is found to be 14.31 ± 0.19 MeV which is very consistent with known binding energy value 13.59 ± 0.15 MeV. Therefore, ${}_{\Lambda}^{15}\text{N} \rightarrow {}_4^9\text{Be} + {}_2^3\text{He} + {}_1^2\text{H} + \text{n}$ decay mode is chosen as the acceptable decay mode of single- Λ hypernucleus track #1.

Moreover, ${}_{\Lambda}^{15}\text{N} \rightarrow {}_4^{10}\text{Be} + {}_2^3\text{He} + {}_1^1\text{H} + \text{n}$ decay mode has comparable Q-value and E_{total} in which 130.51 ± 0.16 MeV Q-value and 129.53 ± 0.03 MeV E_{total} value. Moreover, it is observed that the calculated mass of single- Λ hypernucleus is 14141.36 ± 0.19 MeV/c². This value is consistent with the known experimental mass 14142.34 ± 0.16 MeV/c² of ${}_{\Lambda}^{15}\text{N}$ hypernucleus. Furthermore, the calculated binding energy for ${}_{\Lambda}^{15}\text{N}$ hypernucleus is found to be 14.53 ± 0.19 MeV which is very consistent with known binding energy value 13.59 ± 0.15 MeV. Therefore, ${}_{\Lambda}^{15}\text{N} \rightarrow {}_4^{10}\text{Be} + {}_2^3\text{He} + {}_1^1\text{H} + \text{n}$ decay mode is also chosen as the acceptable decay mode of single- Λ hypernucleus track #1. But, in the decay mode ${}_{\Lambda}^{15}\text{N} \rightarrow {}_4^{10}\text{Be} + {}_2^3\text{He} + {}_1^1\text{H} + \text{n}$, ${}_4^{10}\text{Be}$ is unstable particle and these decay mode is rejected.

Finally, a single- Λ hypernucleus track #1 is uniquely identified as ${}_{\Lambda}^{15}\text{N}$ which has 14141.58 ± 0.19 MeV/c² mass and 14.31 ± 0.19 MeV binding energy value. The most probable decay mode is found as ${}_{\Lambda}^{15}\text{N} \rightarrow {}_4^9\text{Be} + {}_2^3\text{He} + {}_1^2\text{H} + \text{n}$ in which 125.93 ± 0.16 MeV energy is released for this decay mode.

Conclusions

A single- Λ hypernucleus event of J-PARC E07 experiment is analyzed kinematically. According to our analysis, a single- Λ hypernucleus track #1 is uniquely identified as ${}_{\Lambda}^{15}\text{N}$. The Q-values of decay mode, total energy, mass and binding energy of ${}_{\Lambda}^{15}\text{N}$ hypernucleus is obtained in this analysis. The results are very useful for hypernuclear identification research work. We can support the identification data to extend the nuclear chart with strangeness.

Acknowledgements

The authors would like to thank Lieutenant Colonel Saw Myint Oo, Dean of Faculty of Physics, Defence Services Academy for his encouragement and permission to complete this work. The authors also would like to thank all collaborators of KEK-PS E373 experiment for their discussions, supports and valuable advices to carry out hypernuclear research.

References

- Bando H., *et al.*, (1990), International Journal of Modern Physics **A5**, pp. 4021-4198
- Ichikawa A., *et al.*, (2001), Physical Review Letters **B500**.
- Nakazawa K., (2018), Private Communication.
- Nakazawa K., *et al.*, (2013), Physical Review Letters **C 88**.
- Samanta C., and Schmitt A. T., (2019), “AIP Conference Proceedings, Vol. 2130, pp. 040004.
- Takahashi T., *et al.*, (2012) Progress of Theoretical and Experimental Physics 02B010.

INVESTIGATION OF TRIAXIALITY IN MEDIUM-MASS GERMANIUM ISOTOPES

Khaing Pwint Wai¹, Nyein Wint Lwin²

Abstract

The shape evolution for some selected germanium isotopes have been investigated from calculated potential energy surfaces on beta-gamma ($\beta - \gamma$) plane and analyzed by the single-particle energy levels. The Ev8 program with a 3-dimensional Cartesian mesh which solves the Skyrme-Hartree-Fock+BCS problem is employed. From the ($\beta - \gamma$) plane, these results are pointed out that ^{64}Ge is to be triaxial while both ^{68}Ge (oblate) and ^{78}Ge (prolate) have axially symmetric whereas ^{82}Ge gives the spherical nature. The calculated binding energies of all selected nuclei in this work fairly agree with experimental data.

Keywords: Skyrme Hartree-Fock + BCS method, ($\beta - \gamma$) plane

Introduction

One of the major challenges in nuclear physics is to study the nuclear structure of neutron-rich nuclei far from the beta stability line. For that reason, many researchers are trying to find out the valuable observations either experimentally or theoretically. There are about 4000–7000 nuclei which are expected to be bound from several theoretical calculations but have not yet been discovered experimentally. At present, both experimental results and theoretical calculations concluded that most of the deformed nuclei have a quadrupole deformation of the prolate kind (cigar-like shape) that preserves to a great extent axial symmetry. Therefore, those regions of the nuclide chart showing deformation with axial symmetry or deformed triaxial distributions breaking axial symmetry are of great interest to deepen the understanding of the mechanisms underlying the appearance of deformation [Robledo, L. M., R. R. Guzman and P. Sarriuguren, (2009)].

The microscopic models with effective interactions are widely used to investigate the properties of nuclei in stable and unstable regions. These can be divided into two different approaches; the shell model and self-consistent mean-field models. The shell model plays a main role for calculating the ground-state properties and excitations of nuclei with a mean-field description which is built from phenomenological single-particle basis wave functions such as the harmonic oscillator. However, it cannot explain some observed parities of heavier excited nuclei and magnetic moments. In the past decades, the relativistic and non-relativistic self-consistent mean-field approaches have been popular to study the structures of nuclei. The self-consistent mean-field (SCMF) theory is the only approach that aims closer to a fully microscopic description of nuclei that is computationally tractable over the entire mass table, it becomes the successful approach to describe and predict the properties of heavy nuclei. Many of these nuclei are located in the neutron-rich region and they play an important role in explaining the nucleosynthesis mechanism beyond iron. Therefore, it is necessary to gain knowledge of the structures of neutron-rich nuclei which are quite different from that of stable nuclei.

The aim of this present work is to predict the shapes of medium-mass nuclei with quadrupole deformation using self-consistent mean field approach. In this work, we chose four germanium isotopes (^{64}Ge , ^{68}Ge , ^{78}Ge , ^{82}Ge) because they can exhibit a pronounced competition between different configurations. The structures of these nuclei will be investigated by calculating the potential energy surfaces on ($\beta - \gamma$) plane which can clearly show the shapes of nuclei. To

¹ Assistant Lecturer, Department of Physics, Monywa University.

² Professor, Department of Physics, University of Mandalay.

this end, the Ev8 program will be employed in this work [Ryssens, W. et al, 2014]. This report is organized as: firstly, background theory of spherical shell model and deformed shell model will be discussed. Then Hartree-Fock equations with Skyrme interaction are presented. In addition constrained-Hartree-Fock method is also discussed. Finally, we concluded the results with the descriptions of the shapes which are obtained from the calculated potential energy surfaces.

Formalism

I. Background Theory of Spherical and Deformed Shell Model

The shell model which is based on the Schrödinger equations for the single-particle levels can be seen as follows

$$\left(-\frac{\hbar^2}{2m} \nabla^2 + V(\mathbf{r}) \right) \psi_i(\mathbf{r}) = \varepsilon_i \psi_i(\mathbf{r}) \quad (1)$$

where the central potential $V(r)$ will be approximated by the phenomenological potential such as square well, the Woods-Saxon or harmonic oscillator potential. It was realized, however, that use of such a phenomenological potential alone cannot even reproduce the empirical shell closures without the inclusion of a spin-orbit coupling term, as shown by Mayer

$$H = -\frac{\hbar^2}{2m} \nabla^2 + V(\mathbf{r}) + V_{so}(\mathbf{r}) \hat{\ell} \cdot \hat{s} \quad (2)$$

where \hat{s} and $\hat{\ell}$ are spin and angular momentum operators for a single nucleon. The degeneracy of oscillator level was partially removed with the introduction of this $\hat{\ell} \cdot \hat{s}$ term and the levels split up as $j = \ell \pm 1/2$, where j is the total angular momentum.

Since the potential for the shell model was spherically symmetric so that a new potential was needed for deformed nuclei. The Nilsson model, modified shell model, has been one of the most successful models that ever developed in nuclear theory. The modified harmonic-oscillator potential introduced by Nilsson et al., has been extensively employed in the interpolation of deformed nuclei [Zhang, J.Y. et al., 1989]. For axially symmetric deformed shapes, the potential extension along the nuclear z-axis is different from the two equal frequencies in the x and y-axes. The single-particle Hamiltonian in the form as follows

$$H_{nil} = -\frac{\hbar^2}{2M} \nabla^2 + \frac{M}{2} \left[\omega_x^2 (x^2 + y^2) + \omega_z^2 z^2 \right] - 2k\hbar\omega_0 \vec{\ell} \cdot \vec{s} - \mu'\hbar\omega_0 \left(\ell^2 - \langle \ell^2 \rangle_N \right) \quad (3)$$

where ω_0 is the oscillator frequency for the spherical case related to each of the three dimensions, κ controls the strength of the spin-orbit part of the potential, and μ' controls the strength of the correction term. The correction term, $(\ell^2 - \langle \ell^2 \rangle_N)$ originally had the form of $\mu\ell^2$. It served the purpose of suppressing (repressing) the energy of the higher lying shells; however, it was noted that this shift was too large for large N quantum numbers [Gustafson C. et al., 1968].

For triaxial nuclear shapes, the Hamiltonian in term of anisotropic harmonic oscillator potential becomes

$$H_{nil} = -\frac{\hbar^2}{2M} \nabla^2 + \frac{M}{2} \left(\omega_x^2 x^2 + \omega_y^2 y^2 + \omega_z^2 z^2 \right) - 2k\hbar\omega_0 \vec{\ell} \cdot \vec{s} - \mu'\hbar\omega_0 \left(\ell^2 - \langle \ell^2 \rangle_N \right) \quad (4)$$

The triaxial shape associated with the harmonic oscillator potential can be seen as follows

$$V_{osc} = \frac{M}{2} (\omega_x^2 x^2 + \omega_y^2 y^2 + \omega_z^2 z^2) \quad (5)$$

with $\omega_x \neq \omega_y \neq \omega_z$ and their relationships with the parameter (β) and the triaxiality angle (γ) are

$$\omega_x = \omega_0(\beta, \gamma) \left[1 - \frac{2}{3} \beta \cos\left(\gamma + \frac{2\pi}{3}\right) \right] \quad (6)$$

$$\omega_y = \omega_0(\beta, \gamma) \left[1 - \frac{2}{3} \beta \cos\left(\gamma - \frac{2\pi}{3}\right) \right] \quad (7)$$

$$\omega_z = \omega_0(\beta, \gamma) \left(1 - \frac{2}{3} \beta \cos \gamma \right) \quad (8)$$

The parameter (β) specifies the degree of deformation and the parameter (γ) describes the departure from axial symmetry.

The deformation dependence of $\omega_0(\beta, \gamma)$ is determined from volume conservation of the ellipsoidal equipotential surfaces. For the static nuclei, it is needed only the one sector $0^\circ \leq \gamma \leq 60^\circ$. The nucleus is assumed to have prolate shape when $\gamma = 0^\circ$ and oblate shape for $\gamma = 60^\circ$ and the intermediate γ -values as the triaxial shape. The single-particle energies of the triaxial modified oscillator Hamiltonian are obtained from diagonalisation.

With these definitions and the Nilsson Hamiltonian, the energy eigen states $(\varepsilon_{K^\pi[Nn_z\Lambda]})$, sometimes called Nilsson orbitals, can be extracted from solving the Schrödinger equation.

$$H_{nil} \psi_i = \psi_i \varepsilon_i \quad (9)$$

where i represents the complete set of asymptotic quantum numbers used to specify Nilsson orbitals

$$K^\pi [Nn_z\Lambda] \quad (10)$$

where K is the quantum number defines the overlap of the orbital with the deformed core, π is the parity defined as $\pi = (-1)^\ell = (-1)^N$, N is the oscillator quantum number, n_z is the number of oscillator quanta (number of nodes in the wave function), and Λ is the projection of the particle's orbital angular momentum onto the symmetry axis.

II. Hartree-Fock Equations with Skyrme Interaction

The full many-body Hamiltonian with a one-body kinetic energy term and a two-body force is obtained as follows

$$H = \sum_{i=1}^N \hat{t}_i + \frac{1}{2} \sum_{i \neq j}^N \hat{V}(r_i, r_j) \quad (11)$$

where the first term gives the kinetic energy operator and the second is the two-body force with the Coulomb interaction. Finally, the simplified expression for the Hartree-Fock equations becomes

$$\left(-\frac{\hbar^2}{2m} \nabla^2 + U_H^{(i)}(\mathbf{r}) \right) \varphi_i(\mathbf{r}) - \int d\mathbf{r}' U_F^{(i)}(\mathbf{r}, \mathbf{r}') \varphi_i(\mathbf{r}') = \varepsilon_i \varphi_i(\mathbf{r}). \quad (12)$$

This equation is known as the Hartree-Fock equation. The first term is known as the Hartree potential (the local term). The latter non-local part is also called the Fock term. In the following, the Skyrme approximation which can greatly reduce the number of integrations over single particle states will be discussed.

In the Skyrme-Hartree-Fock approach, the total binding energy of the system is given by the sum of the kinetic, Coulomb energies and the Skyrme energy functional that models the effective interaction between nucleons [Bender M. et al., 2003]. The full Skyrme interaction can be shown in the form of the following equation,

$$E = E_{Coulomb} + E_{kin} + E_{Sk} . \quad (13)$$

The result of the Hartree-Fock equations with Skyrme interaction is

$$\begin{aligned} E_{sk} = & b_1 \rho^2 + b_2 (\rho_n^2 + \rho_p^2) + b_3 \tau \rho + b_4 (\tau_n \rho_n + \tau_p \rho_p) + b_5 \rho \nabla^2 \rho \\ & + b_6 (\rho_n \nabla^2 \rho_n + \rho_p \nabla^2 \rho_p) + b_7 \rho^{\alpha+2}(\mathbf{r}) + b_8 (\rho_n^{\alpha+2} + \rho_p^{\alpha+2}) \\ & + b_9 \rho \vec{\nabla} J + b_{10} (\rho_p \vec{\nabla} J_p + \rho_n \vec{\nabla} J_n) + b_{14} J^2 + b_{15} (J_n^2 + J_p^2) \end{aligned} \quad (14)$$

In constrained Hartree-Fock (CHF) method, a wave function such as $|\Phi(q)\rangle$ is used to minimize the total energy under the constraint that a certain single-particle operator $\langle \hat{Q} \rangle$ which has a fixed expectation value

$$q = \langle \Phi | \hat{Q} | \Phi \rangle. \quad (15)$$

The method to solve this problem is adding to the Hamiltonian H in the condition Eq. (15) with Lagrange multiplier λ with quadrupole operators Q_{20} and Q_{22} which are constrained and can be seen as follows

$$\langle H' \rangle = \langle H \rangle - \lambda_1 \langle \hat{Q}_{20} \rangle - \lambda_2 \langle \hat{Q}_{22} \rangle. \quad (16)$$

In this work, this method is used to calculate the energy surface as a function of collective parameters of "q" such as quadrupole deformation.

Results and Discussion

In this calculation, the potential energy surfaces (PES) for selected even-even germanium isotopes are studied to investigate whether it has axially deformed or not. The axial deformation can give either prolate or oblate shape; on the other hand, the non-axial deformation leads to the triaxial shape. There are many sets of the Skyrme parameters. The Sly4 parameter set is chosen for this calculation because this parameterization can give good agreement for the nuclear root mean square radii and binding energies. The zero-range density dependence pairing force will be used in this calculation.

The relationship between the deformation parameter (q) and the triaxiality angle (γ) can be represented by

$$q_1 = q \cos(\gamma) - \frac{1}{\sqrt{3}} q \sin(\gamma) \quad (17)$$

$$q_2 = \frac{2}{\sqrt{3}} q \sin(\gamma). \quad (18)$$

The representation of deformation parameter $\beta_{\ell m}$ which is related to the total mass of the moment as follows

$$\beta_{\ell m} = \frac{4\pi}{3R_0^\ell A} \langle \hat{Q}_{\ell m} \rangle \quad (19)$$

In this section, the calculated potential energy curves using constrained Hartree-Fock method are depicted in Fig. 1 for four selected germanium nuclei (^{64}Ge , ^{68}Ge , ^{78}Ge and ^{82}Ge).

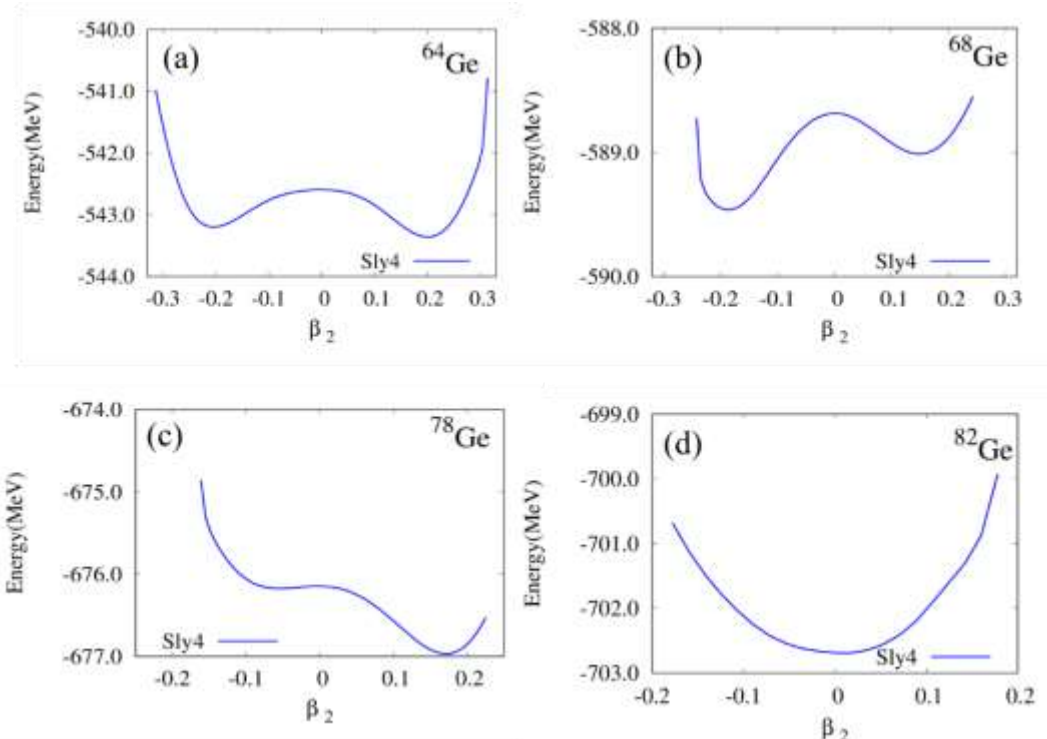


Figure 1 The potential energy curve versus quadrupole deformation (β_2) for (a) ^{64}Ge , (b) ^{68}Ge , (c) ^{78}Ge and (d) ^{82}Ge nuclei obtained with the Sly4 parameter set.

In this section, we first calculate the potential energy surfaces as a function of axial quadrupole deformation parameter. The calculated potential energy surfaces are depicted in Fig. 1(a-d) for ^{64}Ge , ^{68}Ge , ^{78}Ge and ^{82}Ge nuclei. The nuclei having minimum energy located at the positive deformation parameter generally describes the prolate shape while the minimum energy with negative deformation parameter stands for the oblate shape. The ground state energy located at the origin is predicted to have the spherical shape. The shape coexistence is expected in ^{64}Ge nucleus since the energy difference between oblate and prolate shape is less than 0.3 MeV. Shape evolution has been found from oblate to prolate and spherical in ^{68}Ge , ^{78}Ge and ^{82}Ge nuclei. The ^{68}Ge nucleus is predicted to have minimum oblate configuration which can be seen in panel (b) whereas ^{78}Ge to be prolate sides in panel (c), respectively. The semi-magic ^{82}Ge nucleus shows the spherical shape in the last panel (d).

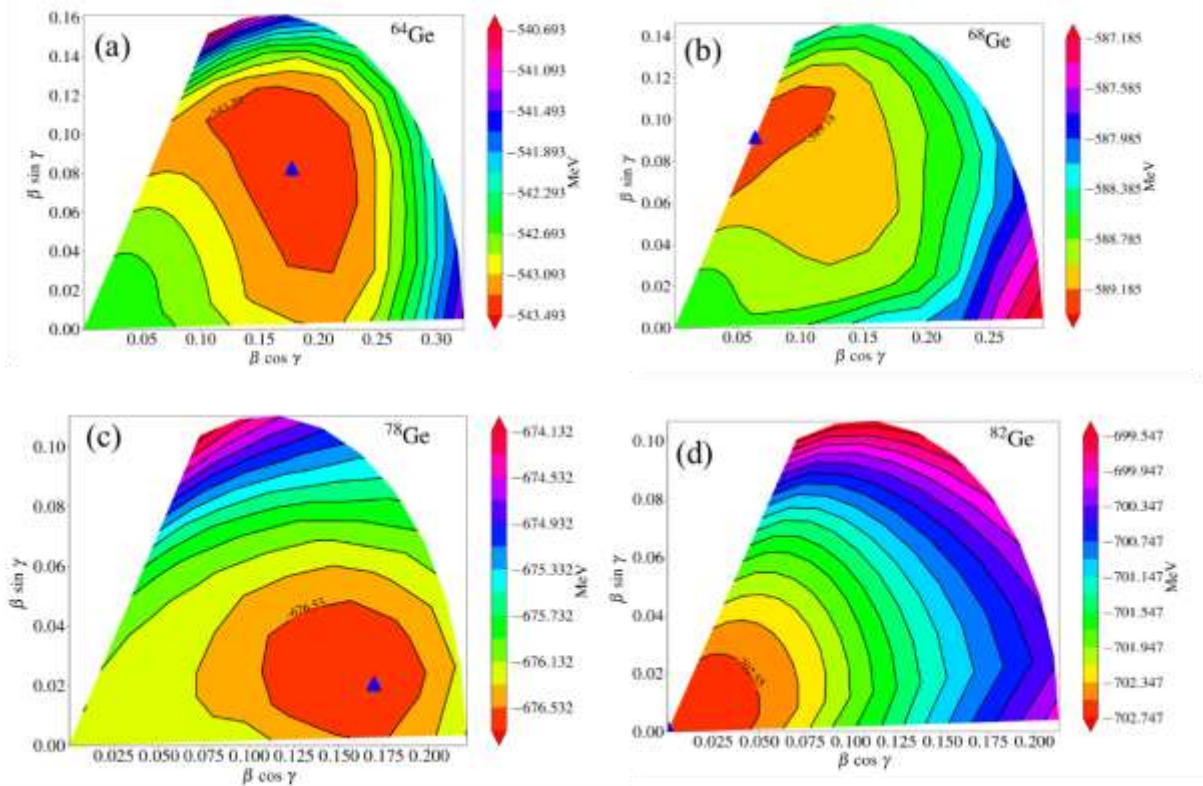


Figure 2 The potential energy surfaces versus quadrupole deformation (β_2) for (a) ^{64}Ge , (b) ^{68}Ge , (c) ^{78}Ge and (d) ^{82}Ge nuclei on $\beta - \gamma$ plane obtained with Sly4 parameter set.

In order to investigate whether there is a deviation from axial symmetry in these nuclei, it is necessary to calculate the potential energy surfaces on $\beta - \gamma$ plane (See: Fig. 2(a)-(d)). In above figures, the contours join the points with the same energy and each contour line is separated by 0.2 MeV. The triangles in these figures indicate the absolute minimum in the potential energy surfaces.

As can be seen in Fig. 2(a), the PES for ^{64}Ge shows its minimum energy at points which is deviating from axial symmetry (ie., the energy minimum does not occur at either $\gamma = 0^\circ$ or $\gamma = 60^\circ$). This fact suggests that this nucleus is expected to have triaxial nature. It has ground state energy of 543.29 MeV at $\beta_2 \approx 0.18$ and triaxiality angle $\gamma = 25^\circ$. The PES of ^{68}Ge shows oblate minimum which is located at $\beta_2 \approx 0.11$ on $\gamma = 60^\circ$ axis having 589.18 MeV as shown in panel (b). On the contrary, the calculated results suggest that ^{78}Ge nucleus can have more prolately deformed configuration rather than the soft-triaxial nature giving ground state energy of 676.53 MeV with the quadrupole deformation nearly 0.17 (See: Fig. 2(c)). Finally, the potential energy surface (PES) for the semi-magic number ^{82}Ge nucleus is showing spherical configuration at the origin with minimum energy of 702.55 MeV.

The variation of single particle energy levels as a function of quadrupole deformation will be discussed in the next section.

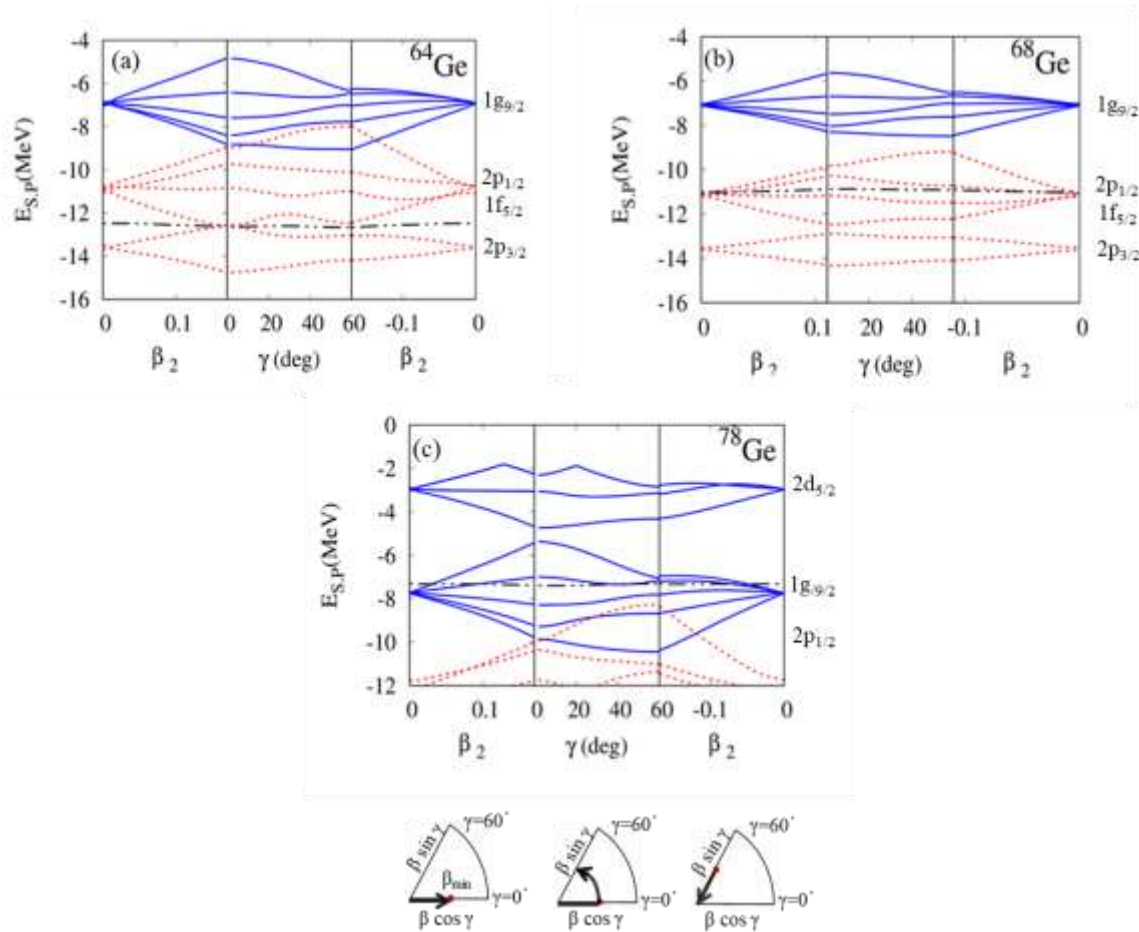


Figure 3 Schematic diagrams for single-particle orbitals along a path (β, γ) are depicted in the lower part of the figures. Combined plot of neutron single-particle energies (a) ^{64}Ge , (b) ^{68}Ge and (c) ^{78}Ge nuclei plotted as a function of the deformation parameter.

In order to get more inside on the resultant nuclear configurations, the single particle levels as a function of triaxial degrees of freedom is plotted in Fig. 3(a-c). It is known that the formation of deformed minima is favored by the occurrence of gaps or low single-particle level density around the highest occupied level. In these figures, the neutron SPE for each selected nuclei are depicted as the combined plot. In the combined plot, the axially symmetric single-particle levels are plotted as a function of deformation parameter (β_2) on the left and right-most panels. In the middle panel, neutron levels are plotted as functions of γ -deformation parameter for a fixed value (β_2) which corresponds to the ground state minimum. Solid blue curves with positive parity, short-dotted red curves with negative parity, and dashed black curve corresponds to the Fermi level and red circles indicated the magic number. Figure 3 (a) is for ^{64}Ge . In this figure, a pronounced gap appears near the Fermi Level which is found between the last occupied $2p_{3/2}$ and first unoccupied states $1f_{7/2}$ sub-shell. The appearance of gap in the triaxial region, $20^\circ < \gamma < 30^\circ$, favors the triaxial shape. The appreciable gap on the oblate axis near the Fermi level is found for ^{68}Ge nucleus which is shown in panel (b). Meanwhile, ^{78}Ge nucleus has the formation of the oblate and prolate neutron gaps which are found above the Fermi level but the largest gap is found on the prolate axis which favours the deep prolate configuration as can be seen in panel (c).

Summary and Conclusion

In this research work, we first calculate the potential energy curves as a function of quadrupole deformation parameter for four even-even germanium isotopes using the Sly4 parameter set. The results suggest that start from shape coexistence in ^{64}Ge nucleus, the shape evolution, ie., oblate-prolate-spherical shapes is found in ^{68}Ge , ^{78}Ge and semi-magic nucleus, ^{82}Ge .

In order to determine the existence of axial asymmetry in these nuclei, the potential energy surfaces of these nuclei are calculated on $\beta - \gamma$ plane. These results confirm oblate, prolate and spherical shapes for ^{68}Ge , ^{78}Ge and ^{82}Ge nucleus, respectively. On the contrary, the energy minimum of ^{64}Ge occurs at $\gamma = 25^\circ$, ie., triaxial shape.

Finally the single-particle energies on $\beta - \gamma$ plane for three deformed germanium nuclei are computed to examine the shapes of nuclei. It can also be concluded that the preference of ground state shape configurations is sensitive on the slope of last occupied single particle level.

Acknowledgements

I am grateful to the respectable person who is devoted their efforts and time for holding the seminar of Myanmar Academy of Arts and Science which is hosted at the University of Yangon. I also thank Dr. Shwe Sin Aung, Professor, and Head of Physics Department at Monywa University for her enthusiasm and permission.

References

- Bender, M., and P. H. Heenen (2003) “Self-consistent mean-field models for nuclear structure.” *Rev. Mod. Phys.* vol. 75, pp. 121.
- C. Gustafson, *et al.*, (1968) “On the spontaneous fission of nuclei with Z near 114 and N near 184” *Nucl. Phys. A* **115**, pp 545.
- J.Y. Zhang, *et al.*, (1989) “Nilsson parameter set in the A=120-140 region.” *Phys. Rev.C* **39**, pp714.
- Robledo, L. M., R. R. Guzman and P. Sarriuren, (2009) “Role of triaxiality in the ground-state shape of neutron-rich Yb, Hf, W, Os and Pt isotopes.” *J. Phys. G: Nucl. Part. Phys.* **36** 115104, pp. 19.
- Ryssens, W., V. Hellemans, M. Bender and P.H. Heenen, (2014) “Solution of the Skyrme HF+BCS equation on a 3D mesh: II. A new version of the Ev8 code.” arXiv: nucl-th **1405.1897v2**, pp. 1.

MEASUREMENTS OF IODINE CONTENTS IN SEAWEED (KALAMOAT SEIGH) (CATENELLA SP) FROM VARIOUS PLACES IN MON STATE

Aye Aye Maw¹, Ni Ni War², Kyi Thar Myint³ and Cho Cho Aung⁴

Abstract

The purpose of this research work was to study the amount of iodine contents and intermolecular bond structure of seaweed from three locations (Waegali, Haigyii and Kyaikkhami) in Mon State. These samples were analysed by using Energy Dispersive X-Ray Fluorescence (EDXRF) and Fourier Transform Infra-Red (FTIR) techniques. From the EDXRF measurement, the result showed that iodine contents of seaweed from three locations (Waegali, Haigyii and Kyaikkhami) were 17.81%, 15.79% and 18.50% respectively. It was found that the iodine isotope as in treatment of diagnosis and diseases of the thyroid gland or thyroid cancers.

Keyword: seaweed (Waegali, Haigyii and Kyaikkhami), EDXRF, FTIR

Introduction

Iodine-131 is the commonly used radioactive isotope of Iodine. It is used in the diagnosis, treatment of disease and localization or tracer studies. To get an adequacy on Iodine levels, the amount of iodine contents in seaweeds were taken up for measuring, with EDXRF techniques by which the elemental contents of the samples were acquired. As it had been mentioned the main objective of this work is to get the iodine level, but it was not come of because instrumental requirements. In EDXRF spectrum of three seaweed samples from represented for iodine contents. To get over this task (FTIR Analysis) would be taken out FTIR Analysis which allows for the determination of specific bonds of molecules and to identify any phase of the elements in compound materials “Nicholas Tsoulfanidls (2009)”.

By means of Vibrational spectroscopic method, it has been obtained frequency or wave number between potassium (K) and iodine (I) in single bond constituted in sample (1). According to this method it would be also carried out for Ca=I double bonds in samples (2) and (3).

From FTIR spectra and EDXRF results for these samples, the iodine concentration percentages could be figure out and these results can be confirmed by S-I₂ bonds because sulphur was assumed to be the largest constituents in the *seaweed* samples and potassium (or) calcium was the second behind.

Materials and Methods

Humans need sufficient iodine to make thyroid hormones which were produced by the thyroid gland. The deficiency of iodine was several important health consequences called IDD (Iodine Deficiency Disorders). Iodine is a mineral that is important for health. It is needed to make the thyroid hormones. These hormones are needed for many body processes including growth, regulating metabolism and for the development of a baby's brain during pregnancy and early life. In this research have been taken out FTIR Analysis which allows for the determination of specific bonds of molecules and identify any phase of the elements in compound materials.

¹ Lecturer, Department of Physics, Mawlamyine University.

² Lecturer, Department of Physics, University of Yangon.

³ Dr, Professor (Retd), Department of Physics, West Yangon University.

⁴ Dr, Professor, Department of Physics, Lashio University.

By means of Vibrational spectroscopic method, it has been obtained frequency or wave number between sulphur (S) and iodine (I) in double bonds constituted in sample 1, samples 2 and 3.

From EDXRF results for these samples, the iodine concentration percentages could be figured out and FTIR spectra results can be confirmed by S - I₂ bonds because sulphur was assumed to be the largest constituents in the seaweed samples and potassium (or) calcium were the second behind it.

Collection of Sample

Three samples of seaweed were collected from different locations, sample 1 from Waegali township, sample 2 from Haigyii township and sample 3 from Kyaikkhami township in Mon State in month of January to April. The seaweed were thoroughly cleaned with seawater and finally cleaned with running water to remove salt and foreign materials. The cleaned seaweed were dried and ground into fine powder and it was stored at room temperature and used for further analysis “Pereira, (2011)”.

Sample Preparation

The samples were dried at room temperature for 34 days in the open air and blended. The dried sample were crushed and ground into powder by using grinding machine. The samples were fine dried and ground enough to meet the conditions for homogeneous dense material, and ensure reproducibility in measurement. And then, these powder sample were weighed with scientific balance to get about 5 grams. Then poured into a disc made of steel and pressed into pellets by using 3 ton weight of Hydraulic press, Cambridge Elective Industries. The diameter of each pellet is 2.5 cm and samples of seaweed were shown in Figure 1 and 2 “Pereira, (2011)”.

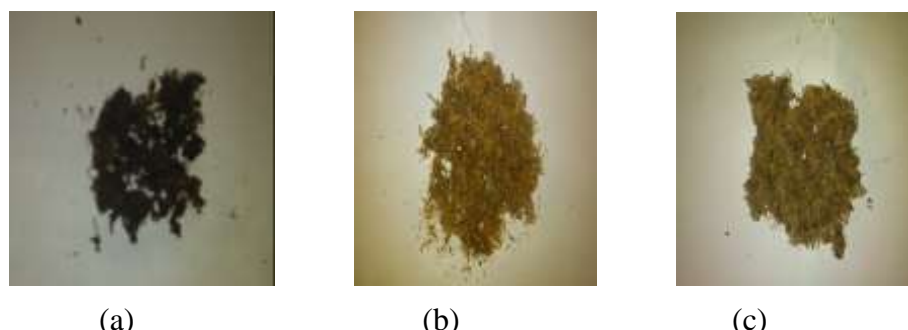


Figure 1 Photograph of samples from (a) Waegali township (b) Haigyii township (c) Kyaikkhami township

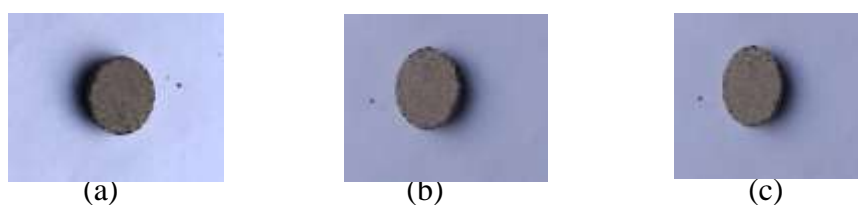


Figure 2 Pallets Sample of seaweed from (a) Waegali Township (b) Haigyii Township (c) Kyaikkhami Township

Energy Dispersive X-Ray Fluorescence (EDXRF)

Energy Dispersive X-Ray Fluorescence Spectrometer (EDXRF) is an analytical method to determine the elemental composition of many types of materials. It can be used to determine the

thickness and composition of layers, coatings, and plating. It is fast, accurate and non-destructive and requires minimal sample preparation. Samples can be soil, liquid, powder. EDXRF spectrometer provides one of the simplest, most accurate and most economic analytical methods for the determination of the chemical composition. It can be used for a wide range of elements, from Sodium (11) to Uranium (92), and provides detection limits at the sub-ppm level; it can also measure concentrations of up to 100% easily and simultaneously “Raquel Salamo Clapera (2006)”.

Measurement Condition of Rigaku NEX CG EDXRF Spectrometer

Cartesian Geometry Energy dispersive X-ray fluorescence (EDXRF) is a routinely used analytical technique for the qualitative and quantitative determination of major and minor atomic elements in a wide variety of sample types. The heart of its versatility stems from the ability to provide rapid, non-destructive, multi-element analyses – from low

parts-per-million (ppm) levels to high weight percent (wt%) concentrations – for elements from sodium (^{11}Na) to uranium (^{92}U) “Raquel Salamo Clapera (2006)”.

The versatile Rigaku NEX CG EDXRF spectrometer delivers routine elemental measurements across a diverse range of matrices – from homogeneous, low viscosity liquids – to solids, metals, slurries, powders and pastes. Especially well suited to the semi-quantitative determination of elemental content in complete unknowns, the superior analytical power, flexibility and ease-of-use of the NEX CG add to its broad appeal for research, industrial and in-plant monitoring applications. The schematic diagram of the Cartesian Geometry Energy Dispersive X-Ray Fluorescence Spectrometer (Rigaku NEX CG EDXRF) [Mawlamyine University, Department of Physics] as shown in Figure 3 “Raquel Salamo Clapera (2006)”.



Figure 3 Energy Dispersive X-ray Fluorescence NEX CG EDXRF Spectrometer

Table 1 The Specification of Rigaku NEX CG EDXRF spectrometer

Excitation	X-ray tube with pd anode 50 W max power 50 W max voltage Four standard polarization and secondary targets depending on application for optimum excitation Optional fifth target for optional excitation of Na and Mg
Detector	High performance SDD Peltier electronic cooling Large active detection area Optimum balance of spectral resolution and high count rate

FTIR Spectroscopic Measurement

FTIR spectrometers have several prominent advantages.

(i) The signal-to-noise ratio of spectrum is significantly higher than the previous generation infrared spectrometers. (ii) The accuracy of wavenumber is high, the error is within the range of ± 0 cm^{-1} . (iii) The scan time of all frequencies is short (approximately 1s). (iv) The resolution is extremely high ($0.1\text{--}0.005 \text{ cm}^{-1}$). (v) The scan range is wide ($10000\text{--}10 \text{ cm}^{-1}$). (vi) The interference from stray light is reduced.

The collected lines in the observed FTIR spectra indicate the vibrational characteristics of constituent molecules in the samples or it indicates the phase formation of the samples (with molecular vibration). Infrared (IR) refers to that part of the electromagnetic spectrum between the visible and microwave regions. The electromagnetic spectrum can be considered as a wave or particle traveling at the speed of light. These waves differ from each other in the length and frequency.

The obtained data (observed wavenumber) are found experimentally that the octahedral site molecular networks in the sample emitted frequencies with $\frac{1}{\lambda} = \bar{v}$ wavenumbers.

FTIR 8400 Spectrophotometer is combined with the IR solution- a 32 bit high performance FTIR software- to analyze samples easily and securely. Universities' Research Centre (URC), University of Yangon (YU) at room temperature.

Experimental conditions were as follows:

Measurement mode : %T

Wavenumber range : $400 \text{ cm}^{-1} \text{--} 4000 \text{ cm}^{-1}$

Time of scan : 60 s

Method : KBr pellet

Vibrational Frequency from Spectroscopic Technique

Vibrational spectroscopic method or Fourier Transform Infrared (FTIR) spectroscopy is the analysis of the sample by using infrared radiation. Infrared radiation refers broadly to electromagnetic spectrum between the visible and microwave regions. When infrared radiation of wave number in the range from about $10000\text{--}100 \text{ cm}^{-1}$ interacts with matter it can be absorbed, causing the chemical bonds in the material to vibrate. The presence of chemical bonds in a material is a necessary condition for infrared spectrum can provide quantitative information as well, such

as the concentration of a molecule in a sample. The relation between absorbance (A) and transmittance (T) is

$$A = \log_{10} \frac{1}{T}$$

The infrared bond gives information about the strength and nature of molecular interactions. Thus, an infrared spectrum provides a great deal of information about a sample. The frequency of absorptions depends on the relative mass of the atoms, the force constants of the bonds and the geometry of the atoms.

The following equation derived from Hooke's Law states the relationship between of oscillation atomic mass and force constant (F) of the bond. For single bond force constant is 5×10^5 dynes/cm.

$$\bar{\nu} = \frac{1}{2\pi c} \left[\frac{F}{\frac{M_x M_y}{M_x + M_y}} \right]^{1/2}$$

Where, $\bar{\nu}$ = the vibrational frequency or wave number

c = velocity of light = 3×10^{10} cms⁻¹

M_x = mass of carbon

M_y = mass of sulphur

According to the above equation vibrational frequency or wave number between carbon (C) and sulphur (S) is carried out^[1].

Common Functional Group in Organic Compound

Any organic compound continuous chain of carbon atoms which has the various functional group. To get the di-iodoethane the basic structure is $\text{---C}^{\text{I}}\text{---I}$ and carbon constituted in chemical group of C S with C = S stretching mode. Modified wave number for two successive bond is 1017cm^{-1} . From this use, it can be deduce the conversion factors for iodine contents interms of sulphur in phenols and di-iodoethane organic compounds.

Results and Discussion

From EDX - NEXCG spectrometer, the results show the presence of different chemical elements in the seaweed as shown in Figure (4) to (6). The element contents of seaweed was listed in Table (2) and diagram of the iodine contents for three samples of seaweed in Figure (7). In this table, the iodine (I) constituents in these seaweed samples are 17.81 % in sample 1, 15.79 % in sample 2 and 18.50 % in sample 3 respectively. Among this iodine content in sample 3 is higher than that of samples 1 and sample 2.

The EDXRF spectroscopic analysis, the qualitative results were analyzed by $\text{C}_6\text{H}_{10}\text{O}_5$ constituted in seaweed is 12.500 mg cm^{-2} in total analyze 12.503 mg cm^{-2} . Iodine contents of three seaweed samples were 17.87 %, 15.79 % and 18.50 % of elemental concentration in Si-U analyzes.

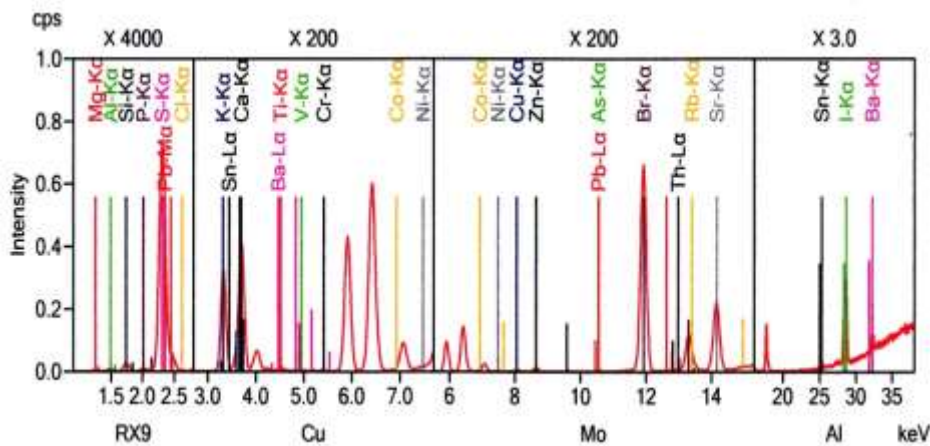


Figure 4 Spectrum of elemental concentration in seaweed from Waegali by NEXCG Spectrometer

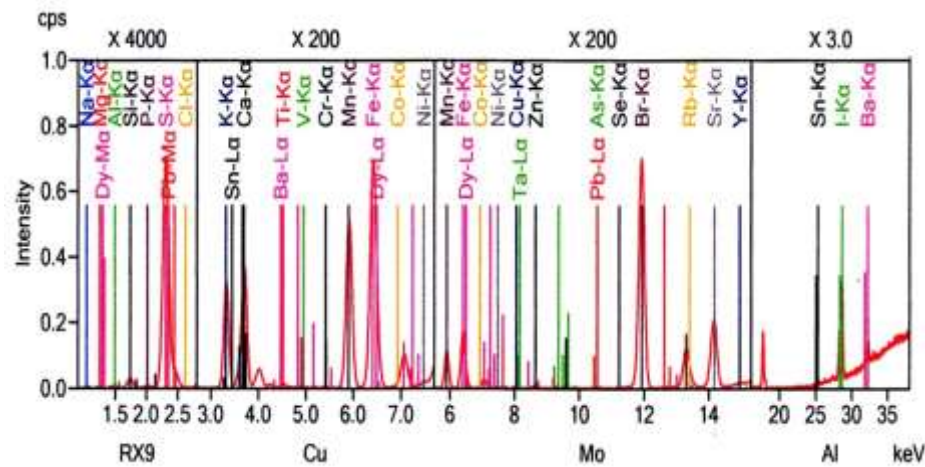


Figure 5 Spectrum of elemental concentration in seaweed from Haigyi by NEXCG Spectrometer

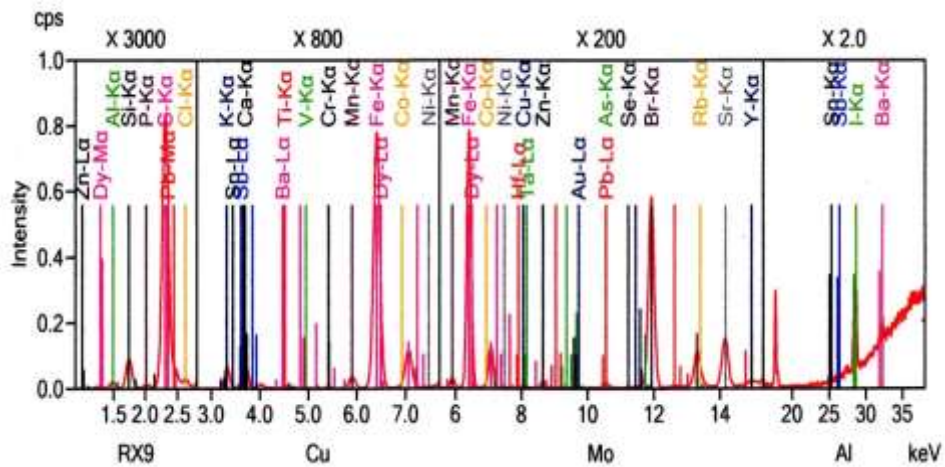
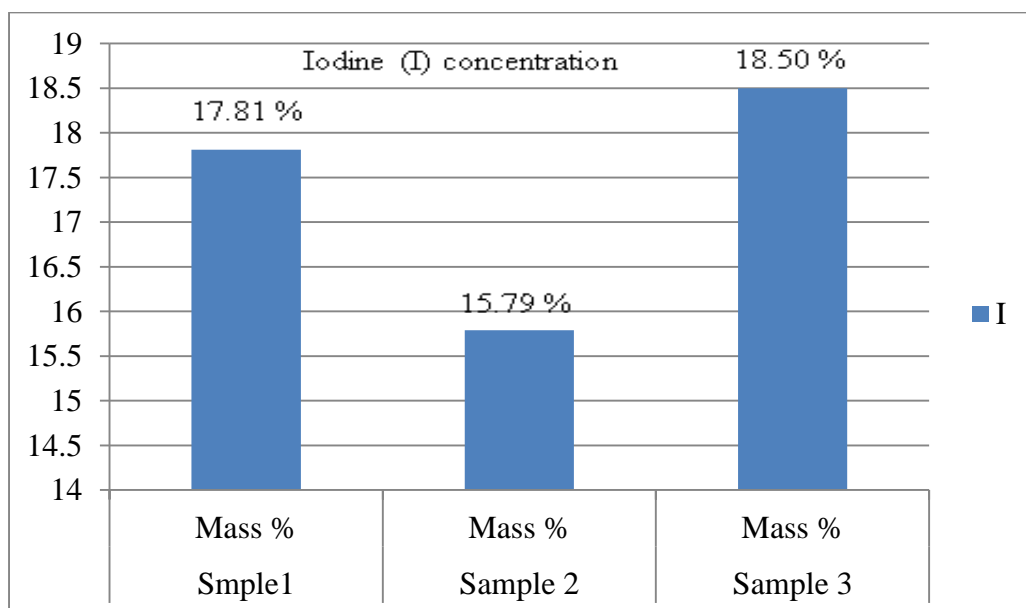


Figure 6 Spectrum of elemental concentration in seaweed from Kyaikkhami by NEXCG Spectrometer

Table 2 Element contents of seaweed (mass%)

No	Element	Smple1 Mass %	Sample 2 Mass %	Sample 3 Mass %
1	Na	-	-	0.44
2	Mg	0.21	-	0.70
3	Al	0.47	-	0.24
4	Si	4.80	4.13	1.21
5	P	1.00	4.30	-
6	S	40.05	42.69	36.32
7	Cl	1.47	2.10	0.02
8	K	16.72	17.42	21.80
9	Ca	15.90	14.80	13.62
10	Ti	0.43	-	-
11	Mn	-	0.51	-
12	Fe	2.40	6.10	5.35
13	Zn		0.17	0.15
14	As	-	-	0.17
15	Br	1.70	-	1.61
16	I	17.81	15.79	18.50
17	Sr	-	0.30	-
18	Cu	-	-	0.14

**Figure 7** Diagram of the iodine contents for three samples of seaweed

FTIR Spectroscopic Study

According to molecular vibrational theory, in the present work, FTIR transmission spectrum of, sample 1 is C = S stretching mode and C S group in the wavenumber range of 1029 cm^{-1} region with KBr pellet method is shown in Fig 8, sample 2 is C = S stretching mode and C S group in the wavenumber range of 1003 cm^{-1} region with KBr pellet method is shown in Figure 9 and sample 3 is C = S stretching mode and C S group in the wavenumber range of

1017 cm⁻¹ region with KBr pellet method is shown in Figure 10. The observed wavenumbers were assigned by using wavenumbers of free ions or molecules. Vibrational characteristics and corresponding mode assignments of molecules are tabulated in Table 3, 4 and 5.

Inclusive iodine results were determination of the iodine contents in seaweed by using vibrational spectroscopic method. In this research, the Fourier Transform Infrared FTIR were used for the vibrational analysis. The concentration of other constitutions are also expressed in modified content percentages.

From analysis the results, the calibrated iodine contents in the samples have to be verified by conventional volumetric method (WHO recommended). It has been known that the contents would be obtained in ppm (parts per million) by HATR (Horizontal Attenuated Total Reflectance) technique. The information and results of this research will contribute to our common goal of the elimination of iodine deficiency disorder (IDD).

Table 3 Intermolecular structure of sample-1 from FTIR spectrum

No.	wave number (cm ⁻¹)	Mode	Chemical group
1	3437.28	N - H stretching	Amino acid I
2	2926.11	C-H stretching	characteristic of aliphatic (- CH) groups
3	1643.41	C ≡ O stretching C = C stretching	Carbonyl groups
4	1535.38	N = N – O stretching	aromatic group
5	1384.94	N – O stretching	Nitro compound
6	1244.13	Vibration stretching	C - O group of ester
7	1028.09	C = S stretching	C S group
8	922.00	C - O H stretching	C - H groups
9	788.91	Vibration stretching	C-H out of plane deformation
10	528.51	K – I stretching	K-I single bond
11	466.79	C - OH ₃ stretching	CO ₂ groups

Table 4 Intermolecular structure of sample-2 from FTIR spectrum

No.	wave number (cm ⁻¹)	Mode	Chemical group
1	3685.49	N - H stretching	Amino acid I
2	2297.30	C ≡ N stretching	C N group
3	1523.82	N - H stretching	Amino acid II
4	1365.65	NO ₂ symmetric stretching	Aromatic nitro compound
5	1003.02	C = S stretching	C S group
6	677.040	Ca = I stretching	Ca = I

Table 5 Intermolecular structure of sample-3 from FTIR spectrum

No.	wave number (cm ⁻¹)	Mode	Chemical group
1	3421.83	N - H stretching	Amino acid I
2	2926.11	C-H stretching	characteristic of aliphatic (- CH) groups
3	2303.08	C ≡ N stretching	C N group
4	1631.83	C = C stretching	Carbonyl groups
5	1531.53	N - H stretching	Amino acid II
6	1377.22	N – O stretching	Nitro compound
7	1016.52	C = S stretching	C S group
8	675.110	Ca = I stretching	Ca = I

Quantitative Analysis

In present research elemental concentrations in seaweed samples were obtained in two categories; exclusive iodine percentage and inclusive iodine percentage. Exclusive iodine elemental concentrations were determined by EDXRF spectrometer. The elemental concentrations in sample 1, 2 and 3 were determined as shown in table 2.

The estimation of quantity due to EDXRF spectrum in sample 1 and sulphur S concentration is 49.052% and from FTIR spectrum 1028.09 cm⁻¹ absorbtion peak correspond to C = S bond. From this research the I₂ contents in di-iodoethane can be deduced as 49.052 % exclusive I₂ and 29.537% inclusive I₂.

The estimation of quantity due to EDXRF spectrum in sample 2 and sulphur S concentration is 50.706% and from FTIR spectrum 1003.02 cm⁻¹ absorbtion peak correspond to C = S bond. From this research the I₂ contents in di-iodoethane can be deduced as 50.706% exclusive I₂ and 30.398 % inclusive I₂.

The estimation of quantity due to EDXRF spectrum in sample 3 and sulphur S concentration is 45.412 % and from FTIR spectrum 1006.52 cm⁻¹ absorbtion peak correspond to C = S bond. From this research the I₂ contents in di-iodoethane can be deduced as 45.412% exclusive I₂ and 27.64 % inclusive I₂.

Conclusion

The present results showed the inclusive iodine contents in three samples from different location by EDX- NEXCG spectrometer. Among these iodine contents in sample 3 is (18.50 %) higher than that of other sample 1(17.81 %) and sample 2 (15.79 %). The iodine contents have been studied in seaweed for consumer levels.

From the result showed that iodine contents in three samples from different location by Rigaku NEX CG EDXRF spectrometer. Among these iodine contents in sample3 is (0.0085 %) higher than that of other sample 1 and sample 2 are (0.0065 %) and (0.0046 %) respectively.

The resultant contents should be recommended, the contents percentage are calibrated with each others resulted from two elements. In table 6 the contents of elements in two rows deduce from potassium and calcium row 1 and deduce from sulphur row 2 are roughly in same order.

From analysis the results, the calibrated iodine contents in the samples have to be verified by conventional volumetric method (WHO recommended). It has been known that the contents would be obtained in ppm (parts per million) by HATR (Horizontal Attenuated Total Reflectance)

technique. The information and results of this research will be hoped for contribution to our common goal of the elimination of iodine deficiency disorder (IDD).

Acknowledgements

The authors would like to knowledge the Department of Physics, Mawlamyine University for facilitating this work with high-tech equipment.

References

- L.Pereira, (2011) “A Review of the nutrient composition of selected edible seaweeds,” in Seaweed: Ecology, Nutrient Composition and Medicinal Uses, V.H. Pomin, Ed, pp.15-47, Science, New York, NY, USA.
- Nicholas Tsoulfanidls (2009) “Measurement and Detection of Radiation Second Edition” (Washington, DC Taylor Francis)
- Raquel Salamo Clapera (2006) “Energy Dispersive X-Ray Fluorescence: Measuring Elements in Solid and Liquid Matrices”
- Topliss, D.J. and Eastman, C.J. (2004) “Diagnosis and management of hyperthyroidism and hypothyroidism”. The Medical Journal of Australia, 180(4):186-193.
- World Health Organization 2000 “Progress towards the Elimination of Iodine Deficiency Disorders” (Geneva: WHO)

INVESTIGATION OF THE RADON GAS CONCENTRATION INSIDE HEINDA TIN MINE IN DAWEI TOWNSHIP, TANINTHARYI DIVISION, MYANMAR

Ei Ei San¹, Aye Kyaw², Aye Aye Hnin³, Thet Naing⁴,
Maung Maung Shwe⁵, Khin Swe Oo⁶

Abstract

This investigation aims to report the radon gas concentration inside of the Heinda Tin Mine in Dawei Township, Tanintharyi Division of Myanmar. In this research, the determinations of the radon gas concentration have been carried out in soil samples of some places inside Heinda Tin Mine. Soil samples were collected from four different parts inside of the Mine. RAD 7 detector was used to obtain the results. The experimental results were compared with the recommended values of ICRP and EPA. And then, a precious message concerned with the radon gas hazard could be given to the public for health.

Keywords: – *radon gas, RAD 7, soil samples*

Introduction

When the earth was formed, billions of years ago, there were probably many radioactive elements included in the mix of material that became the earth. Radioactive elements are unstable. At some indeterminate moment, it will change to another element, emitting some form of radiation in the process. While it is impossible to predict exactly when the transformation of an individual atom will take place, there have been a very good measure of the probability of decay chain, within a given time slot. A natural radioactive transformation is accompanied by the emission of one or more of alpha, beta or gamma radiation. There are several types of radon monitors on the market. Nearly all of these are designed to detect alpha radiation, but not beta or gamma radiation. Because it is very difficult to build a portable detector of beta or gamma radiation that has both low background and high sensitivity.

An important fact is that uranium, thorium and their progeny are the main source of ionizing radiation in the earth crust. Therefore, uranium is a radiotoxic element. Radon (^{222}Rn), one of the decay products of uranium, continually decays to its daughters. The natural decay of ^{222}Rn emits alpha particles entering into the air through the earth crust. And then it exposes to the population and causes to be the natural radiation dose. Radon is a chemically inert gas and do not combine with other. Radon and its daughters can lead to change the respiratory function and can cause to the lung cancer. For these reason, the tracking of radon gas concentration is an important role of the radiation protection. There are many types of radon detection technique. To perform this research, the radon gas concentrations were detected by using RAD 7 detector.

Health Effects of Radon

All radon risk comes from breathing the air that consists of radon gas. These dust particles can easily be inhaled into the lung by the human being and then decay by emitting the alpha radiation which damage cells in lung. Alpha radiation can destroy DNA of these lung cells and can

¹ Lecturer, Department of Physics, Dawei University

² Lecturer, Department of Physics, Dawei University

³ Associate Professor, Department of Physics, Bago University

⁴ Professor, Department of Physics, East Yangon University

⁵ Professor, Department of Physics, Dawei University

⁶ Head & Professor, Department of Physics, Dawei University

lead to cancer. Because of a low solubility in body fluids, it can lead to a uniform distribution of the gas throughout the body. Alpha radiation travels only extremely short distances in the body. Therefore, when we breathe that radiation, it cannot reach cells in any other organs. Especially it is important lung cancer hazarded by radon. There is no safe level of radon any exposure poses some risk of cancer.

Radon concentration depends upon the environmental conditions. The soil and rocks characteristics also control the transportation of radon. Radon concentration varies with time by time, day by day, year by year, grain size, content of radium and uranium.

Situation of Heinda Tin Mine

Heinda Mine is one of the tin mine in Dawei township, Tanintharyi Division in Myanmar. Tanintharyi Region is covering the long narrow southern part of the country on the Kra Isthmus. It borders the Andaman Sea to the west and Thailand to the east. To the north is the Mon State. It is the main manufacturing place for Myanmar's Natural resources like pearl and sea food. Dawei is the capital city of the Division. Especially, Maungmagan Beach is a well-known landmark of Dawei because of its very beautiful sigh seeing. Many local and foreign visitors have frequently paid a visit to this Region.

Heinda Mine is situated on the north-east of Dawei. It is about 142 kilometers or 35 miles far away from Dawei. Its location is north latitude $14^{\circ} 8'49''$ and east longitude $98^{\circ} 28'19''$. Heinda Mine is a large old tin mine in the northern part of the Great Tenasserim River Basin in Tanintharyi Region of Myanmar. This mine is in the proximity of Myitta town. The area of the Mine is about 2100 acres. Myaung Pyo is the closest village to Heinda Mine. Myaung Pyo village is the community most directly and adversely affected by the mining operation. The small tin mine has expanded into a large mining operation using modern technologies today. The map of the Heinda Mine is as shown in Figure 2.

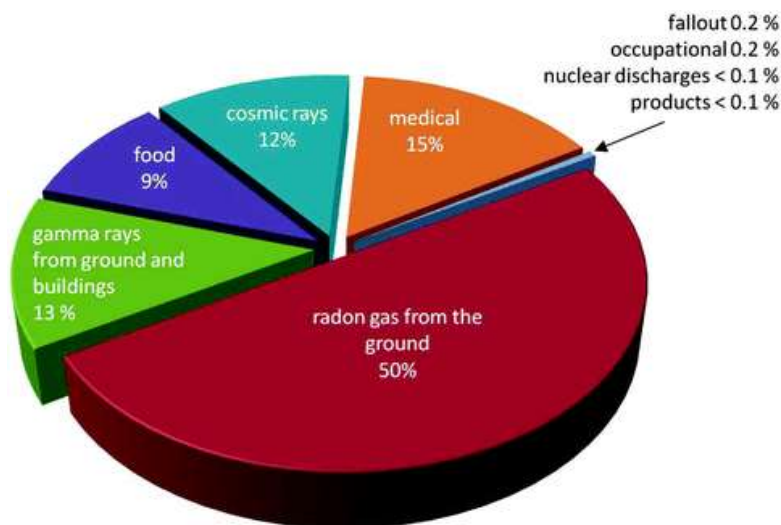


Figure 1 Proportion of the average annual radiation doses to the UK population [Watson et al., 2005]

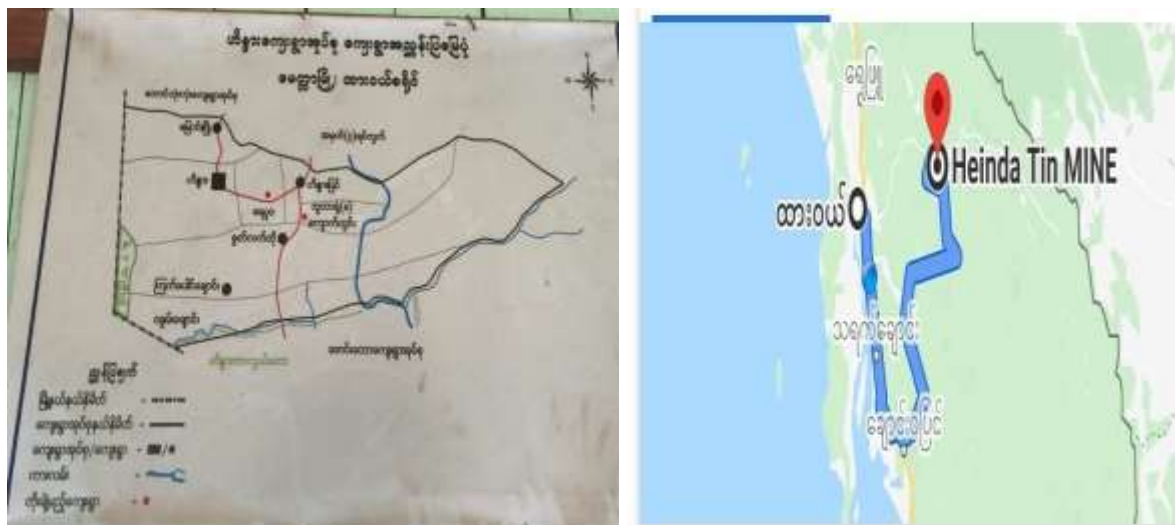


Figure 2 Map of the Heinda Tin Mine

Experimental Procedures

The Collection of Soil Samples

For this experiment, the soil samples were collected from the different parts of Heinda Mine. These are four different parts inside of the Mine. The collected soil samples were packed with the plastic bags and covered with zip. And then the balance was used to know their weights. The photographs of collected soil samples are as shown in Figure.

Measurement Procedure

The RAD 7 Durridge detector which consists of small drying tube with computer connectivity was used to obtain the measurement results. Firstly, the soil sample was filled in the plastic can through the sampling point. The soil gas probe should be inserted into the plastic can and it made sure that a reasonable seal between the probe shaft and the surrounding soil, so that ambient air does not descend around the probe and dilute the soil gas sample. The detector draws air from within the enclosed space, through the desiccant and inlet filter, and into the measurement chamber. The RAD 7 pulls samples of air through a fine inlet filter, which excludes the progeny, into a chamber for analysis. The radon in the RAD 7 chamber decays, producing detectable alpha emitting progeny, particularly the polonium isotopes. Though the RAD 7 detects progeny radiation internally, the only measurement it makes is of radon gas concentration.

Generally, soil gas is normal high concentration so it always uses the short cycle times to gain precision. The total time of the short cycle is 15 minutes. This time to complete a test is the pump sample time 5 minutes plus the delay period 5 minutes plus the count period 5 minutes. This is also called 5 minutes' cycle. The counted data from the detector is transferred to the display monitor computer system. It provides a wealth of graphing and data analysis options and then offers the best precision data acts as a graph. The preparations of RAD professional 7 detector with Computer PC are setup as shown in Figure 4.

The RAD Professional 7 detector always gives the unit of concentration with Bqm^{-3} . Becquerel is the favored unit in Europe and Canada. The favored unit of radon activity in US is PicoCurie. Therefore, to calculate the concentration with PicoCurie and the annual effective dose, the following calibration coefficients were used.

$$1 \text{ pCi/L} = 37 \text{ Bqm}^{-3}$$

$$1 \text{ Bqm}^{-3} = 0.0172 \text{ mSv y}^{-1} (\text{ICRP}, 2007)$$



Figure 3 (a) and (b) The photographs of Heinda Tin Mine where were collected the soil samples
(c) The photographs of the soil samples inside of the Mine.

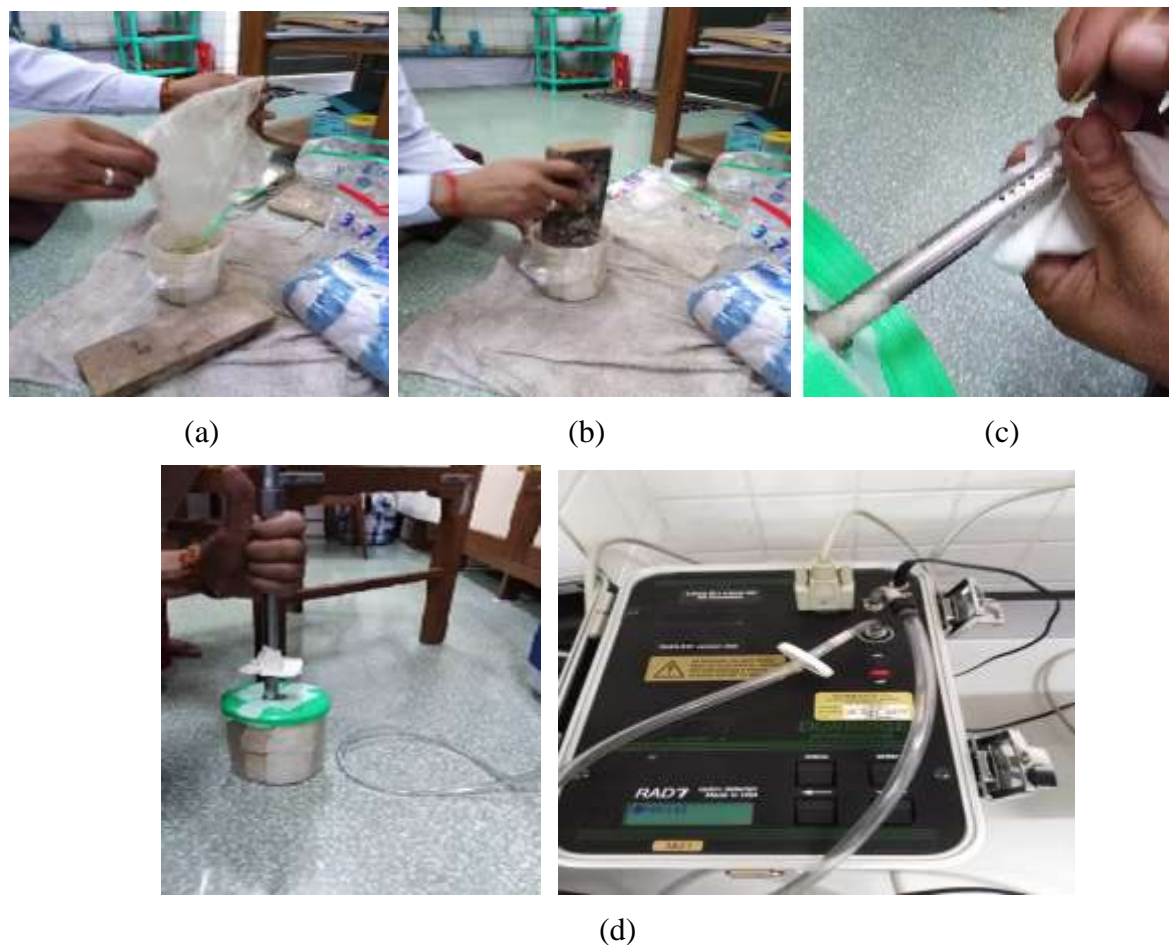


Figure 4 (a), (b), (c) and (d) The photographs of the laboratory preparations for the detection of soil samples.

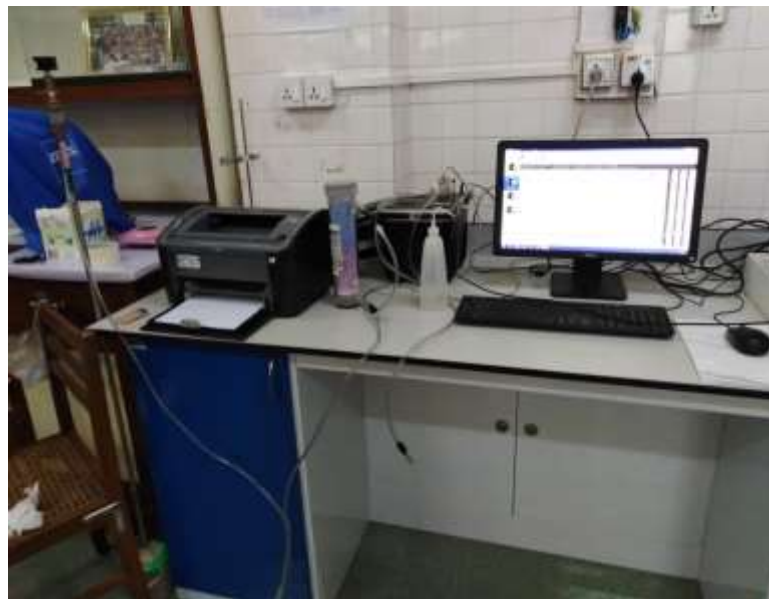


Figure 5 The photograph that was measuring soil sample with RAD 7 detector connected to PC.

Result and Discussion

Table 1 Average radon concentrations of soil samples inside Heinda Mine

No	Sample	Average Radon Concentration		Annual Effective Dose (mSv ⁻¹)
		(Bq m ⁻³)	(pCi/L)	
1	A1	24.8 ± 29	0.67 ± 0.78	0.43 ± 0.50
2	A2	0.00 ± 60	0.00 ± 1.62	0.00 ± 1.03
3	A3	11.9 ± 20	0.32 ± 0.54	0.21 ± 0.34
4	A4	14.2 ± 15	0.38 ± 0.41	0.24 ± 0.26

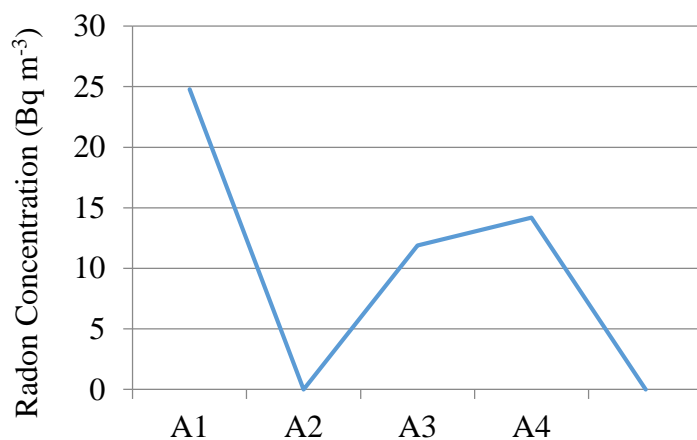


Figure 6 Histogram representing measured radon concentration of four soil samples inside Heinda Mine

The radon gas concentration is association with geology, weather and content of Uranium in the earth crush. As well as radon concentration varies with time by time, day by day and year by year. Therefore, many countries have defined an Action Level of radon concentration to guide their program to control domestic exposure to radon. The Action Level is not a boundary between safe and unsafe, but rather a level at which action on reduction of radon level will usually be

justified. There is not acceptance level of radon in soil. Thus the annual effective dose is variable from country to country and from region to another. The Environmental Protection Agency (EPA) states that any radon exposure carries some risk; no level of radon exposure is always safe.

In Myanmar, an action level hasn't been recommended for the public yet. Therefore, there is no an action level which is recommended in Myanmar. In this research, the recommendation values of ICRP have been used for the action level. In 2007, the International Commission on Radiological Protection (ICRP) Publication 103 issued the recommendation value of 600 Bqm^{-3} for dwelling and 1500 Bqm^{-3} for the workplaces corresponding to the annual effective dose limits of $10\text{--}20 \text{ mSv y}^{-1}$ (ICRP 1993, 2007). In 2009, ICRP issued to reduce radon exposure to upper reference level for dwelling to 300 Bqm^{-3} and 1000 Bqm^{-3} as the entry point for applying occupational radiological protection requirements in existing exposure situations. The Environmental Protection Agency (EPA) in US sets its action level as 148 Bqm^{-3} .

In the recent year, some Myanmar researchers have started to study on radon concentration at various parts in Myanmar. Mostly former researchers have been studied the concentration of radon inside the caves and buildings. There is very little number of researchers who studied at the Mines. There was no one who studied at the Heinda Tin Mine. Therefore, the present results could not be compared with the previous result data.

Conclusion

From the result data, the average radon concentrations of inside the Mine have very few amount of 2009 indoor radon level. The average annual effective doses were under the safe limits of ICRP ($10 \text{ to } 20 \text{ mSv y}^{-1}$). Moreover, it does not reach to EPA's action level (148 Bqm^{-3}). Its highest effective does was $0.43 \pm 0.50 \text{ mSv y}^{-1}$. This means that the people who stay inside the Mine for the whole year can accept the absorbed dose $0.43 \pm 0.50 \text{ mSv}$. This value is very low under the safe limits of ICRP. So it will not be very dangerous for them. For these reasons, the radon concentration of inside the Heinda Tin Mine cannot seriously harmful to the public in health concern for a long time.

Acknowledgements

I would like to express appreciation to Acting Rector Dr Theingi Shwe, Pro-rector Dr Khin May Aung and Dr Cho Cho Myint, Dawei University for their encouragement and kind permission to undertake the present research. I also would like to express my profound thanks to Professor Dr Khin Swe Oo, Head of Department of Physics, and Professor Dr Maung Maung Shwe, Department of Physics, Dawei University, for their kind permission to carry out this work, their encouragement and help during this work.

References

- Chauhan R P, Kant K, Mahesh K & Chakarvarti S K (2001) Indian Journal of Pure Applied Physics 39 491.
- Durrani S A et al (1987) "Solid State Nuclear Track Detector: Principles, Methods and Application" (Oxford, Pergamon)
- Environment International, pp. 47-51, (1999) Copyright©1999 Elsevier Science Ltd Printed in the USA, Vol.25, No.1.
- ICRP: "The Recommendations of International Commission on Radiological Protection." (2007) ICRP Publication 103
- Niles Jonassen (1983) "The Determination of Radon Exhalation Rates" Health Physics 45 (2) 369
- American Journal of Applied Sciences (2012) ISSN 1546-9239 © Science Publication.
- Muramasu H, Hasegawa N et al (1999) "Journal of Health Physics Society 380 77(1)47
- PRAMANA– April (2004) "journal of physics ©Indian Academy of Sciences" 861-8, Vol. 62, No. 4.

ESTIMATION OF BINDING ENERGY OF XI-MINUS HYPERON IN A NUCLEUS FROM SINGLE- Λ HYPERNUCLEUS EVENT

Khin Than Tint¹, Aye Moh Moh Myo², Yi Yi Myint³, K. Nakazawa⁴

Abstract

The binding energy of Xi-minus (Ξ^-) hyperon in nitrogen nucleus was estimated from single- Λ hypernucleus event which was detected in nuclear emulsion of J-ARC E07 experiment. The type of hypernucleus, its production and decay mode were obtained based on the conservation laws of energy and momentum. Moreover, the estimated value of the binding energy of Ξ^- hyperon in nitrogen nucleus was 0.51 ± 0.17 MeV.

Keywords: Xi-minus hyperon, binding energy, single- Λ hypernucleus event, nuclear emulsion

Introduction

Ξ^- hyperons were produced via the (K^-, K^+) reaction in a diamond target with the momentum of the K^- meson beam, 1.81 GeV/c in J-PARC E07 experiment. The Ξ^- hyperons were captured by nuclei in nuclear emulsion and become compound nuclei with $S = -2$. At the decay of compound Ξ^- nuclei, single- Λ hypernucleus, twin single- Λ hypernuclei, double Λ hypernucleus can be emitted. The binding energy of Ξ^- hyperon in a nucleus can be obtained more exactly from twin single- Λ hypernuclei event. In the twin single- Λ hypernuclei event, two single- Λ hypernuclei were emitted back to back from the stopping point of Ξ^- hyperons. The kinetic energy and momentum of two single- Λ hypernuclei can be obtained from their range. The binding energy of Ξ^- hyperon can be obtained from the momentum balance of two single- Λ hypernuclei. On the other hand, one single- Λ hypernucleus track and Λ hyperon (invisible in nuclear emulsion) were emitted at the stopping point of Ξ^- hyperon, i.e. decay point of Ξ^- nucleus in single- Λ hypernucleus event. In this case, the energy and momentum of the single- Λ hypernucleus can be measured from its range. However, the energy and momentum of Λ hyperon cannot determine exactly due to invisible in nuclear emulsion. In this analysis, binding energy of Ξ^- hyperons in nitrogen nucleus is obtained from, the difference between Q value and total energy (single- Λ hypernucleus + invisible Λ hyperon).

Event Analysis

Event Description of A Single- Λ hypernucleus Event

The single- Λ hypernucleus event was detected at up-stream of Module #26, plate #5. Figure 1 shows a photograph and a schematic drawing of the single- Λ hypernucleus event. The Ξ^- hyperon came to rest at vertex A, where two charged particle tracks (track #1, track #2) and uncharged particle track (invisible) Λ hyperon were emitted. The particle of track #1 decayed into a π^- meson (track #4) and other charged particle (track #3) at point B. Hence, #1 was identified as a single- Λ hypernucleus. The end of tracks #2, #3 were traced manually and found the stopping points in the same layer of nuclear emulsion. Track #4 (thin track) was passed through the upper layer of emulsion plate # 5 and stopped in plate # 2.

¹ Dr, Associate Professor, Department of Physics, University of Mandalay

² MSc, Department of Physics, Yadanabon University

³ Dr, Professor and head, Department of Physics, Yadanabon University

⁴ Dr, Senior Professor, Department of Physics, Gifu University, Japan.

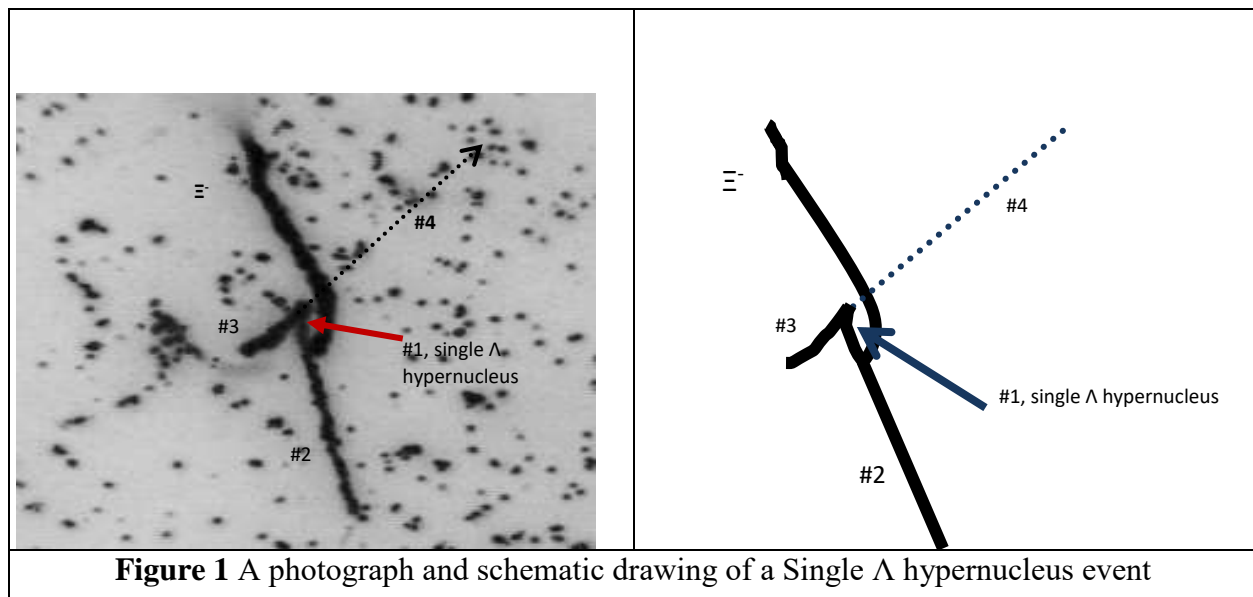


Figure 1 A photograph and schematic drawing of a Single Λ hypernucleus event

Range and Angle Measurement

We measured the ranges and emission angles of the tracks from single- Λ hypernucleus event by using the microscope system. The range of the tracks, R , can be obtained from measured (x , y , z) coordinates of tracks by using the following equation,

$$R = \sqrt{\Delta X^2 + \Delta Y^2 + (\Delta Z \times S)^2} \quad (1)$$

where, ΔX , ΔY and ΔZ as the length in the x , y and z direction respectively. The shrinkage factor of dried emulsion, S , is defined by the ratio of the thickness of the emulsion plate at the time of beam exposure and measurement. The zenith angle (θ) and azimuthal angle (ϕ) of each track were obtained from the coordinates at vertex and suitable clicked point on the track.

Range-Energy Relation Calibration in Nuclear Emulsion

The observable things in nuclear emulsion were ranges, angles, and a grain density of charge particle tracks. In order to calculate the masses of hypernuclei, the energy of the decay daughters was necessary. The kinetic energy of a charged particle is provided by measuring the range if we assume the nuclear species. The range-energy relation is essential for emulsion analysis.

The alpha decays which have topologies of Thorium series were used as range energy calibration source. Total 57 events have straight and long range track, alpha particle decays from ^{212}Po , were used. The method of range-energy relation calibration or the estimation of density nuclear emulsion plate was already described elsewhere. The density and Shrinkage factor of an emulsion plate of Pl#5, Mod #26 were $3.59 \pm 0.02 \text{ gcm}^{-3}$ and 2.2 ± 0.01 , respectively.

Event Reconstruction

The event construction in nuclear emulsion was based on the conservation laws of energy and momentum. The kinetic energies of the charged particles were calculated from their range by means of a range-energy relation and for neutral particles it was calculated from the momentum balance. The errors of kinetic energy come from the errors of range. On the other hand, the errors of total energy come from the errors of range, angles and rest mass.

Firstly, we considered that the Ξ^- hyperon was absorbed by a light nucleus (C, N, and O) in nuclear emulsion at the point A. Since the length of track #1 is as short as $3.3 \pm 0.2 \mu\text{m}$, the Ξ^- hyperon was assumed to be captured in a light nucleus. In nuclear emulsion at point A from which single Λ hypernucleus (track #1), track #2 and invisible Λ hyperon were emitted. The Q value, the total kinetic energy of emitted particles (E_{Total}) were calculated and compared. Table (1), Table (2), Table (3) and Table (4) summarized the some possible production reaction modes from $\Xi^- + {}_6^{12}\text{C}, {}_7^{14}\text{N}, {}_8^{16}\text{O}$ to a Λ hyper nucleus (track #1, track #2) and invisible Λ hyperon.

Table 1 Some production reaction modes of the single Λ hypernucleus without neutron emission.

Possible Production Reaction	Q-value (MeV)	E_{total} (MeV)	B_{Ξ^-} (MeV) = Q - E_{Total}
$\Xi^- + {}_7^{14}\text{N} \rightarrow {}_{10}^{\Lambda}\text{Be} + {}^4\text{He} + \Lambda^0$	19.01	18.51 ± 0.17	0.51 ± 0.17
$\Xi^- + {}_6^{12}\text{C} \rightarrow {}_{10}^{\Lambda}\text{Li} + {}^4\text{He} + \Lambda^0$	10.78	14.45 ± 0.14	-3.66 ± 0.14
$\Xi^- + {}_6^{13}\text{C} \rightarrow {}_{10}^{\Lambda}\text{Li} + {}^4\text{He} + \Lambda^0$	9.57	14.66 ± 0.14	-5.09 ± 0.14
$\Xi^- + {}_6^{12}\text{C} \rightarrow {}_{10}^{\Lambda}\text{Be} + {}^3\text{H} + \Lambda^0$	8.14	24.75 ± 0.17	-6.66 ± 0.17
$\Xi^- + {}_8^{16}\text{O} \rightarrow {}_{12}^{\Lambda}\text{B} + {}^4\text{He} + \Lambda^0$	16.86	25.07 ± 0.22	-8.21 ± 0.22
$\Xi^- + {}_7^{13}\text{C} \rightarrow {}_{10}^{\Lambda}\text{Be} + {}^3\text{H} + \Lambda^0$	7.26	15.73 ± 0.16	-8.47 ± 0.16
$\Xi^- + {}_8^{17}\text{O} \rightarrow {}_{13}^{\Lambda}\text{B} + {}^4\text{He} + \Lambda^0$	17.20	26.20 ± 0.22	-8.99 ± 0.22
$\Xi^- + {}_6^{12}\text{C} \rightarrow {}_{10}^{\Lambda}\text{Be} + {}^2\text{H} + \Lambda^0$	5.45	16.42 ± 0.16	-10.48 ± 0.16
$\Xi^- + {}_7^{14}\text{N} \rightarrow {}_{12}^{\Lambda}\text{B} + {}^2\text{H} + \Lambda^0$	13.75	25.895 ± 0.21	-12.15 ± 0.21
$\Xi^- + {}_7^{14}\text{N} \rightarrow {}_{13}^{\Lambda}\text{B} + {}^1\text{H} + \Lambda^0$	16.01	29.633 ± 0.20	-13.63 ± 0.20

Table 2 Some production reaction modes of the single Λ hypernucleus with one neutron emission

Possible Production Reaction	Q-Value (MeV)	E_{total} (MeV)	B_{Ξ^-} (MeV) = Q - E_{Total}
$\Xi^- + {}_6^{12}\text{C} \rightarrow {}_7^{\Lambda}\text{Li} + {}^4\text{He} + \Lambda^0 + \text{n}$	2.31	> 10.25	< -7.94
$\Xi^- + {}_6^{12}\text{C} \rightarrow {}_{10}^{\Lambda}\text{Be} + \text{d} + \Lambda^0 + \text{n}$	1.89	> 9.98	< -8.10
$\Xi^- + {}_6^{12}\text{C} \rightarrow {}_{10}^{\Lambda}\text{Be} + \text{p} + \Lambda^0 + \text{n}$	3.72	> 11.14	< -7.42
$\Xi^- + {}_6^{13}\text{C} \rightarrow {}_8^{\Lambda}\text{Li} + {}^4\text{He} + \Lambda^0 + \text{n}$	5.84	> 10.34	< -4.49
$\Xi^- + {}_6^{13}\text{C} \rightarrow {}_{10}^{\Lambda}\text{Be} + \text{t} + \Lambda^0 + \text{n}$	3.19	> 9.72	< -6.53
$\Xi^- + {}_6^{13}\text{C} \rightarrow {}_{10}^{\Lambda}\text{Be} + \text{d} + \Lambda^0 + \text{n}$	1.00	> 10.54	< -9.54
$\Xi^- + {}_7^{14}\text{N} \rightarrow {}_{10}^{\Lambda}\text{Be} + {}^4\text{He} + \Lambda^0 + \text{n}$	15.46	> 12.55	< 2.90
$\Xi^- + {}_7^{14}\text{N} \rightarrow {}_{12}^{\Lambda}\text{B} + \text{p} + \Lambda^0 + \text{n}$	11.52	> 17.07	< -5.54
$\Xi^- + {}_7^{15}\text{N} \rightarrow {}_{10}^{\Lambda}\text{Be} + {}^4\text{He} + \Lambda^0 + \text{n}$	8.19	> 12.87	< -4.69
$\Xi^- + {}_6^{17}\text{O} \rightarrow {}_{12}^{\Lambda}\text{B} + {}^4\text{He} + \Lambda^0 + \text{n}$	12.72	> 16.71	< -4.07

Table 3 Some production reaction of single Λ hypernucleus with two neutron emission

Possible Production Reaction	Q-Value (MeV)	E_{total} (MeV)	$B_{\Xi} (\text{MeV}) = Q - E_{\text{Total}}$
$\Xi^- + {}^{12}_6C \rightarrow {}^6_\Lambda\text{Li} + {}^4\text{He} + \Lambda^0 + 2\text{n}$	-4.42	> 8.72	< -13.14
$\Xi^- + {}^{12}_6C \rightarrow {}^9_\Lambda\text{Be} + p + \Lambda^0 + 2\text{n}$	-0.35	> 8.26	< -8.61
$\Xi^- + {}^{13}_6C \rightarrow {}^8_\Lambda\text{Li} + {}^4\text{He} + \Lambda^0 + 2\text{n}$	-14.73	> 7.92	< -22.64
$\Xi^- + {}^{13}_6C \rightarrow {}^9_\Lambda\text{Be} + d + \Lambda^0 + 2\text{n}$	-3.06	> 7.97	< -11.03
$\Xi^- + {}^{13}_6C \rightarrow {}^{10}_\Lambda\text{Be} + p + \Lambda^0 + 2\text{n}$	-1.73	> 8.67	< -10.40
$\Xi^- + {}^{14}_7N \rightarrow {}^8_\Lambda\text{Be} + {}^4\text{He} + \Lambda^0 + 2\text{n}$	-3.31	> 10.36	< -13.67
$\Xi^- + {}^{14}_7N \rightarrow {}^{11}_\Lambda\text{B} + p + \Lambda^0 + 2\text{n}$	-1.06	> 12.35	< -13.41
$\Xi^- + {}^{15}_7N \rightarrow {}^{12}_\Lambda\text{B} + p + \Lambda^0 + 2\text{n}$	0.69	> 12.97	< -12.28
$\Xi^- + {}^{17}_8O \rightarrow {}^{11}_\Lambda\text{B} + {}^4\text{He} + \Lambda^0 + 2\text{n}$	0.13	> 13.28	< -13.15
$\Xi^- + {}^{18}_8O \rightarrow {}^{12}_\Lambda\text{B} + {}^4\text{He} + \Lambda^0 + 2\text{n}$	4.67	> 13.68	< -9.10

Table 4 Some production reaction of single Λ hypernucleus with three neutron emission

Possible Production Reaction	Q-value (MeV)	E_{total} (MeV)	$B_{\Xi} (\text{MeV}) = Q - E_{\text{Total}}$
$\Xi^- + {}^{13}_6C \rightarrow {}^6_\Lambda\text{Li} + {}^4\text{He} + \Lambda^0 + 3\text{n}$	-9.37	> 7.96	< -17.33
$\Xi^- + {}^{13}_6C \rightarrow {}^9_\Lambda\text{Be} + p + \Lambda^0 + 3\text{n}$	-5.29	> 7.08	< -12.36
$\Xi^- + {}^{14}_7N \rightarrow {}^7_\Lambda\text{Be} + {}^4\text{He} + \Lambda^0 + 3\text{n}$	-15.67	> 9.24	< -24.91
$\Xi^- + {}^{14}_7N \rightarrow {}^{10}_\Lambda\text{B} + p + \Lambda^0 + 3\text{n}$	-10.85	> 9.89	< -20.73
$\Xi^- + {}^{15}_7N \rightarrow {}^8_\Lambda\text{Be} + {}^4\text{He} + \Lambda^0 + 3\text{n}$	-14.15	> 9.37	< -23.53
$\Xi^- + {}^{15}_7N \rightarrow {}^9_\Lambda\text{Be} + {}^3\text{He} + \Lambda^0 + 3\text{n}$	-15.95	> 8.96	< -24.91
$\Xi^- + {}^{15}_7N \rightarrow {}^{11}_\Lambda\text{B} + {}^4\text{He} + \Lambda^0 + 3\text{n}$	-11.89	> 10.36	< -22.25
$\Xi^- + {}^{17}_8O \rightarrow {}^{10}_\Lambda\text{B} + {}^4\text{He} + \Lambda^0 + 3\text{n}$	-9.65	> 11.47	< -21.13
$\Xi^- + {}^{17}_8O \rightarrow {}^{13}_\Lambda\text{C} + p + \Lambda^0 + 3\text{n}$	0.70	> 14.47	< -13.77
$\Xi^- + {}^{17}_8O \rightarrow {}^{10}_\Lambda\text{B} + {}^4\text{He} + \Lambda^0 + 3\text{n}$	-7.91	> 11.77	< -19.67

Secondly, the single Λ hypernucleus (track#1) was identified from its decay point B. The particle species of decay daughters, track#3 and #4 are assigned and considered all the possible decay modes of the single Λ hypernucleus. The Q values for decay modes are obtained and compared with the total kinetic energy of track #3 and #4. All decay modes of the single Λ hypernucleus (track #1) at vertex point B were shown in Table (5a) and Table (5b).

We also checked the angle between two tracks, track #3 and track #4. Take the coordinates of two points, vertex A and end point of each track, we obtained the vector of each track. The angle between two tracks emitted from vertex B is defined as

$$\theta = \cos^{-1}(\vec{v_3} \cdot \vec{v_4}) \quad (2)$$

where θ is the angle between track #3 and #4. Its value was $133.7 \pm 4.5^\circ$. That angle value was less than 180° , it pointed out that another neutral particle could be emitted from vertex B according to conservation of momentum. Among them, the most possible decay mode of the single Λ

hypernucleus is non-mesonic decay with neutron emission. Only Lamba Beryllium 10 was found to be acceptable for track #1 candidate.

Table 5 (a) Some decay modes of single lambda hypernucleus track #1

Decay mode	Q-value (MeV)	E total (MeV)	Q – E _{Total} (MeV)
$^4_{\Lambda}He \rightarrow p + p + 2n$	166.01	> 77.34	< 77.36
$^5_{\Lambda}He \rightarrow p + p + 3n$	144.70	> 69.79	< 74.91
$^5_{\Lambda}He \rightarrow p + d + 2n$	146.92	> 137.86	< 9.07
$^5_{\Lambda}He \rightarrow d + p + 2n$	146.92	> 75.41	< 71.41
$^5_{\Lambda}He \rightarrow ^3_2He + \pi^- + 3n$	34.72	> 29.85	< 4.87
$^6_{\Lambda}He \rightarrow p + d + 3n$	146.60	> 116.72	< 29.87
$^6_{\Lambda}He \rightarrow d + p + 3n$	146.60	> 68.57	< 78.02
$^6_{\Lambda}He \rightarrow d + d + 2n$	148.82	> 134.19	< 14.63
$^6_{\Lambda}Li \rightarrow ^3_2He + p + 3n$	153.00	> 73.14	< 79.86
$^7_{\Lambda}He \rightarrow ^3_2He + p + 2n$	145.74	> 114.31	< 31.43
$^7_{\Lambda}He \rightarrow t + p + 3n$	149.77	> 67.71	< 82.06
$^7_{\Lambda}He \rightarrow t + d + 2n$	152.00	> 131.43	< 20.56
$^7_{\Lambda}Li \rightarrow ^3_2He + p + 2n$	146.26	> 67.77	< 78.48
$^7_{\Lambda}Li \rightarrow ^3_2He + d + 2n$	148.48	> 126.86	< 21.61
$^7_{\Lambda}Li \rightarrow ^4_2He + p + 2n$	166.84	> 72.40	< 94.44
$^7_{\Lambda}Li \rightarrow ^4_2He + d + 2n$	169.06	> 169.02	< 0.038
$^8_{\Lambda}He \rightarrow t + d + 3n$	150.80	> 112.48	< 38.31
$^8_{\Lambda}Li \rightarrow ^3_2He + d + 3n$	140.01	> 110.05	< 29.96
$^8_{\Lambda}Li \rightarrow ^3_2He + d + 3n$	158.37	> 67.36	< 91.00
$^8_{\Lambda}Li \rightarrow ^4_2He + d + 2n$	160.59	> 124.16	< 36.43
$^9_{\Lambda}Li \rightarrow ^4_2He + d + 2n$	156.86	> 108.31	< 48.55
$^9_{\Lambda}Be \rightarrow ^6_3Li + p + 2n$	144.90	> 75.28	< 69.62
$^{10}_{\Lambda}Be \rightarrow ^6_3Li + p + 3n$	141.34	> 70.30	< 71.04

Table 5 (b) Some decay modes of single lambda hypernucleus track #1

Decay mode	Q value	E_{total}	Q – E_{Total}
$^{10}_{\Lambda}Be \rightarrow {}^6_3Li + d + 2n$	143.57	> 119.06	< 24.51
$^{10}_{\Lambda}Be \rightarrow {}^7_3Li + p + 2n$	148.59	> 76.33	< 72.26
$^{10}_{\Lambda}Li \rightarrow {}^4_2He + t + 3n$	158.13	> 152.49	< 5.65
$^{11}_{\Lambda}Be \rightarrow {}^6_3Li + d + 3n$	137.15	> 105.86	< 31.30
$^{11}_{\Lambda}Be \rightarrow {}^7_3Li + p + 3n$	142.17	> 71.06	< 71.14
$^{11}_{\Lambda}Be \rightarrow {}^7_3Li + d + 2n$	144.40	> 118.21	< 26.18
$^{12}_{\Lambda}B \rightarrow {}^7_3Li + p + 2n$	146.71	> 87.51	< 59.19
$^{12}_{\Lambda}Be \rightarrow {}^7_3Li + d + 3n$	143.27	> 105.33	< 37.93
$^{13}_{\Lambda}C \rightarrow {}^9_5B + p + 3n$	128.58	> 87.33	< 41.25
$^{13}_{\Lambda}C \rightarrow {}^9_5B + d + 2n$	130.81	> 126.57	< 4.23
$^{13}_{\Lambda}B \rightarrow {}^9_4Be + p + 3n$	142.22	> 79.62	< 62.00
$^{13}_{\Lambda}B \rightarrow {}^9_4Be + d + 3n$	144.45	> 121.03	< 23.42
$^{14}_{\Lambda}C \rightarrow {}^{10}_5B + p + 3n$	131.59	> 90.19	< 41.39
$^{14}_{\Lambda}C \rightarrow {}^{10}_5B + d + 2n$	133.81	> 128.60	< 5.21
$^{14}_{\Lambda}B \rightarrow {}^9_4Be + d + 3n$	138.44	> 108.29	< 30.15
$^{14}_{\Lambda}N \rightarrow {}^{12}_6C + p + 2n$	150.03	> 125.53	< 24.49
$^{15}_{\Lambda}C \rightarrow {}^{10}_5B + d + 3n$	124.65	> 114.47	< 10.17
$^{16}_{\Lambda}N \rightarrow {}^{12}_6C + p + 3n$	139.02	> 107.50	< 31.52
$^{16}_{\Lambda}N \rightarrow {}^{13}_6C + p + 2n$	143.97	> 131.44	< 12.53
$^{17}_{\Lambda}N \rightarrow {}^{12}_6C + d + 3n$	138.05	> 126.02	< 12.03
$^{17}_{\Lambda}N \rightarrow {}^{13}_6C + p + 3n$	140.78	> 111.54	< 29.23
$^{17}_{\Lambda}N \rightarrow {}^{14}_6C + p + 2n$	148.95	> 137.36	< 11.59
$^{18}_{\Lambda}N \rightarrow {}^{13}_6C + d + 3n$	136.66	> 128.70	< 7.84
$^{18}_{\Lambda}N \rightarrow {}^{14}_6C + p + 3n$	142.50	> 115.59	< 26.91
$^{18}_{\Lambda}N \rightarrow {}^{15}_6C + p + 2n$	143.72	> 143.33	< 0.388

Results and Discussions

Results of Range and Angle Measurement of Tracks in Single Λ Hypernucleus Event

Ranges and angles of all the tracks in single Λ hypernucleus event were measured by using the microscope system under constant temperature and humidity. We obtained the range and angles from measured coordinates at the vertex and click points on the track. The measured lengths and emission angles of those tracks were expressed in Table (6).

Table 6 Range and angles of all the tracks in single- Λ hypernucleus event

Vertex	Track Number	Range (μm)	θ (Degree)	ϕ (Degree)
A	#1	3.3 ± 0.2	108.4 ± 3.6	292.3 ± 13.1
	#2	15.5 ± 0.4	122.9 ± 3.8	104.8 ± 3.6
B	#3	14.1 ± 0.8	158.3 ± 3.3	48.7 ± 12.2
	#4	11111.1 ± 5.9	67.9 ± 3.1	233.1 ± 0.5

Results of Determination of Density and Shrinkage factor of Nuclear Emulsion Plate

In event analysis, kinetic energies of charged particles were obtained from their ranges. Kinetic energy of particles, ranges and density of the medium was related to each other. We used the thorium decay series in nuclear emulsion as range-energy relation calibration source. We measured the coordinates of alpha tracks emitted from ^{212}Po in thorium decay series. The coordinates (x, y, z) at the end points of the tracks were measured by using the overall viewer. From measured coordinates, $\Delta x^2 + \Delta y^2$ and Δz^2 were obtained. We plotted the scattered graphs, Δz^2 versus $\Delta x^2 + \Delta y^2$ graphs for ^{212}Po . The plotted data are fitted with straight line.

The range of alpha particles emitted from ^{212}Po and shrinkage factor of nuclear emulsion plate were obtained by fitting the straight line equation with scattered plotted graphs. Its values were $49.87 \pm 0.22 \mu\text{m}$ and 2.2 ± 0.01 , respectively.

By changing the density of nuclear emulsion plate in energy-range relation, we produced a corresponding range of alpha particles for average kinetic energy of α particles from ^{212}Po of 8.785 MeV. Densities of nuclear emulsion plate of sheet #5, Module #26 was $3.59 \pm 0.02 \text{ gcm}^{-3}$. That density value was used when we obtained the kinetic energy of the charge particle track which were included in Single Λ hypernucleus event.

Results of Event Reconstruction

We constructed the single Λ hypernucleus event which was found in plate #5 of Mod# 26 of JPARC E07 Experiment. Firstly, we consider at the production point of the single Λ hypernucleus. We considered as Ξ^- hyperon was absorbed by a light nucleus (C, N, and O) in nuclear emulsion at the point A. We obtained the kinetic energy of charged particles were obtained from their ranges. The kinetic energy of neutral particles was obtained from momentum balance. We assigned the particle species which were emitted from point A and obtained the Q values for each production mode. Results were shown in the 2nd column of Table (7). The total kinetic energy (E_{Total}) which includes kinetic energy of charged and uncharged particles were obtained. The results were shown in the 3rd column of Table (7). The binding energy of Ξ^- hyperon was obtained from the difference between the Q value and E_{Total} . The corresponding binding energies were presented in the 4th column of Table (7). For the production modes with negative Q value and large values of B_{Ξ^-} were rejected. The most acceptable production mode of single lambda hypernucleus and binding energy of Ξ^- hyperon in $^{14}_7\text{N}$ nucleus were $\Xi^- + ^{14}_7\text{N} \rightarrow ^{10}_\Lambda\text{Be} + ^4\text{He} + \Lambda^0$ and $0.51 \pm 0.17 \text{ MeV}$, respectively. On the other hand, we considered at the decay point of the single Λ hypernucleus event at point B.

Table 7 Possible production reaction of single Λ hypernucleus

Possible Production Reaction	Q-value (MeV)	E _{total} (MeV)	B Ξ^- (MeV) = Q - E _{Total}	Comments
$\Xi^- + {}^{14}_7N \rightarrow {}^{10}_\Lambda Be + {}^4He + \Lambda^0$	19.01	18.51 ± 0.17	0.51 ± 0.17	acceptable
$\Xi^- + {}^{12}_6C \rightarrow {}^8_\Lambda Li + {}^4He + \Lambda^0$	10.78	14.4 ± 0.14	-3.66 ± 0.14	rejected
$\Xi^- + {}^{12}_6C \rightarrow {}^7_\Lambda Li + {}^4He + \Lambda^0 + n$	2.31	10.25 ± 0.14	-7.94 ± 0.01	rejected
$\Xi^- + {}^{12}_6C \rightarrow {}^9_\Lambda Be + d + \Lambda^0 + n$	1.89	9.979 ± 0.17	-8.10 ± 0.17	rejected
$\Xi^- + {}^{12}_6C \rightarrow {}^6_\Lambda Li + {}^4He + \Lambda^0 + 2n$	-4.42	8.72 ± 0.14	-13.14 ± 0.14	rejected
$\Xi^- + {}^{12}_6C \rightarrow {}^9_\Lambda Be + p + \Lambda^0 + 2n$	-0.35	8.26 ± 0.17	-8.61 ± 0.17	rejected
$\Xi^- + {}^{16}_8O \rightarrow {}^{12}_\Lambda B + {}^4He + \Lambda^0$	16.86	25.07 ± 0.22	-8.21 ± 0.22	rejected

Possible decay modes of the single Λ hypernucleus (track #1) are expressed in Table (8). Possible decay mode, Q value, E_{Total}, difference of Q value and E_{Total} and comment are described in that Table. According to collinear checking between track #3 and track #4, we can concluded that neutron(s) will be emitted at point B. By comparing with production mode and decay modes, possible decay mode of single lambda hypernucleus is ${}^{10}_\Lambda Be \rightarrow {}^6_3 Li + d + 2n$. The type of hypernucleus was lambda beryllium 10 hypernucleus.

Table 8 Possible decay modes of the single Λ hypernucleus

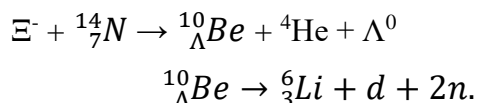
Decay mode	Q value	E _{total}	Q - E _{Total}	Comments
${}^4_\Lambda He \rightarrow p + p + 2n$	166.01	> 77.34	< 77.36	rejected
${}^5_\Lambda He \rightarrow p + p + 3n$	144.70	> 69.79	< 74.91	rejected
${}^5_\Lambda He \rightarrow p + d + 2n$	146.92	> 137.86	< 9.07	rejected
${}^5_\Lambda He \rightarrow d + p + 2n$	146.92	> 75.41	< 71.41	rejected
${}^5_\Lambda He \rightarrow {}^3_2 He + \pi^- + 3n$	34.7	> 29.85	< 4.87	rejected
${}^6_\Lambda He \rightarrow p + d + 3n$	146.60	> 116.72	< 29.87	rejected
${}^6_\Lambda He \rightarrow d + p + 3n$	146.60	> 68.57	< 78.02	rejected
${}^6_\Lambda He \rightarrow d + d + 2n$	148.82	> 134.19	< 14.63	rejected
${}^6_\Lambda Li \rightarrow {}^3_2 He + p + 3n$	153.00	> 73.14	< 79.86	rejected
${}^7_\Lambda He \rightarrow t + d + 2n$	152.00	> 131.43	< 20.56	rejected
${}^7_\Lambda Li \rightarrow {}^3_2 He + p + 2n$	146.26	> 67.77	< 78.48	rejected
${}^8_\Lambda He \rightarrow t + d + 3n$	150.80	> 112.48	< 38.31	rejected
${}^8_\Lambda Li \rightarrow {}^3_2 He + d + 3n$	140.01	> 110.05	< 29.96	rejected
${}^9_\Lambda Li \rightarrow {}^4_2 He + d + 2n$	156.86	> 108.31	< 48.55	rejected
${}^9_\Lambda Be \rightarrow {}^6_3 Li + p + 2n$	144.90	> 75.28	< 69.62	rejected
${}^{10}_\Lambda Be \rightarrow {}^6_3 Li + p + 3n$	141.34	> 70.30	< 71.04	rejected
${}^{10}_\Lambda Be \rightarrow {}^6_3 Li + d + 2n$	143.57	> 119.06	< 24.51	accepted
${}^{11}_\Lambda Be \rightarrow {}^6_3 Li + d + 3n$	137.15	> 105.86	< 31.30	rejected
${}^{11}_\Lambda Be \rightarrow {}^7_3 Li + p + 3n$	142.17	> 71.06	< 71.14	rejected
${}^{12}_\Lambda B \rightarrow {}^7_3 Li + p + 2n$	146.71	> 87.51	< 59.19	rejected
${}^{12}_\Lambda Be \rightarrow {}^7_3 Li + d + 3n$	143.27	> 105.33	< 37.93	rejected
${}^{13}_\Lambda C \rightarrow {}^9_5 B + p + 3n$	128.58	> 87.33	< 41.25	rejected
${}^{16}_\Lambda N \rightarrow {}^{12}_6 C + p + 3n$	139.02	> 107.50	< 31.52	rejected

Discussions

We checked and choose suitable events among many single Λ hypernucleus events to analyze. We have analyzed one of the single Λ hypernuclues events found in the upper layer of emulsion plate #5 of Module #26. We measured the range and angles of all the tracks in single Λ hypernuclues event in temperature and humidity controlled room by using the microscope system. Since the kinetic energies of charged particles were obtained from their ranges and range-energy of the particle depends on the density of material medium. Therefore, we made range energy relation calibration by using α particles tracks, emitted from ^{212}Po in Thorium decay series. The density of emulsion plate which detected our analyzed event was $3.59 \pm 0.02 \text{ gcm}^{-3}$. When we obtained kinetic energy of each charged particle in the event from its range, that density value was used. Event reconstruction in the emulsion was based on the conservation laws of energy and momentum. Firstly, we considered at the production point of single Λ hypernucleus event point A. All possible production reactions were considered and obtained. Q value for each production mode was obtained with known mass of hypernucleus. The total kinetic energy of particles was also obtained. By comparing with the Q value and total kinetic energy, the most possible production was estimated. A Ξ^- hyperon was captured by nitrogen nucleus and decayed into lambda beryllium 10 hyprnucleus, helium and one Λ hyperon were emitted, $\Xi^- + ^{14}_7\text{N} \rightarrow ^{10}_\Lambda\text{Be} + ^4\text{He} + \Lambda^0$. On the other hand, we considered at the point B, decay point of the single Λ hypernucleus event with the same manner as considering in production mode. The angle between track #3 and #4, which were the decay daughters of the single Λ hypernucleus, were checked. Its angle value was 135 ± 4.5 d. It shows that another neutral particle such as neutron(s) can be emitted from point B. We estimated the decay mode of the single Λ hypernucleus was lambda beryllium 10 hypernucleus decay into lithium 6, deuteron and two neutrons were emitted, $^{10}_\Lambda\text{Be} \rightarrow ^6_3\text{Li} + d + 2n$.

Conclusion

We have analyzed a single Λ hypernucleus which was found in the J-PARC E07 experiment based on the conservation laws of energy and momentum. The type of hypernucleus was beryllium 10 hypernucleus and the production and decay modes of the event were,



Moreover, the binding energy of Ξ^- hyperon in nitrogen nucleus was $0.51 \pm 0.17 \text{ MeV}$.

Acknowledgements

Our gratitude to Rectors and Pro-rectors from University of Mandalay and Yadanabon University. We would like to thank Professor Dr Lei Lei Win, Head of Department of Physics, Professor Dr Kalyar Thwe, Professor Dr Nyein Wint Lwin, Professor Dr Nay Win Oo, Department of Physics, University of Mandalay for their kind encouragement to carry out research work.

References

- Aoki. S., *et al.*, (1991), Prog. Theor. Phys. 85, 951–956.
- Ahn. J. K. *et al.*, (2001), Phys. Rev. Lett. 87, 132504.
- Bando. H. et.al, (1990), Intl. J. Mod. Phys.A, **5**, 4023.
- Dover.C. B, et.al, (1991), Phys. Rev. C44 1905
- Davis, D. H., (2005), Nucl. Phys. A **754**, 3c.
- Dalitz R. H, *et al.*, (1989), Proc. Roy. Soc. Lond. A **426**, 1
- Danysz. M, *et al.*, (1963), Nucl. Phys. **49**, 121.
- Hiyama. E and K. Nakazawa, (2018), Annu. Rev. Nucl. Part. Sci. **68**, 13159.
- Imai. K, et.al J-PARC E07 Proposal
- Khaustov. P. *et al.*, Phys. Rev. C61 (2000) 054603.
- Mondal, A. S. et.al, (1975), Nuov. Cim. A **28**, 42.
- Myo. A. M. M, (2019), M. Sc Thesis, Yadanabon University.
- Takahashi. H, *et al.*, (2001), Phys. Rev. Lett. **87**, 212502.
- Tint. K. T. (2017), Myingyan Deg. Col. Res. J, 8,1, 90-97.
- Yoshida. J, Nakazawa. K and Umehara. K, (2014), JPS Conf. Proc. **1**, 013070..

MEASUREMENT OF RADON CONCENTRATION IN SOIL GAS USING RAD7 FROM BYUT MYAUNG AND KALAIN GOLD MINES AT BAGO REGION

Hein Nay Zar Wann¹, Win Win Maw², Tun Myint³, Tin Tin Phyto Lwin⁴, Yin Maung Maung⁵

Abstract

Soil gas Radon, ^{222}Rn , concentrations were measured in Buut Myaung and Kalain gold mines of Shwe Kyin Township at Bago region. The soil samples were tested by using RAD7 radon technique detector. In each location of four different depths were taken for soil gas measurements, starting from the ground surface. It was found that the largest radon concentration was 29.5 ± 1.37 Bqm-3 at 6ft depth and smallest radon concentration was 11.2 ± 0.91 Bqm-3 at 12ft depth from Byut Myaung gold mine. The largest radon concentration was 25.7 ± 1.49 Bqm-3 at 6 ft depth and the smallest radon concentration was 10.9 ± 0.68 Bqm-3 at 12 ft depth from Kalain gold mine. All the mentions were taken by using International Commission on Radiological Protection (ICRP) method for under or over safety concentration level that effects on human inspiration system especially lung's tissue. The results obtained from this study are not dangerous for that region.

Keywords: Soil, Radon, Gold Mines and RAD7.

Introduction

Radon gas (^{222}Rn) exhalation rate and concentration are associated with its ultimate precursor uranium in the earth crust. Uranium, a radiotoxic element, is a naturally occurring radioactive element and is decay lead to radon in the environment such as gas, oil, groundwater and soil deposits. The half-life of radon isotope ^{222}Rn takes enough for long 3.82 days. And then, it spreads out through the soil and freely moves to the atmosphere and the environment where the human live. Radon- 222 gas, commonly called radon is colorless, odorless and tasteless and therefore undetectable by human senses. Radon can only be detected or measured with special detectors. Two methods can be used for measuring of radon concentration as short term and long term methods. In this research, RAD-7 solid state detector (short term) was used because RAD-7 was simply set up of its all apparatus. It could work out the data faster than other machines not to be waste time. So, it was used to determine the radon concentration in soil samples from Byut Myaung and Kalain gold mines, Shwe Kyin Township, Bago Region.

Health Effects of Radon

Radon mainly occurs as gaseous condition in the environment. Radon gas decays or breaks down continuously to form radioactive elements that can be inhaled into the lungs. In the lungs, decay continues, creating radioactive particles that release small bursts of energy. When long-term exposure (drinking water and breathing air) occurs radon increases the chances of developing lung cancer. Radon can only cause cancer after several years of exposure. Radon may be radioactive, but gives off little actual gamma radiation.

¹ Lecturer, Physics Department, Pang Long University

² Lecturer, Physics Department, Yangon University of Education

³ Lecturer, Physics Department, Dagon University

⁴ Lecturer, Physics Department, Monywa University

⁵ Professor, Physics Department, University of Yangon

Natural Decay Series of Uranium

Radon exhalation and concentration rate are different from one place to another place according to the content of uranium and radium. Radioactive decay occurs when an unstable (radioactive) isotope transforms to a more stable isotope, generally by emitting a subatomic particle such as an alpha or beta particle. Radon is part of the natural decay series of uranium (U) and thorium (Th) found in all soils and rocks to a varying concentration. There are three radioisotopes of radon naturally present in the environment: Radon-222 from the Uranium-238 decay series, Radon-220 from Thorium-232 decay series and Radon-219 from Uranium-235 decay series. Radon is formed in the ground from the radioactive decay of uranium-238, which is present in small quantities in all rocks and soils. The schematic diagram of the radioactive decay of uranium-238 is shown in Figure 1.

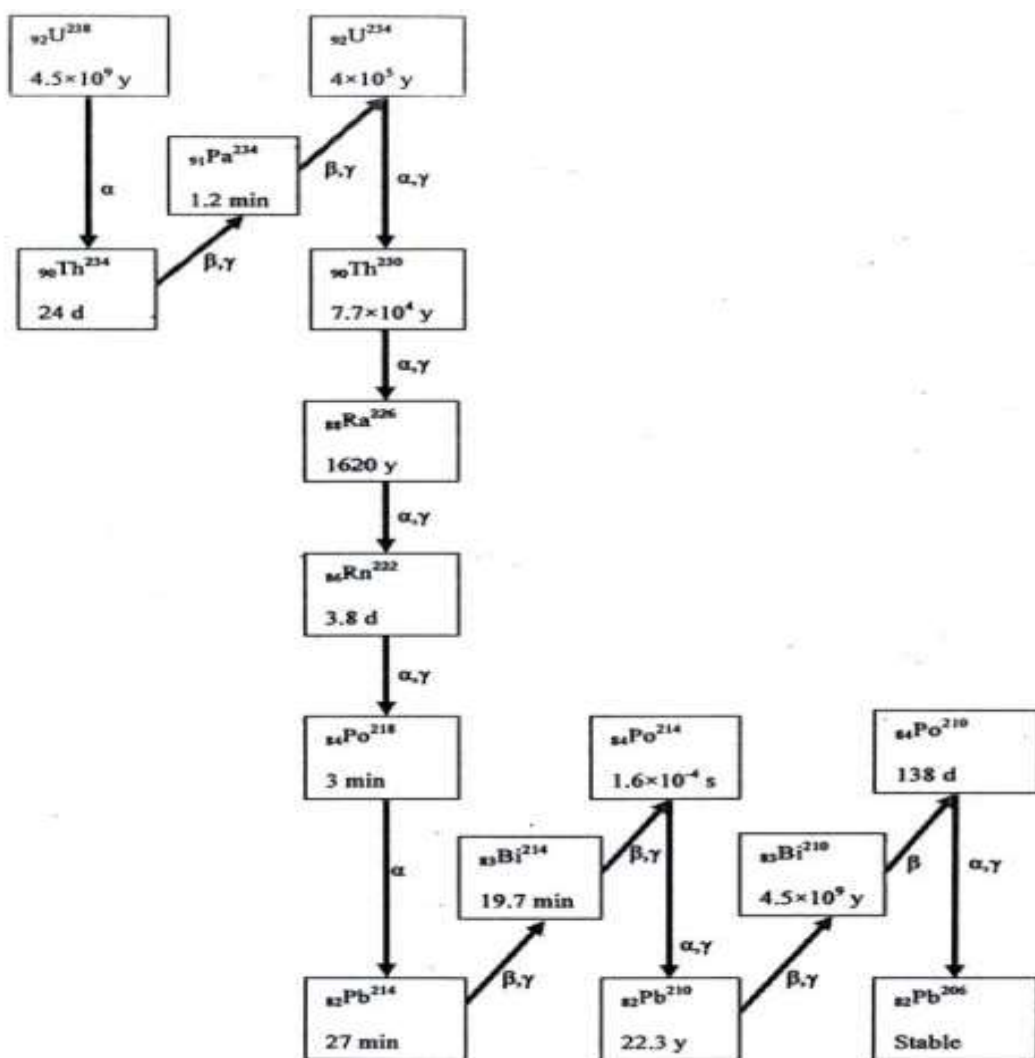


Figure 1 U-238 decay chain and the half-life associated with each element

A Safe Level of Radon Gas

ICRP recognizes that an action level can have two distinct purposes which are to define workplaces either in which intervention should be undertaken and to identify where the system of protection for practice should be applied. There were generally mentioned as three circumstances by ICRP's record. There is no action required for the concentration volume which was lower than 200Bq/m³ as shown in table 1.

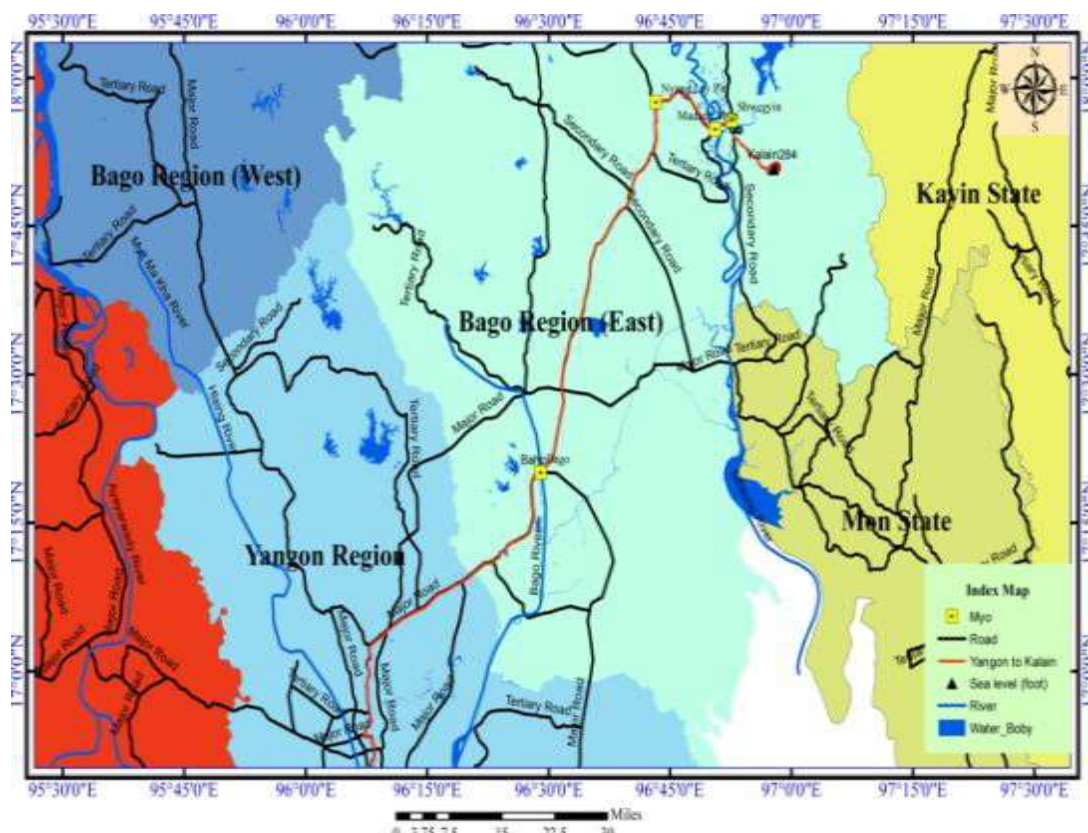
Table 1 Remedial exposure time of concentration period

Radon concentration	Recommended Remedial Exposure Time	References
Greater than 600 Bq/m ³	In less than 1 year	[5,6]
Between 200 Bq/m ³ and 600 Bq/m ³	In less than 3 years	
Less than 200 Bq/m ³	No action required	

Material and Methods

Sample Collection

The RAD 7 detector was performed on soil samples at Byut Myaung and Kalain gold mines at 284 ft above sea level. The samples are collected at 17° 50' 46.08' north latitude, 96° 57' 46.80' east longitude and Kalain and Byut Myaung gold mines with GPS MAP 62 S as shown in figure 2. Soil samples were collected from various depths, recording their depths with long tape measurement as shown in figure 3 and figure 4.



Source: Department of Agricultural Land Management and Statistics, Shwe Kyin Township

Figure 2 Location map of Kalain and Byut Myaung gold mines from Shwe Kyin Township



Figure 3 Kalain gold mine at Shwe Kyin Township



Figure 4 Byut Myaung gold mine at Shwe Kyin Township

Measurement Procedure

After taking an arrangement consists of RAD7 professional Durridge and small drying tube filled with fresh descendant (CaSO_4) positioned vertically, soil gas sample plastic can was filled through a sampling point. Soil gas is normally so high in radon that it is not necessary to use long cycle times to gain precision. Soil sample were placed in to the small tube inlet, and passed through the inlet filter after small drying tube as shown in figure 5 and then took out the results from its clear wide monitor as shown in figure 6. Five minutes cycle times (purge 5 minutes, pumping 5 minutes, waiting 5 minutes and counting 5 minutes) are sufficient. In total, each set of readings included four 5 minutes cycles that took half hour. Other rested depths can also be taken out by running the test and interpretation of the data as the previous processes.

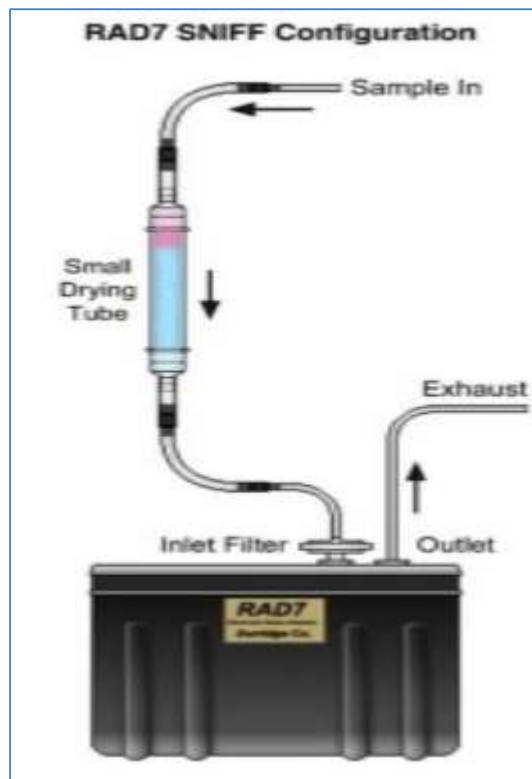


Figure 5 Durridge RAD 7 radon monitor



Figure 6 Experiment of soil samples by using RAD7

Results

In active method, RAD7 radon gas detector will measure the radon concentrations in soil samples at the end of the half hour period. After the determination of the soil sample was used RAD7 detector, coming out four different results. It could be easily note that radon concentration was showing topmost at 6ft depth. These different results data were also described with (chart) in figure 11 and below table 2 and table 3. As shown in table 2, the radon concentration of Byut Myaung gold mine higher than that of Kalain gold mine as shown in table 3. In during testing these samples, the diagrams of alpha energy spectrum of them were also respectively mentioned as below figure 7, figure 8, figure 9 and figure 10.

Table 2 Radon concentration of soil samples with different depths at Byut Myaung gold mine

Samples No:	Depth	Radon concentration(Bqm^{-3})
1	91.44 cm (3 ft)	18.6 ± 1.21
2	182.88 cm (6 ft)	29.5 ± 1.37
3	274.32 cm (9 ft)	14.4 ± 1.14
4	365.76 cm (12 ft)	11.2 ± 0.91

Table 3 Radon concentration of soil samples with different depths at Kalain gold mine

Samples No:	Depth	Radon concentration(Bqm^{-3})
1	91.44 cm (3 ft)	16.4 ± 1.41
2	182.88 cm (6 ft)	25.7 ± 1.49
3	274.32 cm (9 ft)	13.1 ± 1.33
4	365.76 cm (12 ft)	10.9 ± 0.68

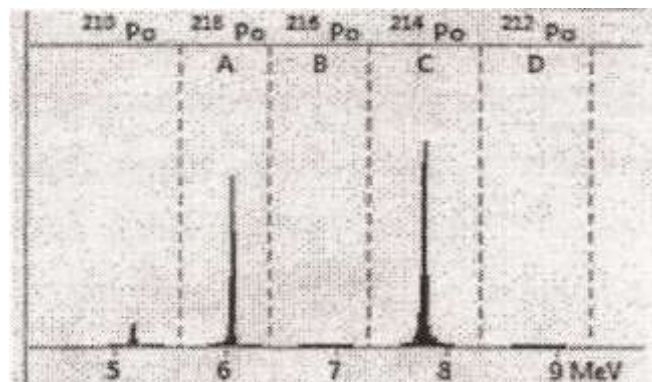


Figure 7 Alpha energy spectrum for 6 ft depth at Byut Myaung gold mine

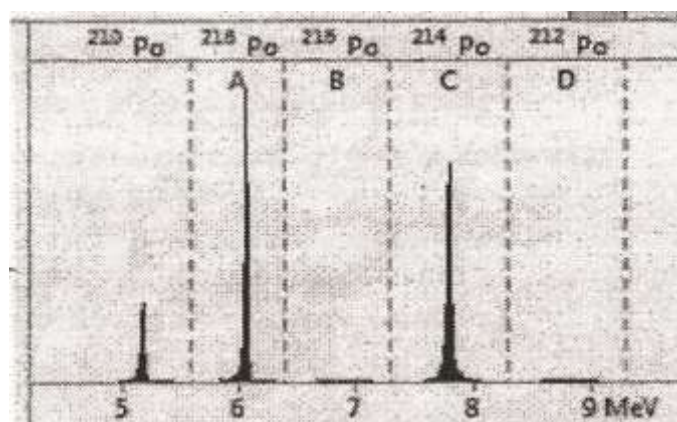


Figure 8 Alpha energy spectrum for 6 ft depth at Kalain gold mine

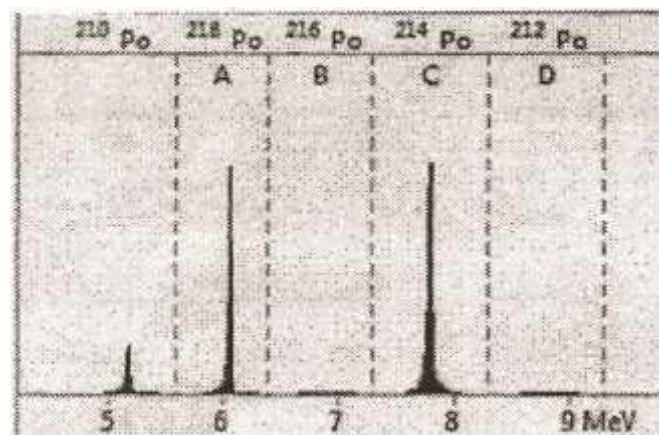


Figure 9 Alpha energy spectrum for 12 ft depth at Byut Myaung gold mine

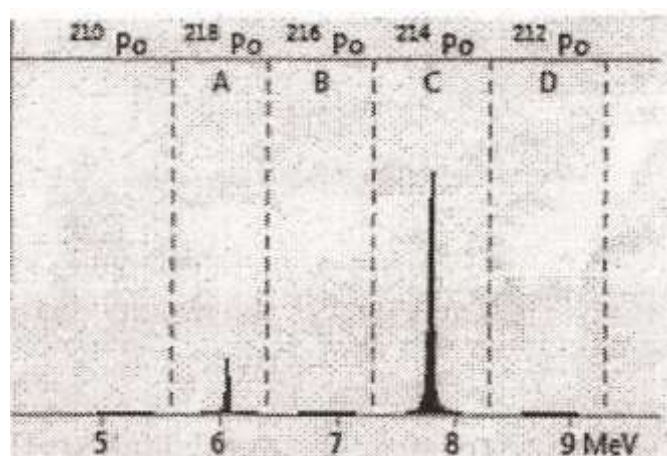


Figure 10 Alpha energy spectrum for 12ft depth at Kalain gold mine

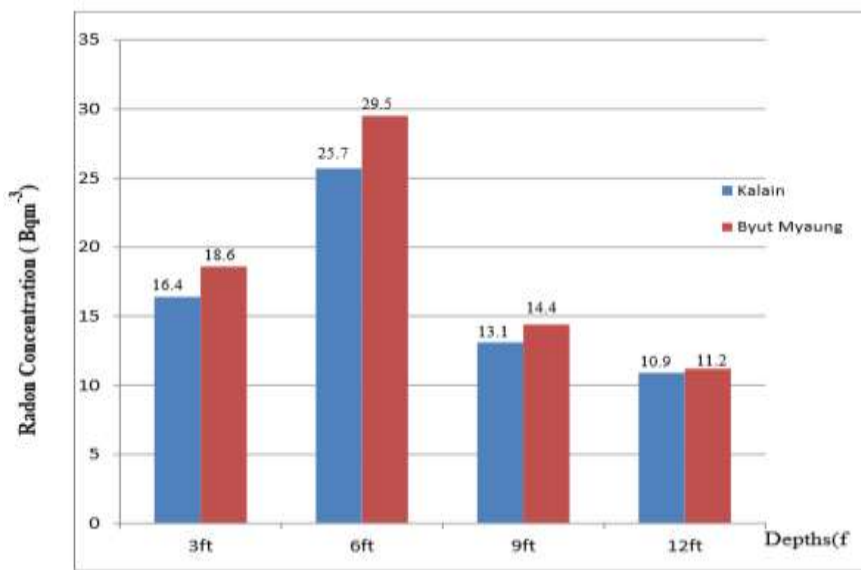


Figure 11 The radon concentrations of soil samples at Byut Myaung and Kalain goldmines by RAD7

Discussion

According to table 2 and table 3, it was found that the radon concentration in soil samples of Byut Myaung gold mine is higher than that of Kalain gold mine. The heights of the peaks on the spectrum depend on the concentration of the radon and to which radon had exposed. Operational Radon Spectra for soil samples at 3 ft, 6 ft, 9 ft and 12 ft depths were obtained from the results of peaks. There were easily can be seen that the highest radon concentration was at 6 ft depth and the lowest was at 12 ft depth. In my practice, concentrations were mentioned to highest at around 6 ft depths even the lowest at 12 ft and deeper. The major cause of this difference should be the states of varies the viscosity, density and air volume in these soil. Then, about the energy spectrum of these different four depths were described as following continue. At 5.3 MeV, a persistent peak will be developed as resultant of Polonium-210 buildup. At 6.00 MeV, after less than one hour of exposure to radon are called new radon Po-218 peak A. At 6.78MeV, the RAD7 spectrum while continuous sampling thoron laden air (new thoron) Po-216 peak B. At 7.69 MeV, the RAD 7 spectrum after purging the instrument with radon-free air for more than 10 minutes (old radon) following exposure to radon Po-214 peak C. At 8.78 MeV, the spectrum after discontinuing a lengthy (old thoron) are sampling of thoron laden air, Po 212 Peak D.

Conclusion

The purpose of this research is focused on the public health point of view why radon is believed to be the second largest cause of lung cancer, after that of smoking. The results evidently show maximum and minimum concentration of radon activity in soil gas having in depths of 6 ft and 12 ft respectively. For the depths of upper soil layer (less than 6 ft) radon prevalence more easily to the air, the activity should be less, although in the depth more than 6 ft the rock soil grains as constituted more compact as to decrease radon activity. No action may be required for maximum concentration activity ($29.5 \pm 1.37 \text{ Bqm}^{-3}$) in 6ft depth at Byut Myaung and ($25.7 \pm 1.49 \text{ Bqm}^{-3}$) in 6 ft depth at Kalain gold mines was less than 200 Bqm^{-3} that had been defined by International Commission on Radiological Protection (ICRP) standard. However it did not seriously effect on people at this location, we have to continuously and widely study

on radon concentration which is usually effected by the moisture, humidity, and temperature in seasonal differences. And it is very important in future for human healthy deal with unseeable radioactive leaking such as radon because of being upon the changes of types of soil and other unpredictable challenges.

Acknowledgements

We would like to thank Dr Khin May Aung, Pro-rector, Panglong University for her permission to write this research. We would like to extend our thanks to Dr Than Than Win, Professor (Head) and Dr Hla Toe, Professor, Department of Physics, Panglong University for their encouragement to conduct this research.

We also deeply thank to Dr Kyi Thar Myint, Professor (Retd), Department of Physics, West Yangon University for her valuable advice and guidance in carrying out this research.

We would like to thank all people who encouraged and supported us during the undertaking of this work.

References

- Ali K. Hasan, Abdul.R.H.Subber and Ahmed R. Shaltakh, (2011), "Measurement of Radon Concentration in soil gas using RAD7 in the environs of Al-Najaf Al-Ashraf city-Iraq" Advalce in Applied Science Research, 2(5):273-278.
- A.K. Singh, P.J. Jojo, A.J. Khan, R. Prasad and T.V. Ramchandran, (1997), "Calibration of track detectors and measurement of radon exhalation from soil samples", Radiation Protection Eruiron, 20.129
- A.Smith, S. Pournis and P. Barretto, (1976), "Radon methods in uranium".
- Canadian Nuclear Safety Commission, (2012), "Radon and Health".
- ICRP, (2014), Radiological Protection against Radon Exposure ICRP Publication 126, Ann. ICRP 43(3).
- ICRP, (2017). Occupational Intakes of Radionuclides: Part 3. ICRP Publication 137, Ann. ICRP 46(3-4).
- M.F. Cwar and L.P. Geraldo, (1981), "Studies of Alpha Particle Registration in LR-155 Types II, A Solid State Nuclear Track Detector".
- M. Tirmarche, et al. (2010), "Lung cancer risk from radon and progeny and statement on radon", Annals of the ICRP.
- P.A.a.M. Colgan, A.T, (2009), "Radon Monitoring and Control of Radon Exposure, in Radiological Protection Institute of Ireland".

RELATIVISTIC AND NON-RELATIVISTIC MOMENTUM SPACE WAVEFUNCTIONS FOR CHARMONIUM AND BOTTOMONIUM STATES

Shwe Sin Oo¹, Khin Maung Maung²

Abstract

In the constituent quark model, charmonium and bottomonium are considered to be the bound states of charm/anti-charm and bottom/antibottom quarks. We use the linear potential to represent the long distance confining part of the potential and a Coulomb like potential to represent the short distance one-gluon exchange part of the potential. In order to study the general features of the wave functions, it is not necessary to include spin dependent parts in the potential. Using the above mentioned potentials, we solved the Schrodinger equation with non-relativistic kinematics and also with relativistic kinematics. We solve these equations by expanding the momentum space wavefunction in a complete set of orthonormal basis functions and turning the Schrodinger equation into a standard matrix eigen-value equation. We vary the masses of the quarks, and the strengths of the potentials until we get a satisfactory fit to the spin averaged mass spectra of the desired $q\bar{q}$ system. The eigenvectors gives the coefficients of the linear combination in the wavefunction expansion from which we can construct the wavefunctions. We compare the non- relativistic and relativistic wavefunctions for each state in $b\bar{b}$ and $c\bar{c}$ systems.

Keywords: quark, linear potential, momentum space

Introduction

Meson as a two-body bound state of quark-antiquark pair has been a fertile ground for the study of two-body relativistic equations and also for phenomenology. Most studies restrict themselves to non-relativistic Schrodinger equation in position space, since the solution methods are well known and in some cases, analytical solutions exist. Commonly used methods are the well known Numerov method combined with wavefunction and its derivative matching at a predetermined location. The input is the eigen-energy and it is varied until the desired tolerance is achieved for the log-derivative matching. For each angular momentum value l this has to be done for all the states of interest. Although this is not an economical way of doing things, it can be done. But if we want to use relativistic kinematics, one can no longer use position space representation of the Schrodinger equation.

The non-relativistic kinetic energy operator $\hat{p}^2/2\mu$ (μ is the reduced mass)is now replaced by $\sqrt{\hat{p}^2 + m_1^2} + \sqrt{\hat{p}^2 + m_2^2}$ in the center of mass frame. Since quantization gives $\hat{p} \rightarrow -i\hbar\nabla$, we will have differential operator under the radical sign. This problem is best treated in momentum representation. In this case both the non-relativistic and the relativistic Schrodinger equations are integral equations and the momentum operator \hat{p} becomes just a number in this representation. In the case of linear potential and Coulomb like potentials, there is a minor complication of removable singularities in the momentum representation of these potentials. Well known subtraction methods exist. We can also add spin-spin and spin-orbit potentials to our problem without any technical complications. But the spin-orbit splitting between 1S_0 and 3S_1 in $b\bar{b}$ system is about 50 MeV while the mass of the meson is about 10,000 MeV. This is of the order of 0.5%. Therefore, in this stage of the study of the wavefunctions, we neglect the spin dependent part of the potential. In the next section, we will describe how we will solve the Schrodinger equation in momentum space with non-relativistic and relativistic kinematics. We will also explain how the wave function can be obtained once the eigen-value problem is solved. In section III, we will show our results of eigen-

¹ Lecturer, Department of Physics, University of Mandalay

² Professor, Department of Physics and Astronomy, University of Southern Mississippi, USA

values and their fit to the spin-averaged meson spectra. We will also compare the relativistic and non-relativistic wavefunctions. We than make conclusions based on our results.

The Solution Method

The Schrodinger equation in momentum representation can be written as

$$D(m_1, m_2, p) + \int V(\bar{p}, \bar{p}') \phi(\bar{p}') d\bar{p}' = E\phi(\bar{p}) \quad (1)$$

Here $D(m_1, m_2, p) = p^2/2\mu$ for the case with non-relativistic kinematics and $D(m_1, m_2, p) = \sqrt{m_1^2 + p^2} + \sqrt{m_2^2 + p^2}$ for the relativistic case. Now $V(\bar{p}, \bar{p}')$ is the Fourier transform of the position space potential.

$$V(r) = \lim_{\eta \rightarrow 0} \left(\sigma r e^{-\eta r} - \frac{C e^{-\eta r}}{r} \right) \quad (2)$$

Here σ and C are the strengths of the linear and the Coulomb like potentials. We have used the exponential damping factor η since the straight forward Fourier transforms of linear potential and Coulomb potential do not exist. After the Fourier transform and partial wave decomposition, we can take the $\eta \rightarrow 0$ limit explicitly.

The Fourier transforms of the damped potentials in equation (2) are given by

$$V(\bar{p}, \bar{p}') = \lim_{\eta \rightarrow 0} \left[\frac{\sigma}{2\pi^2} \frac{\partial^2}{\partial \eta^2} \left(\frac{1}{q^2 + \eta^2} \right) - \frac{C}{2\pi^2} \left(\frac{1}{q^2 + \eta^2} \right) \right] \quad (3)$$

Since we do not have any potential that couples angular momentum, we can take the orbital angular momentum l as a good quantum number and write

$$\phi(\bar{p}) = \phi_{nl}(p) Y_l^m(\hat{p}) \quad (4)$$

Now after the angular decomposition Schrodinger equation can be written for each l as

$$D(m_1, m_2, p^2) \phi_{nl}(p) + \int_0^\infty V_l(p, p') \phi_{nl}(p') p'^2 dp' = E_{nl} \phi_{nl}(p) \quad (5)$$

Here the l^{th} partial wave component of the potential is given by

$$V_l(p, p') = 2\pi \int_{-1}^1 V(p, p') P_l(x) dx \quad (6)$$

$$= \frac{1}{\pi p p'} \lim_{\eta \rightarrow 0} \left(\sigma \frac{\partial^2}{\partial \eta^2} Q_l(y) - C Q_l(y) \right) \quad (7)$$

Here, $Q_l(y)$ is the Legendre polynomial of the second kind and the argument $y = (p^2 + p'^2 + \eta^2)/2pp'$. In the $\lim_{\eta \rightarrow 0}$ limit, $Q_l(y)$ and its derivatives have a removable singularity as can be seen here.

$$Q_l(y) = Q_0(y) P_l(y) - W_{l-1}(y) \quad (8)$$

and $Q_0(y)$ and $W_{l-1}(y)$ are given by

$$Q_0(y) = \frac{1}{2} \ln \left[\frac{y+1}{y-1} \right] \quad (9)$$

and

$$W_{l-1}(y) = \sum_{m=1}^l \frac{1}{m} P_{l-m}(y) P_{m-1}(y) \quad (10)$$

We immediately see that although $W_{l-1}(y)$ has no singularities but $Q_l(y)$ and its derivatives do through $Q_0(y)$ at $y = 1$ which corresponds to $p=p'$ case in the limit of $\eta \rightarrow 0$. In order to handle these singularities, we use the method developed by Maung, Kahana and Norbury [2]. In order to

solve equation (5), we expand the wavefunction $\phi_{nl}(p)$ in complete orthonormal basis set of functions. i.e

$$\phi_{nl}(p) = \sum_{\alpha=1}^N C_{\alpha l} g_{\alpha l}(p) \quad (11)$$

Here, for the $g_{\alpha l}(p)$'s we use a complete orthonormal set of functions given in terms of Jacobi polynomials [4] and $C_{\alpha l}$ are the expansion coefficients. The set of functions $g_{\alpha l}(p)$ are given by

$$g_{\alpha l}(p) = \frac{1}{\sqrt{N_{\alpha l}}} \frac{(p/b)^l}{[(p/b)^2 + 1]^{l+2}} P_{\alpha}^{\left(l+\frac{3}{2}, l+\frac{1}{2}\right)} \left(\frac{p^2 - b^2}{p^2 + b^2}\right) \quad (12)$$

$$N_{\alpha l} = \frac{b^3}{2(2n+2l+3)} \frac{\Gamma(n+l+5/2)\Gamma(n+l+3/2)}{n!\Gamma(n+2l+3)} \quad (13)$$

where $N_{\alpha l}$ is the normalization constant and b is a parameter that be used as the variational parameter. $P_{\alpha}^{(a,c)}(x)$ are the Jacobi polynomials. These expansion functions $g_{\alpha l}(p)$ obey orthonormal condition

$$\int_0^\infty g_{\alpha l}(p) g_{\beta l}(p) p^2 dp = \delta_{\alpha \beta} \quad (14)$$

We now use the expansion given by equation (11) in (5) and furthermore, we multiply by $p^2 g_{\alpha l}(p)$ and integrating over p we obtain

$$\sum_{\alpha=1}^N C_{\alpha l} \left(\int_0^\infty g_{\beta l}(p) D(m_1, m_2, p^2) g_{\alpha l}(p) p^4 dp \right) + \int_0^\infty g_{\beta l}(p) V_l(p, p') g_{\alpha l}(p') p^2 p'^2 dp dp' = E_{\alpha l} C_{\beta l} \quad (15)$$

This is in the form of a simple matrix eigenvalue equation for each l . i.e.

$$\sum_{\alpha=1}^N A_{\beta \alpha} C_{\alpha l} = E_{\alpha l} C_{\beta l} \quad (16)$$

Once the eigen-equation is solved, we obtain the eigen-energies and for each energy we get a set of coefficients C_{α} . Then, by using equation (11) we can construct the wavefunction corresponding to the desired state.

Results

In this section we show the results of our calculations. As explained previously, we do not include spin-spin and spin-orbit potentials. Therefore, before we fit the meson spectrum, we do the spin-averaging of the masses. First of all, meson states are given in the spectroscopic notation as $n^{2S+1}L_J$, where the S is in the superscript is the total spin which is either $S = 0$ (singlet state) or $S = 1$ (triplet state). L is the orbital angular momentum quantum number and they are traditionally named as S , P , D etc. for $L = 0, 1, 2, \dots$ respectively. For example, for $l = 0$ case there are four states, namely 1S_0 (1 state) and 3S_1 (3 states). Therefore, the spin-average masses $M(nS)$ for $l = 0$ states are calculated from

$$M(nS) = \frac{[M(n {}^1S_0) + 3M(n {}^3S_1)]}{4} \quad (17)$$

and the spin-averaged masses for P -states are calculated by

$$M(nP) = \frac{M(n {}^3P_0) + 3M(n {}^3P_1) + 3M(n {}^1P_1) + 5M(n {}^3P_2)}{12} \quad (18)$$

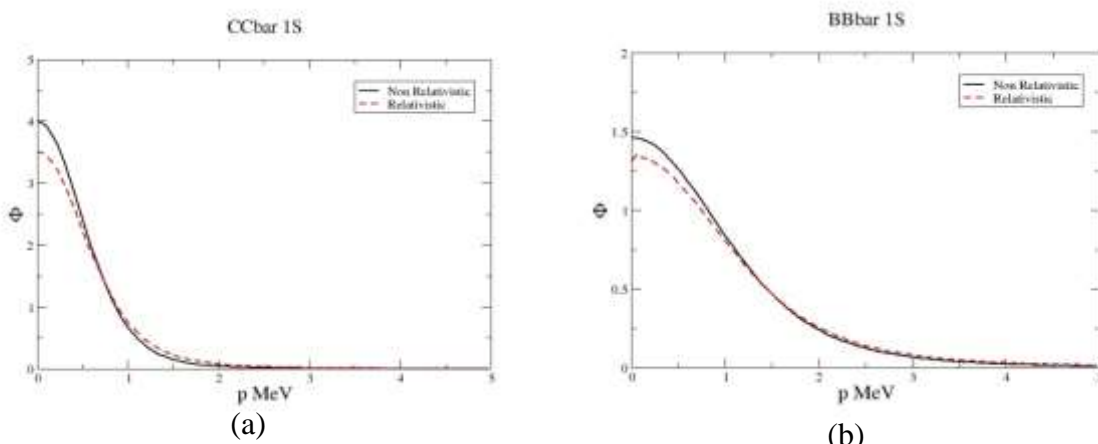
**Table 1 Spin-averaged experimental meson masses(MeV) and calculations (Non-Relativistic)
 $M_c = 1321.5 \text{ MeV}$, $M_b = 4763.8 \text{ MeV}$**

State	$c\bar{c}$ Calculation	$c\bar{c}$ Experiment	$B\bar{B}$ Calculation	$B\bar{B}$ Experiment
1S	3068.84	3068.65	9444.58	9444.98
2S	3720.06	3673.95	10036.25	10017.2
3S	4206.86		10400.47	
4S	4556.18		10696.73	
5S	5000.25		10957.12	
1P	3518.43	3525.31	9928.74	9899.73
2P	4029.52		10303.95	
3P	4462.01		10607.15	
4P	4848.62		10872.57	
5P	5203.97		11113.65	

**Table 2 Spin-averaged experimental meson masses(MeV) and calculations (Relativistic)
 $M_c = 1352.19 \text{ MeV}$, $M_b = 4783.42 \text{ MeV}$**

State	$c\bar{c}$ Calculation	$c\bar{c}$ Experiment	$B\bar{B}$ Calculation	$B\bar{B}$ Experiment
1S	3068.47	3068.65	9444.50	9444.98
2S	3679.80	3673.95	10044.11	10017.2
3S	4123.95		10404.81	
4S	4496.53		10695.39	
5S	4826.01		10949.15	
1P	3480.28	3525.31	99564.39	9899.73
2P	3945.98		10324.25	
3P	4332.98		10620.19	
4P	4673.12		10878.08	
5P	4981.049		11326.93	

In these calculations, we fixed the strength of the linear potential to 0.2 GeV^2 and Coulomb like potential strength to -0.5. We vary only the quark masses. Once the 1S state is adjusted to the experimental value with a tolerance of 0.05% we keep the quark mass value. We then use the same parameter set for $L=1$ p-wave case. We do the same procedure for both the non relativistic and relativistic cases.



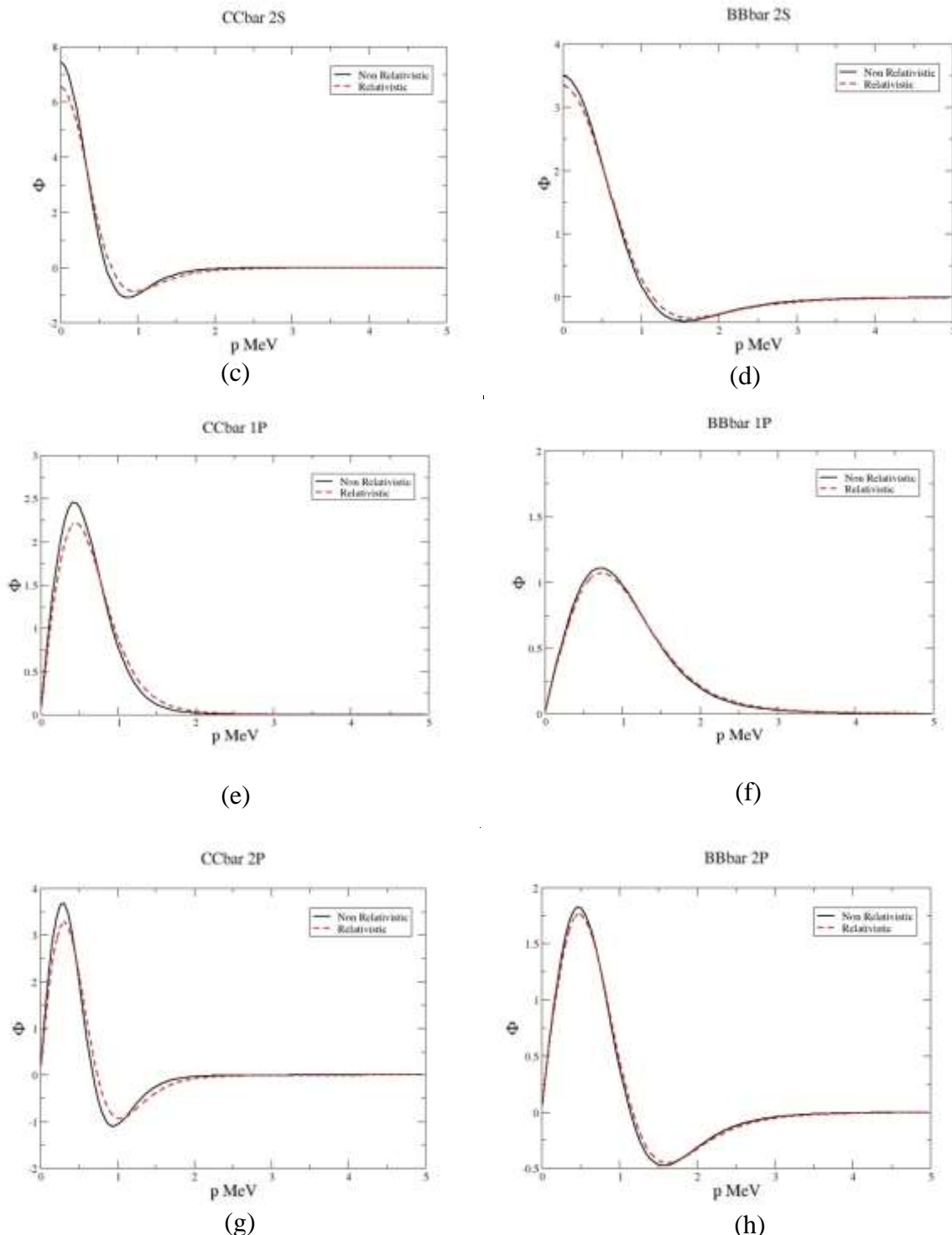


Figure (a-h) Non-relativistic and relativistic wavefunctions for b-bbar and c-cbar systems

Conclusions

In the figures, we compare non-relativistic and relativistic wavefunctions for, $1S$, $2S$, $1P$ and $2P$ states for b-bbar and c-cbar systems. All wavefunctions are normalized. First of all we note that just like in the r-space wavefunctions, the ground state for each angular momentum L has no nodes in the wavefunction. The first excited state has one node etc. We see that the differences

between the relativistic and non-relativistic wavefunctions are small for b-bbar system. It is reasonable since it is a much heavier system. We also note that as L becomes higher, the difference is more pronounced and for the same L , excited states show more difference between relativistic and non-relativistic case. In the future, the prediction of decay rates will be done and compared with experimental results. In these calculations, the differences in the wavefunction will be important.

Acknowledgement

I would like to thank Professor Dr. Lei Lei Win, Head of department of Physics, University of Mandalay for her kind permission to carry out this work.

References

- B. D. Keister and W. N. Polyzou, J. Comp. Phys. 134(2), 1997
- J. A. Tjon and P. C. Tiemeijer, Phys. Rev. C. Vo 49, 494-512, 1994.
- K. M. Maung, D. E. Kahana and J. W. Norbury, Phys. Rev. D. Vol 42,1182, 1993
- Particle data group, Phys. rev. D, Vol 98, 030001, 2018

NUMERICAL SIMULATIONS OF BINARY NEUTRON STAR MERGERS

Thei` Theint Theint Aung¹, Kyaw Zall Linn², Thant Zin Naing³

Abstract

Tidal deformity is assumed to be very important parameters in compact astrophysical objects such as binary neutron stars and black holes. Different kinds of tidal deformity for the binary neutron star mergers have been investigated and relevant numerical simulations have been implemented using mathematica coding.

Keywords: *binary neutron star mergers, tidal deformity, mathematica coding*

Introduction

As neutron stars are massive and compact astrophysical objects, the coalescence of binary neutron star systems is one of the most promising sources of gravitational waves observable by ground-based detectors. The gravitational wave signals emitted during a neutron star merger depend on the behavior of neutron star matter at high densities. So, the detection of gravitational waves opens the possibility to constraint the nuclear matter parameters characterizing the EoS[1]. A significant signature carried by gravitational waves is the tidal deformability of the neutron star and it is well explored analytically. In a coalescing binary neutron star system, during the last stage of inspiral, each neutron star develops a mass quadrupole due to the extremely strong tidal gravitational field induced by the other neutron star forming the binary. The dimensionless tidal deformability describes the degree of deformation of a neutron star due to the tidal field of the companion neutron star and is sensitive to the nature of the equation of state (EOS). This research will firstly study about mass for observable merging neutron star systems, then, tidal deformability and finally tidal deformability of binary neutron star. Besides, c and G are taken by 1 in this research.

Mass for merger neutron star systems

The future investigation of neutron stars merger such as GW170817 will have the factors of masses and spins like to those of known double neutron star systems. Known systems contain at least one pulsar and their masses and spins have been determined by pulsar timing. The total mass $M_T = M_1 + M_2$ is known with precision. For the former systems, it is straightforward to determine q and M . However, even in the latter cases, some information about M and q can be established, using the theoretical model that the minimum neutron star mass is $\geq 1.1M_{\odot}$. Note that one can write the chirp mass

$$M = \frac{M_1^{3/5} M_2^{3/5}}{M_T^{1/5}}$$
$$M = M_T^{2/5} \left(\frac{M_1}{M_T} \right)^{\frac{3}{5}} M_2^{3/5}$$

¹ Lecturer, Department of Physics, Bago University

² Assistant Lecturer, Department of Physics, Yangon University

³ Retired Pro-Rector (Admin), International Theravāda Buddhist Missionary University, Yangon.

$$\begin{aligned} M &= M_T^{2/5} \left(\frac{M_T - M_2}{M_T} \right)^{\frac{3}{5}} M_2^{3/5} \\ M &= M_T^{2/5} \left(1 - \frac{M_2}{M_T} \right)^{\frac{3}{5}} M_2^{3/5}, \end{aligned} \quad (1)$$

$$q = \frac{M_2}{M_1} = \frac{M_2}{M_T - M_2} \quad (2)$$

so the constraint $1.1M_{\square} \leq M_2 \leq M_T/2$ will determine $M(q)$. When M_2 is though smaller than or equal to M_1 , the binary mass ratio $q \leq 1$.

Tidal deformability of neutron star

Consider a static, spherically symmetric star of mass M retained in a static external quadrupolar tidal field \mathcal{E}_{ij} with the response a quadrupole moment Q_{ij} . In the local asymptotic rest frame (asymptotically mass-centered Cartesian coordinates) of the star with large r the metric coefficient g_{tt} is given by

$$\frac{(1-g_{tt})}{2} = -\frac{M}{r} - \frac{3Q_{ij}}{2r^3} \left(n^i n^j - \frac{1}{3} \delta^{ij} \right) + O\left(\frac{1}{r^3}\right) + \frac{1}{2} \varepsilon_{ij} x^i x^j + O(r^3) \quad (3)$$

where $n^i = x^i/r$; this expansion defines ε_{ij} and Q_{ij} . That Q_{ij} is connected to the density perturbation $\delta\rho$ in the Newtonian limit by

$$Q_{ij} = \int d^3x \delta\rho(x) \left(x_i x_j - \frac{1}{3} r^2 \delta_{ij} \right), \quad (4)$$

and \mathcal{E}_{ij} is assumed in terms of the external gravitational potential Φ_{ext} as

$$\mathcal{E}_{ij} = \frac{\partial^2 \Phi_{ext}}{\partial x^i \partial x^j} \quad (5)$$

To linear order in ε_{ij} , the induced quadrupole will be of the form

$$Q_{ij} = -\lambda \varepsilon_{ij} \quad (6)$$

The tensor multipole moments Q_{ij} and ε_{ij} can be decomposed as

$$\varepsilon_{ij} = \sum_{m=-2}^2 \varepsilon_m y_{ij}^{2m}, \quad (7)$$

$$Q_{ij} = \sum_{m=-2}^2 Q_m y_{ij}^{2m}, \quad (8)$$

where the symmetric traceless tensors y_{ij}^{2m} are defined by (Thorne 1980)

$$y_{2m}(\theta, \varphi) = y_{ij}^{2m} n^i n^j \quad (9)$$

with $n = (\sin \theta \cos \varphi, \sin \theta \sin \varphi, \cos \theta)$. Thus, equation (6) can be written as

$$Q_m = -\lambda \varepsilon_m \quad (10)$$

Without loss of generality, only one ε_m can assumed no vanishing, this is enough to compute λ .

Here λ is a constant related to the $l = 2$, tidal Love number (apsidal constant) k_2 by

$$k_2 = \frac{3}{2} \lambda R^{-5} \quad (11)$$

Here R is the radius of neutron star and the constant of proportionality λ is the tidal deformability of the neutron star. It measures the magnitude of the quadrupole moment induced by an external tidal field and is proportional to the (dimensionless) $l = 2$ tidal Love number

$$k_2 = \frac{3}{2} \lambda R^{-5} \quad (12)$$

To find the tidal deformability λ from Eq. (12), k_2 must be firstly calculated by using the method described by Hinderer: A perturbation of the spherically symmetric background metric

$$g = -e^{2\nu} dt^2 + \frac{1}{1-2m/r} dr^2 + r^2 (d\theta^2 + \sin^2 \theta d\phi^2), \quad (13)$$

In the Regge-Wheeler gauge, $\nu(r)$ is determined by

$$\left(1 - \frac{2m}{r}\right) \frac{d\nu}{dr} = \frac{1}{r^2} (m + 4\pi r^3 p), \quad (14)$$

with δg a linear, quadrupolar, static, polar parity perturbation given by

$$\delta g = \left(-e^{2\nu} dt^2 + \frac{1}{1-2m/r} dr^2 \right) H_{2,m}(\theta, \phi) + r^2 (d\theta^2 + \sin^2 \theta d\phi^2) K_{2,m}(\theta, \phi), \quad (15)$$

where H and K are both functions of r . The perturbed Einstein equation gives a differential equation for H :

$$0 = \frac{d^2 H}{dr^2} \left(1 - \frac{2m}{r}\right) + \frac{dH}{dr} \left[\frac{2}{r} - \frac{2m}{r^2} + 4\pi r(p - \varepsilon) \right] - H \left[\frac{6}{r^2} - 4\pi \left(5\varepsilon + 9p + \frac{\varepsilon + p}{dp/d\varepsilon} \right) + 4 \left(1 - \frac{2m}{r}\right) \left(\frac{d\nu}{dr} \right)^2 \right]. \quad (16)$$

In vacuum, H can be written as a linear combination of $P_2^2(r/M-1)$ and $Q_2^2(r/M-1)$ where P_2^2 and Q_2^2 are the $l=m=2$ associated Legendre functions. When expanded in powers of $M=r$ at infinity, $P_2^2(r/M-1)=O(M/r)^3$ and $Q_2^2(r/M-1)=O(r/M)^2$. The coefficient of P_2^2 is therefore related to the quadrupole moment of the star, and the coefficient of Q_2^2 is related to the tidal field applied by the neutron star. By matching $H(r)$ and its derivative across the surface of the star, one can show

$$\begin{aligned} k_2 = & \frac{8C^5}{5} (1-2C^2) [2+2C(y-1)-y] \{2C[6-3y+3C\times(5y-8)] \\ & + 4C^3[13-11y+C(3y-2)+2C^2(1+y)] + 3(1-2C^2)[2-y+2C(y-1)] \log(1-2C)\}^{-1} \end{aligned} \quad (17)$$

where $C=M/R$ is the compactness of the star and the quantity of $y=y(R)$ can be numerically integrated and evaluate y at the surface of the star.,

$$y(r) = r \frac{H'(r)}{H(r)}, \quad (18)$$

which gives rise to the first-order differential equation

$$r \frac{dy(r)}{dr} + y(r)^2 + y(r)F(r) + r^2Q(r) = 0 \quad (19)$$

with

$$F(r) = \frac{r - 4\pi r^3 (\varepsilon(r) - p(r))}{r - 2m(r)} \quad (20)$$

$$Q(r) = \frac{4\pi r \left(5\varepsilon(r) + 9p(r) + \frac{\varepsilon(r) + p(r)}{\partial p(r)/\partial \varepsilon(r)} - \frac{6}{4\pi r^2} \right)}{r - 2m(r)} - 4 \left[\frac{m(r) + 4\pi r^3 p(r)}{r^2 (1 - 2m(r)/r)} \right]^2 \quad (21)$$

To find $y = y(R)$, Eq. (19) can be numerically integrated and evaluate y at the surface of the star. where $m(r)$ is mass enclosed within the radius r , $\varepsilon(r)$ and $p(r)$ are, the energy density and pressure respectively in terms of radial coordinate r of a star. Then, by using polytrope equation of state, numerical integration Love number of Eq. (17) is shown in Figure (1). To pronounce the stellar equation of state (EOS), these quantities are calculated within the nuclear matter model chosen. For a given equation of state (EOS), Eq. (19) can be integrated together with the Tolman-Oppenheimer-Volkoff equations with the boundary conditions $y(0) = 0$, $p(0) = p_c$ and $m(0) = 0$, where $y(0)$, p_c and $m(0)$ are the dimensionless quantity, pressure and mass at the center of the NS, respectively. The dimensionless tidal deformability can be defined as

$$\Lambda \equiv \frac{\lambda}{m^5} = \frac{1}{m^5} \frac{2}{3} k_2 R^5 = \frac{2}{3} k_2 \frac{R^5}{m^5} = \frac{2}{3} k_2 C^{-5} \quad (22)$$

R and M are the radii and masses of the binary components, respectively. k_2 can be readily determined from a first-order differential equation simultaneously integrated with the two usual TOV structural equations and has values ranging from about 0.05 to 0.15 for neutron stars. So, the visualization figure of dimensionless tidal deformability Λ for TOV equation is shown in Figure (2). For black holes, $k_2 = 0$. The tidal deformations of the neutron stars result in excess degeneracy of orbital energy and speed up the final stages of the inspiral. Tidal deformations act oppositely to spin effects, which tend to be more important during earlier stages of the observed gravitational wave signal. Then, the tidal deformability of the neutron stars present in the binary neutron star system can be combined to yield the weighted average as,

$$\tilde{\Lambda} = \frac{16}{13} \frac{(12q+1)\Lambda_1 + (12+q)q^4\Lambda_2}{(1+q)^5} \quad (23)$$

where Λ_1 and Λ_2 are the individual tidal deformabilities corresponding to the two components in the NS binary with masses m_1 and m_2 , respectively with $q = m_2/m_1 < 1$.

Polytrope equation of state and Tidal deformability of binary neutron star

To investigate impressive a common EOS constraint, a piecewise polytrope scheme is employed to simulate thousands of equations of state. Every one EOS follows causality, attaches at densities to the familiar EOS of neutron star crusts, is reserved by experimental and theoretical

studies of the symmetry properties of matter near the nuclear saturation density, and satisfies the observational constraint for the maximum mass of a neutron star, $m \geq 2M_{\odot}$. Since the compactness parameter is defined by $C \equiv m/R$, the star's tidal deformability Λ is related to compactness parameter C by Eq. (14) and gives $\Lambda \propto C^{-5}$. However, a better description $\Lambda \propto C^{-6}$ is provided by for moderate masses because the behavior $k_2 \propto C^{-1}$ is observed for a wide variety of EOS in the mass range $(1.1M_{\odot} \leq M \leq 1.6M_{\odot})$. This mass range is the predictable range if perceived double neutron star binaries are typical merger candidates. But $m \rightarrow 0, k \rightarrow 0$ so that k_2 is related to C with positive power. So, in this relevant range the important result become

$$\Lambda = aC^{-6} \quad (24)$$

where $a = (2/3)k_2 = 0.0093 \pm 0.0007$ bounds the results for $1.1M_{\odot} \leq M \leq 1.6M_{\odot}$. The C -dependence of Λ has interesting consequences for the binary deformability $\tilde{\Lambda}$, equation (13). An immediate result motivated by the observation with piecewise polytropes that $\Lambda \approx aC^{-6}$ and $R_1 \approx R_2$ is

$$\Lambda_1 \approx q^6 \Lambda_2 \quad (25)$$

The above correlation is used in the analysis of the gravitational wave signal from GW 170817. Then the binary tidal deformability $\tilde{\Lambda}$ with different q values is shown in Figure (2). The common equation of state (EOS) constraint allows to show that the binary tidal deformability $\tilde{\Lambda}$ is essentially a function of the chirp mass M , the common radius R , and the mass ratio q [4], but that its dependence on q is very weak. Substituting the expressions $\Lambda \approx aC^{-6}$ and $R_1 \approx R_2 \approx R$ into Equation (23)

$$\begin{aligned} \tilde{\Lambda} &= \frac{16}{13} \frac{(12q+1)\Lambda_1 + (12+q)q^4\Lambda_2}{(1+q)^5} \\ \tilde{\Lambda} &= \frac{16}{13} \frac{(12q+1)\Lambda_1 + (12+q)q^{-2}\Lambda_1}{(1+q)^5} \\ \tilde{\Lambda} &= \frac{16}{13} \frac{((12q+1)+(12+q)q^{-2})\Lambda_1}{(1+q)^5} \\ \tilde{\Lambda} &= \frac{16}{13} \frac{(q^2(12q+1)+12+q)\Lambda_1}{q^2(1+q)^5} \\ \tilde{\Lambda} &= \frac{16}{13} \frac{(1+q)(12q^3+q^2+12+q)\Lambda_1}{q^2(1+q)^5} \\ \tilde{\Lambda} &= \frac{16}{13} \frac{(12q^2-11q+12)\Lambda_1}{q^2(1+q)^4} \\ \tilde{\Lambda} &= \frac{16}{13} \frac{(12q^2-11q+12)}{q^2(1+q)^4} \left(\frac{2}{3}k_2\right) \left(\frac{R}{M}\right)^6 \end{aligned}$$

$$\tilde{\Lambda} = \frac{16}{13} a' \left(\frac{R}{M} \right)^6 \frac{(12q^2 - 11q + 12)}{q^2 (1+q)^4}$$

$$\tilde{\Lambda} = \frac{16}{13} a' \left(\frac{R}{M} \right)^6 f(q) \quad (26)$$

where $f(q) = \frac{(12q^2 - 11q + 12)}{q^2 (1+q)^4}$ which is very weakly dependent on q . Then Equation (26) becomes

$$\tilde{\Lambda} = \frac{16}{13} a' \left(\frac{R}{M} \right)^6 \quad (27)$$

where $a' = 0.0042 \pm 0.0004$ bounds the results for $1.1M_{\odot} \leq M \leq 1.6M_{\odot}$. In this research the masses of binary neutron are taken as $m_1 \geq m_2$, $q \leq 1$. Each equation of state in the piecewise polytrope scheme can compute $\tilde{\Lambda}$ for all stellar pairs along the corresponding to $M - R$. Then, Figure 4 show the results of $\tilde{\Lambda}$, where equations of state are identified by their corresponding value of $R_{1.4}$, the radius of a $1.4M_{\odot}$ star[5].

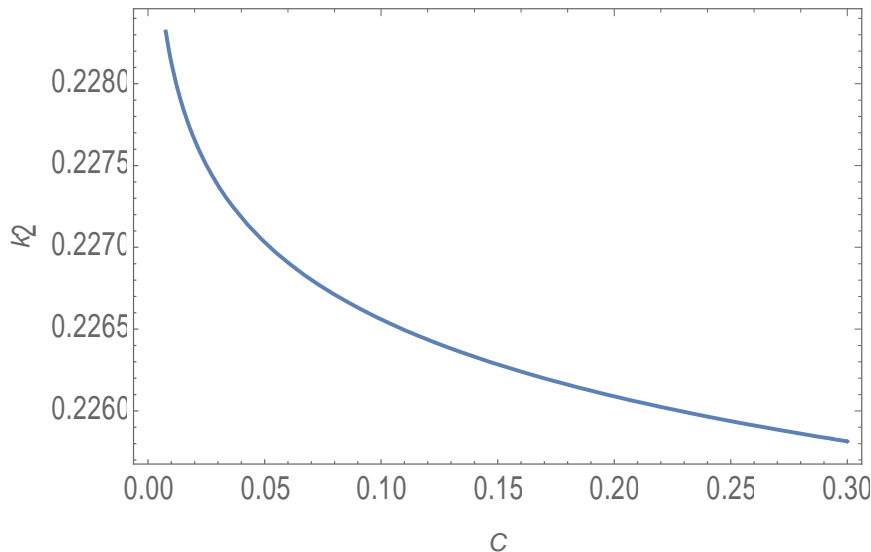
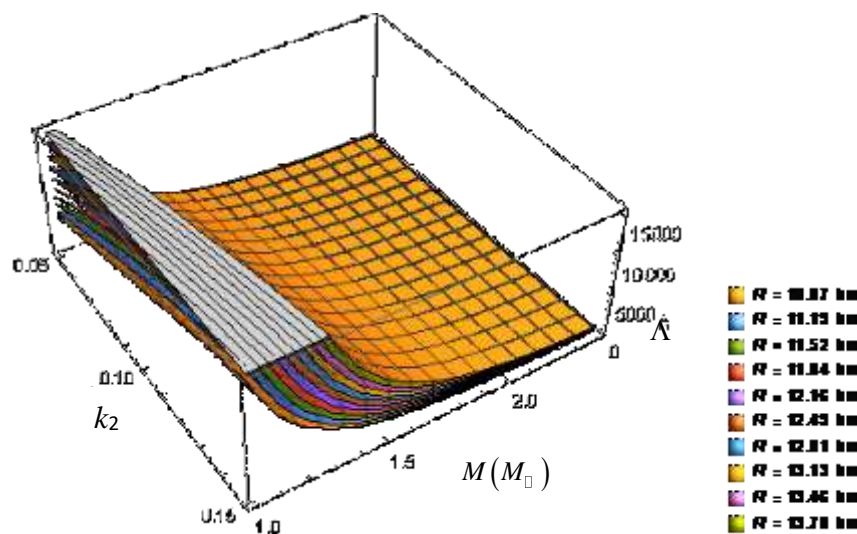
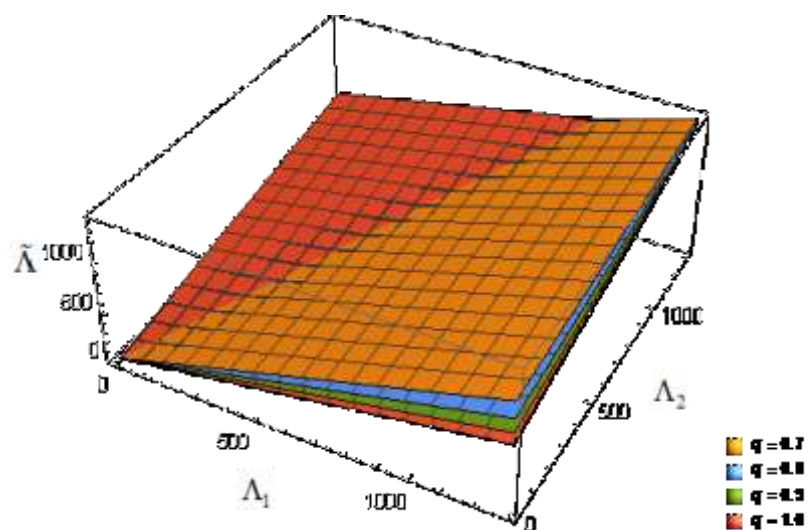
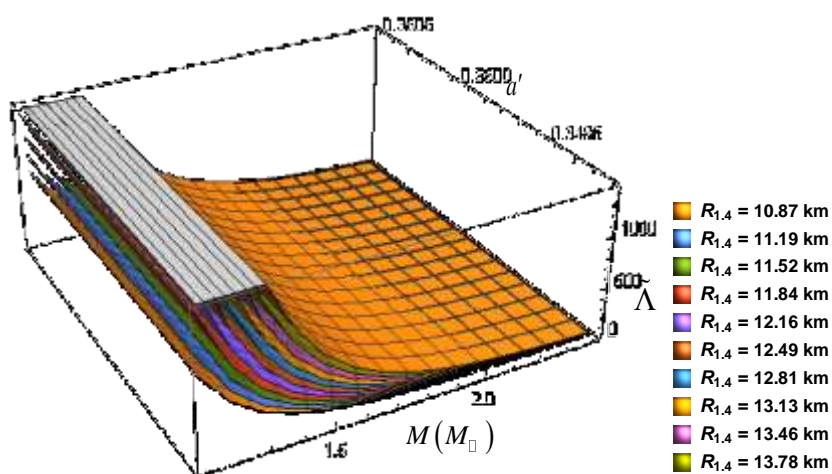


Figure 1 Dimensionless Love number (k_2) as a function of Compactness (C)

**Figure 2** 3D visualization of tidal deformity Λ **Figure 3** 3D visualization of tidal deformity $\tilde{\Lambda}$ with Λ_1 and Λ_2 **Figure 4** 3D visualization of tidal deformity $\tilde{\Lambda}$

Concluding Remarks

In the present research, the tidal deformability of neutron star Λ and the dimensionless binary tidal deformability $\tilde{\Lambda}$ have been studied with the Love number k_2 and the radius of neutron stars. So, the corresponding tidal Love number is firstly calculated and the tidal deformability of static neutron star is calculated. So, tidal Love number (k_2) as a function of compactness (C) is shown in Figure 1. From this figure, the numerical range of Love number for polytrope equation of state are obtained. By using this range, tidal deformability as a function of mass for physically realistic polytropes is shown by Figure (2). In this figure, TOV integration with each EOS parameter set results in a series of values that are shown as points colored by their radii R . There are well-defined upper and lower bounds for $\Lambda(M)$, with the upper (lower) bound defined by the stars with the largest (smallest) radii. The lower bound for $\Lambda(M)$ is an important constraint that should be taken into account in gravitational waveform modeling of BNS mergers. The dimensionless binary tidal deformability deformity $\tilde{\Lambda}$ with Λ_1 and Λ_2 is demonstrated in Figure (3) with $q \leq 1$. Then, for each equation of state in the piecewise polytrope scheme, one can compute $\tilde{\Lambda}$ for all stellar pairs along the corresponding to mass and radii. The results are displayed in Figure (4) which is similar to Figure (2), except that the dimensionless binary tidal deformability as a function of chirp mass M . Finally, in the case of binary neutron star system, many situations are possible, depending on the mass of components and EOS of matter. Besides, system with larger masses and less deformable matter result to prompt collapse to black hole after the merger. Binaries with smaller masses and more deformable matter lead to the formation of an unstable, possibly long-lived remnant.

Acknowledgements

I would like to express my sincere thanks to Professor Dr Thant Zin Naing, Retired Pro-Rector (Admin), International Theravāda Buddhist Missionary University, for his valuable guidance and helpful advice to carry out this work.

References

- B. P. Abbott *et al.*, “Properties of the Binary Neutron Star Merger GW170817,” *Phys. Rev. X*, vol. 9, no. 1, p. 11001, 2019.
- S. De, D. Finstad, J. M. Lattimer, D. A. Brown, E. Berger, and C. M. Biwer, “Tidal Deformabilities and Radii of Neutron Stars from the Observation of GW170817,” *Phys. Rev. Lett.*, vol. 121, no. 9, 2018
- T. Malik *et al.*, “GW170817: Constraining the nuclear matter equation of state from the neutron star tidal deformability,” *Phys. Rev. C*, vol. 98, no. 3, pp. 1–11, 2018.
- T. V. Collaboration, “Properties of the binary neutron star merger GW170817,” no. September, 2018.
- T. Zhao and J. M. Lattimer, “Tidal deformabilities and neutron star mergers,” *Phys. Rev. D*, vol. 98, no. 6, 2018

ASSESSMENT OF SOLAR ENERGY POTENTIAL FOR TWO SELECTED AREAS IN YANGON REGION

Khin Sandar Khaing¹, Khet Khet Tun², Kalyar Thwe³

Abstract

Solar energy is the most abundant energy resource on Earth. It can be captured and used in several ways such as photovoltaic technology. In order to investigate a potential use of concentrating solar power technologies and select an optimum site for these technologies, it is necessary to obtain information on the geographical distribution of monthly average daily solar irradiation over an area of interest. This paper aims to evaluate the potential of renewable energy source of solar in two selected areas of South Aye Village in Khayan Township and Kyutawwa Village in Thongwa Township at Yangon Region. Additionally, solar energy collected data were analyzed for six months starting from January till June, 2020. Feasibility of harnessing for monthly mean solar energy was investigated by using 50 W photovoltaic solar panels. The solar power received on one day for month was checked by solar panel checker. From all the records measured, it was found that the measurements value for the solar energy from South Aye Village was more than that of Kyutawwa Village. In South Aye Village, the highest solar irradiation was estimated as 7.47 kWh/m²/day in May and the lowest was 4.47 kWh/m²/day recorded in June. The annual average daily solar radiation for Kyutawwa Village has been between 4.27 kWh/m²/day and 7.26 kWh/m²/day. This study indicates that selected areas had great potentials for utilizing solar energy system. It is also wanted to get benefits the development of the society and to have an impact on solar power generation technology and solar power generation.

Keywords: solar energy, photovoltaic technology, 50 W photovoltaic solar panels

Introduction

Renewable energy sources such as solar energy, hydropower, wind power, geothermal energy and biomass in its various forms. There is one natural energy resource without pollution: the solar energy. Every location on Earth receives sunlight at least part of the year. The amount of solar radiation that reaches any one spot on the Earth's surface varies according to geographic location, time of day season, local landscape and local weather. Because the Earth is round, the sun strikes the surface at different angles, ranging from 0° (just above the horizon) to 90° (directly overhead). When the sun's rays are vertical, the Earth's surface gets all the energy possible. The Earth revolves around the sun in an elliptical orbit and is closer to the sun during part of the year. When the sun is nearer the Earth, the Earth's surface receives a little more solar energy. The rotation of the Earth is also responsible for hourly variations in sunlight. In the early morning and late afternoon, the sun is low in the sky. Its rays travel further through the atmosphere than at noon, when the sun is at its highest point. On a clear day, the greatest amount of solar energy reaches a solar cell around solar noon.

Human life is inseparable from the sun, and the vast majority of energy human need is directly or indirectly from the sun. Solar energy is the energy obtained by capturing heat and light from the Sun. The method of obtaining electricity from sunlight is used to as the photovoltaic method. The solar energy that the sun radiates every hour is potentially sufficient to ensure one-year world energy consumption. This is the case when all sunlight is captured and completely converted into electricity.

Myanmar is well suited for solar energy, as it receives good amounts of solar energy due to its near equatorial location. Solar radiation has a vast potential to be converted into power, but

¹ Dr, Lecturer, Department of Physics, East Yangon University

² Dr, Lecturer, Department of Physics, East Yangon University

³ Dr, Professor, Department of Physics, University of Mandalay

due to dependence on weather conditions and seasonal change, solar energy can be unpredictable and unreliable.

Solar power is the resources of much energy, for example, the wind power, chemical energy, potential energy of water and other are all converted by the solar power. Some main methods of using solar power are such as solar cells, photoelectric conversion by the energy contained in sunlight into electricity. Solar power is the conversion of energy from sunlight into electricity, either directly using photovoltaic (PV). Photovoltaic cells convert light into an electric current using the photovoltaic effect. Solar panels use the power of the sun to generate clean power. The reason for their huge popularity is that solar power is reliable, affordable, easy to install and causes no pollution.

This research aims to report on the amount of solar energy impact mainly in two selected Villages of Khayan and Thongwa Townships. The solar panels will be used to identify electricity availability in the study areas. It is also wanted to investigate an area of solar energy consumption for the development of Myanmar, to select suitable areas for development requires a preliminary investigation.

Materials and Methods

Location of Solar Home System in Some Selected Areas

Solar home system is beginning to the benefits of power and light to solar energy. In this research, the roof mounted 50 W solar panel (3.178 ft^2 or 0.295 m^2) was used for the period of January to June in 2020. The suitable solar energy collected areas such as system I (South Aye Village in Khayan Township) and system II (Kyutawwa Village in Thongwa Township) at Yangon Region were selected. The geographical location of Khayan Township is between Latitude $16^{\circ} 54' 20'' \text{ N}$ and Longitude $96^{\circ} 33' 47'' \text{ E}$. Thongwa Township is situated between Latitude $16^{\circ} 45' 35.93'' \text{ N}$ and Longitude $96^{\circ} 31' 29.93'' \text{ E}$. The map of Yangon Region, showing the selected Township is shown in Figure 1 and 2. The Roof-mounted 50 W solar panels in South Aye Village at Khayan Township and Kyutawwa Village at Thongwa Township are shown in Figure 3 and 4. The monthly output solar power received on the system I and II were recorded with solar panel checker. The monthly average solar energy received per area per day on the system I and II were calculated.



Figure 1 The map of Yangon Region, showing the selected Township (Khayan)

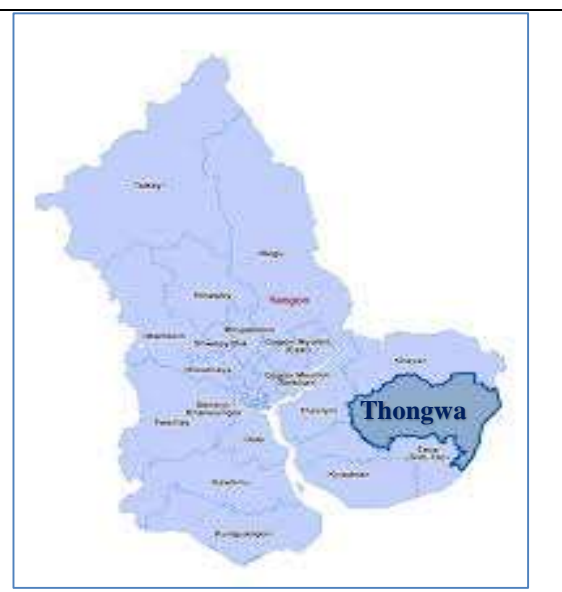


Figure 2 The map of Yangon Region, showing the selected Township (Thongwa)



Figure 3 Roof-mounted 50 W solar panel in South Aye Village at Khayan Township



Figure 4 Roof-mounted 50 W solar panel in Kyutawwa Village at Thongwa Township

Solar Energy Potential Using Photovoltaic (PV) Technology

Solar energy is converted sunlight directly into electricity using photovoltaic technology. The two types of PV technologies are flat plate and concentrating PV. Both PV technologies use solar cells that are made of semiconductor materials to absorb sunlight. When light is incident upon solar cell can generate and support an electric current without being attached to any external voltage source. The schematic block diagram of the solar power home system is shown in Figure 5. A solar photovoltaic (PV) system consists of a solar PV panel (module), a charge controller, a battery, an inverter, and interconnection wiring.

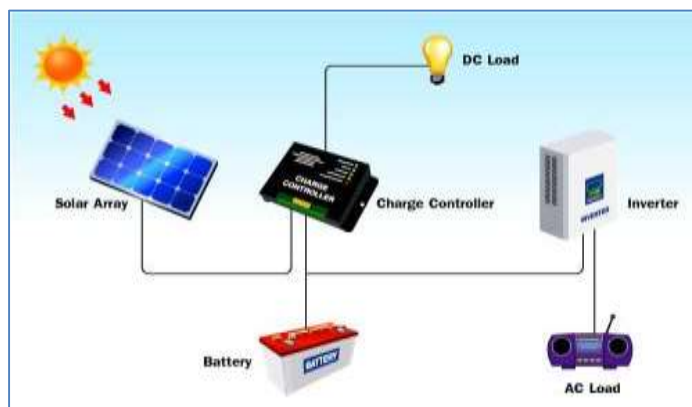


Figure 5 The schematic block diagram of the solar power home system

Working Principle of Solar Cell

When a solar cell is illuminated by sun-light, photons energy of the incident light is converted to direct current electricity through the process of photovoltaic effect of the solar cell. The solar cell works in three steps: (1) Photons in sunlight hit the solar panel and are absorbed by semiconductor materials, such as silicon. (2) Electrons (negatively charged) are knocked loose from their atoms, causing an electric potential difference. Current starts flowing through the material to cancel the potential and this electricity is captured. (3) An array of solar cells converts solar energy into a usable amount of direct current (DC) electricity. Figure 6 shows the working principle of solar panel.

When sunlight strikes the surface of a solar cell, some of the photons are energetic enough to free electrons from the N-type semiconductor. Incident light causes electron-hole pairs to be generated in the semiconductor and there is increase in the concentration of minority carriers (electrons in the p-type region and holes in the n-type region) in the depletion region. Some of the electron-hole pairs immediately recombine. But if the electron-hole pairs are near the P-N junction, the junction potential barrier (due to diffusion) causes the “charge” pairs to separate. The negative electrons move to the N-type side of the cell and the “positive” holes move to the P-type side. The separation of the charges gives rise to a “terminal” voltage. When connected to an external circuit, a current flow as long as sunlight illuminates the cell. The solar panel charges the batteries during the day and the batteries run the light at night.

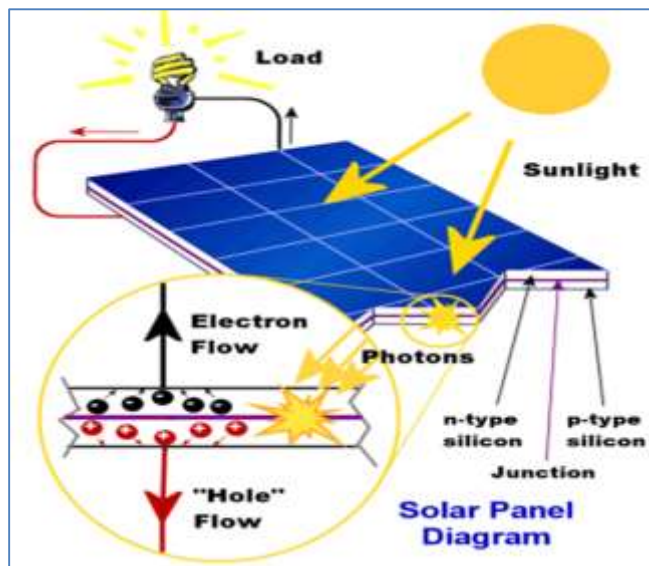


Figure 6 The working principle of solar panel

Results and Discussion

Experimental Recorded Data of Solar Energy

The mathematical method was used to calculate the total output power (P), the average solar energy (E_{av}) and the average solar energy per area per day (E/A) for two selected areas. The daily irradiation energy is hence obtained and then repeated for every one hour and its summation for one day. The hourly variation with the power output for May from 50 W solar panel at studied areas are shown in Figure 7 and 8. On average, these studied areas receive about 6 hours of sunshine per day. Solar radiation is closely related to the sunshine duration. Its seasonal and spatial variations are thus very much the same as in the case of sunshine.

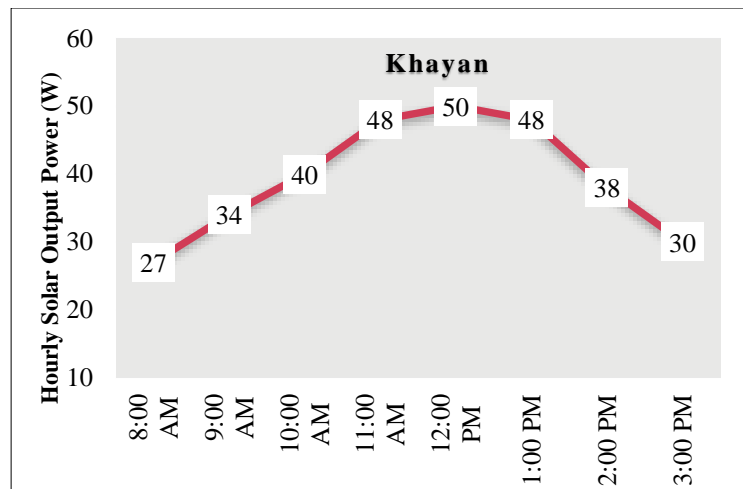


Figure 7 The hourly variation with the power output for May from 50 W solar panel at Khayan Township

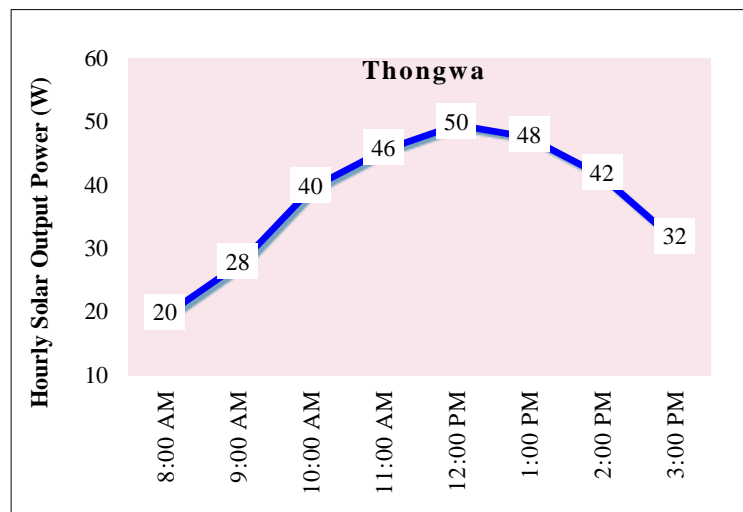
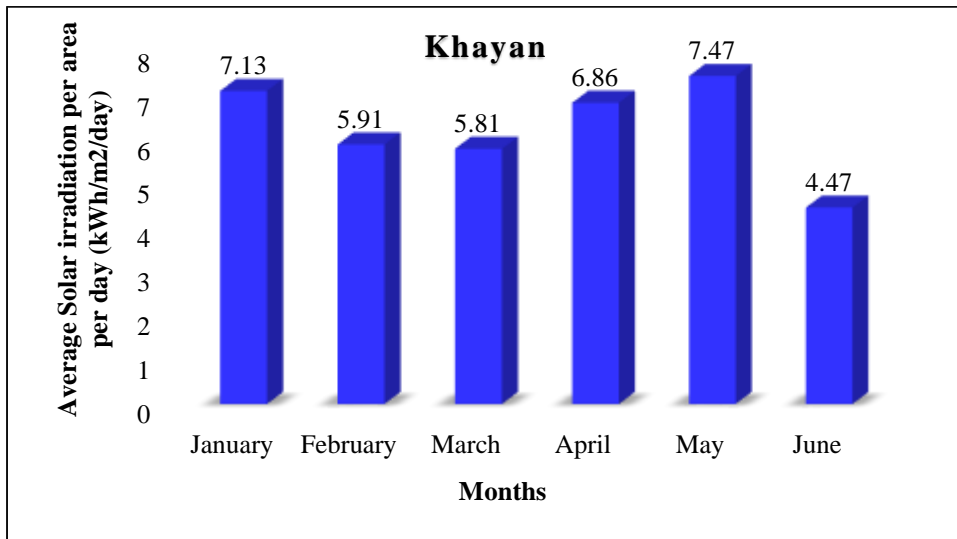


Figure 8 The hourly variation with the power output for May from 50 W solar panel at Thongwa Township

To calculate monthly average daily solar irradiation intensity, data for the number of days in one month were averaged. The average solar energy per area per day (E/A) received on the system I and II (50 W solar panels) were calculated from the experimental recorded data of solar energy. The monthly average solar energy received per area per day for South Aye Village in Khayan Township is given in Table 1 and Figure 9. The solar radiation of South Aye Village in Khayan Township ranges from 7.47 kWh/m²/day in the month of May and drops lower to 4.47 kWh/m²/day in the month of June. The monthly average solar energy received per area per day for Kyutawwa Village in Thongwa Township is shown in Table 2 and Figure 10. The values of monthly average solar radiation received per area per day ranging from 4.27 kWh/m² to 7.26 kWh/m² for Kyutawwa Village in Thongwa Township.

Table 1 The monthly average solar energy received per area per day for South Aye Village in Khayan Township

Month	Total sunshine hours per day t (hrs)	Total Solar Output Power received in a day P (W)	Calculated Solar Energy received in a day E _{av} (kWh)	Collected Area A (m ²)	Average Solar Energy received per area per day E/A (kWh/m ² /day)
January	7	300	2.10	0.295	7.13
February	6	291	1.74	0.295	5.91
March	6	286	1.71	0.295	5.81
April	7	289	2.02	0.295	6.86
May	7	315	2.21	0.295	7.47
June	5	264	1.32	0.295	4.47
Average	6	291	1.85	0.295	6.28

**Figure 9** The graph of the monthly average solar energy received per area per day for South Aye Village in Khayan Township**Table 2** The monthly average solar energy received per area per day for Kyutawwa Village in Thongwa Township

Month	Total Sunshine hours per day t (hrs)	Total Solar Output Power Received in a day P (W)	Calculated Solar Energy Received in a day E (kWh)	Collected Area A (m ²)	Average Solar Energy received per area per day E/A (kWh/m ²)
January	7	296	2.07	0.295	7.02
February	6	284	1.70	0.295	5.78
March	7	287	2.01	0.295	6.81
April	6	274	1.64	0.295	5.57
May	7	306	2.14	0.295	7.26
June	5	252	1.26	0.295	4.27
Average	6	283	1.80	0.295	6.12

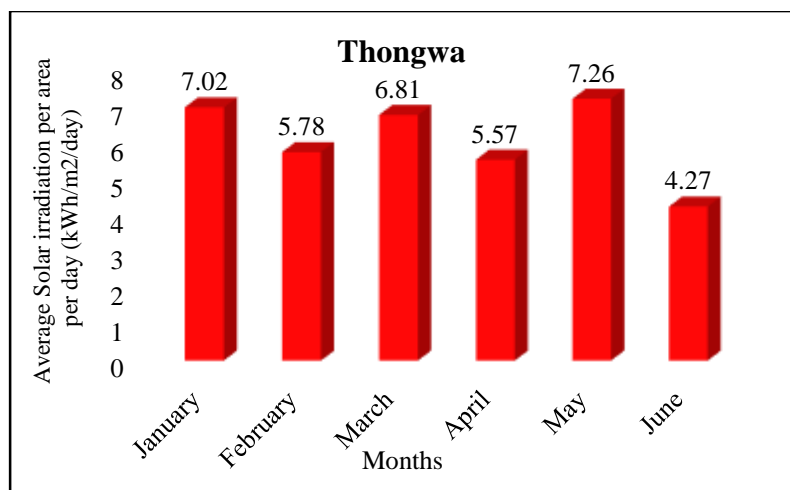


Figure 10 The graph of the monthly average solar energy received per area per day for Kyutawwa Village in Thongwa Township

Discussion

The comparison results of solar energy received in one day for two studied areas are shown in Table 3 and Figure 11. In all results, the highest solar irradiation was in May and the lowest was in June. The comparison results of solar Energy Received per area per day in two studied areas are displayed in Table 4 and Figure 12. Myanmar Electric Power Enterprise (MEPE) experimental measurements indicate that irradiation intensity of more than 5 kWh/m² was observed during the dry season. So, according to all solar energy data, the average daily solar irradiation in two selected Villages of Khayan and Thongwa Townships were considered to be well. Due to variating monthly global solar radiation, the energy output by a solar energy conversion system would vary from month to month. The two most important effects that must be allowed for are due to the variable temperature and irradiance. Temperature has an important effect on the power output from the cell. Irradiance is directly proportional to the short-circuit current of a solar cell.

Table 3 The comparison results of solar energy received in one day for two studied areas

Month	Solar Energy received in one day	
	E_{av}(kWh)	
	Khayan	Thongwa
January	2.10	2.07
February	1.74	1.70
March	1.71	2.01
April	2.02	1.64
May	2.21	2.14
June	1.32	1.26
Average	1.85	1.80

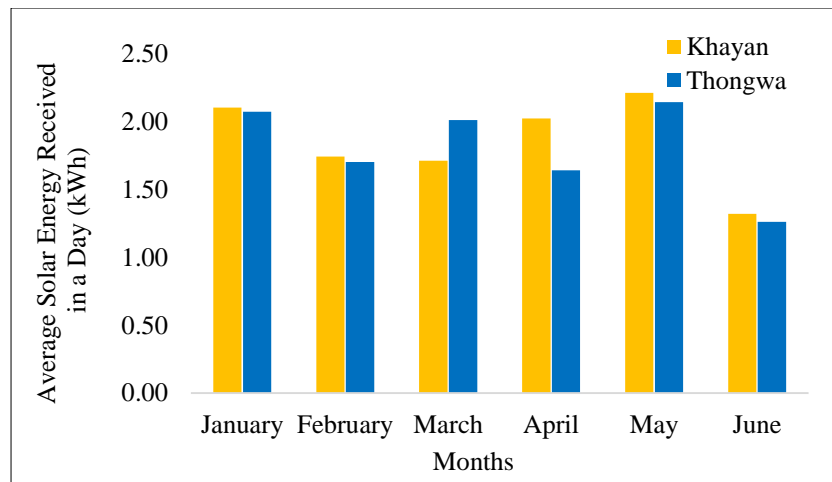


Figure 11 The graph of the comparison results of solar energy received in one day for two studied areas

Table 4 The comparison results of solar Energy Received per area per day in two studied areas

Month	Average Solar Energy Received per area per day E/A ($\text{kWh}/\text{m}^2/\text{day}$)	
	Khayan	Thongwa
January	7.13	7.02
February	5.91	5.78
March	5.81	6.81
April	6.86	5.57
May	7.47	7.26
June	4.47	4.27
Average	6.28	6.12

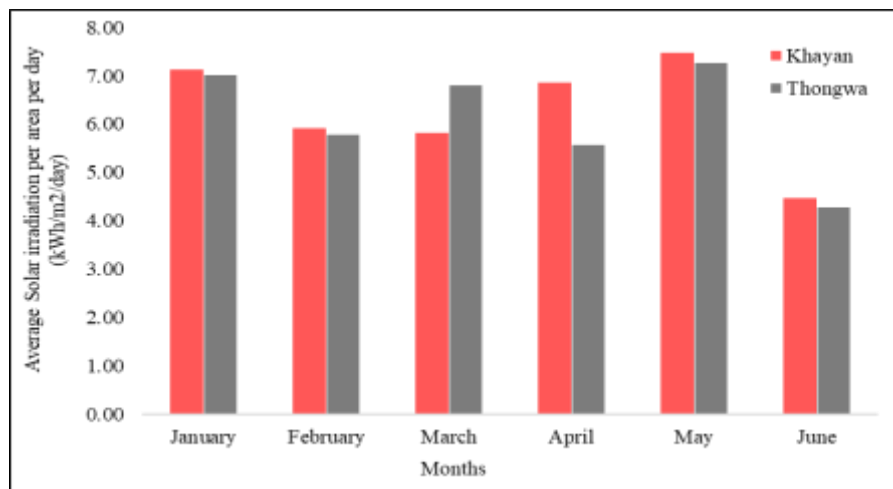


Figure 12 The graph of the comparison results of solar energy received in one day for two studied areas

Table 4 shows for 50 W solar panel of studied areas the list of the most common household appliances used with typical wattage rating with time tendencies of use. By studying the daily habits and energy requirements of the households in these areas, the present household energy consumption is estimated.

The block diagram of the uses of home appliances for 50 W solar panel is shown in Figure 13. For example, four 10 W light bulbs and a 60 W fan require 100 watts of power. To use these appliances for 3 hours, we will need a total of 300 watts of power. Divide a total of 300 watts of energy by six hours of sunlight a day to get 50 W. So, we need to use a 50 W solar panel to use four 10 W light bulbs and a 60 W fan for 3 hours.

Table 4 The list of the most common household appliances for 50 W solar panel

Electrical application of Household type	Effect [W]	Normally time of use/ Remarks
2 light bulbs to 5 light bulbs	From 3 to 12 W	05:00-06:00, 18:00-20:00
Stereo	30	19:00-22:00
Radio	7	10:00-12:00, 13:00-14:00
Fan	35	19:00-22:00
Mobile charger	6	05:00-06:00, 19:00-21:00



Figure 13 The block diagram of the uses of home appliances for 50 W solar panel

Concluding Remarks

This study indicates that the region of South Aye Village in Khayan Township has more abundant availability of solar energy. According to most of results, South Aye Village in Khayan and Kyutawwa Village in Thongwa Townships are good regions for solar photovoltaic system because the average daily solar radiation intensity is more than 5 kWh/m². The amount of electricity generated from solar energy depends upon the available sunlight. In this research, 50 W off-grid solar system was used for lighting, mobile charging and battery charging.

People can see the applications everywhere in the life. Such as solar photovoltaic power plant, household solar photovoltaic power generation system, solar lights, solar cars and some other applications. Solar energy usage in Myanmar is still very low, but it is currently used to charge battery back-up systems for radio telephones, telephone switchboards, television relay stations, water pumping stations and solar freezers for hospitals in rural areas. Nowadays, even government is offering rebate and tax exemptions to those who install Solar Power in their home. In the most remote locations, solar energy is the ideal source of electricity.

Today's electricity supply in Myanmar is generated by fuel generators and hydroelectric power plants. However, far-flung areas which are away from National Grids cannot enjoy the electricity generated by these sources. The possible applications of the successful development of economic solar energy conversion to meet needs for mechanical or electrical energy are wide. Applications of solar power will require the substantial development of new technology.

People in South Aye Village of Khayan and Kyutawwa Villages of Thongwa Townships at Yangon Region believe that they are enjoying the development of the solar energy system. Since Myanmar is a land of plentiful sunshine, solar energy is available around the country. So, researchers have also been doing research concerning about solar cells in Myanmar. If so, everywhere away from National Grids can enjoy the electricity generated by solar energy. It is hoped that the data obtained from this research will be useful to generate electricity from solar energy in the studied areas.

Acknowledgements

First and foremost, the authors would like to express appreciation to Rector Dr Kyaw Kyaw Khaung and Pro-Rector Dr Min Min Yee, East Yangon University, for their kind permission to undertake the research. The authors would like to express my deep appreciation to Professor Dr Khin Mya Mya Soe, Professor & Head, Department of Physics, East Yangon University, who generously provided feedback and constructive suggestions for improving this research. The authors also would like to express thankful to Professor Dr Thet Naing, Professor of Physics Department, East Yangon University, for his guidance with this research.

References

- Aghil Shavalipour, (2013), November, "New Formulation for the Estimation of Monthly Average Daily Solar Irradiation for the Tropics: A Case Study of Peninsular Malaysia", Solar Energy Research Institute, Universiti Kebangsaan Malaysia (UKM), 43600 Bangi, Selangor, Malaysia.
- R. R. King, (2009), September, "24th European Photovoltaic Solar Energy Conference" Hamburg, Germany, 21-25.
- San Tint, Dr. (1998), November, "Commercialization of Renewable Energy for Sustainable Development": Yangon Technological University.
- Thet Thet Han Yee, Su Su Win, and Nyein Nyein Soe, (2008), "Solar Energy Potential and Applications in Myanmar", World Academy of Science, Engineering and Technology.
- Tomas Markwart, (1992), "Solar Electricity", University of Southampton, UK.
- Win Khaing, (2003), "Solar Power Development for Rural Areas in Myanmar". Myanmar Times, Pg-10. (<http://www.myanmar.gov.mm/myanmartimes>).
- <http://www.energy.gov/eere/solar>

FIREBASE AS A BACKEND SERVICE IN MOBILE AND WEB APPLICATION DEVELOPMENT*

Chaw Su Lwin¹, Nem Khan Dim², Soe Mya Mya Aye³

Abstract

Nowadays, mobile applications are widely used in organizations. Moreover, mobile applications have become more and more reliant upon large amount of database and unorganized data such as videos, images, audio, text, files and other arbitrary types. It is difficult for Relational Database Management System (RDBMS) to handle the unstructured data. Firebase is a powerful web and mobile application platform to solve the key challenges of app development. This platform is a Backend-as-a-Service (BaaS) solution both for mobile and web-based applications. Moreover, firebase is a relatively new technology for handling large amount of unstructured data. It is very fast when compared to RDBMS. This paper develops a university student attendance system using Firebase and intend its concepts, related terminologies, advantages and limitations. Student attendance systems rely on large amount of database, require prompt system responses and the number of user access to the applications is unpredictable. Therefore, student attendance system was developed to demonstrate the real-time affordances of Firebase and its features.

Keywords: Firebase, Mobile app, Cloud storage, NoSQL, Student Attendance System

Introduction

In today society, everyone uses mobile phones and daily operations of organizations can be expanded by implementing a number of businesses as a mobile application. In this paper, we look to create an application and determine how useful Firebase is, in the case of development of student attendance system. This paper implements an application with which teachers can easily record student attendance using their mobile phones. In addition to collecting a class attendance, the application also allows teachers to record their personal information, check their daily class schedule, review the attendance list at any time, submit daily attendance to department head and send/read department notifications. There are about 1,000 teachers who are in charge of teaching at a university, and the number of times they can access information from the app is unpredictable. Therefore, every time data is read/ written into a database, the cost may increase. To solve these problems, we tried to develop a mobile app with Firebase.

Firebase is a toolset to “build, improve, and grow app”, and the tools cover a large portion of the services that developers would normally have to build themselves, because they had rather be focusing on the app experience itself. This includes application analytics, authentication, databases, configuration, file storage, push messaging, and the list goes on. The services are hosted in the cloud, and scale with little to no effort on the part of the developer.

Therefore, this paper aims to implement a Student Attendance System for all universities. The system will be implemented using the services provided by Firebase. This paper will show the use of Firebase services. In addition, the implemented student attendance system will be available at all universities.

The paper is structured as follows. Section 2 briefly presents the basic concepts and services of Firebase. Section 3 presents the related work. Section 4 describes the application

¹ Dr, Lecturer, Department of Computer Studies, University of Yangon.

² Dr, Demonstrator, Department of Computer Studies, University of Yangon.

³ Dr, Professor and Head, Department of Computer Studies, University of Yangon.

* Best Paper Award Winning Paper in Computer Studies (2020)

development: the implementation stage is depicted in detail. Section 5 is result and discussion. Finally, section 6 concludes the paper.

Firebase

Firebase was established by Andrew Lee and James Tamplin in 2011 and launched formally in April 2012. Started as a realtime database, now Firebase has 18 services (4 of them currently in beta), and dedicated APIs.

The Firebase platform is a Backend-as-a-Service (BaaS) solution both for mobile and web-based applications. Firebase services include features building, testing, and managing apps. With easy development, Firebase developers can focus more on crafting fantastic user experiences. Developers do not have to manage servers and write APIs. Firebase serves as a server for API and data store. The most important feature of Firebase is its generality that allows developers to modify it to suit their needs. Additionally, developers will occasionally need to use other bits of the Google Cloud for their advanced applications.

Firebase is suitable for developing student attendance systems because it is a useful framework for building portable and web applications for businesses which require real-time database which means when one user updates a record in the database, the update should be conveyed to every single user instantly. A host of other Google features packed- in with the service gives a basic and unified platform to many applications along with. Firebase handles most of the server-side work when it comes to the development of applications. Firebase has several elements that helps maintain a state of harmony between the developer and the client by causing minimal delay of work. Firebase has several features that make this platform essential as shown in Figure 1. These features include unlimited analytics and reporting, cloud messaging, authentication and hosting.

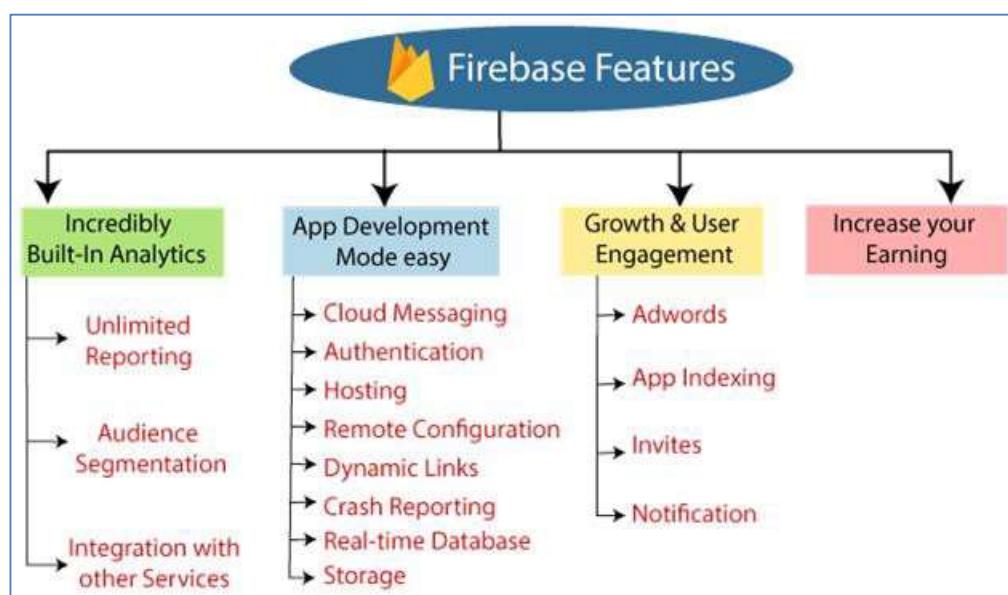


Figure 1 Available Firebase Features

There are many services that can be integrated to our application to enable the features, some of the services. Services such as (1) Authentication, (2) Hosting (3) Crash Reporting (4) Real-time Database (5) Analytics, and (6) Cloud messaging are used in implementing our proposed work.

Table 1 Firebase services

No.	Service	Description
1.	Authentication	Firebase has little friction with acclaimed authentication.
2.	Hosting	Firebase has little friction with acclaimed authentication.
3.	Crash Reporting	Prioritize and fix issues with powerful, real-time crash reporting.
4.	Real-time Database	It can store and sync app data in real-time.
5.	Analytics	Get free and unlimited app analytics.
6.	Cloud messaging	Firebase allows us to deliver and receive messages in a more reliable way across different platforms

Proposed Work

The system was implemented into two sides: Admin side and Teacher side. At admin side, professor or staff can set up all required information to use the system such as student information, teachers, courses, modules and timetables. Professors can also see daily, monthly and semester-based reports on student. At teacher side, a teacher can sign up for an account, check their weekly timetables and check student attendance. Admin side is a web-based application and teacher side is a mobile application with which teachers can easily check student attendance on their phone during the class. This is the part where Firebase is especially suitable for the system because data from the webapp needs to be effectively synchronized on the mobile app and Firebase supports it best. Details will be discussed along with the users interfaces shown below.

Professor or staff can login to their account and this user authentication can be easily done. Most tasks that can be done in professor and staff account are nearly the same but staffs cannot see attendance reports or cannot approve re-submission of attendance requests from teachers as professors can do. User can login to the system by the following firebase authentication code.

```

FirebaseAuth authentic=FirebaseAuth.getInstance();
authentic.signInWithEmailAndPassword(email, password)
.addOnCompleteListener(new OnCompleteListener())
{
    @Override
    public void onComplete (Task task)
    {
        if(task.isSuccessful())
        {
            FirebaseUser user=task.getResult().getUser();

            String email=user.getEmail();
            //...
        }
    }
});
```

Figure 2 is where professor can assign and view teacher to courses. If an assignment for a teacher is redundant for the same lecture time, the system will notify it to the professor and thus the professor can avoid redundant schedule assignment for the teachers.

Figure 2 Assign Teacher to Course

Professor can approve or reject requests from staffs and teachers as shown in Figure 3. Requests from staffs can be made when they have submitted student data for use but need to edit student information due to their errors. Requests from teachers can happen when teachers want to modify student attendance for some reasons. After teachers have submitted daily student attendance to the professor, they cannot modify without professor permission. In that case professors can approve or reject those requests in the following form.

Figure 3 Approve/Reject Requests by Professor

In Figure 4, professor can select a class (second year, third year) and modules to see the attendance of the students.

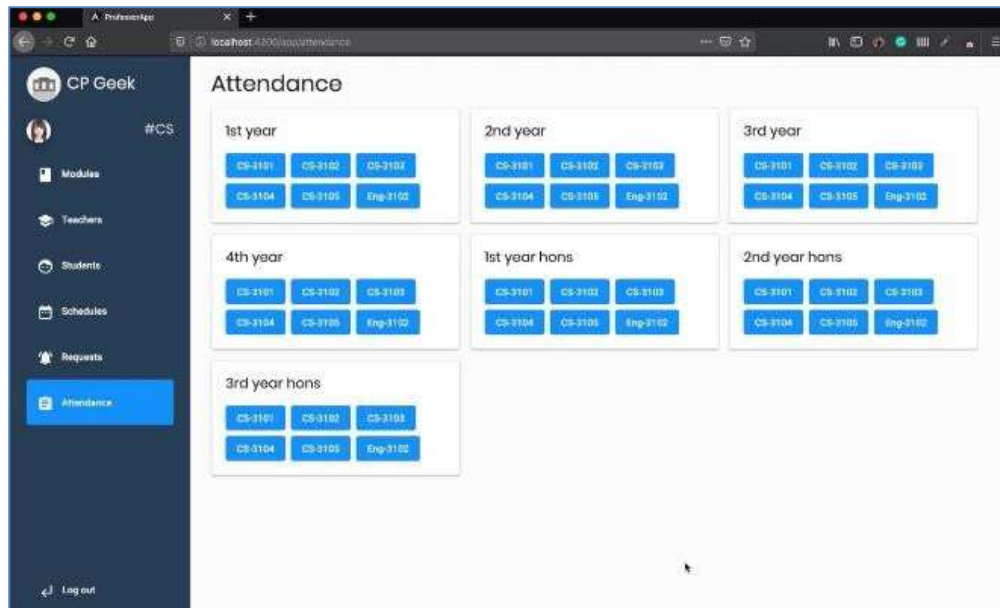


Figure 4 Select Class and Module to check student attendance

Professors can check student attendance by means of day, month and semester. They can also filter students with attendance under 75% or above. This attendance report (Figure 5) can be printed or exported to an excel file format.

Sr. No.	Roll No.	Name	No of Periods	Out of (14) periods	Percentage	Remark
1	3-CS-1	Mg Kyaw Thira	14	10	71	
2	3-CS-2	Mg Min Myat Kyaw	14	14	100	
3	3-CS-E	Mg Zu Wut Yi	14	8	57	
4	3-CS-B	Ma Thet Thinzar Aung	14	12	86	
5	3-CS-7	Mg Thit Htoo Pyow Sone	14	14	100	

Figure 5 Attendance report

A teacher can sign up for an account on their mobile app. The following code can be used to add Firebase as a dependency to android project:

```
{ compile 'com.firebaseio:firebase-client-android:2.5.0+'  
}
```

Once the Firebase and storage dependency are added to the application, Firebase storage and hosting tasks can be easily done with the following built in codes:

```
FirebaseStorage storageObj = FirebaseStorage.getInstance();
StorageReference fileRef = storageRef.child("filePath");
```

All departments have their staff data filled up before teachers use the mobile application. When a teacher signs up, the sign up information such as staff number and NRC number match with teacher information in the department staff database, the teacher account is approved and created. Teachers will be able to retrieve as the Figure 6.



Figure 6 Teacher profile page after signing up

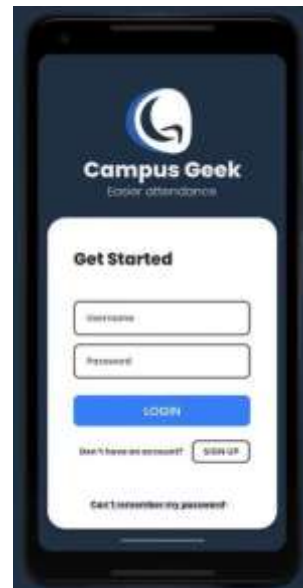
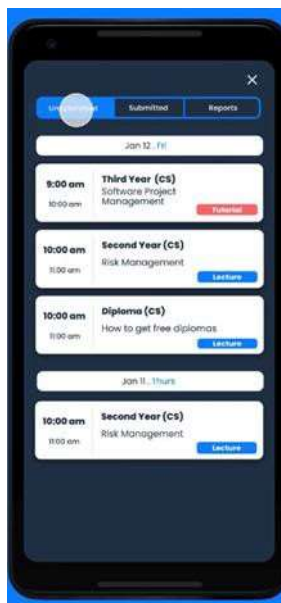
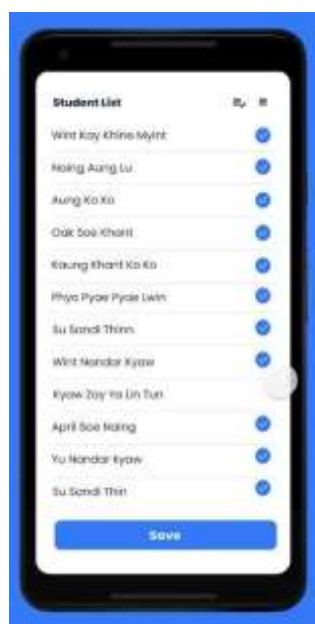
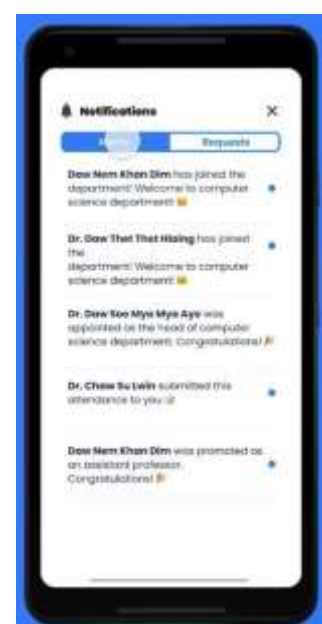


Figure 7 Teacher log in page.

A teacher can log in Figure 7 after signing up to the application. Data entry in signing up can be readily performed using the following code in Firebase:

Call: ref.push().setValue(object) or ref.setValue(object)

A teacher can check their weekly schedule (Figure 8 a) and daily schedule (Figure 8 b). Teachers can check and pay student attendance as in Figure 9. Each teacher can also view monthly report of student attendance as the Figure 10. Because of Firebase's auto synchronization web services, teachers can concurrently check their daily schedules and attendance report with almost no concurrency error. Teachers can also check notifications and announcement within the department as shown in Figure 11.

**Figure 8 (a)** Teacher weekly Schedule**Figure 8 (b)** Teacher daily schedule**Figure 9** Check student attendance**Figure 10** Monthly student attendance percentage**Figure 11** Notificaiton page

In Figure 12, admin can see detail app analytics; how many users are using, current quota period and how many transactions occur over time. The analytics show the number of database read/write transactions on which database costs can be estimated.

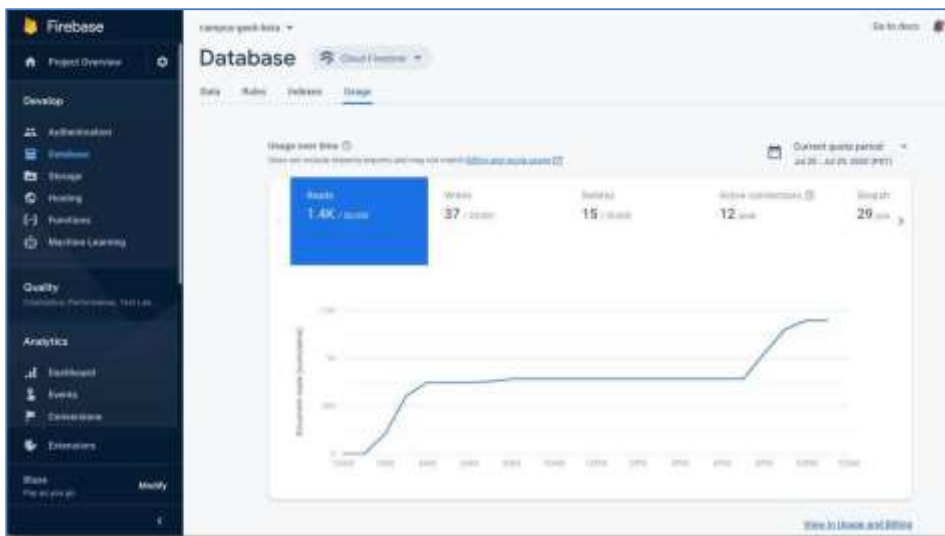


Figure 12 User feedback analytics on the proposed work

Results and Discussion

A pilot study was conducted at Department of Computer Studies, University of Yangon (YUCS). During the study, professor, Department staff and teachers from YUCS use the system performing their respective tasks, and record their feedbacks regarding their experiences in using the system and answer some follow up questions. The pilot study took one month.

The proposed system receive positive comments from users. The efficiency in doing tasks and user experiences are greatly appreciated by the users. Users found it easy to learn and use the system. User satisfaction, fatigue, ease of learn, ease of use of the system are recorded using a seven-point Likert scale after the pilot study (for example, 1 for not satisfied at all and 7 for very satisfied).

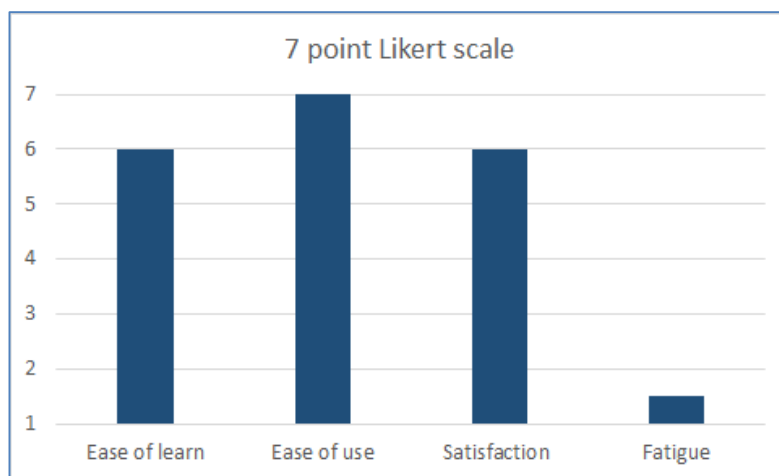


Figure 13 User feedback on the system

In Figure 13, users gave high rating for all items: ease to learn, ease to use and user satisfaction. Less score in fatigue means that the system offered good users experience that users feel less stressed and tired using the system.

Subjective comments from users were also analyzed to find opportunities for improvements of the system. Some users suggest to add export function for attendance report at

teacher side too. Some other users suggest to link the system to other school software such as HR management and student registration system so that some tasks for data entry can be reduced at the current system. Some other users also suggest to consider about teachers transfer so that the system can be used for any University in Myanmar. Those comments and suggestions will be considered for further improvement of the system in the future. Firebase framework is oriented toward real-time and synchronization and there is a few limitation in data migration because there can be restriction in exporting data from servers that users do not own.

Conclusion

This paper demonstrates the use of Firebase framework to develop a student attendance system that is a portable web application which require real-time database transactions. Affordable services in Firebase eases the development processes. Also, the proposed system receives positive feedback and receptivity from its potential users. The contributions of this paper are the demonstrations of implementation of a mobile web application using Firebase services and a student attendance system that can be used in all universities. The present study was conducted and the proposed system was pilot tested in Yangon University. In the future, current work will be extended to test the system in other universities to better understand the affordances and limitations of Firebase.

Acknowledgement

We would like to express my deepest gratitude to the following individuals who extended their invaluable support for the completion of this study. Firstly, we would like to express my special gratitude to Dr. Pho Kaung (Rector, University of Yangon) for his administrative support that assisted greatly in the preparation of this study. We would like to offer respectful gratitude to our Professor and head, Dr. Soe Mya Mya Aye for her precious guidance and suggestions. We also owe a special debt to the teachers from Department of Computer Studies, University of Yangon for their cooperation in this research.

References

- Abdullah A., Yahya A. H., Mohammed A. D., Ibrahim A., (2017), “*Real-Time Communication Network Using Firebase Cloud IoT Platform for ECMO Simulation*”, IEEE International Conference on Internet of Things IEEE Green Computing and Communications IEEE Cyber, Physical and Social Computing IEEE Smart Data, pp 178-182.
- Chunnu K., Pritam S., (2018), “*Application of Firebase in Android App Development-A Study, International Journal of Computer Applications*”, Volume 179 – No.46, pp 0975 – 8887.
- Fu C., (2018), “*Build Mobile Apps with Ionic 4 and Firebase: Hybrid Mobile App Development*”, Second Edition, ISBN-13 (pbk): 978-1-4842-3774-8 ISBN-13 (electronic): 978-1-4842-3775-5.
- Guido A., Fikru G. D., Waqar H., Dario S., (2020), “*On the performance of web services, google cloud messaging and firebase cloud messaging, Digital Communications and Networks*”, Volume 6, Issue 1, Pages 31- 37.
- Mayuri C. W., Priyanka P. P., (2018), “*Traditional Infrastructure vs. Firebase Infrastructure, International Journal of Trend in Scientific Research Development (IJTSRD)*”, International Open Access Journal, Volume 2, Issue 4, pp 2050-2053.
- Nilanjan C., Souvik C., Aakash D., Dr. Asoke N., (2018), “*Real-time Communication Application Based on Android Using Google Firebase*”, Volume 6, Issue 4, International Journal of Advance Research in Computer Science and Management Studies.
- Neil S., (2017), “*Firebase Essentials Android Edition*”, First Edition, Payload Media, Inc., 2017.
- Sai Spandhana R. E., Sirisha P., (2019), “*Android Based Instant Messaging Application Using Firebase*”, International Journal of Recent Technology and Engineering (IJRTE) ISSN: 2277-3878, Volume-7 Issue-5S2, pp 352-255.
- Sonam K., Swapnil T., (2017), “*Real Time Databases for Applications*”, International Research Journal of Engineering and Technology (IRJET), Volume: 04 Issue: 06, pp 74-79.

EFFECTIVE STUDENT COLLBORATIVE SYSTEM BASED ON CLUSTERING ANALYSIS

Kyaw Thiha¹, Khin Myo Sett²

Abstract

In most recent years, many educational research workers pointed out that collaborative learning should be widely used in education systems because collaboration skill has increasingly become an essential skill of modern society. Moreover, collaborative learning can encourage the improvement of students' comprehension about their studying. However, it is vitally important to notice that students have different common interests which mean various habits, likes and dislikes, and different learning styles. From the view of educational informatization, we therefore propose Student Collaborative System (SCS) to help in grouping students in accordance with their common interests in this paper. In our proposed system (SCS), students are grouped based on the analysis of common interests using K-Means clustering method. This system is developed using Python as programming language and Spyder (Python 3.7) as integrated development environment (IDE).

Keywords: collaborative learning, common interests, educational informatization, K-Means clustering

Introduction

Alongside with the influence of educational informatization, Data Mining techniques are widely used in education industry to gain the valuable insight from data. This is namely called Educational Data Mining (C. Romero, S. Ventura (2007)). Following the steps of most Data Mining system, Educational Data Mining also has three steps; data preprocessing, mining or using one of Data Mining techniques and providing finalized results.

Although the use of Educational Data Mining is increasingly spread, it is mainly convenient in developed countries because data collecting is the indispensable process of Data Mining and it is easily performed in developed countries through many information system and successful E-Learning classrooms. Educational Data Mining is rarely used in developing countries as traditional classrooms are essential roles of education system and data collection is not that much easy.

On the one hand, collaborative learning which can provide collaborative skill in real life and has a lot of benefits for students has become one of popular learning styles. Moreover, it can help student-center learning which can promote student engagements (Singhal, Divya. (2017)). On top of that, student-center learning is the education system which is used in our country, Republic of the Union of Myanmar.

Due to the above reasons, student collaborative system (SCS) is designed to meet the requirements in developing countries, especially in Myanmar. Regardless of being homogeneous or heterogeneous grouping, our paper mainly focus on grouping students according to their common interests. In our research work, questionnaire approach is used as primary data collection method and K-Means clustering method is applied to classify students into proper groups.

Related Works

A lot of educational data mining researches are developed to enhance collaborative learning although there many open source tools such as Keel, Weka and we can adopt many seldom paywares, e.g. SPSS and DBMiner. Among these previous researches, a research

¹ Part-Time Demonstrator, Department of Computer Studies, University of Mandalay

² Professor(Head), Department of Computer Studies, University of Mandalay

paper by TangJie et.al., (2012) explored a peer-model that was designed for Mobile Computer Supported Learning in order to find partners for students in 2012. Moreover, there are many researches about educational data mining tools such as Pdinamet (E. Gaudioso et al., (2009)) and E-learning Web Miner (Zorrilla, Marta & García-Saiz, Diego. (2013)) which apply clustering or association rules.

In 2009, Wen-Yan Kao developed a learning style classification mechanism for e-learning. A hybrid approach which is composed of genetic algorithm and k-NN classification is used in this research. And In 2014, Enhanced Ant Colony Optimization (EACO) algorithm is proposed by Hu Hui based on the ability, interests and comprehensions of students in order to enhance cooperative learning. On top of that, Ma Yanyun measured students' learning ability to improve the effectiveness of collaborative learning in 2016.

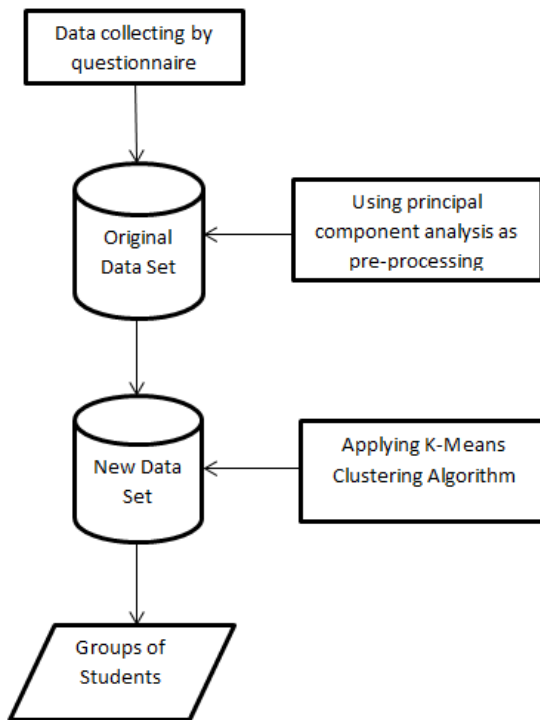
Through these previous researches, we can clearly see that many educational researchers applied Educational Data Mining in terms of improving effectiveness and efficiency of student collaboration.

Proposed System

Our proposed system, student collaborative system (CSC) is inspired by these related works. However, the main difference between our work and these related researches are data sources. The data sources of these related studies are mostly collected from E-Learning systems and computerized school management systems which can acquire data of student learning activity. Apart from these researches, we developed a questionnaire to collect data because E-Learning system and computerized school management systems cannot be adopted widely in developing countries and so teachers in those portions of the world need a questionnaire as a mean to gather students' data. After we gathered students' data through the developed questionnaire, K-means clustering method was employed to analyze collected data. The system flow diagram of our proposed system is illustrated in figure 1.

Data Collecting

Following the rules of Data Mining processes, data collecting came in first place of our research work. To collect data, we developed a questionnaire that can catch students' opinions which can be used to identify the groups. Moreover, this questionnaire was comprised in accordance with students in Myanmar currently enrolling in computer science because it is vitally important to guarantee comprehensiveness, usability, quality and to reflect the targeted people and to meet requirements in research areas. Therefore, the questionnaire was developed with 20 questions in which number one to ten are about lifestyle and habits while number eleven to fifteen are about their opinions on their specialization and last five question are about their learning styles that are extracted from Dunn's theory of learning style (Dunn, R. (1984)). Each question consists of three answers to be chosen as shown in Table 1.

**Figure 1** System Flow Diagram**Table 1** Questionnaire to collect students' opinions

Questions	Choices	Answers
1. Which is the most and usually habit you would like to do in the following?	(a) Gaming (b) Music/Watching TV (c) Photography	
2. What time of weekend day would you be most available?	(a) Morning (b) Afternoons (c) Evening	
:	:	:
11. Which programming language you would prefer the most?	(a) Java (b) C# (c) C++	
:	:	:
20. What will you do when you need to make a decision while shopping?	(a) Make the decision right away (b) Make the decision after deep consideration (c) Hesitate to make decision	

These questionnaires are handed out to 30 computer science students from Department of Computer Studies, University of Mandalay. And 27 questionnaires were collected with a collecting rate of nearly 90% (exactly 89.99%).

Data Pre-processing

After collecting data sources, next step we must perform is data pre-processing on original data set, which is an indispensable and important initial stage of data mining. Moreover, we can solve the noises, missing values and inconsistent data via data pre-processing. In other words, we can say that the main objective of data pre-processing is to minimize the dimensionality or size of data, normalize the original data set, discover the interconnection between data, detect outliers and extract features for data. Data pre-processing consists of data cleaning, data integration, data transformation. These stages are illustrated by figure 2 and figure 3 (Tamilselvi et al.,2015). In our research work, we performed data conversion and principal component analysis for dimensionality reduction on original data set.

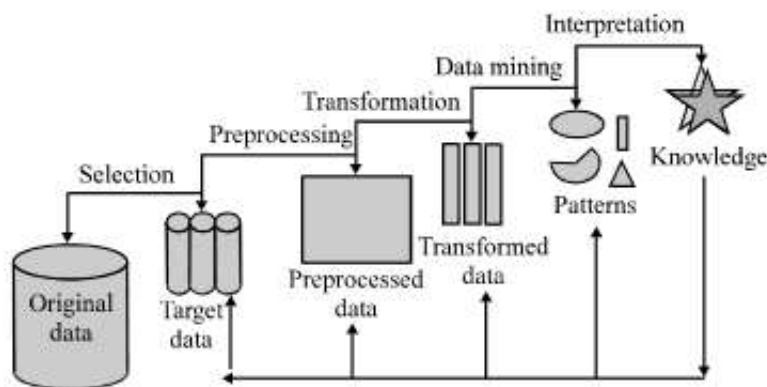


Figure 2 Data pre-processing in Knowledge discovery

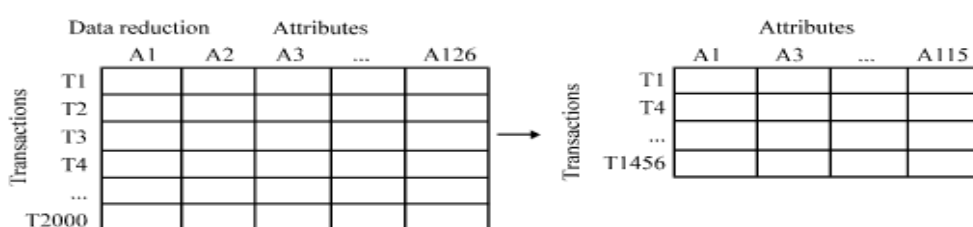
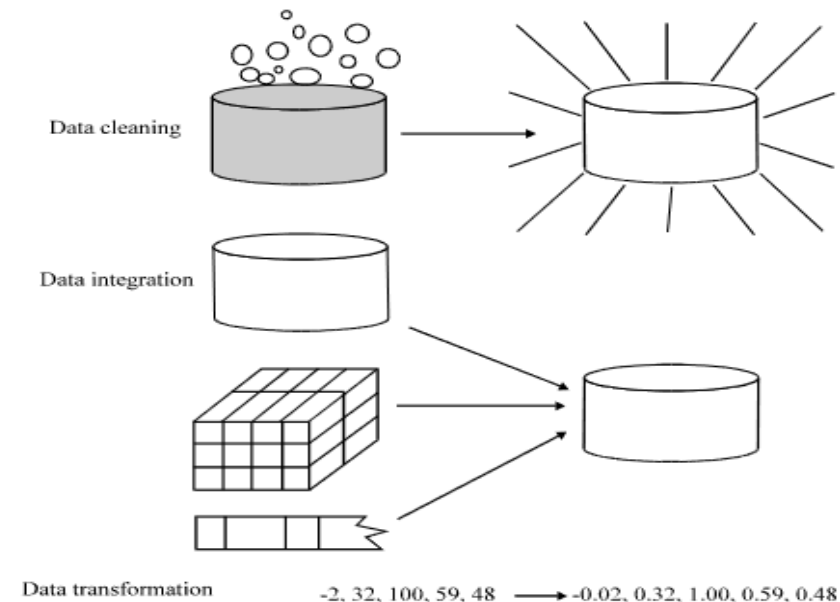


Figure 3 Data pre-processing Form Data Conversion

According to the structure of questionnaire we designed as shown in Table 1, every students staring from the sequences of their roll number R possess 20 attributes from A1 to A20. A range of choice for each answer A is {a, b, c}.Therefore, we can say that $R_i = \{A_1, A_2, A_3, \dots, A_{19}, A\}$, i= number of students {1,2,3,.....,40} as shown in Table 2. Due to the fact that our proposed system (SCS) need numeric values to conduct clustering analysis, a, b, and c is transformed to the values of 1, 2, and 3 respectively as shown in Table 3.

Table 2 Original data

Roll Num	Q1	Q2	Q10	Q19	Q20
R1	B	b	B	C	A
R2	C	c	C	C	a
:	:	:	:	:	:
R10	B	a	B	C	A
:	:	:	:	:	:
R26	B	c	B	B	a
R27	B	a	C	C	B

Table 3 Converted data

Roll Num	Q1	Q2	Q10	Q19	Q20
R1	2	2	2	3	1
R2	3	3	3	3	1
:	:	:	:	:	:
R10	2	1	2	3	1
:	:	:	:	:	:
R26	2	3	2	2	1
R27	2	1	3	3	2

Dimensionality Reduction of Original Data by Principal Component Analysis

Principal component analysis can be defined as a process to reduce the size of data that has multi dimension; in other words, data which has a lot of attributes with the minimum loss of data. The goals of principal component analysis are (1) to extract the most important information from the data table;(2) to compress the size of the data set by keeping only this important information;(3) to simplify the description of the data set; and (4) to analyze the structure of the observations and the variables;(5) to compress the data, by reducing the number of dimensions, without much loss of information (Mishra et al., 2017). In our research work, principal component analysis was applied as pre stage to K-Mean Clustering algorithm which need the least data size as much as possible.

Although principal component analysis has several stages which are also related to mathematical backgrounds, we applied the Python programming libraries built in Python 3.7 supported by Spyder IDE to perform the principal component analysis on original data. As a result, we can reduce the data size of original data from 20 attributes to 15 attributes. As shown in figure 4, there is no variation among data when the variation line reaches 15 principal components. This means that the original data which has 20 components can be covered by first 15 components. This leads to $R_1 = \{A_1, A_2, A_3, \dots, A_{14}, A_{15}\}$.

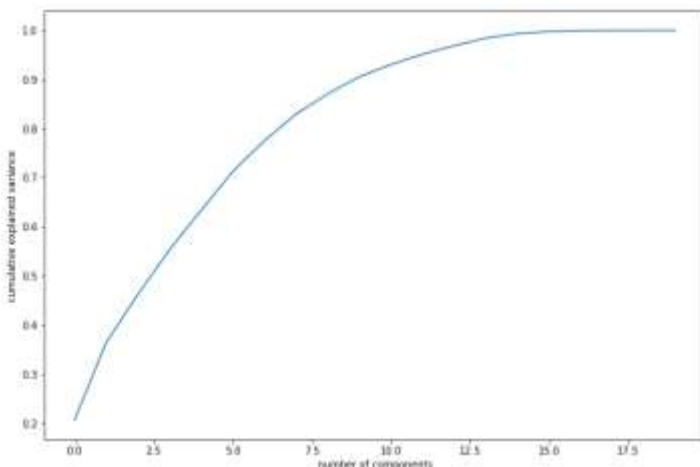


Figure 4 Variance of data

After deciding number of principle component as 15, we derived a new data set as shown in figure 5.

K-Means Clustering Algorithm

Clustering Analysis can be defined as partitioning the data into different groups according to their attributes or characteristics. We can also say that data in one group are similar and have same properties compared to data in different groups (Han et al., 2004). Unlike supervised learning, clustering is an unsupervised learning method in which we analyze the data to be put into similar groups and to create different groups instead of predicting a target. There are many types of clustering; connectivity-based clustering, also known as hierarchical clustering, centroid-based clustering, also known as k-means clustering, distribution-based clustering, density-based clustering, gird-based clustering.

With the rapid development of data mining technology, there are a lot of areas in which clustering method is highly applied. It is widely used not only in business and market research but also in image segmentations. Moreover, clustering analysis can identify Web files by looking at their attributes such as their subjects. In education sector, clustering analysis is applied by many research workers as we discussed in related works section.

PC1	PC2	...	PC13	PC14	PC15
0.365854	9.985776e-02	...	5.367860e-01	4.289935e-02	-2.091347e-01
0.228457	-1.976134e-01	...	-1.864872e-01	-3.129605e-01	-1.545044e-01
0.240936	2.272357e-01	...	2.562431e-02	-3.072779e-01	3.729338e-01
-0.223152	-1.778080e-01	...	5.115909e-01	-3.347983e-01	-1.468264e-01
-0.306658	2.655403e-01	...	-1.414196e-01	-5.341031e-01	-3.054365e-01
-0.279119	2.836098e-01	...	1.588858e-01	1.548743e-01	4.285242e-01
-0.269030	1.417237e-01	...	-1.710357e-01	-2.862694e-01	1.748827e-01
0.015183	1.883671e-01	...	-3.601613e-02	9.955013e-03	-4.493631e-01
0.308539	-1.669531e-01	...	-7.023506e-02	-3.336279e-01	5.829103e-03
-0.209130	-2.105387e-01	...	7.172767e-02	-1.656067e-01	8.181922e-02
-0.129787	2.876661e-01	...	2.602901e-01	1.585640e-01	-3.538935e-01
0.000000	-3.388132e-21	...	2.775558e-17	-2.090342e-16	5.551115e-17
-0.092111	3.357913e-01	...	-5.945705e-02	1.304645e-02	3.872300e-02
-0.205322	-3.288269e-01	...	-1.753506e-01	1.690723e-01	-2.050590e-01
0.172279	4.370517e-02	...	1.411913e-01	-3.058368e-01	1.518661e-01
0.129435	-1.249319e-01	...	4.477161e-02	-2.326388e-02	4.124667e-02
-0.246579	2.143753e-01	...	3.709259e-02	-6.813678e-02	-2.923280e-02
0.308030	3.826778e-01	...	6.075898e-02	1.144206e-02	-1.328249e-02
0.185212	2.497981e-01	...	-4.039612e-01	1.898060e-02	-2.375823e-01
0.136815	1.142839e-01	...	-1.913203e-01	1.027712e-01	6.752292e-02

Figure 5 New Data Set Via Principal Component Analysis

In our proposed system, K-Means clustering algorithm was adopted because it is much better than other clustering algorithm in term of computation. Another reason is that K-means clustering is very convenient if the number of student is very large and is easy to implement. Last but not least, K-mean clustering is less time consuming compared to other algorithm. John A. Hartigan (1975) proposed five steps for K-Means algorithm: (1) Arbitrarily choose k objects from D as the initial cluster centers; (2) Repeat; (3) (Re) assign each object to the cluster to which the object is the most similar, based on the mean value of the objects in the cluster; (4) Update the cluster means, i.e., calculate the mean value of the objects for each cluster; and (5) Until no change; where k is the number of clusters, and D is a data set containing n objects.

The most important stage of K-Mean clustering algorithm is to determine the number of cluster; in other word deciding the value of K. In our proposed system, we decided the value of K as 6 targeting that the number of student in one group is about four due to the reason that at least 2 and at most 5 students should be in a group collaborative learning according to Johnson & Johnson (1999).

Clustering Analysis Result and Discussion

After we had done all data pre-processing stages and get a new data set via principle component analysis as shown in Figure 5, we applied K-Means Clustering algorithm to this new data set. As a result, we got an output in which clusters of components of new data set can be seen as shown in Figure 6. After that, we integrated this result to initial data which means data with same size to original data in order to get finalized data. According to final results shown in figure 7, we found that cluster 0 and cluster 4 had two students respectively while cluster 2 and cluster 5 stands with six students in each. Unlike other clusters, cluster 3 has seven students and cluster 1 possesses four students.

PC1	PC2	PC3	...	PC14	PC15	ClusterID
1.595324	0.105983	-0.875856	...	0.219723	0.030235	3
2.496133	0.852213	2.382664	...	-0.321496	0.087751	3
-1.351051	1.429692	0.281185	...	0.612708	-0.563851	5
-1.173077	-1.168322	2.354893	...	-1.047280	0.339959	1
-1.466784	-1.980877	-1.651553	...	-0.174610	-1.250551	1
1.284443	0.098350	1.987432	...	0.409770	-0.880005	3
0.408275	-0.294704	-0.576540	...	0.230531	0.511582	3
0.450440	0.494688	-0.942574	...	-0.484379	-0.031278	5
-0.765306	-0.242670	2.498679	...	-1.030195	-0.404444	2
-1.056105	1.379964	0.449117	...	0.007582	0.137108	0
-3.247024	0.269276	-2.105386	...	-0.282511	-0.269802	5
0.886622	-2.328942	0.007489	...	0.045342	-0.117104	2
2.163281	0.981455	-1.468905	...	0.688552	0.243300	3
0.857690	-2.036056	0.002346	...	-0.588359	-0.053659	2
-1.638978	-0.064278	-1.945133	...	-0.348003	0.377057	5
-2.368671	-2.230059	1.356742	...	0.571551	0.202716	1
-0.994854	2.726695	0.554623	...	-0.513644	0.566621	4
4.597196	0.921338	-1.073432	...	-0.438596	-0.195548	3
-1.097413	3.173216	1.045240	...	0.772549	-0.303755	4
1.706604	-1.982412	0.855020	...	0.466852	0.223135	2
-0.873590	1.532422	0.584746	...	-0.129518	0.047030	0
-3.247024	0.269276	-2.105386	...	-0.282511	-0.269802	5
0.521591	-2.633858	-0.263768	...	0.319542	0.063051	2
1.980765	0.828998	-1.604534	...	0.825652	0.333378	3
0.675175	-2.188514	-0.133282	...	-0.451259	0.036419	2
-1.821493	-0.216736	-2.080761	...	-0.210903	0.467135	5
-2.551186	-2.382516	1.221113	...	0.708651	0.292793	1
-0.994854	2.726695	0.554623	...	-0.513644	0.566621	4

Figure 6 Principal components with cluster ID

Roll Num	Q1	Q2	Q3	Q4	Q5	Q6	...	Q15	Q16	Q17	Q18	Q19	Q20	ClusterID
R1	2	2	2	2	2	1	...	2	3	2	2	3	1	3
R2	3	3	3	1	1	1	...	1	3	2	2	3	1	3
R3	2	1	2	2	3	2	...	3	1	2	1	3	3	5
R4	2	3	1	2	1	1	...	2	1	1	1	2	2	1
R5	1	1	1	2	3	1	...	2	3	1	1	2	1	1
R6	3	2	3	2	1	1	...	2	2	2	2	3	1	3
R7	2	3	2	2	3	1	...	2	2	2	2	3	1	3
R8	2	3	3	1	3	1	...	2	3	2	2	3	2	5
R9	2	3	3	3	1	3	...	1	1	2	1	3	3	2
R10	2	1	3	3	1	1	...	1	2	1	2	3	1	0
R11	1	2	2	3	3	3	...	1	3	2	1	3	1	5
R12	2	3	1	3	1	1	...	2	3	1	1	3	3	2
R13	2	3	3	2	3	1	...	2	2	1	2	3	3	3
R14	2	3	2	3	1	1	...	2	2	1	1	3	2	2
R15	2	1	2	3	3	2	...	2	3	2	1	3	2	5
R16	2	3	1	3	3	1	...	1	2	2	1	2	2	1
R17	2	1	1	2	3	2	...	2	2	2	2	3	2	4
R18	3	3	3	2	1	1	...	2	3	1	3	3	2	3
R19	2	3	3	3	3	3	...	2	2	2	2	3	2	4
R20	2	3	3	3	1	1	...	2	3	1	1	3	3	2
R21	2	1	3	3	3	1	...	1	2	1	2	3	2	0
R22	1	2	2	3	3	3	...	1	3	2	1	3	1	5
R23	2	3	1	3	1	1	...	2	3	1	1	3	1	2
R24	2	3	3	2	3	1	...	2	2	1	2	3	2	3
R25	2	3	2	3	1	1	...	2	2	1	1	3	1	2
R26	2	1	2	3	3	2	...	2	3	2	1	3	1	5
R27	2	3	1	3	3	1	...	1	2	1	2	1	1	1

Figure 7 Finalized Result

These are the result of our proposed system (SCS), which applied K-Means clustering to group the students based on students' common interests with a goal to promote collaborative learning. By the final results, our proposed system focus on grouping students based on their opinions, their answers to questionnaire. Moreover, the data size of our data set can be effectively reduced by principal component analysis and it is also an advantage to K- Means clustering algorithm. K-Means clustering algorithm is also better compared to other algorithm in terms of speed and simplicity.

Conclusion and Outlook

Although educational informatization is widely spread and improved in developed countries in order to promote collaborative learning, it is still hard to implement in developing countries because of the lack of data sources. In developed countries, it is easy and convenient to acquire the required data sources for collaborative learning because of the availability and mushroom existence of E-Learning classrooms. However, E-Learning classrooms and school information system are not prospered in developing countries. Therefore, we designed a questionnaire that reflects the common interests of the students especially in computer science to collect data and then we applied K-Means clustering to data in order to group students in accordance with their common interests after principal component analysis was performed as data pre-processing. By the results of our proposed system, teachers can group their students based on their common interests and enhance the collaborative learning.

In the future, researchers can perform more clustering algorithm by combining two or more them as a hybrid approach to make more reliability of clustering. Moreover, the research material (30 students) we used in this study is relatively small because we use the students in one classroom as research objects. Therefore, further studies should be carried out with larger amount of class size improving the proposed system. By conducting these researches more, our education system should be moved forward and better with the help of educational informatization.

Acknowledgements

My sincerest gratitude to my supervisor, Professor Khin Myo Sett, for her insights and guidance throughout the research. She was always happy to meet me and discuss our work. She encouraged and motivated me throughout the process. I would also like to thank all the teachers in our department, for guiding me throughout my this study. I also thank to final students who are cooperative in my questioner approach to obtain data. Finally, I also owe much to my family; my special appreciation and gratitude go to my parents for being a source of encouragement.

References

- C. Romero, S. Ventura. (2007) Educational data mining: A survey from 1995 to 2005[J]. *Journal of Expert Systems with Applications*, (1-33): 135-146.
- Chang, Y.C., Kao, W.Y., Chu, C.P., Chiu, C.H. (2009): A learning style classification mechanism for e-learning. *Comput. Educ.* 53, 273–285.
- Dunn, R. (1984): Learning style: state of the science. *Theory Pract.* 23(1), 10–19.
- E. Gaudioso, M. Montero, L. Talavera, and F. Hernandez-del-Olmo. (2009) Supporting teachers in collaborative student modeling: A framework and an implementation [J]. *Expert System with Applications*, (36): 2260-2265.
- Han, J.W., Kamber, M., Pei, J. (2004): Data Mining, 3rd edn. Morgan Kaufmann Publishers Inc., San Francisco.
- Hu, H., He, J.H. (2014): Research of composing cooperative learning group based on enhanced ant colony optimization algorithm. *Comput. Eng. Appl.* 50(13), 137–141.
- John A. Hartigan. (1975): Clustering Algorithms, John Wiley & Sons New York, London, Sydney, Toronto.
- Johnson, D. W., & Johnson, R. T. (1999). Making cooperative learning work. *Theory Into Practice*, 38, 67–73. 10.1080/00405849909543834
- Ma, Y.Y., Yuan, J. (2016): Based on GSDBK – means grouping algorithm research for networked collaborative learning. *Electron. Sci. Technol.* 29(12), 89–92.
- Mishra, Sidharth & Sarkar, Uttam & Taraphder, Subhash & Datta, Sanjoy & Swain, Devi & Saikhom, Reshma & Panda, Sasmita & Laishram, Menalsh. (2017). Principal Component Analysis. *International Journal of Livestock Research*. 1. 10.5455/ijlr.20170415115235.
- Singhal, Divya. (2017). Understanding Student- Centered Learning and Philosophies of Teaching Practices. *International Journal of scientific research and management*. 10.18535/ijsr/v5i2.02.
- Tamilselvi, R., Sivasakthi, B. and Kavitha, R., (2015). AN EFFICIENT PREPROCESSING AND POSTPROCESSING TECHNIQUES IN DATA MINING.
- Tang, J., Li, H.J., Qiu, F.Y. (2012): A research on collaborative grouping peer-model in mCSCL. *Distant Educ.* China 2, 48–51.
- Zorrilla, Marta & García-Saiz, Diego. (2013). A service oriented architecture to provide data mining services for non-expert data miners. *Decision Support Systems*. 55. 399-411. 10.1016/j.dss.2012.05.045.

KNOWLEDGE-BASED RECOMMENDATION SYSTEM FOR TRAVEL DESTINATION

Tin Nilar Win¹, Wint Pa Pa Kyaw²

Abstract

Recommendation systems are software tools and techniques providing suggestions for items to be of interest to a user and can help to overcome the problem of information overload. Tourism is a primary application area for mobile applications to support the travellers before, during and after the travel. A mobile based travel recommendation system can effectively help the customers to find their trip destination according to their interests. Knowledge-based systems generate recommendations using specific domain knowledge about how certain item features meet user preferences, and ultimately, how the item is of interest to the user. A specific type of knowledge-based recommenders are constraint-based recommenders. In this research, the system suggests personalized travel locations to a user by exploiting predefined knowledge bases that contain explicit rules about how to relate customer requirements with item features based on knowledge-based filtering method.

Keywords: Recommendation System, Constraint-based, Knowledge-based Filtering

Introduction

The explosive growth of online environments has made the issue of information search and selection increasingly cumbersome; users are overwhelmed by options which they may not have the time or knowledge to assess. Recommendation systems have proven to be a valuable tool for online users to cope with the information overload. Recommendation systems use details of registered user profiles and habits of the whole user community to compare available information items against reference characteristics in order to present item recommendations. Typically, a recommendation system compares a user profile to some reference attributes and seeks to predict the ‘rating’ or ‘preference’ that a user would give to an item she has not yet considered.

Recommendation systems originally found success on e-commerce web sites to present information on items and products that are likely to be of interest to the user (e.g. films, books, news, web pages etc). Lately, they have been increasingly employed in the field of electronic tourism (e-tourism), providing services like trip and activities advisory, lists of points of interest (POIs) that match user preferences, recommendations of tourist packages, etc. Existing recommendation systems in e-tourism typically emulate services offered by tourist agents where prospective tourists refer to seeking advice for tourist destinations under certain time and budget constraints. The users typically state their needs, interests and constraints based upon selected parameters. The system then correlates user choices with catalogued destinations annotated using the same vector of parameters.

A relatively recent development in e-tourism lies in the use of mobile devices as a primary platform for information access, giving rise to the field of mobile tourism. In the tourism field, travel recommendation systems aim to match the characteristics of tourism and leisure resources or attractions with the user needs. The travel companies have to aware of these preferences from different tourists and serve more attractive packages to get more business and profit. Therefore, the demand for intelligent tour services, from both travellers and tour companies, is expected to increase dramatically. The unique characteristics of mobile tourism bring forward new challenges and opportunities for the evolution of innovative personalized

¹ Dr, Assistant Lecturer, Department of ICT, Co-operative University (Thanlyin)

² Dr, Associate Professor, Department of Computer Studies, University of Yang

services which have no place in the field of e-tourism. Since recommendation systems have been successfully applied to enhance the quality of service for customers in a number of fields, it is natural direction to develop knowledge-based recommendation system for travel destination.

Recommendation Filtering Methods

The use of efficient and accurate recommendation method is very important for a system that will provide good and useful recommendation to its individual users. Based on a particular prediction method, recommendation systems have been classified into three main categories. These are collaborative filtering, content-based filtering and knowledge-based filtering methods.

- (1) In Content-Based Filtering, where the system makes use of the user's profile to recommend items that exhibit similar characteristics to what he has liked in the past.
- (2) In Collaborative Filtering, the recommendation compares the user's past ratings with those of other users to find users with similar taste. Highly rated items by these neighbors will be recommended.
- (3) Knowledge-Based recommendations make use of domain specific information to match user interests with items.

Knowledge-Based Filtering

Knowledge-based recommendation systems are particularly useful in the context of items that are not purchased very often. Examples include items such as real estate, automobiles, tourism requests, financial services, or expensive luxury goods. In such cases, sufficient ratings may not be available for the recommendation process. As the items are bought rarely, and with different types of detailed options, it is difficult to obtain a sufficient number of ratings for a specific instantiation (i.e., combination of options) of the item at hand.

This problem is also encountered in the context of the cold-start problem, when sufficient ratings are not available for the recommendation process. Furthermore, the nature of consumer preferences may evolve over time when dealing with such items. For example, a user who went to the beach, coast, and island for his or her holiday trip doesn't want to go there again, as a result of which the preferences of user may show a corresponding evolution.

In other cases, it might be difficult to fully capture user interest with historical data such as ratings. A particular item (tour package) may have attributes associated with it that correspond to its various properties, and a user may be interested only in items with specific properties. For example, a tour package may have several properties such as type (drive or fly), night stay, depart date, return date, number of travellers, the cost of trip, and things to do while travelling. User interests may also be regulated by a very specific combination of these options. Thus, in these cases, the tourism domain tends to be *complex* in terms of its varied properties, and it is hard to associate sufficient ratings with the large number of combinations at hand.

Such cases can be addressed with knowledge-based recommendation systems, in which ratings are not used for the purpose of recommendations. Rather, the recommendation process is performed on the basis of similarities between user requirements and item descriptions, or the use of constraints specifying user requirements. The process is facilitated with the use of *knowledge bases*, which contain data about rules and similarity functions to use during the retrieval process.

In fact, the knowledge bases are so important to the effective functioning of these methods that the approach takes its name from this fact. The explicit specification of requirements results in greater control of users over the recommendation process. In both collaborative and content-based systems, recommendations are decided entirely by either the user's past actions, ratings of user's peers, or a combination of the two. Knowledge-based systems are unique in that they allow the users to explicitly specify what they want. Figure 1 shows the paradigm of knowledge-based recommendation.

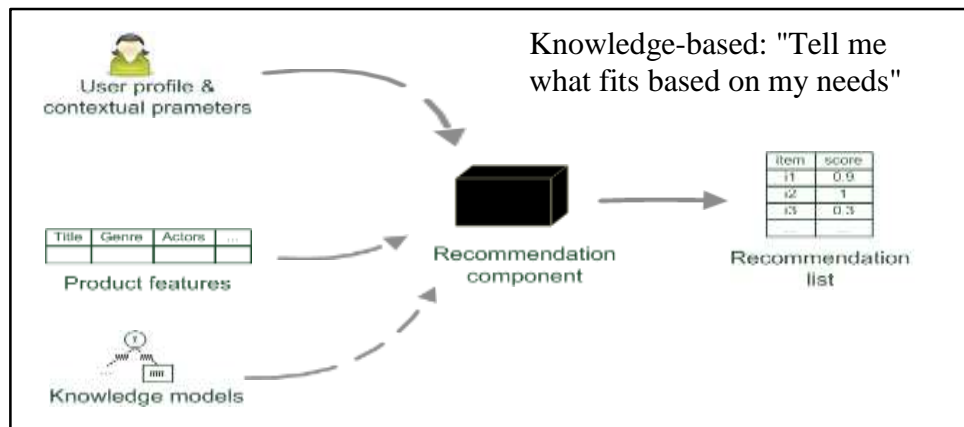


Figure 1 Paradigm of Knowledge-based Recommendation System

Constraint-based Recommendation System

In constraint-based systems, users typically specify requirements or constraints (e.g., lower or upper limits) on the item attributes. Domain-specific rules are used to match the user requirements to item attributes. These rules represent the domain-specific knowledge used by the system. Such rules could take the form of domain-specific constraints on the item attributes. Furthermore, constraint-based systems often create rules relating user attributes to item attributes. In such cases, user attributes may also be specified in the search process. Depending on the number and type of returned results, the user might have an opportunity to modify their original requirements. For example, they might relax some of their constraints when too few results are returned, or they might add more constraints. This search process is interactively repeated until the user arrives at her desired results.

In general, knowledge-based systems rely on detailed knowledge about item characteristics. Roughly speaking, the recommendation problem consists of selecting items from this catalog that match the user's needs, preferences, or hard requirements. The user's requirements can, for instance, be expressed in terms of desired values or value ranges for an item feature, such as “the cost should be lower than \$100” or in terms of desired functionality, such as “the activity should be suited for art and culture” in travel domain.

A constraint-based recommendation problem can, in general, be represented as a *constraint satisfaction* that can be solved by a constraint solver or in the form of a *conjunctive query* that is executed and solved by a database engine.

Knowledge Representation and Reasoning

In general, knowledge-based systems rely on detailed knowledge about tour package characteristics. A snapshot of such tour packages list is shown in Table 1 for the travel domain. Roughly speaking, the recommendation problem consists of selecting tour packages from this table that match the user's needs, preferences, or hard requirements. The user's

requirements can, for instance, be expressed in terms of desired values or value ranges for a tour package feature.

Table 1 Sample Tour Package Assortment

id	Type	Depart City	Stay	Depart Date	Return Date	Traveler	Activity	Cost (ks)	Tour Place
p1	drive	yangon	2	4/8/20	6/8/20	35	hill & mountain, heritage	15000	Kyaik tiyo
p2	drive	yangon	2	4/8/20	6/8/20	15	beach & coast, honeymoon	30000	Ngwe Saung
p3	fly	mandalay	3	4/8/20	6/8/20	35	food & drink, hill &mountain	150000	Myit kyina
p4	fly	yangon	3	11/8/20	13/8/20	15	beach & coast, surfing	180000	Nga pali
p5	drive	mandalay	3	11/8/20	13/8/20	35	honey moon, hill & mountain	50000	Hpa-An
p6	drive	mandalay	3	11/8/20	13/8/20	35	adventure, mountain biking	35000	Taung gyi
p7	fly	yangon	2	13/8/20	16/8/20	15	art & culture, heritage	170000	Mrauk -U
p8	drive	yangon	2	13/8/20	16/8/20	35	art & culture, heritage	50000	Bagan
p9	drive	yangon	2	16/8/20	19/8/20	35	beach & coast, surfing	30000	Chaung Thar
p10	drive	yangon	3	16/8/20	19/8/20	35	adventure, hill & mountain	120000	Nat-Ma-Taung

Constraints

A classical constraint satisfaction problem (CSP) can be described by a-tuple (V, D, C) where V is a set of variables, D is a set of finite domains for these variables, and C is a set of constraints that describes the combinations of values the variables can simultaneously take. A solution to a CSP corresponds to an assignment of a value to each variable in V in a way that all constraints are satisfied.

Table 2 Sample Recommendation Task (V_C , V_{PK} , C_R , C_F , C_{PK} , REQ) and the Corresponding Recommendation Result (RES)

V_C	$\{type(\dots), depart_city(\dots), stay(\dots), depart_date(\dots), return_date(\dots), traveler(\dots), activitiy(\dots), max_cost(\dots)\}$
V_{PK}	$\{type (\text{drive or fly}), depart_city (\text{yangon, mandalay, \dots}), stay (1\dots10), depart_date (4/8/20\dots16/4/20), return_date (6/8/20\dots19/8/20), traveler (1\dots35), activitiy (\text{heritage, art \& culture, surfing, beach \& coast, adventure, mountain biking, sky diving, hill \& mountain, honeymoon, food \& drink}), cost (15000\dots180000)\}$
C_F	$\{activity = \text{art \& culture}, stay=3\}$ ($activity$ is customer property and $stay$ are tour package property)
C_R	$\{activitiy = \text{hill \& mountain}, max_cost \leq 50000\}$ ($activitiy$ and max_cost are customer properties)
C_{PK}	$\{(id=p1, type=drive, depart_city=yangon, stay=2, depart_date=4/8/20, return_date= 6/8/20, traveler=35, activitiy = hill \& mountain, heritage, cost=15000, tour_place=Kyaiktiyo) \dots (id=p10, type=drive, depart_city=yangon, stay=3, depart_date=16/8/20, return_date= 19/8/20, traveler=35, activitiy = adventure, hill \& mountain, cost=120000, tour_place=Nat-Ma-Taung)\}$
REQ	$\{type=drive, depart_city= yangon, stay=2, depart_date=4/8/20, return_date=6/8/20, traveler=1, activitiy = hill \& mountain, max_cost \leq 30000\}$
RES	$\{type=drive, depart_city= yangon, stay=2, depart_date=4/8/20, return_date= 6/8/20, traveler=1, activitiy = hill \& mountain, heritage, max_cost \leq 50000, id=p1, type=drive, depart_city= yangon, stay=2, depart_date=4/8/20, return_date=6/4/20, traveler \leq 35, activitiy = hill \& mountain, heritage, cost=15000, tour_place=Kyaiktiyo\}$

Constraint-based recommendation systems can build on this formalism and exploit a *recommender knowledge base* that typically includes two different sets of variables ($V = V_C \cup V_{PK}$), one describing potential user requirements and the other describing product properties. Three different sets of constraints ($C = C_R \cup C_F \cup C_{PK}$) define which items should be recommended to a user in which situation. Sample for such variables and constraints for tour package recommendation is shown in Table 2 where the corresponding recommendation result according to the user's constraints are queried from Table 1.

- (a) Customer properties (V_C) describe the possible customer requirements. The customer property max_cost denotes the maximum cost acceptable for the customer, the property $activities$ is the type of activities such as heritage, surfing, adventure, etc.
- (b) Package properties (V_{PK}) describe the properties of tour packages in an assortment; for example, $type$ denotes possible means of transport in tour package.
- (c) Filter conditions (C_F) define under which conditions which tour package should be selected – in other words, filter conditions define the relationships between customer properties and package properties. An example filter condition is *heritage, art & culture activities require cost should be at least 50000*.
- (d) Compatibility constraints (C_R) define allowed instantiations of customer properties – for example, *if beach & coast activity is required, the minimal accepted cost must be greater than or equal to 30000*.

- (e) Package constraints (C_{PK}) define the currently available tour package assortment. Each conjunction in this constraint completely defines a package (item) – all package properties have a defined value.

The task of identifying a set of products (tour packages) matching a customer's wishes and needs is denoted as a *recommendation task*. The user requirements REQ can be encoded as unary constraints over the variables in V_C and V_{PK} – for example, $max_cost = 50000$.

Formally, each solution to the CSP ($V = V_C \cup V_{PK}$, D , $C = C_R \cup C_F \cup C_{PK} \cup REQ$) corresponds to a consistent recommendation. In many practical settings, the variables in V_C do not have to be instantiated, as the relevant variables are already bound to values through the constraints in REQ . The task of finding such valid instantiations for a given constraint problem can be accomplished by every standard constraint solver.

Conjunctive Queries

A slightly different way of constraint-based item retrieval for a given item (tour package) catalog is to view the item selection problem as a data filtering task. The main task in such an approach, therefore, is not to find valid variable instantiations for a CSP but rather to construct a conjunctive database query that is executed against the item catalog. A *conjunctive query* is a database query with a set of selection criteria that are connected conjunctively.

For example, $\sigma [activity=hill \ \& \ mountain, max_cost \leq 50000] (P)$ is such a conjunctive query on the database table P , where σ represents the selection operator and $[activity=hill \ \& \ mountain, max_cost \leq 50000]$ the corresponding selection criteria. Conjunctive queries for item selection purposes is exploited, V_{PACK} and C_{PACK} are represented by a database table P . Table attributes represent the elements of V_{PACK} and the table entries represent the constraint(s) in C_{PACK} .

Queries can be defined that select different item subsets from P depending on the requirements in REQ . Such queries are directly derived from the filter conditions (C_F) that define the relationship between customer requirements and the corresponding item properties. The filter condition $activity = beach \ \& \ coast \rightarrow stay = 2$ denotes the fact that if customers want to have *beach & coast activity*, the *stay* must be 2. If a customer defines the requirement $activity = beach \ \& \ coast$, the corresponding filter condition is active, and the consequent part of the condition will be integrated in a corresponding conjunctive query. The existence of a recommendation for a given set REQ and a product assortment P is checked by querying P with the derived conditions (consequents of filter conditions). Such queries are defined in terms of selections on P formulated as $\sigma[criteria](P)$.

Tour Packages Design for Knowledge-based Recommendation

Table 3 shows the tour packages list in travel recommendation system. In this table, there are twenty-five tour packages for the month of August, 2020 and also corresponding their attributes such as drive or fly (0 means “drive”, 1 means “fly” in database table), depart from (city), night stay, depart date, return date, things to do, and trip price (cost) and trip name, etc. Knowledge-based system uses this knowledge sources and recommends tour packages according to the user's constraints.

Table 3 Tour Packages List in Travel Recommendation System

id	drive _or_ fly	depart _from	night _stay	depart _date	return _date	total _seats	thing_todo	trip _price	trip _name
1	0	Yangon	3	16-08-20	19-08-20	35	#Horse Riding #Scuba Driving #Beaches & Swimming	50000	Ngwe Saung
2	0	Manda lay	3	16-08-20	19-08-20	35	#Heritage #Art & Culture	30000	Bago Travel
3	0	Yangon	3	16-08-20	19-08-20	35	#Heritage #Art & Culture	70000	Mrauk U Travel
4	1	Yangon	3	16-08-20	19-08-20	35	#Hills & Mountains #Adventure #Mountain Biking	180000	HpaAn (Kyauk Ka Lat)
5	0	Manda lay	3	16-08-20	19-08-20	35	#Adventure #Hills & Mountains #Wildlife & Nature #Heritage	20000	Kyaik htiyo Travel
6	0	Yangon	3	16-08-20	19-08-20	35	#Hills & Mountains #Honeymoon & Romance	120000	Lake Inle
7	0	Mandalay	3	16-08-20	19-08-20	35	#Art & Culture #Heritage	50000	Bago
8	0	Yangon	3	16-08-20	19-08-20	35	#Honeymoon & Romance #Food & Drink	70000	Pyin Oo Lwin Travel
9	0	Mandalay	3	16-08-20	19-08-20	35	#Heritage #Art & Culture #Hills & Mountains	70000	Pindaya Caves
10	0	Yangon	3	16-08-20	19-08-20	35	#Art & Culture #Heritage #Food & Drink	80000	Mingun
11	1	Yangon	2	24-08-20	26-08-20	35	#Wildlife & Nature #Mountain Biking #Heritage #Adventure	120000	Mount Popa
12	0	Yangon	2	24-08-20	26-08-20	35	#Heritage #Art & Culture #Food & Drink	65000	Amara pura
13	0	Naypyi taw	2	24-08-20	26-08-20	35	#Heritage #Art & Culture	52000	Shwebo Travel
14	1	Yangon	2	24-08-20	26-08-20	35	#Adventure #Wildlife & Nature #Coasts & Islands	250000	Myit kyina Travel
15	0	Yangon	2	24-08-20	26-08-20	35	#Coasts & Islands #Beaches & Swimming #Surfing #Food & Drink	80000	Satse Beach
16	0	Yangon	2	24-08-20	26-08-20	35	#Beaches & Swimming #Coasts & Islands #Food & Drink	70000	Gaw Yin Gyi Island

id	drive _or_ fly	depart _from	night _stay	depart _date	return _date	total _seats	thing_todo	trip _price	trip _name
17	0	Bago	2	24-08-20	26-08-20	35	#Coasts & Islands #Adventure #Hills & Mountains	50000	Mawtin sune Pagoda
18	0	Manda lay	2	24-08-20	26-08-20	35	#Food & Drink #Honeymoon & Romance #Coasts & Islands #Art & Culture	60000	Mawlam ying
19	0	Yangon	2	28-08-20	30-08-20	35	#Heritage #Art & Culture #Hills & Mountains #Adventure	20000	Kyaik Htee Yo
20	0	Yangon	2	28-08-20	30-08-20	35	#Art & Culture #Heritage #Food & Drink	60000	Sagaing Trip
21	0	Yangon	2	28-08-20	30-08-20	35	#Food & Drink #Heritage #Horse Riding	50000	Mawlam ying
22	0	Yangon	2	28-08-20	30-08-20	35	#Rafting #Beaches & Swimming #Surfing #Coasts & Islands	30000	Ngwe Saung Beach
23	0	Yangon	2	28-08-20	30-08-20	35	#Art & Culture #Food & Drink #Hills & Mountains	80000	Kayah State
24	0	Yangon	2	28-08-20	30-08-20	35	#Mountain Biking #Wildlife & Nature #Adventure #Hills & Mountains	80000	Goteik Bridge
25	0	Manda lay	2	28-08-20	30-08-20	35	#Art & Culture #Food & Drink #Heritage	70000	Shwe Ti Gone

Result and Discussion for Knowledge-based Recommendation

The following Table 4 shows the user's requirements and the corresponding recommendation result according to the constraints that are queried from Table 3. A consistent recommendation result (*RES*) for user's requirements (*REQ*) is depicted as follows.

Table 4 User Requirement (REQ) and the Recommendation Result (RES)

REQ1	<code>{drive_or_fly=drive, depart_from= Yangon, night_stay=2, depart_date=28/8/20, return_date=30/8/20, traveler=2, trip_price= Between 20000 and 50000, things_todo = #Art & Culture #Heritage #Hills & Mountains#Beaches, Coast #Surfing}</code>
RES1	<code>{id=22, drive_or_fly =0, depart_from = Yangon, night_stay =2, depart_date=28/8/20, return_date=30/8/20, traveler<=35, things_todo = #Rafting #Beaches & Swimming #Surfing #Coasts & Islands, trip_price=30000, tour_place= Ngwe Saung Beach}</code>
RES2	<code>{id=21, drive_or_fly =0, depart_from = Yangon, night_stay =2, depart_date=28/8/20, return_date=30/8/20, traveler<=35, things_todo = #Food & Drink #Heritage #Horse Riding, trip_price=50000, tour_place= Mawlamying}</code>
RES3	<code>{id=19, drive_or_fly =0, depart_from = Yangon, night_stay =2, depart_date=28/8/20, return_date=30/8/20, traveler<=35, things_todo = #Heritage #Art & Culture #Hills & Mountains #Adventure, trip_price=20000, tour_place= Kyaik Htee Yo}</code>
REQ2	<code>{drive_or_fly=Drive, depart_from= Mandalay, night_stay=2, depart_date=24/8 /20, return_date=26/8/20, traveler=2, trip_price= Between 50000 and 100000, things_todo = #Adventure #Beaches, Coast #Food & Drink #Hills & Mountains #Surfing}</code>
RES1	<code>{id=18, drive_or_fly =0, depart_from = Mandalay, night_stay =2, epart_date=24/8/20, return_date=26/8/20, traveler<=35, things_todo = #Food & Drink #Honeymoon & Romance #Coasts & Islands #Art & Culture, trip_ price=60000, tour_place= Mawlamying}</code>
REQ3	<code>{drive_or_fly=Fly, depart_from= Yangon, night_stay=2, depart_date=24/8/20, return_date=26/8/20, traveler=2, trip_price= Between 100000 and 250000, things_todo = #Adventure #Art & Culture #Hills & Mountains #Beaches, Coast #Food & Drink}</code>
RES1	<code>{id=14, drive_or_fly =1, depart_from = Yangon, night_stay =2, depart_ date=24/8/20, return_date=26/8/20, traveler<=35, things_todo =#Adventure #Wildlife & Nature #Coasts & Islands, trip_price=250000, tour_place= Myitkyina Travel}</code>
RES2	<code>{id=11, drive_or_fly =1, depart_from = Yangon, night_stay =2, depart_ date=24/8/20, return_date=26/8/20, traveler<=15, things_todo = #Wildlife & Nature #Mountain Biking #Heritage #Adventure,trip_price=120000, tour_place= Mount Popa}</code>

From the above Table 4, it can be concluded that the user requirement (REQ1) is the most similar to the recommendation results such as tour package id22 for RES1, id21 for RES2, and id19 for RES3. The user requirement (REQ2) is the most similar to the recommendation results such as tour package id18 for RES1. The user requirement (REQ3) is the most similar to the recommendation results such as tour package id14 for RES1, and id11 for RES2. From the fact that knowledge-based method gives consistent recommendation according to user constraints that fit his or her requirements.

Conclusion

Knowledge-based recommendation systems perform a needed function in a world of ever-expanding information resources. Unlike other recommendation systems, they do not depend on large bodies of statistical data about particular rated items or particular users. The knowledge component of these systems need not be prohibitively large, since we need only enough knowledge to judge items as similar to each other.

Further, knowledge-based recommendation systems actually help users explore and thereby understand an information space. Users are an integral part of the knowledge discovery process, elaborating their information needs in the course of interacting with the system. One need only have general knowledge about the set of items and only an informal knowledge of one's needs; the system knows about the tradeoffs, category boundaries, and useful search strategies in the domain. Knowledge-based recommendation systems are strongly complementary to other types of recommendation systems.

This paper proposes a recommendation system that offers knowledge-based recommendations for travel destinations to individuals. It can help overcome information overload problem by exposing users to interesting, novel, surprising and relevant items based on preferences users have expressed explicitly constraints. It can introduce users to new items that have not been known or have not been retrieved. So, these recommendations can help users in meeting their information needs for travel destinations.

Acknowledgement

I would like to express my profound gratitude to Dr. Soe Mya Mya Aye, Professor and Head of the Department of Computer Studies, Yangon University, for her kind permission to carry out this research. I would like to thank Dr. Ohn Mar San, Professor and Head of the Department of ICT, Co-operative University (Thanlyin), for her encouragement to do this research. I also would like to thank my supervisor Dr. Wint Pa Pa Kyaw, Associate Professor, Department of Computer Studies, Yangon University, for her close supervision and invaluable suggestions. I wish to thank all who help and give me advice on this research.

References

- Aggarwal, C.C. (2016), *Recommendation System: The Textbook*, ©Springer International Publishing Switzerland, ISBN 978-3-319-29657-9
- Alexander, F. (2008), *Persuasion in knowledge-based recommendation* in: *Persuasive Technology*, Springer, Page 71~82.
- Friedrich, G., Jannach D., Zanker M. and Felfernig (2011), *Developing Constraint-based Recommenders*
- Gavala, D., Konstantopoulos C., Mastakas K. and Pantziou, G. (2014), *Mobile Recommender Systems in Tourism*, Journal of Network and Computer Applications
- Isinkaye, F.O., Folajimi, Y.O. and Ojokoh, B.A. (2015), *Recommendation systems: Principles, methods and evaluation*, Egyptian Informatics Journal, Vol.16, Page 261~273
- Jannach D., Zanker M., Felfernig A. and Friedrich, G. (2011), *Recommendation Systems: An Introduction*, Cambridge University Press, ISBN 978-0-521-49336-9
- Naaz, D. and Danish, M. (2018), *Knowledge Based Tourism Recommendation System Using Knowledge Base Filtering with Protégé Framework*, IJCSN- International Journal of Computer Science and Network, Volume 7, Issue 3, ISSN (Online: 2277-5420)
- Ricci, F., Rokach, L., Shapira B., Paul, B. and Kantor (2011), *Recommendation Systems Handbook*, Springer New York Dordrecht Heidelberg London, ISBN 978-0-387-85819-7